The many-body ground states of the graphene quantum Hall effect and their edge channels

Alexis Coissard

THÈSE

Pour obtenir le grade de

DOCTEUR DE L'UNIVERSITÉ GRENOBLE ALPES

Spécialité : Physique de la Matière Condensée et du Rayonnement

Arrêté ministériel : 25 mai 2016

Présentée par

Alexis COISSARD

Thèse dirigée par **Hervé COURTOIS**
et codirigée par **Benjamin SACÉPÉ**

préparée au sein de l'**Institut Néel, CNRS**
dans l'**École Doctorale de Physique de Grenoble**

Les états fondamentaux du graphène en régime Hall quantique et leurs canaux de bord

The many-body ground states of the graphene quantum Hall effect and their edge channels

Thèse soutenue publiquement le **22 novembre 2021**
devant le jury composé de :

Clément FAUGERAS
Directeur de recherche, Laboratoire National des Champs Magnétiques Intenses, Grenoble, Président

Christian GLATTLI
Directeur de recherche, CEA Saclay, Rapporteur

Dimitri RODITCHEV
Professeur, ESPCI Paris, Rapporteur

Mitali BANERJEE
Professeure assistante, École Polytechnique Fédérale de Lausanne, Examinatrice

Mark Oliver GOERBIG
Directeur de recherche, Laboratoire de Physique des Solides, Orsay, Examinateur

Hervé COURTOIS
Professeur, Université Grenoble Alpes - Institut Néel, Directeur de thèse

Benjamin SACÉPÉ
Directeur de recherche, Institut Néel, Grenoble, Co-directeur de thèse

Abstract - Résumé

Graphene exhibits a two dimensional electron gas directly exposed to vacuum, thus accessible by scanning tunneling microscopy (STM) and spectroscopy. In this PhD thesis we present a systematic STM spectroscopy study performed on high-quality graphene samples, where the charge carrier density is tuned with a back-gate, and in which we have investigated the physics of the graphene quantum Hall regime under strong magnetic fields using a home-made AFM/STM operating at 4 K and up to 14 T. By carrying out high-resolution Landau level spectroscopy we unveil the pinning of the Fermi level in the Landau levels, a key phenomenon in the quantum Hall physics. We performed the first Landau level spectroscopy at the native edges of a graphene flake residing atop an insulating substrate and we show that the quantum Hall edge channels are confined in a few magnetic lengths from the graphene edges. When the Fermi level fills the zeroth Landau level, we observed the opening in the bulk of the interaction-induced gap at charge neutrality, resulting from a magnetic-like Stoner instability. This gap is found to be in excellent agreement with the Coulomb energy scale. We further show that the Coulomb interaction can be screened using a suitable high-k dielectric substrate. Last, scanning graphene at the atomic scale enabled us to image the different ground states of charge-neutral graphene, which emerge as a function of the strength of the Coulomb interaction. Our results eventually point towards a quantum phase transition driven by the substrate-screening of the Coulomb interaction.

Le graphène présente un gaz d'électrons bidimensionnel directement exposé au vide, donc accessible par microscopie et spectroscopie à effet tunnel (STM). Dans cette thèse de doctorat, nous présentons une étude systématique de spectroscopie STM réalisée sur des échantillons de graphène de haute qualité, où la densité de porteurs de charge est contrôlée avec une grille, et dans lesquels nous avons étudié la physique du régime de Hall quantique du graphène sous de forts champs magnétiques, en utilisant un AFM/STM de notre conception fonctionnant à 4 K et jusqu'à 14 T. En effectuant des spectroscopies haute résolution des niveaux de Landau, nous avons observé le piégeage du niveau de Fermi dans les niveaux de Landau, un phénomène clé dans la physique de l'effet Hall quantique. Nous avons réalisé la première spectroscopie des niveaux de Landau aux bords natifs d'un échantillon de graphène reposant sur un substrat isolant et nous montrons que les canaux de bord de l'effet Hall quantique sont comprimés au bord sur quelques longueurs magnétiques. Lorsque le niveau de Fermi remplit le niveau de Landau zéro, nous avons observé l'ouverture du gap d'interaction à la neutralité de charge, résultant de l'instabilité de Stoner de type magnétique. Ce gap est en excellent accord avec l'échelle d'énergie de Coulomb. Nous montrons en outre que l'interaction de Coulomb peut être écrantée à l'aide d'un substrat diélectrique approprié. Enfin, l'imagerie du graphène à l'échelle atomique nous a permis de visualiser les différents états fondamentaux du graphène à la neutralité de charge, qui apparaissent en fonction de l'intensité de l'interaction de Coulomb. Nos résultats mettent finalement en évidence une transition de phase quantique pilotée par l'écrantage de l'interaction de Coulomb par le substrat.

Remerciements

Le temps est relatif, comme le dirait un fameux docteur, et je pense que faire une thèse donne un très bon exemple de cette relativité. Trois années de travail sur un projet, cela semble si long et lointain quand on commence. Et quand elles s'achèvent, on ne cesse de se demander comment on a pu arriver à cette fin tant redoutée si rapidement. Tant et si bien qu'une quatrième année apparaît vite comme une panacée, bien qu'elle se consume à son tour avec la même célérité. Et maintenant que le temps attribué à cette étape de ma vie s'achève, vient le moment de me remémorer et de remercier ceux qui m'ont guidé, assisté, aidé, soutenu, supporté et partagé mon quotidien pendant ces quatre formidables années de thèse.

Je remercie tout d'abord Benjamin Sacépé, mon superviseur, qui a imaginé et monté tout ce projet, et qui a accepté de me le confier il y a maintenant plus de quatre ans. Merci, sincèrement, pour ta confiance et tout ce savoir, théorique et pratique, que j'ai pu acquérir à tes côtés.

Je remercie aussi Hervé Courtois pour avoir accepté d'être mon directeur de thèse et qui, malgré ses nombreuses responsabilités, a toujours gardé un œil attentif sur l'avancement de mes travaux et m'a conseillé quand ceux-ci étaient fortement ralentis.

J'exprime aussi ma gratitude envers Hermann Sellier pour toute son aide et son expertise quant à l'implémentation et l'optimisation du mode AFM sur notre STM, ainsi que pour les nombreuses et longues discussions que nous avons eu sur mes résultats. Un véritable puits de science qui aura eu quelques fois, bien malgré moi et à ma plus grand honte, raison de mon attention.

Je souhaite remercier les membres du jury pour m'avoir fait l'honneur d'accepter d'y figurer. J'en profite pour remercier tout particulièrement Dimitri Roditchev, mon professeur à l'ESPCI Paris, qui m'aura initié au STM et donné envie de faire une thèse dans ce domaine.

Merci aussi à tous les membres de mon équipe QuNES au sein du laboratoire avec qui j'aurai partagé mon quotidien. Un grand merci à Marco pour ces quatre années de bonne humeur qu'il a toujours su instiller dans le bureau, tout en supportant mon mauvais caractère. Merci à Corentin de m'avoir extirpé des affres de la capitale pour m'emmener avec lui à Grenoble. Merci à Hadrien, mon camarade de ronchonnade. Merci à Louis et Arthur qui m'auront formé à mon arrivée. Une pensée aussi aux différents stagiaires qui nous ont rejoint temporairement et que j'ai pris plaisir à former en retour.

David Wander mérite aussi mes plus sincères remerciements. Les malheurs de son STM auront fait le bonheur du nôtre et le mien. Bien qu'étant en rédaction active de ce manuscrit, j'ai apprécié d'avoir enfin l'occasion de transmettre mes connaissances et mon expertise concernant notre STM et nos mesures, et vu les superbes résultats que tu as obtenus par toi-même, je n'ai pas dû être trop mauvais (juste une tendance à trop radoter...). Les derniers résultats présentés dans cette thèse n'auraient jamais pu être obtenus sans lui, faute comme toujours de temps.

Merci à Adolfo Grushin et Cécile Repellin, nos deux théoriciens avec qui nous avons partagé nos résultats et avancées et qui nous ont grandement aidés à mieux les comprendre et à les modéliser.

Une grande partie de cette thèse a été dédiée à la fabrication des échantillons en salle blanche, et je souhaite donc remercier l'équipe NanoFab, et en particulier Thierry Crozes, qui a toujours été présent pour mes problèmes de lithographie électronique, ainsi que Bruno Fernandez et Gwenaëlle Julie pour toute leur aide au quotidien en salle blanche. La plateforme AFM aura été grandement utile, et je tiens donc aussi à remercier Simon Le-Denmat pour son aide, sa disponibilité et son expertise dans ce domaine. Merci aussi à David Barral pour les dépôts par sputtering et à Murielle Legendre pour avoir sauvé nos derniers échantillons sur STO.

Je remercie grandement Frédéric Gay pour tout son support technique et son expertise qu'il m'aura apporté pendant ces quatre années. Merci aussi à Florent Blondelle. Ma gratitude à Jean-Baptiste Cully, Laurent Del-Rey, Didier Dufeu, Dominique Grand, Julien Jarreau, Grigor Kapoujyan et Philippe Plaindoux du pôle mécanique pour toute leur aide et leur savoir d'ingénierie qui auront été grandement nécessaires à la conception, l'entretien et l'amélioration de notre plateforme STM. Merci aussi à Sylvain Dumont, Olivier Exshaw et Daniel Lepoittevin du pôle électronique.

Ma reconnaissance à Anne-Laure Jaussent, Florence Pois et Angélique Simoes pour leur aide concernant toute la partie administration et gestion, ainsi qu'à Patrick Belmain du service informatique.

Un grand merci à Juliette pour avoir passé tant de temps à m'encourager pendant la rédaction. Une pensée à Nicolas, Thibault, Danial ainsi qu'aux autres doctorants, notamment ceux de l'équipe Hybrid, avec qui j'ai partagé ces années de thèse. Et une dédicace spéciale à Guilliam pour ces inoubliables soirées passées à boire du bon vin rouge et à raconter nos vies.

Enfin, bien sûr, un grand merci à toute ma famille. Merci à ma sœur Emilie pour son indéfectible soutien et ses mots d'encouragement, et à Henji et Inou qui m'auront grandement aidé à supporter ces quatre années et leur lot inévitable de problèmes et de remises en question. J'ai aussi une pensée toute particulière à ma mamie Simone, dont j'aurais tant aimé qu'elle puisse assister à l'apogée de mes études. Ces mêmes études cependant qui m'auront au final, le temps étant traître, fait perdre de vue l'essentiel en me faisant oublier de profiter d'elle comme je l'aurais ardemment souhaité et négliger de l'accompagner dans ses moments difficiles.

Je remercie au final, de tout mon cœur, ma mère et mon père, Brigitte et Pierre, pour simplement tout, pour avoir fait de moi l'homme que je suis aujourd'hui, d'avoir toujours veillé sur moi et de m'avoir toujours permis, accompagné et donné les moyens de suivre ma propre voie. Je ne pourrais sûrement jamais assez exprimer ma reconnaissance et ma gratitude pour tout ce qu'ils m'ont donné, mais je souhaite leur dédier cette thèse.

Alexis

À mes très chers parents,

Qui n'ont jamais cessé de me soutenir et de m'épauler pour que je puisse atteindre mes objectifs.

Il faut toujours se réserver le droit de rire le lendemain de ses idées de la veille.

– Napoléon Bonaparte

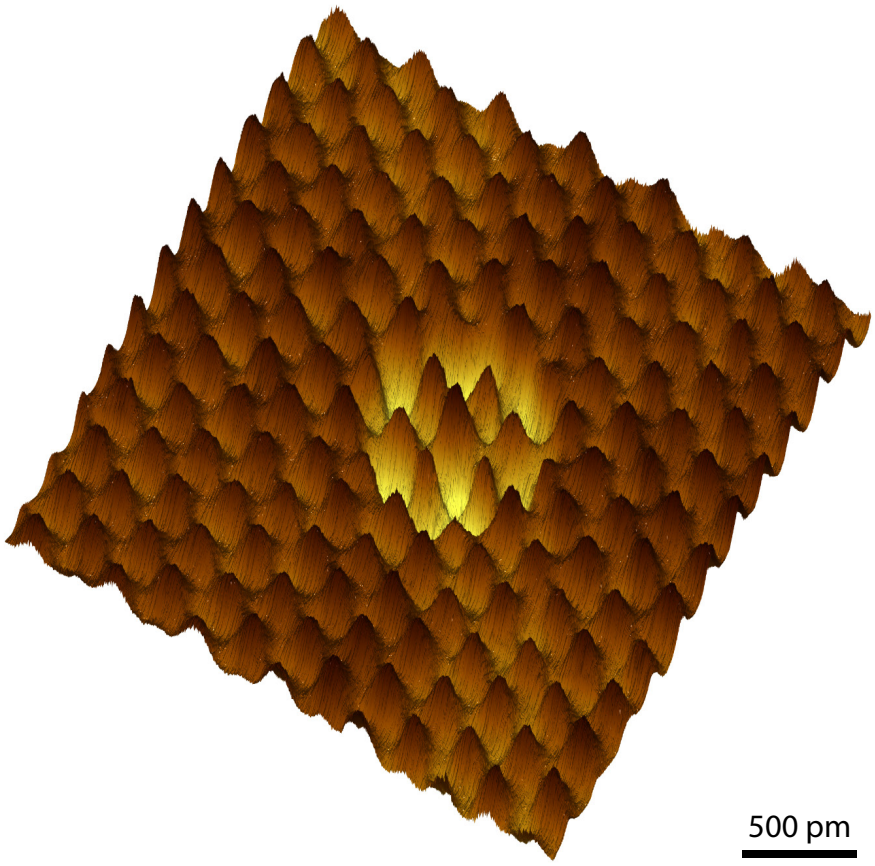

Charge-density wave in graphene with a defect at the center.

Table of Contents

Experimental results

Appendix

List of fundamental constants

e	Elementary charge	1.602×10^{-19}	C
h	Planck constant	6.626×10^{-34}	J.s
ε_0	Vacuum electric permittivity	8.854×10^{-12}	$\mathrm{F.m^{-1}}$
m_e	Electron mass	9.109×10^{-31}	kg
k_B	Boltzmann constant	1.381×10^{-23}	$\mathrm{J.K^{-1}}$
$\hbar = h/2\pi$	Reduced Planck constant	1.054×10^{-34}	J.s
$R_\mathrm{K} = h/e^2$	von Klitzing constant	25.813×10^3	Ω
$\Phi_0 = h/e$	Magnetic flux quantum	4.135×10^{-15}	$\mathrm{T.m^2}$
$\mu_\mathrm{B} = e\hbar/2m_\mathrm{e}$	Bohr magneton	9.274×10^{-24}	$\mathrm{J.T^{-1}}$

Introduction

Among all the striking phenomena that condensed matter physics has offered us to observe and understand this last century, the quantum Hall effect is still nowadays a major topic of research. Discovered by von Klitzing in 1980 for which he was awarded the Nobel Prize in 1985, it occurs in two dimensional electron systems subjected to low temperatures and strong perpendicular magnetic fields. Its manifestation is the precise quantization of the transverse conductance as a function of charge carrier density which forms plateaus at multiples of the quantum of conductance e^2/h, while the longitudinal resistance simultaneously vanishes. This peculiar transport regime results from the splitting of the density of states of the 2D electron gas (2DEG) into discrete highly degenerate levels, known as the Landau levels, and separated by cyclotron gaps. It has been shown by Halperin in 1982 that the Landau level spectrum bends up in the vicinity of the electron gas edge, due to the confinement of charge carriers. As a consequence, when the Fermi level lies in a cyclotron gap, an integer number of Landau levels that are filled in the bulk eventually cross the Fermi level at the edges. Each crossing defines unidimensional edge channels that carry the current while the bulk of the electron gas remains insulating, inducing the quantization of the conductance as a function of the number of edge channels.

Although the quantum Hall effect has been considerably studied, especially in transport measurements, the exact nature of those edge channels, or their spatial structure, have remained little addressed. The best method to obtain further experimental insights is studying edge channels directly by using scanning tunneling microscopy (STM) and spectroscopy (STS). By approaching a metallic tip at a few Å from a 2DEG such that a tunneling current flows between both, we can probe the local density of states of the 2DEG at the atomic scale, where Landau levels emerge as well-defined peaks. The edge dispersion of the Landau level spectrum, and thus the edge channels, can then be spatially imaged by moving the tip toward the edge of the electron gas. However, a major challenge for such experiment is that it is not possible to use STM on conventional 2D systems such as GaAs where the electron gas is buried deep below the surface of the sample, and therefore remains inaccessible for the tip.

Graphene, a bidimensional crystal consisting of a monolayer of carbon atoms arranged in a honeycomb lattice, thus becomes a system of choice for this study. Although it was used back to the middle of the twentieth century as a toy model, graphene was eventually isolated by Novoselov and Geim in 2005 using a mechanical exfoliation technique. This allowed them to study the graphene transport properties and observe a non-conventional relativistic quantum Hall effect, which originates from the peculiar linear bandstructure of graphene. This discovery, which opened the field of 2D materials, enabled Novoselov and Geim to win the Nobel Prize in

2010. The main advantage of graphene for this PhD work is that the 2D electron gas is surface accessible, which enables us to study by STS its bulk physics as well as the edge states at the physical edges of graphene.

In this PhD thesis, we investigated the quantum Hall effect in graphene and our first objective has been to visualize the quantum Hall edge channels in graphene by scanning tunneling spectroscopy. For this purpose we fabricated high quality samples of graphene on hexagonal boron nitride (hBN) on a standard highly doped substrate of silicium with a oxide layer atop, which are common devices used in transport measurements of the quantum Hall effect in graphene. We eventually performed the first STM study of the evolution of the density of states upon approaching the native edges of graphene and our results therefore provide new insights on transport observations.

Charge-neutral graphene has also been shown to develop an unusual correlated topological phase based on Landau levels that has been dubbed quantum Hall topological insulator. This phase emerges in the zeroth Landau level when the Coulomb potential is screened by a high-k dielectric environment, and exhibits spin-filtered helical edge channels and the resulting quantum spin Hall effect, which are of high interest for spintronics and topological superconductivity. In a second part of this thesis, we fabricated new samples on the high-k dielectric strontium titanate $SrTiO_3$ substrate. We measured by STS the interaction-induced gap which opens in the half-filled zeroth Landau level due to quantum Hall ferromagnetism and we showed that the Coulomb interaction in such samples is indeed strongly screened with respect to usual samples on silicon oxide. We then unveiled the different ground states that emerge in charge-neutral graphene as a function of the efficiency of the substrate-screening.

This PhD thesis is structured as follows :

Chapter 1 introduces the basics of graphene physics at zero magnetic field and the theoretical tools that will be required in the next chapters. We notably derive the electronic bandstructure and the density of states. In a second part we present the two main experimental techniques employed to probe graphene physics that are considered in this thesis : STM and STS that we used to study the physics of graphene under strong magnetic field at the atomic scale, and transport measurements which are mostly used as references. We then briefly see how graphene physics can be strongly altered by the substrate on which it lies.

Chapter 2 presents the quantum Hall effect in graphene. We first derive the relativistic Landau level physics which makes graphene quantum Hall physics strongly different from that of a conventional 2D electron gas such as GaAs. We then deal with theories of the edge dispersion of the Landau level spectrum at the native edges of graphene. Finally, we focus on the physics of charge-neutral graphene and its resulting quantum Hall ferromagnetism. We notably investigate how it is possible to induce a quantum Hall topological insulator phase in graphene.

Chapter 3 consists of a review chapter of the state of the art of Landau level spectroscopy in graphene, mainly based on the scanning tunneling spectroscopy technique.

Chapter 4 is the instrumental chapter where we present our home-made cryogenic AFM/STM operating under strong magnetic fields. The working principles of the two scanning probe microscopy we used in this thesis, Atomic Force Microscopy (AFM) and Scanning Tunneling Microscopy (STM), are introduced in **Appendix A**. The fabrication of our graphene samples is detailed in **Appendix B**.

Chapter 5 addresses the characterization of our high quality graphene samples by tunneling spectroscopy. We study the particular square root dispersion of the Landau levels. We also describe how Landau levels disperse as a function of the charge carrier density and we show that this measurement is fully consistent with the observation of the quantum Hall effect in mesoscopic transport devices. We finally investigate how many-body effects alter our Landau level spectra. We also show additional results in **Appendix C**.

Chapter 6 presents our results on the quantum Hall edge states spectroscopy. We describe our methodology in order to bring the metallic STM tip at the edges of graphene which lies on an insulating hBN substrate. We then show that the confinement potential at the edges happens to be very sharp, on the scale of a few tens of nanometers from the edge, such that the quantum Hall edge channels are eventually squeezed in this very narrow region, which is a completely different case from that of a conventional 2D electron gas such as GaAs. We also present a series of numerical simulations of the density of states on graphene edge for different ground states.

Chapter 7 is our final result chapter where we study the physics of charge-neutral graphene in the quantum Hall regime. We demonstrate that the gap which opens in the zeroth Landau level due to the Stoner instability, and which is responsible for the strong insulating behavior observed in transport measurements at charge neutrality, originates from the Coulomb interaction. Moreover, we show that it is possible to screen these Coulomb interactions in graphene by using a strontium titanate substrate for our samples. Finally, we image two different ground states of charge-neutral graphene in those two systems where the Coulomb energy is screened or not. Our results eventually point towards a magnetic-field-induced quantum phase transition in charge-neutral graphene tuned by the screening of electron-electron interactions.

Elements of graphene physics

Chapter 1

In this introductory chapter we describe physical and electronic properties of graphene. Due to its honeycomb lattice, this unconventional 2D electron gas exhibits a bandstructure consisting of two inequivalent Dirac cones where the energy varies linearly with the wave vector. We introduce several theoretical tools that we will use in the following chapters. We then present two kinds of experiments used to probe graphene physics : transport measurements, which we will mostly consider as reference for this thesis, that give global quantities such as resistivity, and on the other hand tunneling spectroscopy, the main focus on this thesis, that allows us to directly measure the local density of states. We discuss how the disorder induced by the substrate on which graphene lies can alter its electronic properties. Finally, we quickly deal with many-body physics and the consequences on graphene bandstructure. In particular, we describe how the substrate can also tune interactions in graphene through its dielectric properties. These preliminary results are useful in order to understand what happens when graphene is placed in a magnetic field, which is the topic of the Chapter 2.

Contents

1.1 Electronic properties

Graphene is a bidimensional 2D crystal consisting of a monolayer of carbon atoms arranged in a honeycomb lattice, and is the structural element of other allotropes such as graphite, carbon nanotubes and fullerenes. The resulting band structure gives graphene unusual electronic properties, characteristic of a Dirac material. Though graphene was theoretically predicted by P. R. Wallace in 1947 [1], it was not until 2005 that K. Novoselov and A. Geim successfully managed to isolate, and study with transport measurements, a graphene flake mechanically exfoliated from a bulk graphite crystal [2], which awarded them the Nobel Prize in physics in 2010. Since then, graphene has been heavily studied and shown to offer many technological applications : graphene is an excellent conductor of heat and electricity but also a strong, light and transparent material, and may serve as the basis for new and more efficient electronic devices.

Furthermore graphene is also extremely interesting from a fundamental point of view. Its honeycomb lattice structure makes that charge carriers behave like massless relativistic particles, which gives electronic properties that greatly differ from conventional bidimensional electron gases and unique features like the Dirac cone bandstructure and the ensuing density of states, the Klein tunneling or the relativistic quantum Hall effect.

1.1.1 Honeycomb lattice

The honeycomb lattice of graphene consists of a hexagonal pattern filled with carbon atoms (see Figure 1.1), each one being connected to its three nearest-neighbors through σ-bonds originated from the sp_2 hybridization between the s, p_x and p_y orbitals of carbons, involving three valence electrons, with the distance between two neighboring atoms being $a = 1.42$ Å. These bonds are responsible of the planar structure of graphene and its thermal and mechanical properties. The remaining p_z orbitals of the carbon atoms form π-bonds with neighbors, which gives one free electron per atom and determines the transport properties of graphene.

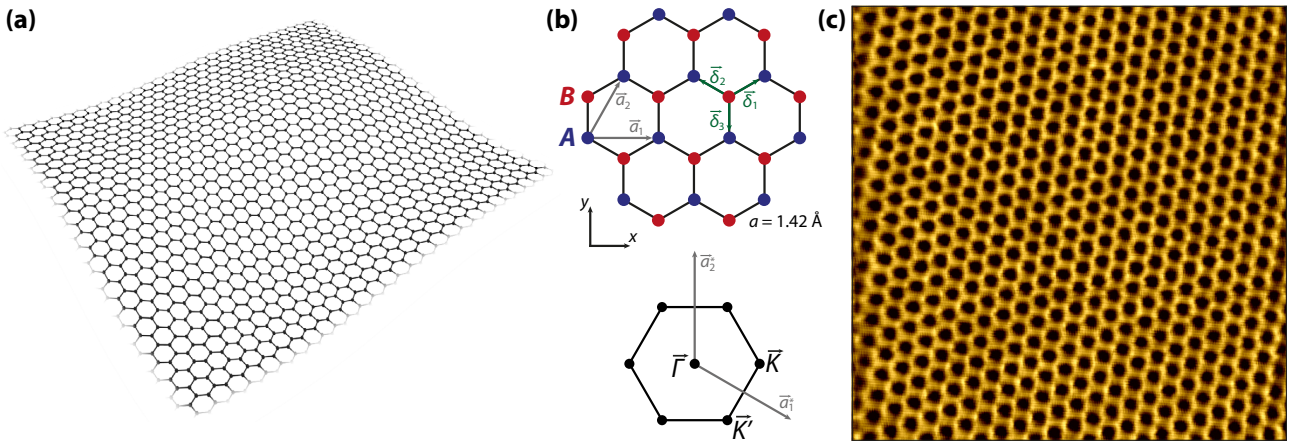

Figure 1.1: Graphene honeycomb lattice. **(a)** Graphene is a 2D crystal with a one-atom thick honeycomb lattice and can be seen as a monolayer of graphite. **(b)** Top : real-space honeycomb lattice of graphene, made out of two interpenetrating triangular sublattices A and B, with lattice vectors $\boldsymbol{a}_1$ and $\boldsymbol{a}_2$. The $\boldsymbol{\delta}_i$ vectors are the nearest-neighbor vectors and $a = 1.42$ Å is the distance between two neighboring carbons. Bottom : Brillouin zone of the reciprocal lattice of graphene with basis vectors $\boldsymbol{a}_1^*$ and $\boldsymbol{a}_2^*$, centered on the $\boldsymbol{\Gamma}$ point with two inequivalent Dirac points K and K' where the Dirac cones are located. **(c)** 5×5 nm STM topography image showing the honeycomb lattice of graphene (see Chapter 4 for further measurements).

Since the honeycomb lattice of graphene is not a Bravais lattice, it must be considered as two triangular sublattices with two atoms A and B per unit cell, where in the particular case of graphene A and B are both carbon atoms. We introduce $\boldsymbol{a}_1$, $\boldsymbol{a}_2$ and $\boldsymbol{a}_3$ the basis vectors of the Bravais triangular sublattice. We can also define the hopping vectors $\boldsymbol{\delta}_1$, $\boldsymbol{\delta}_2$ and $\boldsymbol{\delta}_3$ as the vectors connecting each A atom to its three nearest-neighbor B atoms. We then have :

$$\begin{aligned} &\boldsymbol{a}_1 = a\sqrt{3}\boldsymbol{e}_x \qquad \boldsymbol{a}_3 = \boldsymbol{a}_2 - \boldsymbol{a}_1 \qquad \text{and} \qquad \boldsymbol{\delta}_{1/2} = \frac{a}{2}\left(\pm\sqrt{3}\boldsymbol{e}_x + \boldsymbol{e}_y\right) \\ &\boldsymbol{a}_2 = \frac{a}{2}\left(\sqrt{3}\boldsymbol{e}_x + 3\boldsymbol{e}_y\right) \qquad\qquad\qquad\qquad\quad \boldsymbol{\delta}_3 = -a\boldsymbol{e}_y \end{aligned}$$

The reciprocal lattice of the graphene honeycomb lattice is a hexagonal lattice, rotated by an angle of $\pi/2$ compared to the real space one. The first Brillouin zone is a hexagon centered on the $\boldsymbol{\Gamma}$ point and defined by the basis vectors $\boldsymbol{a}_1^*$ and $\boldsymbol{a}_2^*$ given by :

$$\boldsymbol{a}_i^*.\boldsymbol{a}_j = 2\pi\delta_{ij} \qquad \Rightarrow \qquad \boldsymbol{a}_1^* = \frac{2\pi}{a\sqrt{3}}\left(\boldsymbol{e}_x - \frac{\boldsymbol{e}_y}{\sqrt{3}}\right) \qquad , \qquad \boldsymbol{a}_2^* = \frac{4\pi}{3a\sqrt{3}}\boldsymbol{e}_y$$

1.1.2 Electronic bandstructure

The Hamiltonian for the system can be written as a tight-binding Hamiltonian that describes how electrons can hop from one lattice site to another one. Since the rate of tunneling events from one site to another exponentially decreases with the distance, we only consider in the first order tunneling terms between the nearest neighbor sites. The hopping amplitude t can be estimated using ab initio calculations as $t \approx 2.7\,\text{eV}$. We also do not consider the spin since the associated Zeeman energy $E_\text{Z} \sim g\mu_\text{B}B \sim 0.1\,\text{meV} \ll t$ for common laboratory magnetic fields. We then write the Hamiltonian as :

$$\widehat{\mathcal{H}} = -t\sum_{\langle i,j\rangle}\left(\hat{c}^\dagger(\boldsymbol{r}_i)\hat{c}(\boldsymbol{r}_j) + h.c.\right) \tag{1.1}$$

where the sum is over the nearest neighbors and $\hat{c}^\dagger$ and $\hat{c}$ are respectively the creation and annihilation operators in the second quantization formalism. We can rewrite $\widehat{\mathcal{H}}$ using a summation over the $\boldsymbol{r}_A$ of the sublattice A which gives :

$$\widehat{\mathcal{H}} = -t\sum_{\boldsymbol{r}_A}\sum_{\alpha=1,2,3}\left(\hat{c}_B^\dagger(\boldsymbol{r}_A + \boldsymbol{\delta}_\alpha)\hat{c}_A(\boldsymbol{r}_A) + h.c.\right) \tag{1.2}$$

The annihilation operators relative to the sublattices A and B can be written in the Fourier space as :

$$\hat{c}_{A/B}(\boldsymbol{r}_i) = \frac{1}{\sqrt{N}}\sum_{\boldsymbol{k}} e^{-i\boldsymbol{k}.\boldsymbol{r}_i}\,\hat{c}_{A/B}(\boldsymbol{k}) \tag{1.3}$$

which gives the new expression for the Hamiltonian :

$$\widehat{\mathcal{H}} = -t\sum_{\boldsymbol{k}}\left(\gamma(\boldsymbol{k})\hat{c}_B^\dagger(\boldsymbol{k})\hat{c}_A(\boldsymbol{k}) + h.c.\right) \tag{1.4}$$

where we used the relation $\sum_{\boldsymbol{r}_A} e^{-i(\boldsymbol{k}-\boldsymbol{k'}).\boldsymbol{r}_A} = N\delta_{\boldsymbol{k},\boldsymbol{k'}}$ and we have introduced :

$$\gamma(\boldsymbol{k}) = \sum_{\alpha=1,2,3} e^{i\boldsymbol{k}.\boldsymbol{\delta}_\alpha} = 2e^{ik_ya/2}\cos\left(\frac{\sqrt{3}}{2}k_xa\right) + e^{-ik_ya} \tag{1.5}$$

We can write the Hamiltonian in the following form as a product :

$$\widehat{\mathcal{H}} = -t\sum_{\boldsymbol{k}}\begin{pmatrix}\hat{c}_A^\dagger(\boldsymbol{k}) & \hat{c}_B^\dagger(\boldsymbol{k})\end{pmatrix}\begin{pmatrix}0 & \gamma^*(\boldsymbol{k}) \\ \gamma(\boldsymbol{k}) & 0\end{pmatrix}\begin{pmatrix}\hat{c}_A(\boldsymbol{k}) \\ \hat{c}_B(\boldsymbol{k})\end{pmatrix} \tag{1.6}$$

The diagonalization of $\widehat{\mathcal{H}}$ allows us to obtain the dispersion relation with two solutions $\varepsilon_\lambda(\boldsymbol{k}) = \lambda t|\gamma(\boldsymbol{k})|$, indexed by $\lambda = \pm 1$ [3, 4] :

$$\varepsilon_\lambda(\boldsymbol{k}) = \lambda t\sqrt{3 + 2\sum_{i=1}^{3}\cos\left(\boldsymbol{k}.\boldsymbol{a}_i\right)} = \lambda t\sqrt{1 + 4\cos\frac{\sqrt{3}k_x a}{2}\cos\frac{3k_y a}{2} + 4\cos^2\frac{\sqrt{3}k_x a}{2}} \tag{1.7}$$

which gives two symmetric bands, the conduction band for the positive ($\lambda = +1$) solution and the valence band for the negative ($\lambda = -1$) solution. The bandstructure of graphene is shown on Figure 1.2(a). Each carbon atom contributes one π-electron (either spin up or down) to the system. In the case of a perfect undoped graphene sheet, since every electronic state can be occupied by two electrons of opposite spin, half of the total number of states are therefore occupied and the valence band is completely filled whereas the conduction band is empty. The Fermi energy lies then at $\varepsilon = 0$. The two bands touch at this point when the equation $\varepsilon(\boldsymbol{k}) = 0 \Rightarrow \gamma(\boldsymbol{k}) = 0$, which is satisfied for two inequivalent points, located at the corners of the Brillouin zone, called the Dirac points and noted K and K', given by :

$$\boldsymbol{K} = \frac{4\pi}{3\sqrt{3}a}\boldsymbol{e}_x \qquad \text{and} \qquad \boldsymbol{K'} = -\frac{4\pi}{3\sqrt{3}a}\boldsymbol{e}_x \tag{1.8}$$

We can index the Dirac points using $\xi = \pm 1$ where $\xi = +1$ for K and $\xi = -1$ for K'. The Dirac points energy is labeled E_D : both bands thus touch at $E_\mathrm{D} = \varepsilon(\xi\boldsymbol{K}) = 0$. Around the Dirac points, we can linearize the dispersion relation by introducing the wave vector $\boldsymbol{q}$ as $\boldsymbol{k} = \boldsymbol{K} + \boldsymbol{q}$, where $|\boldsymbol{q}| \ll |\boldsymbol{K}|$, to obtain :

$$\varepsilon_\lambda^\xi(\boldsymbol{q}) = \lambda\hbar v_\mathrm{F}|\boldsymbol{q}| + \mathcal{O}\left(\left|\frac{q}{K}\right|^2\right) \tag{1.9}$$

which gives Dirac cones around the vertices of the Brillouin zone : the low-energy dispersion relation depends linearly with the wave vector. It is also independent of ξ since K and K' are indistinguishable, which results in a two-fold valley degeneracy in graphene, with the associated degree of freedom - the valley index ξ - called the isospin, that adds to the already existing spin degeneracy. Each electronic state has then a four-fold degeneracy. The group velocity v_F is the Fermi velocity and is defined by :

$$v_\mathrm{F} = \frac{1}{\hbar}\frac{\partial\varepsilon_\lambda^\xi(q)}{\partial q} = \frac{t}{\hbar}\left.\frac{\partial\gamma(k)}{\partial k}\right|_{\boldsymbol{k}=\boldsymbol{K}} \approx \frac{3at}{2\hbar} \tag{1.10}$$

Numerically, $v_\mathrm{F} \sim 1 \times 10^6\ \mathrm{m.s^{-1}}$. The linear dependence of the dispersion relation with the wave vector also implies that charge carriers in graphene behave as relativistic and massless Dirac fermions, with the energy-independent velocity v_F, which is a striking difference with the conventional 2D electron gas where $\varepsilon(\boldsymbol{q}) = q^2/2m$ and the velocity of charge carriers is given by $v = k/m = \sqrt{2\varepsilon/m}$ and hence depends on the energy.

If we also consider hopping terms between the next-nearest-neighbors, whose hopping amplitude can be estimated numerically as $t_2 \approx 0.2\,\mathrm{eV} \ll t$, we obtain [4] :

$$\varepsilon_\lambda^\xi(\boldsymbol{q}) \simeq 3t_2 + \lambda\hbar v_\mathrm{F}|\boldsymbol{q}| - \left(\frac{9t_2a^2}{4} + \lambda\frac{3ta^2}{8}\sin(3\theta_q)\right)|\boldsymbol{q}|^2 \tag{1.11}$$

where $\theta_q = \arctan(q_y/q_x)$. The presence of t_2 shifts the position of the Dirac point and breaks the particle-hole symmetry, making the conduction and valence bands asymmetric, but without changing the shape of the low-energy spectrum. However at higher energies the terms up to order $|q/K|^2$ induce a dependence of the dispersion relation with the direction in the momentum space, which gives a three fold symmetry, known as the trigonal warping of the electronic spectrum [5, 6]. We then for the following only consider the low-energy spectrum Dirac cones in the vicinity of the Dirac points K and K'.

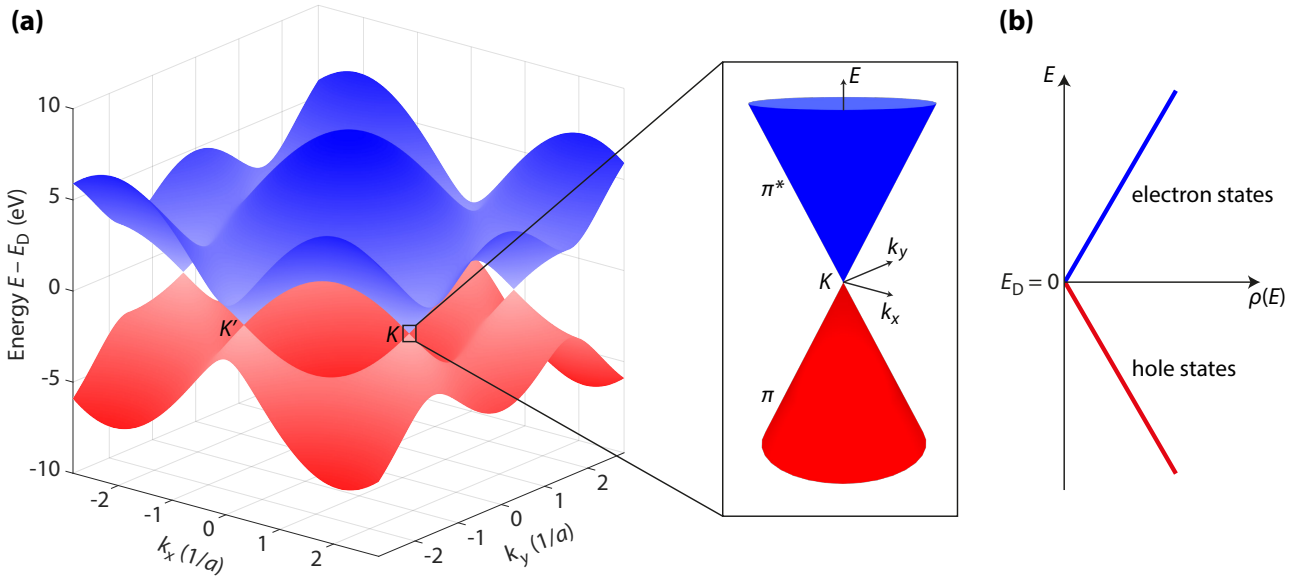

Figure 1.2: Graphene bandstructure and density of states. **(a)** Left : Energy dispersion of graphene, with the conduction π^* band on the top and the valence π band on the bottom. Both bands touch at the Dirac points where the Fermi level is located in undoped graphene. Right : zoom around the Dirac point where the low-energy dispersion can be linearized, giving the electron-hole symmetric Dirac cone structure. **(b)** Low-energy density of states of graphene, which is linear in energy, vanishes at the Dirac point and presents an electron-hole symmetry.

1.1.3 Density of states

In a 2D electron gas, the density of states per unit area is given by $\rho(\boldsymbol{q}) = \mathrm{d}N(\boldsymbol{q})/\mathrm{d}|\boldsymbol{q}|$ with $N(\boldsymbol{q}) = g_s q^2/4\pi$ the number of states in reciprocal space within a circle of radius $|\boldsymbol{q}|$, where $g_s = 2$ is the spin degeneracy. Adding the valley degeneracy $g_v = 2$ of graphene gives $N(\boldsymbol{q}) = g_s g_v q^2/4\pi$. Since the low-energy dispersion relation (1.9) implies $|\boldsymbol{q}| = |\varepsilon|/\hbar v_F$ around one Dirac point, the density of states per unit area is :

$$\rho(\varepsilon) = \rho(\boldsymbol{q})\frac{\mathrm{d}|\boldsymbol{q}|}{\mathrm{d}\varepsilon} = \frac{1}{\hbar v_F}\frac{\mathrm{d}N(\boldsymbol{q})}{\mathrm{d}|\boldsymbol{q}|} = \frac{g_s g_v}{\hbar v_F}\frac{2|\boldsymbol{q}|}{4\pi} \tag{1.12}$$

so that the density of states in graphene close to the Dirac point is :

$$\rho(\varepsilon) = \frac{g_s g_v}{2\pi(\hbar v_F)^2}|\varepsilon| = \frac{2}{\pi(\hbar v_F)^2}|\varepsilon| \tag{1.13}$$

The density of states in graphene is linear in energy, with an electron-hole symmetry and vanishes at E_D, giving a V-shape as shown in Figure 1.2(b). This greatly differs from the non-relativistic case where the energy dispersion is quadratic and the density of states is constant.

The general expression for charge carrier density n at temperature T is :

$$n(T) = \int_{-\infty}^{+\infty} \rho(\varepsilon) f_{FD}(\varepsilon, T)\mathrm{d}\varepsilon \tag{1.14}$$

where f_{FD} is the Fermi-Dirac distribution. At $T = 0$, we then have :

$$n = \int_{E_D=0}^{E_F} \rho(\varepsilon)\mathrm{d}\varepsilon = \mathrm{sign}(E_F)\frac{E_F^2}{\pi\hbar^2 v_F^2} \tag{1.15}$$

so that the carrier density n is linked to the Fermi energy E_F in graphene such as :

$$E_F = \hbar v_F\,|\boldsymbol{k}_F| = \mathrm{sign}(n)\hbar v_F\sqrt{\pi|n|} \tag{1.16}$$

1.1.4 Low-energy Hamiltonian

Two-spinor representation Using the linearization around the Dirac points, it is possible to write the Hamiltonian of the system as a 2D Dirac Hamiltonian. We write the wave vector in the Fourier space as $\boldsymbol{k} = \xi\boldsymbol{K} + \boldsymbol{q}$ with $\xi = \pm 1$ indexing the two Dirac points K and K' and $|\boldsymbol{q}| \ll |\boldsymbol{K}|$. We then have :

$$\gamma(\boldsymbol{k}) \approx \underbrace{\gamma(\xi\boldsymbol{K})}_{=0} - \frac{3}{2}a(\xi q_x + iq_y) + \mathcal{O}\left(\left|\frac{q}{K}\right|^2\right) \tag{1.17}$$

which gives for the low-energy Hamiltonian, considering Equation (1.6) :

$$\widehat{\mathcal{H}}^{\xi} = \hbar v_{\mathrm{F}} \sum_{\boldsymbol{k}} \begin{pmatrix} \hat{c}^{\dagger}_{A,\xi}(\boldsymbol{k}) & \hat{c}^{\dagger}_{B,\xi}(\boldsymbol{k}) \end{pmatrix} \begin{pmatrix} 0 & \xi q_x - iq_y \\ \xi q_x + iq_y & 0 \end{pmatrix} \begin{pmatrix} \hat{c}_{A,\xi}(\boldsymbol{k}) \\ \hat{c}_{B,\xi}(\boldsymbol{k}) \end{pmatrix} \tag{1.18}$$

that we can write as :

$$\widehat{\mathcal{H}}^{\xi} = \sum_{\boldsymbol{k}} \hat{c}^{\dagger}_{\xi}(\boldsymbol{q}) \widehat{\mathcal{H}}^{\xi}_{D}(\boldsymbol{q}) \hat{c}_{\xi}(\boldsymbol{q}) \tag{1.19}$$

where $\hat{c}^{\dagger}_{\xi}(\boldsymbol{q}) = \begin{pmatrix} \hat{c}^{\dagger}_{A,\xi} & \hat{c}^{\dagger}_{B,\xi} \end{pmatrix}$. This yields the effective low-energy Hamiltonian which takes the form of a Dirac Hamiltonian for a 2D massless fermion :

$$\widehat{\mathcal{H}}^{\xi}_{D}(\boldsymbol{q}) = \hbar v_{\mathrm{F}} \left(\xi q_x \sigma_x + q_y \sigma_y\right) = \hbar v_{\mathrm{F}} \begin{pmatrix} 0 & \xi q_x - iq_y \\ \xi q_x + iq_y & 0 \end{pmatrix} \tag{1.20}$$

where $\boldsymbol{\sigma} = (\sigma_x, \sigma_y)$ are the Pauli matrices[1] of the sublattice pseudospin.

A more convenient representation is obtained by switching the pseudospins for the K' valley such as $\hat{c}^{\dagger}_{\xi=-1}(\boldsymbol{q}) = \begin{pmatrix} \hat{c}^{\dagger}_{B,K'} & \hat{c}^{\dagger}_{A,K'} \end{pmatrix}$. In this case, the low-energy Dirac Hamiltonian is :

$$\widehat{\mathcal{H}}^{\xi}_{D}(\boldsymbol{q}) = \xi\hbar v_{\mathrm{F}} \boldsymbol{q}.\boldsymbol{\sigma} = \xi\hbar v_{\mathrm{F}} \left(q_x \sigma_x + q_y \sigma_y\right) = \xi\hbar v_{\mathrm{F}} \begin{pmatrix} 0 & q_x - iq_y \\ q_x + iq_y & 0 \end{pmatrix} \tag{1.21}$$

The low-energy Hamiltonian of graphene takes the form of a Dirac Hamiltonian in 2D : the low-energy excitations can thus be described as ultra-relativistic particles of spin 1/2, where the velocity of light c is replaced by the Fermi velocity v_{F} which is about 300 times smaller. The low-energy quasiparticles in graphene are then qualified of massless Dirac fermions.

The appearance of the Dirac Hamiltonian is a direct consequence of the development of the dispersion relation around the Dirac points, as opposed to the general Dirac equation which arises from fundamental symmetries such as the Lorenz invariance. Moreover, the negative energy states have in graphene a natural interpretation in terms of valence electrons or holes. It must also be highlighted that, contrary to the general Dirac equation, the Pauli matrices $\boldsymbol{\sigma} = (\sigma_x, \sigma_y)$ correspond to the sublattice pseudospin and not the real electron spin : pseudospin-up corresponds to the case where the charge carrier density is concentrated on one sublattice whereas the pseudospin-down corresponds to the other sublattice.

The eigenfunctions describing the Hamiltonian (1.20) such as $\widehat{\mathcal{H}}^{\xi=+1}_{D} \Psi^{\lambda}_{K} = \varepsilon^{\xi=+1}_{\lambda} \Psi^{\lambda}_{K}$ can be written as a two-component spinor :

$$\Psi^{\lambda}_{K}(\boldsymbol{q}) = \begin{pmatrix} \Psi_{A,K} \\ \Psi_{B,K} \end{pmatrix} = \frac{1}{\sqrt{2}} \begin{pmatrix} 1 \\ \lambda e^{i\theta_q} \end{pmatrix} \tag{1.22}$$

[1] $\sigma_x = \begin{pmatrix} 0 & 1 \\ 1 & 0 \end{pmatrix}$ / $\sigma_y = \begin{pmatrix} 0 & -i \\ i & 0 \end{pmatrix}$ / $\sigma_z = \begin{pmatrix} 1 & 0 \\ 0 & -1 \end{pmatrix}$

with $\theta_q = \arctan(q_y/q_x)$ and $\lambda = \pm 1$ the band index. The two components $\Psi_{A,K}$ and $\Psi_{B,K}$ are the amplitudes of the wave function on the A and B sublattices. This two-component representation, which is analogous to the one of a spin, corresponds to the projection of the electron wave function on each sublattice of graphene. $\Psi^{\lambda}_{K'}(\boldsymbol{q})$ is the time reversal symmetric of $\Psi^{\lambda}_{K}(-\boldsymbol{q})$, since by time reversal symmetry $\boldsymbol{k} = \boldsymbol{K'} + \boldsymbol{q} \longmapsto -\boldsymbol{k} = \boldsymbol{K} - \boldsymbol{q}$, with the anti-unitary time reversal operator $\mathcal{T}$ being equivalent to the complex conjugation operator $\mathcal{C}$:

$$\Psi^{\lambda}_{K'}(\boldsymbol{q}) = \begin{pmatrix} \Psi_{A,K'} \\ \Psi_{B,K'} \end{pmatrix} = \mathcal{T}\Psi^{\lambda}_{K}(-\boldsymbol{q}) = \Psi^{\lambda,*}_{K}(-\boldsymbol{q}) = \frac{1}{\sqrt{2}} \begin{pmatrix} 1 \\ \lambda e^{-i\theta_q} \end{pmatrix} \tag{1.23}$$

In real space, with the position representation $\boldsymbol{k} \longmapsto -i\boldsymbol{\nabla}$, the eigenfunctions obey the 2D Dirac equation :

$$-i\hbar v_{\mathrm{F}} \boldsymbol{\sigma}.\boldsymbol{\nabla}\Psi(\boldsymbol{r}) = \varepsilon_{\lambda}\Psi(\boldsymbol{r}) \tag{1.24}$$

with $\varepsilon_{\lambda} = \lambda\hbar v_{\mathrm{F}} k$ the eigenenergies for both valence and conduction bands.

Four-spinor representation It is also possible the write the low-energy Hamiltonian taking into account both valleys K and K' as a 4×4 matrix. Introducing the following operator $\widehat{c}^{\,\dagger}(\boldsymbol{q}) = \begin{pmatrix} \widehat{c}^{\dagger}_{A,K} & \widehat{c}^{\dagger}_{B,K} & \widehat{c}^{\dagger}_{A,K'} & \widehat{c}^{\dagger}_{B,K'} \end{pmatrix}$, the low-energy Hamiltonian can be written as two copies of the Hamiltonian (1.20) :

$$\widehat{\mathcal{H}}_D(\boldsymbol{q}) = \begin{pmatrix} \widehat{\mathcal{H}}_D^{\xi=+1}(\boldsymbol{q}) & 0 \\ 0 & \widehat{\mathcal{H}}_D^{\xi=-1}(\boldsymbol{q}) \end{pmatrix} = \hbar v_{\mathrm{F}} \begin{pmatrix} 0 & q_x - iq_y & 0 & 0 \\ q_x + iq_y & 0 & 0 & 0 \\ 0 & 0 & 0 & -(q_x + iq_y) \\ 0 & 0 & -(q_x - iq_y) & 0 \end{pmatrix} \tag{1.25}$$

Note that in this four-spinor representation, the first two components represent the sublattice components for valley K whereas the last two represent those for valley K'. A more convenient representation is also obtained using the operator $\widehat{c}^{\,\dagger}(\boldsymbol{q}) = \begin{pmatrix} \widehat{c}^{\dagger}_{A,K} & \widehat{c}^{\dagger}_{B,K} & \widehat{c}^{\dagger}_{B,K'} & \widehat{c}^{\dagger}_{A,K'} \end{pmatrix}$ where sublattices have been swapped for valley K'. The Hamiltonian can thus be written as :

$$\widehat{\mathcal{H}}_D(\boldsymbol{q}) = \hbar v_{\mathrm{F}}\, \tau_z \otimes \boldsymbol{q}.\boldsymbol{\sigma} = \hbar v_{\mathrm{F}} \begin{pmatrix} \boldsymbol{q}.\boldsymbol{\sigma} & 0 \\ 0 & -\boldsymbol{q}.\boldsymbol{\sigma} \end{pmatrix} \tag{1.26}$$

The Pauli matrix τ_z describes the valley isospin and its eigenvalues $\xi = \pm 1$ label the Dirac points. In this representation, eigenfunctions are four-spinors with two components for the sublattices and two others for the valleys.

1.1.5 Chirality and suppression of backscattering

Adding to the previous indexes, we can also introduce the helicity $\widehat{\eta}$ defined as the projection of the spin $\boldsymbol{\sigma}$ onto the direction of propagation of the wave vector $\boldsymbol{q}$:

$$\widehat{\eta} = \frac{\boldsymbol{q}.\boldsymbol{\sigma}}{|\boldsymbol{q}|} \tag{1.27}$$

For massless fermions, $\widehat{\eta}$ commutes with the Hamiltonian and helicity is then a good quantum number with eigenvalues $\eta = \pm 1$: $\eta = +1$ (right-handed) if the spin is parallel to the wave vector and $\eta = -1$ (left-handed) in the antiparallel case, and helicity is conserved. For instance, in nature, this conservation applies to neutrinos, where all neutrinos are left-handed whereas antineutrinos are right-handed. Helicity and chirality are also equivalent if we consider valley isospin rather than the electronic spin. The Hamiltonian around a given Dirac point can then be written as :

$$\widehat{\mathcal{H}}^{\xi}_D(\boldsymbol{q}) = \xi\hbar v_{\mathrm{F}} |\boldsymbol{q}| \widehat{\eta} \tag{1.28}$$

$\widehat{\eta}$ is therefore proportional to the Hamiltonian. The two valleys K and K' have opposite chirality due to the time reversal symmetry [7] : electrons have a positive chirality in the K-valley while they have a negative one in the K'-valley. Band index, valley isospin and helicity are related by :

$$\lambda = \xi\eta \tag{1.29}$$

and then are not independent, as shown in Figure 1.3.

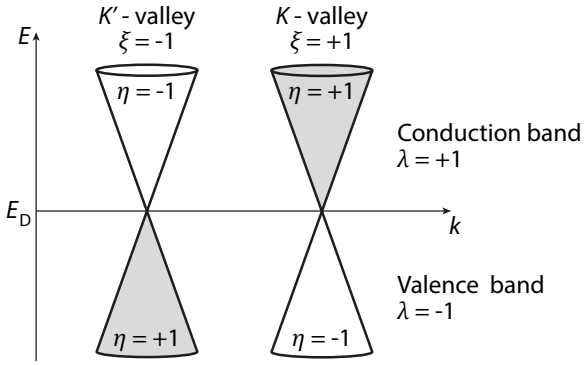

Figure 1.3: Helicity η, band index λ and valley isospin ξ.

This leads to an important consequence that backscattering in graphene is suppressed. Let us consider the intravalley backscattering probability, which is obtained from the projection of the wave function corresponding to a quasiparticle moving forward $\Psi_K^+(\boldsymbol{q}(\theta_q))$ on that of the backscattering particle $\Psi_K^+(\boldsymbol{q}(\theta_q+\pi))$ where the momentum has been inverted $\boldsymbol{q} \longmapsto -\boldsymbol{q}$. Within the same valley we have $\Psi_K^+(\boldsymbol{q}(\theta_q+\pi)) = \Psi_K^-(\boldsymbol{q}(\theta_q))$ using Equation (1.22), and :

$$\left\langle \Psi_K^+(\boldsymbol{q}(\theta_q)) \,|\Psi_K^+(\boldsymbol{q}(\theta_q+\pi))\right\rangle = \left\langle \Psi_K^+(\boldsymbol{q}(\theta_q)) \,|\Psi_K^-(\boldsymbol{q}(\theta_q))\right\rangle = 0 \tag{1.30}$$

which means that intravalley backscattering is suppressed. This selection rule is a consequence of the fact that backscattering within the same valley would reverse the direction of the sublattice pseudospin $\sigma \longmapsto -\sigma$, which can not happen if the impurity does not mix K and K'.

We now consider the intervalley backscattering probability, which is given by the projection of the moving forward quasiparticle in K valley $\Psi_K^+(\boldsymbol{q}(\theta_q))$ on the backscattering quasiparticle in the K' valley $\Psi_{K'}^+(\boldsymbol{q}(\theta_q+\pi))$. Therefore we have, using Equation (1.23) :

$$\left\langle \Psi_K^+(\boldsymbol{q}(\theta_q)) \,|\Psi_{K'}^+(\boldsymbol{q}(\theta_q+\pi))\right\rangle = \left\langle \Psi_K^+(\boldsymbol{q}(\theta_q)) \,|\Psi_K^-(\boldsymbol{q}(\theta_q))\right\rangle = 0 \tag{1.31}$$

so that intervalley backscattering is also suppressed. In this case the selection rule comes from the fact that intervalley backscattering would inverse the chirality of the quasiparticle.

Intra and intervalley backscattering in graphene are then impossible within this single particle approach, which leads to physical consequences on transport properties in graphene such as ballistic transport at low temperature [8, 9], extremely large room temperature conductivity [10] and weak antilocalisation [11].

Summary Let us sum up the different degrees of freedom and indexes in graphene :

- the spin, for the true electronic spin ($s = \pm 1$),
- the pseudospin, for both sublattices A and B,
- the isospin, for both valleys K and K' ($\xi = \pm 1$),
- the band index, for the conduction and valence bands ($\lambda = \pm 1$),
- the helicity, for right- and left-handed particles ($\eta = \pm 1$).

1.1.6 Cyclotron mass

In a conventional 2D electron gas, the quadratic dispersion energy is given as :

$$\varepsilon(\boldsymbol{k}) = \frac{\hbar^2 k^2}{2m^*} \tag{1.32}$$

where m^* is the effective mass of charge carriers. The Fermi velocity is there defined as :

$$v_\mathrm{F} = \frac{1}{\hbar}\left.\frac{\partial\varepsilon}{\partial|\boldsymbol{k}|}\right|_{\boldsymbol{k}=\boldsymbol{k}_\mathrm{F}} = \frac{\hbar k_\mathrm{F}}{m^*} \tag{1.33}$$

and depends on the effective mass m^*.

For graphene, the effective mass rather reads as a function of the Fermi velocity :

$$m^* = \frac{\hbar k_\mathrm{F}}{v_\mathrm{F}} = \frac{\hbar}{v_\mathrm{F}}\sqrt{\pi n} \tag{1.34}$$

One can show that this effective mass as defined above is identical to the cyclotron mass m_c that is measurable for instance in a cyclotron resonance experiment, since in the semi-classical limit, the cyclotron mass is defined as [12] :

$$m_\mathrm{c} = \frac{\hbar^2}{2\pi}\left.\frac{\partial\mathcal{A}(\varepsilon)}{\partial\varepsilon}\right|_{\varepsilon=E_\mathrm{F}} \qquad \text{where} \qquad \mathcal{A}(\varepsilon) = \pi k^2(\varepsilon) = \frac{\pi\varepsilon^2}{\hbar^2 v_\mathrm{F}^2} \tag{1.35}$$

$\mathcal{A}$ is the area in the reciprocal space enclosed by an orbit of energy ε, so that $m_\mathrm{c} = m^*$. We can conclude that the cyclotron mass of relativistic charge carriers in graphene depends on the charge carrier density as its square root $n^{1/2}$, whereas the usual parabolic dispersion would imply a constant cyclotron mass. This square root dependence was observed experimentally using Shubnikov-de Haas oscillations, which provides evidence for the existence of massless Dirac quasiparticles in graphene [2, 13, 14, 15].

1.1.7 Berry phase

In quantum mechanics the Berry phase γ is the phase acquired by a wave function which undergoes an adiabatic cyclic evolution in the parameter space. It is an invariant and an observable of the system, which can lead to important physical consequences in diverse fields such as atomic, condensed matter, nuclear and elementary particle physics or optics [16]. We use a gauge invariant definition for the Berry phase [17] :

$$\gamma = \oint_{\mathcal{C}} \mathrm{d}\boldsymbol{k}\, \langle\Psi(\boldsymbol{k})\,|i\boldsymbol{\nabla}_{\boldsymbol{k}}\,\Psi(\boldsymbol{k})\rangle \tag{1.36}$$

where $\mathcal{C}$ is a closed path in the parameter space and the wave function $\Psi(\boldsymbol{k})$ has to be single-valued. Applying this definition with the wave function given in Equation (1.22) and taking a contour $\mathcal{C}$ that encloses one of the Dirac points, we find that the Berry phase in graphene is [5] :

$$\gamma = \pi \tag{1.37}$$

which means that when an electron moves in a complete circle corresponding to a full rotation of the wave vector or pseudospin, the wave function acquires a phase of π. This non-zero Berry phase is experimentally measurable in graphene in Shubnikov-de Haas oscillations, causing a phase shift of π, and in the quantum Hall regime, where it is responsible of the existence of the zero-energy Landau level as well as the anomalous quantum Hall effect [13].

For further insights on the electronics properties of graphene, see the works of Ando [18], Castro Neto *et al.* [4], Goerbig [19], Das Sarma *et al.* [20], Bennaceur [21] and Andrei *et al.* [22].

1.2 Probing graphene physics

We briefly discuss in this section about how we can probe some of the graphene physics established above. We first present how the electric field effect allows the tuning of the charge carrier density in graphene. We then focus on two different measurements : transport that measures global quantities like conductivity and mobility, and tunneling spectroscopy which locally probes the density of states of graphene.

1.2.1 Electric field effect

Due to its low charge carrier density close to the Dirac point, it is easy to apply an electric field effect by using an external gate in order to dope graphene, and tune the carrier density n or the position of the Fermi level. At zero doping, $E_F = E_D$ and the lower valence band of graphene is completely filled up to the Dirac point, and applying a gate voltage allows the injection of electrons in the conduction band or holes in the valence band. Experimentally, gating effect is commonly enabled by depositing a graphene flake on an insulating layer such as silicon oxide SiO_2 atop a highly doped silicon substrate, as shown in Figure 1.4(a). By applying a gate voltage V_g on the silicon gate, the carrier density n in graphene is thus given by :

$$e\,n = C_g V_g \tag{1.38}$$

with $C_g = \epsilon_0 \epsilon_r / t$ the gate capacitance per unit area, ϵ_0 the vacuum permittivity, t the thickness of the insulating layer and ϵ_r its relative dielectric constant. The gating is ambipolar due to the electron-hole symmetry and it is equivalent to inject electrons in the upper half of the Dirac cone (for $V_g > 0$) or holes in the lower half (for $V_g < 0$). The gate-induced density changes sign at the Dirac point, which justifies why it is also commonly called the charge-neutrality point (CNP).

In practice, graphene will always have a residual unintentional doping from contaminants coming from the fabrication process so that $E_F \neq E_D$. The gate voltage which brings E_F to E_D, and changes the polarity from holes to electrons or vice-versa, is called the charge neutrality point V^{CNP}. A hole (electron) -doped graphene will therefore have a positive (resp. negative) V^{CNP}. The carrier density must then be written as :

$$e\,n = C_g \left(V_g - V^{CNP}\right) \tag{1.39}$$

The position of the Fermi level in graphene as a function of the gate voltage is therefore :

$$E_F = \hbar v_F k_F = \mathrm{sign}(n)\hbar v_F \sqrt{\frac{4\pi|n|}{g_s g_v}} = \mathrm{sign}\left(V_g - V^{CNP}\right)\hbar v_F \sqrt{\frac{\pi C_g}{e}\left|V_g - V^{CNP}\right|} \tag{1.40}$$

1.2.2 Transport properties

Transport measurements have been the first ever done to characterize graphene in 2005 by Novoselov *et al.* [2] and Zhang *et al.* [13]. Using a Hall bar configuration device of graphene exfoliated on SiO_2, they show that the resistivity (resp. conductivity) of graphene shows a maximum (resp. minimum) when the Fermi level is brought with gating close to the Dirac point, see Figure 1.4(b,c), corresponding to the vanishing of the density of states at E_D. The Fermi level can be continuously tuned from holes at negative V_g to electrons at positive V_g, and the carrier density n changes of sign when E_F crosses the charge neutrality point, demonstrating the bipolar behavior of graphene. The hole and electron branches are qualitatively symmetric,

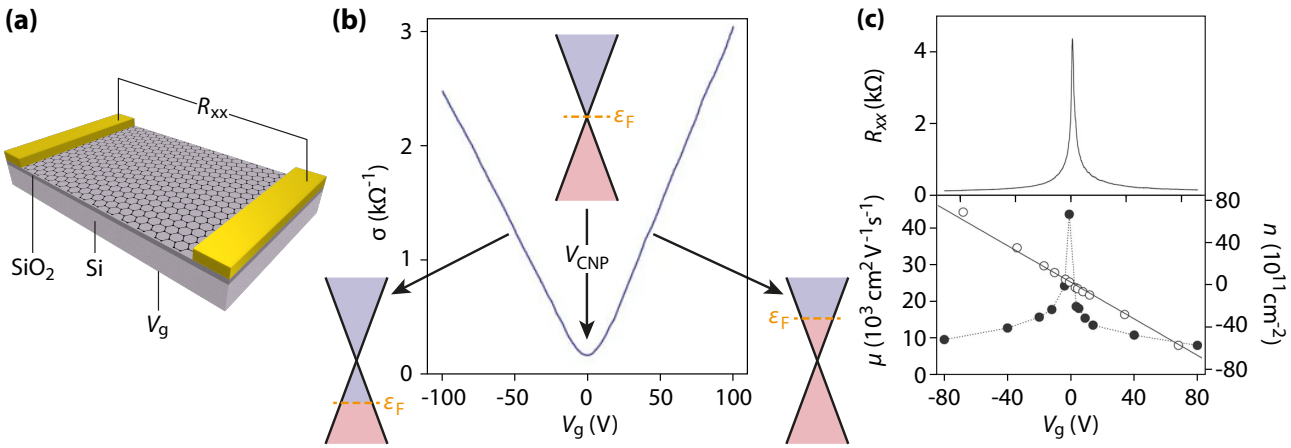

Figure 1.4: Electric field effect in graphene. **(a)** Typical transport device where a graphene flake is exfoliated atop a silicon substrate with an insulating SiO_2 layer to allow field effect. The charge carrier density in graphene is then given by $n = C_g V_g/e$ with V_g the gate voltage and C_g the gate capacitance. **(b)** Graphene conductivity σ measured as a function of gate voltage V_g showing the electric field effect in graphene. The transition from electrons to holes occurs at the minimum of the conductivity at the Dirac point. Figure taken from [23]. **(c)** Resistance R_{xx}, mobility μ (black dots) and carrier density n (white dots) of graphene measured as a function of gate voltage V_g. Figure taken from [13].

which is a direct consequence of the electron-hole symmetry of the bandstructure. A separate Hall measurement provides a measure of the charge carrier density n which varies linearly with the gate voltage as expected. The mobility μ of graphene can be extracted from these two measures of the conductivity σ and the carrier density n as :

$$\sigma = |e| n \mu \tag{1.41}$$

by assuming a simple Drude model, where the mobility μ is related to the transport time τ_{tr}, that is the time between two backscattering events, and their effective mass m^* with :

$$\mu = \frac{|e|\tau_{tr}}{m^*} \Rightarrow \sigma = \frac{n e^2 \tau_{tr}}{m^*} \tag{1.42}$$

Note that Klein tunneling in graphene [24, 25] enables forward scattering of carriers by impurities, without it affecting transport. τ_{tr} is thus greater than the elastic scattering time τ_e, which is the carrier lifetime between two scattering events that we will estimate in Chapter 2.1.3. Note also that the mobility μ can hardly be estimated at the Dirac point where the density n, the conductivity σ and the effective mass m^* vanish.

1.2.3 Tunneling spectroscopy

Scanning Tunneling Microscopy (STM) is a powerful technique used to study the topography of surfaces, being able to easily access the atomic resolution, as shown for graphene in Figure 1.1(c). On the other hand, Scanning Tunneling Spectroscopy (STS) allows to directly measure the local density of states of the material, which is then simply proportional to the derivative of the tunneling current I_{tunnel} with respect to the bias voltage V_{bias} (see Appendix A.1.3) :

$$\frac{dI_{tunnel}}{dV_{bias}} \propto \rho(eV_{bias}) \tag{1.43}$$

which can then gives access to the density of states of graphene. Figure 1.5(b) shows a tunneling spectrum measured on graphene on SiO_2. We find the expected V-shape for high V_{bias}, but

there are two minima : one at negative bias is induced by the vanishing of the density of states at $eV_{\text{bias}} = E_{\text{D}}$, the other is a zero bias anomaly which is a gap that occurs at the Fermi level (which is by definition at $V_{\text{bias}} = 0$) and attributed to inelastic tunneling into graphene via phonon scattering [26]. Several peaks appear, marked by black ticks, that we deal with in Chapter 5. The asymmetry in the V-shape is attributed to the existence of disorder in graphene that introduces a random potential, which we will talk about in the next section.

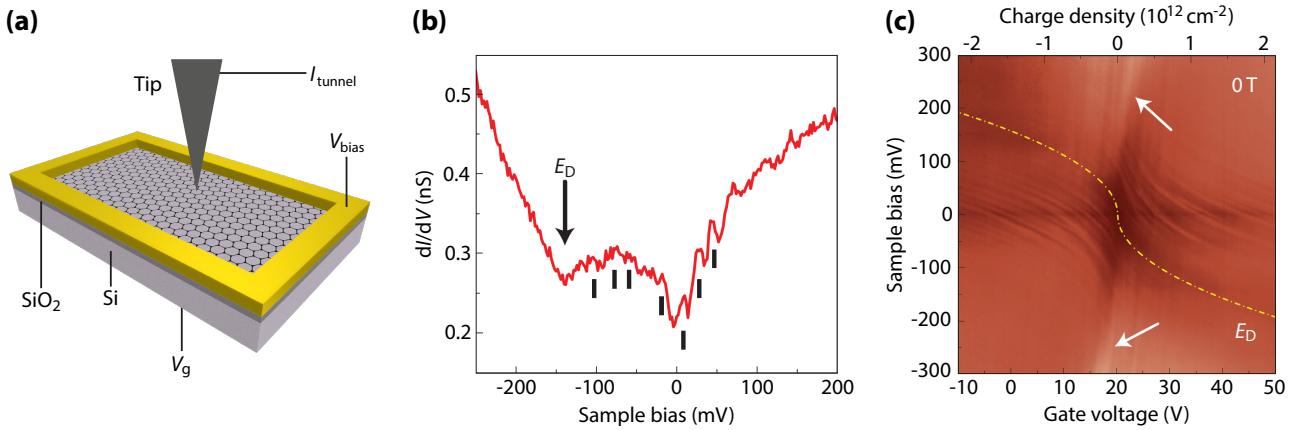

Figure 1.5: Observation of the Dirac point with STS. (a) Typical device for STM measurements. Applying a bias voltage V_{bias} on the sample allows the metallic tip to extract tunneling electrons from graphene which gives the tunneling current I_{tunnel}. The gate voltage V_{g} tunes the position of the Fermi level in graphene. **(b)** $\mathrm{d}I/\mathrm{d}V$ spectrum on graphene on SiO_2 at $V_{\text{g}} = 40\,\text{V}$ showing a minimum at the Dirac point. A second minimum occurs at the Fermi level (zero sample bias) due to the zero-bias anomaly. **(c)** $\mathrm{d}I/\mathrm{d}V$ gate map as a function of sample bias and gate voltage. The yellow dash-dotted line shows the evolution of the Dirac point as a function of gate voltage. Figures (b,c) taken from [27].

By applying a gate voltage V_{g}, the Fermi level E_{F} of graphene varies. Since E_{F} is fixed at $V_{\text{bias}} = 0$ in STM, equivalently the Dirac point energy varies in the opposite direction, which gives the theoretical equation derived from Equation (1.40) :

$$E_{\text{D}} = \text{sign}\left(V^{\text{CNP}} - V_{\text{g}}\right) \hbar v_{\text{F}} \sqrt{\frac{\pi C_{\text{g}}}{e} \left|V_{\text{g}} - V^{\text{CNP}}\right|} \tag{1.44}$$

The square-root dependence of the Dirac point position with the gate voltage is well observed on the gate map of Figure 1.5(c), where each vertical line of the plot is an individual spectrum measured at the given gate voltage. For each gate voltage, the Dirac point position is attributed with the same method than for the spectrum of Figure 1.5(b) and a fit with Equation (1.44) gives the yellow dash-dotted line, with fitting parameters $V^{\text{CNP}} = 20\,\text{V}$, which means that this sample is naturally hole-doped, and $v_{\text{F}} = 1.12 \times 10^6\,\text{m.s}^{-1}$ with this latter being closed to the theoretical value of $1 \times 10^6\,\text{m.s}^{-1}$. STS then allows the tracking of the Dirac point and the direct measure of the Fermi velocity which is not possible with transport measurements.

1.3 Influence of the substrate

We discuss in this section how the substrate affects the electronic and transport properties of the graphene sheet that lies on it, starting from usual SiO_2/Si substrates, which can limit the performances of such devices. We then detail how the use of better substrates such as hBN helps improving graphene quality and even inducing new physics and transport properties, at the cost of more complicated fabrication process, as detailed in Appendix B.

1.3.1 Disorder potential and charge puddles

Graphene was first isolated by Geim and Novoselov using a mechanical exfoliation technique on silicon with a layer of SiO_2 as a substrate. Though this common substrate allows field effect gating, the roughness of the SiO_2 layer induces random corrugations, or even ripples, in the graphene sheet which limits its mobility. Moreover, since insulating substrates such as SiO_2 host randomly distributed charged impurities trapped inside or on the surface, charge carriers in graphene are subjected to a disordered impurity potential and the graphene flake to spatially random gating, with the Dirac point energy relative to the Fermi level displaying random fluctuations as illustrated in Figure 1.6(a).

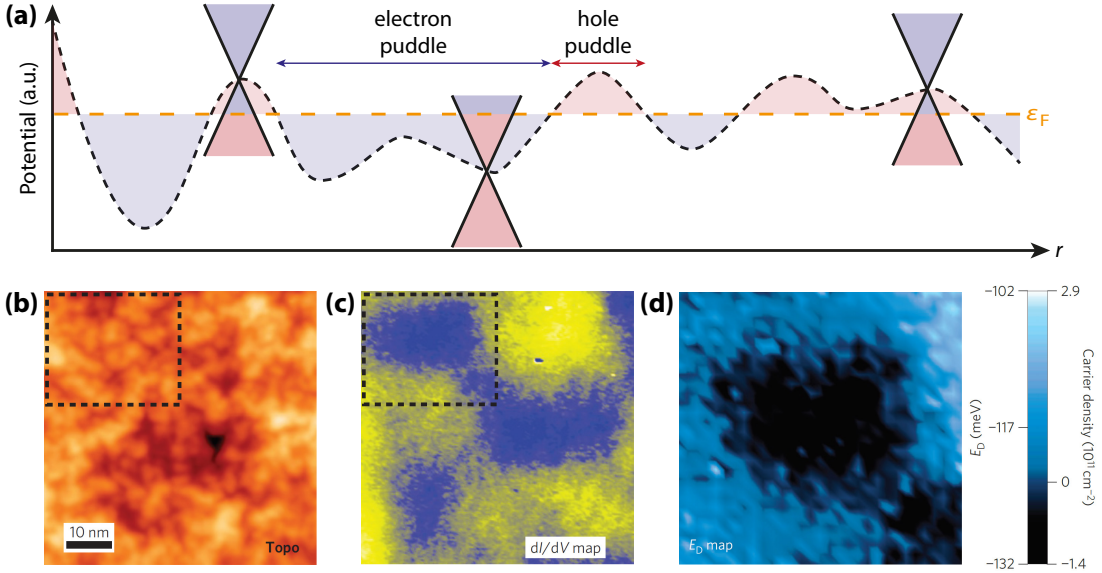

Figure 1.6: Charge puddles in graphene. **(a)** Schematic diagram of the disorder potential variation as a function of spatial location. The relative position of the Fermi level E_F to the Dirac point is tuned with a gate voltage. At a given gate voltage, the local position of the Dirac point relatively to the Fermi level gives hole or electron puddles. **(b,c)** $60 \times 60\,\text{nm}^2$ STM topography image of graphene on SiO_2 in (b) and the corresponding dI/dV map ($V_{\text{bias}} = -225\,\text{mV}$) in (c) showing electron puddles with a characteristic length of $\sim 20\,\text{nm}$. **(d)** Dirac point energy E_D map of a single charge puddle corresponding to the dashed square in (b) and (c). Figures (b-d) are taken from [28].

At high carrier densities, the screening of the carriers is strong enough to efficiently screen the impurity potential. But at low carrier density, close to the Dirac point, the weak screening makes electronic properties of graphene very sensitive to electrostatic potential fluctuations. This random potential causes the charges to break into charge puddles (or electron-density inhomogeneities) : electron (resp. hole) puddles when the local potential is below (resp. above) the Fermi energy. Zhang *et al.* [28] and Martin *et al.* [29] showed that charge puddles are prevalent in graphene on SiO_2 and have width up to 20 nm, see Figure 1.6(b-d), but they are also uncorrelated to topographic corrugations originating from the substrate roughness, leaving charge traps in SiO_2 or even molecules from air trapped between graphene and SiO_2 during the device fabrication being possible sources of the puddles.

These charge puddles create midgap states which fill out graphene density of states near the Dirac point [22, 30] making it impossible to reach the zero carrier density condition at charge neutrality for any applied gate voltage. Furthermore, for graphene deposited on SiO_2 the fluctuations of the random potential smear the Dirac point over a typical energy range of $30 - 100\,\text{meV}$. When the Fermi energy is close to the Dirac point inside this range, a gate voltage

change transforms electrons into holes but leaves the net carrier density almost unchanged. The spatial extent of the puddles significantly increases as the Dirac point is approached as shown by Samaddar *et al.* [31, 32], see Figure 1.7. At high carrier concentrations n, the underlying disorder potential is strongly screened by charge carriers which reduces the size ξ of the puddles, expected to decrease as $\xi \sim n^{-1/2}$.

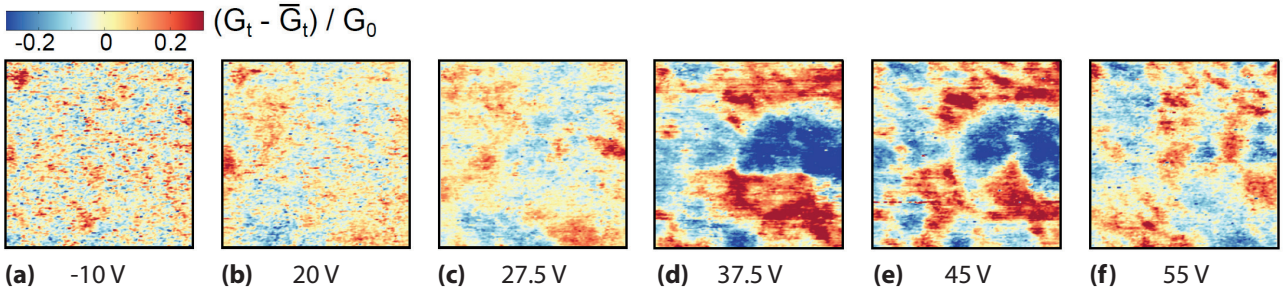

Figure 1.7: Spatial extension of charge puddles close to the Dirac point. Spatial maps of the variations of the normalized differential tunneling conductance over an area of $100 \times 100\,\mathrm{nm}^2$ at different gate voltages showing the evolution of charge disorder with carrier concentration. As the gate voltage gets closer to $V^{\mathrm{CNP}} = 30\,\mathrm{V}$, the charge puddles grow and become more intense. Figures are taken from [31].

Graphene can be seen in this regime as a disordered system with countless pn junctions, and the charge transport is possible thanks to Klein tunneling [24, 25] which allows the transmission of carriers across such barriers with a 100% efficiency on normal incidence, explaining the anomalous non-zero minimal conductivity at zero carrier density observed in measures on graphene on SiO_2 devices, see Figure 1.4(b,c). Charge puddles also make the linear density of states close to the Dirac point, and its vanishing at the Dirac point, become inaccessible, and justify as well the absence of a clear universal minimum conductivity in graphene devices [33, 34]. Charged impurities are also responsible for backscattering of Dirac fermions [28]. Surface roughness, charge puddles and backscattering are the three main reasons that explain the limitation of the mobility of graphene placed on SiO_2.

1.3.2 Moiré pattern with hBN substrate

With such limitations intrinsic to the SiO_2 substrate, the need of putting graphene atop better substrates quickly arises. One of them is hexagonal boron nitride (hBN). In such systems, graphene is placed atop hBN, forming a Van der Waals heterostructure (whom fabrication is detailed in Appendix B), the latter stack lying on a SiO_2 substrate to allow field effect. hBN is a layered material with the same honeycomb lattice of graphene, with a 1.8 % longer lattice constant, where each atom B and N occupies one of the two triangular sublattices. This breaking of the sublattice symmetry opens a large gap of about 6 eV in the bandstructure of hBN, making this material a Semenov insulator where charge carriers act as massive Dirac fermions. Moreover, hBN is relatively inert, coupling weakly to graphene, is free of surface charge traps and has a dielectric constant $\epsilon_{\mathrm{BN}} \sim 3 - 4$ similar to SiO_2. hBN is therefore a suitable insulator for electric field gating.

Once exfoliated on SiO_2, this 2D crystal is atomically flat and hBN flakes can be used as substrates for graphene. The main advantages of such graphene/hBN heterostructure is that the hBN layer suppresses charge inhomogeneities that graphene may feel when placed directly on SiO_2 and also reduces topographic corrugations [35], up to more than one order of magnitude with respect to graphene on SiO_2, as shown in Figure 1.8 by scanning both systems with STM.

The stacking method developed by Dean *et al.* in 2010 [36] enabled to boost graphene mobility, reaching mobilities above 1 000 000 $cm^2/V.s$ (several orders of magnitude higher than devices on SiO_2). hBN is thus a substrate of choice for our samples.

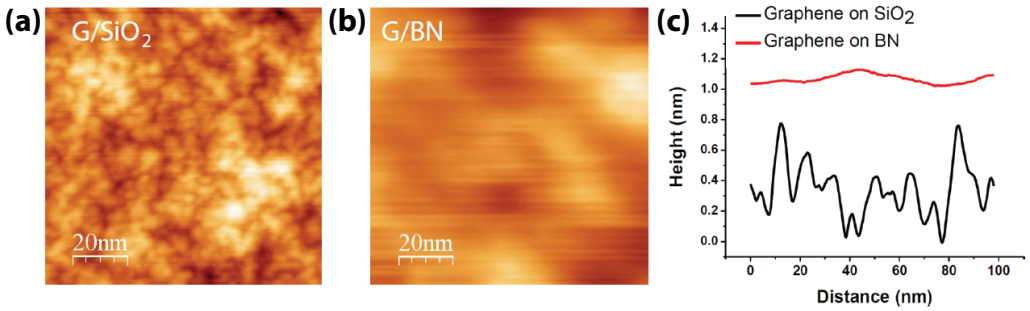

Figure 1.8: Graphene roughness due to the substrate beneath. (a,b) Comparison between the topography of two 100 nm × 100 nm areas of (a) graphene on SiO_2 and (b) graphene on hBN. **(c)** The comparison between two line cuts across (a) and (b) shows a more than one order of magnitude decrease in corrugation on hBN compared to SiO_2. Figures taken from [37].

However the mismatch $\delta \approx 1.8\%$ between the lattices of graphene and hBN induces the appearance of a superlattice also known as a Moiré pattern [38], see Figure 1.9(b). The Moiré wavelength λ is a function of the relative rotation angle ϕ between the two lattices :

$$\lambda = \frac{(1+\delta)a\sqrt{3}}{\sqrt{2(1+\delta)(1-\cos\phi)+\delta^2}} \tag{1.45}$$

where $a\sqrt{3}$ is the graphene lattice constant. We can also write the relative rotation angle θ of the Moiré pattern with respect to the graphene lattice as :

$$\tan\theta = \frac{\sin\phi}{(1+\delta)-\cos\phi} \tag{1.46}$$

Most of the time, ϕ is a random variable due to fabrication process. We plot the Moiré wavelength λ and its rotation angle θ as a function of ϕ in Figure 1.9(c).

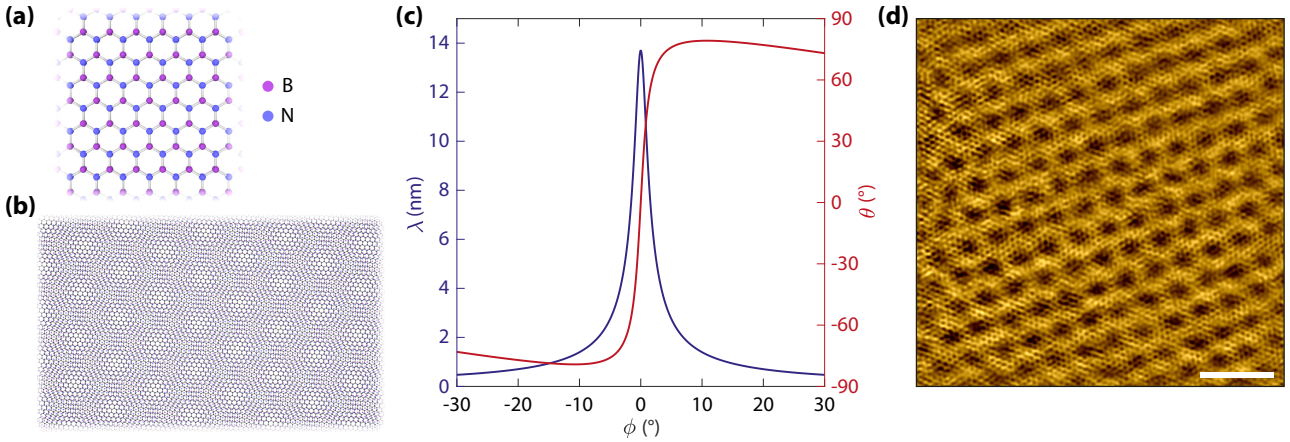

Figure 1.9: Moiré pattern. (a) Hexagonal boron nitride (hBN) lattice, similar to graphene, where each atom B and N occupies one of the triangular sublattice. **(b)** When superimposed, graphene and hBN honeycomb lattices form a superlattice or Moiré pattern. **(c)** Superlattice wavelength λ and rotation with respect to graphene θ as a function of the rotation angle ϕ of the graphene lattice atop the hBN one. **(d)** STM topography image showing a Moiré pattern atop graphene with a wavelength of $\lambda \simeq 1.2$ nm measured in our 4 K STM. Scalebar : 3 nm.

The existence of a superlattice also alters the electronic properties of graphene, as studied using STM by Yankowitz *et al.* [38], by generating new Dirac points in the bandstructure due to the periodic potential induced by the hBN substrate. They appear in the density of states as two dips at energies $\pm\hbar v_{\mathrm{F}}|\boldsymbol{G}_\alpha|/2 = \pm 2\pi\hbar v_{\mathrm{F}}/\sqrt{3}\lambda$ around the graphene Dirac point $E_{\mathrm{D}} = 0$, where $\boldsymbol{G}_\alpha$ with $\alpha = 1, 2, 3$ are the reciprocal superlattice vectors. These dips are generally of asymmetric strength. In a STS gate map, they move parallel to the original Dirac point when varying the gate voltage. Furthermore, as they cross the Fermi energy, the Moiré dips move quickly due to the vanishing of the density of states at the superlattice Dirac points, in a similar fashion to that of the original Dirac point whose behavior is described by Equation (1.44). Finally, the local density of states displays a periodic modulation in real space with the same period as the Moiré pattern.

1.3.3 Effects of substrate-driven interactions

So far we have described the low energy excitations in graphene in a single-particle picture. Many-body interactions alter the energy dispersion, which then mainly depends on the carrier density n, the momentum k and the Coulomb interaction [39, 40, 41, 42, 43, 44]. A way to quantify these interactions is by introducing the interaction parameter α_{G}, also called the fine-structure constant, given by the ratio of the Coulomb potential to the kinetic energy [20] :

$$\alpha_{\mathrm{G}} = \frac{E_{\mathrm{C}}}{E_{\mathrm{K}}} \tag{1.47}$$

The Coulomb potential is :

$$E_{\mathrm{C}} = \frac{e^2}{4\pi\epsilon_0\epsilon_{\mathrm{m}}\langle r\rangle} \tag{1.48}$$

where ϵ_{m} is the effective dielectric constant of the medium in which the graphene sheet is embedded. Typically, for STM measurements, since graphene is always atop the substrate and in contact with vacuum, ϵ_{m} is the arithmetic mean of the substrate dielectric constant and the unitary vacuum relative permittivity. $\langle r\rangle$ is the averaged interparticle separation which is expressed in a two dimensional system as $\langle r\rangle = 1/(\pi|n|)^{1/2}$. On the other hand, the kinetic energy is the Fermi energy of the system which is given by $E_{\mathrm{F}} = \hbar v_{\mathrm{F}}\,\mathrm{sign}(n)(\pi|n|)^{1/2}$. Since both the kinetic energy and Coulomb potential scale as the square root of the carrier density, α_{G} is independent of the density and we therefore obtain :

$$\alpha_{\mathrm{G}} = \frac{e^2}{4\pi\epsilon_0\epsilon_{\mathrm{m}}\hbar v_{\mathrm{F}}} \simeq \frac{2.2}{\epsilon_{\mathrm{m}}} \tag{1.49}$$

Nonetheless, α_{G} depends on the dielectric medium surrounding graphene, described by ϵ_{m}. The interactions in the system can then be driven by the dielectric properties of the substrate on which the graphene flake lies, from a non-interacting system with $\alpha_{\mathrm{G}} \to 0$ for $\epsilon_{\mathrm{m}} \to \infty$, to a weakly-interacting one with $\alpha_{\mathrm{G}} \sim 2$ for $\epsilon_{\mathrm{m}} = 1$.

Another effect of interactions is the reshaping of the Dirac cone. Many-body theories predict that the ensuing spectrum can be characterized by a renormalized velocity v_{F}^* with a logarithmic divergence at charge neutrality [39, 40, 45], see Figure 1.10 :

$$\frac{v_{\mathrm{F}}^*}{v_{\mathrm{F}}} = 1 - \frac{\alpha_{\mathrm{G}}}{\pi}\left[\frac{5}{3} + \ln(\alpha_{\mathrm{G}})\right] + \frac{\alpha_{\mathrm{G}}}{8}\ln\left(\frac{n_{\mathrm{C}}}{n}\right) \tag{1.50}$$

where v_{F} is the bare Fermi velocity in the absence of interactions and n_{C} is the density corresponding to the ultraviolet cutoff energy $\Lambda \simeq 3$ eV [42], using Equation (1.16). The dispersion velocity then increases with decreasing density due to electron-electrons interactions [46, 47, 48].

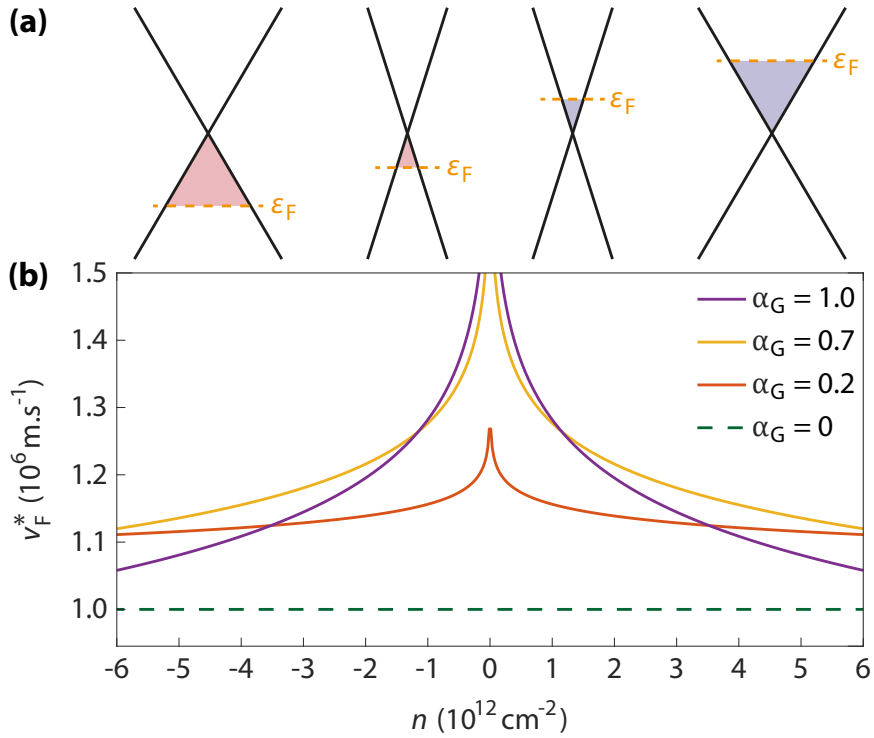

Figure 1.10: Dirac cone reshaping and Fermi velocity renormalization due to electron-electron interactions. (a) As the density decreases, the Fermi velocity increases and the Dirac cone is squeezed. **(b)** Renormalization of the Fermi velocity v_F^* as a function of the carrier density n as given by Equation (1.50), for different interaction parameters α_G. The non-interacting case ($\alpha_G = 0$) is given by the dashed green curve.

Conclusion

In this chapter we introduced most of the physics of graphene at zero magnetic field that is needed in this thesis, starting from its special bandstructure that arises from its honeycomb lattice to the density of states, which has a typical V-shape form. We then briefly presented how transport measurements and tunneling spectroscopy allow us to probe graphene physics. We also explained how hBN can be used as an atomically flat substrate for graphene to reduce the charge puddles. Finally we showed that the many-body interactions in graphene can be substrate-driven via the dielectric environment of graphene. This result is used in Chapter 2 to induce a quantum Hall topological insulator phase in graphene via the use a high-k dielectric substrate.

Quantum Hall effect in graphene

Chapter 2

We study in this chapter the physics of graphene under a perpendicular magnetic field. We describe the relativistic Landau levels that disperse with the square root of the magnetic field and Landau index as well as the corresponding wave functions and density of states in presence of disorder. We then see how quantum Hall edge channels appear at the physical edges of graphene in this regime. The edge physics is investigated with two points of view : by using an electrostatic model developed to depict edge channels in a conventional 2D electron gas and by solving the eigenvalue problem with suitable boundary conditions for both zigzag and armchair edges of graphene. In the last section, we explain how interactions in graphene lift the spin and valley degeneracies, and we present the quantum Hall ferromagnetism. Finally, we focus on the zeroth Landau level, where graphene can exhibit a quantum Hall topological insulator phase with helical transport at charge neutrality.

The results of the transport measurements presented here will be necessary to understand the physics of graphene in the quantum Hall regime probed at the atomic scale by tunneling spectroscopy in the next chapters.

Contents

2.1 Graphene under perpendicular magnetic field

When graphene is placed under a transverse magnetic field, its density of states splits into discrete Landau levels (LLs). For a conventional 2D electron gas with a parabolic dispersion relation, the LLs dispersion is that of a harmonic oscillator $E_N = \hbar\omega_c\,(N + 1/2)$, where $\omega_c = eB/m^*$ is the cyclotron pulsation and m^* the effective mass of electrons. It is thus linear with the magnetic field B and the Landau index N [1] and LLs are equally spaced. We show in this section how the Dirac linear dispersion relation of graphene changes the energetic quantification of the LLs. An important length scale we will introduce is the magnetic length l_B defined as [2] :

$$l_B = \sqrt{\frac{\hbar}{eB}} \simeq 25.65\ \text{nm}\,/\sqrt{B[\text{T}]} \tag{2.1}$$

We then explain how the electronic conduction in graphene under perpendicular magnetic field is done via chiral edge channels, so that graphene exhibits a relativistic quantum Hall effect with a peculiar sequence of plateaus of transverse conductance.

2.1.1 Relativistic Landau levels

The Hamiltonian of graphene in a perpendicular magnetic field $\boldsymbol{B} = B\boldsymbol{e}_z$ is obtained by using the Peierls substitution, which replaces the canonical momentum $\boldsymbol{p} = \hbar\boldsymbol{q}$ by the gauge-invariant kinetic momentum $\boldsymbol{\pi}$:

$$\boldsymbol{p} \longmapsto \boldsymbol{\pi} = \boldsymbol{p} + e\boldsymbol{A} \tag{2.2}$$

where $\boldsymbol{A}$ is the potential vector defined by $\boldsymbol{B} = \boldsymbol{\nabla} \times \boldsymbol{A}$. The substitution is valid as long as l_B is much larger than the lattice constant a. Neglecting the Zeeman effect, the Hamiltonian under magnetic field is therefore deduced from combining the last equation with Equation (1.21) :

$$\widehat{\mathcal{H}}_D^{\xi}(\boldsymbol{B}) = \xi v_{\text{F}}(\pi_x\sigma_x + \pi_y\sigma_y) = \xi v_{\text{F}} \begin{pmatrix} 0 & \pi_x - i\pi_y \\ \pi_x + i\pi_y & 0 \end{pmatrix} \tag{2.3}$$

[1] For a conventional 2DEG with a quadratic energy dispersion, the Schrödinger equation reads as :

$$\left[\frac{(\boldsymbol{p} + e\boldsymbol{A})^2}{2m^*}\right]\Psi(\boldsymbol{r}) = E\Psi(\boldsymbol{r}) \tag{2.a}$$

In the Landau gauge, the potential vector can be written as $\boldsymbol{A} = -By\boldsymbol{e}_x$:

$$\left[\frac{(p_x - eBy)^2 + p_y^2}{2m^*}\right]\Psi(x,y) = E\Psi(x,y) \tag{2.b}$$

We consider a plane wave propagating in the x direction, $\Psi(x,y) = e^{-ik_x x}\psi(y)$, so that the previous equation can be written as :

$$\left[\frac{p_y^2}{2m^*} + \frac{1}{2}m^*\omega_{\text{c}}^2\left(y - \frac{\hbar k_x}{eB}\right)^2\right]\psi(y) = E\psi(y) \tag{2.c}$$

We obtain a one-dimensional Schrödinger equation of a free particle in a quadratic potential, which describes an harmonic oscillator in the y direction with the centre coordinate :

$$y_* = \frac{\hbar k_x}{eB} \tag{2.d}$$

and whose eigenvalues give the linear spectrum :

$$E_N = \hbar\omega_c\left(N + \frac{1}{2}\right) \tag{2.e}$$

[2] l_B depends only on the perpendicular component of the magnetic field.

Since $\boldsymbol{p} \longmapsto -i\hbar\boldsymbol{\nabla}$ and using the commutation relations of the momentum $\boldsymbol{p}$ and position $\boldsymbol{r}$:

$$[x, y] = 0 \qquad [p_x, p_y] = 0 \qquad [r_i, p_j] = i\hbar\delta_{ij} \tag{2.4}$$

then the commutation relation of the kinetic momentum is :

$$[\pi_x, \pi_y] = -ie\hbar\left(\frac{\partial A_y}{\partial x} - \frac{\partial A_x}{\partial y}\right) = -ie\hbar B = -i\frac{\hbar^2}{l_B^2} \tag{2.5}$$

We therefore introduce the ladder operators as :

$$\widehat{a} = \frac{l_B}{\sqrt{2}\hbar}(\pi_x - i\pi_y) \qquad \widehat{a}^\dagger = \frac{l_B}{\sqrt{2}\hbar}(\pi_x + i\pi_y) \tag{2.6}$$

with the commutation relation $[\widehat{a}, \widehat{a}^\dagger] = 1$. We obtain for the kinetic momentum :

$$\pi_x = \frac{\hbar}{\sqrt{2}l_B}(\widehat{a} + \widehat{a}^\dagger) \qquad \pi_y = \frac{i\hbar}{\sqrt{2}l_B}(\widehat{a}^\dagger - \widehat{a}) \tag{2.7}$$

so that the Hamiltonian can be written as :

$$\widehat{\mathcal{H}}_D^\xi(\boldsymbol{B}) = \xi\frac{\sqrt{2}\hbar v_\mathrm{F}}{l_B}\begin{pmatrix} 0 & \widehat{a} \\ \widehat{a}^\dagger & 0 \end{pmatrix} = \xi\hbar\Omega_\mathrm{c}\begin{pmatrix} 0 & \widehat{a} \\ \widehat{a}^\dagger & 0 \end{pmatrix} \tag{2.8}$$

where we have introduced $\Omega_\mathrm{c} = \sqrt{2}v_\mathrm{F}/l_B$ the cyclotron pulsation in the case of relativistic particles. We can now solve the Schrödinger equation to calculate the energy spectrum of relativistic particles in a magnetic field $\boldsymbol{B}$:

$$\widehat{\mathcal{H}}_D^\xi(\boldsymbol{B})\Psi_n = E_n\Psi_n \qquad \text{with the spinor } \Psi_n = \begin{pmatrix} u_n \\ v_n \end{pmatrix} \tag{2.9}$$

which gives the coupled equations :

$$\begin{cases} \xi\hbar\Omega_\mathrm{c}\widehat{a}v_n &= E_n u_n \\ \xi\hbar\Omega_\mathrm{c}\widehat{a}^\dagger u_n &= E_n v_n \end{cases} \quad \Rightarrow \quad (\xi\hbar\Omega_\mathrm{c})^2\,\widehat{a}^\dagger\widehat{a}v_n = E_n^2 v_n \quad \Rightarrow \quad \widehat{a}^\dagger\widehat{a}v_n = \frac{E_n^2}{(\xi\hbar\Omega_\mathrm{c})^2}v_n \tag{2.10}$$

Since $\widehat{a}^\dagger\widehat{a}$ is the number operator, we have $\widehat{a}^\dagger\widehat{a}v_n = nv_n$ with $n \in \mathbb{N}$, and we can derive the energy spectrum of the relativistic Landau levels [49] :

$$E_n = \pm v_\mathrm{F}\sqrt{2\hbar enB} \tag{2.11}$$

Equation (2.11) has two solutions corresponding to LLs at positive and negative energies, with respect to $E_\mathrm{D} = 0$. A better indexation using $N \in \mathbb{Z}$ so that $n = |N|$ gives :

$$E_N = \mathrm{sign}(N)v_\mathrm{F}\sqrt{2\hbar e|N|B} \tag{2.12}$$

where $N > 0$ (resp. $N < 0$) corresponds to electron (resp. hole) -like LLs. Landau levels in graphene disperse as the square root of the index N and the magnetic field B, which differs from the conventional 2D electron gas where $E_N = \hbar\omega_c\,(N + 1/2)$. The dispersion relation for relativistic LLs is shown in Figure 2.1.

In the density of states, this dispersion relation translates as a series of Landau peaks appearing at energies E_N :

$$\rho(E) \propto \sum_{N=-\infty}^{+\infty}\delta(E - E_N) \tag{2.13}$$

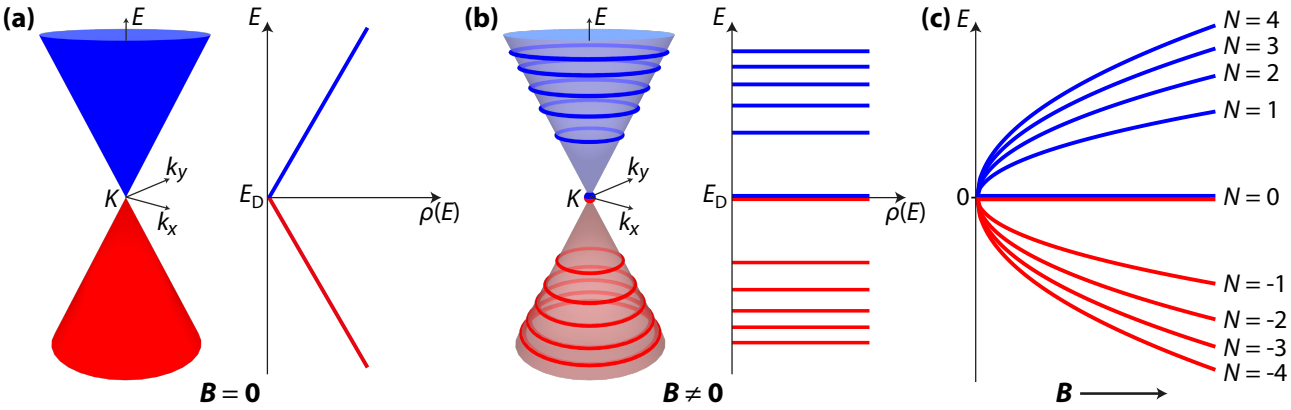

Figure 2.1: Landau levels in graphene. **(a)** Graphene low-energy bandstructure and its linear density of states at zero magnetic field. **(b)** Under a magnetic field, the density of states of graphene splinters into discrete Landau levels. Each LL has a four-fold degeneracy coming from the spin and valley degrees of freedom. **(c)** The Landau levels dispersion with the magnetic field B is given by $E_N = \pm v_\mathrm{F}\sqrt{2\hbar e N B}$ where N is the index of the Landau level.

Compared to the non-relativistic case, the Landau levels are no longer equally spaced and the cyclotron gap decreases with increasing index at a given magnetic field :

$$\hbar\Omega_\mathrm{c} = \Delta E_N = v_\mathrm{F}\sqrt{2\hbar e B}\left(\sqrt{N+1} - \sqrt{N}\right) \propto \frac{1}{\sqrt{N}} \text{ for } N \gg 1 \tag{2.14}$$

Graphene has much larger cyclotron gaps than conventional 2DEGs : for instance the energy gap between the zeroth and first LL in graphene is about $\hbar\Omega_\mathrm{c} = 36.2\,\mathrm{meV}.\sqrt{B[\mathrm{T}]}$ whereas in a 2D electron gas such as GaAs the gap is only about $\hbar\omega_\mathrm{c} = 1.72\,\mathrm{meV}.B[\mathrm{T}]$.

The energy spectrum of Landau levels is independent of the valley isospin ξ, so that LLs are two-fold valley degenerate. With the additional two-fold spin degeneracy (since we neglected the Zeeman effect), each LL has a four-fold degeneracy. LLs are therefore highly degenerate, the degeneracy per unit area being equal to :

$$D = g_\mathrm{s} g_\mathrm{v} \frac{B}{\phi_0} = \frac{4B}{\phi_0} \tag{2.15}$$

where B/ϕ_0 is the orbital degeneracy and $\phi_0 = h/e$ the flux quantum.

Another particularity of graphene is the existence of a zeroth Landau level ($N = 0$) at zero energy, which does not disperse with the magnetic field. Since it lies at zero energy, it belongs to both the valence and conduction bands : this level comprises electrons and holes. The existence of this zeroth Landau level is a direct manifestation of the Berry phase in graphene $\gamma = \pi$ [13, 20] and holds special properties that we will study latter in this chapter.

One can also define the filling factor ν, which represents the ratio between the electron density n and the density of flux quanta n_B :

$$\nu = \frac{n}{n_B} = \frac{n\phi_0}{B} \tag{2.16}$$

ν quantifies the filling of the LLs. In the case of graphene with its four-fold degenerate LLs, filling the N-th LL implies a variation of ± 4 in terms of ν. At charge neutrality ($\nu = 0$), the zeroth LL is half-filled.

2.1.2 Eigenfunctions and cyclotron radius

We describe here the structure of the eigenfunctions of graphene under magnetic field. We consider plane waves propagating in the x direction. Eigenfunctions are specified by the Landau index N, the valley K or K' and the momentum in the x direction $\boldsymbol{k} = k_x \boldsymbol{e}_x$. For each valley, eigenfunctions can be written as two-component spinors with their components on sublattices A and B such that, for the N-th Landau level (LL_N) with $N \neq 0$ [19, 50] :

$$\Psi^{K}_{N\neq 0}(\boldsymbol{r}) = \begin{pmatrix} \Psi^{A,K}_{N} \\ \Psi^{B,K}_{N} \end{pmatrix} = \frac{e^{-ik_x x}}{\sqrt{2L_x}} \begin{pmatrix} \mathrm{sign}(N)\ \phi_{|N|-1}(y - l_B^2 k_x) \\ \phi_{|N|}(y - l_B^2 k_x) \end{pmatrix} \tag{2.17}$$

$$\Psi^{K'}_{N\neq 0}(\boldsymbol{r}) = \begin{pmatrix} \Psi^{A,K'}_{N} \\ \Psi^{B,K'}_{N} \end{pmatrix} = \frac{e^{-ik_x x}}{\sqrt{2L_x}} \begin{pmatrix} \phi_{|N|}(y - l_B^2 k_x) \\ -\mathrm{sign}(N)\ \phi_{|N|-1}(y - l_B^2 k_x) \end{pmatrix} \tag{2.18}$$

$\phi_{|N|}$ is the solution of the 1D harmonic oscillator [51] :

$$\phi_{|N|}(y) = \frac{1}{\pi^{1/4}\sqrt{2^{|N|}|N|!\, l_B}} H_{|N|}\left(\frac{y}{l_B}\right) \exp\left[-\frac{1}{2}\left(\frac{y}{l_B}\right)^2\right] \tag{2.19}$$

where $H_{|N|}$ is a Hermite polynomial[3]. The guiding center, similar to the one for conventional 2DEG, locks the position in the y direction with the momentum in the x direction :

$$y_* = \frac{\hbar k_x}{eB} = l_B^2 k_x \tag{2.20}$$

Zeroth Landau level LL_0 is a special case, its eigenfunctions are given by :

$$\Psi^{K}_{0}(\boldsymbol{r}) = \begin{pmatrix} \Psi^{A,K}_{0} \\ \Psi^{B,K}_{0} \end{pmatrix} = \frac{1}{\pi^{1/4}\sqrt{l_B}} \frac{e^{-ik_x x}}{\sqrt{L_x}} \begin{pmatrix} 0 \\ \exp\left[-(y - l_B^2 k_x)^2/2l_B^2\right] \end{pmatrix} \tag{2.21}$$

$$\Psi^{K'}_{0}(\boldsymbol{r}) = \begin{pmatrix} \Psi^{A,K'}_{0} \\ \Psi^{B,K'}_{0} \end{pmatrix} = \frac{1}{\pi^{1/4}\sqrt{l_B}} \frac{e^{-ik_x x}}{\sqrt{L_x}} \begin{pmatrix} \exp\left[-(y - l_B^2 k_x)^2/2l_B^2\right] \\ 0 \end{pmatrix} \tag{2.22}$$

so that in each valley K and K', its wave functions reside solely on one sublattice, B or A respectively : **valley and sublattice degrees of freedom are equivalent for $\mathbf{LL_0}$.**

Cyclotron radius The broadening of LL_N eigenfunction is given by its squared amplitude :

$$|\Psi_N|^2 \propto \left|H_{|N|}(y/l_B)\right|^2 e^{-y^2/l_B^2} \tag{2.23}$$

which gives a spatial extent for the wave functions of LL_N [52] :

$$R_c = l_B\sqrt{2|N|+1} \tag{2.24}$$

where R_c is the quantized cyclotron radius which scales as the magnetic length l_B : electrons are spatially localized and describe, in a semiclassical picture, quantized cyclotron orbits[4].

[3] $$H_n(y) = (-1)^n e^{y^2} \frac{\mathrm{d}^n}{\mathrm{d}y^n} e^{-y^2} \tag{2.f}$$

Landau level degeneracy The full description of the Landau level quantum states requires to take into account the quantization of the momentum $k_x = k_{x,m} = 2\pi m/L_x$ with the integer $m \geq 0$ being the orbital degeneracy. From Equation (2.20), we obtain a quantization condition on the guiding center coordinate :

$$0 \leq y_* = l_B^2 \frac{2\pi m}{L_x} < L_y \quad \Rightarrow \quad 0 \leq m < \frac{\mathcal{A}}{2\pi l_B^2} \tag{2.25}$$

with $\mathcal{A} = L_x L_y$ the size of the sample, which gives $M = \mathcal{A}/(2\pi l_B^2)$ states, or Landau sites, in each LL. Since each site is spin and valley degenerate, the degeneracy for each LL is therefore :

$$4 \times \frac{\mathcal{A}}{2\pi l_B^2} = 4\frac{eB}{2\pi\hbar}\mathcal{A} = \frac{4B}{\phi_0}\mathcal{A} = D \times \mathcal{A} \tag{2.26}$$

and we retrieved Equation (2.15). Furthermore, a Landau site in LL_N, which can accommodate four electrons, occupies an area :

$$\Delta S = 2\pi l_B^2 \tag{2.27}$$

This result can also be obtained by considering the Heisenberg uncertainty principle on the coordinates of the guiding center, which is thus smeared out over the surface $2\pi l_B^2$. The distance between two Landau sites, which is the minimal distance $\langle r \rangle$ between two electrons in a same LL, is therefore given by :

$$\langle r \rangle \sim l_B \tag{2.28}$$

This has consequences for the Coulomb interaction, whose relevant length scale is thus l_B, as we will discuss in Section 2.3 when considering electron-electron interactions.

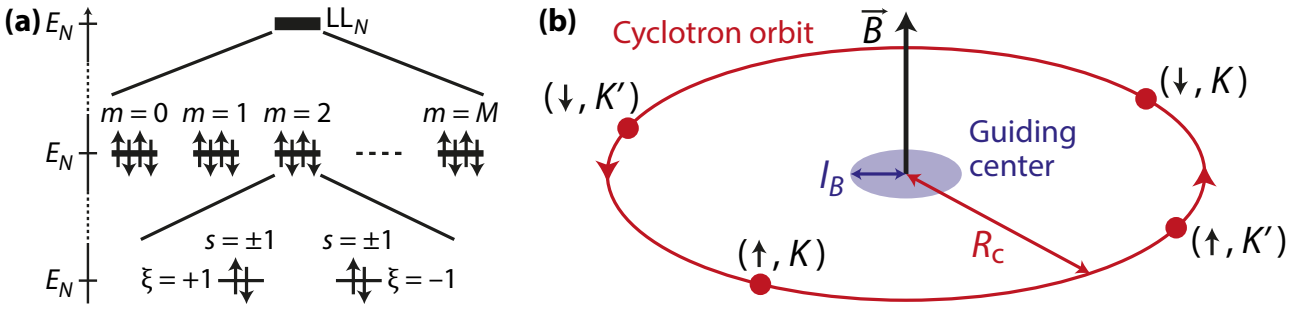

Figure 2.2: Landau level degeneracy and sites. (a) Orbital ($0 \leq m < M$), valley ($\xi = \pm 1$) and spin ($s = \pm 1$) degeneracies. **(b)** Semiclassical picture of the cyclotron motion of electrons. One Landau site is described by an orbital index m, with the corresponding guiding center position - which is the only dynamical variable and is smeared out over an area $2\pi l_B^2$ - and by a LL index N, with its quantized cyclotron radius R_c scaling as $l_B(2|N|+1)^{1/2}$.

[4]This scaling can also be obtained within a semiclassical image using the Bohr-Sommerfeld quantization :

$$\oint \mathrm{d}\boldsymbol{r}.\boldsymbol{k} - \frac{e}{\hbar}\oint \mathrm{d}\boldsymbol{r}.\boldsymbol{A} + \gamma = 2\pi\left(n + \frac{1}{2}\right) \quad , \quad n \in \mathbb{N} \tag{2.g}$$

where the first term is the dynamic phase $\Delta\phi_\mathrm{d}$, the second is the Aharonov-Bohm phase $\Delta\phi_\mathrm{AB}$, $\gamma = \pi$ is the graphene Berry phase, and the integration is done along the closed loop of the cyclotron orbit. Classically the cyclotron radius is given by $R_c = \hbar k/eB = k l_B^2$. We then obtain :

$$\Delta\phi_\mathrm{d} = 2\pi R_c k = 2\pi R_c^2/l_B^2 \quad , \quad \Delta\phi_\mathrm{AB} = -\frac{e}{\hbar}\iint \mathrm{d}\boldsymbol{S}.\boldsymbol{B} = -\frac{e}{\hbar}\pi R_c^2 B = -\pi R_c^2/l_B^2$$

so that Equation (2.g) now reads :

$$\Delta\phi_\mathrm{d} + \Delta\phi_\mathrm{AB} = 2\pi n \Rightarrow R_c = l_B\sqrt{2n}$$

Note that this semiclassical approach fails to retrieve the zeroth Landau level, which is of purely quantum origin.

2.1.3 Local density of states with disorder

In real systems graphene is subjected to various disorder potentials that broaden the LL peaks in the density of states. Champel and Florens [52] computed the electronic Green's function of graphene $\hat{G}(\boldsymbol{r}, \boldsymbol{r}', \omega)$ for an arbitrary disorder potential in the high magnetic field regime, and obtained the local density of states at zero temperature via the formula :

$$\rho^{\text{loc}}(\boldsymbol{r}, E = \hbar\omega) = -\frac{1}{\pi}\Im\text{m Tr}\,\hat{G}(\boldsymbol{r}, \boldsymbol{r}, \omega) \tag{2.29}$$

For locally flat disorder potentials, that is with smooth spatial variations at the scale of the magnetic length l_B, they obtained an expression of the local density of states as a function of the disorder potentials. Though this result can hardly be used to analyze experimental data, where the disorder potential is difficult to evaluate, they concluded that the width of the N-th LL peak grows as $\sqrt{N}$ with increasing LL index N, which originates from the broadening of the wave functions that scales as $\sqrt{2N+1}$. Such behavior was observed experimentally by Li *et al.* [53] and Miller *et al.* [54] by STS measurements. Moreover, they also showed that the density of states in graphene spatially averaged over the disorder :

$$\rho(E) = \overline{\rho^{\text{loc}}(\boldsymbol{r}, E)} \tag{2.30}$$

can be written as a sum of Gaussian peaks :

$$\rho(E) = \frac{1}{2\pi l_B^2}\frac{4}{\sqrt{\pi}}\left[\frac{1}{\Gamma_0}\exp\left\{-\left(\frac{E}{\Gamma_0}\right)^2\right\} + \sum_{N=1}^{+\infty}\frac{1}{2}\sum_{\epsilon=\pm}\frac{1}{\Gamma_N}\exp\left\{-\left(\frac{E-\epsilon E_N}{\Gamma_N}\right)^2\right\}\right] \tag{2.31}$$

where Γ_N is the width of LL_N that can be expressed as a function of the disorder potential.

This typical density of states of graphene is shown in Figure 2.3. One remarks that for $N \gg 1$, the LLs merge due to the cyclotron gap decreasing with N, see Equation (2.14), while $\Gamma_N \propto \sqrt{N}$, forming an overall increasing background for large N. Note also that the density of states increases with the magnetic field, $\rho(E) \propto l_B^{-2} \propto B$: the larger the magnetic field is, the more states there are in each LL. In other words, at fixed carrier density, by increasing the magnetic field, LLs move up in energy, their number of states grows, and fewer electrons occupy the top levels.

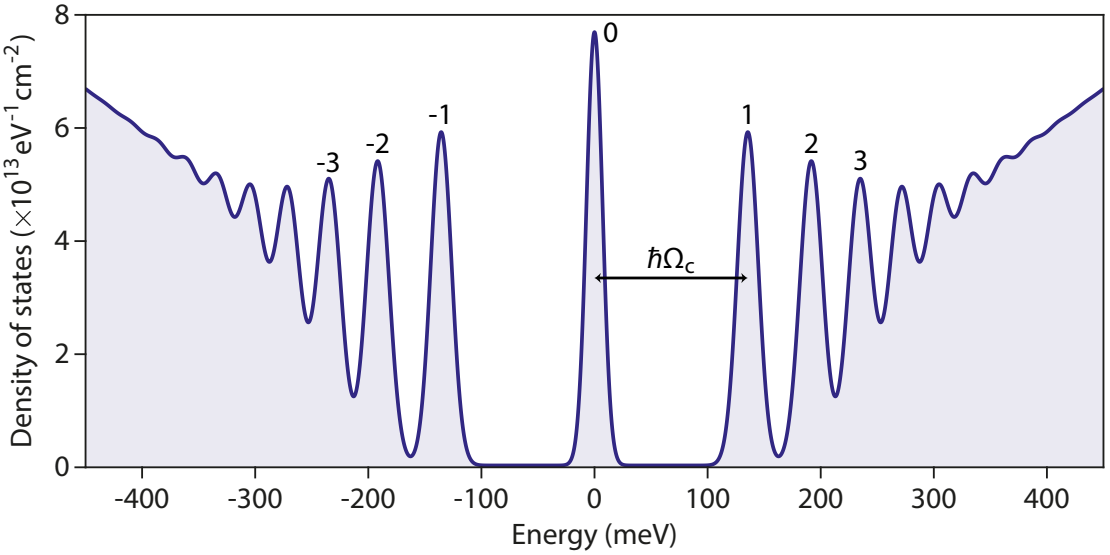

Figure 2.3: Density of states of graphene in magnetic field with Landau levels, at zero temperature plotted using Equation (2.31) with $B = 14\,\text{T}$, $v_\text{F} = 1.0 \times 10^6\,\text{m/s}$, $\Gamma_0 = 10\,\text{meV}$ and $\Gamma_N = \Gamma_0 + 3\,\text{meV} \times \sqrt{N}$. Landau index N is indicated for the first LLs.

The density of states at finite temperature, as measured with STS, is then obtained by convoluting with the derivative of the Fermi-Dirac function, which adds a thermal broadening $\sim k_B T \ll \Gamma_N$ to the intrinsic broadening from disorder. In most STS works on graphene under magnetic field, the width of the LLs is found to be $\Gamma \sim 10$ - 30 meV. This width is related to the elastic scattering time τ_e corresponding to the charge carrier lifetime as $\tau_e \approx \hbar/\Gamma \sim 22$ - 66 fs, which is consistent with values extracted from Shubnikov-de Haas oscillations by Monteverde *et al.* [55]. Notably, they also estimated that τ_e measured from STS and τ_{tr} obtained in transport via the Drude conductivity (introduced in Chapter 1.2.2) are related as $\tau_{tr}/\tau_e \sim 1.8$.

One must also keep in mind that, asides from broadening the peaks, disorder also induces a spatial dispersion of the Dirac point, see Chapter 1.3.1, and as a consequence spatial fluctuations of the positions of the LL peaks. The resulting potential landscape makes electrons in states inside cyclotron gaps, in the tails of the disorder-broadened LL peaks, move around potential hills and valleys, on equipotential lines, see Figure 2.4(a) : such electrons are localized and thus can not contribute to transport. Those states are called *localized states*, in opposition to the *extended states* that, as we will see next, carry the electronic current.

Disorder has a significant impact on the physics of graphene in magnetic field and defines two regimes. The Shubnikov-de Haas regime appears when the cyclotron gap $\hbar\Omega_c$ becomes larger than the broadening due to disorder $\Gamma \approx \hbar/\tau_e$ ($\Omega_c\tau_e \gtrsim 1$). The LLs are there not well separated and the density of states oscillates, see Figure 2.4(b) : the longitudinal conductivity σ_{xx} thus oscillates with the magnetic field and the carrier density, as given by Einstein relation, $\sigma_{xx} = e^2 D \rho(E_F)$, where D is the diffusion coefficient and $\rho(E_F)$ the density of states at the Fermi level. Increasing further the magnetic field, when the cyclotron gap becomes far greater than the width of the peaks ($\Omega_c\tau_e \gg 1$), the LLs are there fully separated, see Figure 2.4(c), and the density of states reaches its minimum value between the peaks, which corresponds to a background density of localized states [56] that pin the Fermi level inside the cyclotron gaps. For these high magnetic fields, we enter in the quantum Hall regime, which is the topic of the next section.

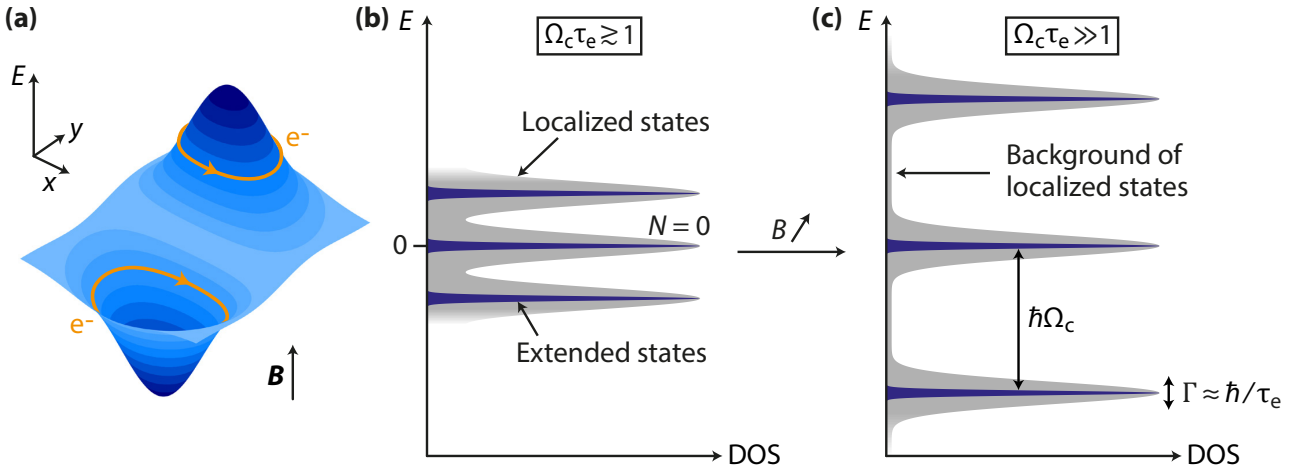

Figure 2.4: Disorder and broadening of Landau levels. **(a)** Localized states around hills and valleys of potential due to disorder. Such electrons move on equipotential lines and can not contribute to transport. **(b)** Shubnikov-de Haas regime ($\Omega_c\tau_e \gtrsim 1$) : the broadening of the LLs is greater than the cyclotron gap, the density of states oscillates and the longitudinal conductivity features oscillations as a function of the magnetic field B and the carrier density n. **(c)** Quantum Hall regime ($\Omega_c\tau_e \gg 1$) : the LL peaks are fully separated with the density of states falling to its minimum value in the gaps.

2.1.4 Relativistic quantum Hall effect

The quantum Hall effect was discovered by von Klitzing in 1980 [57] when he observed in a 2D electron gas under a high magnetic field the appearance of well defined plateaus in the transverse resistance R_{xy} versus the gate voltage while the longitudinal resistance R_{xx} vanishes. The plateaus are precisely quantified to the values :

$$R_{xy} = \frac{h}{e^2 \nu} \tag{2.32}$$

where ν is an integer value of the filling factor, hence the integer quantum Hall effect. The quantum Hall plateaus occur whenever the filling factor ν is close to an integer values (when the Fermi level lies in a cyclotron gap), with the appearance of chiral edge channels at the physical edges of the sample that carry the current, while at the same time the bulk is insulating, preventing backscattering of charge carriers. A striking feature is that this quantization is robust even in the presence of a moderate amount of disorder, this disorder being actually essential for the appearance of quantum Hall plateaus.

In 1982, Tsui, Stormer and Gossard [58] discovered a plateau at a fractional value $\nu = 1/3$ which opened the field of fractional quantum Hall physics. Such fractional plateaus can no longer be explained using a one-particle picture as in the integer case, electron-electron interactions must be considered. Nonetheless, the fractional quantum Hall physics is beyond the scope of this thesis and we focus here on the integer quantum Hall physics of graphene.

2.1.4.a Relativistic quantum Hall effect in graphene

Integer quantum Hall effect was observed in graphene in 2005 by Novoselov *et al.* [2] (see Figure 2.5) and by Zhang *et al.* [13]. Due to the relativistic nature of charge carriers, the quantum Hall plateaus appear at specific integer values of the quantum of conductance :

$$G_{xy} = 4\left(N + \frac{1}{2}\right)\frac{e^2}{h} \quad , \quad N \in \mathbb{Z} \tag{2.33}$$

which gives the series of filling factors $\nu = 2(2N+1) = \pm 2, \pm 6, \pm 10 \ldots$

We show in the following that this peculiar quantification $4N + 2$ of the filling factor comes from the four-fold degeneracy of LLs in graphene, which implies of variation of $\Delta\nu = \pm 4$ for filling or emptying LL_N. Moreover, the shift of 2 originates from the existence of the zero-energy LL, which is half-filled at $\nu = 0$ [59].

New plateaus outside the above sequence were later discovered, at $\nu = \pm 1$ and $\nu = \pm 4$ by Zhang *et al.* [60] and also plateaus at $\nu = \pm 3$ in suspended graphene by Du *et al.* [61]. In 2011, Dean *et al.* [36] developed the fabrication process to stack graphene on an atomically flat flake of hBN, improving graphene quality and boosting the mobility. Young *et al.* [62] eventually observed plateaus at every integer value of the filling factor ν on such graphene/hBN devices. The appearance of those plateaus is a consequence of the breaking of the spin and valley symmetries of the LLs, which is the topic of Section 2.3. Fractional quantum Hall effect was also measured in suspended graphene by Bolotin *et al.* in 2009 [63] and in graphene/hBN samples by Dean *et al.* in 2011 [64].

For further insight on the quantum Hall effects, see works of Goerbig [19, 65] and Weis and von Klitzing [66], as well as books [67, 68, 69].

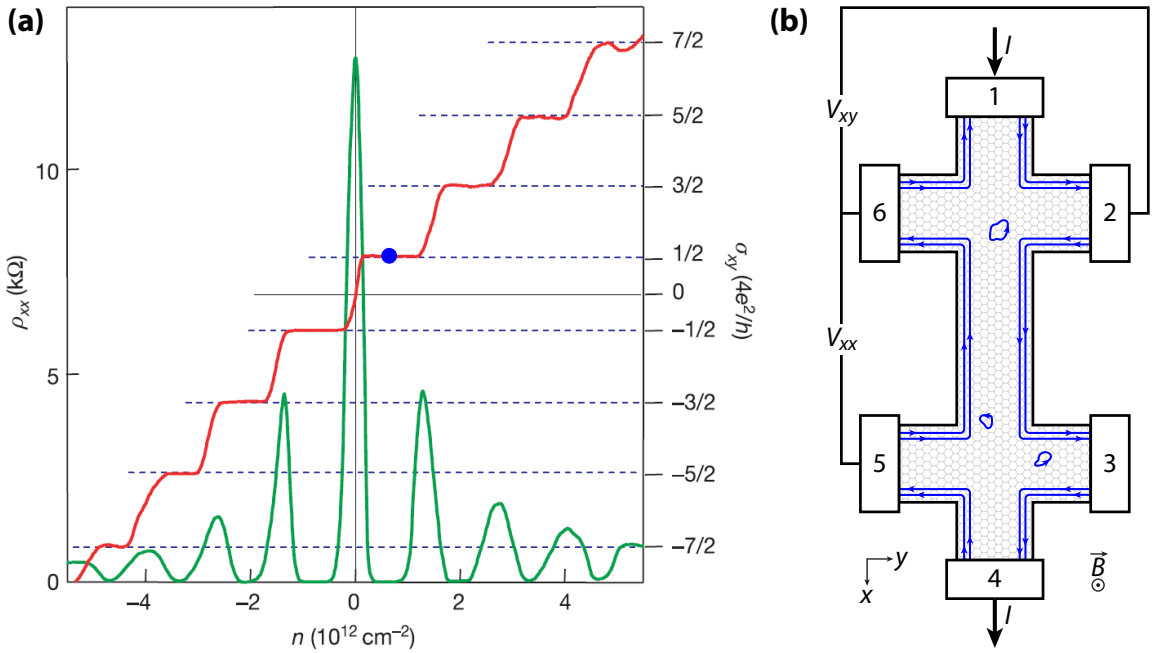

Figure 2.5: Relativistic quantum Hall effect in graphene. (a) Hall conductivity σ_{xy} (red) and longitudinal resistivity ρ_{xx} (green) of graphene as a function of charge carrier density n at $B = 14\,\mathrm{T}$ and $T = 4\,\mathrm{K}$: the transverse conductivity σ_{xy} exhibits quantized plateaus following the sequence given by Equation (2.33) while the longitudinal resistivity ρ_{xx} simultaneously drops to zero. Figure taken from [2]. **(b)** In the six-terminal configuration of a Hall bar, edge channels circulate in a clockwise direction and connect neighboring contacts. The current I is driven from contact 1 to 4. The longitudinal (resp. transverse) resistance is determined by the voltage drop V_{xx} between 2 and 3 or between 5 and 6 (resp. V_{xy} between 2 and 6 or between 3 and 5). Graphene state corresponds to the blue dot in (a).

2.1.4.b Conduction channels at the edges

We suppose in this paragraph that the Fermi level E_F lies in a cyclotron gap. In the bulk of graphene (or other 2DEG), charge carriers move, in a semiclassical image, in closed circular cyclotron orbits and are spatially localized. They therefore do not carry any current and the bulk is insulating. This result is retrieved with the energy dispersion of charge carriers given by Equation (2.e) for a 2DEG and Equation (2.12) for graphene, which is independent of the wave vector $\boldsymbol{k}$. The group velocity is thus zero :

$$v_\mathrm{g} = \frac{1}{\hbar}\frac{\partial E_N}{\partial k} = 0 \tag{2.34}$$

We now consider the physical finite size of the device in the y direction. The wave function of electrons ψ must vanish at the edges of the sample, which justifies that the electron density $|\psi|^2$ is zero at the edge. In 1982, Halperin [70] showed, in the case of a conventional 2DEG, that this condition at the edge consequently shifts the energies of the eigenstates away from the Landau energies toward higher energies (see also the work of MacDonald *et al.* [71]). Edge states can thus be described by introducing a confining potential $V(y) > 0$ that diverges at the edges of the device, preventing electrons from leaving the 2DEG. Equation (2.c) now reads as :

$$\left[\frac{p_y^2}{2m^*} + \frac{1}{2}m^*\omega_\mathrm{c}^2\,(y - y_*)^2 + V(y_*)\right]\psi_N(y) = E_N\psi_N(y) \tag{2.35}$$

with $y_* = l_B^2 k_x$ the guiding center coordinate, see Equation (2.20), which yields eigenenergies :

$$E_N(y_*) = \hbar\omega_\mathrm{c}\left(N + \frac{1}{2}\right) + V(y_*) \tag{2.36}$$

Equivalently, the confining potential in graphene adds to the relativistic LL spectrum and induces a bending at the edges. For both cases, the group velocity with the confining potential is then :

$$v_{\mathrm{g}} = \frac{1}{\hbar}\frac{\partial E_N(y_*)}{\partial k} = \frac{1}{\hbar}\frac{\partial V(y_*)}{\partial k_x} = \frac{1}{eB}\left.\frac{\partial V(y_*)}{\partial y_*}\right|_{y_*=l_B^2 k_x} \tag{2.37}$$

The confining potential causes the group velocity to become non-zero at the edges of the sample and edge states therefore appear at the perimeter of the device, at the intersections of those bended LLs with the Fermi level. In a semiclassical image, those extended states can be seen as cyclotron orbits bouncing on a hard wall. They carry the current and do not become localized in the presence of a disorder potential weak compared to the cyclotron gap.

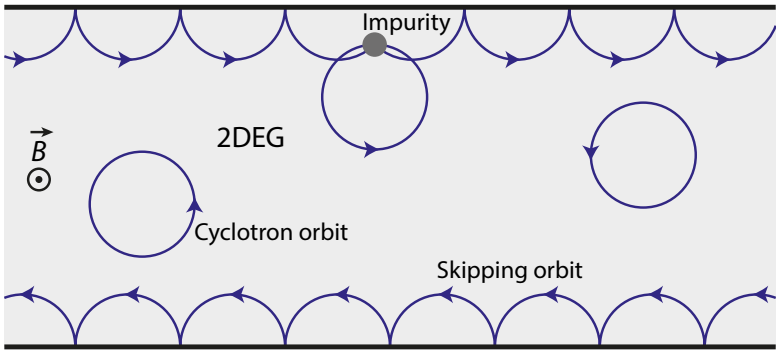

Figure 2.6: Cyclotron and skipping orbits, forming localized states in the bulk and extended states at the edge. The presence of an impurity on the edge only induces forward scattering.

For the following we apply Halperin's image in the case of graphene in a one-electron picture, for instance the typical Hall bar represented in Figure 2.5(b). The confining potential $V(y)$ can either originate from the vanishing of the wave functions at the edge condition alone, or from an external electrostatic potential. In both cases, the confining potential causes the electron-like LLs ($N > 0$) to bend upward when approaching the edges of the sample, see Figure 2.7. Symmetrically, the confinement of holes makes the hole-like LLs ($N < 0$) bend downward when approaching the edges. Note that in the case of the zeroth LL, half of it (electron-like states) bends upward on the edges while the other half (hole-like states) bends downward.

Let us consider $E_{\mathrm{F}} > 0$. On the edges, since each electron-like LL bends up, every $N \geq 0$ LL below the Fermi energy crosses it at both sides of the samples. At the intersecting points, one-dimensional conducting channels appear at the sample edges, see Figure 2.7(a). From Equation (2.37), the group velocity depends directly on the slope of the confining potential, which has opposite signs on both sides of the sample. This results in chiral edge channels, which are counter-propagating at the opposite edges of the sample. Furthermore, all the edge channels on one side of the sample propagate in the same direction. In Section 2.2.2 we will elaborate on the exact dispersion of the LLs at the graphene edges.

2.1.4.c Transport through edge channels

Let us now see how the appearance of edge channels translates in terms of longitudinal and transverse conductance as measured in a graphene Hall bar. Due to the macroscopic distance between the edges and the insulating bulk, backscattering is entirely suppressed and the transport is ballistic : no voltage drop happens and contacts connected by the edge channels have the same potential. The longitudinal resistance R_{xx} measured in the Hall bar is therefore zero.

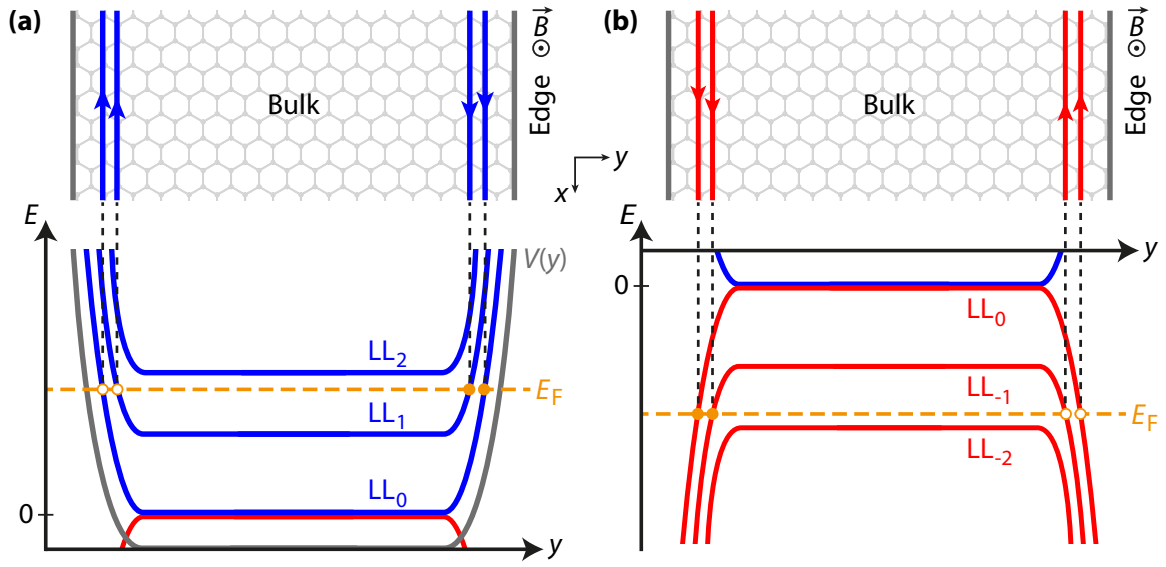

Figure 2.7: Emergence of edge channels. **(a)** Under a perpendicular magnetic field $\boldsymbol{B}$, graphene bulk is insulating. At the edges, the confining potential $V(y)$ makes the electron-like LLs bend up. When the LLs cross the Fermi energy, one-dimensional edge channels arise. **(b)** Hole-like LLs bend downward due to the confinement potential, and the resulting edge channels have opposite direction with respect to the electron-like ones.

In this ballistic regime, the transverse conductance is quantized and function of the number of propagating edge channels, given by the filling factor ν which is the integer number of filled LLs from charge neutrality. Each edge channel is degenerate four times in graphene, except the ones coming from the zeroth LL, which are only two times degenerate (only half of this level bends upward), which gives the series of the filling factor $\nu = \pm 2, \pm 6, \pm 10 \ldots$ for the number of edge channels when E_F is inside a cyclotron gap. Since each edge channel carries a quantum of resistance, defined by the von Klitzing constant $R_\mathrm{K} = h/e^2 \simeq 25.8\,\mathrm{k\Omega}$, the transverse resistance of the Hall bar is $R_{xy} = h/e^2\nu$. In terms of conductivity, since the conductivity tensor $\boldsymbol{\sigma}$ for bidimensional transport is equal to the inverse of the resistivity tensor $\boldsymbol{\rho}$:

$$\boldsymbol{\sigma} = \begin{pmatrix} \sigma_{xx} & \sigma_{xy} \\ \sigma_{yx} & \sigma_{yy} \end{pmatrix} = \boldsymbol{\rho}^{-1} \quad \Rightarrow \quad \sigma_{xx} = \frac{\rho_{xx}}{\rho_{xx}^2 + \rho_{xy}^2} \quad , \quad \sigma_{xy} = \frac{\rho_{xy}}{\rho_{xx}^2 + \rho_{xy}^2} \tag{2.38}$$

one thus notices that when the longitudinal resistance ρ_{xx} is zero, the longitudinal conductivity σ_{xx} is also zero, and $\sigma_{xy} = 1/\rho_{xy}$ so that both the transverse resistivity and conductivity are quantized and present plateaus.

For further insight on magnetotransport in a Hall device, see works of Halperin [72] and Büttiker [73].

2.1.4.d Role of disorder

Finally, we describe how transport measurements in the quantum Hall regime yield consecutive plateaus of quantized transverse conductance as a function of the filling factor ν, which is tuned either with the carrier density (through the gate voltage) or with the magnetic field, see Equation (2.16). Previously in Figure 2.7 the LLs have been assumed to be flat with no spatial dependence. We suppose now the existence of a disorder potential, which makes the LLs in the bulk exhibit spatial fluctuations with random hills and valleys of potential.

When the Fermi level $E_F > 0$ lies inside a cyclotron gap between two LLs, edge channels appear for every LL below E_F which bends up, forming extended states circulating on the whole perimeter of the sample. In bulk graphene, the potential fluctuations of the closest LL locally cross E_F and form localized states, where electrons are trapped, circulating on closed equipotential lines around potential valleys, see Figure 2.8(a), and thus do not contribute to the electronic transport : the transverse conductance is here quantized. The localized states exist in the tail regions of the broadened LLs due to disorder, see Figure 2.4, and are fundamental for the occurrence of the quantum Hall effect : as long as E_F is pinned inside the cyclotron gap due to those localized states, the bulk remains insulating and transverse conductance is quantized, which gives a finite width to quantum Hall plateaus. On the contrary, for an ideally clean sample with no disorder and hence no states in the cyclotron gaps, E_F would jump from one LL directly to the next one and the plateaus width would shrink to zero.

The transitions between quantum Hall plateaus as for them correspond to the regime where one LL is being filled by increasing the carrier density : the valleys of potential, and the ensuing localized states, grow larger and merge together, eventually forming a percolating state in the bulk which connects the opposite edges of the sample, see Figure 2.8(b). Bulk graphene becomes conductive and backscattering of electrons between counterpropagating edge channels is possible, such that transport is not quantized anymore. Increasing further the carrier density, the percolating state fully expands, forming a new extended state, and yields one new set of edge channels, while electrons in the bulk become localized again, this time in states around hills of potential, and transport get quantized, see Figure 2.8(c). Furthermore, this evolution from localized to extended states has been observed by Hashimoto *et al.* in 2008 [74] by STS measurements on an InSb surface.

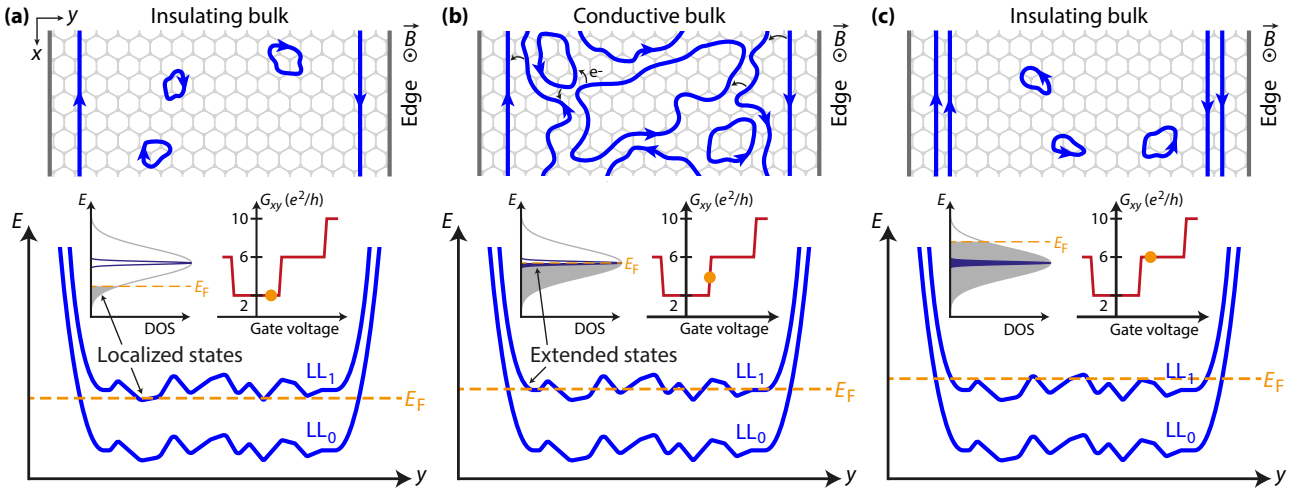

Figure 2.8: Quantum Hall effect and percolation of edge channels. Evolution of the state of graphene as we increase the Fermi level, from (a) to (c), and fill the first LL. **(a)** At $\nu \gtrsim 2$ and E_F below LL_1, potential fluctuations of LL_1 locally cross the Fermi level and form localized states in the insulating bulk graphene, while edge channels (extended states) from LL_0 circulate around the perimeter of the sample. The transverse conductance G_{xy} is quantized at $2\,e^2/h$. **(b)** Increasing ν by filling LL_1, localized states increase in number and size, eventually forming a percolating state in bulk graphene through which electrons can backscatter from one side of the sample to the other. The device bulk undergoes a metal-insulator transition and the transverse resistance is no longer quantized. **(c)** At $\nu \lesssim 6$, the percolating state fully extends on the whole sample and forms one new set of two counterpropagating edge channels. The bulk transits into an insulating state, with few localized states, and the transverse conductance G_{xy} becomes quantized at $6\,e^2/h$.

2.2 Quantum Hall edge physics

In this section we study the physics of the quantum Hall edge channels in graphene. Though the addition of a confining potential to the Landau level spectrum easily explains the band bending at the edge of the 2D gas, and the appearance of one-dimensional edge channels, this naive one-electron picture does not embody the full edge physics and fails to give exact dispersion solutions and edge states. We consider two cases in the following. First we study the electrostatics of edge channels as modeled by Chklovskii, Shklovskii and Glazmann for a smooth gate-induced confining potential as in conventional 2DEGs such as GaAs. Secondly we solve exactly the problem at the edges of graphene, with the vanishing of the wave functions at the last row of atoms on the edge as boundary conditions, for both zigzag and armchair edges.

2.2.1 Electrostatics of edge channels

If the naive one-electron picture presented in Section 2.1.4 is enough to understand the overall physics of the quantum Hall effect, it suffers serious drawbacks to describe the edge channels themselves. For instance, the positions of the edge states are given by the intersections, at one single point, of the bended LLs with the Fermi level, which results in infinitely narrow channels. Those zero-width edge channels cause singularities in the charge carrier density in graphene as we approach the edge, which is not physically possible. Furthermore, this one-electron picture also fails to account for the screening in the 2DEG, which depends strongly on the filling factor due to the oscillating density of states.

We study here the self-consistent model of edge channels reconstruction as developed by Chklovskii, Shklovskii and Glazmann in 1992 [75], where they addressed quantitatively the electrostatics of edge channels in a conventional 2DEG with a gate-induced confinement in the quantum Hall regime. This results in a splitting of the electron gas into alternating strips of incompressible and compressible liquid, as previously introduced qualitatively by Beenakker [76] and Chang [77] in 1990. See also works of Chklovskii *et al.* [78] and Lier *et al.* [79].

2.2.1.a Screening in a 2DEG in strong magnetic fields

In a 2D electron gas under perpendicular magnetic field, only partially filled LLs contribute to the screening. This implies that regions of integer filling factor ν do not screen the external potential, while the screening is strong at half-filling factor when the Fermi level lies at a maximum of the density of states, as shown by Efros in 1988 [80, 81]. To understand this we can introduce the compressibility of the electron gas :

$$\kappa = \frac{1}{n^2}\frac{\partial n}{\partial \mu} \tag{2.39}$$

with n the charge carrier density and μ the chemical potential. When the Fermi level lies in the cyclotron gap, the carrier density does not vary with the potential so that $\partial n/\partial \mu = 0$ which implies $\kappa = 0$: the system is incompressible. The electron gas can not be rearranged to screen an external potential. On the contrary, when the Fermi energy is pinned inside a LL, the system becomes compressible. Since the density of states at the Fermi level is at its maximum, the electrons can rearrange themselves and screening is possible. Screening is therefore highly dependent on the filling factor ν, which varies toward the edge on the gas, from its bulk value to zero at the boundary.

2.2.1.b Gate-induced boundary in a conventional 2DEG

We consider in this section a conventional 2DEG, obtained for instance in GaAs semiconducting heterostructures, with a confining potential formed by an external gate with a negative voltage $-V_g$, which creates the boundary of the 2DEG. This potential is supposed smooth at the scale of the magnetic length l_B. The negative gate voltage repels electrons in the 2DEG and creates a depleted strip of width $2l$ where the electron density is zero. The depletion layer length l is given by [75] :

$$l = \frac{V_g(4\pi\epsilon_0)\epsilon_r}{4\pi^2 n_0 e} \tag{2.40}$$

with ϵ_r the dielectric constant of the semiconductor surrounding the 2DEG, and n_0 the electron density far from the boundary. The electron density grows gradually from zero at the end of the depletion strip ($y = l$) to n_0 in the bulk. At zero magnetic field, the electron density in the 2DEG for $y > l$ varies as :

$$n_0(y > l) = n_0\sqrt{\frac{y-l}{y+l}} \tag{2.41}$$

Note that l defines both the width of the depletion strip and the electron density variation length, see Figure 2.9. Moreover, in this system, the gate-induced confining potential varies on the scale of l, which is usually of the order of 1 µm [5]. This is much more important than in the case of graphene, where the confining of the electron is done by the native edge of graphene on a scale of a few l_B as we see in Section 2.2.2.

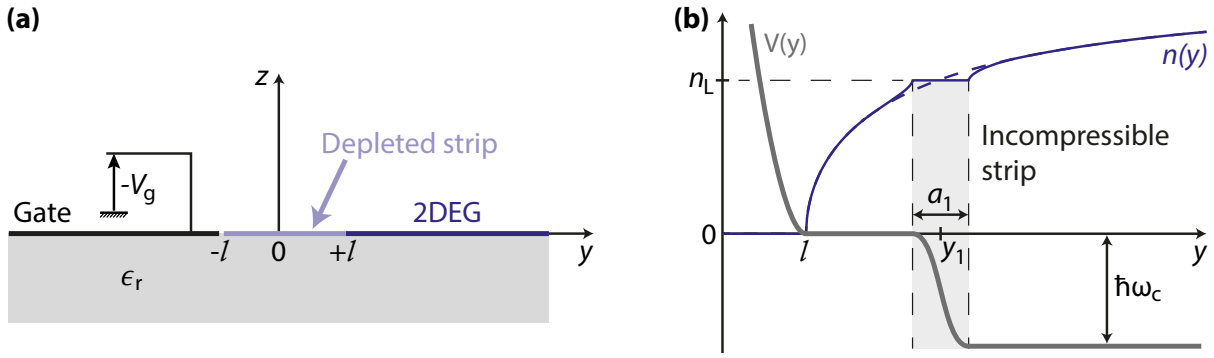

Figure 2.9: Electrostatic confinement and bending. (a) Gate-induced boundary in a 2DEG. A negative gate voltage $-V_g$ creates a depleted strip in the 2DEG. **(b)** Formation of an incompressible strip at the edge of the 2DEG for a bulk filling factor $\nu_0 = 1.5$. $n(y)$ is the electron density and $V(y)$ is the gate-controlled electrostatic confining potential. The dashed blue line is the electron density at zero magnetic field as given by Equation (2.41).

2.2.1.c Edge channels reconstruction

Applying a magnetic field causes the screening in the 2DEG to be periodic on the filling factor ν. Let us consider the case where the Fermi level lies in the cyclotron gap between LL_2 and LL_3. The bulk is then insulating and all the LLs below E_F are filled, giving an integer bulk filling factor $\nu_0 \gtrsim 2$ (we ignore the electron spin).

Near the boundary of the 2DEG, when the electrostatic confining potential $V(y)$ starts to diverge, the LLs bend up until LL_2 crosses E_F. An edge channel appears and LL_2 starts to be emptied, which decreases locally the filling factor $1 < \nu < 2$. A strong screening consequently develops locally, the confining potential becomes completely screened and is constant as in

[5] The distance between the gate and the 2DEG, of the order of 100 nm, can thus be neglected.

a metal. The LLs do not bend up anymore and LL_2 stays pinned at the Fermi energy. The corresponding edge channel therefore acquires a finite spatial lateral expansion, see Figure 2.10(a), and this regime keeps going as long as there are some states in LL_2 to be emptied after what LLs start again to bend up. This mechanism is then repeated for the lower LLs.

Eventually, this leads to the formation of alternating strips, parallel to the gate edge, of conductive compressible liquid - the edge channels, characterized by a non-integer filling factor ν with screened constant electrostatic potential - and of insulating incompressible liquid - characterized by integer ν with no screening and constant electron density[6].

2.2.1.d Compressible and incompressible strips

Since one Landau site occupies an area $2\pi l_B^2$, the electron density corresponding to one completely filled LL is :

$$n_{\mathrm{L}} = \frac{1}{2\pi l_B^2} \tag{2.42}$$

Chklovskii *et al.* [75] computed the position and width of the incompressible and compressible strips. For a bulk with N completely filled LLs, N incompressible strips form at the edge. The position y_k of the k-th incompressible strip with a filling factor $\nu = k$ $(1 < k < N)$ is then found by substituting $n(y) = k/2\pi l_B^2$ in Equation (2.41) :

$$y_k = l\frac{\nu_0^2 + k^2}{\nu_0^2 - k^2} \tag{2.43}$$

with $\nu_0 = n_0/n_{\mathrm{L}}$ the filling factor in the bulk. In the vicinity of y_k, the electron density $n(y)$ is flattened due to charge relocation from LL_{k+1} to LL_k, on the width of the incompressible strip a_k, which is given by :

$$a_k = \left[\frac{2\hbar\omega_{\mathrm{c}}(4\pi\epsilon_0)\epsilon_{\mathrm{r}}}{\pi^2 e^2\ \mathrm{d}n/\mathrm{d}y|_{y=y_k}}\right]^{1/2} = \frac{4}{\sqrt{\pi}}\left[\frac{\nu_0 k^{1/2}}{\nu_0^2 - k^2}\right](a_{\mathrm{B}}l)^{1/2} \tag{2.44}$$

This width is shown to be very small compared to the depletion length l : $a_k/y_k \sim (a_{\mathrm{B}}/l)^2 \ll 1$ with a_{B} the Bohr radius defined by :

$$a_{\mathrm{B}} = \frac{4\pi\epsilon_0\epsilon_{\mathrm{r}}\hbar^2}{m^* e^2} \sim 10\ \mathrm{nm} \tag{2.45}$$

for GaAs with dielectric constant ϵ_{r} and effective electron mass m^*. Consequently, the width of the compressible strips b_k can be approximated as $b_k = y_k - y_{k-1}$ for the compressible strip on the left from y_k, and is given by, for ν_0 , $k \gg 1$:

$$b_k = \frac{n_{\mathrm{L}}}{\mathrm{d}n/\mathrm{d}y|_{y=y_k}} \Rightarrow \frac{a_k}{b_k} = \frac{1}{\sqrt{\pi}}\frac{\nu_0^2 - k^2}{\nu_0 k^{1/2}}\left(\frac{a_{\mathrm{B}}}{l}\right)^{1/2} \tag{2.46}$$

As a result, the widths of the incompressible strips scale as $(a_{\mathrm{B}}l)^{1/2}$ while those of the compressible strips scale as l. Note also that $a_k/b_k \sim (a_{\mathrm{B}}/l)^{1/2} \ll 1$: the incompressible strips are narrower than the adjacent compressible ones. Both strips get narrower as we move closer to the edge : the innermost strips are the widest. Finally, widths of incompressible and

[6]Note that there is some debate with this model as to where the current actually circulates. On the one hand, there is a non-zero density of states at the Fermi level in the compressible strips, but the group velocity is zero (since the confining potential is there screened and flat). On the other hand, the group velocity is not zero in the incompressible strips but there is no density of states at the Fermi level.

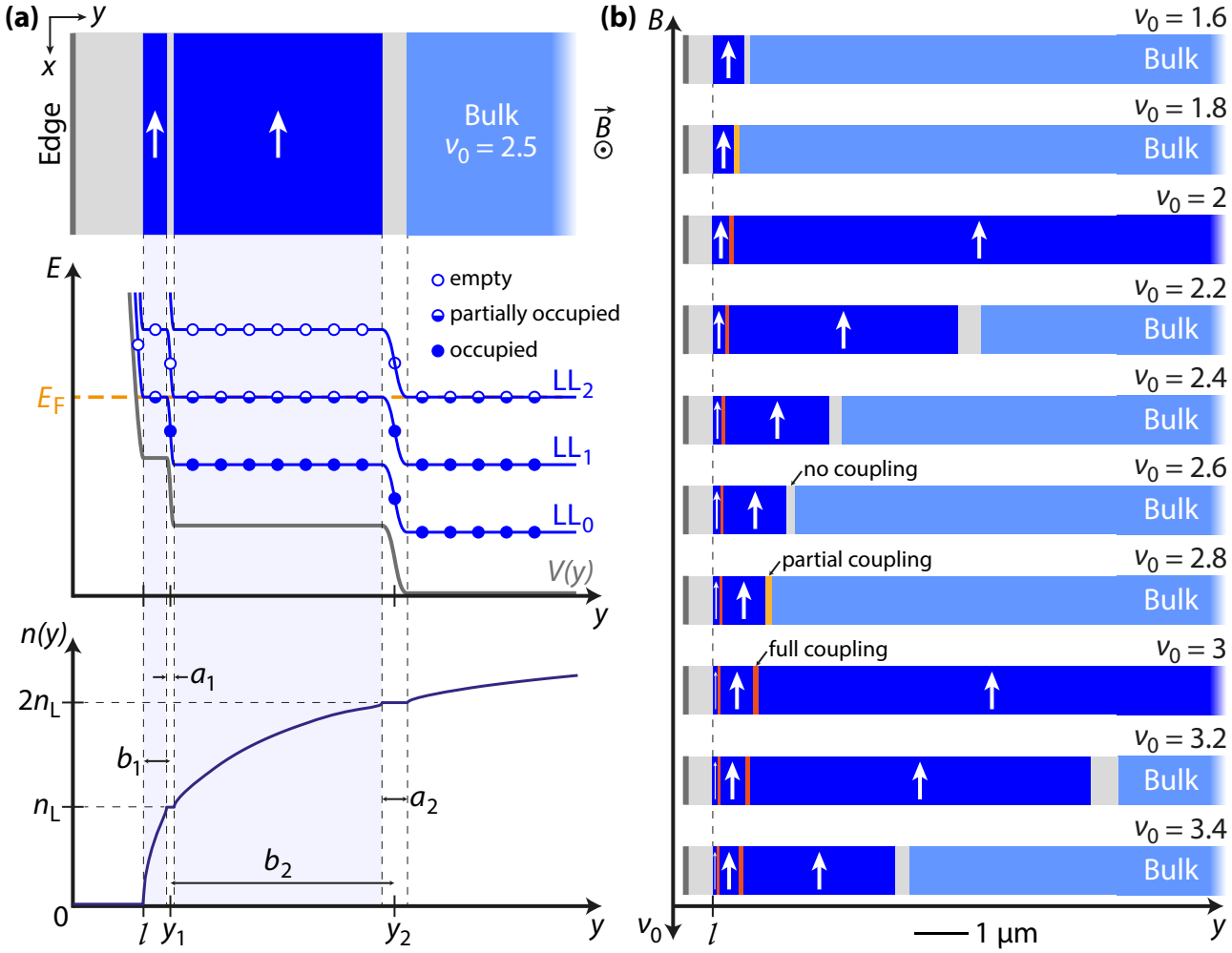

Figure 2.10: Self-consistent electrostatic model of edge channels. **(a)** Top : 2DEG near the edge for bulk filling factor $\nu_0 = 2.5$. Blue regions are compressible liquids (non-integer filling factor) while gray regions are incompressible liquids (integer filling factor). Middle : Electrostatic potential $V(y)$ and LLs at the edge. Circles represent the local filling of the LLs. In compressible strips, $V(y)$ is screened. Bottom : Electron density $n(y)$ variation at the edge. In incompressible strips, the density flattens at integer values of the filling factor. **(b)** Evolution of the spatial distribution of edge channels with the magnetic field. Red incompressible strips are small enough to enable full coupling between adjacent compressible strips, bigger yellow strips only enable partial coupling while gray ones are too wide to allow any coupling. Transport is quantized only when the bulk is completely decoupled from the edge channels.

compressible strips were also shown to obey to an universal relation that does not depend on the magnetic field, the distance from the 2DEG boundary nor the charge density gradient :

$$a_k^2 = \frac{4}{\pi} b_k a_B \tag{2.47}$$

Typically, the lengths of the compressible strips are of the order of 100 nm in GaAs.

2.2.1.e Evolution with the magnetic field

Here we describe the transition that occurs in the 2DEG when increasing the magnetic field as interpreted by Chklovskii *et al.* [75]. Figure 2.10(b) shows the evolution of the compressible and incompressible strips at the edge of the 2DEG as a function of the magnetic field B, using Equations (2.43) and (2.44) to compute the positions and widths of the incompressible strips as a function of the bulk filling factor $\nu_0 \propto B^{-1}$.

Let us start at a magnetic field B such as $\nu_0 \gtrsim N \in \mathbb{N}$. The innermost N-th incompressible strip is wide enough to separate the bulk from the N equilibrated edge channels, preventing backscattering of electrons through the compressible bulk : the transverse resistance is quantized at $R_{xy} = h/e^2N$. By increasing B, ν_0 decreases, the strips grow and move away from the edge toward the bulk, see Figure 2.10(b). When $\nu_0 = N$, the N-th incompressible strip becomes infinitely large and eventually disappears. Decreasing ν_0 further, equilibration[7] between the N-th edge channel and the others becomes more and more difficult as the $(N-1)$-th incompressible strip grows larger : the transverse resistance increases. Equilibration is suppressed when $\nu_0 \lesssim N$ and the $(N-1)$ edge channels become completely decoupled from the infinitely large N one which becomes the new bulk. The transverse resistance gets quantized at $R_{xy} = h/e^2(N-1)$, and the reasoning starts again when $\nu_0 \gtrsim N-1$.

2.2.1.f Case of graphene

The electrostatic model of edge channels developed by Chklovskii *et al.* [75] is valid for a conventional 2DEG. Gutiérrez *et al.* [82] and Kim *et al.* [83] adapted it to the case of graphene with a gate-induced boundary. They derived a similar equation for the k-th incompressible strip width at position y_k from the edge :

$$a_k = \left[\frac{4(4\pi\epsilon_0)\epsilon_{\mathrm{m}} \Delta E_{\mathrm{LL}}}{\pi^2 e^2 \ \mathrm{d}n/\mathrm{d}y|_{y=y_k}} \right]^{1/2} \tag{2.48}$$

with $\Delta E_{LL} = E_{k+1} - E_k$ the cyclotron gap given by Equation (2.14). The main difference is the geometry of the system. Here graphene lies between two dielectric media. If graphene is exposed to vacuum, the effective dielectric constant is $\epsilon_{\mathrm{m}} = (\epsilon_{\mathrm{r}} + 1)/2$ with ϵ_{r} the dielectric constant of the substrate below graphene. There is also a difference in the numerical prefactor : 2 in Equation (2.44) instead of 4 here.

2.2.2 Edge states in graphene

We study in the following the edge states that appear at the physical edges of graphene. Since graphene is a 2D crystal, one can obtain exact solutions for the edge states with the boundary condition that the wave function must vanish at the edge[8]. The honeycomb lattice presents two different terminations : zigzag and armchair edges (see Figure 2.11). In a zigzag edge, the atoms of the last row belong to the same sublattice A or B whereas, in an armchair edge, the last row is comprised of A-B dimers. We explain the edge dispersion at both types of graphene edge. We see that for both edges, the number of dispersing states is the same, which is consistent with the observation of the relativistic quantum Hall effect in real-system graphene, where edges can be zigzag, armchair or a succession of both.

In the following we consider graphene ribbons, infinite in one dimension, with the geometry shown in Figure 2.11(a) : for the ribbon with armchair (resp. zigzag) edges, the boundaries are along the x (resp. y) axis and the graphene ribbon is infinite in the x (resp. y) direction. We also suppose that the ribbon is large enough so that the two edges are decoupled.

[7] Tunneling between adjacent edge channels is determined by the overlap between the corresponding wave functions, which decreases exponentially with the distance.

[8] Note here the absence of an external electrostatic confining potential. We go back to Halperin's approach [70] where the confinement of charge carriers is naturally achieved with the vanishing of the wave functions at the edges of the crystal, which has been shown to induce a dispersion of the eigenenergies toward higher energies.

2.2.2.a Boundary conditions

The tight-binding model of graphene is valid up to the last row of atoms near the boundary : the wave function must vanish on the first next line that does not contain any atom. The boundary conditions thus depend on the type of the edge. For a zigzag edge, the boundary consists of atoms from the same sublattice : for the left edge in Figure 2.11, the wave function has to vanish on all A sites at the edge, hence the boundary conditions for a zigzag edge :

$$\Psi_A|_{\text{edge}} = 0 \qquad \text{and} \qquad \Psi_B|_{\text{edge}} \text{ free} \tag{2.49}$$

For the armchair edge, the boundary consists of atoms from both sublattices. The wave function has to vanish on both sites A and B at the edge, which is done by mixing the two valleys K and K'. The boundary conditions are therefore :

$$\Psi_A|_{\text{edge}} = \Psi_B|_{\text{edge}} = 0 \tag{2.50}$$

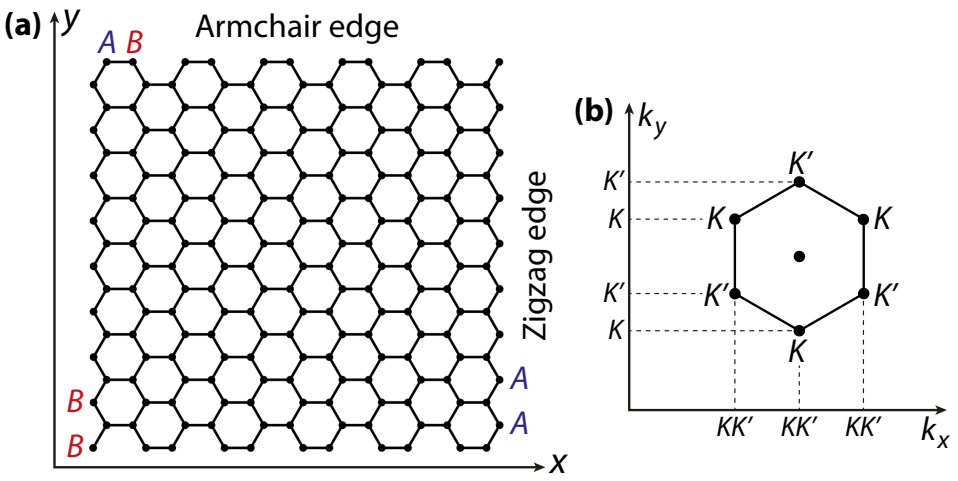

Figure 2.11: **(a)** Graphene lattice with edges : top and bottom are armchair edges, left and right are zigzag edges. Sublattices A and B are marked. **(b)** First Brillouin zone : for the armchair edge, the two valleys K and K' are admixed.

2.2.2.b Edge states in the tight-binding model

Edge spectrum at zero magnetic field We start by considering briefly the edge states of graphene at zero magnetic field, which enables us to introduce important concepts to understand the edge dispersion in the quantum Hall regime. The tight-binding spectra of graphene at zero magnetic field for both armchair and zigzag edges [84, 85] are shown in Figure 2.12.

We can make two important remarks. Firstly, the edge spectra correspond to the projection of the bulk spectrum, see Figure 1.2(a), on the directions of both edges : along the k_x direction for the armchair edge and along the k_y direction for the zigzag edge. In the first Brillouin zone, the projections of the Dirac points coincide for the armchair boundary ($K_x = K'_x$) but do not for the zigzag one ($K_y \neq K'_y$), see Figure 2.11(b) : for the armchair edge, it is necessary to admix the two valleys to fulfill the boundary conditions. Secondly, the zigzag edge hosts a band of zero-energy dispersionless edge states [86, 87, 88, 89], linking both Dirac points, and which are referred as surface states in opposition to the dispersing edge states. These surface states were also shown to persist when a magnetic field is applied [84], and will therefore play a role in the formation of quantum Hall edge states at the zigzag boundary.

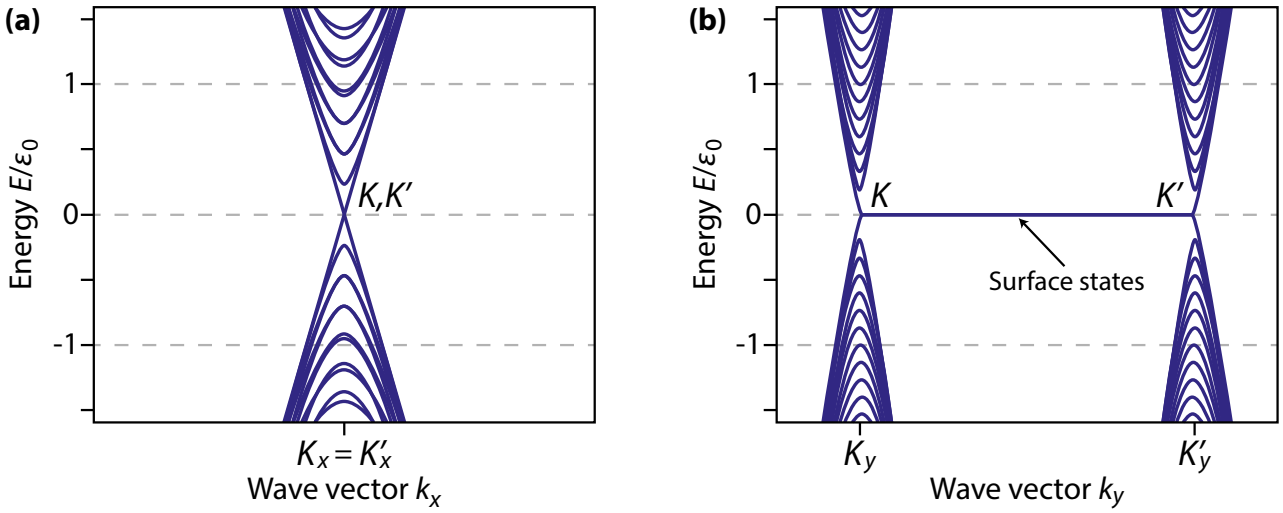

Figure 2.12: Edge spectra of graphene at zero magnetic field. **(a)** Tight-binding spectrum for an armchair ribbon. **(b)** Tight-binding spectrum for a zigzag ribbon, with a zero-energy dispersionless edge mode. Figures adapted from [85].

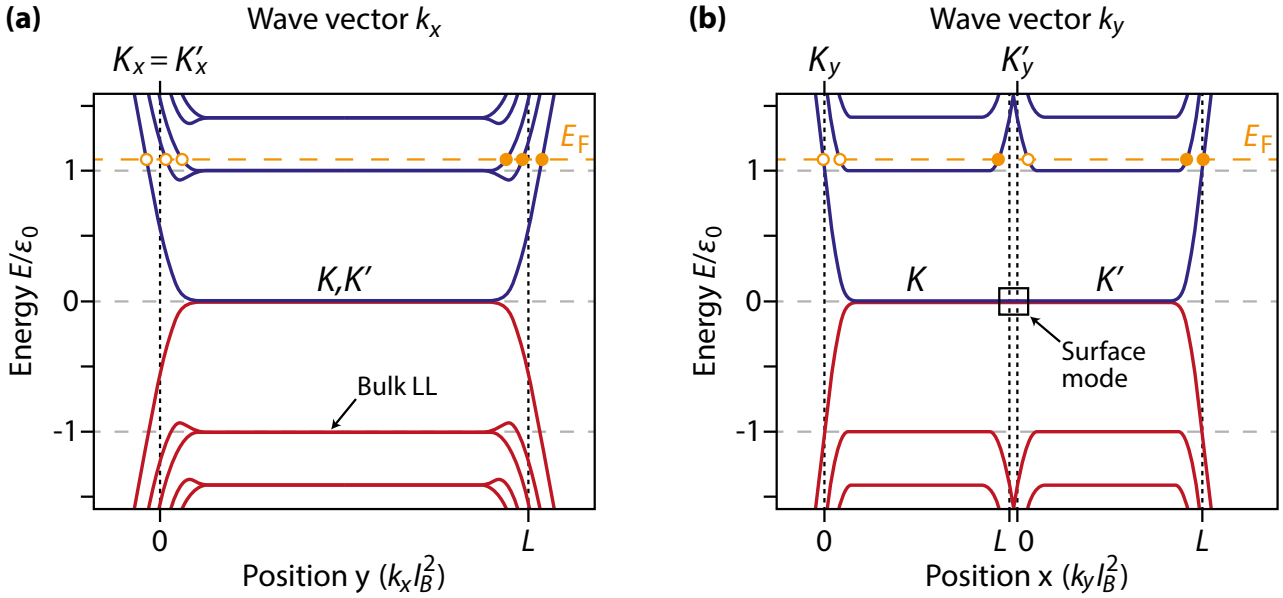

Figure 2.13: Edge spectra of graphene in a strong magnetic field. **(a)** Tight-binding spectrum for an armchair ribbon. **(b)** Tight-binding spectrum for a zigzag ribbon. For both armchair and zigzag edges, the number of dispersing edge states for integer filling factor is an odd number (fill and empty yellow dots, for both physical edges of the ribbon). In both figures, $B = 100\,\mathrm{T}$ and edges are represented by black dashed lines. Figures adapted from [90].

Edge spectrum at high magnetic field We now consider the edge dispersion for a graphene ribbon in the quantum Hall regime. Tight-binding edge spectra for both armchair and zigzag edges were computing numerically by Brey and Fertig in 2006 [90] and are shown in Figure 2.13. The LLs as given by Equation (2.12) appear as flat bands in the bulk, whereas dispersing edge states emerge at the boundaries, which correspond to the quantum Hall edge states as first discussed by Halperin [70]. For both armchair and zigzag edges, the number of edge bands crossing the Fermi level at one edge, at integer filling factor $\nu_0 = N$, is the odd number $2N + 1$: when adding the spin degeneracy, we retrieve the relativistic quantum Hall conductance of $G_{xy} = 2(2N + 1)e^2/h$.

In both figures, one must remember that in a LL problem, we have the position-momentum locking : there is a relation between the momentum parallel to the edge and the position perpendicular to it, see Equation (2.20). Tight-binding spectra can then be also drawn as a function of position. For each valley K and K', the position of one edge in the k-space is fixed by the Dirac point while the other edge is located at a distance $\Delta k_\alpha = L/l_B^2$ with L the width of the ribbon and $\alpha = x, y$ [85].

The edge dispersion itself in graphene clearly depends on the type of edge. For the zigzag edge, we obtain two spectra, one for each valley. The zeroth LL supports two types of edge states, dispersing quantum Hall edge states and dispersionless states as discussed above which link both spectra. The spectrum for a given valley is asymmetric. For the armchair edge, we obtain only one spectrum, since the valleys are admixed, with valley-degenerate bulk LLs. This degeneracy is lifted at the edges, giving two dispersing branches, one of them being non monotonous.

We now present in the following an analytical model for the edge dispersion in graphene based on the Dirac equation with the appropriate boundary conditions.

2.2.2.c Edge states in the massless Dirac model

We analyze here the edge dispersion and states as established by Abanin, Lee and Levitov in 2006 [91, 92], using the massless Dirac model [93], where they provided a continuum description of the edge states for both zigzag and armchair edges.

Low-lying states near both Dirac points K and K' are described as superpositions of four zero-energy Bloch functions with slow varying envelope functions u_K, v_K, $-u_{K'}$ and $-v_{K'}$ [9]. In these functions, u and v correspond to the wave function components on both sublattices A and B, and u_K, v_K (resp. $u_{K'}$ and $v_{K'}$) describe excitations near the Dirac point K (resp. K'). The $\boldsymbol{k}.\boldsymbol{p}$ theory is used [93] to obtain an effective low-energy Hamiltonian by keeping only the lowest-order gradients of the envelope functions u and v. This Hamiltonian takes the form of the Dirac Hamiltonian given in Equation (1.20). The low-energy Hamiltonian under magnetic field, written for each of the Dirac points in terms of u and v, is then given in the basis defined above by :

$$\widehat{\mathcal{H}}_K = iv_{\mathrm{F}} \begin{pmatrix} 0 & \pi_x + i\pi_y \\ -(\pi_x - i\pi_y) & 0 \end{pmatrix} \quad , \quad \widehat{\mathcal{H}}_{K'} = iv_{\mathrm{F}} \begin{pmatrix} 0 & \pi_x - i\pi_y \\ -(\pi_x + i\pi_y) & 0 \end{pmatrix} \tag{2.51}$$

where we used the Peierls substitution : $\boldsymbol{\pi} = \boldsymbol{p} + e\boldsymbol{A}$ and $\boldsymbol{B} = \boldsymbol{\nabla} \times \boldsymbol{A}$.

Armchair edge We consider a graphene sheet in the half-plane $y < 0$ with an armchair edge parallel to the x axis. We here choose the gauge for the potential vector $A_x = -By$ and $A_y = 0$. Since the system is infinite in the x direction, we consider states with a plane wave component in the x direction, giving a x dependence as $e^{-ip_x x/\hbar}$. Equation (2.51) can thus be written as, using $\boldsymbol{p} \longmapsto -i\hbar\boldsymbol{\nabla}$:

$$\widehat{\mathcal{H}}_K = iv_{\mathrm{F}} \begin{pmatrix} 0 & p_x - eBy + \hbar\partial_y \\ -p_x + eBy + \hbar\partial_y & 0 \end{pmatrix}$$
$$\widehat{\mathcal{H}}_{K'} = iv_{\mathrm{F}} \begin{pmatrix} 0 & p_x - eBy - \hbar\partial_y \\ -p_x + eBy - \hbar\partial_y & 0 \end{pmatrix}$$

[9] The sign convention for the K' valley is convenient for treating the armchair edge.

which gives, by factoring out $\hbar/l_B$:

$$\widehat{\mathcal{H}}_K = \frac{i\hbar v_\mathrm{F}}{l_B}\begin{pmatrix} 0 & l_B\partial_y - y/l_B + p_x l_B/\hbar \\ l_B\partial_y + y/l_B - p_x l_B/\hbar & 0 \end{pmatrix}$$
$$\widehat{\mathcal{H}}_{K'} = \frac{i\hbar v_\mathrm{F}}{l_B}\begin{pmatrix} 0 & -l_B\partial_y - y/l_B + p_x l_B/\hbar \\ -l_B\partial_y + y/l_B - p_x l_B/\hbar & 0 \end{pmatrix}$$

We introduce $\varepsilon_0 = \sqrt{2}\hbar v_\mathrm{F}/l_B = v_\mathrm{F}\sqrt{2\hbar eB}$ and the reduced variables $\tilde{y} = y/l_B$ and $\tilde{p}_x = p_x l_B/\hbar$. Finally we obtain :

$$\widehat{\mathcal{H}}_{K,K'} = \frac{i\varepsilon_0}{\sqrt{2}}\begin{pmatrix} 0 & \pm\partial_{\tilde{y}} - (\tilde{y} - \tilde{y}_*) \\ \pm\partial_{\tilde{y}} + (\tilde{y} - \tilde{y}_*) & 0 \end{pmatrix} \tag{2.52}$$

where we wrote the guiding center coordinate, as given by Equation (2.20), with $\tilde{y}_* = \tilde{p}_x \Rightarrow y_* = p_x/eB$. One can note that the spectrum of $\widehat{\mathcal{H}}_{K,K'}$ gives the LLs as derived previously in Equation (2.11) : $E_n = \pm\varepsilon_0\sqrt{n}$ with $n \geq 0$. We now consider edge states. The energy levels are determined by computing the eigenvalues of the Dirac equation $\widehat{\mathcal{H}}_{K,K'}\Psi = E\Psi$ where $\Psi = (u_{K,K'}, v_{K,K'})$. For valley K, this reads as :

$$\frac{i}{\sqrt{2}}\begin{pmatrix} 0 & \partial_{\tilde{y}} - (\tilde{y} - \tilde{y}_*) \\ \partial_{\tilde{y}} + (\tilde{y} - \tilde{y}_*) & 0 \end{pmatrix}\begin{pmatrix} u_K \\ v_K \end{pmatrix} = \frac{E}{\varepsilon_0}\begin{pmatrix} u_K \\ v_K \end{pmatrix} \tag{2.53}$$

which gives the system of coupled equations :

$$\begin{cases} \frac{i}{\sqrt{2}}\left[\partial_{\tilde{y}} - (\tilde{y} - \tilde{y}_*)\right] v_K = (E/\varepsilon_0) u_K \\ \frac{i}{\sqrt{2}}\left[\partial_{\tilde{y}} + (\tilde{y} - \tilde{y}_*)\right] u_K = (E/\varepsilon_0) v_K \end{cases} \tag{2.54}$$

We substitute v_K to obtain an eigenvalue equation for u_K. The same is done for valley K'. Finally, introducing the spectral parameter $\lambda = (E/\varepsilon_0)^2$, we obtain, for sublattice A, the eigenvalue equations for $u_{K,K'}$ in both valleys :

$$\frac{1}{2}\left[-\partial_{\tilde{y}}^2 + (\tilde{y} - \tilde{y}_*)^2 + 1\right] u_K = \lambda u_K \tag{2.55a}$$
$$\frac{1}{2}\left[-\partial_{\tilde{y}}^2 + (\tilde{y} - \tilde{y}_*)^2 - 1\right] u_{K'} = \lambda u_{K'} \tag{2.55b}$$

where the ± 1 terms come from the commutator $[\partial_y, y] = 1$. We now have to include the boundary conditions. Since the armchair edge has both A and B lattice sites (see Figure 2.11), the wave function on both sublattices must be zero. The boundary conditions at the armchair edge for the envelope functions are then :

$$u_K = u_{K'} \quad , \quad v_K = v_{K'} \tag{2.56}$$

To solve the system of eigenvalue equations on the negative half-plane $y < 0$ with the boundary conditions at $y = 0$, Abanin *et al.* [91, 92] simplified the problem by transposing $u_{K'}$ on the positive half-plane $y > 0$ by writing $u_{K'}(y) \longmapsto u_{K'}(-y)$, while still keeping u_K on the negative half-plane $y < 0$. We thus obtain an eigenvalue problem on the whole y axis with the wave function given by u_K for $y < 0$ with Equation (2.55a) and given by $u_{K'}$ for $y > 0$ with Equation (2.55b). The boundary conditions for u implies the continuity of the wave function at $y = 0$. Using Equation (2.54) (and its counterpart for valley K'), the boundary conditions for v eventually implies the continuity of the derivative of the wave function at $y = 0$. So we have :

$$u_K(y \to 0^-) = u_{K'}(y \to 0^+) \quad , \quad \left.\frac{\partial u_K}{\partial y}\right|_{y\to 0^-} = \left.\frac{\partial u_{K'}}{\partial y}\right|_{y\to 0^+} \tag{2.57}$$

The system of Equations (2.55) defined on $y < 0$ can finally be written with a single equation on the entire y axis :

$$\left[-\frac{1}{2}\frac{\partial^2}{\partial\tilde{y}^2} + V(\tilde{y})\right] u = \lambda u \tag{2.58}$$

with the asymmetric double harmonic wells potential $V(y)$ defined by :

$$V(\tilde{y}) = \frac{1}{2}\left(|\tilde{y}| + \tilde{y}_*\right)^2 - \frac{1}{2}\text{sign}(\tilde{y}) \tag{2.59}$$

We therefore have to solve a 1D Schrödinger equation. The spectrum $\lambda(\tilde{y}_*)$ was computed numerically by Abanin *et al.* [91, 92] and the energy levels of the Dirac fermions are eventually obtained as :

$$E(\tilde{y}_*) = \pm\varepsilon_0\sqrt{\lambda(\tilde{y}_*)} \tag{2.60}$$

The electron-hole symmetry of graphene is implied by the $\pm$ signs. The edge dispersion for the armchair case is shown in Figure 2.14(a). We remark that the valley degeneracy of the LLs in the bulk of graphene is lifted at the edge[10]. An immediate conclusion of this analysis is that for an integer bulk filling factor, $\nu_0 = N$, there is an odd number $(2N+1)$ of edge modes crossing the Fermi level. This implies the quantization of the transverse conductance as $G_{xy} = 2(2N+1)e^2/h$, as already mentioned in Section 2.1.4, with the factor 2 coming from the remaining spin degeneracy.

Zigzag edge We now consider a graphene sheet in the half-plane $x > 0$ with a zigzag edge parallel to the y axis. We here choose the gauge for the potential vector $A_x = 0$ and $A_y = Bx$. This time the system is infinite in the y direction so states have a y dependence as $e^{-ip_y y/\hbar}$. Similar calculations enable us to write the Dirac Hamiltonians of Equation (2.51) for both Dirac points in this geometry as :

$$\widehat{\mathcal{H}}_{K,K'} = \frac{\varepsilon_0}{\sqrt{2}}\begin{pmatrix} 0 & \partial_{\tilde{x}} \mp (\tilde{x} - \tilde{x}_*) \\ -\partial_{\tilde{x}} \mp (\tilde{x} - \tilde{x}_*) & 0 \end{pmatrix} \tag{2.61}$$

where we have introduced the reduced variables $\tilde{x} = x/l_B$ and $\tilde{p}_y = p_y l_B/\hbar$ and the guiding center coordinate as $\tilde{x}_* = -\tilde{p}_y \Rightarrow x_* = -p_y/eB$. The spectrum is found once again by solving the eigenvalue equation $\widehat{\mathcal{H}}_{K,K'}\Psi = E\Psi$ with $\Psi = (u_{K,K'}, v_{K,K'})$. As previously, we obtain a system of two eigenvalue equations for $u_{K,K'}$ for both Dirac points after substituting v and introducing $\lambda = (E/\varepsilon_0)^2$:

$$\frac{1}{2}\left[-\partial_{\tilde{x}}^2 + (\tilde{x} - \tilde{x}_*)^2 - 1\right] u_K = \lambda u_K \tag{2.62a}$$

$$\frac{1}{2}\left[-\partial_{\tilde{x}}^2 + (\tilde{x} - \tilde{x}_*)^2 + 1\right] u_{K'} = \lambda u_{K'} \tag{2.62b}$$

For a zigzag edge, the last row of atoms just before the boundary is comprised of atoms of the same sublattice, for instance B (see Figure 2.11). As a consequence, the wave function must vanish on all A sites at $x = 0$. We thus have hard-wall boundary conditions for the envelope functions $u_{K,K'}$ on sublattice A :

$$u_K = 0 \quad , \quad u_{K'} = 0 \tag{2.63}$$

[10] This result can be easily understood when considering that, at the edge of graphene, the valleys K and K' are not equivalent anymore (as in the bulk) due to the breaking of the sublattice symmetry.

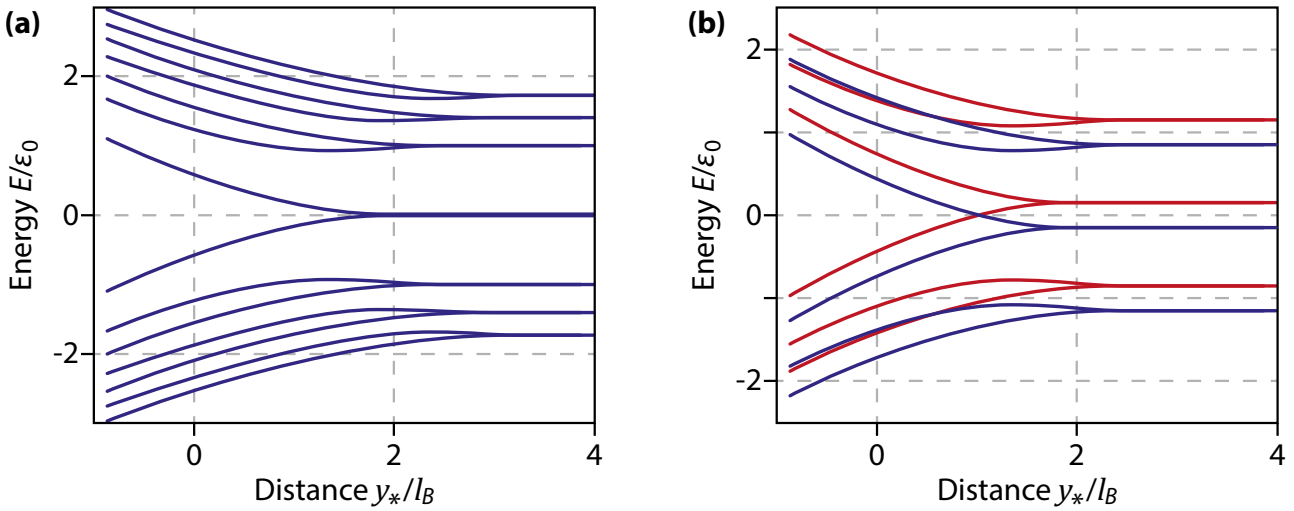

Figure 2.14: Graphene energy spectrum at the armchair edge. **(a)** The valley degeneracy is lifted at the edge, which forms an odd number of electron-like or hole-like edge channels. **(b)** Spin-split edge states, the blue (resp. red) curves represent spin down (resp. spin up) states. At charge neutrality ($\nu = 0$), we obtain helical edge channels, see Section 2.3.4. Figures adapted from [92].

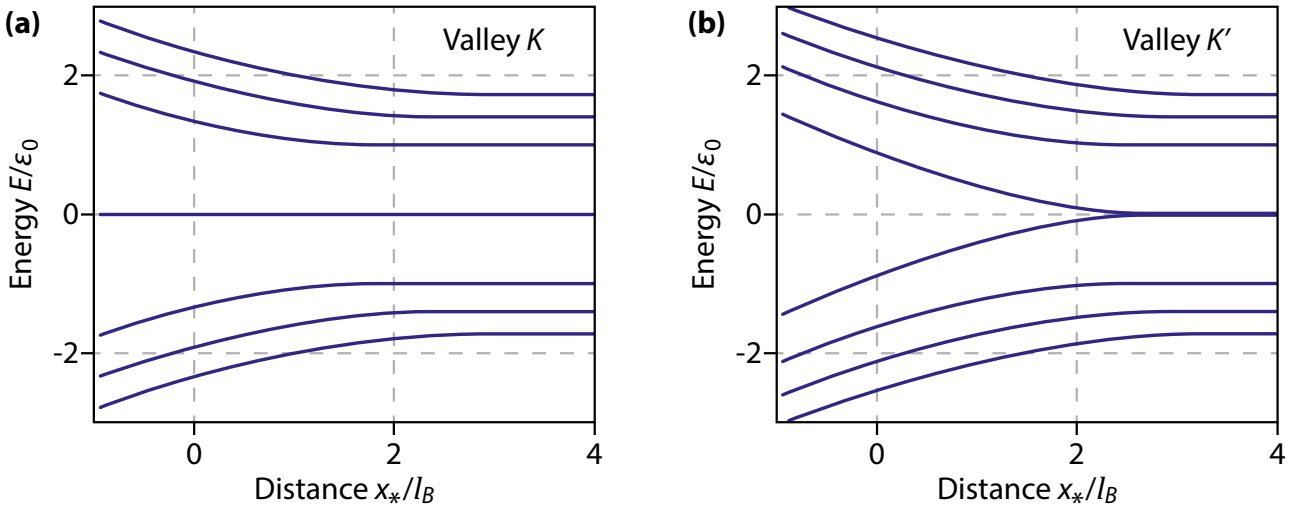

Figure 2.15: Graphene energy spectrum at the zigzag edge. **(a)** Dispersion for the valley K : the zeroth LL morphs into a dispersionless surface mode at the edge. **(b)** Dispersion for the valley K' : the zeroth LL mixes with the surface mode, which yields two branches of dispersing edge states. The valley degeneracy is also lifted at the edge. Figures adapted from [92].

The spectrum $\lambda(\tilde{x}_*)$ of the eigenvalue problem (2.62) with hard-wall boundary conditions was computed numerically by Abanin *et al.* [92], from which the Dirac fermion energy dispersion is obtained as :

$$E(\tilde{x}_*) = \pm\varepsilon_0\sqrt{\lambda(\tilde{x}_*)} \tag{2.64}$$

The edge dispersions for the zigzag case, for each valley K and K' separately, are shown in Figure 2.15. For the $N \neq 0$ LLs, we obtain an edge spectrum similar to that for an armchair edge : two branches of dispersing edge states, one for each valley, and with the valley degeneracy of the bulk that is lifted at the edge[11].

[11]Note that for both armchair and zigzag edges, the Landau level spectra are computed as a function of the momentum, which is afterward converted into a function of the position using the position-momentum locking,

In the following we focus on the special behavior of the zeroth LL at the zigzag edge. The zeroth LL coexists with the zero-energy surface states introduced above and shows as a consequence a peculiar edge dispersion, different for both valleys : it presents a dispersionless mode for the valley K and two dispersing branches for the valley K'. To explain this feature, we recall that, as seen in Section 2.1.2, the eigenstates for the two valleys K and K' for the zeroth LL can be written as :

$$\begin{pmatrix} u_{K,0} \\ v_{K,0} \end{pmatrix} = \begin{pmatrix} 0 \\ \phi_0(x - x_*) \end{pmatrix} \quad , \quad \begin{pmatrix} u_{K',0} \\ v_{K',0} \end{pmatrix} = \begin{pmatrix} \phi_0(x - x_*) \\ 0 \end{pmatrix} \tag{2.65}$$

with ϕ_0 the eigenfunction of the harmonic oscillator. Therefore the zeroth Landau states reside solely for valley K on the sublattice B and for valley K' on the sublattice A : in valley K the zeroth LL states automatically satisfy the hard-wall boundary condition $u_K = 0$. Consequently, the zeroth LL for valley K morphs into the dispersionless surface mode, which does not contribute to the edge transport. For states of valley K', the zeroth LL and the surface mode mix, from which two dispersing edge modes arise. Abanin *et al.* [92] computed the energies for both branches of the dispersing edge states as :

$$E_{\pm}(x_*) \approx \pm\varepsilon_0 \pi^{-1/4} \sqrt{\frac{2x_*}{l_B}} \exp\left(-\frac{x_*^2}{2l_B^2}\right) \tag{2.66}$$

Eventually, despite the existence of the zero-energy surface mode, the number of dispersing modes (for both valleys) at integer values of the bulk filling factor $\nu_0 = N$ is $2N+1$: there is the same odd number of edge channels than in the armchair edge, for both electron and hole carriers. This ensures the observation of the relativistic quantum Hall effect in graphene, for both zigzag and armchair edges, but also for more realistic edges made of a succession of these two ideal cases.

A final observation is that the LLs disperse at the edge on a scale of a few l_B only, which is much smaller than the electrostatic gate-induced edge dispersion, where the reconstruction of edge channels as described by Chklovskii *et al.* [75] happens on a scale of around 1 µm.

For further insights on the quantum Hall edge states in graphene, see also the works of Peres, Guinea, and Castro Neto [4, 84, 94, 95], Gusynin *et al.* [96] and Delplace *et al.* [85, 97].

2.2.2.d Edge dispersion at charge neutrality

In this section we supposed that electrons in the bulk of graphene are degenerate in both spin and valley. Let us quickly see how the lifting of the spin degeneracy by the Zeeman effect changes the edge dispersion. This is shown in Figure 2.14(b). A peculiar feature happens at zero energy, where the edge states carry opposite spins and propagate in opposite directions, giving spin-filtered edge states, which differs from quantum Hall edge states that are not spin-polarized. As we shall see later, this yields a quantum spin Hall effect in graphene.

This picture is nonetheless incomplete since we also have to take into account the valley gap that opens likewise in the bulk due to the breaking of the valley symmetry, and the edge dispersion at zero energy will therefore depend on the interplay of those spin and valley splitting energies. This is the topic of the next section.

see Equation (2.20). However this relation is strictly valid only in the continuum model, at a scale much larger than the lattice parameter, which is not the case anymore at the edges and the last rows of atoms. This justifies the fact that the spectra continue beyond the $x_* = 0$ and $y_* = 0$ axes.

2.3 Quantum Hall topological insulator

We deal in this section with the quantum Hall ferromagnetism in graphene that appears in high-quality samples where spin and valley degeneracies are lifted. We also describe the special properties that arises in the zeroth LL and its quantum Hall ground states, and then how exotic phases may appear, in particular a quantum Hall topological insulator phase induced by a substrate-screening of the Coulomb interaction.

2.3.1 Quantum Hall ferromagnetism

In Section 2.1.1 we derived the LLs of graphene under perpendicular magnetic field using a one-particle picture, neglecting all kinds of interaction. Each electron has four degrees of freedom due both spins $\uparrow\downarrow$ and the two valleys K and K', which results in a four-fold degeneracy of each LL with a SU(4) symmetry. This four-fold degeneracy explains the quantization of the transverse conductance with the series $G = \pm 4(N + 1/2)e^2/h$. In low-disorder samples, the observation of plateaus outside this series, and notably at each integer filling factor $G = \pm\nu e^2/h$, see Figure 2.16(a), arises due to the breaking of spin and valley symmetries, which mainly stems from Zeeman effect, as well as electron-phonon and Coulomb interactions.

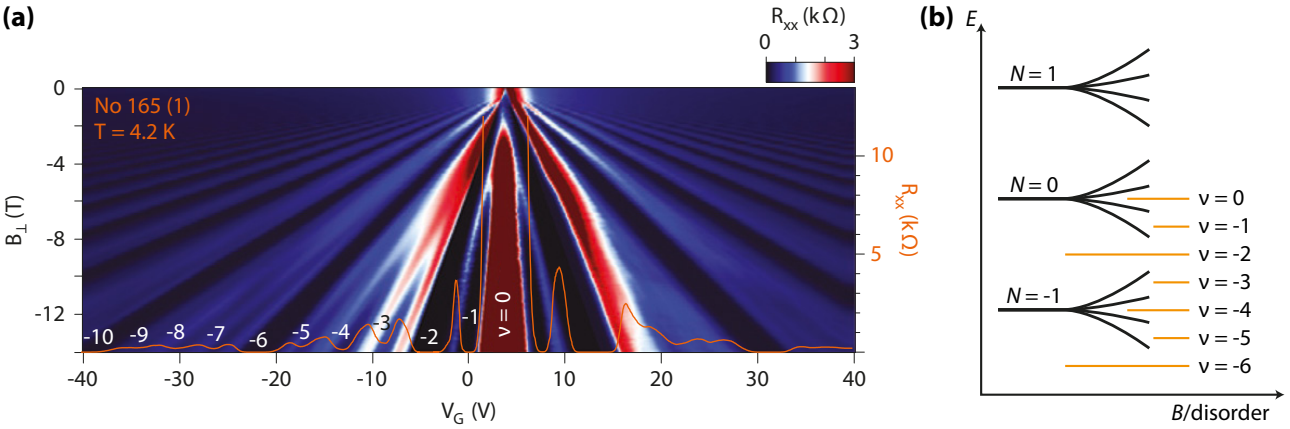

Figure 2.16: Quantum Hall ferromagnetism in graphene. **(a)** Quantum Hall plateaus at every integer filling factors ν in high-mobility graphene/hBN device. Figure taken from [62]. **(b)** Broken-symmetry states emerging from LLs at high magnetic field B in low-disorder samples.

2.3.1.a Spin gap

The Zeeman effect lifts the spin-degeneracy of the Landau levels with an energy gap :

$$E_{\mathrm{Z}} = g\mu_{\mathrm{B}}B \simeq 0.116\,\mathrm{meV} \times B[\mathrm{T}] \tag{2.67}$$

where $g \approx 2$ is the Landé factor and $\mu_{\mathrm{B}} = e\hbar/2m_{\mathrm{e}} \simeq 5.8 \times 10^{-5}\,\mathrm{eV.T}^{-1}$ the Bohr magneton. This gap depends only on the amplitude of the magnetic field, regardless of its direction. Typically, for $B = 10\,\mathrm{T}$, $E_{\mathrm{Z}} \simeq 1.2\,\mathrm{meV}$ so the Zeeman splitting is very small and negligible compared to the cyclotron gap $\Delta E_{0/1} \simeq 115\,\mathrm{meV}$ for the same magnetic field. However, tunneling spectroscopy performed by Song *et al.* [98] as well as magnetotransport measurements made by Young *et al.* [62] in graphene have shown that the gap between the spin-polarized states happens to be several times larger than the one expected from the Zeeman effect.

This enhancement of the spin splitting is attributed to the exchange interaction between electrons [99]. This interaction arises from the principle that the interchange of the wave functions of two fermions has to be antisymmetric, as a consequence of Pauli principle (so electrons of opposite spins have no exchange contribution), and can be approximated to be of the order of the Coulomb energy :

$$E_{\mathrm{X}} \sim E_{\mathrm{C}} = \frac{e^2}{4\pi\epsilon_0\epsilon_{\mathrm{r}} l_B} \simeq 56.2\,\mathrm{meV} \times \frac{\sqrt{B[\mathrm{T}]}}{\epsilon_{\mathrm{r}}} \tag{2.68}$$

where the magnetic length l_B is the relevant length scale for interactions within a LL, see Equation (2.28). ϵ_{r} is the effective dielectric constant seen by the graphene sheet. The Coulomb energy, and so the exchange interaction, both scale as $\sqrt{B}$, which differs from the linear scaling of the Zeeman effect with magnetic field.

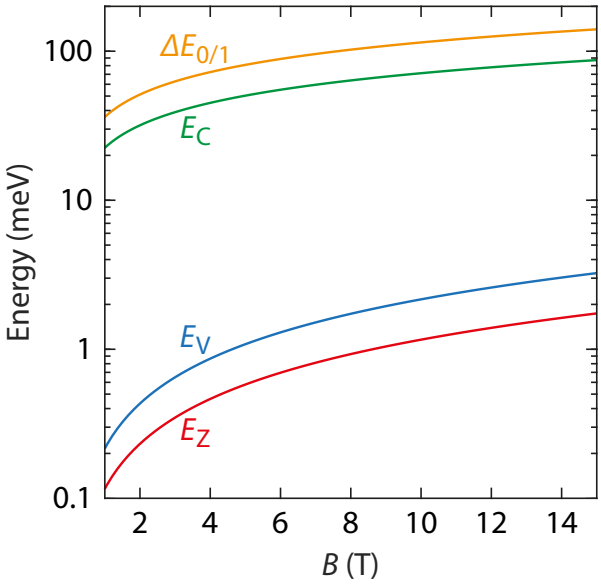

Figure 2.17: Energy scales for spin and valley gaps. $\Delta E_{0/1}$ is the cyclotron gap between the zeroth and first LL and E_{C} is the Coulomb energy, both scale as $\sqrt{B}$. E_{V} is the valley gap and E_{Z} is the Zeeman splitting, both scale as B and are at least one order of magnitude smaller.

2.3.1.b Valley gap

The valley symmetry is on the other hand broken by valleys anisotropies induced by lattice distortions which result from short-range electron-electron interactions [100] and electron-phonon interactions [101]. The latter may introduce a Kekulé distortion where both atoms A and B of the hexagonal lattice have an in-plane displacement. Another possible lattice distortion appears when both sublattices A and B vibrate vertically out of plane and out of phase. These lattice distortions open a gap which is enhanced by the Coulomb interaction [62, 102] :

$$E_{\mathrm{V}} \sim \frac{a}{l_B} E_{\mathrm{C}} \simeq 0.31\,\mathrm{meV} \times \frac{B[\mathrm{T}]}{\epsilon_{\mathrm{r}}} \tag{2.69}$$

where $a = 1.42\,\text{Å}$ is the interatomic distance. The valley gap therefore increases linearly with the magnetic field. The valley symmetry is also broken at the edges where the sublattices become inequivalent, see Section 2.2.2. Figure 2.17(c) plots the different energy scales. The dielectric constant used for E_{C} is $\epsilon_{\mathrm{r}} = 4$, a typical value for substrate like SiO_2 or hBN/SiO_2. We remark that the Coulomb energy is two orders of magnitude larger than the valley and spin gaps, and therefore is the dominant interaction.

2.3.1.c Quantum Hall ferromagnetism and broken-symmetry states

In graphene the immediate consequence of the Coulomb interaction is an instability towards quantum Hall ferromagnetism. Due to exchange interactions, a spontaneous breaking of the SU(4) isospin symmetry lifts the spin and valley degeneracies and splinters the LLs into quartets of broken-symmetry states that are polarized in one or a combination of the spin and valley degrees of freedom [48, 62, 103, 104].

This multicomponent quantum Hall ferromagnetism can be understood considering the Stoner instability [105]. In a metal, a spontaneous spin polarization may decrease the total interaction energy of the system, which makes the metal ferromagnetic (F). In the unpolarized state, each site is occupied by two electrons of opposite spins, with an on-site repulsion energy $U > 0$. The spin polarization of the F phase appears when electrons from the unpolarized phase flip their spin and move, as a consequence of Pauli principle, to unoccupied states above the Fermi level. Each spin-flip lowers the total interaction energy ΔE_{pot} (given by the exchange energy, which is of the order of the Coulomb energy), but also on the other side moves upward the Fermi level and thus increases the total kinetic energy ΔE_{kin}, see Figure 2.18(a). Ferromagnetism appears when the gain in exchange energy is larger than the cost in kinetic energy, which gives the Stoner criterion :

$$\Delta E_{\text{kin}} + \Delta E_{\text{pot}} < 0 \Rightarrow U \times \rho(E_{\text{F}}) > 1 \tag{2.70}$$

with $\rho(E_{\text{F}})$ the density of states at the Fermi energy : ferromagnetism only appears in partially filled bands with large density of states at the Fermi level. In metals, this criterion leads to a partial spin polarization of the band.

The particularity of the quantum Hall regime is that the kinetic energy is quenched (due to electrons being localized in the cyclotron orbits) : the cost in kinetic energy for rearranging electrons in the LLs flat bands is then zero $\Delta E_{\text{kin}} = 0$, see Figure 2.18(b). The Stoner criterion is therefore always fulfilled, whatever the strength of the interaction. This means that partially filled LLs in a 2DEG spontaneously splits into two spin-polarized broken-symmetry states due to the Coulomb interaction given by Equation (2.68) : we obtain a quantum Hall ferromagnet. Note that the interaction-induced gap that opens between those broken-symmetry states at half-filling differs from the cyclotron gap between two LLs.

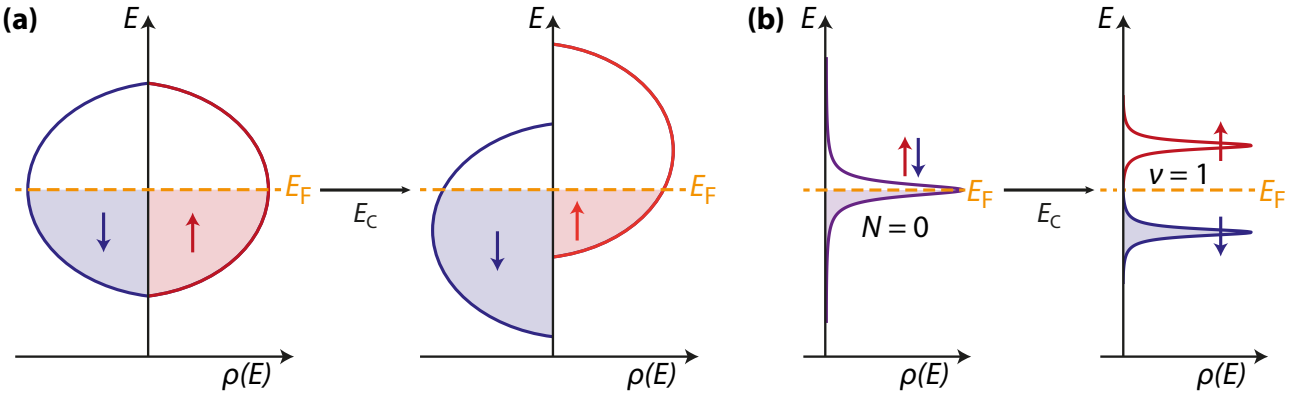

Figure 2.18: Stoner instability. (a) In a metal, the competition between exchange and kinetic energies in a partially filled band leads to a ferromagnetic state with a partial spin polarization. **(b)** For a 2DEG in the quantum Hall regime, LLs are flat bands. The Coulomb interaction then completely lifts the spin degeneracy in partially-filled LLs and we obtain a quantum Hall ferromagnet with two spin-polarized broken-symmetry states.

Things become slightly more complicated in the case of graphene. When the Fermi energy is pinned inside a LL, the Stoner instability applies for both the spin and valley isospin degrees of freedom and spontaneously breaks the SU(4) symmetry of the LLs, which opens interaction-induced gaps at every quarter filling, see Figure 2.19(a). This gives four broken-symmetry states, whose polarizations are given by different directions in the SU(4) space spanned by the four different combinations of both isospin and spin $(K, K', \uparrow, \downarrow)$. Observation of broken-symmetry states is only possible if the exchange gap is greater than disorder. Since $E_C \propto \sqrt{B}$, this defines a minimum magnetic field for a given mobility μ above which the ferromagnetism is observable. Nomura and MacDonald [103] derived in 2006 a Stoner criterion for the occurrence of broken-symmetry states :

$$B[10\ \mathrm{T}]\ \mu[10^4\ \mathrm{cm}^2.\mathrm{V}^{-1}.\mathrm{s}^{-1}] \gtrsim 1/\nu_s^* \tag{2.71}$$

where $\nu_s \propto 1/\mu B$ is the ratio of the density of Coulomb scatterers to the density of a full LL, which has to be lesser than the maximum value ν_s^* for broken-symmetry states to appear. This defines the phase diagram shown in Figure 2.19(b). For low-quality graphene devices, disorder broadens the LLs such that the interaction-induced gaps disappear and only the cyclotron gaps and the quantum Hall plateaus at $\nu = 4N + 2$ are observable. Notice that the first broken-symmetry state which opens by increasing the magnetic field B is the one at $\nu = 0$: we deal with this peculiar state at charge neutrality in the following discussion.

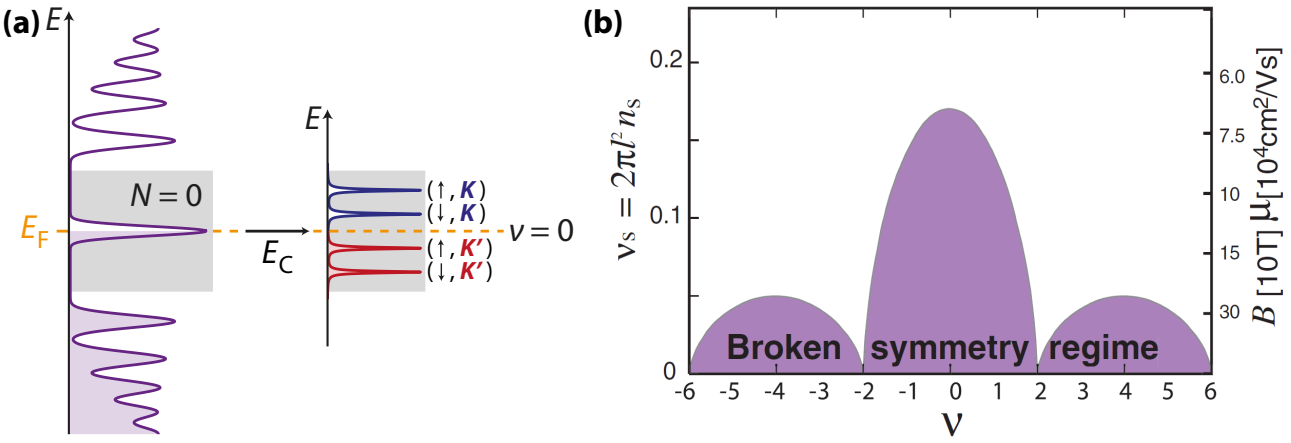

Figure 2.19: Quantum Hall ferromagnetism in graphene. **(a)** The Coulomb interaction lifts both spin and valley degeneracies in graphene, for instance here in the half-filled zeroth LL, which gives four broken-symmetry states. One among many possible polarization is shown for the $\nu = 0$ state, with a valley-polarized ground state. **(b)** Phase diagram for the SU(4) quantum Hall ferromagnetism in the $N = 0$ and $N = \pm 1$ LLs of graphene. The ordered region, where broken-symmetry states occur, is bounded by $\nu_s < \nu_s^*$ and the right axis then gives the minimal value of B required to observe the quantum Hall plateau at ν for a given sample mobility μ. Figure taken from [103].

2.3.2 Edge dispersion in the zeroth Landau level

For the rest of this chapter we focus on the zeroth LL in graphene. When the spin and valley degeneracies are lifted, charge-neutral graphene at $\nu = 0$ state can be probed with transport measurements. Since this LL lies at zero energy, it holds special properties and notably its edge dispersion can lead to either gapped or gapless edge excitations, making charge-neutral graphene either insulating or conductive with the emergence of the quantum spin Hall (QSH) effect.

2.3.2.a Quantum Hall ferromagnetism in the zeroth Landau level

As in other LLs, the exchange interactions split the zero-energy LL into a quartet of four broken-symmetry states. The bulk of graphene at $\nu = 0$ is insulating and its ground state polarization lies somewhere in the SU(4) space, that we can roughly approximate as a SU(2)$\otimes$SU(2)$= KK' \otimes \uparrow\downarrow$ space. However the polarization of edge states is more complicated.

As seen in Section 2.2.2, for an armchair edge both valleys K and K' are mixed at the edge, while for a zigzag armchair the edge dispersion depends on the valley, and the overall edge dispersion then results from the linear combination of both K and K' valleys. Eventually, for both types of boundary, the bulk isospin states evolve into two edge modes (that can not anymore be simply described by one valley or the other only), with one mode dispersing as an electron-like branch while the other disperses as a hole-like branch. With the spin splitting, we obtain four dispersing edge modes : two electron-like and two hole-like branches. Depending if the spin gap Δ_S (given by the Zeeman spin-splitting enhanced by exchange interaction) overcomes the valley splitting Δ_V or not, two typical scenarii of symmetry breaking can happen at the edges, which result in gapped or not edge excitations, as shown in Figure 2.20.

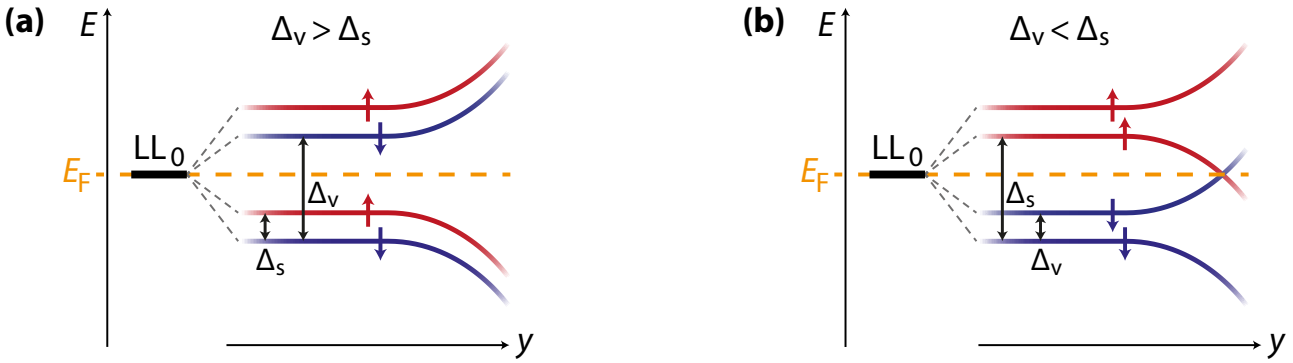

Figure 2.20: Edge dispersions of the zeroth Landau level. (a) If the valley gap Δ_V is greater than the spin gap Δ_S, the edge excitations at $\nu = 0$ are gapped. **(b)** If $\Delta_V < \Delta_S$, there is a topological inversion between the lowest electron-type and highest hole-type sublevels which makes the edge excitations at $\nu = 0$ gapless and helical edge channels emerge. Blue (resp. red) curves represent spin down (resp. spin up) states.

If $\Delta_V > \Delta_S$, electron-like and hole-like bands are separated in doublets and disperse in opposite directions at the edge. The resulting edge excitations are then gapped, hence giving a quantum Hall insulator $\nu = 0$ state, see Figure 2.20(a).

If $\Delta_V < \Delta_S$, a topological inversion between the lowest electron-type and highest hole-type bands occurs, and the spin-up hole band crosses the spin-down electron band at the edge, see Figure 2.20(b). This results in gapless edge excitations, and two counter-propagating, spin-filtered helical edge channels appear at $\nu = 0$ [91, 106], one carrying electrons and the other holes. We obtain an analogous of the quantum spin Hall effect in time-reversal symmetric 2D topological insulators (see Figure 2.21). The immunity of helical edge channels to backscattering here relies on the continuous U(1) axial rotation symmetry of the spin polarization [107, 108].

2.3.2.b Insulating ground state of the charge-neutral graphene

Charge-neutral graphene has been characterized in transport measurements on SiO_2 or hBN substrates as an insulator [60], with gapped edge excitations. Abanin *et al.* observed in 2007 [109] that the transverse conductance of graphene on SiO_2 devices at charge neutrality features

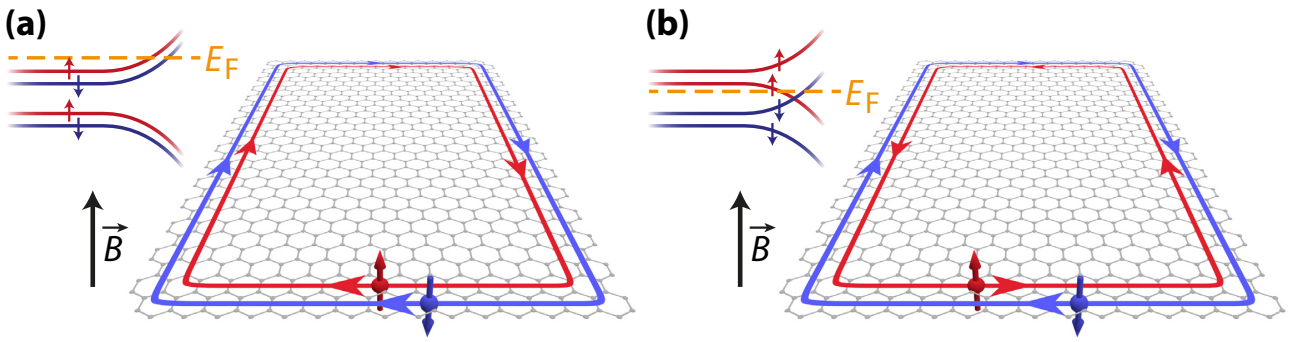

Figure 2.21: Chiral and helical edge channels. **(a)** Quantum Hall effect at $\nu = 2$: the edge channels are chiral, both are electron-like and propagate in the same direction, no matter the spin of the charge carriers. **(b)** Quantum spin Hall effect at $\nu = 0$: the edge channels are helical, the blue one carries spin-down electrons while the counter-propagating red one carries spin-up holes.

a step-like structure at zero conductance, however neither the transverse resistance exhibits a quantized plateau, nor the longitudinal resistance possesses a minimum, see Figure 2.22(a,b). In 2008 Checkelsky *et al.* showed [110, 111] that graphene on SiO_2 samples displays a strongly insulating behavior around charge neutrality that increases with the magnetic field. The same behavior was characterized in suspended graphene by Du *et al.* in 2009 [61] and Bolotin *et al.* [63], as well as in graphene on hBN by Young *et al.* in 2012 [62], see Figure 2.22(c). The tendency of higher quality samples to be more resistive at charge neutrality signifies that the insulating behavior is an intrinsic property of an ideal defect-free system, rather than being a consequence of disorder-induced localization effects [101].

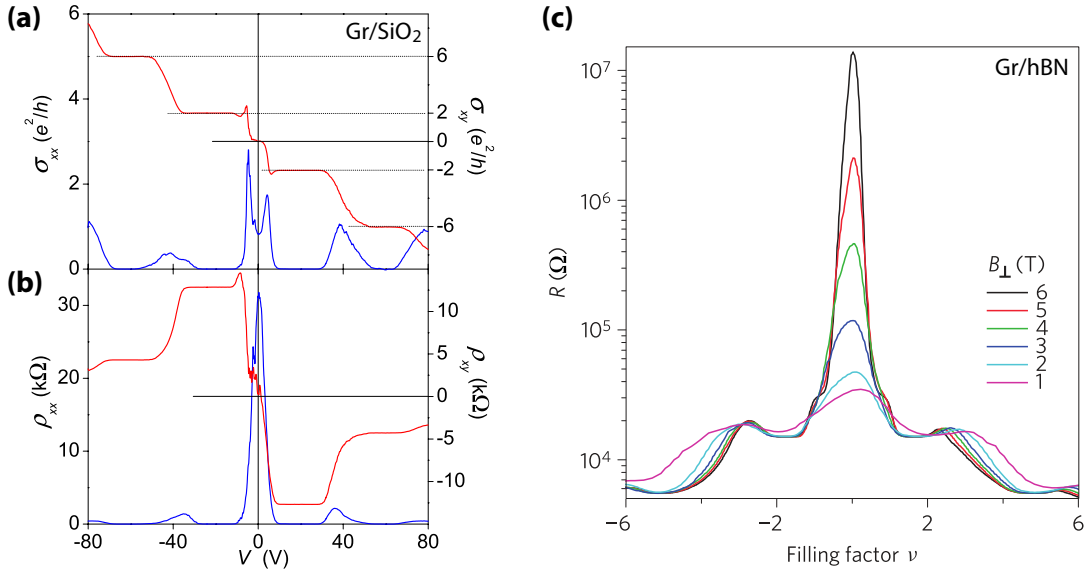

Figure 2.22: Charge-neutral graphene insulating state at $T = 4.2$ K. **(a)** The transverse conductance σ_{xy} (red) features a step-like structure at $\nu = 0$, while the longitudinal conductance σ_{xx} (blue) exhibits a double-peak structure. **(b)** At charge neutrality, neither the transverse resistance ρ_{xy} (red) exhibits a quantized plateau nor the longitudinal resistance ρ_{xx} (blue) vanishes, which would be the hallmarks of the quantum Hall effect. **(c)** Resistance R as a function of the filling factor ν around charge neutrality at various magnetic fields B. The insulating behavior of the $\nu = 0$ state increases with B. Figures (a,b) taken from [109]. Figure (c) taken from [62].

The explanation of the insulating behavior of charge-neutral graphene led to many theories [112, 113, 114, 115], with the prediction of several ground states. In the next section, we focus on the possible many-body ground states of the $\nu = 0$ state in graphene and their edge excitations.

2.3.3 Phase diagram of the $\nu = 0$ state

The physics of charge-neutral graphene, where orbitals of the half-filled zeroth LL are occupied by two electrons, greatly depends on the spin and valley gaps that break the SU(4) symmetry, and the $\nu = 0$ ground state is determined by the competition between these two energies. The Zeeman effect naturally favors a spin-polarized ferromagnetic (F) state, whereas electron-electron and electron-phonon interactions break the valley and sublattice symmetry at the lattice scale. These many-body mechanisms induce valley anisotropies which favor valley-polarized states such as charge-density waves (CDW) or bond-density waves, such as the Kekulé distortion (KD). Since for the zeroth LL the wave functions in each valley are localized on only one real-space sublattice, which makes equivalent the valley K (resp. K') and the sublattice B (resp. A), a valley polarization also implies a sublattice polarization.

In this section we study the phase diagram of the $\nu = 0$ state as established by Kharitonov in 2012 [101, 108, 116].

2.3.3.a Model and Hamiltonian

The low-energy Hamiltonian describing electron dynamics in graphene in the vicinity of the Dirac point is written as :

$$\widehat{\mathcal{H}} = \widehat{\mathcal{H}}_0 + \widehat{\mathcal{H}}_{\text{e-e}} + \widehat{\mathcal{H}}_{\text{e-ph}} \tag{2.72}$$

$\widehat{\mathcal{H}}_0$ describes non-interacting electrons in graphene. $\widehat{\mathcal{H}}_{\text{e-e}}$ describes electron-electron interactions and can be written as a sum of two terms :

$$\widehat{\mathcal{H}}_{\text{e-e}} = \widehat{\mathcal{H}}_{\text{e-e},0} + \widehat{\mathcal{H}}_{\text{e-e},1} \tag{2.73}$$

where $\widehat{\mathcal{H}}_{\text{e-e},0}$ describes the long-range Coulomb interactions, which are symmetric in the valley-sublattice space, and $\widehat{\mathcal{H}}_{\text{e-e},1}$ describes the short-range electron-electron interactions, at the honeycomb lattice scale, that break the valley and/or sublattice symmetry.

$\widehat{\mathcal{H}}_{\text{e-ph}}$ describes the electron-phonon interactions. Electrons in graphene couple mainly to two in-plane optical phonons [117] : two E_2 modes with the phonon wave vector at the Γ point, see Figure 2.23(a), and A_1, B_1 modes with the wave vector at the K and K' points, see Figure 2.23(b). Furthermore, the lattice deformation due to the A_1 and B_1 modes corresponds to the Kekulé distortion.

The valley anisotropies arise from the short-range electron-electron and electron-phonon interactions. They are asymmetric in the valley-sublattice space and can be described in this space by two energies $u_\perp$ and u_z. These terms favor valley-polarizations in different directions in the valley Bloch sphere : a strong negative u_z favors a K or K' valley-polarization (isospin at the poles of the valley Bloch sphere) whereas a strong negative $u_\perp$ favors a $K + K'$ valley-polarization (isospin on the equator of the valley Bloch sphere), see Figure 2.24. On the contrary, valley-polarized states are unfavored by positive $u_{\perp,z}$, which thus favors spin polarizations.

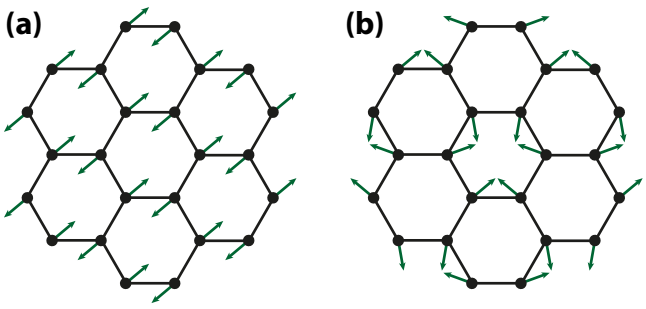

Figure 2.23: In-plane optical phonon modes with the strongest e-ph coupling. (a) Linear combination of the two degenerate E_2 modes, with the phonon wave vector at the Γ point. **(b)** Linear combination of the degenerate A_1 and B_1 modes with the wave vector at the K and K' points, producing a Kekulé distortion of the lattice.

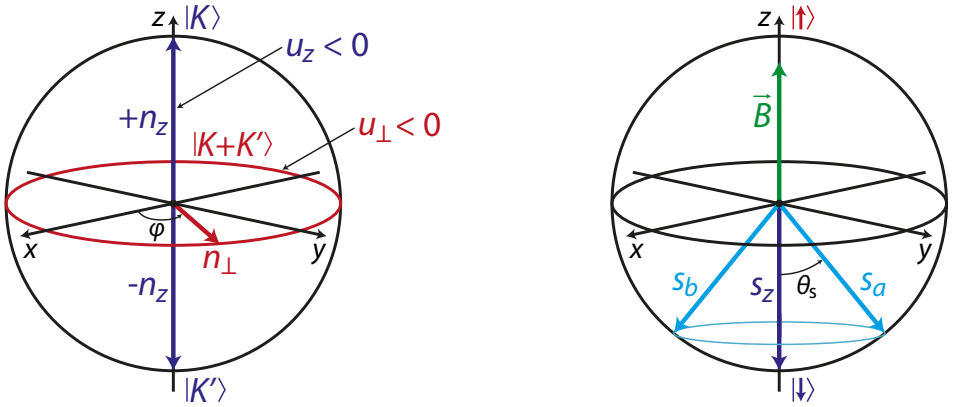

Figure 2.24: Isospin and spin Bloch spheres. In each sphere, the valley and spin polarizations for the four possible ground states described later and presented in Figure 2.25 are indicated. Valley anisotropies are characterized in the valley Bloch sphere by energies $u_\perp$ and u_z which favor valley polarizations respectively in the equatorial plane or at the poles.

Kharitonov studied [101] the renormalization of these anisotropy energies due to the long-range part of the Coulomb interaction. He showed that, depending on their initial values, renormalized $u_{\perp,z}$ are enhanced and even exceed the Zeeman energy, while their sign may also change. The difficulty here is that is not possible to know exactly the initial values of $u_{\perp,z}$, and thus their final value and sign after renormalization can not be predicted. The ground state of the $\nu = 0$ depends on the signs of the anisotropy energies $u_{\perp,z}$ and their relation between each other and the Zeeman energy E_Z. In particular, the short-range e-e interactions alone could favor any state of the phase diagram, depending on the details of interactions at the lattice scale, while the e-ph interactions always favor the Kekulé distortion order.

2.3.3.b Phase diagram and ground states

The $\nu = 0$ ground state is the configuration $\mathcal{P}$ which minimizes the sum of the valley anisotropy and Zeeman energies. Since any scenario for $(u_\perp, u_z)$ after renormalization could take place in graphene, one must consider all possibilities. The phase diagram of the $\nu = 0$ state is obtained in the parameter space $(u_\perp, u_z, E_\mathrm{Z})$, see Figure 2.25. The system can be driven to four possible ground states. Each phase is characterized by an energy $\mathcal{E}$, which is the sum of the anisotropy energy and the Zeeman energy, and an order parameter $\mathcal{P}$ in the $KK' \otimes \uparrow\downarrow$ space which can be written as $\mathcal{P} = \mathcal{P}_n \otimes \mathcal{P}_s$ where $\mathcal{P}_n$ (resp. $\mathcal{P}_s$) is the order parameter for a valley polarization $\boldsymbol{n}$ (resp. spin polarization $\boldsymbol{s}$) in the valley (resp. spin) Bloch sphere. The different polarizations for each state are represented in Figure 2.24.

Charge-density wave (CDW) This phase is a fully valley-polarized spin-singlet state characterized by the order parameter and energy :

$$\mathcal{P}^{\mathrm{CDW}} = \mathcal{P}_{\pm n_z} \otimes \mathbb{1}_s \quad / \quad \mathcal{E}^{\mathrm{CDW}} = u_z \tag{2.74}$$

The isospin in the CDW phase can be either K or K' (Z_2 symmetry), with both electrons per orbital occupying the same sublattice A or B.

Kekulé distortion (KD) This phase is also a fully valley-polarized spin-singlet state characterized by order parameter and energy :

$$\mathcal{P}^{\mathrm{KD}} = \mathcal{P}_{n_\perp} \otimes \mathbb{1}_s \quad / \quad \mathcal{E}^{\mathrm{KD}} = u_\perp \tag{2.75}$$

The isospin in the KD phase is a linear combination of both valleys $K + e^{i\varphi}K'$ and is free to rotate in the equator of the isospin Bloch sphere. We have a dimerization of one bond over three, hence the bond-density wave. The KD phase has a U(1) symmetry.

Spin-polarized ferromagnet (F) This phase is a fully spin-polarized isospin-singlet state characterized by order parameter and energy :

$$\mathcal{P}^{\mathrm{F}} = \mathbb{1}_n \otimes \mathcal{P}_{s_z} \quad / \quad \mathcal{E}^{\mathrm{F}} = -2u_\perp - u_z - 2E_{\mathrm{Z}} \tag{2.76}$$

Sublattices are equally occupied by both electrons with the same spin. Note that the F phase also preserves the valley symmetry. Without the Zeeman effect, the F phase is SU(2) symmetric in the spin phase, however under a perpendicular magnetic field the F phase becomes non-degenerate, with the spin directed along the Zeeman effect.

Canted antiferromagnet (CAF) This phase is a partial spin-polarized isospin-singlet state[12] characterized by order parameter and energy :

$$\mathcal{P}^{\mathrm{CAF}} = \mathcal{P}_{n_z} \otimes \mathcal{P}_{s_a} + \mathcal{P}_{-n_z} \otimes \mathcal{P}_{s_b} \quad / \quad \mathcal{E}^{\mathrm{CAF}} = -u_z - \frac{E_{\mathrm{Z}}^2}{2\,|u_\perp|} \tag{2.77}$$

Electrons equally occupy both valleys, but their spin is tilted with respect to the direction of the magnetic field. The optimal angle θ_{s} between the spins and the magnetic field is given by :

$$\cos\theta_{\mathrm{s}} = \frac{E_{\mathrm{Z}}}{2|u_\perp|} \tag{2.78}$$

In the absence of the Zeeman effect, an antiferromagnetic (AF) phase appears instead, with both electrons having simultaneously opposite spin and isospin polarizations. The noncollinear orientation of the spins in the CAF phase allows electron to lose some of the anisotropy energy but also to gain more in the Zeeman energy, and therefore is favored over the antiparallel orientation ($\theta_{\mathrm{s}} = \pi/2$) of the AF phase. The CAF phase is U(1)-degenerate in the spin-space, with the rotation of the spins being free around the direction of the magnetic field.

Note that the CDW and KD phases only depend of anisotropy energies and therefore are unaffected by the Zeeman effect. When the valley anisotropies dominate the Zeeman effect, the ground state can either be a CAF, CDW or KD.

[12] There is also a spin-valley entanglement [118] since each valley has a different spin polarization, yet this can not be represented in the $KK' \otimes \uparrow\downarrow$ approximation of the SU(4) space and would require a third Bloch sphere.

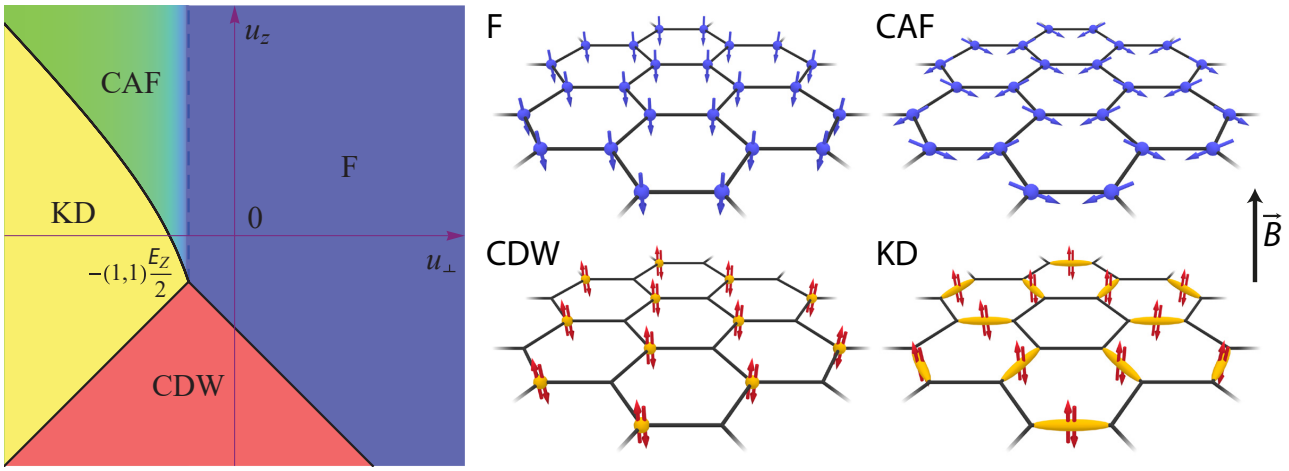

Figure 2.25: Quantum Hall ferromagnetism in the zeroth Landau level. The phase diagram of the $\nu = 0$ quantum Hall ferromagnet, in the space of the anisotropy energies $(u_\perp, u_z)$ and with the Zeeman energy E_Z as parameter (left, figure taken from [101]), predicts four possible quantum Hall ground states : spin ferromagnet (F), canted antiferromagnet (CAF), charge-density wave (CDW) or Kekulé distortion (KD).

The boundaries between the different phases are :

$$u_\perp = -\frac{E_\mathrm{Z}}{2} \qquad \text{between F and CAF phases} \tag{2.79}$$

$$u_\perp = u_z \qquad \text{between CDW and KD phases} \tag{2.80}$$

$$u_\perp + u_z = \frac{E_\mathrm{Z}^2}{2u_\perp} \qquad \text{between CAF and KD phases} \tag{2.81}$$

$$u_\perp + u_z = -E_\mathrm{Z} \qquad \text{between F and CDW phases} \tag{2.82}$$

All four lines intersect at the point $(u_\perp, u_z) = -(1,1)E_\mathrm{Z}/2$. Without the Zeeman effect, the intersection occurs at the origin $(u_\perp, u_z) = (0,0)$, where the anisotropy energy vanishes and every ground state has the same energy. All phase transitions are first-order (including the AF/F transition), except the CAF/F one which is second-order.

2.3.3.c Charge excitations

Charge excitations are gapped in the bulk for every ground state. The edge excitations are gapped in the CDW, KD and CAF phases, with an edge spectrum as shown in Figure 2.20(a), and these three phases therefore exhibit an insulating behavior, making them strong candidates for the insulating $\nu = 0$ state usually observed experimentally. On the other hand, the F phase has gapless edge excitations with the edge spectrum of Figure 2.20(b).

The transition from the AF phase to the phase F, with the evolution of the edge gap, has also been theoretically studied by Kharitonov [116]. Following the edge dispersion obtained for an armchair edge $E(y_*)$ given in Equation (2.60), as derived by Abanin *et al.* [91, 92] (see Section 2.2.2), the mean-field spectrum of the AF/CAF/F phases of the $\nu = 0$ state consists of four branches with the edge dispersions :

$$E_{\pm\pm}(y_*) = \pm\sqrt{\left[E(y_*) \pm (E_\mathrm{Z} + \Delta_\mathrm{F})\right]^2 + \Delta_\mathrm{AF}^2} \tag{2.83}$$

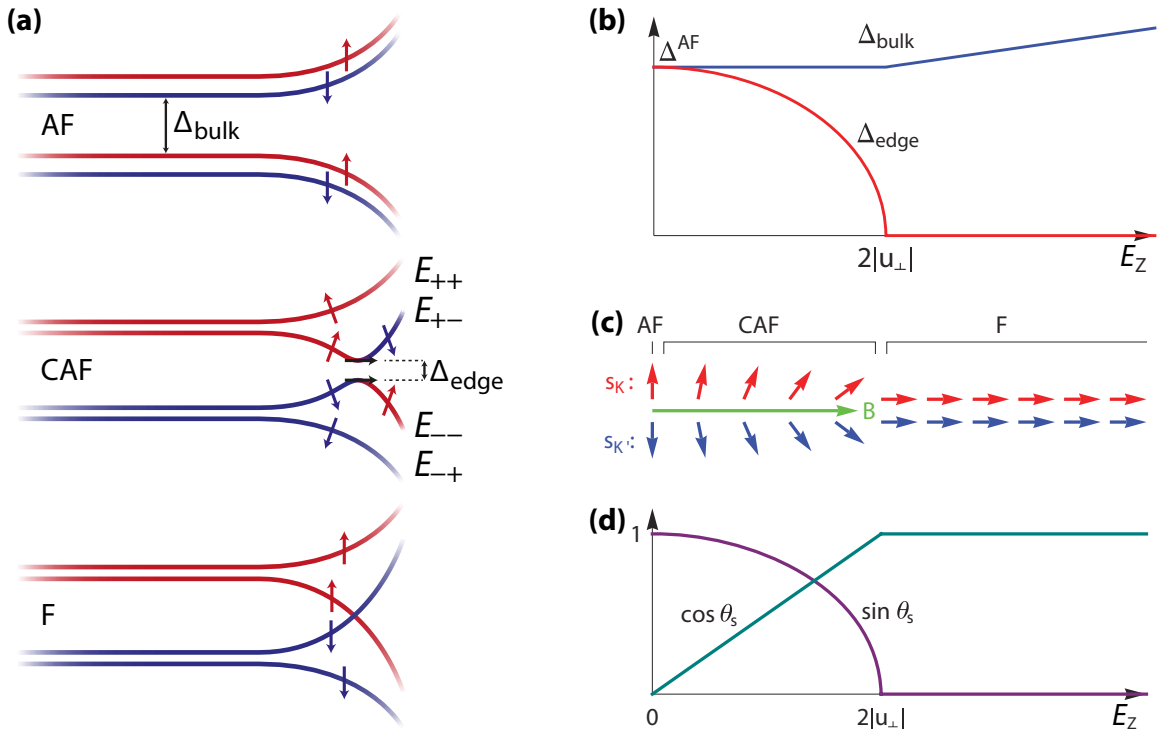

Figure 2.26: Edge excitations of the AF, CAF and F phases. **(a)** Band structure of the AF ($E_\mathrm{Z} = 0$), CAF ($0 < E_\mathrm{Z} < 2|u_\perp|$) and F ($E_\mathrm{Z} > 2|u_\perp|$) phases. The edge gap Δ_edge is maximal in the AF phase, takes smaller values in the CAF phase and vanishes in the F phase, where the gapless helical edge excitations emerge. **(b)** Evolution of the edge Δ_edge and bulk Δ_bulk gaps as a function of the Zeeman energy E_Z at fixed anisotropy energies $u_{\perp,z}$. **(c)** Spin orientation with respect to the magnetic field in the three phases. **(d)** Evolution of the spin polarization in the three phases. θ_s is the angle between the spin and the magnetic field and is given by Equation (2.78). Figures (b-d) taken from [116].

with the mean-field potentials of the F and AF phases :

$$\Delta_\mathrm{F} = \frac{1}{2}\left(u_0 + u_z - 2|u_\perp|\right)\cos\theta_\mathrm{s} \tag{2.84}$$

$$\Delta_\mathrm{AF} = \frac{1}{2}\left(u_0 + u_z + 2|u_\perp|\right)\sin\theta_\mathrm{s} \tag{2.85}$$

and where u_0 describes the exchange term of the Coulomb interaction Hamiltonian $\widehat{\mathcal{H}}_{\text{e-e},0}$. These edge spectra are shown in Figure 2.26(a). The gap in the edge spectrum of the CAF phase monotonically decreases from the AF gapped phase to the F gapless phase, as the Zeeman energy is increased at fixed anisotropy energies. The CAF phase then continuously interpolates between the spin-unpolarized phase to the fully spin-polarized one without closing the bulk gap, see Figure 2.26(b). This results in a gradual insulator-metal transition, where the conductance grows exponentially in the insulating CAF phase and saturates to metallic values in the F phase, where helical edge channels appear when the gap closes. Furthermore, the canted angle inverts in the CAF phase close to the edge, which yields a skyrmion spin texture.

In practice, such evolution - increasing E_Z with $u_{\perp,z}$ constant - is realized by tilting the magnetic field, in order to keep the perpendicular component $B_\perp$ constant while increasing the total value B_T. Indeed the anisotropy energies $u_{\perp,z}$ only depend on $B_\perp$ while the Zeeman energy depends on B_T as $E_\mathrm{Z} = g\mu_B B_\mathrm{T}$, and therefore upon increasing $B_\mathrm{T}/B_\perp$, the system eventually transits into in the F phase.

Similarly, Knothe *et al.* [119, 120] derived in 2015 the edge spectra for both the CDW and KD phases for an armchair edge. For the CDW phase, the four dispersing branches are :

$$E_{\pm\pm}^{\mathrm{CDW}}(y_*) = \pm E_{\mathrm{Z}} \pm \sqrt{E(y_*)^2 + \Delta_{\mathrm{CDW}}^2} \tag{2.86}$$

$$\Delta_{\mathrm{CDW}} = \frac{1}{2}\left(u_0 - 3u_z + 2|u_\perp|\right) \tag{2.87}$$

while the edge spectrum for the KD phase is given by :

$$E_{\pm\pm}^{\mathrm{KD}}(y_*) = \pm E_{\mathrm{Z}} \pm \left[E(y_*) + \Delta_{\mathrm{KD}}\right] \tag{2.88}$$

$$\Delta_{\mathrm{KD}} = \frac{1}{2}\left(u_0 - u_z + 4|u_\perp|\right) \tag{2.89}$$

Nonetheless, these edge spectra were derived assuming that the anisotropy energies $u_{\perp,z}$ stay constant at their bulk value, which is less and less exact when approaching the boundary. Knothe *et al.* also stated that the order parameter $\mathcal{P}$ may undergo spatial variations, with a transition from the bulk phase to a Kekulé distorted region close to the edge. Finally, they predicted that the metal-insulator transition when increasing the Zeeman energy should occur not only from the CAF phase but also from the CDW and the KD phases.

The phase diagram of the quantum Hall ferromagnetic states established by Kharitonov has also been obtained by Atteia, Lian and Goerbig in 2021 [118]. Moreover, they derived in their work the phase diagram of the skyrmionic excitations in charge-neutral graphene, see also [121]. Indeed, adding an electron with opposite spin or isospin perturbs locally the magnetization, and the quasiparticle is thus dressed as a skyrmion, with a spin-isospin texture, to minimize the exchange energy. The skyrmion is spatially localized (so possibly observable by STM) and, far from its center, the background phase (F/CAF/CDW/KD) is retrieved.

2.3.4 Helical quantum Hall phase

We focus in this last section on how the F phase can be induced in graphene. This quantum Hall spin-polarized ferromagnetic phase at charge neutrality, with an edge dispersion that exhibits two counter-propagating and spin-filtered helical edge channels, as shown in Figure 2.21(b), is a quantum Hall topological insulator (QHTI), which belongs to the class of interaction-induced topological insulators [108].

However, the formation of the F phase in charge-neutral graphene in usual transport devices is presumably hindered by the valley anisotropies that dominate the Zeeman effect, which gives the insulating state commonly observed at charge neutrality, as illustrated in Figure 2.22. We present in the following two methods that have been found to induce the F phase : by using extreme tilted magnetic fields to boost the Zeeman effect [107] and by screening the Coulomb interactions to mitigate the valley anisotropy energies [122].

2.3.4.a Ferromagnetic phase in extreme tilted magnetic fields

It is expected from the phase diagram of the $\nu = 0$ state that by boosting the Zeeman effect, using tilted magnetic fields in order to keep the perpendicular component $B_\perp$ constant while increasing the total value B_{T}, the system should transit to the F phase. Such a transition was demonstrated by Young *et al.* in 2014 [107] in high-mobility graphene/hBN/SiO_2 transport devices. They show that as B_{T} was increased with $B_\perp$ kept constant, the $\nu = 0$ state of graphene undergoes a continuous transition from an insulating state to a metallic state, see Figure 2.27(a).

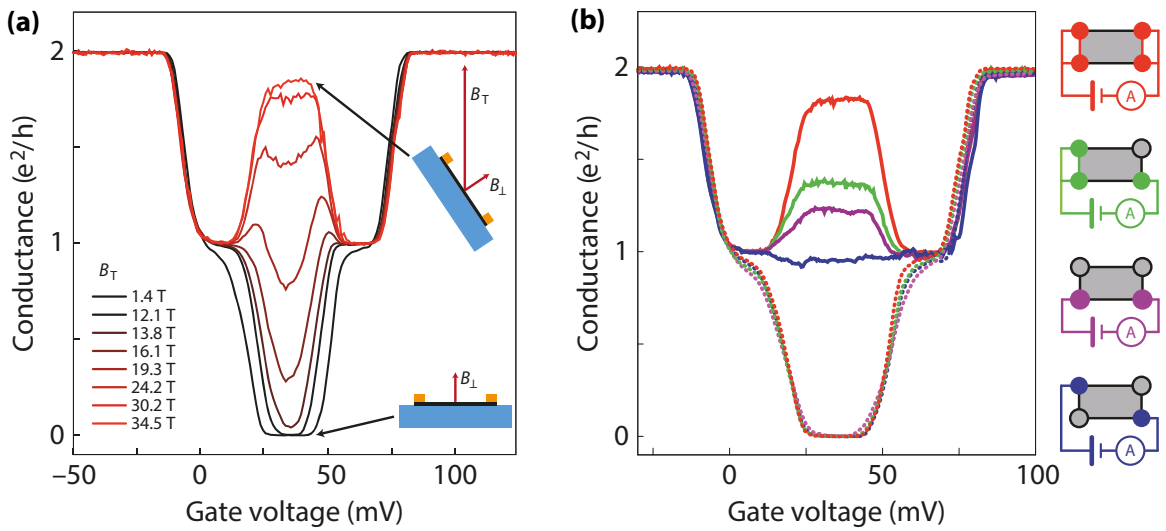

Figure 2.27: QSH state in graphene in extreme tilted magnetic fields and non-local transport. **(a)** Conductance at $B_\perp = 1.4\,\mathrm{T}$ for different values of B_T. As B_T increases, the insulating state at $\nu = 0$ is gradually replaced by a high-conductance state. **(b)** Two-terminal conductance measurements for $B_\perp = 1.4\,\mathrm{T}$, color-coded to match the four different measurement configurations represented on the right (open circles indicate floating contacts whereas filled colored circles indicate measurements contacts). Dashed curves correspond to $B_\mathrm{T} = 1.4\,\mathrm{T}$, solid curves correspond to $B_\mathrm{T} = 34.5\,\mathrm{T}$ (QSH regime) where the conductance at $\nu = 0$ is well fitted by Equation (2.90). Figures taken from [107].

Helical edge transport presents unambiguous signatures in multi-terminal devices. Contrary to chiral edge channels of a quantum Hall state which carry current in only one direction, preventing backscattering, the helical edge channels in the QSH regime carry current either way, and the conservation of spin within the edge states hinders backscattering. An edge section between two successive contacts is thus an ideal helical quantum conductor of quantized resistance h/e^2. However, carriers do not maintain their spin coherence within a metallic contact, which thus acts as a source of backscattering for the counter-propagating helical edge channels with opposite spin-polarizations [123]. The two-terminal resistance R_2t of a device therefore results from the parallel resistance of both edges, each of them being the sum of contributions of each helical edge section, which gives [107] :

$$R_\mathrm{2t} = 1/G_\mathrm{2t} = \frac{h}{e^2}\left(\frac{1}{N_\mathrm{L}} + \frac{1}{N_\mathrm{R}}\right)^{-1} \tag{2.90}$$

where $N_\mathrm{L,R}$ is the number of helical conductor sections delimited by floating contacts for the left (L) and right (R) edge between the source and drain contacts. Helical transport is thus characterized by resistance plateaus given by Equation (2.90) and function of the source and drain contact configuration. This is shown in Figure 2.27(b), and these QSH signatures imply that charge-neutral graphene ground state is indeed a spin ferromagnet.

The continuous transition from the insulating ground state to the F phase as the magnetic field is tilted was explained by Young *et al.* [107] as a progressive closing of the edge gap as the spins align themselves in the magnetic field direction starting from a canted angle. Such a continuous transition, which is expected only between CAF and F phases, has since then placed the CAF phase as a strong candidate for the insulating ground state of charge-neutral graphene in transport devices.

2.3.4.b Ferromagnetic phase induced by substrate-screening

Another approach to induce the F phase in charge-neutral graphene was done in our group in 2020, see Veyrat *et al.* [122]. Instead of boosting the Zeeman effect with a large tilted magnetic field, we mitigated the effects of the lattice-scale interaction terms by a suitable substrate-screening of the Coulomb interactions, in order to restore the dominant role of the spin-polarizing terms. We thus used a high-k dielectric substrate, the quantum paraelectric $SrTiO_3$, which is known to exhibit a very large static dielectric constant of the order of $\epsilon_{STO} \approx 10^4$ at low temperature [124, 125, 126]. This substrate acts both as an electrostatic screening environment and back-gate dielectric [127], see Figure 2.28(b).

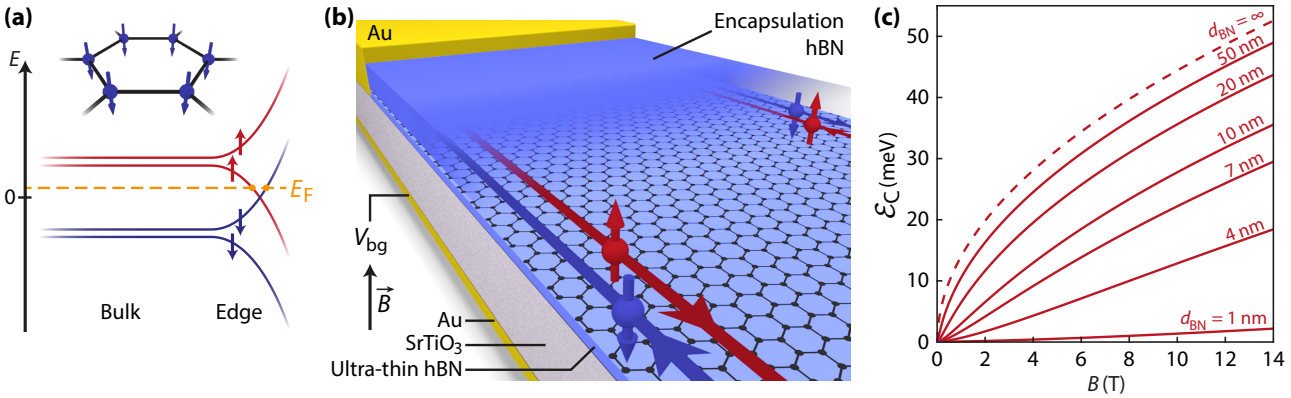

Figure 2.28: F phase induced by dielectric screening. **(a)** F phase in the $\nu = 0$ state of graphene. The bulk is insulating and edge excitations yield helical edge channels. **(b)** Cross section of the hBN-encapsulated graphene device placed on a $SrTiO_3$ substrate that serves both as high-k dielectric and back-gate dielectric. Due to the screening of the Coulomb interaction, the F phase is induced in charge-neutral graphene and helical spin-filtered edge channels appear. **(c)** Variation of the Coulomb energy $\mathcal{E}_C$ with the magnetic field B in the $SrTiO_3$-based heterostructures for different thicknesses of the hBN layer d_{BN} (red curves). The dashed red curve corresponds to the case where there is no screening due to the $SrTiO_3$ feeling by the graphene (typically the case for usual SiO_2 substrates).

The distance between the graphene sheet and the $SrTiO_3$ substrate is a primordial variable here : graphene must be sufficiently close to the substrate in order to have an efficient screening of the Coulomb interactions. The separation should thus be less than the magnetic length l_B which is the average distance between two electrons in the quantum Hall regime. We then made high-mobility hBN encapsulated graphene heterostructures[13] with an ultra-thin bottom hBN layer with a thickness d_{BN} between $2 - 5\,\text{nm} < l_B \simeq 11\,\text{nm}$ at 5 T.

The substrate-screened Coulomb energy scale $\mathcal{E}_C$ is given by [129, 130] :

$$\mathcal{E}_C = E_C \times S(B) \tag{2.91}$$

where E_C is the bare Coulomb energy :

$$E_C = \frac{e^2}{4\pi\epsilon_0\epsilon_{BN} l_B} \tag{2.92}$$

[13] Encapsulating graphene between two hBN flakes protects it from pollutants and greatly improves its mobility [128].

and $S(B)$ is the screening factor :

$$S(B) = 1 - \frac{\epsilon_{\text{STO}} - \epsilon_{\text{BN}}}{\epsilon_{\text{STO}} + \epsilon_{\text{BN}}} \frac{l_B}{\sqrt{l_B^2 + 4d_{\text{BN}}^2}} \tag{2.93}$$

where ϵ_{BN} and ϵ_{STO} are respectively the relative permittivities of hBN and $SrTiO_3$. Figure 2.28(c) shows the evolution of the substrate-screened $\mathcal{E}_C$ as a function of magnetic field, for different d_{BN}. Screening is B-dependent with the ratio l_B/d_{BN} and is more efficient at low magnetic fields, where the Coulomb energy becomes comparable with the Zeeman energy. In particular, at low magnetic fields, the potential becomes dipolar with $\mathcal{E}_C \sim B^{3/2}$. Asymptotically, the bare Coulomb energy is retrieved for very thick hBN layer where the graphene plane does not feel any screening effect from the $SrTiO_3$ substrate.

The F phase appears in our hBN encapsulated graphene devices at low magnetic fields : in Figure 2.29(a), a resistance plateau at h/e^2 around charge neutrality develops over a B-range from 1.5 to 4 T whereas at $B > 5$ T, the resistance departs from h/e^2 towards insulation. Line-cuts at fixed magnetic fields in Figure 2.29(b) clearly show the appearance of a conductance plateau at charge neutrality in addition to standard graphene quantum Hall plateaus at $\nu = 2$ and 6. The transport properties of the plateau at $\nu = 0$ are characterized by swapping the source and drain contacts and the number of helical edge sections between, which gives the curves in Figure 2.29(c). The resistance at charge neutrality reaches the expected values from Equation (2.90) for each contact configuration, which is the signature of the QSH effect and that the $\nu = 0$ ground state is a spin ferromagnet.

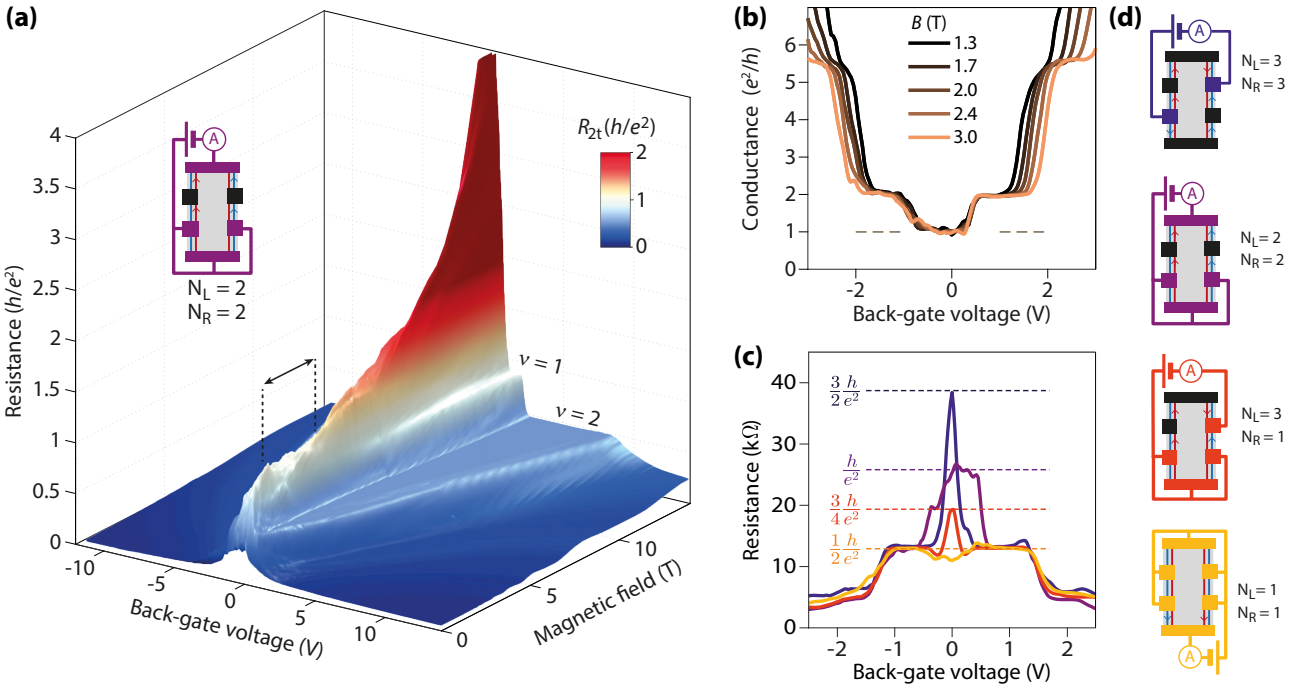

Figure 2.29: Low magnetic field quantum spin Hall effect in graphene. **(a)** Two-terminal resistance R_{2t} versus magnetic field B and back-gate voltage V_{bg}. In addition to standard quantum Hall plateaus at filling factors $\nu = 1$ and 2, the resistance exhibits a plateau at $\nu = 0$ between $B = 1.5$ and 4 T (delimited by the black arrow), which signals the regime of the QSH effect. **(b)** Two-terminal conductance $G_{2t} = 1/R_{2t}$ versus V_{bg} at different B. The QSH plateau of conductance e^2/h emerges at charge neutrality. **(c)** Two-terminal resistance versus V_{bg} at 2.5 T for different contact configurations schematized in (d) (black contacts are floating). Each contact configuration yields a resistance at charge neutrality reaching the expected value for helical edge transport, given by Equation (2.90). Figures taken from [122].

Similar measurements on a device with a very thick hBN spacer ($d_{\mathrm{BN}} \gg l_B$), where the substrate-screening from $SrTiO_3$ is negligible, showed that the resistance at charge neutrality strongly diverged upon applying a small magnetic field [122], indicating therefore an insulating ground state without edge transport. This demonstrates that the F phase indeed emerges as the ground state of charge-neutral graphene due to the substrate-screening of electron-electron interactions. Finally, as seen in Figure 2.29(a), increasing further the magnetic field (which decreases the substrate-screening) induces a topological quantum phase transition from the QHTI ferromagnetic phase to an insulating quantum Hall ground state.

Conclusion

In this chapter we showed that the physics of graphene under a perpendicular magnetic field greatly differs from conventional 2DEG. Its relativistic Landau levels disperse as the square root of the magnetic field and Landau index and are four-fold degenerate due to the spin and valley degrees of freedom of charge carriers. We saw how the relativistic quantum Hall effect arises from the appearance of edge channels, which makes the transverse conductance of a graphene device quantized as $G_{xy} = \nu e^2/h$, where the filling factor ν counts the number of edge channels. We also studied how Landau levels disperse on the last few l_B at the zigzag and armchair edges of graphene. Due to the Zeeman effect and Coulomb interaction in graphene, the spin and valley degeneracies are lifted and we introduced the ensuing quantum Hall ferromagnetism. Finally, we focused on the special case of the zeroth Landau level and how, depending of the interplay of the Zeeman energy and valley anisotropies, four different ground states can emerge at the $\nu = 0$ state. One in particular, the spin-polarized ferromagnetic F phase, which appears when the spin splitting becomes predominant, features helical spin-filtered edge channels and a quantum spin Hall effect in graphene.

Landau levels spectroscopy in graphene

CHAPTER 3

SCANNING Tunneling Microscopy (STM) and Spectroscopy (STS) are powerful techniques to investigate graphene electronic properties. The graphene 2D electron gas is directly accessible by a tip, on contrary to conventional 2D electron gases such as GaAs which are buried in semiconductor quantum wells. After graphene discovery in 2005, the first STM imaging of its honeycomb lattice was done in 2007 by Ishigami *et al.* [131] for graphene on SiO_2, soon followed by the first STS [132, 133, 134, 135] on graphene on various substrates. For graphene on SiO_2, interactions with the insulating substrate [136] limits graphene mobility, and disorder induces an important topographic corrugation of the graphene sheet [137] as well as charge puddles [28, 31, 32, 138, 139]. The stacking process to make van der Waals heterostructures of graphene on hexagonal boron nitride (hBN) developed by Dean *et al.* in 2010 [36] has enabled the production of higher quality graphene devices where graphene roughness and charge puddles are greatly reduced, as observed by STM measurements [35, 140, 141], see also Chapter 1.3. Under perpendicular magnetic field, Landau levels appear in the density of states of graphene which can be probed with STS, see Appendix A.1.3 for the working principle. We present in this review chapter the state of the art of Landau levels (LLs) spectroscopy in graphene.

Contents

3.1 Observation of Landau levels of Dirac fermions

Although graphene was first isolated on SiO_2 substrates using mechanical exfoliation from graphite crystals, the first observation of LLs of Dirac fermions was done on conductive highly oriented pyrolytic graphite (HOPG). Li *et al.* measured in 2007 [142] tunneling spectroscopy at the surface of bulk HOPG samples under perpendicular magnetic field B and observed LLs in the density of states corresponding to both massless Dirac fermions - with their position E_N scaling as $(NB)^{1/2}$ - and massive ones - scaling as NB - which suggested partial decoupling of the surface states from the bulk. Eventually, by cleaving the surface of a HOPG substrate, it became possible to find decoupled graphene flakes on the surface of HOPG where the tunneling spectroscopy yields LLs of Dirac fermions with E_N scaling as $(NB)^{1/2}$, as shown by Li, Luican and Andrei [53, 143]. Similarly, LLs of decoupled bilayer graphene flakes were also studied [144] in this system. Another process enables the growth of epitaxial graphene on silicon carbide (SiC) substrates where the graphene layers are electronically decoupled, and LLs of graphene were observed there by STS by Miller *et al.* [54] and Song *et al.* [98].

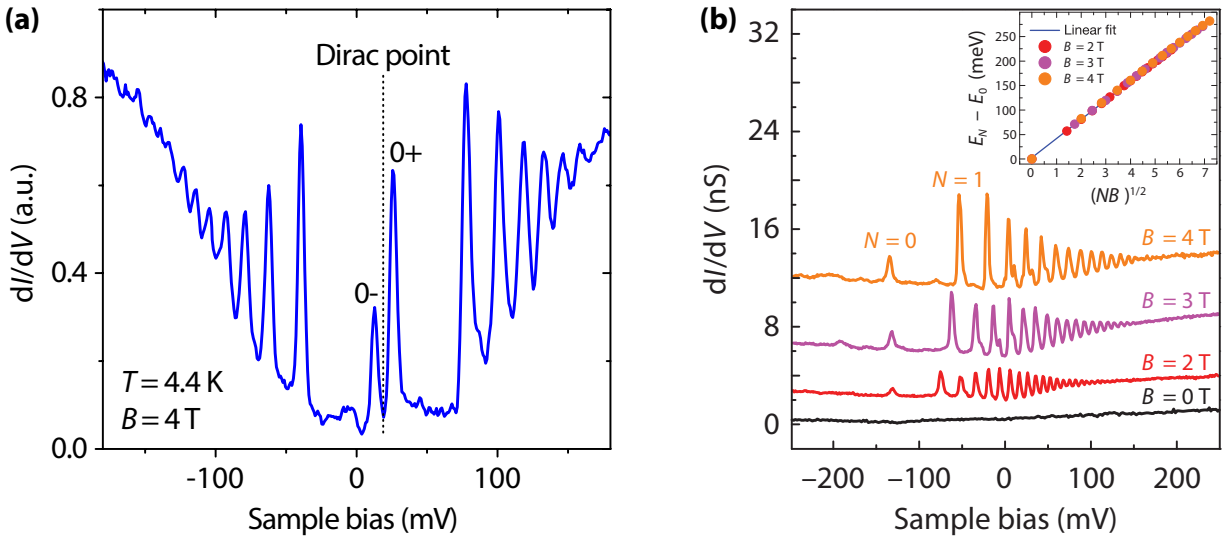

Figure 3.1: Landau level spectroscopy. (a) Tunneling spectrum of decoupled graphene on graphite at $T = 4\,\mathrm{K}$ and $B = 4\,\mathrm{T}$ showing well-resolved LLs. Figure taken from [53]. **(b)** Landau level tunneling spectroscopy of graphene on SiC at $T = 13\,\mathrm{mK}$ and different magnetic fields B. Inset: Landau level peak energy position versus $\sqrt{NB}$. The linear fit yields a carrier velocity of $v_\mathrm{F} = (1.08 \pm 0.03) \times 10^6\,\mathrm{m.s^{-1}}$. Figure taken from [98].

High-quality graphene tunneling spectra are shown in Figure 3.1 where LLs clearly appear as peaks at energetic position given by Equation (2.12). The position of the zeroth LL, which lies at the Dirac point, is not at zero bias which indicates intrinsic doping of graphene. One see that the width of the Landau peaks increases with their index N and, at large N, LLs merge and form a V-shape background, see Section 2.1.3. Last, in the spectrum in Figure 3.1(a), the LL that lies at zero bias splits into two sublevels, with the opening of a gap. This feature that results from electron-electron interactions is the focus of the last Section 3.8.

When studied on such conductive substrates, graphene flakes do not suffer from the drawbacks of SiO_2 substrate and present structural and electronic properties expected for a pristine graphene layer, although it is not possible to apply any gating effect - the Dirac point can consequently not be moved which greatly limits the possible experiments and the comparison to transport measurements.

3.2 Gate dependence of Landau levels

Graphene devices on insulating SiO_2 substrates, with either a hBN flake between or not, enable gating effect to tune the charge carrier density in graphene, hence the filling of the LLs and the position of the Dirac point[1]. At zero magnetic field the V-shape density of states of graphene makes the Dirac point move continuously in STS as the square root of gate voltage, given by Equation (1.44), see Chapter 1.2.3.

However in the quantum Hall regime the gate voltage shifts the Fermi level into areas of very high density of states - the Landau levels - separated by minima of very low density of states in the cyclotron gaps, see Figure 2.4(c). Filling the highly-degenerate LLs requires an important change of carrier density, or equivalently of gate voltage. The filling of one LL therefore results in the pinning of the Fermi energy to this level, as long as there are states to fill, which gives plateaus in the $\mathrm{d}I/\mathrm{d}V$ gate map. On the contrary, filling the low density of states in the cyclotron gap requires only a small change of carrier density and the Fermi level thus quickly jumps from the last occupied state of a filled LL to the first empty state of the next empty LL [147].

Consequently, in a STS gate map, as we vary the carrier density, the LLs form a staircase pattern as a function of gate voltage where each plateau corresponds to the pinning of the Fermi level in one LL, whereas the transitions correspond to the quick variations of the Fermi level in the cyclotron gaps. Such a gate map, shown in Figure 3.2(a), was obtained by Luican *et al.* in 2011 [22, 145] for graphene on SiO_2, as well as Jung *et al.* [27] : each vertical line is a tunneling spectrum $\mathrm{d}I/\mathrm{d}V$ taken at a given gate voltage. Disorder in graphene can then be qualitatively estimated in these maps : the broader the LL peaks are, the larger the slopes

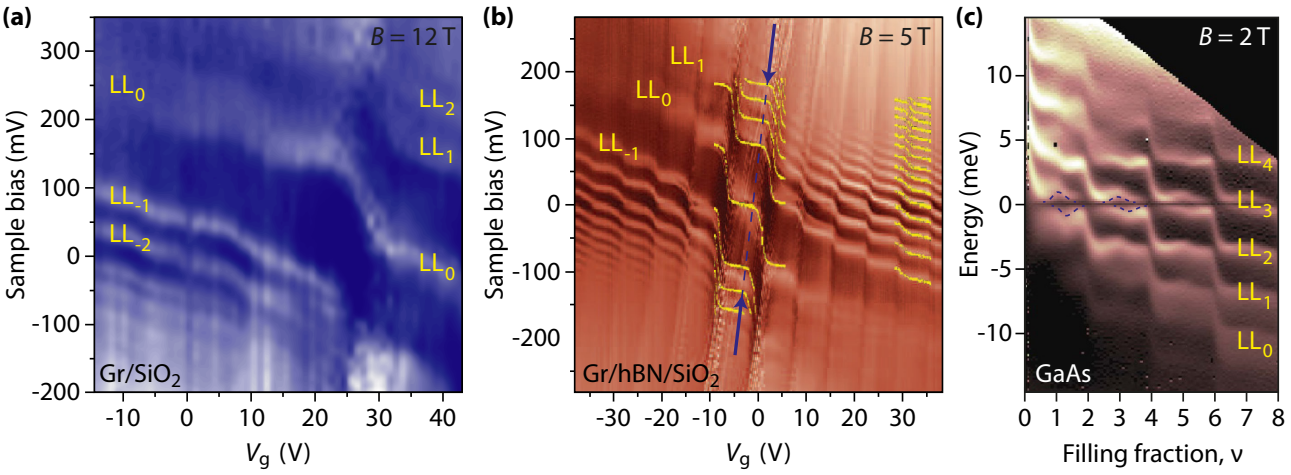

Figure 3.2: Landau level spectroscopy gate maps. (a) $\mathrm{d}I/\mathrm{d}V$ gate map as a function of sample bias and gate voltage V_g on graphene exfoliated on SiO_2 at $T = 4\mathrm{K}$ and $B = 12\mathrm{T}$. Landau levels correspond to the bright stripes and form a staircase pattern due to the successive pinning of the Fermi level. Figure taken from [145]. **(b)** $\mathrm{d}I/\mathrm{d}V$ gate map on graphene/hBN/SiO_2 heterostructure at $T = 4\,\mathrm{K}$ and $B = 5\,\mathrm{T}$. Figure taken from [47]. The blue arrows indicate one isodensity line. **(c)** Landau level spectroscopy in GaAs using time-domain capacitance spectroscopy to measure the single-particle density of states at $T = 100\,\mathrm{mK}$ and $B = 2\,\mathrm{T}$. Figure taken from [146].

[1] In STS, the Fermi level always lies at zero bias, and the Dirac point is moved with respect to the Fermi level by the gate voltage.

of the plateaus are (filling the LL implies a variation of E_F by the width of the peak) and the less abrupt the transitions between them are (the density of states in the cyclotron gap increases with disorder). The pinning effect is thus smeared out in disordered samples. The fact that LL peaks become sharper and better defined when they are brought closer to the Fermi level is attributed by Luican *et al.* [145] to the minimal scattering at the Fermi energy [39].

The first LLs spectroscopy on graphene/hBN/SiO_2 heterostructures was performed in 2012 by Chae *et al.* [47], whose data clearly show significant improvement of the tunneling spectra thanks to lower disorder with the observation of many LLs with enhanced lifetimes. They obtained gate maps for both regimes introduced in Chapter 2.1.3, the Shubnikov-de Haas regime where LLs are not fully separated ($\Omega_c\tau_e \gtrsim 1$) which gives a dI/dV gate map at $B = 2$ T with a continuous evolution of LLs, roughly as the square root of the gate voltage with no observable pinning of the Fermi level, and the quantum Hall regime at $B = 5$ T ($\Omega_c\tau_e \gg 1$) with the successive pinning of the Fermi level inside the LLs, see Figure 3.2(b).

Landau levels gate map in GaAs

Interestingly, similar gate maps were also observed in high mobility 2DEG in GaAs samples by Dial *et al.* in 2007 [146] using time-domain capacitive spectroscopy. They obtained the gate map shown in Figure 3.2(c) - note the equidistant spacing between the LLs for this conventional 2DEG, see Equation (2.e).

An important feature appears in this map due to low disorder : a magnetic-field-induced Coulomb gap opens at the Fermi level which splits LLs into two peaks. This gap is enhanced due to exchange energy and varies as a function of the filling factor. At even integer filling factor, between two plateaus, LLs are completely filled and there is no net spin polarization, and therefore no exchange gap. When one LL starts to be filled by increasing the carrier density, quantum Hall ferromagnetism (see Chapter 2.3.1) splits the spin states : one spin state starts to be filled and the exchange interaction opens a gap with the other spin states, gap which grows until it becomes maximal at odd filling factor with one spin state completely filled and the other empty. Increasing further the carrier density we start filling the upper spin state, decreasing the exchange interaction and the gap until both spin states (and the LL) are filled where the exchange gap closes.

This theory of oscillatory g factor, developed by Ando *et al.* in 1974 [148] and associated with the pinning of the Fermi level inside the LLs in the quantum Hall regime, yields specific patterns for LLs when they cross the Fermi level, see dashed line in Figure 3.2(c). In particular, for graphene case, one can expect that this feature happens not only at half-filling of LLs but also at quarter-filling due to valley degeneracy. Dial *et al.* [146] found that the spin gap in their GaAs samples scales as $B/\sqrt{\nu}$ while it is expected that an exchange-induced spin gap scales as the Coulomb energy with $\sqrt{B}$ at fixed ν [149, 150] (see Chapter 2.3.1).

3.3 Fermi velocity renormalization

Landau level spectroscopy is also a way to directly measure the Fermi velocity of charge carriers in graphene, from the linear fit of the LL positions in the dI/dV spectra as a function of $(NB)^{1/2}$. Although single-particle theory predicts $v_F \sim 1 \times 10^6$ m.s^{-1}, see Equation (1.10), the Fermi velocity is renormalized in real systems by electron-electron interactions. The screening of the Coulomb interaction, and therefore the measured value of the dispersion velocity as we

shall see in this section, strongly depends on the substrate graphene lies on through its dielectric properties (via the interaction parameter α_G), but also on the charge carrier density n (the screening length diverges at charge neutrality). In particular, at zero magnetic field, many-body theories [39, 40, 41, 42, 43, 44] predict a renormalized Fermi velocity v_F^* with a logarithmic divergence at charge neutrality[2] (see Chapter 1.3.3) :

$$\frac{v_F^*}{v_F} = 1 - \frac{\alpha_G}{\pi}\left[\frac{5}{3} + \ln(\alpha_G)\right] + \frac{\alpha_G}{8}\ln\left(\frac{n_C}{n}\right) \tag{3.1}$$

At zero and low magnetic fields, the renormalization of the Fermi velocity induces a squeezing of the Dirac cone, while at high magnetic fields in the quantum Hall regime, it induces an increase of the cyclotron gaps between LLs.

3.3.1 Influence of the substrate

Many works estimated the carrier velocity in graphene on different substrates, and Table 3.1 sums up some results obtained in STS. One remarks that the measured velocity differs from the expected single-particle value $v_F \sim 1 \times 10^6$ m.s^{-1} up to 20 %, depending on the substrate[3]. The differences stem from the dielectric constant ϵ of the medium which surrounds graphene, that depends on the substrate own dielectric constant. This modifies the interaction parameter $\alpha_G \propto 1/\epsilon$ and therefore the screening of electron-electron interactions in the graphene sheet.

System	v_F^* ($\times 10^6$ m.s^{-1})	Reference
Graphene/Graphite	0.79	Li *et al.* [53]
Graphene/Graphite	1.207 ± 0.002	Yin *et al.* [144]
Graphene/Graphene/SiO_2	1.2	Luican-Mayer *et al.* [152]
Graphene/SiC	1.08 ± 0.03	Song *et al.* [98]
Graphene/SiC	0.8	Wang *et al.* [153]
Graphene/SiO_2	1.12 ± 0.1	Jung *et al.* [27]
Graphene/SiO_2	1.07 ± 0.02	Luican *et al.* [145]
Graphene/hBN/SiO_2	1.1	Chae *et al.* [47]

Table 3.1: Fermi velocity v_F^* in graphene estimated by STS in different systems.

Moreover, other methods also enable the estimation of the Fermi velocity. Transport measurements on graphene/SiO_2 [2, 13, 29] estimated $v_F^* \approx 1.1 \times 10^6$ m.s^{-1}. Ponomarenko *et al.* [154] used capacitance measurements in aluminum oxide/graphene/SiO_2 capacitors to measure the density of states and obtained $v_F^* = (1.15 \pm 0.1) \times 10^6$ m.s^{-1}. Infrared spectroscopy of LLs in graphene/SiC measured by Sadowski *et al.* [155] and Orlita *et al.* [156] gives

[2]Under magnetic field B, the cutoff density n_C can be estimated [151] by equating the corresponding number of electrons in the negative filled LLs given by $-n_C = 4N_C/2\pi l_B^2$ (four electrons per Landau site, see Chapter 2.1.2), to that in the filled valence band of intrinsic undoped graphene, given by $2/S_0$ with $S_0 = 3\sqrt{3}a^2/2$ the area of graphene elementary cell which contains two electrons. N_C is the cutoff LL index given by :

$$N_C = \frac{\pi l_B^2}{S_0} \approx \frac{39\,500}{B[\mathrm{T}]}$$

[3]For the same substrate, the value of v_F^* measured in different works can also greatly differ. There may be two possible reasons. The first one is that the Fermi velocity value depends on the carrier density at which it is estimated, see Section 3.3.2. The second one is that the tip can have a level arm effect which renormalizes the LL energies, see Section 3.6, and the measure of v_F^* then becomes tip-dependent.

$v_F^* = (1.02 \pm 0.01) \times 10^6$ m.s^{-1}, while in graphene/SiO_2 infrared spectroscopy performed by Jiang *et al.* [157] yields $v_F^* \approx 1.1 \times 10^6$ m.s^{-1}. Chen *et al.* [158] studied the evolution of the Fermi velocity in graphene/hBN heterostructures as a function of the magnetic field using magneto-infrared spectroscopy. See also the work of Hwang *et al.* [159].

Finally, magneto-Raman spectroscopy measurements were done by Faugeras *et al.* [160] on different systems : suspended graphene, hBN-encapsulated graphene and graphene on graphite. They obtained for the three systems the magnetic field dependence of the Fermi velocity associated with two inter-LLs excitations, see Figure 3.3(b), which ranges between 1.0 and 1.4×10^6 m.s^{-1}. They also concluded that if conductive substrates ($\alpha_G \to 0$) such as graphite or SiC favor the single-particle behavior of graphene with $v_F^* \sim 1 \times 10^6$ m.s^{-1}, graphene on insulating substrates (with a weak dielectric screening) such as SiO_2 or hBN is strongly affected by electron-electron interactions as seen by the observed renormalized v_F^*. Sokolik *et al.* [151] furthermore analyzed these experimental data using a self-consistent screening model of Coulomb interaction which provided them an optimal value of the bare single-particle Fermi velocity $v_F = 0.85 \times 10^6$ m.s^{-1}.

3.3.2 Carrier-density dependence

We now focus on how the Fermi velocity evolves with the carrier density in graphene. In 2011, Luican *et al.* [145] obtained the carrier dependence of the renormalized v_F^* from their STS gate map in graphene/SiO_2, see Figure 3.2(a), by fitting the dI/dV spectra at each gate voltage point. The obtained Fermi velocity is shown in Figure 3.3(c). They found that v_F^* increases toward the Dirac point, which is consistent with the decrease of the screening of electron-electron interactions at lower carrier densities. The same year Elias *et al.* [46] were able to measure the cyclotron mass, and from it the Fermi velocity using Equation (1.34), in suspended graphene through Shubnikov-de Haas oscillations. They clearly obtained a logarithmic dependence of v_F^* with the carrier density n, see Figure 3.4(a), with measured value of $v_F^* \approx 3 \times 10^6$ m.s^{-1} at $n < 10^{10}$ cm^{-2}. This shows that the many-body renormalization described by Equation (3.1) still holds at low magnetic fields.

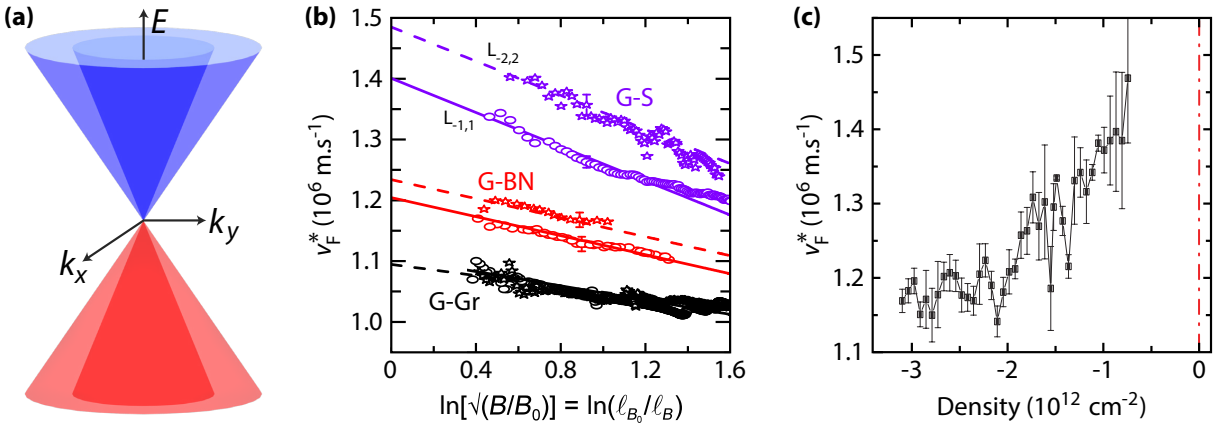

Figure 3.3: Renormalization of graphene Fermi velocity. **(a)** Single-particle (outer cone) and many-body (inner cone) graphene electronic spectra. **(b)** Dispersion velocity obtained from magneto-Raman spectroscopy at $T = 4$ K, associated with two inter-Landau level excitations, for suspended graphene (G-S), hBN-encapsulated graphene (G-BN) and graphene on graphite (G-Gr) samples. Figure taken from [160]. **(c)** Evolution of the Fermi velocity in graphene/SiO_2 as a function of carrier density, extracted from the gate map in Figure 3.2(a) at $T = 4$ K and $B = 12$ T. Figure taken from [145].

A similar result was obtained by Chae *et al.* in 2012 [47] in graphene/hBN/SiO_2 from their STS gate map, see Figure 3.2(b). They extracted the Fermi velocity at constant carrier density (after correcting the tip doping, see Section 3.6) and obtained the plot shown in Figure 3.4(b). They also observed a significant increase of v_F^* near charge neutrality with a logarithmic divergence described by Equation (3.1). Another important result is that the LL dispersion stays linear with $(NB)^{1/2}$ even at low carrier densities, which shows that the single-particle linear dispersion relation of graphene is conserved at low energies even toward charge neutrality where many-body effects become predominant, with only an effective increase of the dispersion velocity v_F^*. The Dirac cone bandstructure is therefore preserved but squeezed at low carrier densities, see Figure 3.3(a). Theoretical model and fit of this observed renormalization of the Fermi velocity were provided by Lozovik *et al.* [161].

High magnetic field regime

The behavior of the Fermi velocity close to charge neutrality in strong magnetic fields is still unclear, in particular concerning the logarithmic divergence described by Equation (3.1). The difference stems from the quantized bandstructure in the quantum Hall regime which may change the effects of electron-electron interactions in graphene. Russell *et al.* [164] found using infrared magnetospectroscopy in hBN-encapsulated graphene at $T = 6\,\mathrm{K}$ a non monotonic variation of v_F^* with the filling factor ν. Notably, they observed a plateau of v_F^* around $\nu = 0$ rather than a divergence. Sonntag *et al.* [162] noticed a similar feature in suspended graphene at $B = 3\,\mathrm{T}$ using magneto-Raman spectroscopy, with the renormalized velocity scaling linearly with the carrier density and therefore staying finite at charge neutrality where it forms a plateau, see Figure 3.4(c). They attributed this change in behavior with respect to the low magnetic field case (where LLs are not fully separated) to the localization of the electronic wave functions on the scale of l_B in the quantum Hall regime : the long-range Coulomb interaction, which is responsible for the divergence of v_F^* at charge neutrality, is suppressed, and therefore so is the logarithmic divergence.

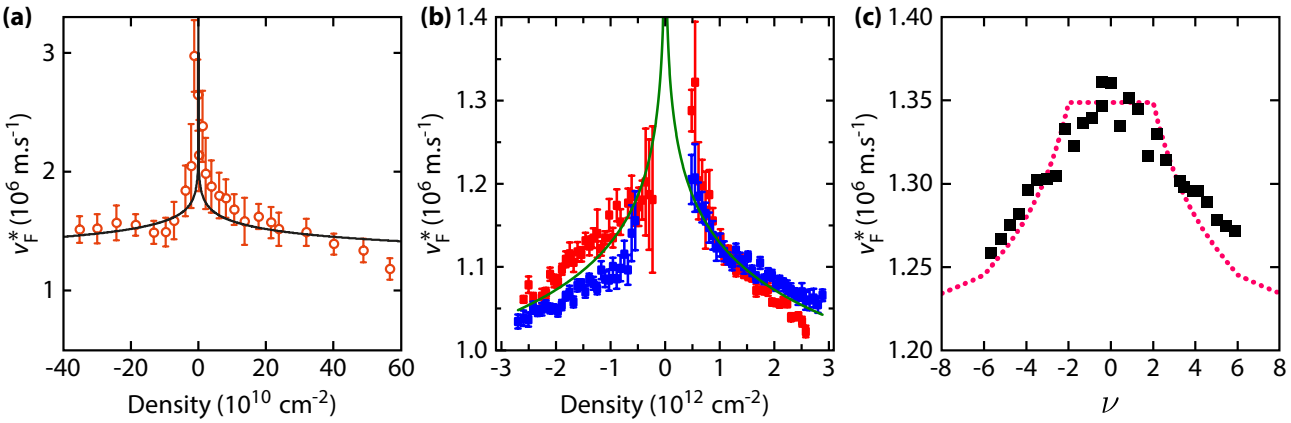

Figure 3.4: Carrier density dependence of graphene Fermi velocity. **(a)** Evolution of the Fermi velocity in suspended graphene as a function of carrier density. Figure taken from [46]. **(b)** Evolution of the Fermi velocity in graphene/hBN/SiO_2 as a function of carrier density, extracted from the gate map in Figure 3.2(b) at $T = 4\,\mathrm{K}$ and $B = 5\,\mathrm{T}$, for electron (red symbols) and hole (blue symbols) puddles. The green curve is a fit using Equation (1.50) with parameters $v_F = 0.957 \times 10^6\ \mathrm{m.s^{-1}}$ and $\alpha_G = 0.69$. Figure taken from [47]. **(c)** Evolution of the Fermi velocity in suspended graphene as a function of the filling factor ν as measured at $T = 4\,\mathrm{K}$ and $B = 3\,\mathrm{T}$ in [162] (black squares) and theoretical fit with a self-consistent screening (dotted red line) from [163] showing a plateau of v_F^* at $-2 < \nu < 2$.

Eventually, Sokolik *et al.* presented in 2019 [163] a theoretical many-body model in strong magnetic fields where they obtained that v_F^* saturates at a finite value at charge neutrality, forming a broad plateau between $-2 < \nu < 2$ as the Fermi level is pinned inside the zeroth LL, and quickly decreases at $|\nu| > 2$ due to enhancement of the screening of electron-electron interactions, see Figure 3.4(c).

However, note that the behavior of v_F^* in the quantum Hall regime observed in STS may differ from the one obtained in optical measurements due to the difference of nature of the quasiparticles - excitons for optical spectroscopy versus single electrons in tunneling spectroscopy [164]. For instance, Chae *et al.* [47] observed the logarithmic divergence of v_F^* at charge neutrality while having clear pinning of the Fermi level inside the LLs in their gate map, see Figure 3.2(b), which is the landmark in STS of the quantum Hall regime.

3.4 Lifting of Landau levels orbital degeneracy

Charged impurities at the surface of the substrate constitute the primary source of disorder and scattering in 2DEG [136, 165] and produce spatially localized signatures in the density of states measurable by STS. In graphene under strong magnetic field, they are notably expected to lift the orbital degeneracy of LLs in their vicinity [166, 167].

Luican-Mayer *et al.* studied in 2014 [152] the local influence of an isolated charged impurity, see inset in Figure 3.5(a), on graphene density of states in a bilayer graphene on SiO_2, where graphene flakes were twisted with a large angle to preserve the single-layer electronic spectrum of the top layer, while the bottom one helps reaching high sample quality. They obtained in this system the STS gate map shown in Figure 3.5(a) where the spectra were acquired far from the impurity. They next fixed the gate voltage to values corresponding to a more or less filled zeroth LL and measure the spatial evolution of the $\mathrm{d}I/\mathrm{d}V$ spectra as they cross the impurity. They observed that as the zeroth LL is filled, the spectra become more and more distorted close to the impurity, see Figure 3.5(b), with a downshift of LLs due to the attractive potential produced by the consequently positively charged impurity. This is the result of the screening of the impurity by the electron gas. As we saw in Chapter 2.2.1, when the Fermi level is pinned inside the zeroth LL, the system is compressible and the electron gas screens the impurity potential. However when the zeroth LL becomes almost empty, the impurity potential is not screened anymore and thus perturbs the LLs spectrum.

Individual $\mathrm{d}I/\mathrm{d}V$ spectra taken when the screening of the impurity is minimal clearly show that the zeroth LL splits into a series of discrete peaks in the vicinity of the impurity, see Figure 3.5(c), which is the consequence of the lifting of the orbital degeneracy m, introduced in Chapter 2.1.2, of LL_0. In particular, numerical simulations performed by Luican-Mayer *et al.* [152] showed that the perturbation due to the impurity appears in the E_{Nm} spectrum as a m-dependent energy downshift, which is maximal for E_{00} and decreases with increasing m and N, until we retrieve the unperturbed spectrum where unresolved sublevels (N, m) merge into a continuous m-independent LL_N.

Note that this impurity-induced orbital splitting happens at full filling of the LLs, which is at the opposite of the interaction-induced gap that emerges at partial filling of a LL (see Chapter 2.3.1). Both splitting therefore occur in different regimes in a STS gate map : broken-symmetry states appear when the Fermi level is pinned inside a LL (and for this level only) while the orbital splitting appear when the Fermi level lies in a cyclotron gap (with a shift of every LL).

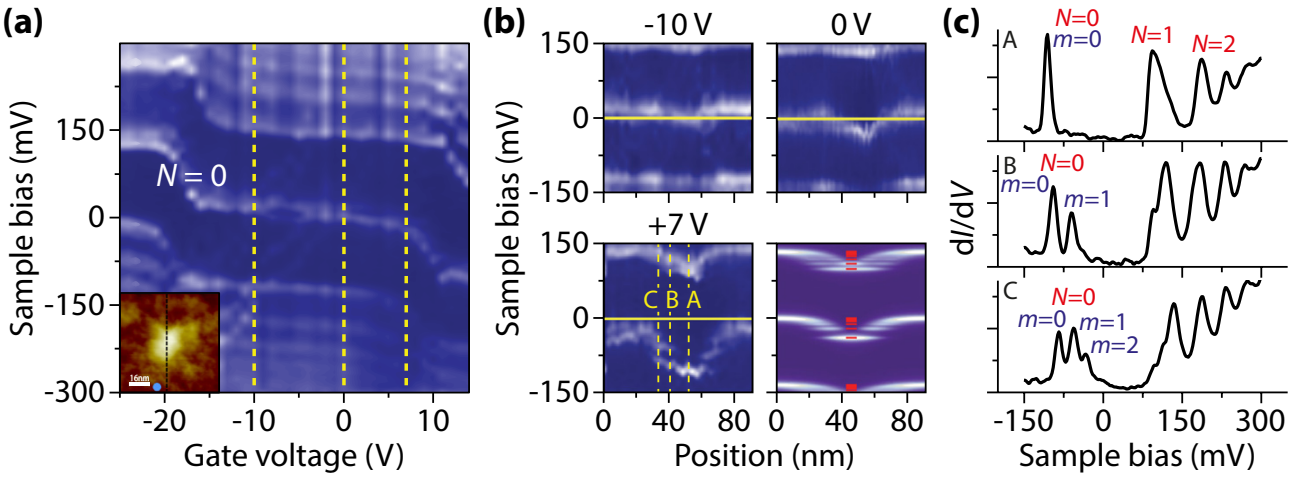

Figure 3.5: Lifting of Landau levels orbital degeneracy by a charged impurity. (a) $\mathrm{d}I/\mathrm{d}V$ gate map at $B = 10\,\mathrm{T}$ far from the impurity (blue dot in the inset, scale bar : 16 nm). **(b)** $\mathrm{d}I/\mathrm{d}V$ spectra measured across the impurity (dashed line in (a) inset) at different gate voltages corresponding to the dashed yellow lines in (a). The Landau levels sequence is distorted in absence of screening at integer filling factor ($V_\mathrm{g} = 7\,\mathrm{V}$) and reveals the lifting of the orbital degeneracy of Landau levels. Lower right panel : simulated DOS near the impurity at $V_\mathrm{g} = 7\,\mathrm{V}$, the red lines represent the computed energies E_{Nm}. **(c)** $\mathrm{d}I/\mathrm{d}V$ spectra corresponding to the dashed lines in the lower left panel of (b) and revealing peaks of the $N = 0$ Landau level with lifting orbital degeneracy m. Figures taken from [152].

3.5 Graphene quantum dots

The electronic properties of graphene, in particular its density of states, are greatly influenced by its electrostatic environment, in particular by the interactions with the substrate beneath. We study in this section how quantum dots appear in bulk graphene, due to the disorder potential and charged impurities, and induce charging effects in the tunneling spectra characteristic of the Coulomb blockade physics.

3.5.1 Coulomb blockade physics and charging peaks

We already discussed in Chapter 1.3.1 how charge puddles appear in graphene at zero magnetic field due to the disorder potential induced by the substrate beneath, in particular for SiO_2 due to its important roughness and the existence of many charged impurities at its surface [136]. However electrons are not confined into one puddle because of the Klein tunneling [24, 25]. Increasing the magnetic field makes electrons move in cyclotron orbits, until they eventually get localized when their cyclotron radius becomes much smaller than the size of the charge puddles, which prevents Klein tunneling between adjacent puddles [168].

Jung *et al.* studied in 2011 [27] the graphene/SiO_2 system in the quantum Hall regime and observed that the electron gas breaks up into conductive compressible regions, which form quantum dots in bulk graphene where electrons are confined [169, 170], see Figure 3.6. Each quantum dot is separated from the others by insulating incompressible strips which form around hills and valleys of the disorder potential of the substrate. Furthermore, when realizing a STS gate map in the quantum Hall regime, they not only observed the successive pinning of the Fermi energy inside the LLs but also some quartets of peaks running diagonally in the $\mathrm{d}I/\mathrm{d}V$ map in opposite direction of that of LLs, and crossing them at the Fermi level, see Figure 3.7. Their

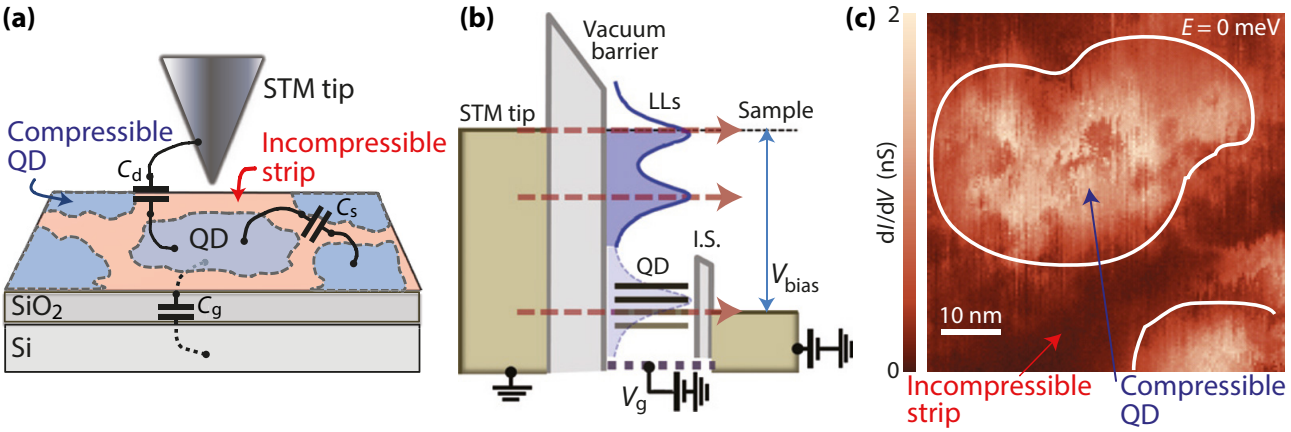

Figure 3.6: Quantum dots in graphene in the quantum Hall regime. **(a)** Quantum dot in graphene with capacitive coupling with the back gate (C_g), the tip (C_d) and other dots (C_s) from which it is separated by insulating strips. **(b)** Single-electron tunneling events through the dot with two tunneling barriers. The discrete charging levels of the dot originate from the confined Landau level at the Fermi level. **(c)** Spatial dI/dV map at $B = 8$ T showing a compressible zeroth Landau level region surrounded by incompressible strips, which defines an isolated graphene quantum dot. Figures taken from [27].

intersection takes the form of a well-defined pattern of four Coulomb diamonds, which is the signature of charging effects of the Coulomb blockade physics in quantum dots [171] : each so-called charging peak corresponds to single-electron charging effects in the graphene quantum dot.

This shows that tunneling from tip to graphene therefore requires an electron to tunnel first from the tip to the graphene quantum dot (through the vacuum barrier) and then from the dot to bulk graphene (through the incompressible strip). Inside the quantum dot, the LL in which the Fermi level is pinned becomes quantized into discrete charging levels that create the charging peaks, which appear as quartets due to valley and spin degeneracies of LLs, see Figure 3.6(b). In particular, Coulomb charging peaks appear in spatial dI/dV maps as four concentric rings inside the quantum dot [27].

3.5.1.a Addition energy in graphene quantum dots

The bias spacing ΔV_{bias} between adjacent dI/dV peaks correspond to the energy required to add a new charge into the quantum dot. This addition energy E_{add} can be written as :

$$E_{\text{add}} = E_{\text{c}} + \Delta \tag{3.2}$$

where the charging energy E_{c} is the electrostatic energy the additional electron must overcome, while Δ includes the spin and/or valley gaps of graphene.

The charging energy is determined by the total capacitance of the dot as [171] :

$$E_{\text{c}} = \frac{e^2}{C_{\text{tot}}} \tag{3.3}$$

where $C_{\text{tot}} = C_{\text{g}} + C_{\text{s}} + C_{\text{d}}$ with C_{g} the capacitance between the dot and the back gate and C_{s}, C_{d} the capacitances between the dot and respectively the source and the drain, each one being either the tip or bulk graphene depending on the sign of V_{bias}.

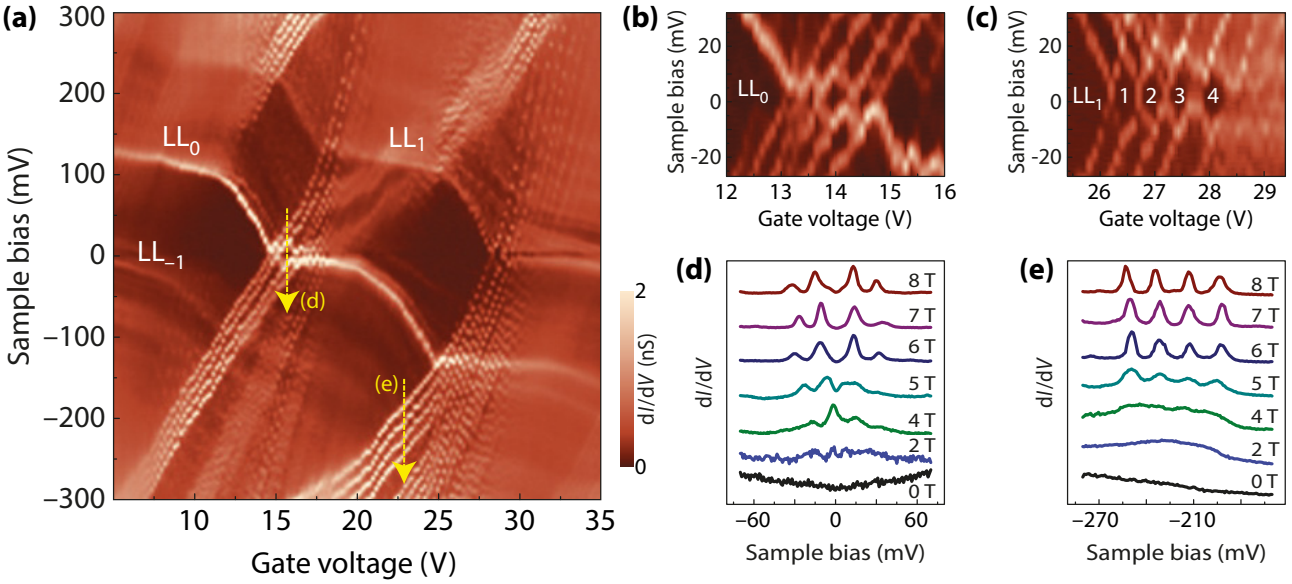

Figure 3.7: STS gate map with quartets of charging peaks. (a) $\mathrm{d}I/\mathrm{d}V$ gate map at $B = 8\,\mathrm{T}$ in graphene/SiO_2 showing quartets of charging peaks intersecting the $N = 0$ and $N = 1$ Landau levels when they cross the Fermi level. **(b,c)** Four Coulomb diamonds appear at the Fermi level when the charging peaks intersect the Landau level $N = 0$ in (b) and $N = 1$ in (c). **(d,e)** $\mathrm{d}I/\mathrm{d}V$ spectra corresponding to the dashed lines in (a) as a function of magnetic field. The charging peaks appear at strong magnetic fields and overshadow the Landau levels peaks in the spectra. Figures taken from [27].

The ratio of capacitances can be obtained from the slopes of the Coulomb diamonds (see Figure 3.8), this enables to write C_{tot} as a function solely of C_{g}, which is the only capacitance one can easily express assuming a parallel plate capacitor model[4] :

$$C_{\mathrm{g}} = \epsilon_0 \epsilon_{\mathrm{r}} \frac{\pi R_{\mathrm{dot}}^2}{d} \tag{3.4}$$

with ϵ_{r} the dielectric constant of the gate insulator and d its thickness, and R_{dot} the size of the quantum dot that can therefore be estimated from the measure of the charging energy E_{c}.

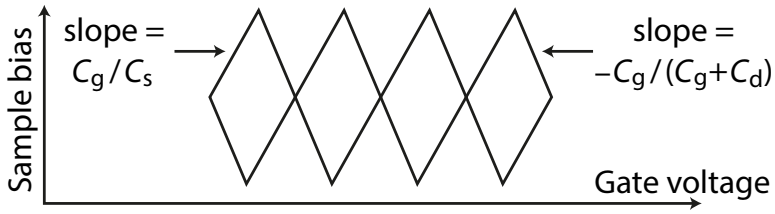

Figure 3.8: The capacitances ratio between C_{g}, C_{s} and C_{d} can be extracted from the slopes of the Coulomb diamonds in a $\mathrm{d}I/\mathrm{d}V$ gate map.

Jung *et al.* [27] observed that the peak spacing ΔV_{bias} inside one quartet is not constant for the zeroth LL, which makes the central diamond larger than the others, see Figures 3.7(b,d). They related that increase to the breaking of the valley symmetry and estimated the valley gap as 10 meV at 8 T. They also extracted the charging energy as $E_{\mathrm{c}} = (16.4 \pm 0.6)$ meV from which they computed the diameter of the graphene quantum dot as $R_{\mathrm{dot}} = (45 \pm 1)$ nm.

[4]We assume the parallel plate capacitor model is valid since the graphene quantum dot is part of a much larger graphene sheet, hence there is no edge effect for the electrical field at the boundaries of the quantum dot.

3.5.2 Interaction effects in confined states

We studied in Chapter 2.2.1 how a confining potential in a 2DEG makes compressible and incompressible strips appear at the edges of the confined region [75, 78, 172]. Due to dependency of the screening with the filling factor, the confining potential flattens in the compressible regions, forming a staircase-like pattern as a function of the distance from the edge. Such a confining potential can be created by a quantum dot in graphene in the quantum Hall regime. The radial confinement here leads to a characteristic wedding cake-like shape of the screened confining potential, see Figure 3.9(b), with the appearance inside the quantum dot of a concentric series of compressible rings separated by incompressible strips.

Edge-free graphene quantum dots can be formed in the graphene/hBN/SiO_2 system using ionized impurities in hexagonal boron nitride created by pulsing a strong electric field with a STM tip [173, 174, 175]. Both n-type and p-type quantum wells can be obtained and they act as circular pn junctions with built-in local nanoscale confining potentials which are, with the dot doping, both tunable by the back-gate voltage. It is therefore possible to control the number of LLs crossing the Fermi energy and thus the number of compressible rings inside the graphene quantum dot.

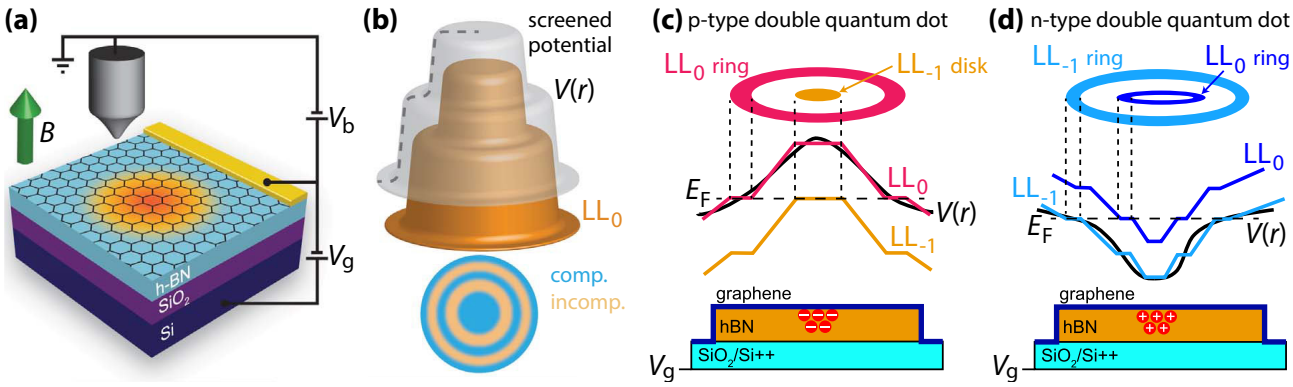

Figure 3.9: . (a) Graphene device with a quantum dot resonator forming a p-doped center inside a n-doped background. **(b)** The screened confining potential inside the quantum dot takes the form of a wedding cake due to electron-electron interactions with alternating compressible and incompressible disks and rings. **(c)** Landau levels in a p-type quantum dot tuned to the double-dot regime : two Landau levels LL_0 and LL_{-1} cross the Fermi energy which results in each one making either a compressible ring or disk inside the dot. **(d)** Same as (c) but for a n-type dot. Figures (a,b) taken from [82] and Figures (c,d) taken from [176].

Magnetic quantization inside quantum dots in a 2DEG has first been probed using Coulomb blockade spectroscopy [171, 177, 178]. Gutiérrez *et al.* studied the case of a p-doped graphene quantum dot in 2018 [82]. They measured the spatial dependence of $\mathrm{d}I/\mathrm{d}V$ tunneling spectra as they pass trough the graphene dot. At zero magnetic field, the confining potential appears as a bright concave band in the spatial map, see Figure 3.10(a), which surrounds resonance states that arise in the dot due to large-angle scattering which circumvent Klein tunneling [173, 179]. The transition from spatial to magnetic confinement occurs when the magnetic length l_B becomes smaller than the width of the confining potential. At $B = 1$ T some resonating states of the dot start to merge into the zeroth LL, see Figure 3.10(a). Increasing further the magnetic field, more and more states merge into LLs which appear as brighter and brighter bands in the maps. Eventually at $B = 4$ T, see Figure 3.10(b), the LLs flatten and form plateaus of compressible regions, taking an overall wedding cake-shape, in agreement with simulations which take into account electron-electron interactions. Spatial $\mathrm{d}I/\mathrm{d}V$ maps

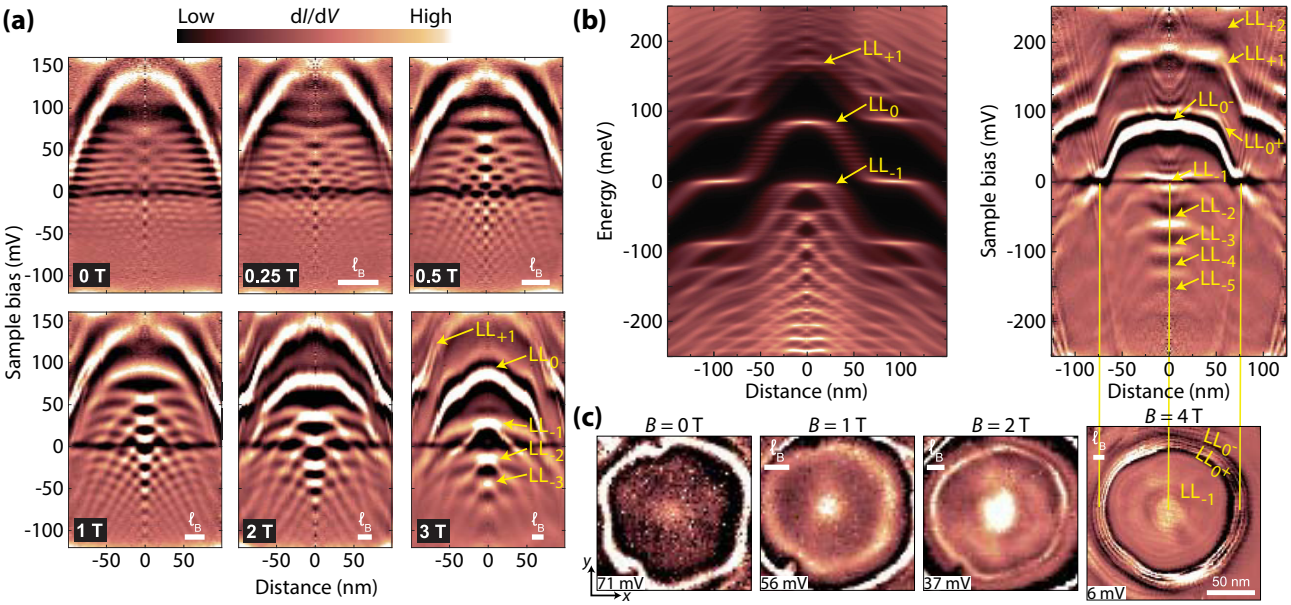

Figure 3.10: Interaction-driven wedding-cake structures in graphene quantum dots in the quantum Hall regime. (a) $\mathrm{d}I/\mathrm{d}V$ spectra as a function of the distance from the center of the p-doped quantum dot, for different magnetic fields, showing the condensation of the dot states into Landau levels as the magnetic field is increased. **(b)** The wedding cake structure of Landau levels inside the quantum dot is well visible at $B = 4$ T (right panel) in agreement with the many-body simulation with the screened confining potential (left panel). **(c)** Spatial $\mathrm{d}I/\mathrm{d}V$ maps at increasing magnetic fields showing the appearance of a $N = 1$ Landau level compressible disk at the center of the dot and an outer $N = 0$ ring, separated by an incompressible ring. In the four figures the scale bar is the same. Figures taken from [82].

presented in Figure 3.10(c) [82] show that under magnetic field, LLs form concentric rings and disks of compressible liquids in the quantum dot, separated by incompressible liquid regions, and simultaneously contract toward the center of the dot as the magnetic field is increased. These compressible islands can be described as LL quantum dots. In particular, when one LL is pinned at the Fermi energy, Coulomb charging peaks appear as seen in Figure 3.10(b) where both $N = 0$ and $N = -1$ LLs cross the Fermi level at $B = 4$ T and charging peaks occur at the intersections. Corresponding quartets of charging rings consequently appear in the right panel of Figure 3.10(c) around the $N = -1$ disk at the center of the dot and the $N = 0$ ring.

Walkup *et al.* studied in 2020 [176] the charging effects and interactions between LLs islands inside a graphene quantum dot, for both p-type and n-type wells, see Figure 3.9(c,d) (though we focus here only on the n-type case). The gate voltage enables the tuning of the confinement geometry : for a certain range of voltage, only one LL dot forms with the corresponding charging effects while for another range two LL dots exist and a double-dot charging pattern can be observed. The evolution of the double-dot tunneling spectroscopy with the gate voltage is shown in Figure 3.11(a). Though the expected staircase pattern is retrieved, many charging peaks[5] appear as slanted bright lines and intersect the LLs when they cross the Fermi energy. At $V_g \approx -10$ V, the $N = -1$ LL is pinned at the Fermi energy and is being filled, which forms a LL_{-1} disk inside the graphene quantum dot, see Figure 3.11(c). Each charging peak which appears in the gate map as the gate voltage is increased corresponds to

[5]The orbital degeneracy of LLs is lifted inside the graphene dot. Each orbital state can be charged four times due to spin and valley degeneracies, so that charging peaks are clustered into quartets, after what the next orbital state can be charged by overcoming an additional energy gap. This was particularly observed for p-type dots [176].

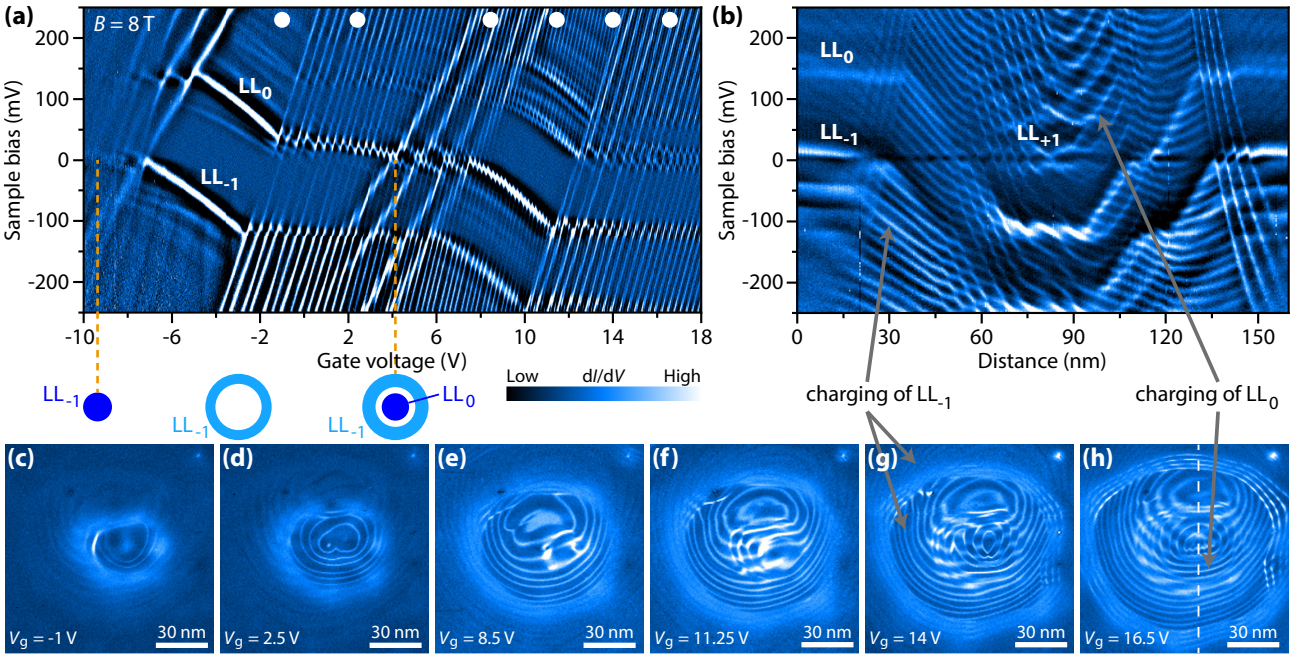

Figure 3.11: Charging and interactions between double Landau level dots. (a) $\mathrm{d}I/\mathrm{d}V$ gate map at the center of the n-doped quantum dot at $B = 8\,\mathrm{T}$. The charging of the LL_{-1} dot starts when the first electron is added at $V_\mathrm{g} \approx -9.5\,\mathrm{V}$ as indicated by the slanted bright line which intersects the Fermi energy at the position marked by the yellow dashed line. Similarly, the charging of the LL_0 dot starts at $V_\mathrm{g} \approx 4\,\mathrm{V}$ with the appearance of a new series of charging peaks which differ from those related to the LL_{-1} ring with a characteristic avoided crossing pattern. **(b)** $\mathrm{d}I/\mathrm{d}V$ spectra taken through the centers of the double-dot system, along the dashed line in (h). Landau levels exhibit an inverted wedding-cake shape and charging events appear as series of convex parabolas with different curvatures. **(c-h)** $\mathrm{d}I/\mathrm{d}V$ spatial maps showing top views of the graphene dot at different gate voltages corresponding to the white circles in (a). As the gate voltage is increased, the LL_{-1} dot appears with an increasing number of concentric charging lines. The LL_0 dot later appears in (f) with a new set of charging lines. Figures taken from [176].

the addition of a single charge to the LL_{-1} dot. As additional charges are added the LL_{-1} dot expands, see Figure 3.11(c-e). When the LL_{-1} is filled and therefore shifted below the Fermi level, its compressible part expands outward in the graphene dot which forms a LL_{-1} ring while the center of the dot becomes incompressible and insulating. The increase of the LL_{-1} dot size can be seen in the gate map as the charging peaks get more and more finely spaced[6].

At $V_\mathrm{g} \approx 4\,\mathrm{V}$ the $N = 0$ LL crosses the Fermi energy inside the graphene dot which forms a concentric double-dot with a LL_0 disk inside the LL_{-1} ring, see Figure 3.11(f-h). In this double-dot regime, a new set of charging peaks with a different slope and corresponding to the charging of the LL_0 dot appears in the gate map. Figure 3.11(b) shows the evolution of the $\mathrm{d}I/\mathrm{d}V$ spectra as the tip pass through the centers of both dots. Alongside the inverted wedding-cake structure of LLs expected for the n-type dot, the charging of the double LL_{-1} and LL_0 dots appear as series of convex parabolas whose vertical spacing is given by the charging energy of the respective dot. Finally, the charging patterns for both LL_{-1} ring and LL_0 disk feature in the gate map a lattice of avoided crossings which results from the interactions between each LL dot [176].

[6]The charging energy decreases with the dot size, see Equations (3.3) and (3.4).

3.6 Tip influence on tunneling spectroscopy

So far we have supposed that the tip does not perturb the graphene, so that the $\mathrm{d}I/\mathrm{d}V$ spectra correctly probe its pristine electronic properties. However tunneling measurements require to bring the metallic tip to very close vicinity of graphene which can make the measure itself invasive, in particular due to the electrostatic interactions between the tip and the sample.

Tip gating An immediate effect of the tip is an unintentional local doping of graphene due to the field effect of the tip[7]. The total doping of graphene from field effects of both the back gate and the tip is therefore :

$$n = \frac{1}{e}\left(C_\mathrm{g} V_\mathrm{g} - C_\mathrm{tip} V_\mathrm{bias}\right) \tag{3.5}$$

with the capacitances C_g between graphene and the back gate and C_tip between the tip and graphene.

As a result, constant carrier densities in a STS gate map $(V_\mathrm{g}, V_\mathrm{bias})$ do not appear as vertical lines at constant gate but as tilted ones, with a slope determined by the ratio between both capacitances $C_\mathrm{g}/C_\mathrm{tip}$. Tip gating effect can be seen in the STS gate map in Figure 3.2(b) where the LLs staircase transitions do not occur at constant V_g, as indicated by the blue arrows.

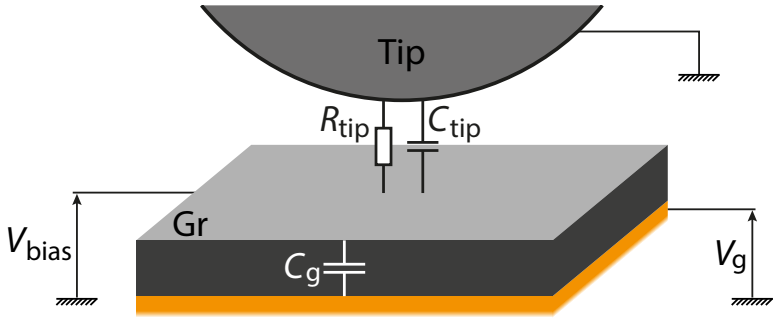

Figure 3.12: Gating of graphene from both back gate and tip through the tunneling junction.

Tip lever arm As shown in Figure 3.12, the sample is capacitively coupled to at least the tip (C_tip) and the back gate (C_g). Because of the capacitive coupling between the sample and the gate, a bias voltage variation ΔV_bias, as measured in a $\mathrm{d}I/\mathrm{d}V$ spectrum, does not strictly induce a shift in energy of the sample density of states of $e\Delta V_\mathrm{bias}$. In fact we rather have an effective energy shift of $\Delta E < e\Delta V_\mathrm{bias}$.

In order to convert correctly bias and energy one must take into account the tip lever arm α_tip which is the ratio between the tip-sample capacitance C_tip to the total capacitance C_tot, that is the sum of C_tip, C_g and other capacitive coupling, for instance in the case of a quantum dot, see Figure 3.6(a). We therefore have :

$$\alpha_\mathrm{tip} = \frac{C_\mathrm{tip}}{C_\mathrm{tot}} \qquad \Rightarrow \qquad \Delta E = \alpha_\mathrm{tip} \times e\Delta V_\mathrm{bias} \tag{3.6}$$

There are several possibilities to estimate the tip lever arm, using electrostatic calculations or directly from experimental data.

[7] In our setup the bias voltage is applied on the sample rather than on the tip which is grounded. We can nonetheless still write the field effect of the back gate as $en = C_\mathrm{g} V_\mathrm{g}$ since $V_\mathrm{bias} \ll V_\mathrm{g}$.

3.6.1 Electrostatic confinement of Landau levels

Confinement of electrons in graphene can also be achieved using the STM tip electrostatic potential. At zero magnetic field, Zhao *et al.* [179] observed electron whispering-gallery modes in graphene inside a circular electron cavity. The cavity itself was created by the confining potential produced by a local pn junction ring induced by the tip bias and the gate voltage. Under magnetic field, the tip-induced electrostatic potential locally shifts the LLs inside the cyclotron gaps, which provides fine tuning of the confinement, especially for the larger gaps such as the one between the zeroth and first LLs, see Figure 3.13(a,b). This approach was done by Freitag *et al.* in 2016 [180]. STS measurements inside this edge-free graphene quantum dot revealed many quartets of charging peaks in the $\mathrm{d}I/\mathrm{d}V$ spectra, see Figure 3.13(c). The addition energy E^i_{add} between charging peaks i and $i+1$ is given by :

$$E^i_{\mathrm{add}} = E^i_{\mathrm{c}} + \Delta_i \tag{3.7}$$

where E^i_{c} is the charging energy already defined in Equation (3.2) and Δ_i consists of the orbital splitting Δ^{o}, the valley splitting Δ^{V} and/or the spin splitting Δ^{S}.

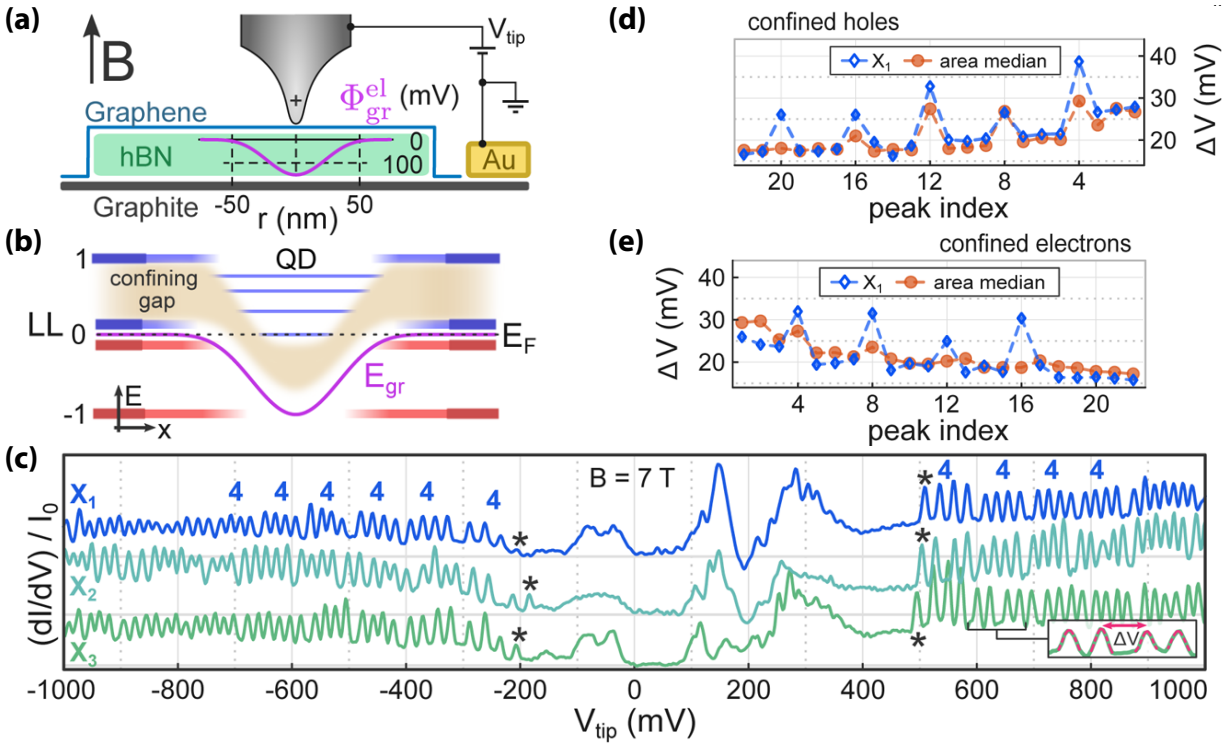

Figure 3.13: Tip-induced graphene quantum dot. (a) The tip induces an electrostatic confinement potential $\Phi^{\mathrm{el}}_{\mathrm{gr}}$ in graphene (magenta line) which creates a quantum dot. **(b)** Inside the dot, Landau levels are downshifted due to the local band bending E_{gr}. States embedded in the cyclotron gap between LL_1 and LL_0 are electrostatically confined. **(c)** $\mathrm{d}I/\mathrm{d}V$ spectra at $B = 7$ T in different points of graphene, with more than 40 charging peaks clustered into quartets. The first charging peaks for both electron and hole sides are marked by an asterisk. **(d,e)** Spacing between successive charging peaks ΔV for one spectrum (blue points) and the median values for an area of 60×60 nm^2 (orange points). Figures taken from [180].

The charging energy was found by Freitag *et al.* [180] to be nearly independent of the charge state i of the dot such as $E^i_{\mathrm{c}} \approx E_{\mathrm{c}} \approx 10$ meV. The charging peaks are clustered into quadruplets due to the additional orbital splitting, see Figure 3.13(d,e), which can therefore be estimated as $\Delta^{\mathrm{o}} \approx 4 - 10$ meV at $B = 7$ T. An additional doublet structure was also observed for the

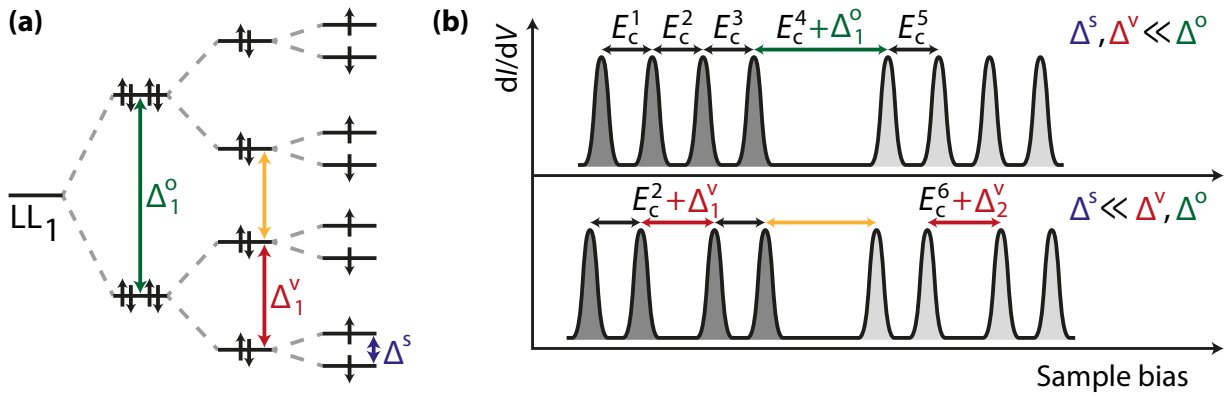

Figure 3.14: Landau level splitting and addition energies of a graphene dot. **(a)** Energy level diagram of a graphene dot for the first two orbital states of the first Landau level, with an orbital gap Δ_1^o. The breaking of the valley symmetry opens an additional gap Δ^V in each orbital state, and the same goes with the spin gap Δ^S which is far smaller than the other two. **(b)** Adding an electron to the dot requires an addition energy given by Equation 3.7. The orbital gap Δ^o clusters charging peaks intro quartets. If Δ^V is not negligible, the quartets are as well separated into doublets.

first orbital states which was attributed by Freitag *et al.* to the lifting of the valley degeneracy, estimated to be $\Delta^V \approx 3$ meV, see Figure 3.14.

Freitag *et al.* studied in 2018 [181] the nanoscale variations of the charging energies in a graphene/hBN/graphite/SiO_2 system, where the superposition of graphene on hBN yields a Moiré superlattice, see Chapter 1.3.2 and Figure 3.15. Because of the inequivalent stacking sites of the C atoms with respect to the B and N atoms of the hBN layer, a spatially dependent sublattice symmetry breaking is expected in graphene. Using the electrostatic potential of the tip to induce a quantum dot in graphene, dot which can be spatially moved by moving the tip, Freitag *et al.* were able to measure the different addition energies between successive charging peaks and their spatial variations. They thus obtained spatial maps of the different addition energies E_{add}^i between the peaks i and $i+1$, which are related to the spatial variations of either the orbital, valley or spin splitting, see Figure 3.14 (the spatial variations of the charging energy are supposed negligible). Figure 3.15 presents the spatial maps of the valley and spin splitting for one orbital state. One can observe that the maps indeed clearly feature short-range superlattice-periodic modulations which appear as dark ring-like structures at the center of the Moiré supercells for the valley addition map E_{add}^6 and spin addition maps E_{add}^5 and E_{add}^7.

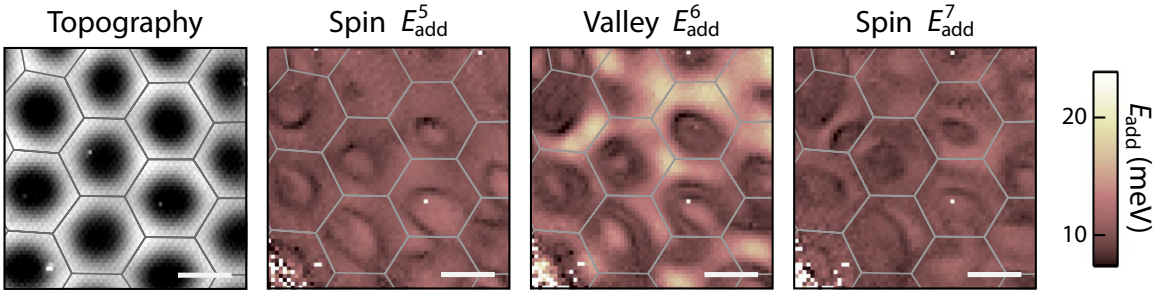

Figure 3.15: Addition energy spatial maps for spin and valley gaps. Left : STM image showing the superlattice of the Moiré pattern of graphene on hBN. Others : E_{add}^i spatial maps imaging the spatial variations of spin or valley gaps. The gray lines mark the Moiré supercells. Scale bars : 10 nm. Figures taken from [181].

3.6.2 Pseudomagnetic fields in strained graphene

The graphene sheet has sometimes been observed to be attracted and deformed locally due to interactions with the STM tip [182], deformation which is then determined by the competition between the attraction force with the tip, the pinning of the graphene layer to its substrate and finally the rigidity of the graphene sheet [136]. A immediate consequence is that the STM image of deformed graphene is not that of the relaxed sheet, which may add an additional corrugation.

Mechanical deformations in graphene were also shown to lead to the introduction of a pseudo-potential vector $\boldsymbol{A}_{\text{ps}}(\boldsymbol{r})$ which is directly proportional to specific strain terms [183, 184, 185]. This results in the appearance of a pseudomagnetic field perpendicular to the graphene plane :

$$\boldsymbol{B}_{\text{ps}} = \left[\boldsymbol{\nabla} \times \boldsymbol{A}_{\text{ps}}\right]_z \, \boldsymbol{e}_z \tag{3.8}$$

$\boldsymbol{A}_{\text{ps}}$ differs from the electromagnetic potential vector $\boldsymbol{A}$ such that $\boldsymbol{A}_{\text{ps}}$ does not break time-reversal symmetry (and the same goes for $\boldsymbol{B}_{\text{ps}}$) : the canonical momentum $\boldsymbol{\pi}$, introduced in Equation (2.2), is thus written with different signs for both valleys K and K' (indexed by $\xi = \pm 1$) [186, 187] :

$$\boldsymbol{\pi} = \boldsymbol{p} + \xi e \boldsymbol{A}_{\text{ps}} \tag{3.9}$$

Using this substitution with the Hamiltonian given by Equation (1.26), we obtain in the four-spinor basis $\Psi = (\psi_{A,K} \ \psi_{B,K} \ \psi_{B,K'} \ \psi_{A,K'})$:

$$\widehat{\mathcal{H}} = v_{\text{F}} \begin{pmatrix} \boldsymbol{\sigma}.\left(\boldsymbol{p} + e\boldsymbol{A}_{\text{ps}}\right) & 0 \\ 0 & -\boldsymbol{\sigma}.\left(\boldsymbol{p} - e\boldsymbol{A}_{\text{ps}}\right) \end{pmatrix} \tag{3.10}$$

The squared Hamiltonian reads as :

$$\widehat{\mathcal{H}^2} = v_{\text{F}}^2 \begin{pmatrix} \left(\boldsymbol{p} + e\boldsymbol{A}_{\text{ps}}\right)^2 \mathbb{1} + e\hbar B_{\text{ps}} \sigma_z & 0 \\ 0 & \left(\boldsymbol{p} - e\boldsymbol{A}_{\text{ps}}\right)^2 \mathbb{1} - e\hbar B_{\text{ps}} \sigma_z \end{pmatrix} \tag{3.11}$$

The sublattice components on A and B of the eigenfunctions are thus given by the equations :

$$E^2 \psi_A^{K,K'} = v_{\text{F}}^2 \left[\boldsymbol{\pi}^2 + e\hbar B_{\text{ps}}\right] \psi_A^{K,K'} \tag{3.12a}$$

$$E^2 \psi_B^{K,K'} = v_{\text{F}}^2 \left[\boldsymbol{\pi}^2 - e\hbar B_{\text{ps}}\right] \psi_B^{K,K'} \tag{3.12b}$$

The first term $\boldsymbol{\pi}^2$ leads to a quantization of the density of states into pseudo-Landau levels with a dispersion relation similar to Equation (2.12), where the external magnetic field B is replaced by the pseudomagnetic field B_{ps} (for homogeneous B_{ps} on the scale of $l_{B_{\text{ps}}}$). The second term $v_{\text{F}}^2 e\hbar B_{\text{ps}}$ is equivalent to a pseudo-Zeeman coupling term between the pseudomagnetic field B_{ps} and graphene pseudospin A/B. The associate pseudo-Zeeman energy scales as $B_{\text{ps}}^{1/2}$ and breaks the pseudospin symmetry by shifting upward in energy states of sublattice A and downward states of sublattice B. As a conclusion, this strain-induced pseudomagnetic field yields locally in graphene a pseudo-Landau quantization (even at zero magnetic field) and a pseudospin polarization, akin to the spin polarization induced by an external magnetic field.

Pseudomagnetic fields in graphene were found to reach extremely high values. For instance, Levy *et al.* [188] observed in 2010, in graphene nanobubbles at zero magnetic field, a pseudo-Landau quantization corresponding to pseudomagnetic fields greater than 300 Teslas, which opens the door to the study of graphene in otherwise inaccessible extreme magnetic field regimes. What is needed now is to find a way to obtain reproducible pseudomagnetic fields in graphene, some methods of strain engineering were then proposed by Pereira *et al.* [189] as well as Zhu *et al.* [190]. Notably, a zero-field quantum Hall effect is expected to emerge in strained graphene

[191]. STS measurements on a strained suspended graphene drumhead by Klimov *et al.* revealed the formation of a quantum dot [192, 193] with spatially confined charge carriers at zero magnetic field. Strained graphene was also observed to exhibit a strong electron-hole asymmetry by Bai *et al.* [194] with different Fermi velocities for both charge carriers. Using a combination of both an external magnetic field and strain-induced pseudomagnetic fields, Li *et al.* observed the splitting of real LLs into valley-polarized pseudo-LLs [195] as well as a valley inversion in the $\mathrm{d}I/\mathrm{d}V$ spectra taken along a graphene ripple, where the inversion occurs at the change of sign of the pseudomagnetic field [196].

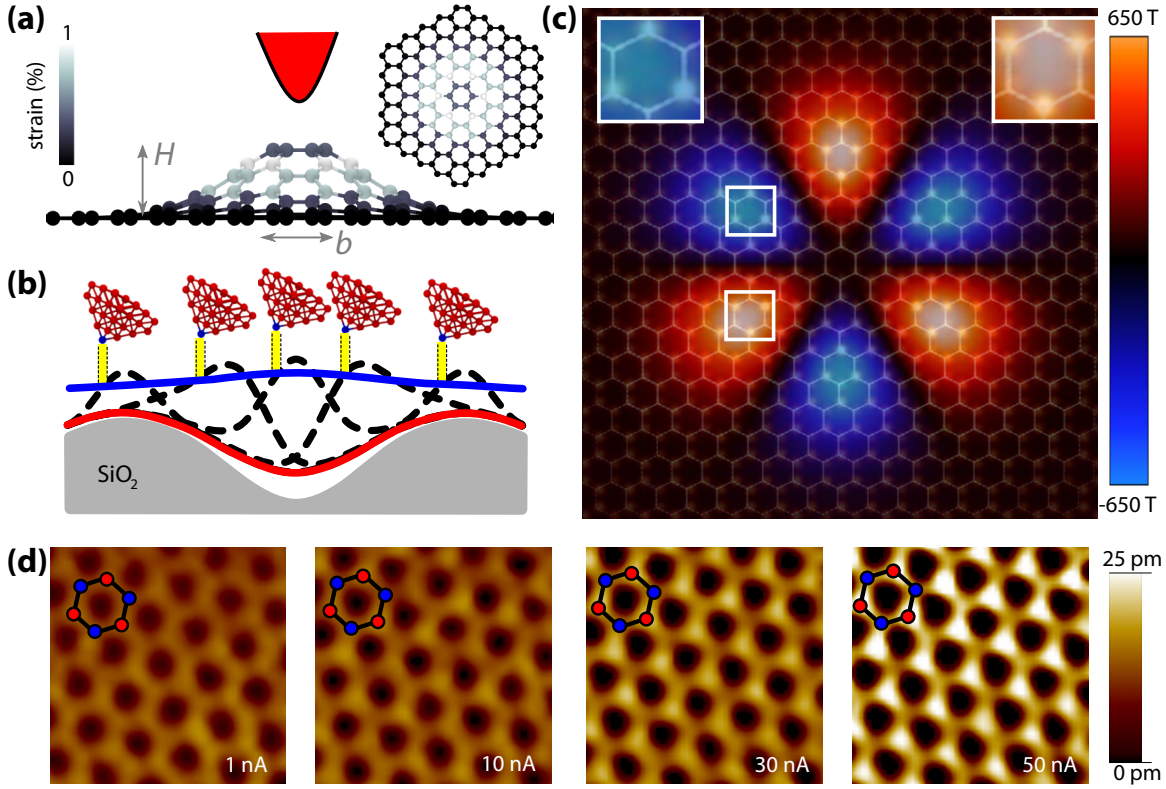

Figure 3.16: Strain-induced sublattice symmetry breaking. **(a)** Tip-induced gaussian deformation in graphene on SiO_2 due to van der Waals interactions (molecular dynamic calculation, $H = 1$ Å and $b = 5$ Å). **(b)** The deformation of the graphene sheet (dashed black lines) follows the scanning tip so that the apparent image (blue curve) is lifted with respect to the relaxed sheet (red curve). Due to the geometrical asymmetry of the tip apex, the tunneling is unlikely to happen at the top of the deformation, but rather on the side in areas of large strains and pseudomagnetic fields. **(c)** Strain-induced pseudomagnetic field pattern. Each atom of the lattice is overlaid by dots whose brightness corresponds to the computed local density of states amplitude, which reveals a sublattice symmetry breaking. **(d)** Constant current STM images of the same graphene area at increasing tunneling currents. Figures taken from [187].

Georgi *et al.* [187] used in 2017 a STM tip to locally strain graphene, where the van der Waals interactions locally lift the graphene sheet from a SiO_2 substrate. The deformation follows the tip as it is scanning graphene surface and the lifting height, typically of 1 Å, can be tuned by varying the tunneling current and so the tip-sample distance, see Figure 3.16(a,b). Their tight-binding numerical simulation presented in Figure 3.16(c) shows a map of the strain-induced pseudomagnetic field $\boldsymbol{B}_{\mathrm{ps}}$ at the atomic scale and the resulting sublattice symmetry breaking. Eventually, they observed a controlled increase of the sublattice symmetry breaking in STM images with increasing tunneling current, or equivalently increasing lifting force, see Figure 3.16(d), where graphene honeycomb lattice becomes distorted and one sublattice becomes brighter than the other one.

3.7 Quantum Hall edge states spectroscopy

We focus in this section on the spectroscopy of the quantum Hall edge states, following the theoretical background introduced in Chapter 2.2. We first consider the case of a boundary induced by a smooth electrostatic confining potential, with edge channels reconstruction on the scale of several hundreds of nanometers, see Chapter 2.2.1 ; and then the case of the physical edges of graphene where LLs disperse on the scale of a few l_B, see Chapter 2.2.2.

3.7.1 Edge channels in a smooth electrostatic confinement

For a 2DEG in the quantum Hall regime with a smooth electrostatic confining potential, it is expected that the electron gas breaks into alternating compressible and incompressible strips at the edge [75]. Many works were done in GaAs in order to image and study those strips by using different techniques, such as scanning single-electron transistor [197], scanning charge accumulation microscopy [198], scanning force microscopy [66, 199], near-field optical microscopy [200], scanning microwave impedance microscopy [201] or scanning capacitance imaging [202] where good agreement was found with the self-consistent electrostatic picture.

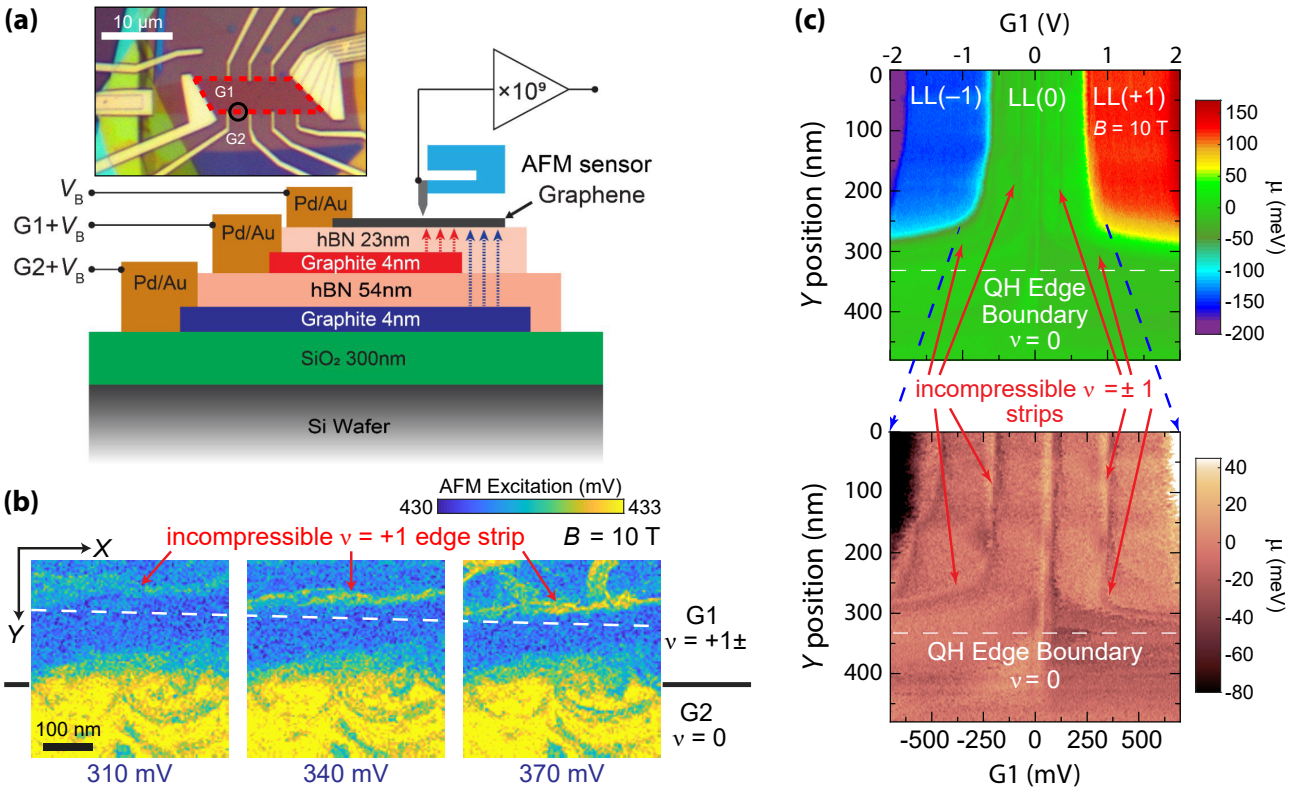

Figure 3.17: Imaging edge channels at a pn junction. **(a)** Schematic of the dual-gated heterostructure. Inset : optical image of the device. The edge is induced at the boundary between the local gate G_1 (outlined by the red dashed line) and the global gate G_2. The black circle corresponds to the scanning area of (b). **(b)** Spatial AFM excitation maps at $B = 10$ T across the quantum Hall boundary for different local gate voltages G_1 around $\nu = 1$. The global gate voltage G_2 is set to $\nu = 0$ to create the boundary with an insulator in the bottom region. The incompressible $\nu = 1$ edge strip appears near the boundary and drifts toward it with increasing local gate voltages. **(c)** Spatial dispersion of Landau levels (top) and broken-symmetry states (bottom) at the boundary observed with KPFM at $B = 10$ T. The higher resolution bottom map clearly shows that the $\nu = \pm 1$ strips disperse away from the $\nu = 0$ one, which points out toward a gapped ground state. Figures taken from [83].

Boundaries can be electrostatically induced in bulk graphene using dual-gated quantum Hall devices [203, 204, 205], see Figure 3.17(a), where one gate (G_1) is used to tune the carrier density in one part only of graphene while the independent second gate (G_2) tunes as usual the density of the whole graphene sheet. In such systems a pn junction is created in graphene at the edge of G_1. A boundary[8] with a smooth electrostatic confining potential is eventually induced by setting graphene density above G_2 to $\nu = 0$, where graphene is insulating at high magnetic fields (see Chapter 2.3.2.b).

Using a SQUID-on-tip setup, Uri *et al.* [206] were able to image the quantum Hall edge currents in such pn junction. Edge channels and broken-symmetry states dispersion at the boundary were observed by Kim *et al.* in 2021 [83] using atomic force microscopy (AFM) and Kelvin probe force microscopy (KPFM) [207, 208] at $T = 10\,\text{mK}$ and $B = 10\,\text{T}$. Figure 3.17(b) shows the formation of the $\nu = 1$ incompressible strip close to the boundary (beyond which graphene is set to its $\nu = 0$ insulating state). As the local gate G_1 is increased, so is the bulk filling factor and the $\nu = 1$ strip is progressively shifted toward the boundary as expected from the edge reconstruction theory, see Figure 2.10. KPFM maps in Figure 3.17(c) show the spatial evolution of edge states close to the boundary. The $\nu = 1$ strip disperses toward higher positive energies (electron-like edge state), the $\nu = -1$ strip disperses toward higher negative energies (hole-like edge state) and the $\nu = 0$ strip does not disperse. This is consistent with a gapped $\nu = 0$ ground state, see Figure 2.20. The width of the incompressible strips is also estimated to be on the order of 40 nm which is consistent with the electrostatic Equation (2.48).

3.7.2 Landau level dispersion at graphene physical edges

We now study the evolution of the LLs at graphene edges, where a completely different behavior is expected due to the sharp confinement potential on a few l_B only, which leaves no room for edge channels reconstruction. The first problem is to be able to locate the edge of graphene in STM. This task becomes significantly easier for a graphene sheet on conductive substrates such as graphite, where the edge of the electronically decoupled graphene flake will simply appears in the STM image as a monoatomic step of height 0.34 nm. The edge type, zigzag or armchair, is then determined using an image with atomic resolution [210, 211], see Figure 3.18 where Li *et al.* [209] identified a graphene zigzag edge.

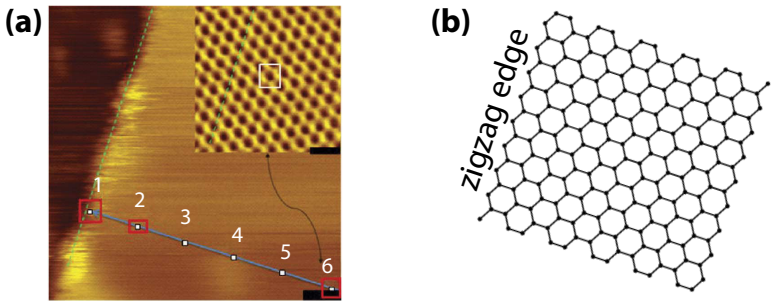

Figure 3.18: STM image of a zigzag edge in **(a)** of a graphene flake on graphite. The edge type is determined using a STM image with atomic resolution far from the edge at 32 nm= $2.5\,l_B$, see inset : the edge direction corresponds to that of the zigzag edge, see **(b)**. The six positions marked in (a) correspond to the points where the $\mathrm{d}I/\mathrm{d}V$ spectra of Figure 3.19(c,e) are taken, at intervals of $0.5\,l_B$. Figure (a) taken from [209].

[8] This boundary in bulk graphene is of higher quality than the physical edge of graphene : it is free of lattice defects or fabrication residues. Moreover scanning probe measurements are easier due to better stability of the junction in bulk graphene with respect to the physical edge (where the layer is more easily deformed by the tip). However, the probed physics is not the same than that at the physical edges of graphene.

In such a graphene/graphite system, Niimi *et al.* performed in 2006 [211] STS measurements at both zigzag and armchair edges at zero magnetic field. They observed near the zigzag edge a clear peak close to the Dirac point in the V-shape density of states of graphene, but not for the armchair edge. They attributed this peak to the dispersionless surface state predicted by Fujita *et al.* [86], see Chapter 2.2.2.b, which only exists at the zigzag edge, whether the magnetic field is zero or not.

In the quantum Hall regime, the LLs dispersion was computed theoretically by Abanin *et al.* [92]. Starting from the analytic model developed in Chapter 2.2.2.c, one can compute the local density of states near the zigzag edge for both sublattices A and B defined by :

$$\rho_A(E,x) = \sum_\alpha |u_\alpha(x)|^2 \, \delta\left(E - E_\alpha\right) \tag{3.13a}$$

$$\rho_B(E,x) = \sum_\alpha |v_\alpha(x)|^2 \, \delta\left(E - E_\alpha\right) \tag{3.13b}$$

with x the distance from the edge, u_α,v_α the eigenstates derived from Equations (2.62) with hard-wall boundary conditions (2.63) and E_α their eigenenergy. Abanin *et al.* obtained the maps shown in Figure 3.19(a,b) for both sublattices, where we can see the LLs bending close to the edge on the scale of a few l_B. Note that the dispersionless surface mode persists at the zigzag edge only for sublattice B whereas in sublattice A the zeroth LL is barely seen to disperse into one electron-like and one hole-like bands.

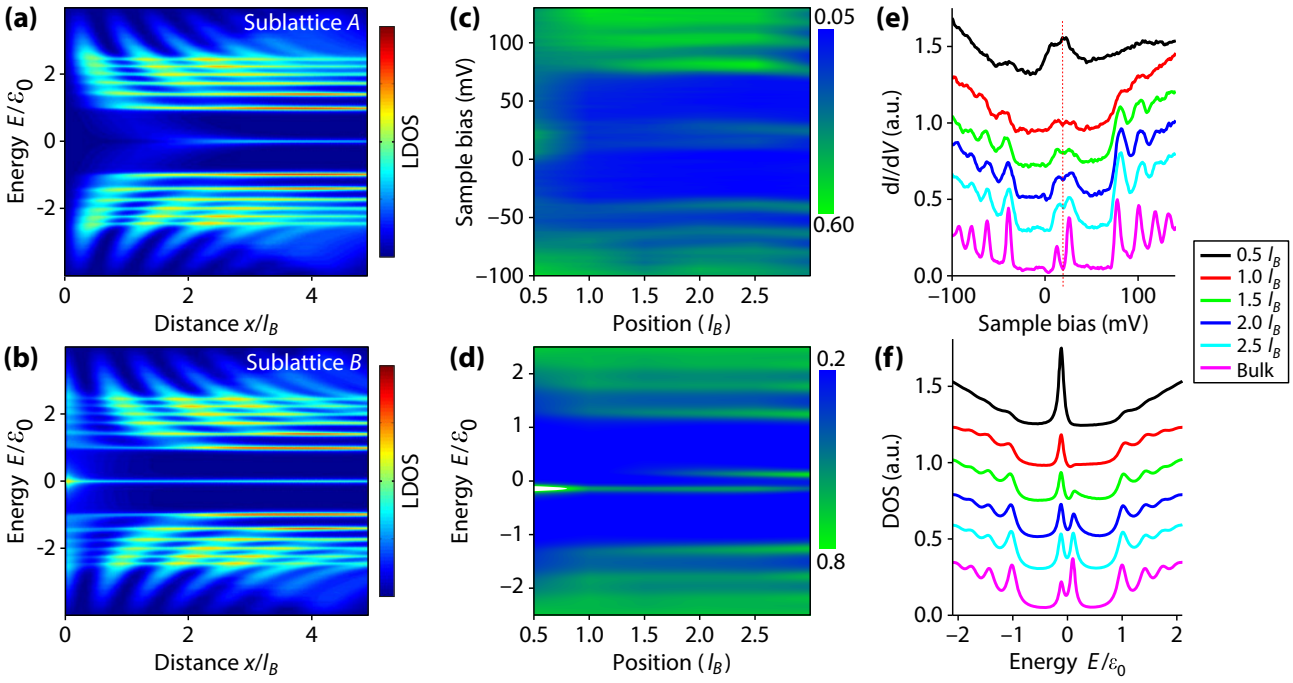

Figure 3.19: Evolution of Landau levels with the distance from the zigzag edge. **(a,b)** Position-dependent theoretical STS near zigzag graphene edge for both sublattices A and B as expected from Abanin *et al.* [92]. The dispersionless surface state persists at the edge only for sublattice B. **(c)** STS map showing the evolution of the $\mathrm{d}I/\mathrm{d}V$ spectra as a function of the distance from the zigzag edge in graphene/graphite at $B = 4\,\mathrm{T}$. **(d)** Simulated STS map corresponding to (c). **(e)** Individual $\mathrm{d}I/\mathrm{d}V$ spectra taken at the positions indicated in Figure 3.18(a) showing the vanishing of the Landau levels close to the edge. **(f)** Simulated local density of states as a function of the distance from the edge. Figures (c-f) taken from [209].

Li *et al.* measured in 2013 [209] the evolution of the LL spectroscopy as they move the tip toward the graphene zigzag edge shown in Figure 3.18. They observed that the proximity of

the edge is not noticeable in the $\mathrm{d}I/\mathrm{d}V$ spectra up to a distance of approximately $2.5\,l_B$, in agreement with theory for an atomically sharp confinement potential. Nonetheless, they do not observe a bending of LLs at the edge but rather a continuous vanishing of the peaks and eventually obtained close to the edge ($0.5\,l_B$) a V-shape-like density of states, with a peak at the Dirac point, see Figures 3.19(c,e). The absence of observable band bending originates from the spatial extent of the wave functions which can be written for LL_N, using Equation (2.24) :

$$\Delta r = 2l_B\sqrt{2|N|+1} \tag{3.14}$$

At a distance x from the edge such that $x \gg \Delta r$, the sharp confinement potential is not felt and one basically probes bulk states. However edge states below a few l_B from the edge happen to be necessarily in close vicinity to bulk states since their spatial extent also scales as l_B : edge states are eventually sensitive to bulk ones up to distances comparable to Δr, and bulk states have thus an important contribution to the probed local density of density near the edge. Therefore, even if the energy of the edge states indeed shifts toward higher energies due to confinement, the position of the peak measured in STS is not seen to be moving and stays close to its bulk position. LLs bending must rather be seen as a continuous redistribution of the spectral weight of the peaks from lower to higher energies : LLs are smeared out toward the edge and the flat density of states observed by Li *et al.* [209] at the zigzag edge is eventually obtained.

Moreover one can remark that the zeroth LL splits into two peaks, see Figure 3.19(e), splitting that Li *et al.* attributed to a substrate-induced sublattice symmetry breaking. Upon approaching the zigzag edge the double peak structure disappears. This feature is also obtained in the simulated $\mathrm{d}I/\mathrm{d}V$ spectra, see Figures 3.19(d,f), and is reminiscent of simulations in Figures 3.19(a,b) : each peak corresponds to one sublattice (or equivalently one valley for the zeroth LL), one is dispersionless and persists toward the zigzag edge while the second disperses and is seen vanishing as the other LLs.

On a side note, a similar study of edge states was performed by Yin *et al.* in 2016 [212] on bilayer graphene decoupled from a graphite substrate.

Charge accumulation at graphene edges

The objective of this thesis is to realize similar STS measurements at the graphene edge on an insulating $\mathrm{hBN/SiO_2}$ substrate, which is the typical gating device used for transport measurements. However Silvestrov *et al.* [213] predicted theoretically that in such systems, a strong charge accumulation at the edge would occur, on a scale defined by the screening length $l_\mathrm{a} \approx 300\,\mathrm{nm}$ from the edge, which is typically the distance between graphene and the silicon back gate. This macroscopic effect should lead to additional edge reconstruction and non-topological edge channels, and should be seen in STS as an important shift of the Dirac point in the $\mathrm{d}I/\mathrm{d}V$ spectra probed as the STM tip is moved toward the edge.

Such charge accumulation was not observed by Li *et al.* [209] since graphene was on a graphite substrate : the screening length is simply the distance between the topmost graphene layer and the nearest one below $l_\mathrm{a} \simeq 0.34\,\mathrm{nm}$. In 2019, Marguerite *et al.* [214] measured an encapsulated-graphene device on an $\mathrm{SiO_2}$ substrate using scanning nanothermometry and scanning gate microscopies and observed dissipation as well as an increase of the resistance at the edge of their device, that they claimed to be the result of edge reconstruction induced by a hole accumulation at the edges of graphene.

3.8 Broken-symmetry states spectroscopy and imaging

Finally, we complete this chapter by a discussion on broken-symmetry states spectroscopy in graphene. As we mentioned in Chapter 2.3.1, these states appear in partially filled LLs due to quantum Hall ferromagnetism, where the spin and valley degeneracies are lifted. As an example, the interaction-induced gap which opens in the half-filled zeroth LL was well seen by Li *et al.* in 2009 [53] in decoupled graphene on graphite, see Figure 3.1(a).

The gap opening at $\nu = 0$ was also noticed by Henriksen *et al.* [215] in bulk graphene on SiO_2 using infrared magneto-spectroscopy, gap which increases with magnetic field. Song *et al.* [98] observed in 2010 at $T = 13$ mK LL splitting into a quartet of broken-symmetry states[9] in STS on graphene on SiC close to the Fermi energy, see Figures 3.20(a,b,c). Their estimations of the valley and spin gaps showed that both gaps increase linearly with the magnetic field, at least for magnetic fields below $B = 7$ T for the valley gap. The linear scaling of both spin and valley gaps was also observed in the topmost layer of multilayer graphene synthesized on rhodium foils by Li *et al.* [216]. In these two works, the valley gap is measured to be greater than the spin one and both also depend on the filling factor, indicating important effects of exchange interaction on the splittings. Using dot-assisted tunneling spectroscopy, Keren *et al.* observed in 2020 [217] the four broken-symmetry states of the zeroth LL up to $B = 33$ T and found the splitting to be dominated by a strongly enhanced Zeeman term greater than the valley gap. Zhang *et al.* probed in 2020 [218] broken-symmetry states induced by some impurities chemisorbed on graphene, such as hydrogen atoms, which locally break the sublattice symmetry and lift the four-fold degeneracy of LLs.

3.8.a $\nu = 0$ interaction-induced gap evolution with magnetic field

Using KPFM measurements [207, 208] on hBN-encapsulated graphene, Kim *et al.* [83] estimated the energy gaps between the broken-symmetry states of the zeroth LL as a function of the magnetic field. KPFM enables to measure directly the local chemical potential as a function of the filling factor, and broken-symmetry states appear as plateaus of chemical potential between successive integer filling factors, see Figure 3.20(c). The gaps corresponding to $\nu = 0, \pm 1$ are then estimated as the differences of chemical potential between these plateaus.

The $\nu = 0$ gap shows distinct low and high field behaviors, see Figure 3.20(d). Above $B = 8$ T, it scales as $\sqrt{B}$, which is consistent with an electron-electron interaction-induced gap opened by the Coulombian interaction $E_C \propto \sqrt{B}$, while below $B = 8$ T it seems constant or even slowly decreases with increasing B. Two behaviors are also observed for the lower $\nu = \pm 1$ gaps, which are seen to increase with B below $B = 8$ T and above rather stay constant and approach the value of the Zeeman gap. Kim *et al.* [83] suggested the occurrence of an isospin phase transition [219] around 6-8 T to explain these two regimes.

In particular, the low-field behavior is supposed to arise due to the existence of a Moiré pattern (see Chapter 1.3.2) in their device. Transport measurements done by Ribeiro-Palau *et al.* [220] indeed showed that a gap opens at the Dirac point at zero magnetic field in devices with a graphene/hBN Moiré, gap which depends on the relative angle between graphene and hBN layers. This gap comes from the breaking of the sublattice symmetry in graphene due to

[9] Interestingly, Song *et al.* [98] also observed the splitting of the individual broken-symmetry states into two peaks as they cross the Fermi level, with the opening of gaps at fractional values of the filling factor, corresponding to the half-filling of one broken-symmetry state. They notably observed fractional states at $\nu = 7/2$, $\nu = 9/2$ at $B = 11$ T and $\nu = 11/2$ at $B = 14$ T, with gaps of about $3 - 5$ meV.

the hBN layer, and may induce a new possible ground state of graphene described by a partially sublattice-polarized (PSP) state [219], along with those introduced in Chapter 2.3.3. A gap around 5-10 meV is expected for an angle of 3.1° as estimated by Kim *et al.* , which is consistent with their low-field value of $\Delta E(\nu = 0)$ [10].

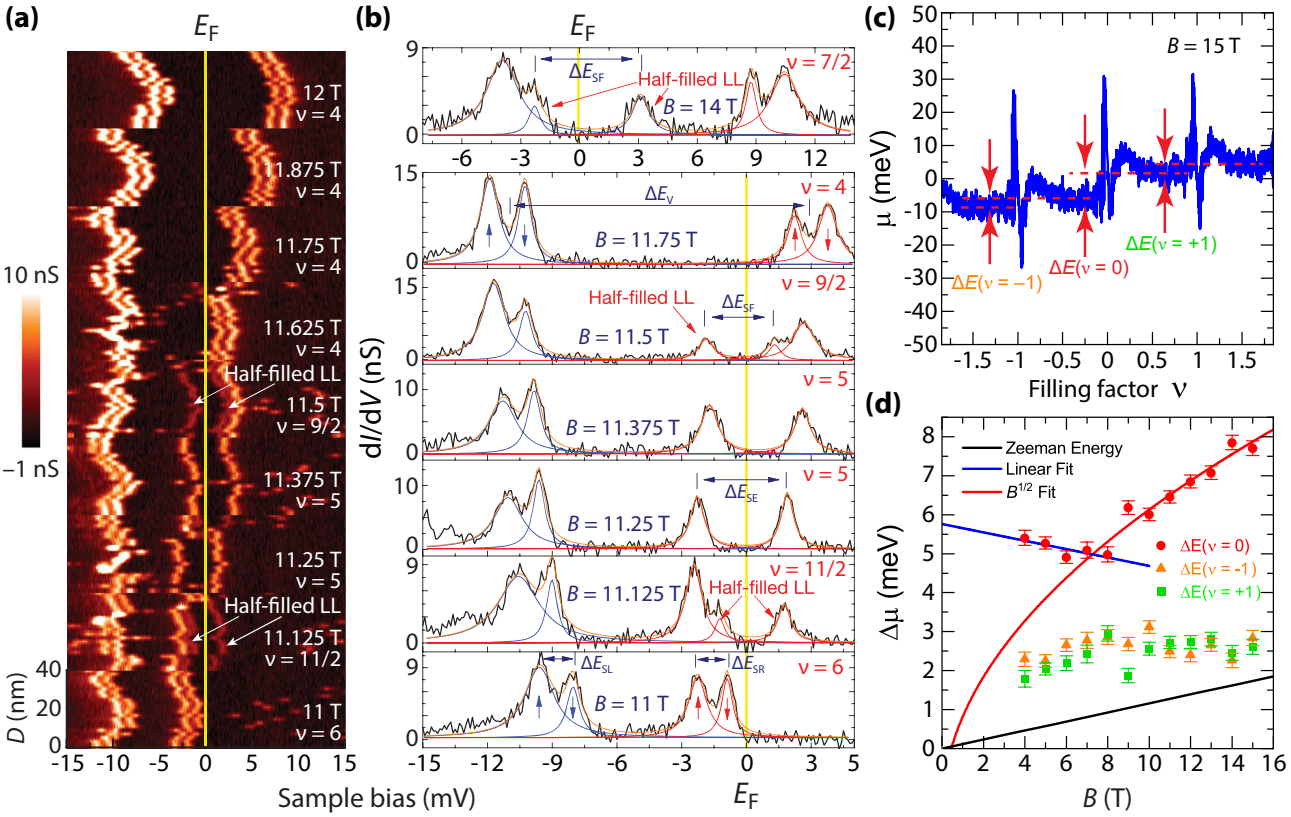

Figure 3.20: Broken-symmetry states spectroscopy. **(a)** Series of $\mathrm{d}I/\mathrm{d}V$ line scans focusing on the crossing of the Fermi level by the broken-symmetry states of the $N = 1$ Landau level in graphene/SiC at $T = 13$ mK. Fractional states appear at $B = 11.125$ T and $B = 11.5$ T. **(b)** $\mathrm{d}I/\mathrm{d}V$ spectra taken at different magnetic fields from which spin and valley gaps can be estimated. The fractional states clearly appear as peaks of half-filled broken-symmetry states. Figures (a,b) taken from [98]. **(c)** Chemical potential as a function of filling factor obtained from KPFM measurements in hBN-encapsulating graphene at $T = 10$ mK and $B = 15$ T. Broken-symmetry states of the zeroth Landau level appear as plateaus between integer filling factors. Each gap $\Delta E(\nu = 0, \pm 1)$ is computed as the difference in chemical potential between the plateaus. **(d)** Estimated gaps from (c) as a function of the magnetic field B. $\Delta E(\nu = 0)$ scales as $\sqrt{B}$ for $B \geq 8\,T$. Figures (c,d) taken from [83].

3.8.b $\nu = 0$ ground state imaging

The identification of charge-neutral graphene ground state still stays ambiguous. Transport measurements, which were employed to study deeply broken-symmetry states physics, can not be used to infer the nature of the $\nu = 0$ state due to their lack of spatial resolution, which makes scanning tunneling techniques the best solution to directly image the charge-neutral ground state. In 2010 Miller *et al.* [221] were able to map the spatial distribution of the zeroth LL at

[10] The interaction-induced gaps which appear at integer filling factors ν are strongly enhanced by exchange interactions, see Chapter 2.3.1. However KPFM enables the measure of these gaps as differences between chemical potential plateaus, occurring between integer ν. The gap is thus measured far from integer ν. Kim *et al.* [83] supposed that the exchange-enhancement may be smaller in this case than that at integer ν, which explains why the gap values they found with this method are smaller than those we measure in Chapter 7.

the scale of l_B in graphene on graphite and found an organized pattern of localized states and evidence for local lifting of the valley degeneracy. Wang *et al.* imaged in 2015 [153] the spatial distribution at the atomic scale of the two split peaks of the zeroth LL of gapped graphene : one peak was mainly localized on one sublattice while the second peak was localized on the other one. This is consistent with the fact that for each valley the wave functions of LL_0 reside solely on one sublattice, see Chapter 2.1.2. Eventually, Li *et al.* visualized in 2019 [216] in graphene on graphite a Kekulé distortion of the honeycomb lattice when tunneling into one of the split peaks of the zeroth LL, see Figure 3.21.

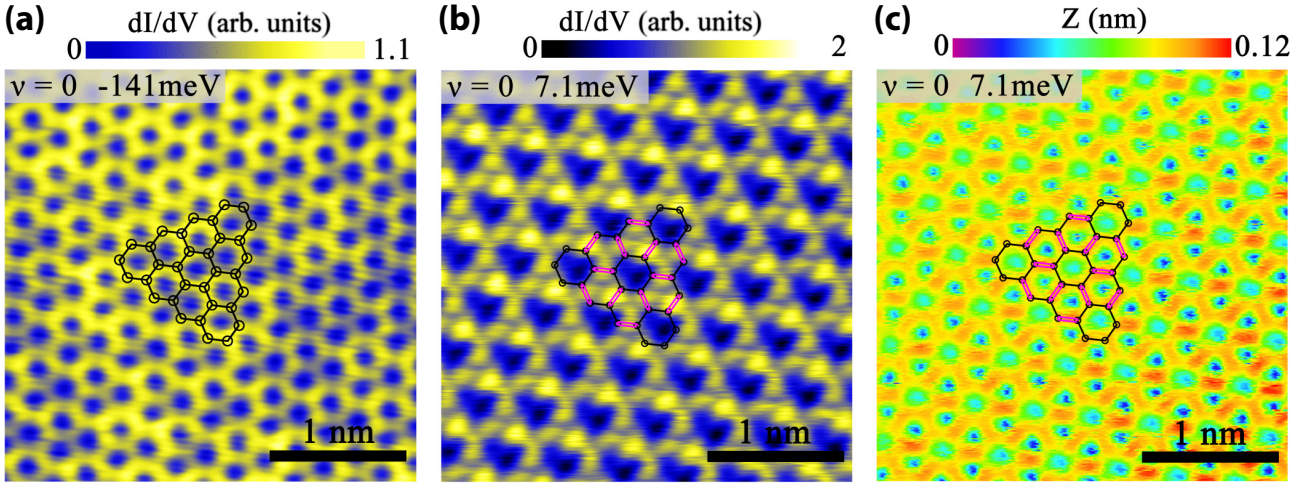

Figure 3.21: Kekulé distortion in charge-neutral graphene. $3 \times 3\,\mathrm{nm}^2$ images at $\nu = 0$ and $B = 13$ T. **(a)** STS map taken at $V_{\mathrm{bias}} = -141$ meV corresponding to the energy of LL_1 : the honeycomb lattice of graphene is well resolved. **(b)** STS map taken at $V_{\mathrm{bias}} = 7.1$ meV which corresponds to the empty peak of the split LL_0. A C-C bond density wave characteristic of the Kekulé distortion is observable. **(c)** STM image taken at $V_{\mathrm{bias}} = 7.1$ meV. We clearly see the Kekulé distortion appearing as a dimerization of one C-C bond over three. Figures taken from [216].

Conclusion

We did in this chapter a review of the state of the art Landau level spectroscopy in graphene, focusing on the topics that will be addressed in our experimental study. The main conclusion we can draw from this bibliographic work is that if tunneling measurements in graphene on conductive substrates such as graphite yield results close to those expected for pristine graphene, they do not enable to truly understand the results obtained in transport measurements where graphene lies on an insulating substrate. The objective of this thesis in the following experimental chapters is to realize LL spectroscopy on graphene/hBN samples which are typical transport devices. It therefore allows direct comparison between the global results from transport and the local ones from tunneling microscopy. We will in particular focus on the LL edge dispersion in Chapter 6, already probed in graphene on graphite [209], as well as the charge-neutral ground state of graphene in Chapter 7, imaged as a Kekulé distortion in graphene on graphite [216], and finally on a quantitative measurement of the interaction-induced gap at $\nu = 0$.

Chapter 4

Cryogenic AFM/STM

We present in this chapter the home-made AFM/STM that we used to bring a metallic tip on a few microns size graphene device to perform tunneling spectroscopy of Landau levels in graphene. We first present the experimental setup. We then focus on the fabrication process of the AFM/STM probes. The working principles of the STM and AFM modes are detailed in Appendix A. Finally we explain how we are able to guide the tip toward graphene at very low temperature, clean and reshape the tip apex, and we show atomic resolution of the graphene honeycomb lattice.

Contents

4.1 AFM/STM at 4 K - 14 T

We use an home-made Scanning Tunneling Microscope which was designed and built by Benjamin Sacépé (with the help of Dominique Grand, SERAS-CNRS, and Louis Veyrat). It is based on the design of Winkelmann [222] and relies on the Pan design [223]. Our microscope can work in both STM and AFM modes, at very low temperatures, using either a 4 K insert or a dilution fridge in a liquid helium cryostat, and is amagnetic to be operated under high magnetic fields up to 14 T using a superconducting solenoid.

4.1.1 STM head

4.1.1.a Description

The STM head, shown in Figures 4.1 and 4.2, is the central part of the whole experimental setup with the sample, the tip and the piezoelectric positioning system.

The inner lower part is hollow and contains the scanner, which consists of a piezoelectric tube inside an alumina prism, both fixed on an alumina base. Atop the piezoelectric tube lies the force-sensor holder receptacle, which is detachable from the microscope, with the tip facing upward. A set of six piezoelectric actuators fixed on the STM body enables a coarse displacement of the scanner in the Z direction. Above is the XY stage with the wagon for the sample holder, that is moved in the XY plane thanks to two other sets of six piezoelectric motors, with the sample facing downward. The sample holder contains 24 contacts in order to enable transport measurements inside the STM for suitable samples. Spring press plates acting on the piezoelectric motors control the displacement steps of both the scanner and the wagon. Both tip and sample holders are top loaded inside the STM head.

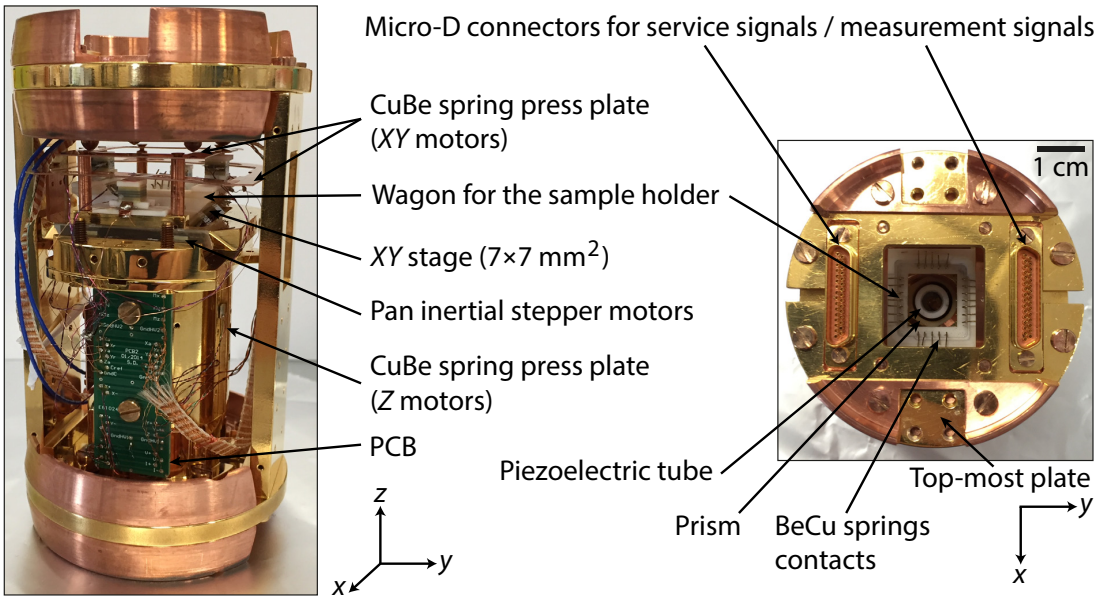

Figure 4.1: STM head. Side and top views of our STM.

Two PCBs are fixed on the inner lower piece, on opposite sides, on which are connected wires for signals related on the one hand to high voltage signals (up to a few hundreds of volts) applied on the piezoelectric tube and motors (called service signals), and the other hand low voltage signals related to measurements on the sensor and the sample. The top-most plate of the STM head is a circular piece on which are fixed two amagnetic Micro-D connectors[1], one for the service signals and the other for the measurement signals. The square hole at the center enables the top-loading of the sensor and sample holders.

4.1.1.b Materials

The choice of the materials of the different mechanical parts during the conception of the STM is primordial. Several parameters must be taken into account. First their thermal conductivity has to be high enough at low temperature, so that the thermalization of the STM during the cooling down is achieved in a reasonable time. Secondly their thermal expansion

[1]made by C&K, MDM connector series, reference MDM-31PFR164FR172.

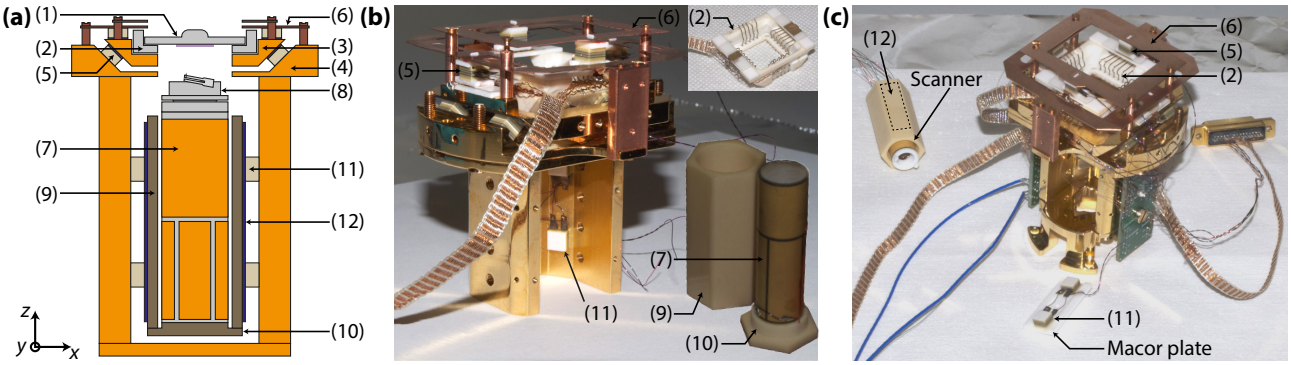

Figure 4.2: Piezoelectric positioning system. (a) Cross section of the STM. The sample holder (1) is inserted in the wagon (2), whose displacements are enabled in the horizontal plane with the XY table. It comprises a X stage (3) and a Y stage (4) that are moved with piezoelectric motors (5). Spring plates (6) are used to tune the displacement steps in each direction. Below is the scanner, that is composed of a piezoelectric tube (7), atop which is inserted the sensor (8), a prism (9) and their common basis (10). Piezoelectric shear stacks (11) slide on sapphire plates (12) glued on the outer faces of the prism for displacement of the scanner in the Z direction. **(b,c)** Images of the mounting of the STM head. The top half contains the XY stage while the piezoelectric scanner is situated inside the bottom half. The piezoelectric tube and prism are shown before their assembly in (b) and after in (c). The inset in (b) shows the wagon with 24 contacts for the sample holder.

coefficients must match with each other, to ensure resilience of the gluing between parts of different materials (e.g. metals and ceramics of the piezoelectric stacks) during the cooling. They must moreover be easily machinable, especially for the choice of ceramics. Finally they must be non magnetic since we do not want the STM head to move when placed into a large magnetic field. The whole STM head must furthermore be rigid, compact and light to be both suitable for cryogenic setups and little sensitive to mechanical vibrations. A rigid head has indeed a high structural (high pass) resonance frequency which damps the low frequency vibrations of the environment.

The head body is in CuZr with a gold coating. CuZr is an alloy of copper with about $0.1 - 0.2\%$ of zirconium with an excellent thermal conductivity down to very low temperature and which is harder than copper, increasing thereby the rigidity of the STM. The prism and its base are in alumina. The piezoelectric tube and stacks are made of PZT, for lead zirconate titanate $Pb(Zr_xTi_{1-x})O_3$, a ceramic with a marked piezoelectric effect, and they slide on sapphire plates. The sensor and sample holders and the wagon are made of Macor, a machinable ceramic. Electrical contacts between both the sample and tip holders with the STM head are done with BeCu springs, another copper alloy with a few percents of beryllium which has a good elasticity and can be shaped into springs of many forms. The whole bolted connection is also done in BeCu. All those materials are amagnetic, and particular care was taken for the choice of non magnetic materials for the different electrodes, for instance those of the piezoelectric actuators. The gluing were done with Stycast 1266, a epoxy glue suitable for cryogenic use.

4.1.2 Piezoelectric positioning system

Scanning probe microscopies rely on the accurate control, at the nanometer scale, of the position of the probe with respect to the sample in the three dimensional space. Such fine positioning is realized by using the piezoelectric material PZT, a ceramic with an important piezoelectric coefficient, about a few hundreds of pm/V at room temperature depending on

the type of ceramic used[2]. The positioning system of our STM is comprised of a piezoelectric tube scanner on which the probe is mounted, that allows a fine positioning of the tip, and of piezoelectric motors that enable coarse motion to move the scanner in the Z direction and the sample holder in both X and Y directions. These different stages are shown in Figure 4.2.

4.1.2.a Piezoelectric scanner

The piezoelectric scanner, shown in Figure 4.3 and visible in Figure 4.2(b), consists of a cylindrical hollow tube (OD = 10 mm, ID = 9 mm) with a length of 33 mm. A first electrode going round the top half of the tube controls its movements in the Z direction while two pairs of electrodes placed on opposites sides of the bottom half control its displacement in the X and Y directions. The interior of the tube is grounded.

The elongation or contraction of the tube, that induces the movement of the tip along the Z axis, is done by applying a voltage V_Z on the top outer Z electrode with respect to the inner grounded electrode : the radial electric field, parallel to the direction of the polarization of the piezoelectric, produces a radial mechanical strain which thins (resp. thickens) the wall of the tube and therefore induces an elongation (resp. contraction) along the Z axis simultaneously. For the lateral displacement in the Y direction, opposite voltages of $+V_Y$ and $-V_Y$ are applied on both Y electrodes on the opposite sides of the tube : a positive V_Y induces an elongation of one electrode while a negative voltage produces a contraction, the overall effect is that the tube therefore bends in one way or the other depending on the sign of V_Y. The same goes for the X direction.

Our piezoelectric tube must satisfy two conditions. On the one hand, its resolution in the three directions must be high enough to enable the imaging of atoms in STM mode, typically of the order of the picometer or below. On the other hand, before performing STM, we first need to localize our sample in AFM (see Section 4.4.1). We then require our tube to have a sufficient scan range at low temperature of several microns for this localization step, nevertheless this high scan range limits the spatial resolution achievable by the microscope.

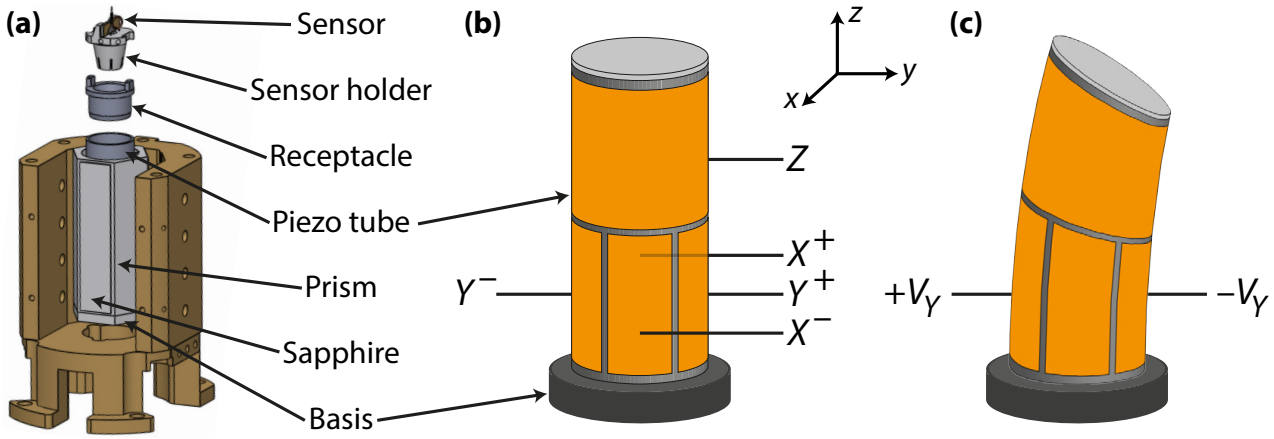

Figure 4.3: Piezoelectric scanner. **(a)** 3D sketch of the piezoelectric scanner of our STM and how the sensor is mounted on top of it. **(b)** Schematic of the piezoelectric tube, the four bottom electrodes allow bending motion for scanning in the XY plane while the top electrode causes extension or contraction of the tube in the Z direction. **(c)** Bending of the piezoelectric tube in the Y direction when applying opposite voltages $\pm V_Y$ on the $Y^{\pm}$ electrodes.

[2]PIC255 for our tube and stacks, made by PI Ceramic GmbH.

Table 4.1 lists the sensitivity (characterized using a calibration sample), resolution and full range scan size of our tube at room and low temperatures. The differences with the temperature come from the lowering of the piezoelectric constant of PZT with decreasing temperatures. Table 4.2 indicates the capacitances of the X, Y, Z electrodes of the tube as measured in the STM. At 4 K, the scan range is about $3 \times 3\,\mu m^2$ and the vertical extension is 340 nm, for a maximum applied voltage on the tube electrodes of ± 150 V. We avoid applying higher voltages that could lead to the depolarization of the tube.

The Nanonis electronics we use (see Section 4.1.3) is a 16-bit system with a maximum output of ± 10 V, followed by a voltage amplifier with gains 4, 15 and 40. We most of the time use the gain 15, we then have a resolution in the voltage applied to the tube of $\delta V \simeq 4.6$ mV, which corresponds to a spatial resolution of $\delta X \simeq 40$ pm at 4 K and a vertical resolution of $\delta Z \simeq 5$ pm.

Sensitivity (nm/V)	$\Delta X/\Delta V$	$\Delta Y/\Delta V$	$\Delta Z/\Delta V$
$T = 293$ K	42.7	50	15.25
$T = 4$ K	9.50	9.85	1.125
Resolution (pm)	δX	δY	δZ
$T = 293$ K	195	230	70
$T = 4$ K	43	45	5.1
Full range (µm)	ΔX	ΔY	ΔZ
$T = 293$ K	12.8	15	1.57
$T = 4$ K	2.85	2.95	0.34

Table 4.1: Sensitivity, resolution (gain 15) **and full range** (for voltages $-150\text{V} < V < 150\text{V}$) **of the piezoelectric scanner** as measured using a calibration sample.

Capacitance (nF)	X^+	X^-	Y^+	Y^-	Z	M_X	M_Y	M_Z
$T = 293$ K	5.0	4.9	4.8	4.9	11.9	8.8	8.8	8.3
$T = 4$ K	1.5	1.6	1.5	1.5	3.0	2.5	2.5	2.3

Table 4.2: Capacitances of the piezoelectric stacks of the scanner and the motors (six actuators for each direction) measured on the STM at room temperature and at 4 K.

4.1.2.b Piezoelectric Pan-type motors and coarse motion

The piezoelectric scanner first needs to be brought in the immediate vicinity of the sample, close enough for it to approach the surface of the sample and then scan on it. We use Z piezoelectric motors to move the scanner in the Z direction, toward the sample, and X and Y motors to move the sample in the XY plane to change to scanning area of the tube.

Those actuators are made of three stacked layers of PZT contacted with amagnetic tantalum electrodes, with a cross section of $5 \times 5\,mm^2$ and a thickness of 3.5 mm. The end plate that is in contact with the pieces to move is made of polished alumina. The stacks are glued directly on the STM body (or are constrained by fixed pieces) and are pressed against sapphire plates glued on either the prism that encircles the tube and the wagon. The roughness of materials is here a fundamental parameter since it controls the friction force between them. The use of sapphire, with a nanometric roughness, and of polished alumina allows the motors to work in a reproducible way at room and low temperatures.

The piezoelectric motors are operated in the shear mode : the electric field $\boldsymbol{E}$ is applied orthogonally to the direction of the polarization $\boldsymbol{P}$ and the mechanical deformation is in the direction of $\boldsymbol{P}$. This allows important deformations of the piezoelectric stack - and thus the use of smaller stacks to achieve a given deformation, which reduces congestion in the STM - since the shear deformation coefficients are usually the largest piezoelectric coefficients. At room temperature, their specified deformation enables a displacement of approximately 1 µm for an applied voltage from −250 V to +250 V and their capacitance is about 1.4 nF.

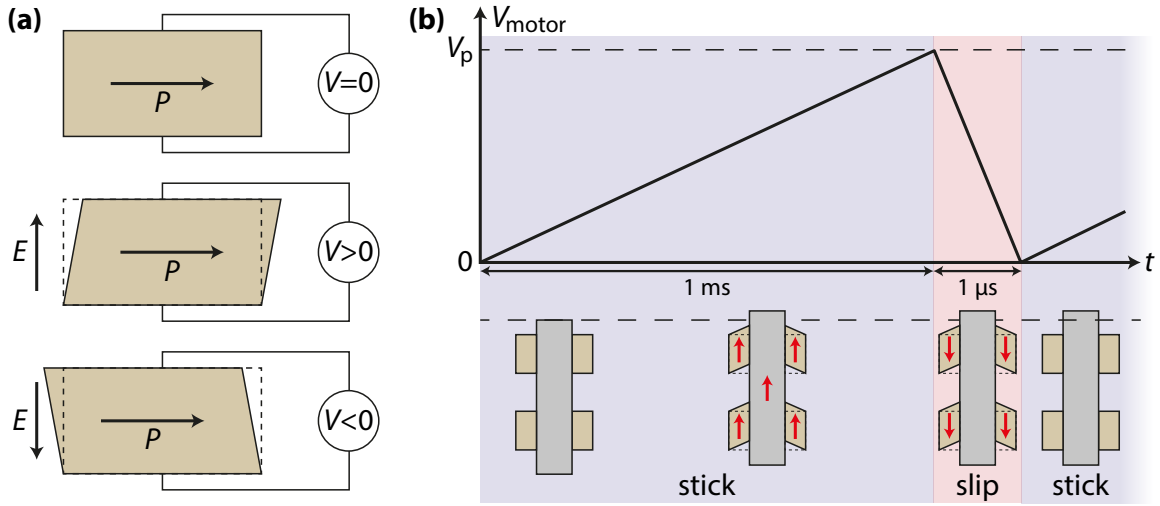

Figure 4.4: Coarse motion with the piezoelectric motors. (a) Shear mode deformation of the piezoelectric actuators. **(b)** Coarse motion by *stick and slip* mechanism : during the slow *stick* step, the central piece follows the deformation of the four piezoelectric motors and moves up ; while during the fast *slip* step, the central piece slides on the motors as they resume their shape at rest.

The displacements of the prism and the wagon are done using a coarse motion based on the *slip and stick* mechanism as shown in Figure 4.4. A sawtooth voltage $V_{\text{motor}}(t)$ is applied to the actuators. It consists of a slow rise on a time of 1 ms followed by a sharp drop on a much faster time of about 1 µs. During the slow rise, the shear deformation force is balanced by the static friction with the sapphire plate the actuator is pressing on : the plate, and the wagon or prism it is glued on, sticks to the motor and gets dragged along the direction of the deformation. When the sharp drop of voltage happens, the actuator quickly deforms back to its shape at rest. However, the static friction is unable to overcome this large acceleration and, as a result, the sapphire plate slips on the piezoelectric stack and does not move. There is then, after each pulse of voltage, a net displacement of either the scanner or the wagon in the direction of the shear deformation of the motors. Such mechanism enables coarse displacements on several millimeters by steps of around 100 nm. Therefore we can bring a tip to a few hundreds of nanometers of the sample (and then use the piezoelectric tube to engage the surface in either STM or AFM mode) starting from a tip at more than one millimeter of distance ; and we can also localize a micron size device on a millimeter size sample.

There are six piezoelectric stacks for the Z motors to move vertically the scanner, as shown in Figure 4.5 : four are fixed on the body of the STM head while the other two are glued on a Macor plate, in two stages of three motors symmetrically placed. The scanner is placed at the center, three sapphire plates are glued on the outer faces of the prism attached to the tube, so that the piezoelectric motors slide on these sapphire plates. An alumina small ball is put between the Macor plate and the Z CuBe spring plate : both plates have a small hole at their center that hold the ball. The Z spring plate is screwed on the STM body,

these screws can be more or less tightened to tune the pressure force of the spring on the Macor plate and the Z piezoelectric motors, we can then control the frictional force between the motors and the prism, and therefore the displacement of the scanner with each step of the motors.

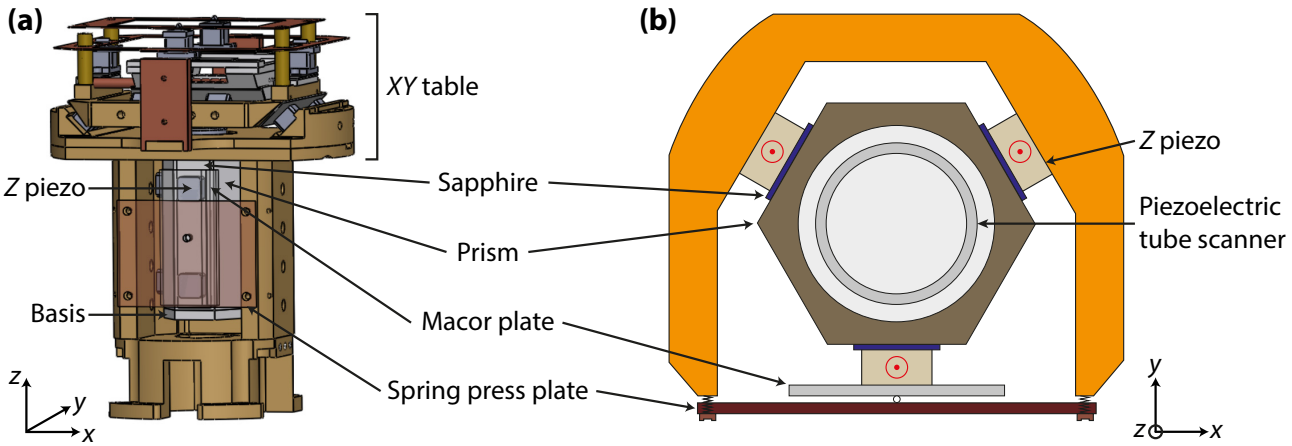

Figure 4.5: Z stage. (a) 3D sketch of the whole Z stage of our STM. **(b)** Cross section of the Z stage. The scanner is mounted on a Macor basis on which a Macor prism is glued. Six piezoelectric motors act on this prism (sliding on sapphire plates) to move it, and the scanner, in the Z direction. A spring press plate is used to tune the motor steps.

The XY stage enables the sample to move on a surface of $7 \times 7\,\mathrm{mm}^2$. It is comprised of two distinct stages with six piezoelectric stacks acting on one direction or the other, see Figure 4.6. First is the bottom Y stage on which are glued four Y piezoelectric stacks. The X stage is positioned on these four stacks, which slide on sapphire plates glued on the X stage, moving it in the Y direction. Two additional Y piezoelectric stacks are placed above the X stage, the Y spring plate press them to ensure good mechanical strength. Four X piezoelectric stacks are glued on the X stage and the wagon for the sample holder is placed on those stacks. As before, they slide on sapphire plates glued on the wagon, which moves it in the X direction. Two additional X piezoelectric stacks are placed above with the X spring plate pressing them. Both X and Y spring plates are screwed on the STM body, they also ensure good parallelism between both stages and the wagon. While one side is anchored, the screws on the other side can be more are less tightened, which tunes the pressure force on the piezoelectric motors below. This controls the displacement of the wagon for one step of the motors in either direction X and Y. Both directions are not completely independent : a motor step in the X direction also causes a small shift in the Y direction.

Displacement (nm/step)	M_{X+}	M_{X-}	M_{Y+}	M_{Y-}	M_{Z+}	M_{Z-}
$T = 293\,\mathrm{K}$	$(-164\,;\,-30)$	$(+212\,;\,+13)$	$(-22\,;\,+274)$	$(+12\,;\,-212)$	$+70$	-160
$T = 4\,\mathrm{K}$	$(-83\,;\,-10)$	$(+63\,;\,-30)$	$(-13\,;\,+120)$	$(+2\,;\,-110)$	$+65$	-140

Table 4.3: Displacement of the XY stage in the XY plane and of the scanner in the Z direction for one motor step, for pulse amplitude of 120 V (at 293 K) and 250 V (at 4 K).

Table 4.2 lists the total capacitance of the three X, Y and Z stages while Table 4.3 indicates the displacement of the wagon and the scanner for one step in each direction. At 4 K, we use pulses of 250 V which move the wagon of around 100 nm by step. For the scanner, displacement in the vertical direction changes by a factor of 2 due to gravity : from 65 nm upward - approaching the sample against gravity - to 140 nm downward - getting away from the sample. This difference allows safer approach of the sample.

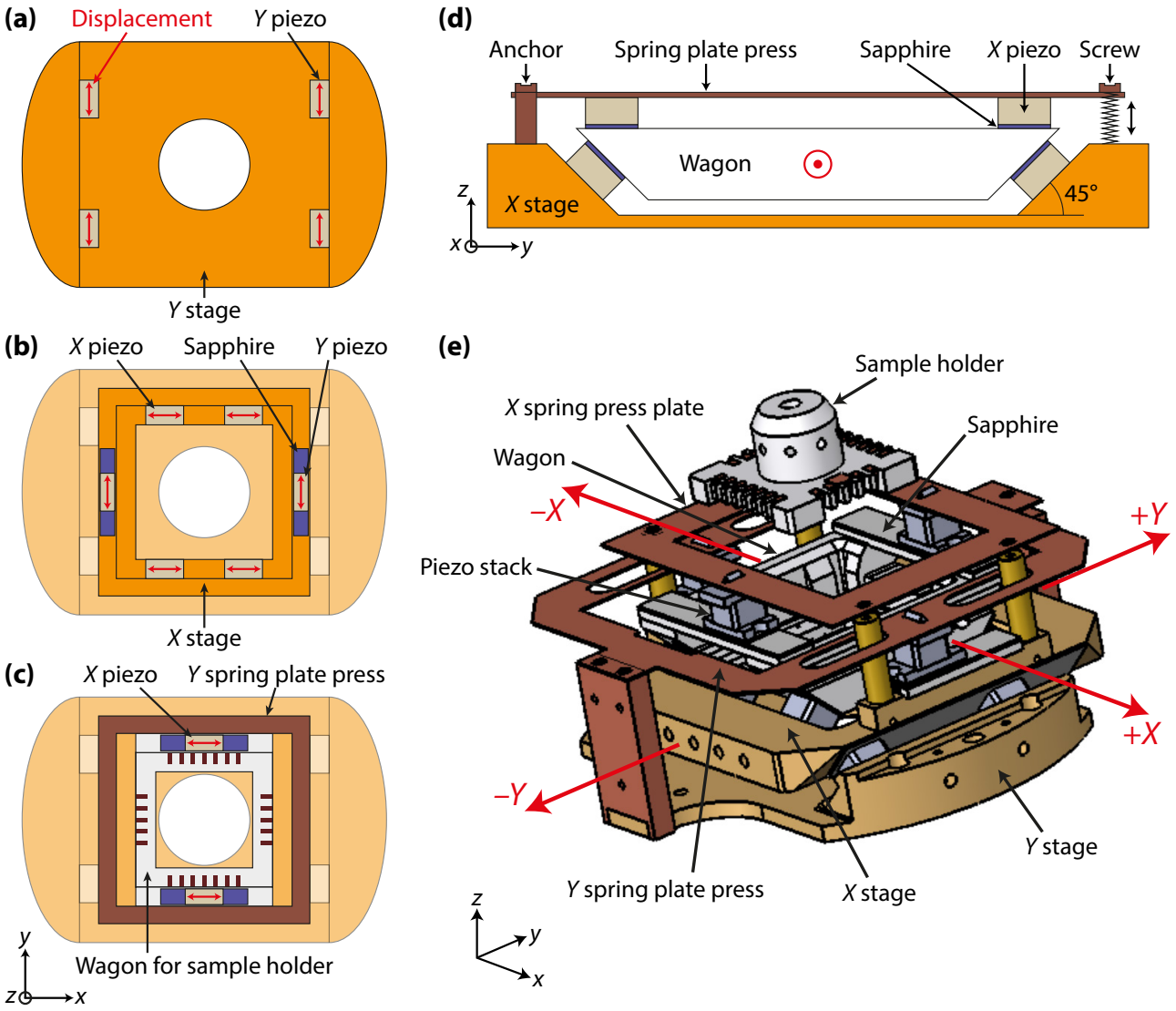

Figure 4.6: *XY* table. **(a-c)** Schematic of the superposition of X and Y stages and the wagon. **(d)** Schematic of the working of the spring press plates to tune the displacement of the wagon for one motor step. **(e)** 3D sketch of the whole XY table of our STM.

4.1.3 Electronics : amplifiers and control unit

The overall control of the microscope is done using Nanonis electronics[3], which allows to operate every input and output of the microscope. It is composed of a PC with a real time operating system with 2 FPGA acquisition cards. The Nanonis is a 16-bit system that mainly consists of 6 modules :

- The SPM Real-Time Controller (RC4), which handles all basic STM experiments, such as the approach, the regulation of the tip-sample distance, the scan control or the bias spectroscopy among others. It is connected to a Signal Conditioning (SC) module that has analog-to-digital and digital-to-analog converters managing 8 input signals and 8 outputs delivering voltages between ± 10 V.

- The Oscillation controller for AFM mode, which provides the excitation oscillatory voltage that drives our tuning fork force sensor, and a PLL to measure the response signal and tune the excitation frequency.

[3]made by SPECS.

- The High Voltage Amplifier (HVA4), which is a low noise amplifier with gains 4, 15 and 40. Its is used to amplify the voltages applied on the piezoelectric scanner, as well as the back-gate voltage applied on the sample. This module is supplied by a High Voltage power Supply (HVS4) which delivers voltages between ±10 V.

- The Piezo Motor Driver (PMD4), which provides voltage pulses to the piezoelectric actuators for coarse motion. It is also supplied by the HVS4 module. The amplitude and frequency of the pulses are user parameters.

We describe in the following two key electronic components : the current amplifiers for STM and AFM.

4.1.3.a STM amplifier

The measurement of the tunneling current I_t is done with a current amplifier[4] that converts currents as low as some pA into voltages that the Nanonis electronics can easily handle. The equivalent electrical circuit of the STM amplifier is shown in Figure 4.7. The output voltage V_t for the input tunneling current I_t is :

$$V_t = -Z_{fb} I_t = -\frac{R_{STM}}{1 + j\omega R_{STM} C_{stray}} I_t \tag{4.1}$$

where $R_{STM} = 100\,\mathrm{M\Omega}$ is the feedback resistance and C_{stray} is the parasitic capacitance, which limits the bandwidth of the amplifier. The gain at low frequency is $-R_{STM}$: the current-voltage converter coefficient is 10^8. The cut-off frequency $f_c = 1/2\pi R_{STM} C_{stray}$ is about 2.5 kHz. The use of such high feedback resistance also reduces the current noise of the amplifier, which is given by the Johnson-Nyquist noise :

$$S_{I_t} = \sqrt{\frac{4k_B T}{R_{STM}}}\,\sqrt{\Delta f} \tag{4.2}$$

Since our feedback resistance is at room temperature, the theoretical noise of our amplifier is $13\,\mathrm{fA}/\sqrt{\mathrm{Hz}}$. Experimentally, the tunneling current power spectral density shows that the noise is a little above, at $18\,\mathrm{fA}/\sqrt{\mathrm{Hz}}$.

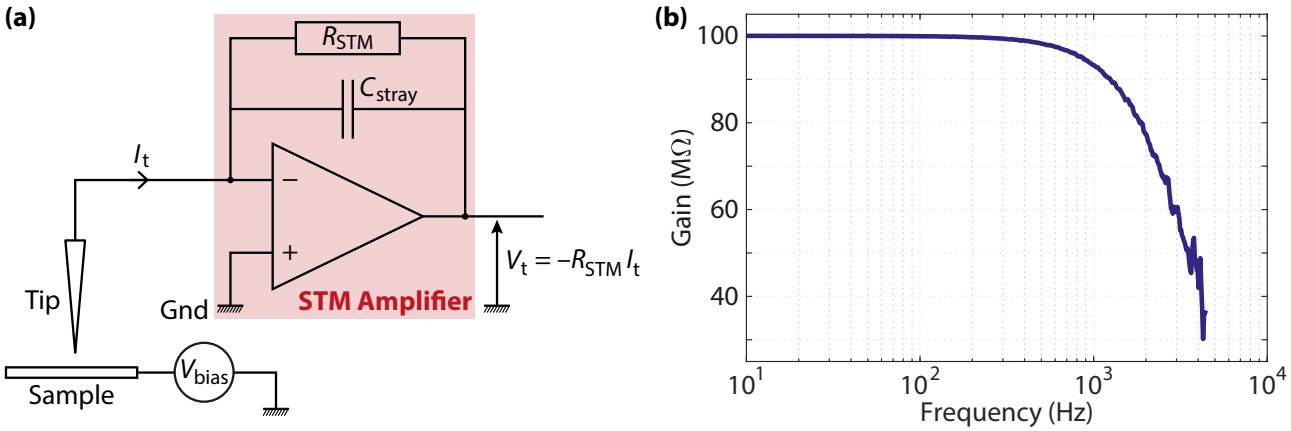

Figure 4.7: STM current amplifier. (a) STM amplifier equivalent electrical circuit with the feedback resistance $R_{STM} = 100\,\mathrm{M\Omega}$ and the stray capacitance C_{stray}. **(b)** Gain $|V_t/I_t|$ of the amplifier as a function of frequency.

[4] made by RHK.

4.1.3.b AFM amplifier

Our sensors use quartz tuning forks for AFM mode. They are excited on one of their electrodes by a driving signal V_{ac} and the piezoelectric effect of the quartz generates a piezoelectric current I_p on the other electrode. This current is measured with our home-made AFM amplifier[5] which is, as previously, a current to voltage converter. The frequency of the signal depends on the resonance frequency of the tuning fork but it ranges most of the time between 15 kHz and 33 kHz. We use a lower feedback resistance $R_{AFM} = 1\,M\Omega$ to increase the bandwidth of the amplifier to such frequencies. This reduced gain is still enough : at 4 K and at resonance frequency of the tuning fork, a driving excitation with an amplitude of a few mV generates a piezoelectric current of a few nA. We also use in the feedback loop of the amplifier a tunable compensation capacitance C_{comp} whose role is to compensate the current originating from capacitive coupling between the electrodes of the tuning fork and from the capacitance of the line (capacitance C_0, see Section 4.3.1). This capacitive current increases with the frequency and could eventually hinder the measurement of the tuning fork resonance.

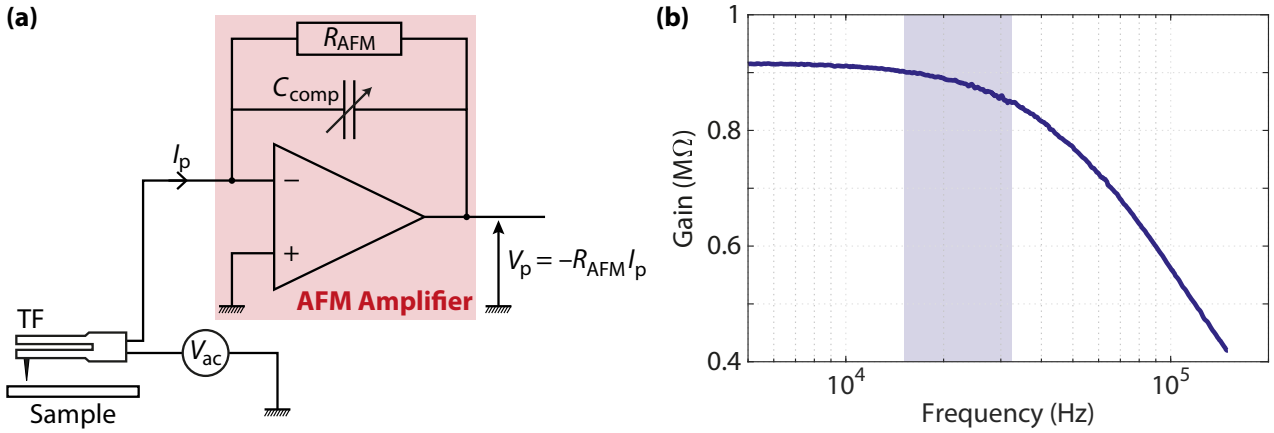

Figure 4.8: AFM current amplifier. (a) AFM amplifier equivalent electrical circuit with the feedback resistance $R_{AFM} = 1\,M\Omega$ and the compensation capacitance C_{comp}. **(b)** Gain $|V_p/I_p|$ of the amplifier as a function of frequency. The blue area is our usual frequency range.

4.1.4 Experimental setup and environment

The STM is mounted on a 4 K insert, in which every service and measurement lines are physically separated to prevent electrical noise from the high voltages on the low level signals such as the tunneling current. It is inserted in a 130 L effective liquid helium cryostat with a holding time superior to 10 days. At the bottom of the cryostat lies the 14 T superconducting solenoid magnet with 103 mm cold bore. The setup has been installed on a two-stage anti-vibration platform, which is critical for the damping of the environmental mechanical vibrations. It is made of a 2.5 tonnes granite bloc on air legs, resting atop a 24 tonnes inertial concrete block on another set of air legs, and it gives a bare noise velocity of ~ 8 nm/s above 30 Hz. Eventually, the tunneling current power spectral density does not show any significant mechanical noise.

Though the results presented in this thesis were obtained at 4 K, our microscope has also been designed to work at very low temperature with an ultra-high vacuum dilution refrigerator, down to temperatures of 20 mK. An UHV chamber mounted on a mobile structure can be connected to the top of the dilution fridge once inserted in the 4 K cryostat. This chamber will

[5] made by D. Leppoitevin from the electronic service in Institut Néel.

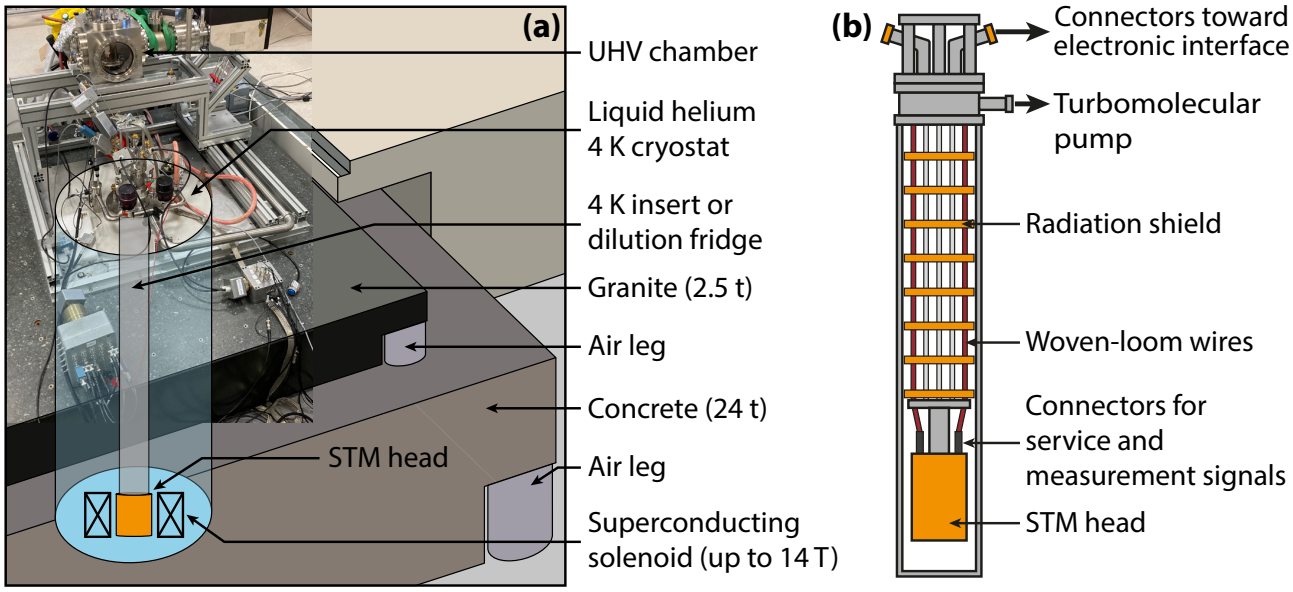

Figure 4.9: STM platform (a) and 4 K insert (b) sketches.

allow in situ annealing of graphene surfaces, field-effect cleaning for the STM tips, and tip and sample top-loading through the fridge inside the STM.

4.2 Graphene device

Our graphene devices consist of a van der Waals heterostructure of graphene on hBN deposited on either a standard SiO_2/Si substrate or a high-k dielectric $SrTiO_3$ substrate. The device, with a typical size of several microns, lies approximately at the center of the $5 \times 5\,mm^2$ substrate. The graphene flakes in the samples we made are contacted with different configurations, from only one contact which allows to apply a bias voltage for STM measurements to a two- or four-probe configuration to also enable transport measurements. Moreover, a back gate enables field-effect gating of the graphene to tune the position of the Fermi level and the filling factor of the Landau levels in the quantum Hall regime. Eventually, a guiding markerfield has been patterned on the whole substrate to help guiding the tip toward graphene in AFM mode.

The fabrication process of our devices is detailed in Appendix B, as well as our cleaning methods to obtain graphene surface suitable for STM measurements.

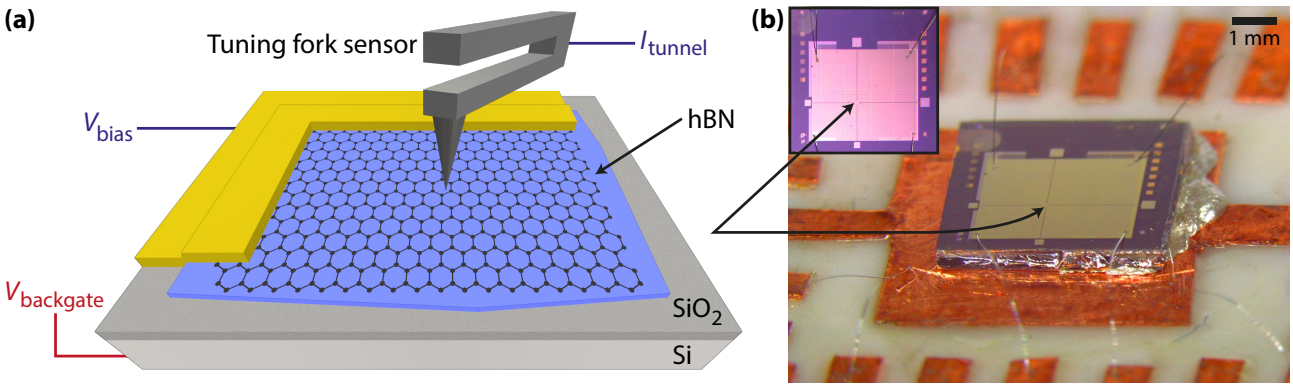

Figure 4.10: Graphene device. (a) Schematics of our typical graphene device. There are two main differences between the samples : the substrate (SiO_2 or $SrTiO_3$) and the graphene contacting. **(b)** Image of the sample once glued and bonded on the 24-contacts sample holder.

The sample is glued on the 24-contacts sample holder with a silver epoxy that realizes the electrical contact between the back gate of the sample and a piece of copper below glued on the Macor sample holder. Two of the 24 contacts of the sample holder are directly connected to that central piece of copper and are therefore used to apply the back-gate voltage. Two other contacts are connected by a 50 Ω resistance which is used as a sample heater. The bonding from the sample holder contacts to the sample are done with a micro-bonding machine with aluminum wires, mostly for the application of the bias voltage but also for transport measurements when available on the sample.

4.3 AFM/STM probe fabrication

Our home-made AFM/STM sensors allow us to work either in AFM mode (for localizing the graphene and its edge[6]) and STM mode (for the measurements). They consist of a tip glued on a tuning fork (TF), where the tip is electrically connected to one of the electrode of the TF. In STM mode, we apply a dc bias voltage on the sample and measure the resulting tunneling current flowing through the tip (the second electrode of the TF is grounded). In AFM mode, an oscillatory signal V_{ac} is applied to one electrode of the TF whereas we measure the piezoelectric current resulting from the deformation on the other electrode. The tip then serves as a sensor for the van der Waals interaction, that shifts the resonance frequency of the TF at the proximity of the surface, and the regulation is done on the resonance frequency shift.

4.3.1 Tuning fork

A tuning fork [224] is made of two parallel coupled oscillating arms linked by a common base, and behaves as a harmonic oscillator with inherent high quality factor. The use of TFs in scanning probe microscopy dates back to 1989 in the scanning near-field acoustic microscopy [225], and later in 1995 in scanning near-field optical microscopy [226], and has been extended since then to many other local microscopies, driven by the need to suppress light from laser-based detection in order to ease experimental setups but also to avoid this potential heat source for very low temperature experiments. Furthermore, Senzier *et al.* [227] demonstrated in 2007 that the use of TFs for combined AFM/STM probes was appropriate in order to perform tunneling spectroscopy at very low temperature.

The TFs are here used as piezoelectric resonators and therefore allow both excitation and detection based on electrical signals. They are made of monocrystalline piezoelectric quartz, a material with high stiffness and low loss. This important stiffness, of the order of 10^3 N/m (see the mechanical model in Appendix C.2), makes TFs quite stable oscillators, which is crucial for STM experiments since it prevents mechanical instabilities, like jumps to contact, from happening. TF are mass-produced by the clockwork industry and used as time references. Figure 4.11(a) shows the TFs[7] we use to realize our sensors. The amplitude and phase responses of the TF correspond to a resonance followed by an anti-resonance, with a background where the amplitude grows linearly with the frequency. When sealed in their ceramic package, their resonance frequency is accurately $2^{15} = 32\,768$ Hz and their quality factor at room temperature is about 50 000. This resonance frequency corresponds to the antisymmetric mode of the TF ; the metallic electrodes are deposited on the arms such that only this oscillatory mode can be electrically excited and detected (see Figure 4.12).

[6] The edge of graphene on hBN is a conductive/insulating interface, preventing us from using STM.
[7] fabricated by Micro Crystal, series CC4V-T1A.

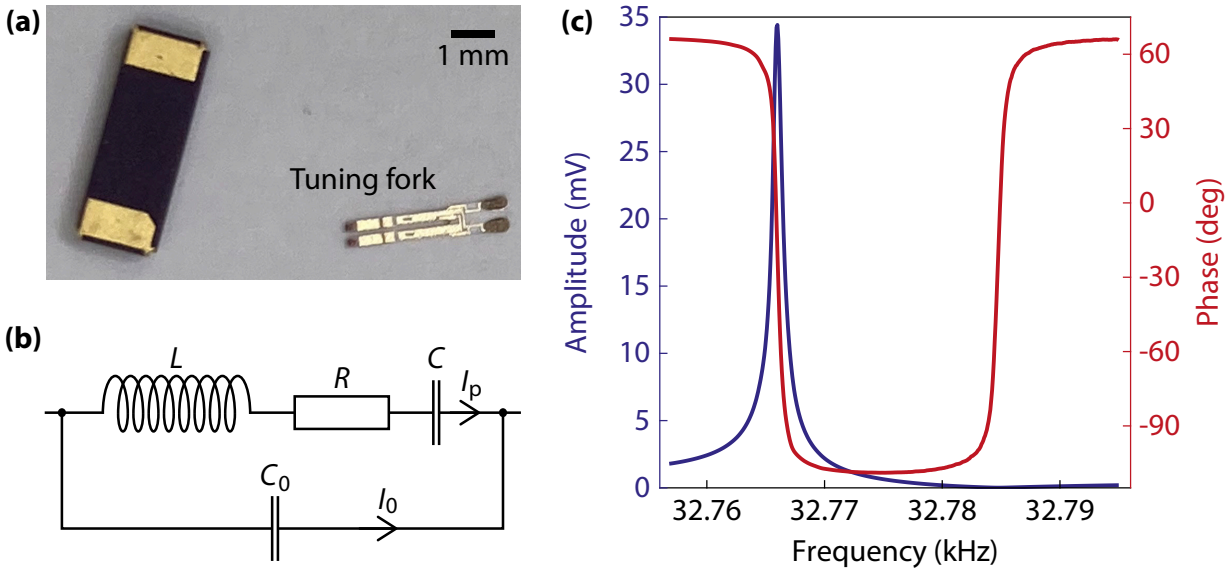

Figure 4.11: Tuning fork. **(a)** Image of the TF used for our AFM/STM sensors : on the left the encapsulated TF as bought, on the right the TF alone once removed from its capsule. **(b)** Equivalent electric schematics of the TF. **(c)** Resonance of the encapsulated TF at 293 K : $f_{\text{res}} = 32.765$ kHz and $Q = 50500$. Drive amplitude of the TF : $U_{\text{d}} = 2$ mV.

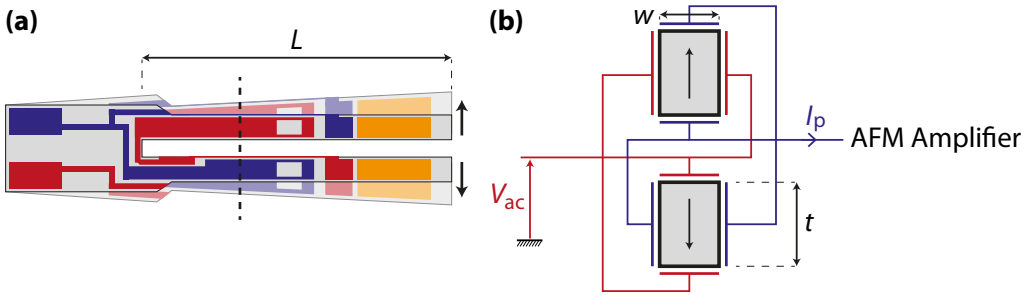

Figure 4.12: Oscillation mode of the tuning fork. **(a)** Antisymmetric oscillation mode of the TF used for our AFM setup. **(b)** Cross section along the black dashed line in (a), showing the pattern of the two electrodes that allows to excite and measure only the antisymmetric mode. One electrode is used to excite the TF with the voltage V_{ac} that oscillates at the TF resonance frequency, while the second electrode is used to collect the piezoelectric charges which form the current I_{p}. L, t and w are respectively the length, thickness and width of the prongs.

It is possible to model the TF with an equivalent electrical schematics as shown in Figure 4.11(b), with a RLC series circuit, modeling a classical second order damped harmonic oscillator, in parallel with a stray capacitance C_0. The resistance R models the damping process, the inductance L represents the effective mass and models the kinetic energy storage, and the capacitance C represents the spring constant and models the potential energy storage. On the other hand, the parallel capacitance C_0 models the geometrical arrangement of the electrodes, the dielectric properties of the quartz but also the capacitive contributions of the cables employed. This electrical circuit fits very well the amplitude and phase signals measured on a TF driven by an excitation signal $V_{\text{ac}} = U_{\text{d}} \cos(2\pi f t)$. The resonance frequency f_{res} is modeled by :

$$f_{\text{res}} = \frac{1}{2\pi} \frac{1}{\sqrt{LC}} \tag{4.3}$$

while the quality factor Q is given by :

$$Q = \frac{1}{R} \sqrt{\frac{L}{C}} \tag{4.4}$$

The greater Q is, the more resolved and separated the resonance and anti-resonance are, which is primordial to have a stable AFM mode. Finally, the background current that increases linearly with the frequency can be written as :

$$I_0 = 2\pi f U_\mathrm{d} C_0 \tag{4.5}$$

where U_d is the drive amplitude applied on the tuning fork.

4.3.2 Probe fabrication

The tuning fork, once unsealed from its ceramic package, is glued on a Macor chip with two gold electrodes, using the Stycast[8] epoxy glue. A very small amount of glue is put on the chip to only glue the common basis of the two prongs of the TF placed on a tilted qPlus configuration, as named by Giessibl *et al.* [228] (see Figure 4.13). The top prong that stands in the void is free to oscillate, however the bottom prong that partially stands on the Macor chip is assumed to be fixed (usually, some glue goes up along this prong by capillarity). After curing the epoxy, we use a bonding machine to bond with aluminum wires each electrode of the chip to the electrodes of the TF. At this point it becomes possible to check if the TF resonates or not, and in the first case if the resonance is still good (the resonance frequency should still be around 32 kHz and the quality factor around 1000 at room temperature and pressure). Only then the TF glued on the chip can be used as a sensor.

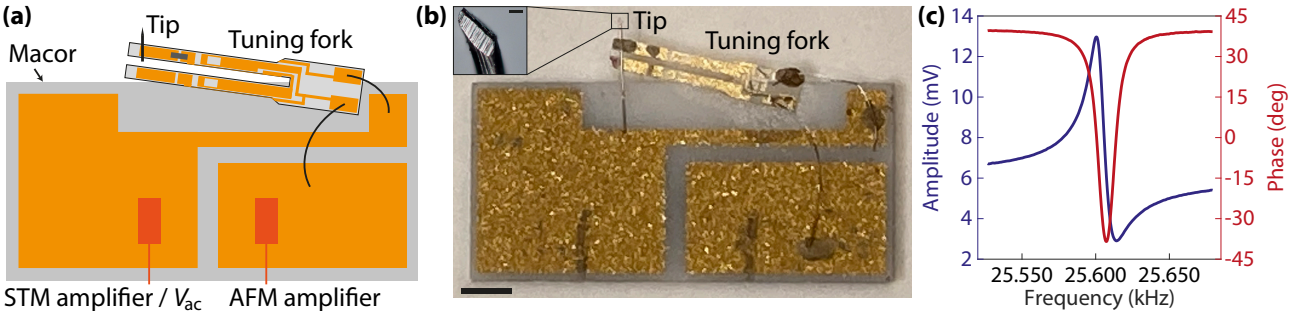

Figure 4.13: AFM/STM sensor. (a) Schematic of our AFM/STM sensor. The TF is glued on one of its prong (tilted qPlus configuration) on a Macor substrate where gold electrodes have been patterned. The PtIr tip is then glued with silver epoxy at the extremity of the free prong. Both electrodes are contacted by the sensor holder on the orange areas by BeCu springs. A patch of silver epoxy contacts the floating electrode where the tip is glued with the electrode of the TF connected to either the STM amplifier (for STM mode) or to the drive amplitude V_ac (for AFM mode). The second TF electrode is connected to the AFM amplifier. **(b)** Image of our AFM/STM sensor, scale bar : 1 mm. Inset : extremity of the PtIr tip (cut by hand) observed with an optical microscope. Scale bar : 20 µm. **(c)** Typical resonance of the TF of the AFM/STM sensor at ambient temperature and atmospheric pressure, with a drive amplitude $U_\mathrm{d} = 30$ mV. Here, $f_\mathrm{res} = 25.600$ kHz and $Q = 1587$.

The next step is to glue the tip at the extremity of the free prong of the TF. We use a PtIr wire (90/10), where the platinum makes the tip stainless while the indium is used to harden the alloy. We cut the wire using a clamp - in most cases the tips we obtain with this rough method are sharp enough to enable us to very well resolve the structures of our guiding markerfield in AFM (the smallest ones have a width of about 200 nm), and can therefore be used for our combined AFM/STM sensors. The tip is glued at the extremity of the free prong

[8] Stycast 1266. Curing : 1 hour at 65 °C.

with a conductive silver epoxy[9] that realizes the electrical contact between the tip and one electrode of the TF. After the curing of the silver epoxy, the resonance of the TF is once again checked. Due to the added mass of the tip and the silver epoxy, the resonance frequency is shifted down of several kHz, usually between 15 and 25 kHz. The quality factor also decreases, but should stay between 500 and 1000 at room temperature and pressure. If the resonance is too bad or not measurable, one can simply remove the tip and glue a new one. The AFM/STM sensor is now ready and can be loaded inside the STM head.

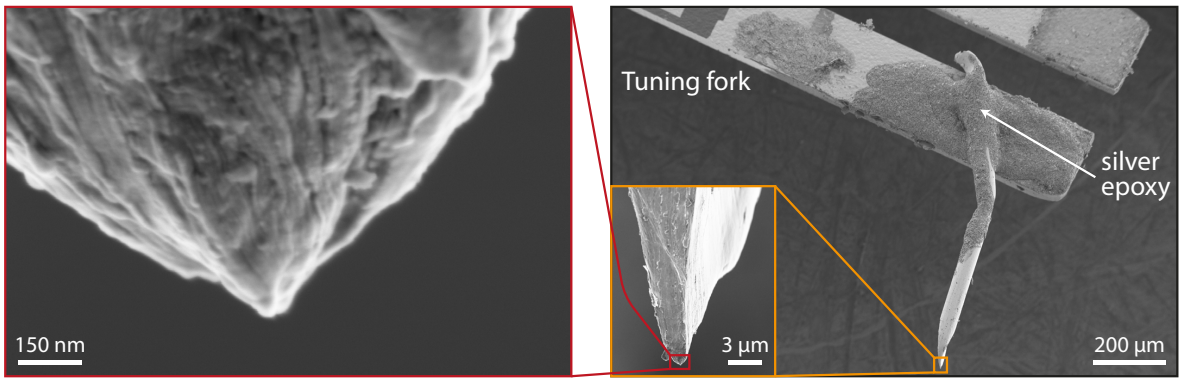

Figure 4.14: Observation of hand-cut tip apex in SEM.

4.3.3 Sensor characterization with temperature and magnetic field

After loading the AFM/STM sensor inside the STM head, the resonance of the TF is continuously measured during the cooling down to 4 K and we obtain the evolution of the resonance frequency and the quality factor as a function of the temperature.

Figure 4.15 shows such evolution for one sensor. The quality factor tends to increase with decreasing temperature [229, 230], yet the variations of f_{res} and Q from room temperature are not monotonic and some spikes may appear due to thermal contractions of the gluing of the TF on its Macor substrate and of the whole mechanical assembly. It is thus not possible to predict the shape of the resonance at 4K, nor if the resonance will still be usable[10]. Only at temperatures below $20 - 30$ K the evolution of the resonance frequency and the quality factor might become stable, and the quality factor can increase to high values such as $Q \sim 10\,000 - 20\,000$ quickly. With the PLL, we regulate the vibration amplitude of the TF at 4 K to typically 5 mV, which corresponds to a vibration amplitude of 10 nm from the estimated calibration of 2 nm/mV.

The evolution of the TF resonance with the magnetic field is also an important parameter since the objective of this thesis is to study the Landau levels physics at the edge of graphene. AFM is there used to localize the edge. We can not simply map the sample at zero magnetic field and afterward increase the magnetic field since the tip position on the sample would inevitably shift. We therefore have to be able to do AFM images at high magnetic fields up to 14 T. As shown in Figure 4.16, the quality factor of the TF resonance decreases with the magnetic field, reaching values of a few thousands at 14 T. It is still enough to perform good AFM images of our devices and locate, even roughly, the edges of graphene. This reduction of the quality factor may come from the eddy currents in the TF electrodes and tip.

[9] DuPont 7713. Curing : 1 hour at 100 °C.

[10] The resonance may have a very low quality factor or may split in two or more weaker resonances, preventing the AFM mode from working.

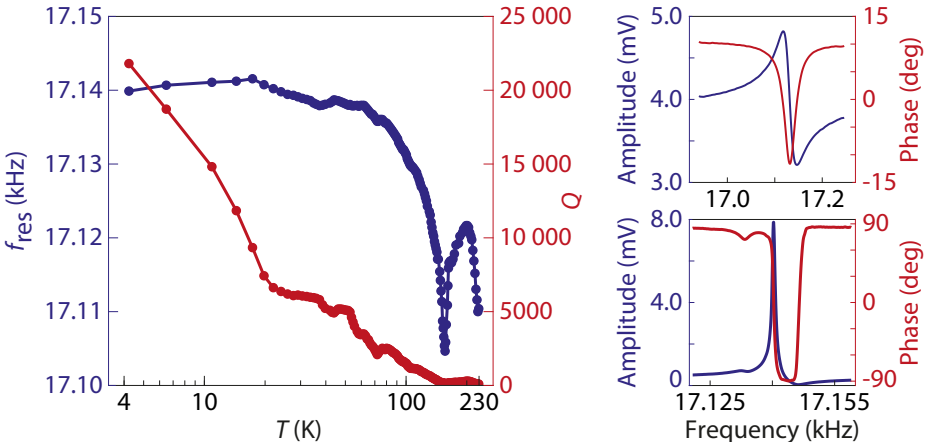

Figure 4.15: Evolution of the resonance with the temperature from 230 K to 4.2 K. (Top right) Resonance at room temperature : $f_{\mathrm{res}} = 17.117\,\mathrm{kHz}$ and $Q = 590$. Drive amplitude : $U_{\mathrm{d}} = 30\,\mathrm{mV}$. (Bottom right) Resonance at 4.2 K after stabilization : $f_{\mathrm{res}} = 17.1402\,\mathrm{kHz}$ and $Q = 30670$. Drive amplitude : $U_{\mathrm{d}} = 5\,\mathrm{mV}$.

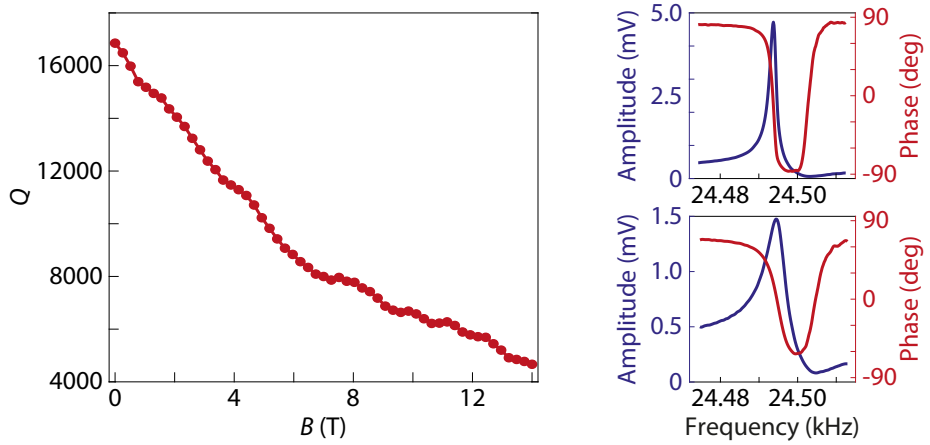

Figure 4.16: Evolution of the quality factor with the magnetic field from 0 T to 14 T at 4 K. The variation of the resonance frequency is smaller than 1 Hz. (Top right) Resonance at 0 T : $f_{\mathrm{res}} = 24.493\,\mathrm{kHz}$ and $Q = 16850$. Drive amplitude : $U_{\mathrm{d}} = 2\,\mathrm{mV}$. (Bottom right) Resonance at 14 T : $f_{\mathrm{res}} = 24.494\,\mathrm{kHz}$ and $Q = 4670$. Drive amplitude : $U_{\mathrm{d}} = 2\,\mathrm{mV}$.

4.4 Towards STM on graphene at 4 K

We detail in this section the consecutive steps once both the sample and sensors are ready, towards putting the tip on the graphene device and then starting preliminary STM measurements, so that it becomes possible to realize tunneling spectroscopy on graphene, which will be the topic of the following chapters.

The AFM/STM sensor is loaded inside the STM head and the resonance of the tuning fork is checked in situ. The sample holder is afterward loaded upside down so that the sample and the tip face each other. The tip is roughly aligned with the eye above the center of the sample where the graphene device lies as shown in Figure 4.17(b). This step is important since it is the only occasion to align the tip, once in the cryostat there is no optical access. The STM head is then mounted on the 4 K insert and cooled down in the liquid helium cryostat. The cooling takes around 90 minutes, a Cernox® resistance glued directly on the STM head with a thermal conductive Stycast is used as a thermometer. During the cooling, the sample holder is heated with a 50 Ω resistance glued on it, with a Joule power of about 100 mW, to desorb water and other gases from the sample surface.

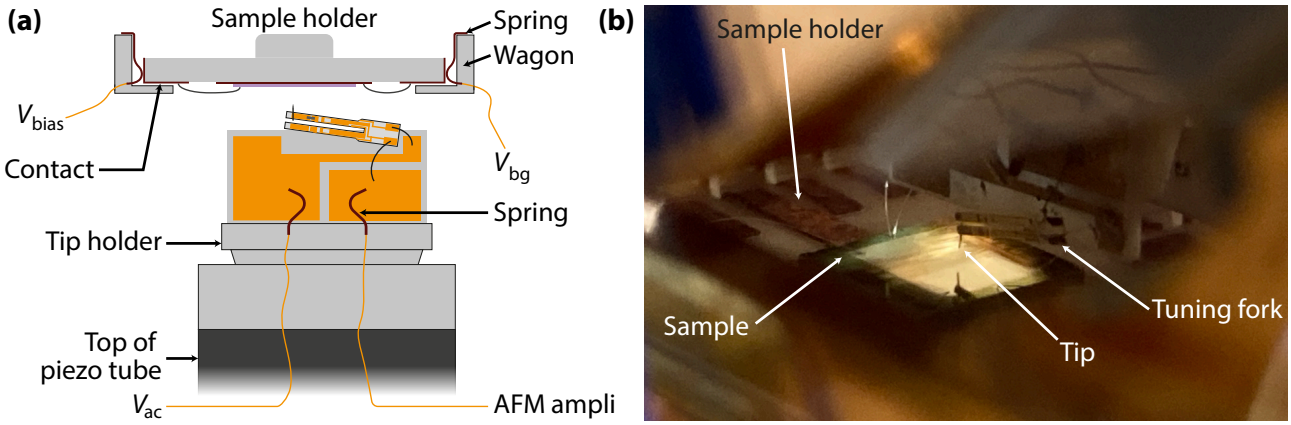

Figure 4.17: Tip and sample holder loaded inside the STM head. **(a)** Schematic of the tip and sample holder in the STM. The sample holder is inserted upside down in the wagon and faces the tip holder mounted at the top of the piezoelectric tube. The electrical contact between the contacts of the sample and tip holders and the STM electronics is done with gold plated BeCu spring wires. **(b)** Image of the reflexion of the tip and sample holder inside the STM head. Using the reflexion of the tip from the sample, it is possible to roughly approach and then align the tip with the eye.

Once at 4 K, the initial approach of the tip toward the sample is done in AFM mode. Both TF electrodes are connected to either the driving excitation V_{ac} and the AFM amplifier while the sample is grounded. The approach ends when the tip eventually feels an attractive interaction with the surface of the sample that results in an increase of the frequency shift Δf of the resonance frequency toward the chosen setpoint, of typically one or a few Hz. The resonance of the TF stays mostly stable and is most of the time not altered by the steps of the Z piezoelectric motors, which results in a steady and swift approach taking about one night.

4.4.1 Tip guiding

For guiding the tip toward the device, a guiding markerfield has been patterned on the $5 \times 5\,\mathrm{mm}^2$ sample substrate with the objective that with a single AFM image, we can determine where the tip is and what is the number of X and Y steps we must do to move the tip toward the graphene sample. The main criterion here is the full range scan size of $3 \times 3\,\mu\mathrm{m}^2$ that we have at 4 K which corresponds to the maximum voltage we can apply to the piezoelectric tube in the X and Y directions[11], which means that the guiding markerfield must be very dense with all the information of one code contained in a square of 3 microns and every code is separated from its neighbors by a distance of 3 microns. The objective is also to be able to reach the graphene device in a few steps, to minimize the hazards the tip might get through (potential crashes due to very high unexpected objects for example) that could pollute or even damage its apex. After having identified the code of the area where the tip landed, the tip is withdrawn of a few tens or hundreds of steps so that we can safely move it to the next target point, after what a new approach is done in AFM mode, we then image the new area, identify its code and keep going toward the graphene device.

We present in Figure 4.18 the working principle of our guiding markerfield and its decoding, while Figure 4.19 shows AFM images at 4 K of different codes. Guiding the tip toward the graphene device usually takes one day, with around 10 scans in AFM.

[11] We limit the voltages applied to the X and Y electrodes of the tube to prevent potential depolarization of the piezoelectric domains with time : $-150\,\mathrm{V} < X, Y < 150\,\mathrm{V}$.

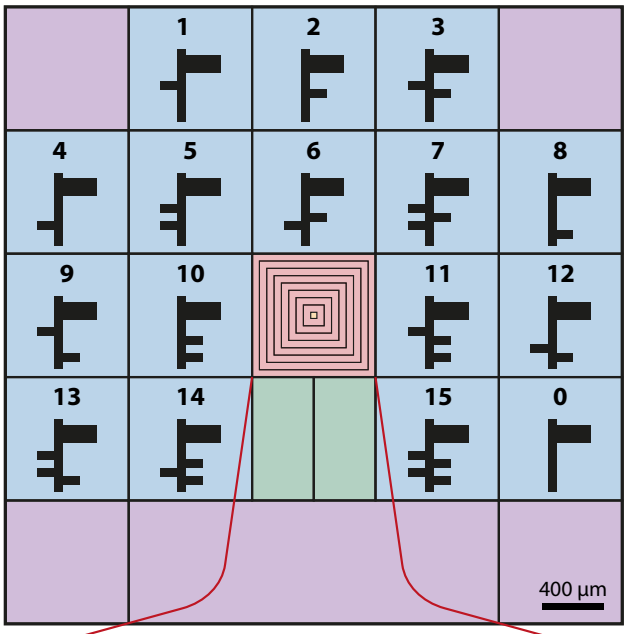

Square	Code	Displacement (µm)	Square	Code	Displacement (µm)
1		X = +825 Y = -1750	9		X = +1750 Y = 0
2		X = 0 Y = -1750	10		X = +825 Y = 0
3		X = -825 Y = -1750	11		X = -825 Y = 0
4		X = +1750 Y = -850	12		X = -1750 Y = 0
5		X = +825 Y = -850	13		X = +1750 Y = +850
6		X = 0 Y = -850	14		X = +825 Y = +850
7		X = -825 Y = -850	15		X = -825 Y = +850
8		X = -1750 Y = -850	0		X = -1750 Y = +850

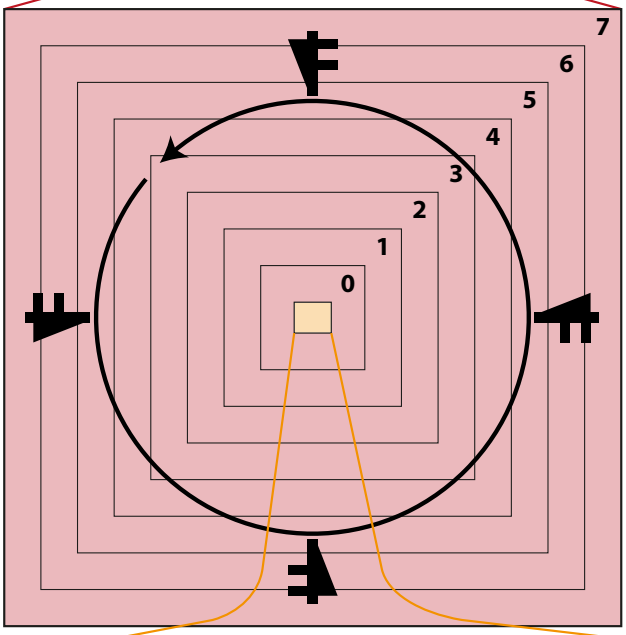

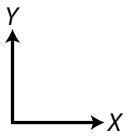

Ring	Code	Displacement (µm) in arrow direction
0		50
1		110
2		155
3		200
4		260
5		310
6		360
7		400

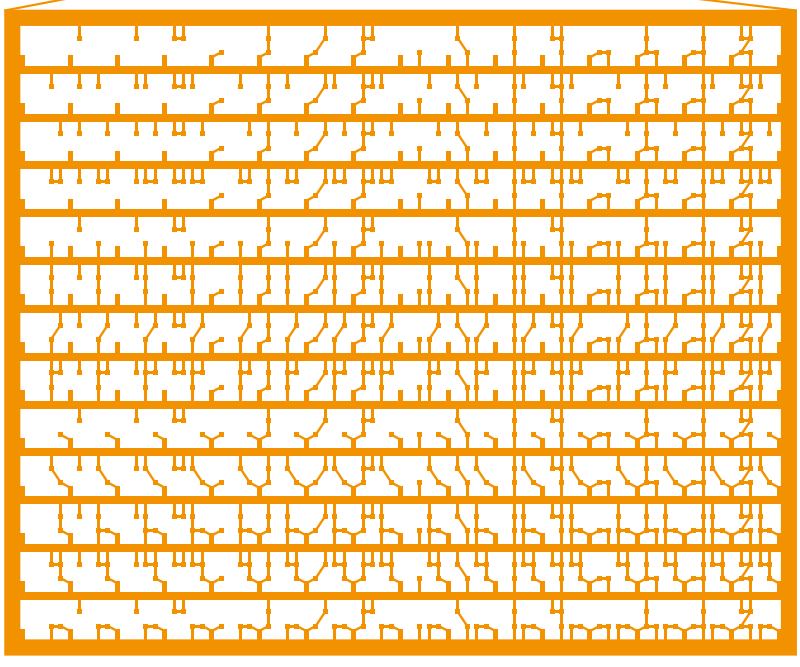

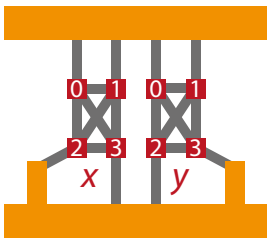

Displacement :

$X = 3\ \mu m \times (x_{target} - x_{tip})$

$Y = 3\ \mu m \times (y_{target} - y_{tip})$

Figure 4.18: Decoding the guiding markerfield.

First coding layer The surface of the sample is separated into 25 squares with the central one containing the graphene device. 16 squares are coded with vertical lines along which a four-digit binary code is repeating (1 : rectangle visible / 0 : rectangle absent). A bigger rectangle separates one code from the next one and is also used as a chirality marker for unambiguous identification. With one AFM image we are able to identify in which square the tip currently is and the displacement we have to do in the X and Y directions, using coarse motors and Table 4.3, to move into the central square. Note that this coding layer only gives coarse localization and displacement. The other nine squares are coded with simple arrows pointing toward the central square, but a tip that has already been aligned with the eye atop the center of the sample is unlikely to land in these distant regions.

Second coding layer The central square is itself divided into 8 concentric rings around a final square in which the graphene device lies. Each ring is coded with lines, along which a three-digit binary code (1 : rectangle visible / 0 : rectangle absent) is repeating on one side on the lines and gives the information on the distance from the central square, while on the other side a triangle indicates the direction of the central square. The lines are rotated around the central square in multiples of 45°.

Final coding layer The central and final square contains the graphene device. Its surface is fully coded by a set of two four-digit binary codes for each x and y coordinates (1 : square visible / 0 : square absent) for precise localization. One chirality marker once again separates each (x, y) code from the next one. Some lines connect the squares in each x and y code which forms unique patterns and eases the identification of the coordinates. After that one can easily move the tip to the targeted position where the device lies (the coding markerfield is absent on the graphene itself).

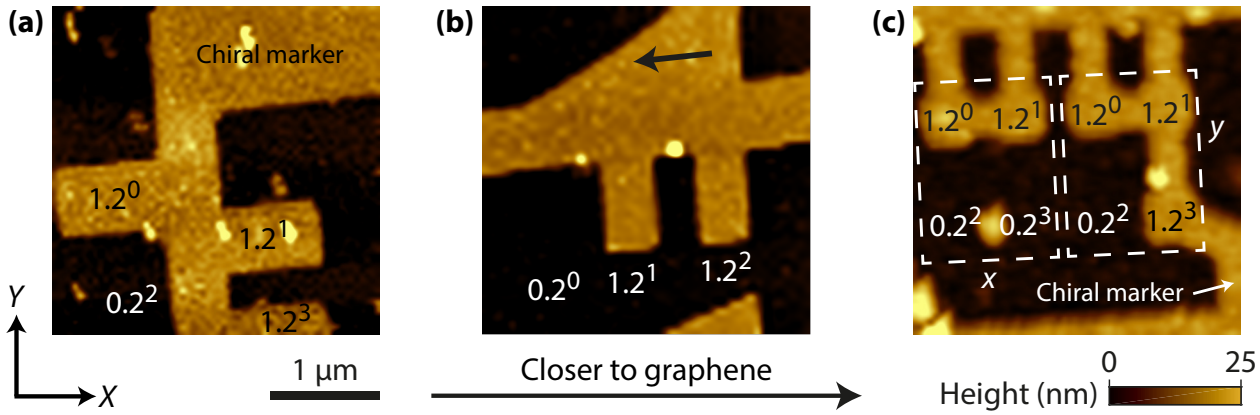

Figure 4.19: Imaging the guiding markerfield. AFM scans at 4 K of markers of the three different coding layers. **(a)** Marker of the first layer that codes the square number $1.2^0 + 1.2^1 + 0.2^2 + 1.2^3 = 11$, which gives for the next displacement with the piezoelectric motors $X = -1750$ µm and $Y = 0$. **(b)** Marker of the second layer that codes the ring number $0.2^0 + 1.2^1 + 1.2^2 = 6$, which gives for the next displacement $X = -360$ µm, the direction is indicating by the arrow. **(c)** Marker of the final layer that codes the position $x = 1.2^0 + 1.2^1 + 0.2^2 + 0.2^3 = 3$ and $y = 1.2^0 + 1.2^1 + 0.2^2 + 1.2^3 = 11$.

Figure 4.20 shows AFM images of the graphene device after we successfully guided the tip on it. With the tip on graphene, we can switch to STM : the driving excitation V_{ac} of the TF is disconnected and replaced with the STM amplifier while the second electrode of the TF is disconnected from the AFM amplifier and grounded. A bias $V_{\text{bias}} \sim 500$ mV is applied on the sample. We then approach the tip toward graphene in STM mode.

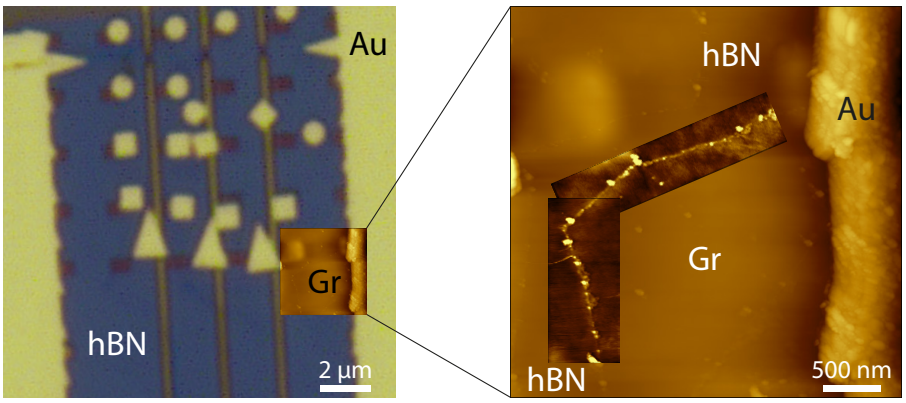

Figure 4.20: Imaging a graphene device in AFM. (Left) Localization of an area of the graphene device imaged in AFM on the optical picture. (Right) Graphene lies atop the hBN flake and is contacted by a gold contact to apply the bias voltage. Two AFM images zoomed on the edge of graphene show that the graphene/hBN interface is polluted at some points by residues that appear as bright spots, but still some places are cleaned and accessible for STM.

4.4.2 Tip cleaning

Usually, the tip can approach graphene in STM and establish a "tunneling" junction : the current measured with the STM amplifier reaches the setpoint value of typically 1 nA. However the junction is not stable and the current does not depend exponentially on the tip-sample distance, which indicates that during the guiding steps the tip apex must have been polluted by impurities such as resist residues. We expose in this section the procedures we have adopted to clean the tip. These procedures are done on a gold surface and are sorted from the less invasive for both the tip and sample to the more hazardous.

Scratching a gold contact This method consists on leaving the tip scanning on a wide area on gold (about 1 micron, tunneling current of 1 nA) to scratch the surface in order to remove the residues at the apex. There are two different approaches : one can increase the bias voltage to high values, such as 1 V or above, to increase the tunneling resistance, or on the opposite decrease the bias voltage to low values, such as 20 mV to decrease the tip-sample distance and increase the "scratching" effect. This method is more efficient if the scanning area contains a high step (a few tens of nanometers) in the scanning direction. By adjusting the regulation of the Z-controller and the tip velocity, the tip can collide smoothly this step for a few seconds (saturation of the tunneling current while the tip moves up). We found that this collision event was enough most of the time to clean the apex of the time without damaging it.

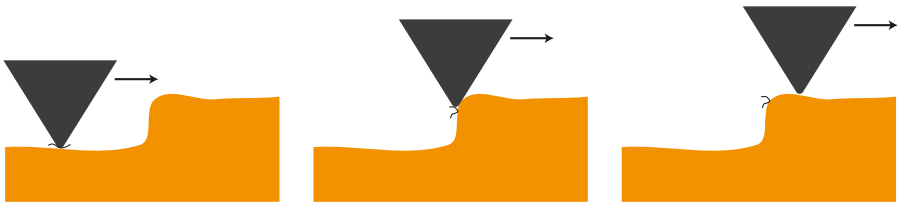

Figure 4.21: Cleaning the tip by scratching. Some resist residues or other pollutant on the tip apex can be simply removed by scratching the tip on gold, especially on high steps.

Bias pulses The tip is brought to tunneling contact on gold (typical values : 1 nA and 300 mV). While keeping the Z-controller on, a bias pulse of several volts (4 V or 10 V for 100 ms) is done. The voltage above the work function of the junction induces a field effect transient regime that is enough to tear off some matter from the tip or the sample (depending on the polarization

and the direction of the electrons) and therefore we deposit the polluted apex on the gold or on the opposite we deposit some gold to cover the pollution. We found that both polarizations may work and restore a pristine apex, but negative pulses of -4 V on the sample, that deposit some gold sputtered from the sample on the tip, gave better results.

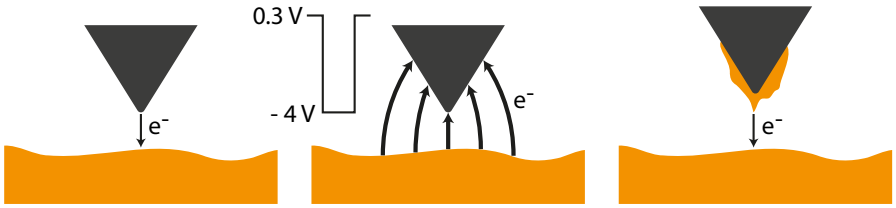

Figure 4.22: Cleaning the tip with bias pulses. Pulses of bias voltage tear off some matter which can create a new pristine tip apex.

Plunging the tip into gold The tip is also brought to tunneling contact on gold (typical values : 1 nA and 300 mV). The regulation of the Z-controller is then turned off and the bias voltage is lowered to 30 mV. The tip is manually brought down by 10 or 20 nm into gold for a quick time (saturation of the tunneling current) before turning on the Z-controller again. The tip should there pick up some gold which gives it a new pristine apex. An important current appears when we plunge the tip into gold that makes both materials melt locally and enhance their sticking. When we retract the tip after less than one second, the ductile gold deforms and stays stuck to the tip, it forms a neck that eventually breaks as the tip is further retracted, which leaves a fine gold tip apex. It is possible to tune the regulation of the Z-controller such that the retraction speed is about 0.5nm/s to give enough time to the neck to get thinner and thinner before breaking.

If this method restores the tip with a new pristine gold apex, it must be used sparingly since it also flattens the tip on a larger scale of tens of nanometers. This flattening is not a problem for STM but it decreases the resolution in AFM mode which could prevent us eventually from recognizing the markers if we have to move later to a new region or from imaging with enough precision the edge of graphene.

Figure 4.23: Plunging the tip. The tip is plunged of several tens of nanometers into gold. When withdrawn, some gold picked up by the tip creates a new pristine apex.

Field effect This procedure is the most hazardous for the tip and the sample. It consists of applying a high bias voltage on the sample and regulating at high current (typically several volts and several tens of nA). Under these conditions, strong electromigration happens that reshapes the tip apex. Depending on the polarization and the direction of the electrons, the current is strong enough to tear off some matter from the tip or the sample on larger scale than the pulses (this method must then be used far from the graphene device to avoid definitive pollution). We start by approaching the tip to tunnel contact at standard values of bias and current (300 mV and 1 nA). The regulation of the Z-controller is then turned off. We change the current setpoint to 80 nA and tune the regulation such that the tip velocity is about 0.5 nm/s. Bias voltage on the sample is turned to 10 V. The Z-controller is turned back on. The Z position of the tip evolves with time which indicates that the shape of the tip apex changes due to electromigration.

We wait enough time to observe the stabilization of the Z value after what we slowly retract the tip. We finally move away from this position before approaching the tip with standard bias and current values to check the tunneling junction.

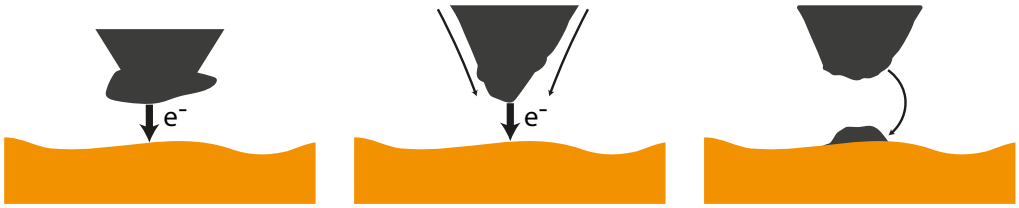

Figure 4.24: Field effect on the tip. Under high bias voltage and current, electromigration reshapes the tip apex. Sometimes, the apex is torn off the tip and pollutes the area of the sample below. Field effect is stopped when the Z position of the tip is stable with time.

It is also possible to increase even more the field effect with values of bias and current such as ~ 100 V and few tens of µA, leaving the tip under these conditions until the Z position stabilizes, but we greatly increase the possibility of tearing off the tip apex which would pollute a large area of the sample below. Nonetheless this outcome is sometimes what we look for when we do not manage to remove the pollution of the tip by any previous mean : we tear off this polluted apex to obtain a new one. But still we can not know the quality of this new tip, we also severely pollute the sample and it may happen that this very high current can make the contact on graphene melt, destroying the sample for good. This field effect method is therefore an all or nothing, and must be used as a last resort.

More sophisticated procedures also exist to clean and reshape the tip apex, mostly based on sputtering and mechanical annealing, with the objective to be robust and reproducible enough so that tips could be prepared *in situ*, see Refs. [231, 232, 233, 234], though such methods were not implemented with our setup.

The quality of the tunneling junction is first and quickly checked after each cleaning test by performing a Z-spectroscopy on gold: starting from the tunneling contact ($V_{\text{bias}} = 300$ mV and $I_{\text{t}} = 1$ nA typically), we turn off the Z-controller and retract the tip of a few nanometers. If the junction is indeed tunnel, we should observe an exponential decay of the tunneling current with a slope of one decade per angström. Such decay is shown in Figure 4.25(a), where we extract

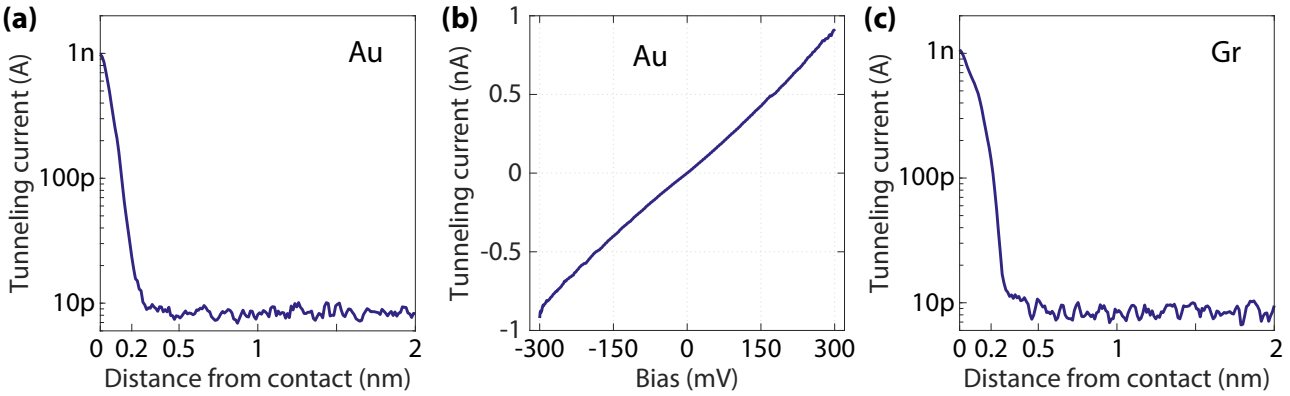

Figure 4.25: Pristine tip for STM. (a) Z-spectroscopy and **(b)** bias spectroscopy for a good tunneling junction on gold which means the tip is cleaned enough and ready for STM and STS on graphene. From (a) we extract a work function on gold of $\Phi_{\text{Au}} \simeq 5.1$ eV. **(c)** Z-spectroscopy on graphene for a good tunneling junction with a rough exponential decay of one decade in current per angström. We estimate on graphene $\Phi_{\text{Gr}} \approx 4$ eV.

a work function of the tunneling junction on gold of $\Phi_{Au} \simeq 5.1$ eV. This value of the barrier height can be retrieved by writing it as $\Phi_{Au} = (\Phi^0_{Au} + \Phi^0_{PtIr})/2$ with $\Phi^0_{Au} = 4.8$ eV [235] and $\Phi^0_{PtIr} = 5.7$ eV [236, 237] the work functions of both sample and tip materials, which gives a similar value $\Phi_{Au} = 5.2$ eV. If the tip is still polluted, we would observe an exponential decay on a larger scale or even a linear decay : a new cleaning procedure is thus needed. If the Z-spectroscopy confirms the tunneling junction, it is possible to go back on graphene to perform good STM images with atomic resolution.

Nonetheless, a good Z-spectroscopy is not enough to ensure a good quality of the tunneling junction when it comes to tunneling spectroscopy. A second test of the quality of the junction consists of a bias spectroscopy on gold to make sure the $I_t(V_{bias})$ spectrum is ohmic, such as the one shown in Figure 4.25(b). This indeed ensures that the dI_t/dV_{bias} spectra will be directly proportional to the local density of states of graphene. If both the Z-spectroscopy and bias spectroscopy on gold are good, we consider the tip is pristine and can be used to perform STM and STS on graphene.

Finally, a Z-spectroscopy on graphene unveils an exponential decay of the tunneling current on a larger scale than on gold, between 250 pm and 600 pm for a decay of two decades, see Figure 4.25(c). This corresponds to work functions of the tunneling junction on graphene of $\Phi_{Gr} \approx 4 - 1.5$ eV. The highest values $\Phi_{Gr} \approx 4$ eV are consistent with the estimations from previous works [32, 238, 239].

4.4.3 Atomic resolution on graphene

Now that the tip is pristine and forms a good tunneling junction with graphene, the STM measurements can start. The next chapters present the experimental results we obtained on tunneling spectroscopy on graphene during this thesis. Beforehand, we eventually focus here on the very first STM experiment we do once we have managed to get a pristine tip on graphene : imaging with atomic resolution in order to observe the honeycomb lattice. Atomic resolution on graphene at 4 K is achieved as shown in Figure 4.26.

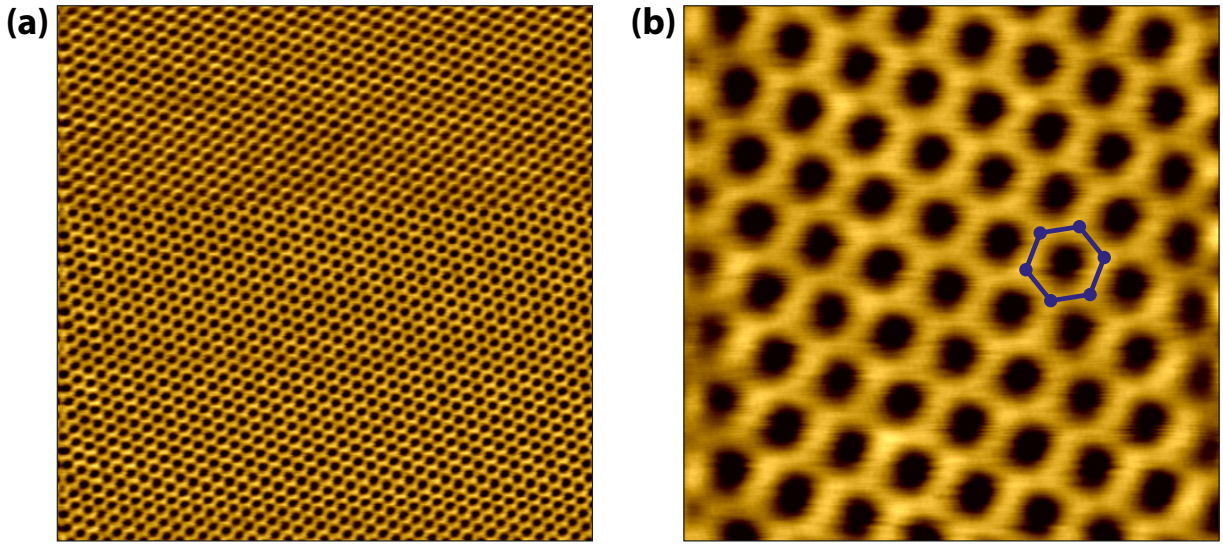

Figure 4.26: Honeycomb lattice of graphene. STM images in sample AC04 with atomic resolution of graphene at different scales : **(a)** 10×10 nm^2 image ($V_{bias} = 400$ mV, $I_t = 1$ nA) and **(b)** 2×2 nm^2 image ($V_{bias} = 300$ mV, $I_t = 1$ nA).

Conclusion

We have introduced in this chapter our home-made AFM/STM, which works at $T = 4\,\mathrm{K}$ and under magnetic fields up to $B = 14\,\mathrm{T}$. We also presented our AFM/STM probes and their fabrication. We then explained how we are able to bring the tip on the graphene/hBN device in one or two days using the AFM mode. The STM imaging of graphene honeycomb lattice is the proof that we are indeed on graphene and that the tip has remained in good shape after the AFM guiding. Our tip cleaning procedures have also been detailed. We now present in the following chapters our experimental STM results.

STS characterization of graphene/hBN devices

CHAPTER 5

THIS first results chapter aims to characterize three of the samples on which we performed our Scanning Tunneling Spectroscopy (STS) measurements at $T = 4\,\mathrm{K}$: one graphene/hBN/SiO_2 (AC04) and two graphene/hBN/$SrTiO_3$ (BNGrSTO-STM-07 and AC23). Optical images of these devices are shown in Appendix B.6 and Table 5.1 sums up their geometrical parameters.

Sample	AC04	BNGrSTO-STM-07	AC23
Substrate	Si^{++}/SiO_2	$SrTiO_3$	$SrTiO_3$
Substrate/oxide thickness	285 nm	500 µm	500 µm
hBN thickness	14 nm	8 nm	12 nm
Graphene size	$5 \times 2\ \mu m^2$	$13 \times 2.5\ \mu m^2$	$10 \times 8\ \mu m^2$

Table 5.1: Geometrical parameters of the three measured samples.

The first step of the measurement consists in finding an area of graphene suitable for STM. We then characterize our devices at zero magnetic field to assess their quality. We eventually apply a perpendicular magnetic field B to study the quantum Hall regime. Using the back-gate voltage to tune the carrier density in graphene, we observe gate-tunable Landau levels and compute the renormalization of the Fermi velocity. Numerical simulations of these LDOS gate maps are performed in order to better understand the different physical effects.

Contents

5.1 Topographic characterization

5.1.1 Graphene corrugation

Even if it lies on an atomically flat hBN spacer, the graphene sheet presents a residual topographic corrugation arising from its intrinsic ripples and from the roughness of the SiO_2 or $SrTiO_3$ substrate. We show in Figure 5.1(a) a large-scale $500 \times 500\,nm^2$ STM image of the graphene/hBN/SiO_2 sample AC04. Though some bright spots indicate the presence of scarce impurities on graphene surface, probably resist residues (see black arrows), the area is mostly clean. Finding a pristine $100 \times 100\,nm^2$ area for the three samples is relatively easy, as shown for the graphene/hBN/$SrTiO_3$ sample BNGrSTO-STM-07 in Figure 5.1(b). Table 5.2 recaps the rms roughness estimated in such areas for the three samples. These values are consistent with the rms roughness of 17 pm obtained by Decker *et al.* [35] on a hBN/SiO_2 sample whereas, for comparison, the rms roughness for graphene on SiO_2 without hBN spacer was found to be much greater, around 150 pm, by Zhang *et al.* [28], see also Figure 1.8. The atomic resolution is achieved and well resolved in STM images below $30 \times 30\,nm^2$. The honeycomb lattice of graphene is shown in Figure 5.1(c). The carbon-carbon distance a can be estimated from the 2D Fourier transform, which is a further confirmation that the tip is indeed being scanning on monolayer graphene.

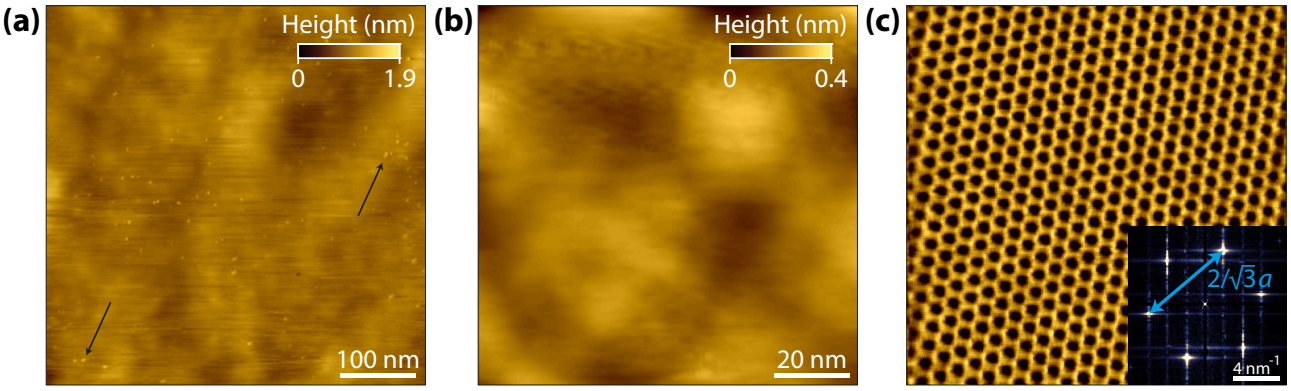

Figure 5.1: STM topography of graphene/hBN. (a) $500 \times 500\,nm^2$ STM image of graphene on hBN/SiO_2 in AC04. **(b)** $100 \times 100\,nm^2$ STM image of graphene on hBN/$SrTiO_3$ in BNGrSTO-STM-07. RMS roughness : $S_q = 42$ pm. **(c)** $5 \times 5\,nm^2$ STM image of graphene honeycomb lattice in BNGrSTO-STM-07 with its 2D Fourier transform in the inset.

5.1.2 Graphene/hBN Moiré superlattice

It is possible that a Moiré superlattice emerges in our graphene/hBN heterostructures. This can not be predicted since we do not control the relative angle ϕ between graphene and hBN lattices during the fabrication process. Furthermore, the annealing we do in order to clean our samples before loading them in the STM, see Appendix B.5, can enable the realignment of both lattices such that a Moiré pattern may eventually appear. We observed Moiré patterns in two samples - BNGrSTO-STM-08 (hBN/$SrTiO_3$ sample, that we only mention here) and AC23 - out of five measured, see Figure 5.2(a,b). The Moiré wavelength λ can be estimated from the 2D Fourier transform in Figure 5.2(c) : the outer blue hexagon corresponds to the reciprocal lattice of graphene while the inner red hexagonal is the reciprocal Moiré superlattice. The relative angle ϕ can then be computed using Equation (1.45), see Figure 1.9(c). In AC23, the Moiré pattern was seen to vary spatially and eventually disappeared in some regions of graphene. Since

Moiré superlattices are known to alter graphene electronic properties, as studied by Yankowitz *et al.* [38], we focus our measurements in regions of graphene devoid of visible Moiré pattern.

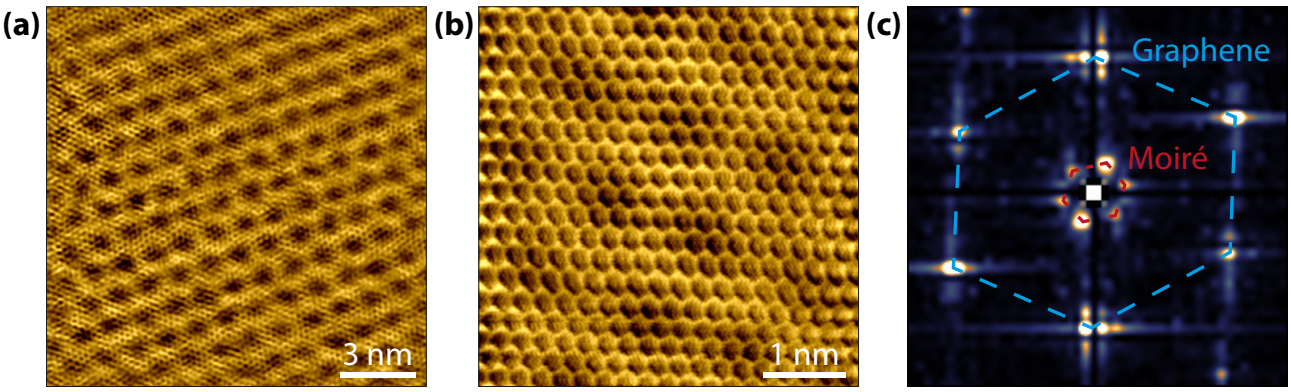

Figure 5.2: Moiré superlattice. (a) $15 \times 15\,\mathrm{nm}^2$ STM image in BNGrSTO-STM-08 showing a graphene/hBN Moiré pattern with a wavelength of $\lambda \simeq 1.2\,\mathrm{nm}$. **(b,c)** $4.5 \times 4.5\,\mathrm{nm}^2$ STM image (b) and its 2D Fourier transform (c) of a Moiré pattern in AC23 with a wavelength of $\lambda \simeq 1.3\,\mathrm{nm}$, corresponding to a rotation angle between graphene and hBN lattices of $\phi \simeq 11°$.

Sample	AC04	BNGrSTO-STM-07	AC23
Substrate	hBN/SiO_2	$hBN/SrTiO_3$	$hBN/SrTiO_3$
S_q	14 pm	17 pm	18 pm
Moiré	–	–	$\lambda = 1.3\,\mathrm{nm}$

Table 5.2: RMS roughness S_q estimated from $20 \times 20\,\mathrm{nm}^2$ STM images and Moiré wavelength λ (when observed) in our three samples.

Additional topographic data are available in Appendix C.

5.2 Zero magnetic field regime

Before going into the quantum Hall regime, we start by characterizing our samples at zero magnetic field. We performed our spectroscopy studies on flat and clean areas of graphene. Our tunneling spectra were obtained using the lock-in detection method, see Appendix A.1.3, with a modulation frequency of about 263 Hz and rms voltage V_{mod} between 1-5 mV depending on the spectral range of interest.

5.2.1 Gating of graphene

We discuss in this section the use of the back-gate voltage V_g to tune the carrier density of graphene, which shifts the Dirac point energy E_D with respect to the Fermi level. We recall that the evolution of E_D with the gate voltage is given by (see Chapter 1.2.3) :

$$E_D = \mathrm{sign}\left(V^{CNP} - V_g\right) \hbar v_F \sqrt{\frac{\pi C_g}{e} |V_g - V^{CNP}|} \tag{5.1}$$

where V^{CNP} is the charge-neutrality point, that is, the gate voltage where $E_F = E_D$ (which means that $E_D = 0$ in the $\mathrm{d}I_t/\mathrm{d}V_{bias}$ spectrum), and $C_g = \epsilon_0 \epsilon_r / t$ is the gate capacitance per unit area, with t the thickness of the insulating layer and ϵ_r its relative dielectric constant.

$\mathrm{d}I_\mathrm{t}/\mathrm{d}V_\mathrm{bias}$ gate maps are obtained by measuring tunneling spectra as the back-gate voltage V_g is swept at fixed tip position. Upward and downward sweeps for both sample bias and back-gate voltage gave similar and reproducible results, with only a slight shift between them. We have observed that the back-gate sweeps induce a slow and reproducible drift of the Z-position of the tip, indicating that the tip-sample distance needed to get the tunneling current setpoint depends on the back-gate voltage. We attribute this feature to the shift of graphene density of states as the back-gate voltage is swept. The setting time between a variation of back-gate voltage and the measurement of the $\mathrm{d}I_\mathrm{t}/\mathrm{d}V_\mathrm{bias}$ spectrum is thus an important parameter for these experiments, so that the Z-controller is given enough time to adjust the tip-sample distance to a stable value.

5.2.1.a LDOS gate map for sample AC04 - graphene/hBN/SiO_2

We start with sample AC04. Figure 5.3(a) shows the Local Density of States (LDOS) $\mathrm{d}I_\mathrm{t}/\mathrm{d}V_\mathrm{bias}$ gate map obtained at zero magnetic field for back-gate voltage swept from -10 V to 10 V and sample bias swept from 300 mV to -300 mV. The drift of the Z-position for this sample is very small, a few hundreds of pm only for the whole sweep. It is then possible to measure directly $\mathrm{d}I_\mathrm{t}/\mathrm{d}V_\mathrm{bias}$ tunneling spectra as the back-gate voltage V_g is swept continuously. Each spectrum appears with an asymmetric V-shape and a minimum around zero sample bias. The Dirac point E_D is characterized by a minimum in the spectra which moves with the back-gate voltage, see Figure 5.3(b), the corresponding minimum can be unambiguously determined with the help of the gate map. We plot in Figure 5.3(c) the Dirac point positions E_D estimated for back-gate voltages $-10\mathrm{V} < V_\mathrm{g} < 4\mathrm{V}$. Using Equation (5.1), we are able to fit these points and we extract the charge-neutrality point $V^\mathrm{CNP} = (-5.0 \pm 0.1)\,\mathrm{V}$, which corresponds to an intrinsic electron-doping of $n \simeq 3.4 \times 10^{11}\,\mathrm{cm}^{-2}$, computed with Equation (1.39), introduced during the device fabrication.

The Fermi velocity can also be extracted from this fit, though it is not straightforward : we first need to estimate the value of the gate capacitance C_g. The back-gate insulator is comprised of two materials : the SiO_2 layer, with a thickness of $d_{SiO_2} = 285$ nm and a dielectric permittivity $\epsilon_{SiO_2} = 3.9$, and the hBN spacer, with a thickness $d_\mathrm{BN} = 14$ nm for AC04. The value of the relative dielectric constant ϵ_BN of hBN is not well known : Wang *et al.* [240] and Laturia *et al.* [241] found that ϵ_BN increases with the number of layers, and ranges from $\epsilon_\mathrm{BN} \simeq 3.3$ for monolayer hBN to $\epsilon_\mathrm{BN} \simeq 3.8$ for bulk hBN. The gate insulator dielectric constant ϵ_r can be obtained by modeling the gate capacitance C_g as the sum of the series capacitances of SiO_2 and hBN assuming plane capacitors :

$$\frac{1}{C_\mathrm{g}} = \frac{1}{C_{SiO_2}} + \frac{1}{C_\mathrm{BN}} \Rightarrow \frac{d_{SiO_2} + d_\mathrm{BN}}{\epsilon_\mathrm{r}} = \frac{d_{SiO_2}}{\epsilon_{SiO_2}} + \frac{d_\mathrm{BN}}{\epsilon_\mathrm{BN}} \tag{5.2}$$

Since $d_\mathrm{BN} \ll d_{SiO_2}$ we write the gate insulator dielectric constant as :

$$\epsilon_\mathrm{r} = \epsilon_{SiO_2} \left(1 + \frac{d_\mathrm{BN}}{d_{SiO_2}} \frac{\epsilon_{SiO_2}}{\epsilon_\mathrm{BN}}\right)^{-1} \tag{5.3}$$

Numerically, we obtain $\epsilon_\mathrm{r} \simeq 3.7$. The gate capacitance is then computed as $C_\mathrm{g} \simeq 10.9\,\mathrm{nF.cm}^{-2}$. Using this value in Equation (5.1), the fit of the Dirac point of Figure 5.3(c) yields $v_\mathrm{F} = (1.18 \pm 0.03) \times 10^6\ \mathrm{m.s}^{-1}$, consistent with the previously reported values for graphene on insulating substrates, see Table 3.1. Nonetheless, note that the determination of v_F at zero magnetic field is merely qualitative due to uncertainties on the position of the Dirac point and on ϵ_BN.

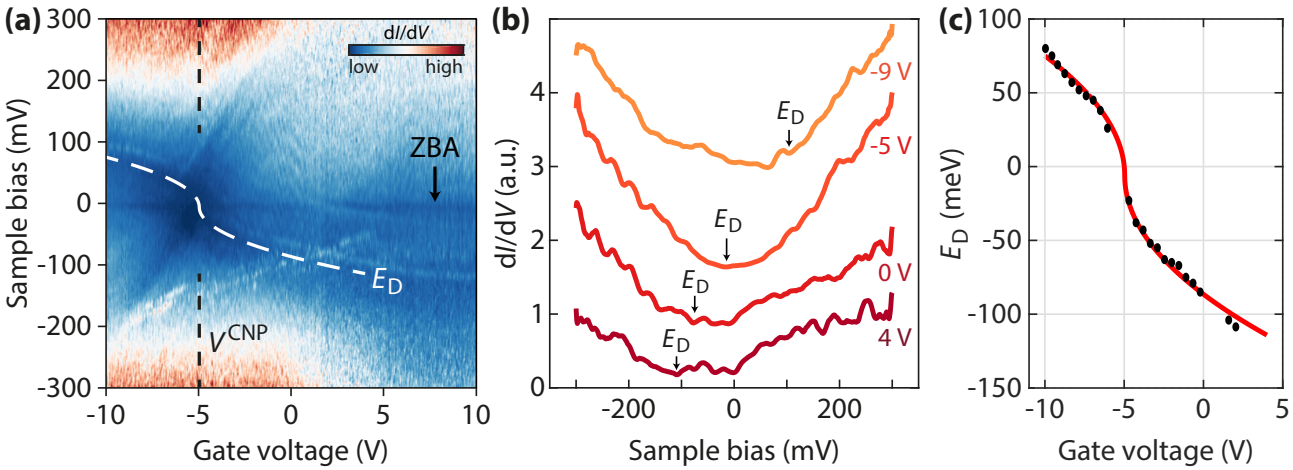

Figure 5.3: Gate map at zero magnetic field. (a) $\mathrm{d}I_\mathrm{t}/\mathrm{d}V_\mathrm{bias}$ gate map as a function of sample bias and gate voltage for sample AC04 ($\mathrm{hBN/SiO_2}$). The white dashed line shows the estimated position of the Dirac point E_D. Spectroscopy parameters : $I_\mathrm{t} = 1\,\mathrm{nA}$, $V_\mathrm{bias} = 300\,\mathrm{mV}$ and $V_\mathrm{mod} = 3\,\mathrm{mV}$. **(b)** Individual spectra of (a) taken at different back-gate voltages. E_D is estimated from the position of a secondary minimum in the spectra, while the minimum at zero bias is due to the zero-bias anomaly. **(c)** Fit of the Dirac point energy E_D as a function of gate voltage, using Equation (5.1), from which we extract $V^\mathrm{CNP} = (-5.0 \pm 0.1)\,\mathrm{V}$ and $v_\mathrm{F} = (1.18 \pm 0.03) \times 10^6\,\mathrm{m.s^{-1}}$.

Zero-bias anomaly We can observe the presence of a narrow horizontal dark strip at zero sample bias in Figure 5.3(a), which arises due to the existence of a gap in the $\mathrm{d}I_\mathrm{t}/\mathrm{d}V_\mathrm{bias}$ spectra that does not disperse with gate voltage [35]. This zero-bias anomaly (ZBA) is characteristic of tunneling into graphene [26, 132] (or other 2D Dirac materials) and arises from the mismatch between the momentum of the tunneling electrons and that of the graphene electrons located on the K and K' points of the Brillouin zone. Notably, Wehling *et al.* [242] showed that the ZBA gap arises from phonon-mediated inelastic tunneling. The ZBA prevents us from estimating E_D precisely close to zero sample bias where the $\mathrm{d}I_\mathrm{t}/\mathrm{d}V_\mathrm{bias}$ spectra flatten, which appears in the gate map of Figure 5.3(a) as a wide dark region around charge neutrality.

We observed that the ZBA was strongly dependent on the tip shape : working the tip on gold enabled us to mitigate the ZBA from a pronounced gap of around 40 meV to the small dip observed in Figure 5.3(a) of less than 10 meV. We also noticed that a pronounced ZBA yields many additional and unexpected features in the $\mathrm{d}I_\mathrm{t}/\mathrm{d}V_\mathrm{bias}$ spectra, especially at strong magnetic fields, which disappear when the ZBA is mitigated after tip cleaning. We therefore in the following only consider experimental data where the ZBA is negligible.

5.2.1.b LDOS gate map for sample BNGrSTO-STM-07 - graphene/hBN/$\mathrm{SrTiO_3}$

We now consider the $\mathrm{d}I_\mathrm{t}/\mathrm{d}V_\mathrm{bias}$ gate map shown in Figure 5.4(a) obtained for sample BNGrSTO-STM-07 with graphene on hBN/$\mathrm{SrTiO_3}$. The back-gate voltage is swept from to 60 V to −20 V. Similarly to sample AC04, the Dirac point E_D is observed to disperse with the back-gate voltage, appearing as a secondary minimum in the individual $\mathrm{d}I_\mathrm{t}/\mathrm{d}V_\mathrm{bias}$ spectra, see Figure 5.4(b).

Particularities of the $\mathrm{SrTiO_3}$ substrate The dielectric constant ϵ_STO of $\mathrm{SrTiO_3}$ is known to display non-linear and hysteretic behaviors with the back-gate voltage [122, 243, 244, 245] due to the existence of ferroelectric domain walls at low temperatures [246, 247, 248, 249]. This

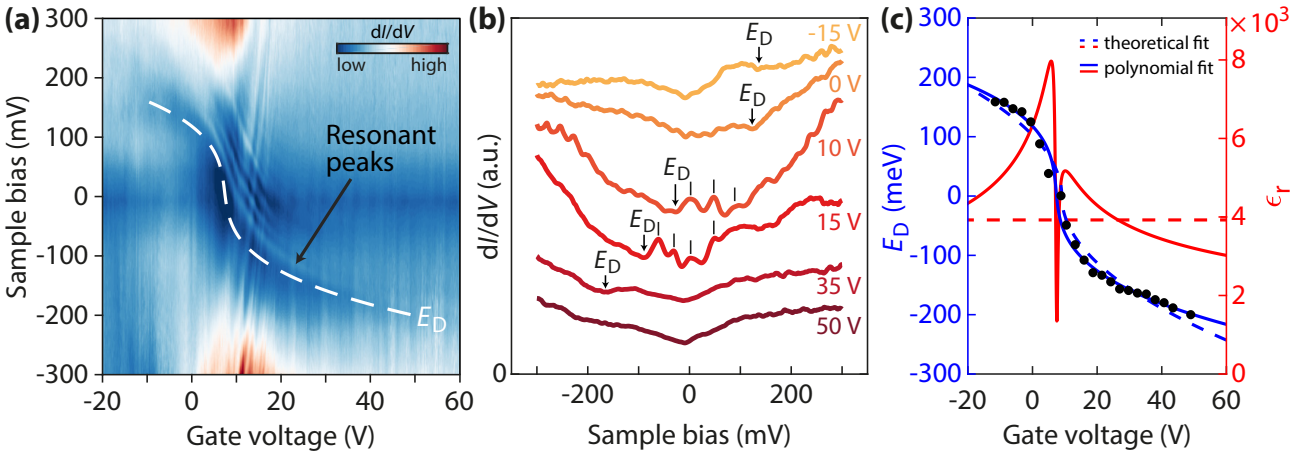

Figure 5.4: Gate map at zero magnetic field with resonant peaks. **(a)** $\mathrm{d}I_\mathrm{t}/\mathrm{d}V_\mathrm{bias}$ gate map as a function of sample bias and gate voltage for sample BNGrSTO-STM-07 (hBN/$SrTiO_3$). The white dashed line shows the estimated position of the Dirac point E_D. Spectroscopy parameters : $I_\mathrm{t} = 1\,\mathrm{nA}$, $V_\mathrm{bias} = 300\,\mathrm{mV}$ and $V_\mathrm{mod} = 4\,\mathrm{mV}$. **(b)** Individual spectra of (a) taken at different gate voltages. E_D is estimated from the position of a secondary minimum in the spectra, while the minimum at zero bias is due to the zero-bias anomaly. Some resonance peaks above the Dirac point, marked with black ticks, are visible. **(c)** (Blue) Fit of the Dirac point positions (black dots) obtained from $\mathrm{d}I_\mathrm{t}/\mathrm{d}V_\mathrm{bias}$ spectra as a function of gate voltage, and (red) estimation from it of the relative permittivity ϵ_r of the gate insulator, with two methods : using the theoretical Equation (5.1) (dashed lines) and a polynomial fit (solid lines).

most of the time induces an important hysteresis with a shift of the charge-neutrality point V^CNP of several volts between upward and downward back-gate sweeps. The direction of the sweeps is consequently an important parameter for samples on $SrTiO_3$ substrate. However for sample BNGrSTO-STM-07 no noticeable shift of V^CNP was observed : we attribute this to the different annealing the sample underwent to clean graphene, which may have probably lowered the dielectric constant of the $SrTiO_3$ substrate and therefore the hysteresis effect. For sample AC23 a shift of 6 V of the charge-neutrality point was observed. $SrTiO_3$ also makes the charge-neutrality point and the efficiency of gating dependent on the hysteresis cycle, and thus on the upper and lower limits of the back-gate sweep which must be kept constant during the consecutive experiments.

Finally, $SrTiO_3$ also displays a strong piezoelectric effect with the back-gate voltage [250, 251], forcing us to maintain the back-gate voltage constant during each sample bias sweep to avoid diverging or vanishing tunneling current, depending if the tip gets closer or moves away from graphene as the gate voltage varies. Figure 5.5 shows the evolution of the Z-position of the tip measured before each bias sweep as a function of back-gate voltage. For both samples on $SrTiO_3$ substrate, we observe a large piezoelectric response $|\mathrm{d}Z/\mathrm{d}V_\mathrm{g}| \simeq 0.4\,\mathrm{nm.V^{-1}}$, consistent with values up to $1\,\mathrm{nm.V^{-1}}$ obtained by Honig *et al.* [251]. The piezoelectric effect is gate-voltage dependent and changes of sign around $V_\mathrm{g} = 5\,\mathrm{V}$.

Estimation of $SrTiO_3$ dielectric constant Using the same reasoning than for sample AC04, the gate map at zero magnetic field can be used to obtain a rough estimation of $SrTiO_3$ dielectric constant for sample BNGrSTO-STM-07. $SrTiO_3$ dielectric constant ϵ_STO is linked to the gate insulator global dielectric constant ϵ_r by a relation similar to Equation (5.3) :

$$\epsilon_\mathrm{r} = \epsilon_\mathrm{STO}\left(1 + \frac{d_\mathrm{BN}}{d_\mathrm{STO}}\frac{\epsilon_\mathrm{STO}}{\epsilon_\mathrm{BN}}\right)^{-1} \tag{5.4}$$

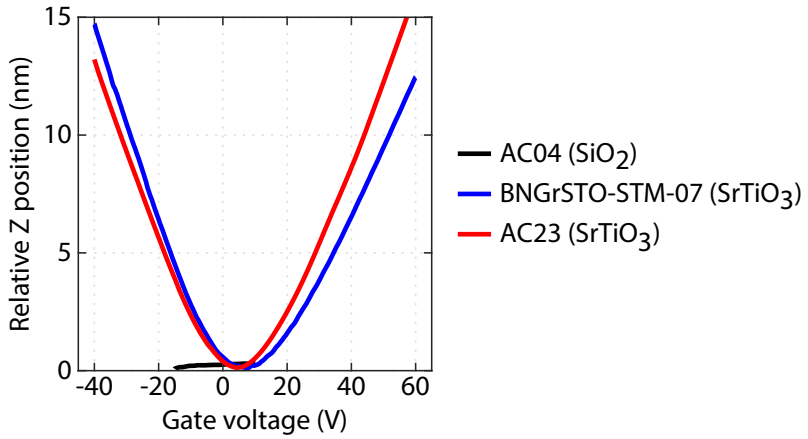

Figure 5.5: Piezoelectric effect of $SrTiO_3$ substrate. Variation of the Z-position of the tip as a function of back-gate voltage for two samples graphene/hBN/$SrTiO_3$ (BNGrSTO-STM-07 and AC23) and one sample graphene/hBN/SiO_2 (AC04). A large piezoelectric effect of about $|\mathrm{d}Z/\mathrm{d}V_\mathrm{g}| \simeq 0.4\,\mathrm{nm.V^{-1}}$ is observed for both $SrTiO_3$ samples. On SiO_2 substrates, the tip position only varies of about 200 pm for a back-gate variation $\Delta V_\mathrm{g} = 25\,\mathrm{V}$.

We have $d_\mathrm{BN} \ll d_\mathrm{STO} = 500\,\mu\mathrm{m}$, $\epsilon_\mathrm{BN} \sim 3.8$ and we expect $\epsilon_\mathrm{STO} \sim 10^4$ at low temperature [124, 125, 126], so that $d_\mathrm{BN}\epsilon_\mathrm{STO}/d_\mathrm{STO}\epsilon_\mathrm{BN} \sim 0.1$. We can thus assume that $\epsilon_\mathrm{r} \simeq \epsilon_\mathrm{STO}$: the gate insulator capacitance is mainly determined by the dielectric constant of $SrTiO_3$.

We fix here the value of the Fermi velocity to $v_\mathrm{F} = 1.4 \times 10^6\,\mathrm{m.s^{-1}}$ (estimated later from CITS map at charge neutrality and $B = 14\,\mathrm{T}$, see Figure 5.8). The positions of the Dirac point E_D are estimated using both the gate map and individual $\mathrm{d}I_\mathrm{t}/\mathrm{d}V_\mathrm{bias}$ spectra as a secondary minimum dispersing with the back-gate voltage, and are reported as black dots in Figure 5.4(c). We then follow two different approaches. First we fit the evolution E_D as a function of V_g using the theoretical Equation (5.1), with V^CNP and ϵ_r (through C_g) as fitting parameters. This yields the dashed blue line in Figure 5.4(c). From the fit we obtain $\epsilon_\mathrm{r} = 3950$[1] as well as $V^\mathrm{CNP} = (9.1 \pm 0.7)\,\mathrm{V}$.

Nonetheless, this fit does not match well the estimated positions of the Dirac point : we suppose this is due to the non-linearity of ϵ_STO, whereas this fit assumes a constant value. We perform a second fit of E_D using a third degree polynomial, which gives the solid blue line in Figure 5.4(c) and yields $V^\mathrm{CNP} = 7.5\,\mathrm{V}$ for an intrinsic hole doping. We then compute ϵ_r using Equation (5.1) with the fitted values of E_D to obtain ϵ_r as a function of V_g shown in Figure 5.4(c) with the red solid line. We obtain a non-linear evolution, with a maximum at charge neutrality[2] and values between 3000 and 8000, which is consistent with previously reported non-linearities of ϵ_STO.

5.2.1.c Resonant peaks

We can observe in the gate map of Figure 5.4 as well as in the individual spectra the existence of resonant peaks above the Dirac point [27, 135], marked by black ticks. Such features may arise from localized quasiparticles either by the disorder potential or by scattering from impurities that form quantum dots [252, 253], where electrons are trapped for a finite time until they finally escape through Klein tunneling [254]. Such quasibound states in quantum dots and the resulting

[1] This rather low value compared to the expected $\epsilon_\mathrm{STO} \sim 10^4$ at low temperature may be due to the different annealing of the sample, see Appendix B.

[2] The dip at V^CNP is due to dividing by $\sqrt{|V_\mathrm{g} - V^\mathrm{CNP}|}$.

resonant peaks in STS were observed in many graphene systems [173, 175, 179, 255, 256]. As we saw in Chapter 3.5.2, these resonant states were shown by Gutiérrez *et al.* [82] to eventually merge into Landau levels as the magnetic field is increased.

Another possible origin for these resonant peaks may be the electrostatic action of the tip rather than disorder in graphene. Indeed Cheng *et al.* showed in 2019 [257] that localized guided modes emerge inside a quantum well in graphene generated by a carbon nanotube placed at a few nanometers away, modes that appear in the density of states as resonances close to the Dirac point. By analogy with this 1D model, we suppose the contact potential difference V_{CPD} of our tip induces a pn junction in the graphene beneath. In such tip-induced dot emerge localized states which then appear as the resonant peaks in the LDOS. We study this in detail in Appendix C.4 using numerical simulations.

5.2.2 Charge puddles

The gate maps of both Figures 5.3 and 5.4 are used to bring graphene in samples AC04 and BNGrSTO-STM-07 to charge neutrality at $V_{\mathrm{g}} = V^{\mathrm{CNP}}$. We then perform Current-Imaging Tunneling Spectroscopy (CITS) which consists of measuring $G(V_{\mathrm{bias}}) = \mathrm{d}I_{\mathrm{t}}/\mathrm{d}V_{\mathrm{bias}}$ spectra at each (x, y) point of an area. Such experiment enables to obtain a 4D matrix $G(x, y, eV_{\mathrm{bias}})$ in parallel to the topographic image $z(x, y)$. Spatial LDOS maps are thus obtained by plotting $G(x, y, eV_{\mathrm{bias}})$ at a constant energy eV_{bias}.

5.2.2.a CITS for sample AC04 - graphene/hBN/SiO_2

We performed on sample AC04 a CITS within an area of $100 \times 100\,\mathrm{nm}^2$ with a grid of 70×70 pixels at $V_{\mathrm{g}} = -4.8\,\mathrm{V}$. Figure 5.6(a) shows the spatial $\mathrm{d}I_{\mathrm{t}}/\mathrm{d}V_{\mathrm{bias}}$ taken at $V_{\mathrm{bias}} = 100\,\mathrm{mV}$. We observe different regions of low and high densities of states which are induced by the spatial variations of the Dirac point E_{D} due to the potential disorder, which eventually breaks graphene electron gas into charge puddles, see Chapter 1.3.1. This map can be roughly seen as an approximate spatial map of the Dirac point. As shown in Figure 5.6(b) areas of positive E_{D} (or equivalently $E_{\mathrm{D}} > E_{\mathrm{F}}$) define hole puddles, while areas of negative E_{D} define electron puddles. Tunneling spectra present the typical V-shape of graphene density of states except it is shifted in energy above zero bias ($E_{\mathrm{D}} > 0$) or below ($E_{\mathrm{D}} < 0$) respectively for hole and electron puddles, see Figure 5.6(d). Therefore, at a fixed $V_{\mathrm{bias}} > 0$, electron puddles are characterized by a high density of states while hole puddles appear with a low density, and the opposite for $V_{\mathrm{bias}} < 0$. Blue (resp. red) areas in Figure 5.6 are thus electron (resp. hole) puddles, defined by $E_{\mathrm{D}} < 0$ (resp. $E_{\mathrm{D}} > 0$) and a minimum (resp. maximum) of the disorder potential [27, 28]. Note that the characteristic length scale of these puddles is greater than 50 nm, superior than that of 20 nm observed in graphene/SiO_2 [27, 28].

Since we brought graphene to charge neutrality, a better way to visualize charge puddles relies on the determination of the Dirac point E_{D} for each spectrum. Beforehand, we plot in Figure 5.6(e) the mean spectrum, averaged on the whole $100 \times 100\,\mathrm{nm}^2$. The spectrum is mostly symmetrical with respect to zero bias and presents a rounded V-shape. We determine E_{D} as the minimum of the parabola which fits locally the minimum of the $\mathrm{d}I_{\mathrm{t}}/\mathrm{d}V_{\mathrm{bias}}$ spectrum and obtain $E_{\mathrm{D}} \simeq -10\,\mathrm{meV}$. The same process is used for each spectrum of the CITS to obtain a spatial map of E_{D} inhomogeneities[3] [31, 32, 222], which is shown in Figure 5.6(b) where an equivalent

[3] This map was eventually convoluted with the normalized 3×3 gaussian filter $\begin{pmatrix} 0.25 & 0.5 & 0.25 \\ 0.5 & 1 & 0.5 \\ 0.25 & 0.5 & 0.25 \end{pmatrix}$.

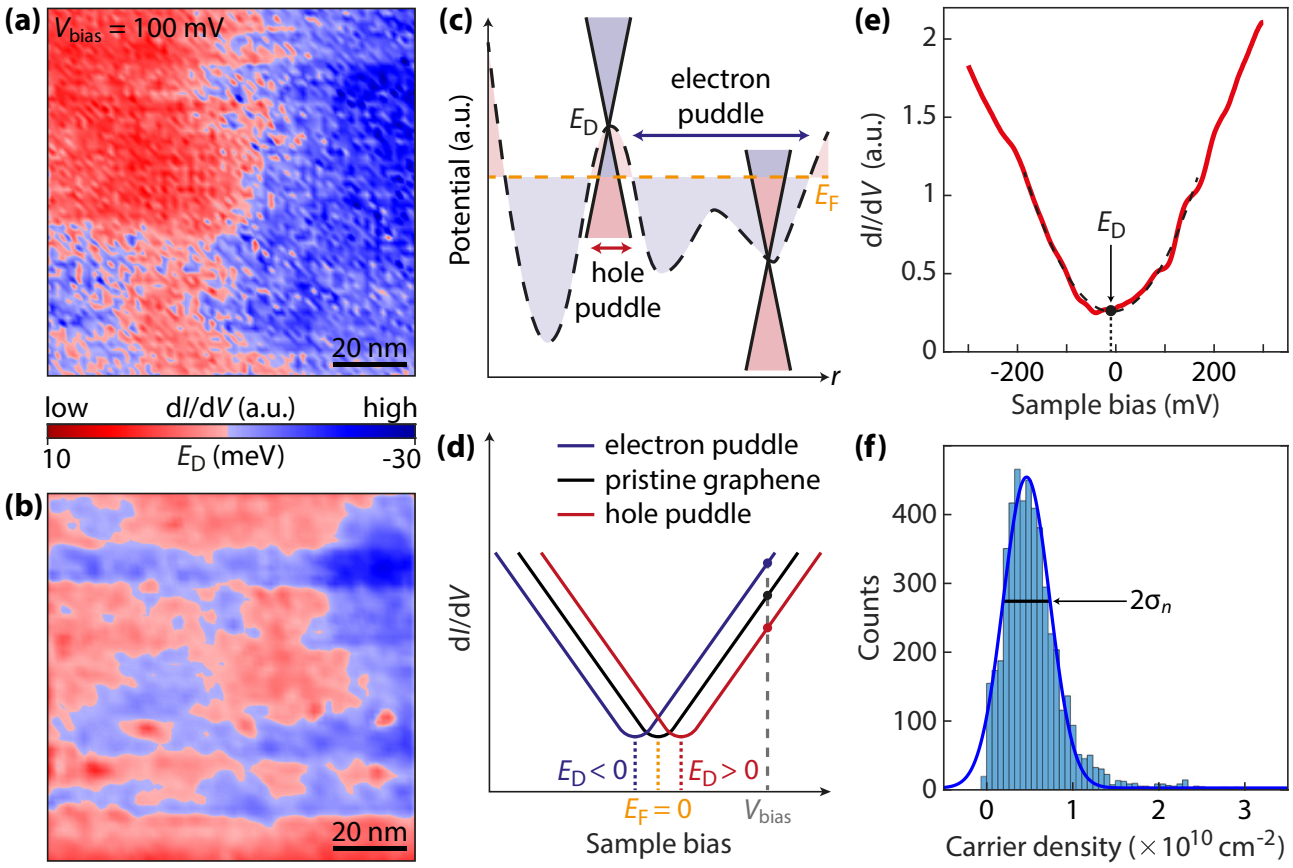

Figure 5.6: Charge puddles in graphene. **(a)** Spatial $\mathrm{d}I_\mathrm{t}/\mathrm{d}V_\mathrm{bias}$ map on a $100 \times 100\,\mathrm{nm}^2$ area of graphene on hBN/SiO_2 in AC04 at $V_\mathrm{g} = -4.8\,\mathrm{V}$, taken at $V_\mathrm{bias} = 100\,\mathrm{mV}$, showing spatial inhomogeneities due to disorder. Spectroscopy parameters : $I_\mathrm{t} = 1\,\mathrm{nA}$, $V_\mathrm{bias} = 300\,\mathrm{mV}$ and $V_\mathrm{mod} = 3\,\mathrm{mV}$. **(b)** Corresponding disorder-induced spatial inhomogeneities of the Dirac point E_D, defining electron and hole puddles as blue and red areas respectively. **(c)** Electron puddles are obtained for $E_\mathrm{D} < E_\mathrm{F} = 0$ while hole puddles are obtained for $E_\mathrm{D} > E_\mathrm{F} = 0$. **(d)** Typical $\mathrm{d}I_\mathrm{t}/\mathrm{d}V_\mathrm{bias}$ spectra for electron and hole puddles. **(e)** Spatially-averaged spectrum over the whole area showing the V-shape of graphene density of states. The Dirac point E_D is determined as the minimum of the parabola which locally fits the minimum of the spectrum. **(f)** Histogram of the carrier densities, determined from E_D at each point of the map, and its gaussian fit, from which we extract the residual doping of graphene $n_0 = (4.6 \pm 0.2) \times 10^9\,\mathrm{cm}^{-2}$ and the charge fluctuations $\sigma_n = (2.7 \pm 0.2) \times 10^9\,\mathrm{cm}^{-2}$.

colormap to that in Figure 5.6(a) is used : red regions correspond to hole puddles with $E_\mathrm{D} > 0$ while blue regions correspond to electron puddles with $E_\mathrm{D} < 0$. The gaussian fit of the histogram of $E_\mathrm{D}(x, y)$ obtained from the whole CITS map confirms the mean value at $E_\mathrm{D} = -10\,\mathrm{meV}$ and yields a standard deviation for the Dirac point of $\sigma_{E_\mathrm{D}} = (2.7 \pm 0.2)\,\mathrm{meV}$. Xue *et al.* [140] observed similar fluctuations of 5.4 meV for E_D in hBN/SiO_2 samples, to compare to their value for SiO_2 samples where they noticed a standard deviation of 55.6 meV. Eventually, the carrier density $n(x, y)$ can be computed from E_D using next relation adapted from Equation (1.16) :

$$n(x, y) = -\mathrm{sign}\left[E_\mathrm{D}(x, y)\right] \frac{1}{\pi} \left[\frac{E_\mathrm{D}(x, y)}{\hbar v_\mathrm{F}}\right]^2 \tag{5.5}$$

where we consider $v_\mathrm{F} = 1.18 \times 10^6\,\mathrm{m.s}^{-1}$ as obtained from the gate map in Figure 5.3(a). We plot in Figure 5.6(f) the histogram of the $n(x, y)$ values. The distribution is mostly gaussian with a pronounced asymmetry. Its mean value obtained from a gaussian fit $n_0 = (4.6 \pm 0.2) \times 10^9\,\mathrm{cm}^{-2}$

represents the residual doping of graphene at $V_g = -4.8$ V. The standard deviation $\sigma_n = (2.7 \pm 0.2) \times 10^9$ cm^{-2} yields the charge fluctuations, similar to the value of 2.5×10^9 cm^{-2} reported by Xue *et al.* [140] in hBN/SiO_2 samples, see also Ref. [35], which is 100 times smaller than carrier density fluctuations measured in graphene/SiO_2 [27, 28, 138, 140]. This gives a first evidence of the high quality of our graphene sample.

5.2.2.b CITS for sample BNGrSTO-STM-07 - graphene/hBN/$SrTiO_3$

We also realized a similar CITS in sample BNGrSTO-STM-07 (100×100 nm^2 area with a 80×80 pixels grid). The gate voltage is set to $V_g = 10$ V to bring graphene to charge neutrality. The spatial dI_t/dV_{bias} map taken at $V_{bias} = 100$ mV is shown in Figure 5.7(a). As in the previous section, the area is separated into regions of high and low densities of states, which

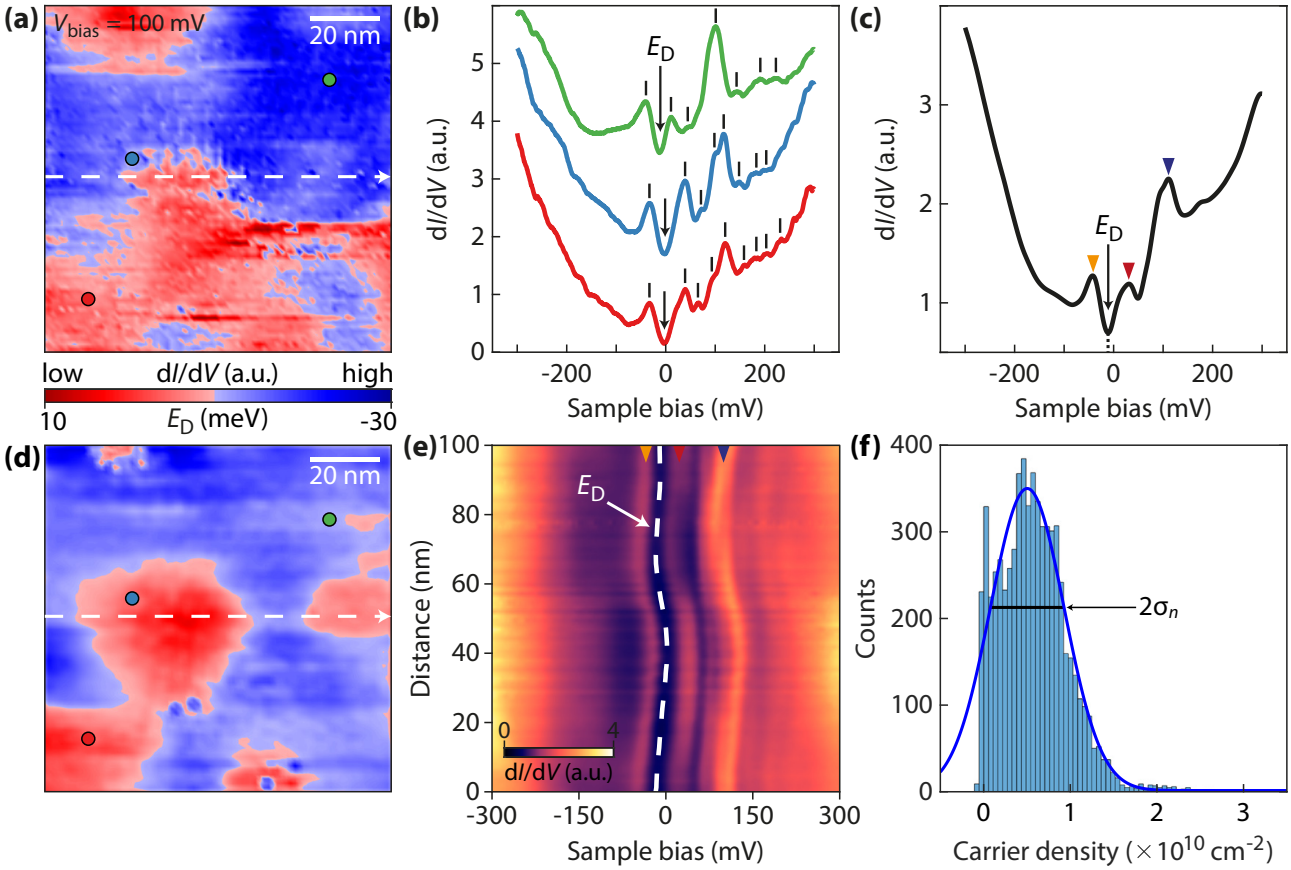

Figure 5.7: Resonant peaks at zero magnetic field. **(a)** Spatial dI_t/dV_{bias} map on a 100×100 nm^2 area of graphene on hBN/$SrTiO_3$ in BNGrSTO-STM-07 at $V_g = 10$ V, taken at $V_{bias} = 100$ mV, showing spatial inhomogeneities due to disorder. Spectroscopy parameters : $I_t = 1$ nA, $V_{bias} = 300$ mV and $V_{mod} = 4$ mV. **(b)** Individual dI_t/dV_{bias} spectra taken at the corresponding colored dots in (a,d). The Dirac point E_D is determined by the minimum of the spectrum around zero bias, and resonance peaks are indicated by vertical ticks. The curves are offset for clarity. **(c)** Spatially-averaged dI_t/dV_{bias} spectrum over the whole area, showing the persistence of the resonance peaks marked by colored triangles matching those in (e). **(d)** Spatial inhomogeneities of E_D, defining electron and hole puddles as blue and red areas respectively. **(e)** dI_t/dV_{bias} spectra taken along the white dashed arrow in (a,d), showing the spatial dispersion due to disorder of E_D and of the resonance peaks, marked by colored triangles. **(f)** Histogram of the carrier densities, determined from E_D at each point of the map, and its gaussian fit, from which we extract the residual doping of graphene $n_0 = (5.0 \pm 0.4) \times 10^9$ cm^{-2} and the charge fluctuations $\sigma_n = (4.2 \pm 0.4) \times 10^9$ cm^{-2}.

correspond respectively to electron and hole puddles. Figure 5.7(b) shows tunneling spectra taken in three different regions of the spatial map. The Dirac point E_D appears as a dip close to zero sample bias, around $E_D \approx -10.7$ meV as determined from the mean spectrum of Figure 5.7(c). We also observe the presence of many resonant peaks [27], especially three major ones whose persistence on the whole 100×100 nm^2 graphene area is clearly visible on the mean spectrum shown in Figure 5.7(c). The spacing between the resonant peaks is approximately 75 meV. The spatial map showing the inhomogeneities of E_D is obtained with the same method than for AC04 and displayed in Figure 5.7(d), where we use the same colormap than in Figure 5.6(b) to enable direct comparison. A hole puddle with a radius of 45 nm is well visible. The gaussian fit of the histogram of $E_D(x, y)$ yields a mean value of $E_D = -12$ meV and a standard deviation of $\sigma_{E_D} = (4.0 \pm 0.3)$ meV. To further study the spatial dispersion of E_D and the resonance peaks, we plot in Figure 5.7(e) the evolution of the dI_t/dV_{bias} spectra taken along the white dashed line in Figure 5.7(a,d). We observe that the Dirac point as well as the resonant peaks have a weak spatial dispersion on 100nm, around $\Delta E_D \simeq 19.6$meV for the Dirac point.

Finally, we show in Figure 5.7(f) the histogram of the carrier densities on the whole area computed using Equation (5.5). Once again we used the value of $v_F = 1.4 \times 10^6$ m.s^{-1} estimated at $B = 14$ T in Figure 5.8. The gaussian fit of the histogram yields a residual doping of $n_0 = (5.0 \pm 0.4) \times 10^9$ cm^{-2} and a carrier density standard deviation of $\sigma_n = (4.2 \pm 0.4) \times 10^9$ cm^{-2}. This larger value than the one we obtained for sample AC04 on hBN/SiO_2 may be due to the thinner hBN spacer ($d_{BN} = 8$ nm) we use for samples on $SrTiO_3$, which thus screens less topographic and charge defects at the surface of the substrate. This is consistent with the smaller mobilities our group obtained for hBN-encapsulated graphene transport devices on $SrTiO_3$ [122] compared to similar devices on SiO_2 with a thicker ($d_{BN} \gg 10$ nm) hBN spacer.

Sample	AC04	BNGrSTO-STM-07
Substrate	hBN/SiO_2	hBN/$SrTiO_3$
σ_{E_D} (meV)	2.7 ± 0.2	4.0 ± 0.3
σ_n (cm^{-2})	$(2.7 \pm 0.2) \times 10^9$	$(4.2 \pm 0.4) \times 10^9$

Table 5.3: E_F and density n standard deviations in hBN/SiO_2 and hBN/$SrTiO_3$ samples.

5.3 Quantum Hall regime

After the characterization of our graphene samples at zero magnetic field, we now present the Landau levels spectroscopy under a perpendicular magnetic field B up to 14 T. We first study the spatial homogeneity of LLs. We then verify that the dispersion of the LLs with respect to both B and the Landau index N is consistent with what is expected for Dirac fermions in graphene (see Chapter 2.1.1) :

$$E_N = E_D + \mathrm{sign}(N) v_F \sqrt{2\hbar e |N| B} \tag{5.6}$$

We next see how the gate dispersion of LLs unveils the successive pinning of the Fermi level, which yields a typical staircase pattern in the LDOS gate maps that is another proof of the high-quality of our devices. Finally we study the many-body renormalization of the Fermi velocity, which differs in samples on hBN/SiO_2 and on hBN/$SrTiO_3$.

Note that, in most figures that follow, a gap opens inside the zeroth Landau level when graphene is at charge neutrality : this interaction-induced gap which was previously introduced in Chapter 2.3 is the focus of Chapter 7 and is therefore only mentioned here.

5.3.1 Landau levels of Dirac fermions

We consider in this section the sample BNGrSTO-STM-07 of graphene on hBN/$SrTiO_3$. We apply a magnetic field of $B = 14$ T and a back-gate voltage $V_g = 13$ V to bring graphene to charge neutrality[4]. We perform a CITS on a 100×100 nm^2 studied in Figure 5.8. dI_t/dV_{bias} spectra reveal many well-defined peaks which correspond to Landau levels as shown in Figure 5.8(d). An interaction-induced gap opens in the zeroth Landau level lying at E_F, which thus splits into two well-resolved peaks $LL_{0^\pm}$. A typical width of $\Gamma_N \approx 20$ meV is obtained for LL peaks, consistent with previously reported values [145] and which tends to slowly increase with N. This corresponds to carrier lifetimes of $\tau_e \approx \hbar/\Gamma_N \approx 33$ fs.

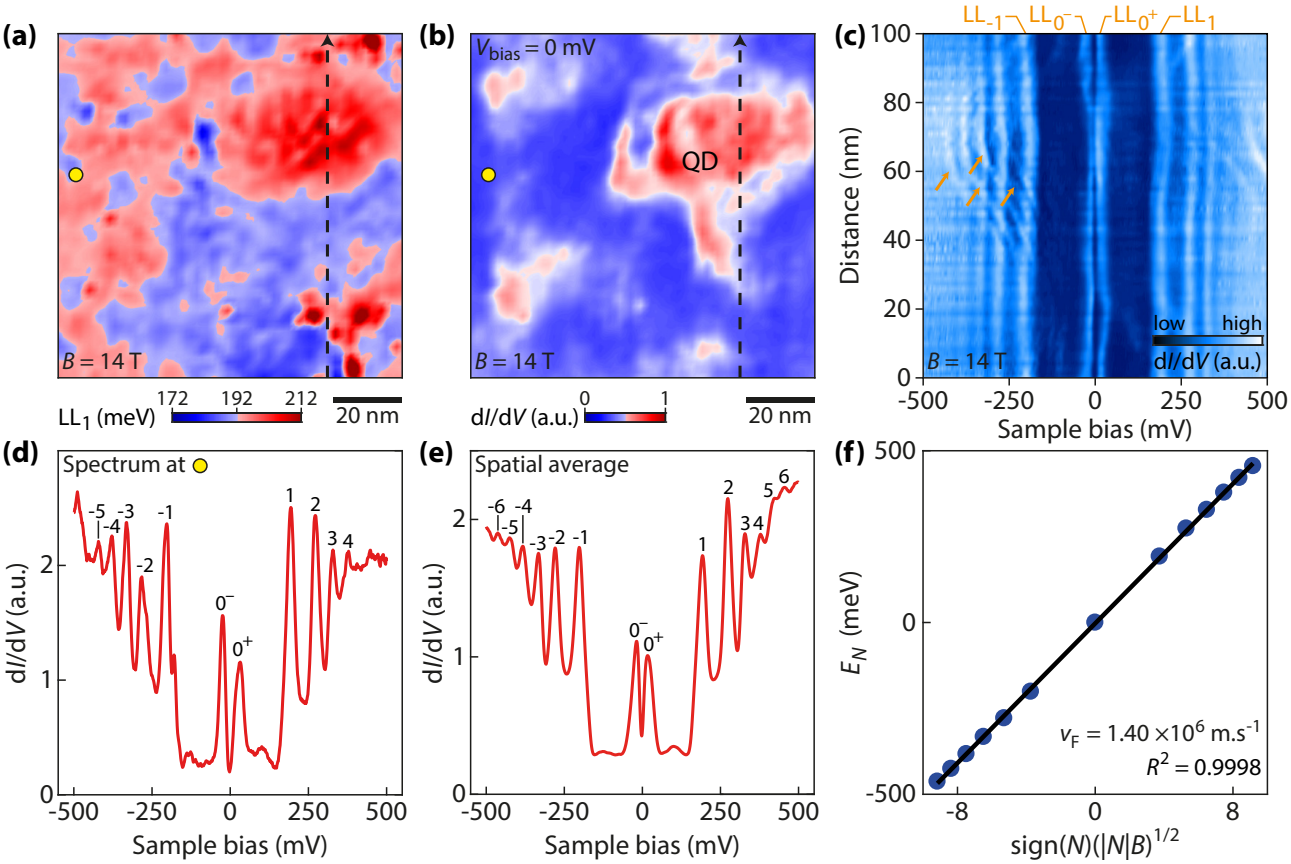

Figure 5.8: Spatial STS map at $B = 14$ T, on a 100×100 nm^2 area of graphene on hBN/$SrTiO_3$ in BNGrSTO-STM-07 at $V_g = 13$ V. Spectroscopy parameters : $I_t = 1$ nA, $V_{bias} = 500$ mV and $V_{mod} = 4$ mV. **(a)** Spatial dispersion map of the position of LL_1. Its mean value is obtained from (e) at $E_1 \simeq 192$ meV. **(b)** Spatial dI_t/dV_{bias} map taken at $V_{bias} = 0$ meV, showing the spatial variations of the $\nu = 0$ gap depth. The red area defines a quantum dot surrounded by blue incompressible regions. **(c)** dI_t/dV_{bias} spectra taken along the black dashed arrow in (a,b). Landau levels display a weak spatial dispersion on a scale of 100 nm. The $\nu = 0$ gap also stays well defined. In the upper left part of the image, a quadruplet of charging peaks (yellow arrows) intersect Landau levels in the dot region. **(d)** dI_t/dV_{bias} spectrum taken at the position marked by a yellow circle in (a,b) showing well-defined Landau level peaks. The zeroth Landau level is split into two peaks. **(e)** Spatially-averaged dI_t/dV_{bias} spectrum on the whole area of (a,b). **(f)** Fit using Equation (5.6) of the positions of Landau levels E_N as a function of $(|N|B)^{1/2}$ with N the Landau level index. An excellent agreement is obtained and the fit yields a Fermi velocity $v_F = (1.403 \pm 0.005) \times 10^6$ m.s^{-1}.

[4]The difference in V^{CNP} with respect to the one at 9 V estimated at zero magnetic field comes from the hysteretic behavior of $SrTiO_3$.

We plot in Figure 5.8(a) the spatial dispersion of the position of LL_1 : we observe around the mean value $E_1 = 192.4$ meV a fluctuation of $\Delta E_1 \approx 20$ meV, with nonetheless large regions of approximately 40 nm of size in which LL_1 features less variations. We also show in Figure 5.8(b) the spatial dI_t/dV_{bias} map taken at $V_{bias} = 0$ meV. This enables a visualization of the spatial variations of the interaction-induced gap depth : in blue regions the gap is well-resolved and the peaks of the broken-symmetry state are completely split, as seen in the spectrum of Figure 5.8(d). In red regions, the tunneling conductance does not fall to zero between the LL_0 peaks : these red regions are conductive at $V_{bias} = 0$ meV. This defines quantum dots as seen by Jung *et al.* [27] which are encircled by incompressible insulating blue regions.

Figure 5.8(c) shows the spatial evolution of the tunneling spectra taken along a line passing through both incompressible regions and a quantum dot. We observe that LLs slowly disperse on a distance of 100 nm, and the main variations occur when crossing the quantum dot. In particular in the dot region, which corresponds to the top half of Figure 5.8(c), a quadruplet of charging peaks [27] (see Chapter 3.5.1) is seen to strongly disperse spatially on the hole side and intersects the underlying negative LLs. Those charging peaks feature an addition energy of about 45 meV. The gap at zero bias also stays well-defined on the 100 nm length, yet inside the dot the $LL_{0^\pm}$ peaks are less resolved. Finally, the spatially-averaged dI_t/dV_{bias} spectrum on the whole area of the CITS is shown in Figure 5.8(e), where we see well-resolved Landau levels up to $N = \pm 6$ as well as both $LL_{0^\pm}$ peaks, with a gap of 35.8 meV. We fit in Figure 5.8(f) the positions of the LLs[5] as a function of $(|N|B)^{1/2}$. We obtain an excellent agreement with the theoretical Equation (5.6), confirming the massless behavior of carriers in graphene. With an uncertainty on the position of LLs of $\Delta E_N \approx 5$ meV, the fit yields a Fermi velocity $v_F = (1.403 \pm 0.005) \times 10^6$ m.s^{-1}. This value is much greater than the expected theoretical one of 1.0×10^6 m.s^{-1}, see Equation (1.10), which we study later in Section 5.3.4. Interestingly, we note that this energy spacing of Landau levels is symmetric with respect to electron and hole levels. This indicates that a possible tip-induced local band bending due to the work-function difference between the tip and graphene does not yield a significant spatial confinement on the Landau levels, which could have modified the Landau level spectrum [258].

We now present a magnetic field sweep from $B = 14$ T to $B = 0$ T in order to observe the dispersion of Landau levels with $B^{1/2}$. Starting from the previous configuration for the CITS in sample BNGrSTO-STM-07, graphene is left at charge neutrality with $V_g = 13$ V, with the tip placed outside the quantum dot. As the magnetic field is decreased at a rate of 0.2 T/min, we simultaneously and continuously acquired dI_t/dV_{bias} spectra. The tunneling junction stayed stable until 4 T, with a slow Z drift of about -0.3 nm/T, and we obtain the map shown in Figure C.4(a). We clearly see LLs disperse with the magnetic field. However the dispersion of positive LLs is not monotone : we suppose it may be a side-effect of the $SrTiO_3$ substrate and its non-linear dielectric constant. Some scattering resonance peaks which quickly disperse with B also emerge in the cyclotron gaps between LL_0 and $LL_{\pm 1}$ (indicating by yellow arrows). dI_t/dV_{bias} spectra taken at different magnetic fields with indexed LLs for $N \leq 0$ are shown in Figure 5.9(b). On the electron side, the indexation is more difficult and only done for unambiguous LL peaks. The interaction-induced gap at zero bias is clearly seen to decrease and to eventually close below $B = 6$ T [6]. For each spectrum, we consider the negative Landau levels with $N = -1, -2, -3$ from 14 to 4 T and fit their position E_N with respect to $(|N|B)^{1/2}$. The fit in Figure 5.9(c) is in good agreement with theory and yields a Fermi velocity $v_F = 1.43 \times 10^6$ m.s^{-1}, consistent with the value obtained at 14 T with Figure 5.8(f).

[5] $E_0 \simeq 0.7$ meV is taken at the middle of the LL_0 peaks.

[6] In fact, as we shall see in Chapter 7, the closure of the gap observed here is not only related to the lowering of the magnetic field but also to a slow drift of the charge-neutrality point V^{CNP} with B.

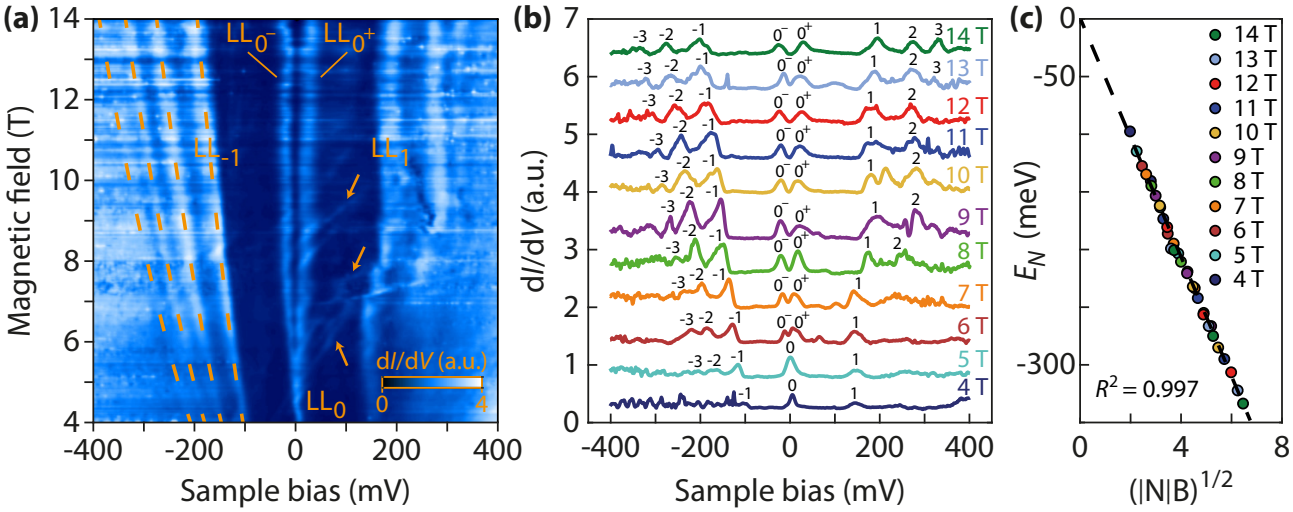

Figure 5.9: Landau levels dispersion with magnetic field. **(a)** $\mathrm{d}I_\mathrm{t}/\mathrm{d}V_\mathrm{bias}$ magnetic field map as a function of sample bias and magnetic field B for sample BNGrSTO-STM-07 at $V_\mathrm{g} = 13$ V. The yellow dashed lines represent the theoretical dispersion resulting from the fit. Spectroscopy parameters : $I_\mathrm{t} = 1$ nA, $V_\mathrm{bias} = 300$ mV and $V_\mathrm{mod} = 4$ mV. **(b)** Individual tunneling spectra taken at different magnetic fields with the Landau levels indexed. The interaction-induced gap opens in the zeroth Landau level beyond $B = 6$ T. **(c)** Results of the fit of the Landau levels positions (for $N < 0$) with respect to $(|N|B)^{1/2}$ using Equation (2.12). The fit yields a Fermi velocity $v_\mathrm{F} = 1.43 \times 10^6$ m.s^{-1}.

5.3.2 Gate tunable Landau levels

Here we study the dispersion of Landau levels with the back-gate voltage V_g, or equivalently with the filling factor ν : by increasing V_g we progressively fill the LLs and move up the Fermi level E_F in the LL spectrum. Since in STS the bias voltage is relative to the Fermi level ($eV_\mathrm{bias} = E - E_\mathrm{F}$), we rather see LLs moving down in energy. Figure 5.10(a) shows the LDOS gate map obtained for sample AC04 at $B = 5$ T, where we observe that each LL forms plateaus. This is the consequence of the successive pinning of the Fermi level inside Landau levels, which produces for each LL a typical staircase pattern characteristic of the quantum Hall regime [47, 145]. A similar result is obtained for sample BNGrSTO-STM-07 at $B = 14$ T as shown in Figure 5.10(c), where the asymmetry between the electron and hole sides arises from the non-linear behavior of ϵ_STO with the gate voltage : ϵ_STO strongly decreases with increasing V_g.

In both maps we observe the opening of different gaps, notably the interaction-induced gap which appears in LLs pinned at zero bias but also other gaps that open in LL peaks as they transit between two plateaus. In Chapter 7 we will study the evolution with the magnetic field of the gate maps and of the interaction-induced gap in LL_0. Nonetheless we will not consider in these chapters effects such as charging states that appear as peaks dispersing with positive slopes - in opposite direction of LLs, see the peaks labeled by red triangles in Figure 5.10(c) - or other LL splittings, whose descriptions are made in Appendix C. Moreover, we will only consider LDOS gate maps where charging effects do not distort the LL spectrum, whereas in Appendix C we deal with some results where charging effects are predominant.

5.3.2.a Pinning of the Fermi level inside Landau levels

We explained in Chapter 3.2 how in the quantum Hall regime the Fermi level does not move continuously with the gate voltage V_g, but rather stays pinned inside LLs for a certain range of V_g that is needed to fill or empty all states of the highly degenerate LLs. This forms

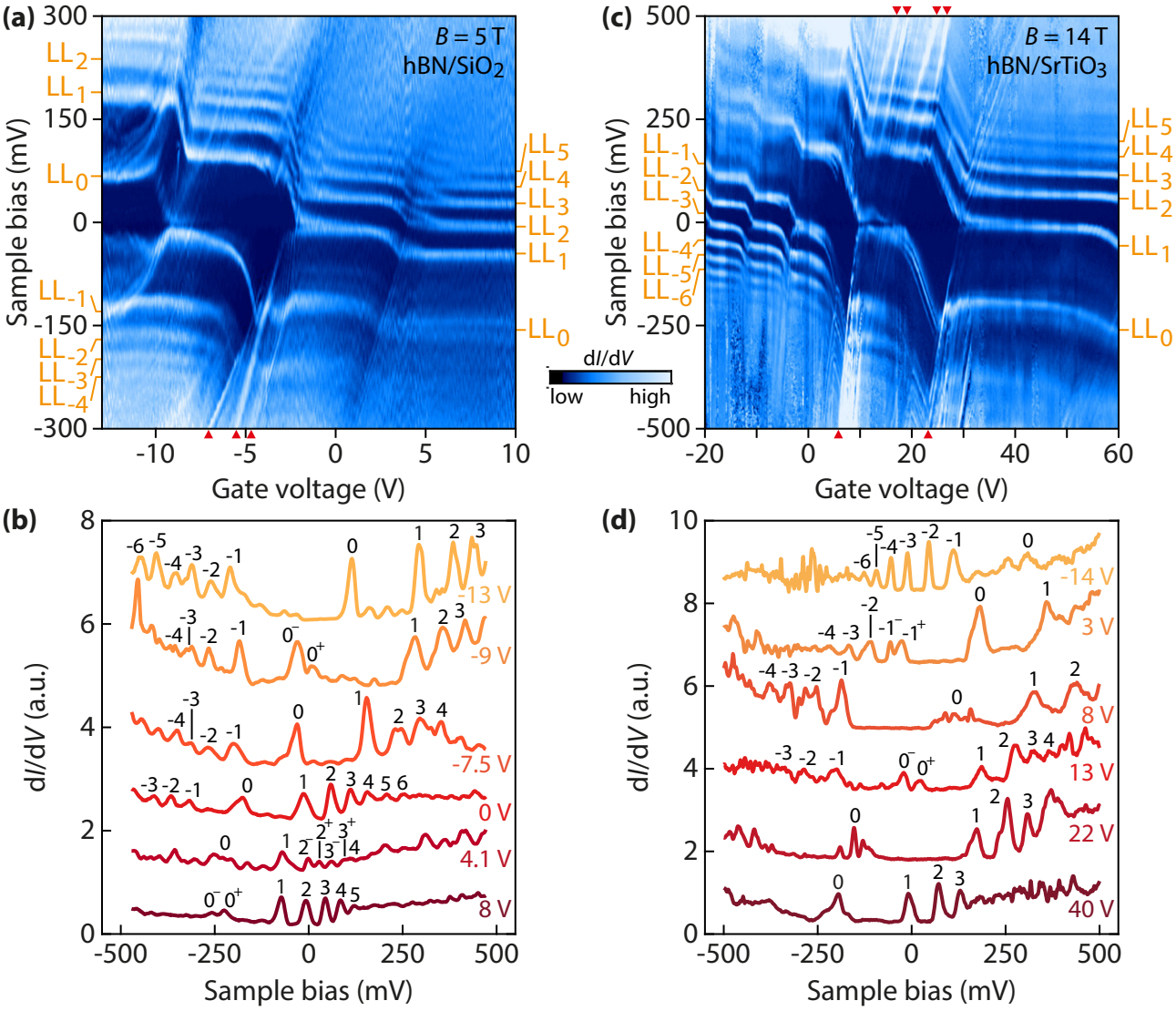

Figure 5.10: LDOS gate maps under magnetic field. **(a)** $\mathrm{d}I_\mathrm{t}/\mathrm{d}V_\mathrm{bias}$ gate map as a function of sample bias and gate voltage for sample AC04 at $B = 5$ T, showing the successive pinning of the Fermi level inside Landau levels. Spectroscopy parameters : $I_\mathrm{t} = 1$ nA, $V_\mathrm{bias} = 300$ mV and $V_\mathrm{mod} = 3$ mV. **(b)** $\mathrm{d}I_\mathrm{t}/\mathrm{d}V_\mathrm{bias}$ spectra taken from (a) at different gate voltages. Landau levels are indexed. **(c)** $\mathrm{d}I_\mathrm{t}/\mathrm{d}V_\mathrm{bias}$ gate map as a function of sample bias and gate voltage for sample BNGrSTO-STM-07 at $B = 14$ T. Spectroscopy parameters : $I_\mathrm{t} = 1$ nA, $V_\mathrm{bias} = 500$ mV and $V_\mathrm{mod} = 4$ mV. **(d)** $\mathrm{d}I_\mathrm{t}/\mathrm{d}V_\mathrm{bias}$ spectra taken from (c) at different gate voltages.

the plateaus that we observe in the gate map, see Figure 5.11. Moreover, E_F jumps quickly between the topmost filled LL and the bottom most empty LL due to the low density of states in the cyclotron gaps. The emergence of plateaus in the LDOS gate map is reminiscent of that of plateaus of transverse conductance G_{xy} as a function of filling factor we observe in the same conditions in transport devices. Note however they have opposite significance : plateaus form in G_{xy} when E_F lies inside a cyclotron gap while pinned to localized states that do not carry current. LDOS gate map must rather be seen as the dual of transport measurements.

The LDOS gate map also gives some insight about the quality and disorder in the sample. The lower the disorder is, the less broad the LLs are. For ideal samples with no disorder, LLs are reduced to Dirac functions and E_F stays constant as the LL at zero sample bias is filled, which yields horizontal plateaus and the transitions width shrinks to zero in absence of states in the

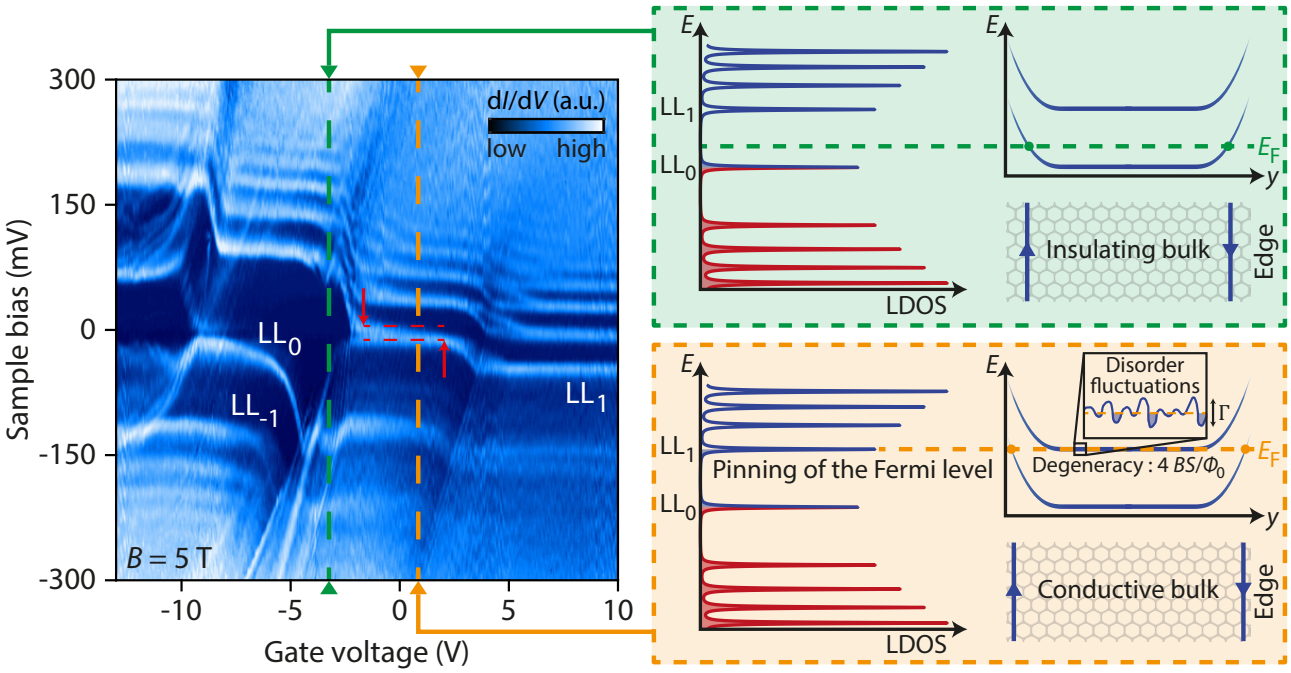

Figure 5.11: Pinning of the Fermi level inside Landau levels. The LDOS gate map of Figure 5.10(a) is characterized by two distinct regimes that define staircase patterns for the evolution of LLs with the gate voltage V_g. Between two LL plateaus at $V_{bias} = 0$ (green inset), the Fermi level E_F lies in a cyclotron gap, pinned to localized states, and varies quickly with V_g, faster for lower disorder. This regime corresponds to the quantized G_{xy} plateaus in transport measurements. On a LL plateau (yellow inset), E_F stays pinned inside one LL as long as there are states to be filled, the lower the disorder the wider the plateau. This implies a variation of E_F with V_g on the plateau of only Γ the width of the LL, which decreases with lower disorder.

cyclotron gap[7]. With disorder, LLs get broadened[8] with a width Γ. This broadening gives the variation of E_F as the LLs are filled and thus explains the shallow slopes downward of the LL plateaus in the LDOS gate map. In Figure 5.11 for AC04 the LL_1 plateau at zero bias displays a shift of -14 meV (see red arrows) between the beginning of the plateau at $V_g \simeq -1.5$ V (filling the first LL_1 state) and its end at $V_g = 2.2$ V (filling the last LL_1 state), which is consistent with the broadening of the LL peak of $\Gamma \sim 20$ meV evaluated from individual spectra. In Figure 5.10(c) for BNGrSTO-STM-07, the same LL_1 shift is found to be greater, around -28 meV, which was expected since we showed at zero magnetic field that this sample on hBN/$SrTiO_3$ features a stronger disorder potential. Eventually, for dirty samples with important disorder, the density of states and consequently the plateaus would be fully smoothed out and LLs would display a pattern in the gate map closer to the square-root dependence expected at zero magnetic field. The emergence of LL plateaus in a LDOS gate map is thus a signature of the quantum Hall regime ($\Omega_c \tau_e \gg 1$), see Figure 2.4(c).

5.3.2.b Estimation of the dielectric constant of $SrTiO_3$ in magnetic field

We already obtained a rough estimation of ϵ_{STO} in BNGrSTO-STM-07 using the LDOS gate map at zero magnetic field, see Figure 5.4(c), by fitting the position of the Dirac point

[7] On the contrary, in transport measurements, quantum Hall plateaus of G_{xy} exist as long as the Fermi level is pinned to localized states inside cyclotron gaps, and are then wider for dirty samples. For high mobility samples with low disorder, the plateaus width shrinks to zero while the transitions between plateaus, which correspond to the filling of LLs, occur on wider ranges of gate voltages.

[8] As we see in Chapter A.1.3, the broadening due to temperature is negligible for LL spectroscopy.

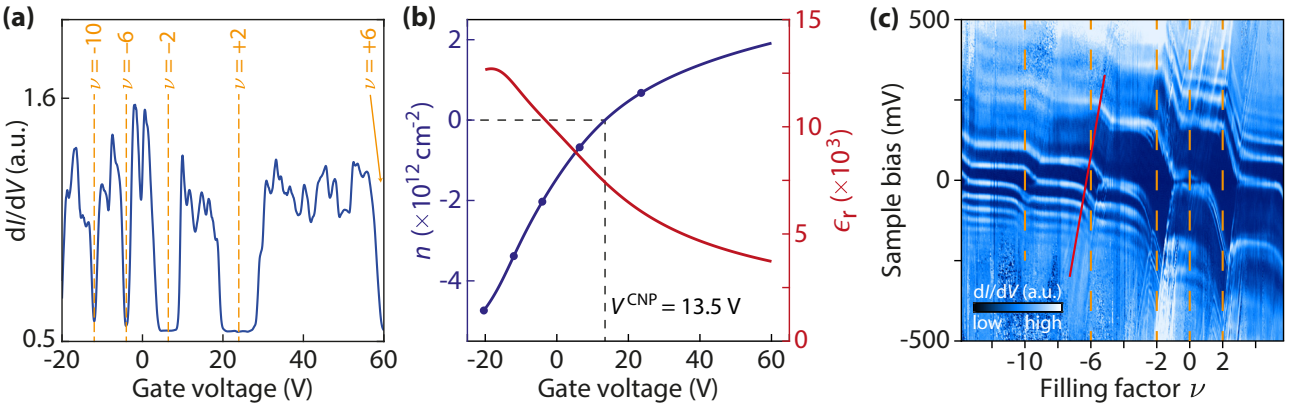

Figure 5.12: Estimation of the dielectric constant of $SrTiO_3$ and rescaling of the gate map. (a) Linecut at $V_{\text{bias}} = 0$, averaged on a range of ± 20 mV, of the LDOS gate map at $B = 14$ T of Figure 5.10(c), which gives back-gate voltages corresponding to filling factors ν of filled LLs. **(b)** Estimation from the filling factors of (a) of the charge carrier density n (blue dots), polynomial fit (blue curve) and computed values of $\epsilon_r \simeq \epsilon_{\text{STO}}$ as a function of gate voltage. The fit also yields $V^{\text{CNP}} \simeq 13.5$ V. **(c)** Rescaling of the gate map as a function of ν.

E_D. Nonetheless it is probable that ϵ_{STO} varies with the magnetic field B. Here we consider the LDOS gate map at $B = 14$ T from Figure 5.10(c) from which we can extract some values of the back-gate voltage corresponding to specific filling factors ν. Since the successive plateaus that form in the gate map correspond to the filling of LLs, the variation of gate voltage to pass through an entire plateau yields a variation in terms of filling factor of $\Delta\nu = \pm 4$.

We plot in Figure 5.12(a) the line cut of the gate map at $V_{\text{bias}} = 0$, averaged on a range of ± 20 meV around this value. We clearly observe the different plateaus forming when E_F is pinned inside one LL, with gaps between : we consider that the gate voltages at the middle of the gaps correspond to completely filled and empty LLs, hence the gate voltages for different values of the filling factor $\nu = -10, -6, -2, 2$. Those values are converted in charge carrier density values n in Figure 5.12(b) using Equation (2.16). A 5-degree polynomial is used to fit these points and interpolate the evolution of the carrier density on the range of gate voltage of the gate map. With this fit, charge neutrality at $n = 0$ is achieved at $V^{\text{CNP}} = 13.5$ V.

We use the field-effect relation (1.38) and the gate capacitance $C_g = \epsilon_0 \epsilon_r / d_{\text{STO}}$ to obtain the equation linking ϵ_r to the carrier density n and the gate voltage V_g :

$$\epsilon_r = \frac{d_{\text{STO}}}{\epsilon_0} \frac{en}{V_g - V^{\text{CNP}}} \tag{5.7}$$

The red curve in Figure 5.12(b) shows the resulting ϵ_r, which decreases with increasing gate voltage and ranges between 12 500 and 3 500. We obtain the same order of magnitude than at zero magnetic field, consistent with the expected value of $\epsilon_{\text{STO}} \simeq \epsilon_r$ at low temperature, but here ϵ_r varies monotonically with V_g. A similar $\epsilon_r(V_g)$ profile but with slightly weaker values is obtained for sample AC23 ($3\,000 < \epsilon_r < 11\,500$).

Finally, using the fit of the filling factor ν, we can rescale the gate map as a function of ν which is shown in Figure 5.12(c). In particular, note that in the rescaled map the interaction-induced gap is maximal at charge neutrality $\nu = 0$, as expected considering that the exchange interaction is maximal at half-filling of the zeroth Landau level.

5.3.3 Unraveling the LDOS gate maps through numerical simulations

LDOS gate map enables the observation of a very rich physics with the appearance of a wealth of features that go beyond the simple theoretical picture of solely dispersing Landau levels. All of these features can make LDOS gate maps rather complicated to decipher. We show in this section how we can simulate the single-particle LL spectrum and the ensuing LDOS gate maps under magnetic field, which reveals quite useful to understand the different physical effects that appear in such maps, and how the LL dispersion depends on many parameters from both graphene density of states and gating effect.

5.3.3.a Algorithm to compute $\rho(E = eV_{\text{bias}}, V_{\text{g}})$

The principle of this simulation is to compute graphene density of states, around $E_{\text{F}} = 0$, as a function of the gate voltage. We then use the theoretical equation proposed by Champel and Florens [52] that we discussed in Chapter 2.1.3 :

$$\rho(E = eV_{\text{bias}}, V_{\text{g}}) = \frac{1}{2\pi l_B^2} \frac{4}{\sqrt{\pi}} \sum_{N=-\infty}^{+\infty} \frac{1}{\Gamma_N} \exp\left\{ -\left(\frac{E - E_{\text{D}}(V_{\text{g}}, V_{\text{bias}}) - E_N}{\Gamma_N} \right)^2 \right\} \tag{5.8}$$

where the parameters are the magnetic length $l_B = \sqrt{\hbar/eB}$, the Dirac point position E_{D}, the Fermi velocity v_{F} (in the LL energies E_N) and the LL widths Γ_N which take into account the disorder potential. The calculation of E_{D} will yield the dependence with the gate voltage V_{g} from the field effect.

We start by calculating the intrinsic graphene density of states with $E_{\text{D}} = E_{\text{F}} = 0$. This step is already tricky : even if we restrain the energies to those of STS measurements, typically $-500\,\text{meV} < E < 500\,\text{mV}$, we need to consider much more LLs beyond this window in order to reproduce the V-shape background of the DOS, that arises due to the decreasing cyclotron gap with N. We choose in our simulations $-100 < N < 100$ and graphene DOS $\rho(E)$ is then obtained using Equation (5.8). Note that $\rho(E)$ is expressed in $\text{eV}^{-1}.\text{cm}^{-2}$.

Next step is the computation of $E_{\text{D}} = f(V_{\text{g}})$. For that we need an estimate of the charge-neutrality point V^{CNP}. First roughly estimated from the LDOS gate maps, it will be refined later as an adjustable parameter of the fit. On the one hand, the carrier density per unit area n is defined by the integration of the density of states $\rho(E)$ from E_{D} to E_{F} which is by convention fixed at zero energy :

$$n = \int_{E_{\text{D}}}^{E_{\text{F}}=0} \rho(E)\text{d}E = \int_{0}^{-E_{\text{D}}} \rho(E)\text{d}E \tag{5.9}$$

since $\rho(E)$ is even. On the other hand, we compute n using the field effect equation given by Equation (1.39) for each V_{g} :

$$n = \frac{C_{\text{g}}}{e}\left(V_{\text{g}} - V^{\text{CNP}}\right) \tag{5.10}$$

with the gate capacitance $C_{\text{g}} = \epsilon_0\epsilon_{\text{r}}/d$ which will play an important role later through the gate insulator dielectric constant ϵ_{r}. For each value of V_{g} the corresponding position of the Dirac point E_{D} is therefore obtained by equalizing both quantities :

$$\int_{0}^{-E_{\text{D}}} \rho(E)\text{d}E = \frac{C_{\text{g}}}{e}\left(V_{\text{g}} - V^{\text{CNP}}\right) \tag{5.11}$$

This equation is resolved numerically and eventually yields $E_{\text{D}} = f(V_{\text{g}})$, from which we can start simulating LDOS gate maps.

5.3.3.b Influence of the local density of states parameters

We first consider that the Dirac point position only depends on the gate voltage : $E_D = E_D(V_g)$. In this case only the dispersion relation $E_D = f(V_g)$ obtained from the previous algorithm is needed and one can easily obtain the LDOS gate map using Equation (5.8). We show in Figure 5.13(a) such gate map, computed with the following parameters : $B = 5$ T, $v_F = 1.0 \times 10^6$ m.s^{-1}, $\Gamma_N = 5$ meV, $V^{CNP} = 0$ and $\epsilon_r = 3.7$. The corresponding graphene density of states $\rho(E)$ is shown in Figure 5.13(b). We observe in Figure 5.13(a) the different plateaus that emerge at partial filling factors. However the transitions between the LL plateaus are discontinuous. This arises from the vanishing of the density of states in the cyclotron gaps : since there is zero in-gap state available, the Fermi level can not be pinned inside the gap and it directly jumps from the topmost filled LL to the bottommost empty LL when increasing the gate voltage.

In order to reproduce the experimental smooth transitions between these plateaus we introduce a flat background ρ_0 in the density of states [56], and therefore some states in the cyclotron gaps to pin the Fermi level, see Figure 5.13(c,d). Such a trick is justified by the fact that experimentally the DOS inside the cyclotron gap between LL_0 and $LL_{\pm1}$ indeed does not fall to zero[9] in the spectra of Figure 5.8(d,e). This effectively reproduces the typical LL transitions observed in experimental gate maps, the more states we add with this flat background the

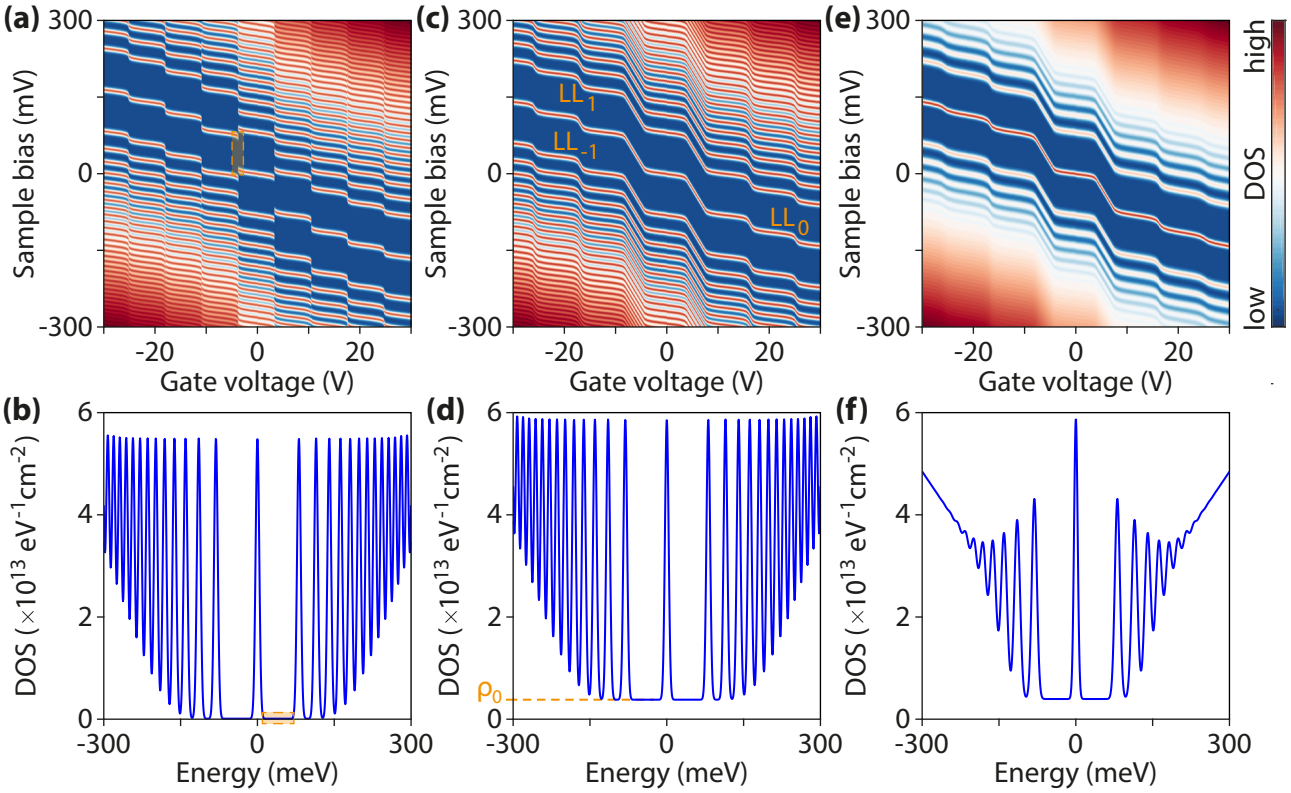

Figure 5.13: Influence of the DOS parameters on the LDOS gate maps. **(a)** LDOS gate map obtained for the DOS shown in (b) at $B = 5$ T. The discontinuous transitions between LL plateaus occur due to the vanishing of the DOS in the cyclotron gap. **(c)** LDOS gate map obtained for the DOS shown in (d). Adding a flat background of $\rho_0 = 4 \times 10^{12}$ eV^{-1}.cm^{-2} to the DOS ensures a continuous transition between LL plateaus : the higher the background the smoother the transition. **(e)** LDOS gate map obtained for the DOS shown in (f) where $\Gamma_N = 5$ meV $+ 2$ meV $\times |N|^{1/2}$.

[9] see also Appendix C.3.

smoother the transitions. Note however that this effect is reduced for high N where LLs merge due to the decreasing cyclotron gap with N which already prevents the density of states from falling to zero in the gaps. The states we introduce in the cyclotron gaps may correspond in the conventional picture to localized states in graphene that appear due to disorder (see Chapter 2.1.3) for instance from charge puddles or impurities. However it is not clear why they produce locally a flat DOS background in a very large cyclotron gap (between LL_0 and $LL_{\pm1}$) and in presumably clean samples.

So far we have assumed LLs have the same width $\Gamma_N = 5\,\text{meV}$. However Γ_N is expected to increase as $|N|^{1/2}$ due to the broadening of the LL wave functions with N, see Chapter 2.1.3. We therefore now consider :

$$\Gamma_N = \Gamma_0 + \delta\Gamma\sqrt{|N|} \tag{5.12}$$

The simulated gate map presented in Figure 5.13(e) is obtained for $\Gamma_0 = 5\,\text{meV}$ and $\delta\Gamma = 2\,\text{meV}$. The increase of Γ_N with $|N|$ induces a blurring of LLs for $|N| > 5$, also visible in the density of states shown in Figure 5.13(f). It also smooths more the transitions between LL plateaus far from charge neutrality with respect to Figure 5.13(c) due to the increase of the density of states inside the cyclotron gaps for high N. We start to obtain gate maps similar to those shown in Figure 5.10, still with noticeable differences that comes from the influence of graphene substrate.

5.3.3.c Non-linear dielectric constant of $SrTiO_3$

We have previously assumed the gate insulator dielectric constant was given by $\epsilon_r = 3.7$, value we estimated using Equation 5.3 for the hBN/SiO_2 gate insulator. This parameter controls the lever arm of the back-gate and therefore the width of the LL plateaus as a function of the gate voltage. Since LL plateaus in hBN/SiO_2 samples display the same width it is quite easy to adjust the parameter ϵ_r to a constant value. A good fit of the LL plateaus widths of Figure 5.10(a) for AC04 is obtained for an unexpectedly high value of $\epsilon_r = 5.4$. For sample $hBN/SrTiO_3$ we must take into account the non-linearity of $\epsilon_r(V_g)$ in order to obtain LL plateaus of different widths. The algorithm is simply modified by writing :

$$\int_0^{-E_D} \rho(E)\mathrm{d}E = \frac{C_g\left[\epsilon_r(V_g)\right]}{e}\left(V_g - V^{CNP}\right) \tag{5.13}$$

We show in Figure 5.14(a) such simulated gate map fitting the experimental map in Figure 5.10(c) of sample BNGrSTO-STM-07. We accurately reproduce the different widths of the LL plateaus by introducing the profile $\epsilon_r = f(V_g)$ obtained from Figure 5.12(b) and using the following parameters : $B = 14\,\text{T}$, $v_F = 1.4 \times 10^6\,\text{m.s}^{-1}$, $\Gamma_0 = 10\,\text{meV}$, $\delta\Gamma = 3\,\text{meV}$, $V^{CNP} = 14\,\text{V}$ and $\rho_0 = 5.4 \times 10^{12}\,\text{eV}^{-1}.\text{cm}^{-2}$.

5.3.3.d Tip-induced gating

The last effect we have to consider for the single-particle LL spectrum is the tip-induced gating, which makes the overall graphene gating dependent of both the gate and bias voltages (see Chapter 3.6). As indicated by the green dashed lines in Figure 5.14(a) the transitions between LL plateaus all occur at the same gate voltage, which means that isodensity lines in this gate map are vertical. This is however not true experimentally, see e.g. Figure 5.10.

Let us consider the gate map in Figure 5.12(c) that we have presumably rescaled as a function of the filling factor ν : if the scaling is indeed good at zero bias, the LL plateau transitions do not occur at constant ν as they should be in a true density map (see the red line) because we

did not compensate the local tip gating. In the LDOS gate maps $\mathrm{d}I_\mathrm{t}/\mathrm{d}V_\mathrm{bias}(V_\mathrm{bias}, V_\mathrm{g})$ isodensity lines eventually appear tilted with a positive slope given by :

$$n = \frac{1}{e}\left(C_\mathrm{g}V_\mathrm{g} - C_\mathrm{tip}V_\mathrm{bias}\right) = \mathrm{cte} \qquad \Rightarrow \qquad \frac{\mathrm{d}V_\mathrm{bias}}{\mathrm{d}V_\mathrm{g}} = \frac{C_\mathrm{g}}{C_\mathrm{tip}} \tag{5.14}$$

with C_tip the tip-graphene capacitance. Experimentally the capacitance ratio $\beta = C_\mathrm{g}/C_\mathrm{tip}$ is seen to decrease with increasing gate voltage, with values ranging between 0.25 and 0.05.

We consider the LDOS gate map shown in Figure 5.10(c) for sample BNGrSTO-STM-07. We estimate β at different gate voltages as the slopes of the isodensity lines defined by the LL plateau transitions, such as the red line in Figure 5.12(c). Following [47, 259] we use a quadratic polynomial to fit these points and interpolate the function $\beta(V_\mathrm{g})$ on the whole range of gate voltage. We then modify the algorithm to take into account this additional gating from the tip as :

$$\int_0^{-E_\mathrm{D}} \rho(E)\mathrm{d}E = \underbrace{\frac{C_\mathrm{g}\left[\epsilon_\mathrm{r}(V_\mathrm{g})\right]}{e}\left(V_\mathrm{g} - V^\mathrm{CNP}\right)}_{\text{back-gate gating}} - \underbrace{\frac{C_\mathrm{g}\left[\epsilon_\mathrm{r}(V_\mathrm{g})\right]}{e} \times \frac{V_\mathrm{bias}}{\beta(V_\mathrm{g})}}_{\text{tip-induced gating}} \tag{5.15}$$

Note that the Dirac point position $E_\mathrm{D}(V_\mathrm{g}, V_\mathrm{bias})$ obtained with this algorithm now features a dependence with the sample bias. The simulated gate map is obtained by computing the density of states $\rho(V_\mathrm{bias}, V_\mathrm{g})$ using Equation (5.8) and the 2D map of the Dirac point $E_\mathrm{D}(V_\mathrm{g}, V_\mathrm{bias})$.

Such map is shown in Figure 5.14(b) (keeping the same other parameters) where the isodensity lines appear tilted with slopes depending on the gate voltage as intended. At this point this simple single-particle simulation already accurately reproduces the experimental LDOS gate map of Figure 5.10(c), see the overlay in Figure 5.14(c).

One must nonetheless note some deviations between simulation and experiment. The first occurs around $\nu = 2$, see yellow rectangle in Figure 5.14(c). While we accurately retrieve other LLs, we underestimate the position of LL_0 in this region. The second happens on the hole

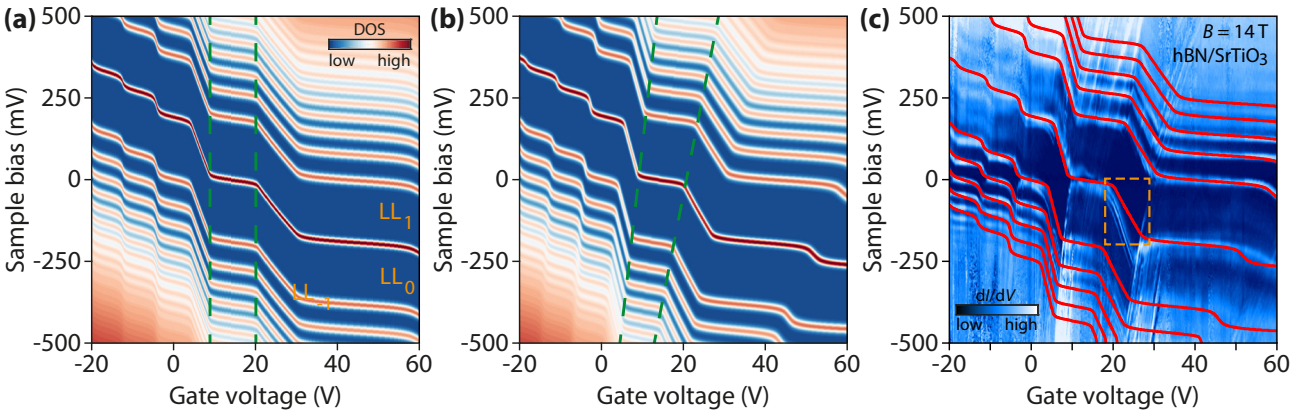

Figure 5.14: Influence of the gating effects on the LDOS gate maps. **(a)** LDOS gate map obtained when introducing a gate voltage dependence in $\epsilon_\mathrm{r}(V_\mathrm{g})$, which controls the widths of the LL plateaus. The vertical dashed green lines represent two isodensity lines. **(b)** LDOS gate map obtained when adding the tip-induced gating, which tilts the isodensity lines with a positive slope $C_\mathrm{g}/C_\mathrm{tip}(V_\mathrm{g})$. The tilted dashed green lines are the same isodensity lines than in (a) and show different slopes. **(c)** Overlay of the final simulated gate map in (b) with the experimental gate map of Figure 5.10(c). The red curves represent the evolution of the maxima of the simulated LL peaks for $-5 < N < 5$.

side where we fail to reproduce precisely the peak spacing at a given gate voltage : this is a consequence of the renormalization of the Fermi velocity as a function of carrier density, which arises from many-body effects that we ignored here by assuming a constant $v_F = 1.4 \times 10^6$ m.s^{-1} as determined in Figure 5.8. This is the topic of the last section.

5.3.4 Fermi velocity renormalization

The objective of this section is to extract the Fermi velocity from the LDOS gate maps, following the work of Chae *et al.* [47]. At zero magnetic field, the only way to do so is to fit the gate dependence of the Dirac point, therefore we obtain one value from each gate map. Under magnetic field, we simply have to fit the LLs dispersion $E_N = \mathrm{sign}(N) v_F^* \sqrt{2\hbar e |N| B}$, at a fixed gate voltage. It is therefore possible to compute the density dependence of the Fermi velocity. As we discussed in Chapters 1.3.3 and 3.3, we should expect a renormalization due to electron-electron interactions, with an increase of v_F^* close to charge neutrality as given by :

$$\frac{v_F^*}{v_F} = 1 - \frac{\alpha_G}{\pi}\left[\frac{5}{3} + \ln(\alpha_G)\right] + \frac{\alpha_G}{8}\ln\left(\frac{n_C}{n}\right) \tag{5.16}$$

Beforehand, we have to convert our LDOS gate maps $\mathrm{d}I_t/\mathrm{d}V_{bias}(V_{bias}, V_g)$ into LDOS density maps $\mathrm{d}I_t/\mathrm{d}V_{bias}(V_{bias}, n)$. As we show in the previous section, there are two effects that must also be taken into account. First is the gate voltage dependence of the gate insulator dielectric constant ϵ_r, in particular for hBN/$SrTiO_3$ samples. We showed in Figure 5.12 how we can estimate $\epsilon_r(V_g)$. We then have to compensate the tip-induced gating. We consider the LDOS gate map shown in Figure 5.15(a), obtained in sample AC23 (hBN/$SrTiO_3$). We estimate $\beta = C_g/C_{tip}$ at different gate voltages to interpolate the profile $\beta(V_g)$ on the whole gate range. Afterward, the gate map is converted into a density map using the transformation :

$$\frac{\mathrm{d}I_t}{\mathrm{d}V_{bias}}(V_{bias}, V_g) \quad \longmapsto \quad \frac{\mathrm{d}I_t}{\mathrm{d}V_{bias}}(V_{bias}, n) = \frac{\mathrm{d}I_t}{\mathrm{d}V_{bias}}\left[V_{bias}, C_g(V_g)\left(V_g - \frac{V_{bias}}{\beta(V_g)}\right)\right] \tag{5.17}$$

where $C_g(V_g)$ takes into account the non-linearity of $\epsilon_r(V_g)$ estimated previously. Figure 5.15(b) shows such LDOS density map (only the square part of the sheared map is displayed) : the

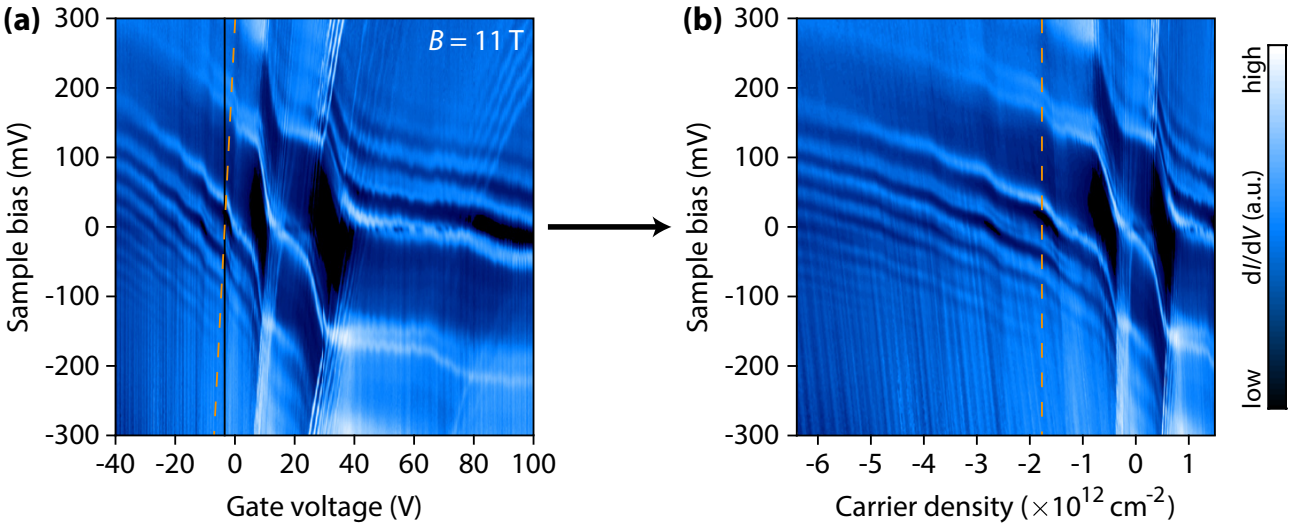

Figure 5.15: Conversion of LDOS gate map as LDOS density map. (a) $\mathrm{d}I_t/\mathrm{d}V_{bias}$ gate map as a function of gate voltage V_g for sample AC23 (graphene/hBN/$SrTiO_3$) at $B = 11$ T. The isodensity lines appear tilted due to local tip gating. **(b)** Same map as a function of carrier density n after correcting the tip gating.

yellow dashed line corresponds to the same isodensity line in Figure 5.15(a) but appears here vertical. Similar treatments are performed for both LDOS gate maps shown in Figure 5.10 for samples AC04 and BNGrSTO-STM-07. This step is important to enable the accurate determination of the renormalized Fermi velocity v_F^* at constant density. Indeed, Chae *et al.* [47] pointed out that the LDOS gate maps overestimate the LL positions, error which varies with density since the capacitance ratio β depends on the gate voltage. Eventually, they estimated this would lead to errors of about 30% on the interaction parameter α_G determined from the fit of $v_F^* = f(V_g)$ compared to the fit of $v_F^* = f(n)$ that we do below.

The renormalized Fermi velocity v_F^* is determined from the fit of the LL positions in the LDOS density maps using Equation (5.6). Figure 5.16 shows such fits performed in sample BNGrSTO-STM-07 using the converted LDOS density map of Figure 5.10(c) at $B = 14$ T : one for a spectrum taken on the hole side at $n = -4.15 \times 10^{12}$ cm^{-2} and the second on the electron side at $n = 1.6 \times 10^{12}$ cm^{-2}. We note that both fits are in excellent agreement with theory, nonetheless an electron-hole asymmetry is observed as they yield different Fermi velocities : $v_F^{*,h} = (1.196 \pm 0.009) \times 10^6$ m.s^{-1} for holes and $v_F^{*,e} = (1.355 \pm 0.014) \times 10^6$ m.s^{-1} for electrons, which is 13% higher. A similar electron-hole asymmetry of 18% is also observed in sample AC23 for the map shown in Figure 5.15.

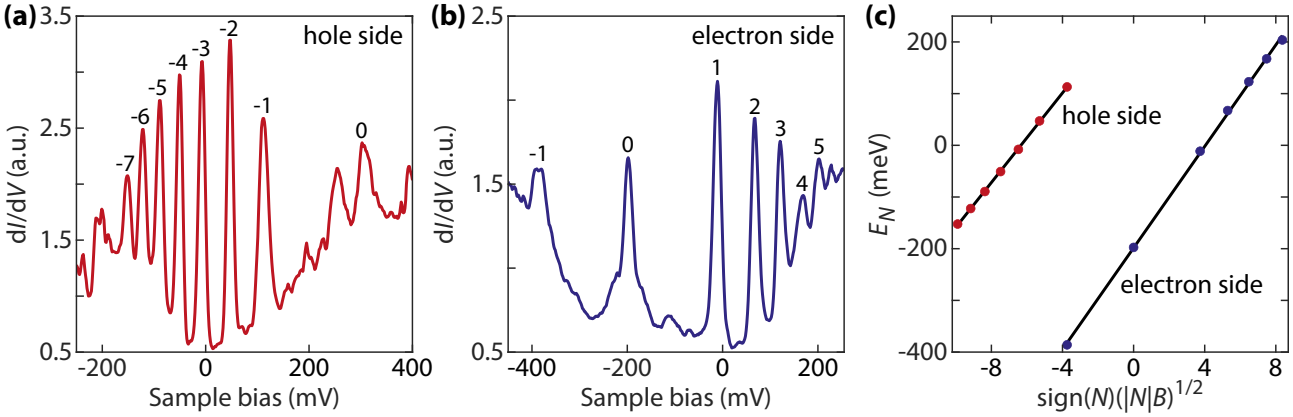

Figure 5.16: Fermi velocity computation and electron-hole asymmetry. **(a)** dI_t/dV_{bias} spectrum in sample BNGrSTO-STM-07 taken from Figure 5.10(c), after its conversion into a LDOS density map, at $n = -4.15 \times 10^{12}$ cm^{-2}. **(b)** Same than (a) but taken at $n = 1.6 \times 10^{12}$ cm^{-2}. **(c)** Fits of LL positions in (a,b) with respect to $(|N|B)^{1/2}$. On the hole side, the fit yields $v_F^{*,h} = (1.196 \pm 0.009) \times 10^6$ m.s^{-1} while, on the electron side, it yields $v_F^{*,e} = (1.355 \pm 0.014) \times 10^6$ m.s^{-1}.

The same procedure is repeated to compute v_F^* for each density point and we obtain the renormalization of the Fermi velocity as a function of carrier density $v_F^* = f(n)$ for the three samples AC04 (graphene/hBN/SiO_2) and BNGrSTO-STM-07 and AC23 (graphene/hBN/$SrTiO_3$). A fit with two adjustable parameters - the bare Fermi velocity v_F and the interaction parameter α_G - is done using Equation (5.16) for the three cases, which gives Figure 5.17.

Let us start with sample AC04 in Figure 5.17(a) where we can distinguish two behaviors for v_F^*. On the electron side we clearly see an increase of the Fermi velocity toward charge neutrality as expected theoretically due to electron-electron interactions. The fit on this side using Equation (5.16) yields a bare Fermi velocity $v_F = (1.030 \pm 0.009) \times 10^6$ m.s^{-1} and an interaction parameter $\alpha_G = 0.66 \pm 0.10$. These values are consistent with those obtained by Chae *et al.* [47], that is, $v_F = (0.957 \pm 0.003) \times 10^6$ m.s^{-1} and $\alpha_G = 0.69 \pm 0.03$ for the same system graphene/hBN/SiO_2. The interaction parameter can be expressed as a function of the

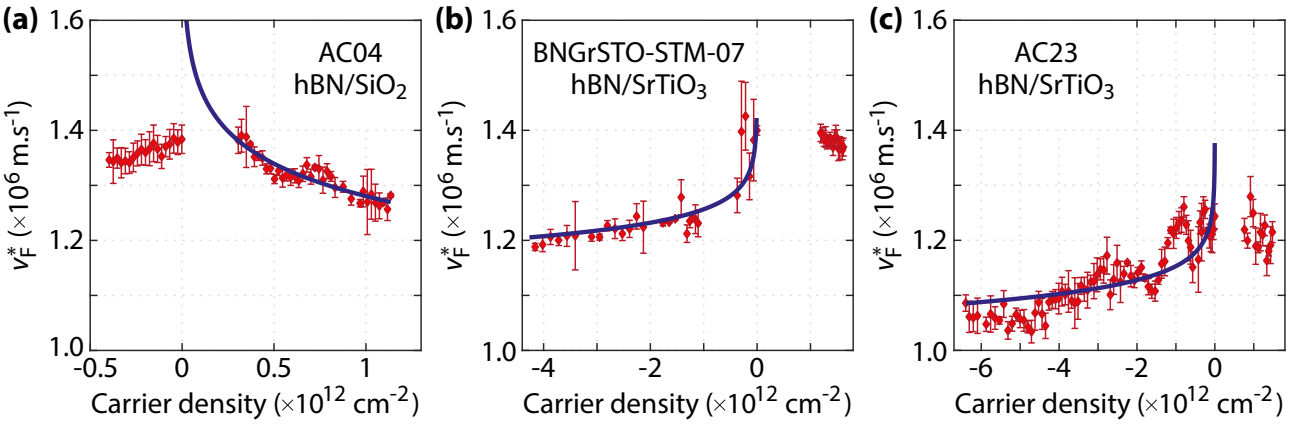

Figure 5.17: Renormalized Fermi velocity v_F^* as a function of carrier density n (red points) determined from the linear fit of the LL positions with respect to $(|N|B)^{1/2}$. **(a)** For sample AC04 (hBN/SiO_2), the fit (blue curve) of $v_F^* = f(n)$ from the LDOS gate map shown in Figure 5.10(a) and using Equation (5.16) yields $v_F = (1.030 \pm 0.009) \times 10^6$ m.s^{-1} and $\alpha_G = 0.66 \pm 0.10$. **(b)** For sample BNGrSTO-STM-07 ($hBN/SrTiO_3$), the fit from the LDOS gate map shown in Figure 5.10(c) yields $v_F = (1.070 \pm 0.024) \times 10^6$ m.s^{-1} and $\alpha_G = 0.26 \pm 0.07$. **(c)** For sample AC23 ($hBN/SrTiO_3$), the fit from the LDOS density map shown in Figure 5.15(b) yields $v_F = (0.972 \pm 0.014) \times 10^6$ m.s^{-1} and $\alpha_G = 0.30 \pm 0.06$.

effective dielectric constant of the medium surrounding graphene, $\alpha_G \simeq 2.2/\epsilon_m$, which gives $\epsilon_m = (\epsilon_r + 1)/2 \simeq 3.33 \pm 0.5$ and $\epsilon_r \simeq 5.67 \pm 1.0$. This value for the gate insulator dielectric constant is close to the one of $\epsilon_r = 5.4$ we estimated with our single-particle simulation in the previous section. On the hole side, v_F^* varies way less with carrier density : this may be the plateau that is expected to arise between $-2 < \nu < 2$ [163] as we discussed in Chapter 3.3.2.

On a side note, for carrier densities $0 < n < 3 \times 10^{11}$ cm^{-2} the fit of LL positions does not follow the theoretical Equation (2.12) so that we could not obtain v_F^* data points in this range. We already observed this problem in the previous section where our single-particle simulation underestimated the position of LL_0 around $\nu = 2$ while the other LLs were accurately obtained, which is consistent with the poor fit we obtain with the experimental data in this range of carrier density. Note also that LLs mostly tend to split in the transitions between plateaus, which decreases the precision on E_N, that we eventually computed as the mean of the split peak energies. Similar observations can be done for the other two samples.

We now deal with the Fermi velocity renormalization in both $hBN/SrTiO_3$ samples in Figure 5.17(b,c). Due to the strong reduction of $SrTiO_3$ dielectric constant on the electron side, we only focus on the hole side where we have a greater range of carrier density[10]. The fits of v_F^* using Equation (5.16) yield similar results for both samples : for BNGrSTO-STM-07 we obtain $v_F = (1.070 \pm 0.024) \times 10^6$ m.s^{-1} and $\alpha_G = 0.26 \pm 0.07$ and for AC23 we get $v_F = (0.972 \pm 0.014) \times 10^6$ m.s^{-1} and $\alpha_G = 0.30 \pm 0.06$. We observe an important decrease of the interaction parameter α_G in $hBN/SrTiO_3$ samples with respect to hBN/SiO_2 ones, by a factor more than 2. This is consistent with the screening of electron-electron interactions by the $SrTiO_3$ substrate which thus strongly mitigates the many-body renormalization of the Fermi velocity[11]. Table 5.4 sums up the α_G values for the three samples.

[10] Note that at charge neutrality, the Fermi velocity in sample BNGrSTO-STM-07 was determined in Figure 5.8 to be $v_F = 1.40 \times 10^6$ m.s^{-1}.

[11] With measurements of electron viscosity in the hydrodynamic regime, Kim *et al.* [260] observed in 2020 a similar strong reduction of electron-electron interactions in hBN-encapsulated graphene when placed in close proximity (a few nanometers) from a bottom screening metallic graphite gate ($\epsilon \to \infty$).

Sample	AC04	BNGrSTO-STM-07	AC23
Substrate	hBN/SiO_2	hBN/$SrTiO_3$	hBN/$SrTiO_3$
v_F ($\times 10^6$ m.s^{-1})	1.030 ± 0.009	1.070 ± 0.024	0.972 ± 0.014
α_G	0.66 ± 0.10	0.26 ± 0.07	0.30 ± 0.06

Table 5.4: Fit parameters of the Fermi velocity renormalization.

However note that these α_G values for $SrTiO_3$ samples are way higher than what we could have naively expected using the relation $\alpha_G \simeq 2.2/\epsilon_m$ with $\epsilon_m \sim 1000$. In order to obtain some quick justification of this observation, we should go back to the definition of the interaction parameter introduced in Chapter 1.3.3 as the ratio of the Coulomb potential to the kinetic energy $\alpha_G = E_C/E_K$. As we studied in Chapter 2.3.4.b, for samples on $SrTiO_3$ substrates we should rather consider the substrate-screened Coulomb potential $\mathcal{E}_C = E_C \times S(B)$ where the screening factor $S(B)$ takes into account the presence of the hBN spacer between graphene and $SrTiO_3$ and is given by Equation (2.93)[12]. We then introduce the substrate-screened interaction parameter $\mathfrak{A}_G$ for hBN/$SrTiO_3$ samples as :

$$\mathfrak{A}_G = \frac{\mathcal{E}_C}{E_K} \simeq S(B)\frac{2.2}{\epsilon_{BN}} \simeq S(B) \times \alpha_G \tag{5.18}$$

with α_G the interaction parameter for hBN/SiO_2 samples. For $B \gtrsim 10$T, we compute $S(B) \approx 0.6$ which gives a ratio between unscreened and substrate-screened interaction parameters consistent with the one we observe in our measurements.

Conclusion

We showed in this chapter the high quality of our hBN/SiO_2 and hBN/$SrTiO_3$ samples and were able to characterize the peculiar dielectric properties of the hBN/$SrTiO_3$ gate insulator. In the quantum Hall regime tunneling spectroscopy measurements unveiled well resolved Landau levels whose energies were in excellent agreement with theory, which enabled us to estimate the Fermi velocity. Landau levels were also seen to weakly disperse spatially, and an interaction-induced gap opened at charge neutrality as expected from quantum Hall ferromagnetism. The study of this gap is the topic of Chapter 7. Using the back-gate voltage to tune graphene carrier density allowed us to obtain LDOS gate map with gate-tunable Landau levels that formed typical staircase patterns due to the successive pinning of the Fermi level, which is another proof of the high quality of our devices. We notably performed a reverse engineering of the LDOS gate maps using numerical simulations. Finally, we extracted from these gate maps the renormalization of the Fermi velocity as a function of carrier density, and observed a reduction by a factor of 2 of the interaction parameter in hBN/$SrTiO_3$ devices with respect to the hBN/SiO_2 one, which is consistent with the substrate-screening of electron-electron interactions due to $SrTiO_3$.

Additional results are available in Appendix C, notably description of features in the LDOS gate maps such as charging peaks and orbital Landau level splitting.

[12]This relation has been obtained for hBN-encapsulated graphene devices, and thus may not be valid for our STM samples where graphene is exposed to both vacuum and the metallic tip.

Quantum Hall edge states spectroscopy

Chapter 6

After characterizing our graphene/hBN samples and studying the bulk Landau levels, we focus in this chapter on the evolution of the local density of states toward graphene edges and on the resulting physics of the edge states. Two similar works were realized on this topic, the first one by Li *et al.* in 2013 [209] for the native edges of graphene on graphite, whereas the second one by Kim *et al.* in 2021 [83] investigated a smooth gate-induced pn boundary in bulk hBN-encapsulated graphene on SiO_2.

Here we present the first tunneling spectroscopy at the native edges of graphene on its insulating hBN/SiO_2 substrate, which is a standard configuration for transport devices, such that our results yield a better comprehension of the edge transport physics in the quantum Hall regime.

We focus on sample AC04 (graphene/hBN/SiO_2) and all the measurements presented in this chapter were done at $T = 4\,\mathrm{K}$ and $B = 14\,\mathrm{T}$. The critical and challenging step consists in localizing the graphene edges and bringing a tip in STM mode at the very last nanometers of this conductive-to-insulating boundary. We notably show that the edge of the graphene sheet is lifted up by the tip interaction from its hBN substrate on a distance of around 10 nm from the edge. We study the evolution of the LDOS toward an armchair edge and show that the Landau level peaks vanish at the edges, as expected from an atomically sharp boundary, which we discussed in Chapter 2.2.2. In particular, this implies that the edge channels are squeezed in the last few magnetic length l_B from the boundary, with no edge reconstruction. We also discuss the charge accumulation at the armchair edge. Finally, we study using tight-binding simulations the Landau level edge dispersions of charge-neutral graphene ($\nu = 0$) for the different ground states discussed in Chapter 2.3.3.

Contents

6.1 Locating the edge of graphene on hBN

The precise localization of graphene edges on the insulating hBN substrate is an experimental challenge. We saw in Chapter 2.2.2 that LLs disperse at the edge on a scale of a few l_B, with $l_B \simeq 6.9$ nm at $B = 14$ T. Visualizing LL edge dispersion therefore requires to bring the tip in STM mode toward the very last nanometers from graphene edge, without losing the tunneling current on the insulating hBN where the tip would inevitably crash.

We first obtain a rough positioning of the graphene edge with an AFM image. Figure 6.1 shows an AFM mapping of the graphene flake of sample AC04 (hBN/SiO_2), with high-resolution images performed at $B = 14$ T of some graphene edges in overlay. These images reveal the vacuum annealing we did to clean graphene[1] left some resist residues that have migrated toward the edges where they have accumulated in a inhomogeneous way. Still some edges appeared to be clean, and we will focus in this chapter on two of them, labeled 1 and 2 in Figure 6.1.

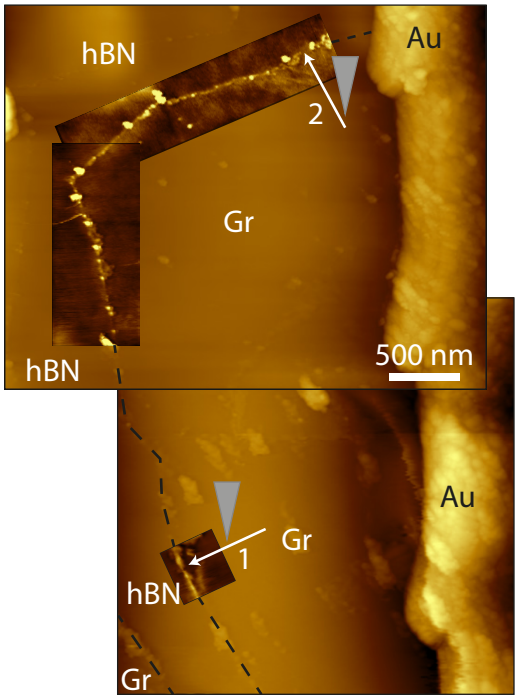

Figure 6.1: AFM mapping of sample AC04 (hBN/SiO_2) and graphene edges at $B = 14$ T. Two edges indicated by the white arrows are next approached by the tip in STM.

6.1.a Methodology to image graphene edge

We show in Figure 6.2(a) an AFM image of the edge of graphene labeled 1 in Figure 6.1. An accumulation of residues of a few nanometers high is well visible and enables us to locate roughly the edge. We focus on the area delimited by the yellow rectangle where residues are seemingly absent. We move the tip of around 20 nm toward bulk graphene and switch to STM mode. In this region the honeycomb lattice of graphene is easily resolved in constant current mode. We then use the constant height mode : before each STM image, we approach graphene in order to measure the setpoint tunneling current (typically 1 nA) and we next switch off the Z-regulation. This mode allows a safe imaging of graphene edge since the tip would not crash down on the insulating hBN, but would rather simply measure zero tunneling current.

[1] see Appendix B.5.

However this constant height mode makes the imaging extremely sensible to the tip-sample distance which varies due to the tilt of the sample. We therefore have to limit the scans to a few nanometers (typically $5 \times 5\,\mathrm{nm}^2$, and up to $20 \times 20\,\mathrm{nm}^2$ in some very flat regions) to ensure the sample tilt does not make the current vanish or diverge.

Starting from the bulk position we consecutively move the scan area toward the edge, see the yellow arrow in Figure 6.2(a), and image the honeycomb lattice in constant height mode. Note that we start this guiding step far away (typically 20 nm) from the edge because it is unlikely the position of the edge in STM coincides with the position obtained in AFM. Since the next objective is to perform tunneling spectroscopy all the way toward graphene edge, this guiding also enables us to know if residues are present or not : they would indeed hinder the imaging of the honeycomb lattice and make the tunneling current measured in constant height mode unstable. When we eventually reach the edge, the tunneling current on the left part of the STM image clearly vanishes due to the tip being atop hBN. However on the very graphene edge, the honeycomb lattice is not resolved and the tunneling current becomes unstable. Figure 6.2(b) shows such STM image, where the meaningful information is the measurement of a zero tunneling current (on hBN) or not (on graphene). This constitutes for now a quite precise estimation of the edge location. Using this image of the edge we can estimate its direction, as indicated by the dashed blue line in Figure 6.2(b). We report this line on the honeycomb lattice of the inset taken a few nanometers away and remark it coincides with an armchair orientation. We therefore conclude the boundary in Figure 6.2(b) is a graphene armchair edge.

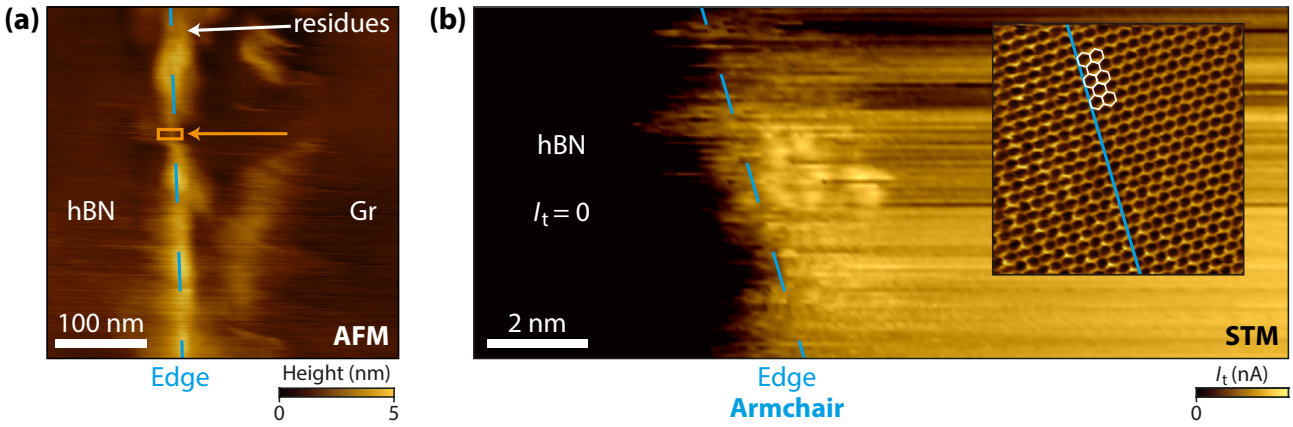

Figure 6.2: Locating graphene armchair edge. **(a)** $380 \times 380\,\mathrm{nm}^2$ AFM image at $B = 14\,\mathrm{T}$ of an edge of graphene on hBN in sample AC04, with an inhomogeneous accumulation of residues along it. **(b)** $16 \times 7\,\mathrm{nm}^2$ STM image in constant height mode of graphene edge in the yellow rectangle of (a). On the left side the tunneling current vanishes, indicating the tip is atop hBN. Inset : $5 \times 5\,\mathrm{nm}^2$ STM image of the honeycomb lattice a few nanometers away from the edge, from which we deduce the boundary is an armchair edge.

We believe the instability of the tunneling current measured on graphene while scanning across the edge arises from the lifting of the graphene sheet due to the electrostatic interaction with the tip (see Chapter 3.6.2), which makes the very edge of the graphene sheet unstable, being lifted from the hBN flake each time the tip scans over it. Indeed scanning on the right part only of Figure 6.2(b), without scanning over the edge, enables the imaging of the honeycomb lattice, see inset, although it was not visible on the overall image where the tip scanned over the edge.

We now consider the edge labeled 2 in Figure 6.1, where an AFM image shown in Figure 6.3(a) reveals a clean 65 nm long boundary devoid of visible residues. Notably, the red profile plotted in Figure 6.2(c) clearly features a step of 0.35 nm at the edge, which is consistent with

the theoretical thickness[2] of 0.34 nm of a graphene sheet. Notably, the second green profile displays a hump of 1Å at graphene edge, that we attribute to the lifting of the graphene sheet edge. A similar protocol as that done for the edge labeled 1 is used to image and locate the edge, see Figure 6.3(b). A $3 \times 3\,\mathrm{nm}^2$ image taken a few nanometers away from the edge unveils the honeycomb lattice. Reporting the dashed blue line on the inset makes it coincide with a zigzag, so that we infer the boundary is a graphene zigzag edge.

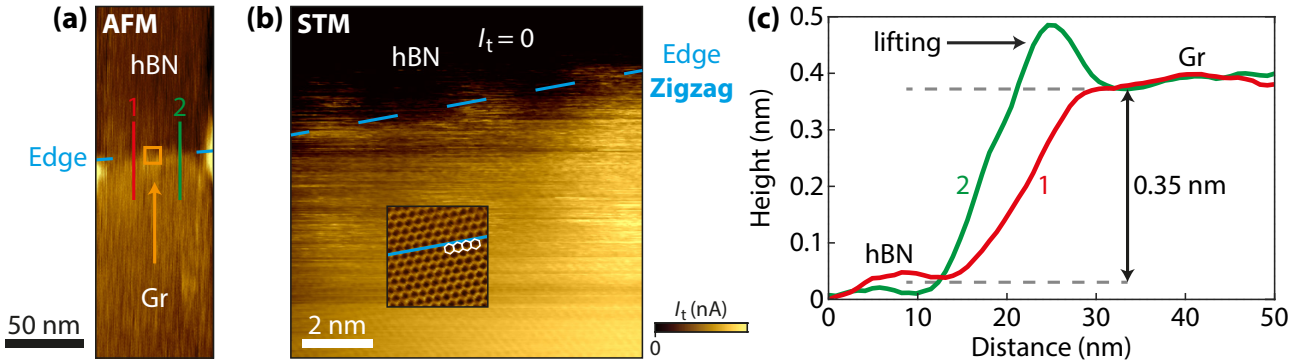

Figure 6.3: Locating graphene zigzag edge. **(a)** $75 \times 225\,\mathrm{nm}^2$ AFM image at $B = 14$ T of a second graphene edge in sample AC04, in a region devoid of visible residues, revealing a clean 65 nm long boundary. **(b)** $10 \times 10\,\mathrm{nm}^2$ STM image in constant height mode of graphene edge in the yellow rectangle of (a). On the top part the tunneling current vanishes, indicating the tip is atop hBN. Inset : $3 \times 3\,\mathrm{nm}^2$ STM image of the honeycomb lattice a few nanometers away from the edge, from which we infer the boundary is a zigzag edge. **(c)** Height profiles in AFM for the red and green lines across the zigzag edge from (a). The red profile confirms the graphene step of 0.35 nm. The green profile unveils the lifting while scanning of the edge on a height of 1 Å.

6.1.b Complementary method and tip-induced lifting of graphene edge

We discuss here another way to precisely locate the edge. We perform a CITS to measure the spatial dispersion of the LL spectrum toward the boundary. The grid is set to start far away in graphene bulk and to finish a few nanometers beyond the edge, previously located with STM images. Moreover, the slow axis direction of the grid is chosen to be perpendicular to the edge. A safety condition is added to the Z-controller to prevent the tip from crashing into hBN : if the Z-position of the tip goes below a threshold (typically 3 nm below the Z-position of the tip estimated close to the edge), the tip is withdrawn and the CITS ends.

We show in Figure 6.4(a) the topographic map $z(d_{\mathrm{edge}}, y)$ obtained from one CITS toward the graphene armchair edge located in Figure 6.2. d_{edge} is the distance from the armchair edge, whose origin will be determined afterward, while y is the lateral coordinate parallel to the edge. The topographic map features a clean and flat bulk graphene on a $80 \times 10\,\mathrm{nm}^2$ next to the edge. When the tip is situated a few nanometers away from the edge, the $z(d_{\mathrm{edge}}, y)$ map reveals inhomogeneous bright spots. Though one can first think about residues, the small height of these spots, around $1 - 3$ Å, rules out this hypothesis.

We rather attribute these large spots to the lifting of the edge of the graphene sheet, see Figure 6.4(d). As we saw in Chapter 3.6.2, the attractive van der Waals force of the tip was shown by Georgi *et al.* [187] to lift locally a graphene sheet lying on a SiO_2 substrate on a typical height of 1 Å. Although we do not observe such lifting in Figure 6.4(a) in bulk graphene

[2]Actually, this is the distance between monolayer graphene sheets in graphite.

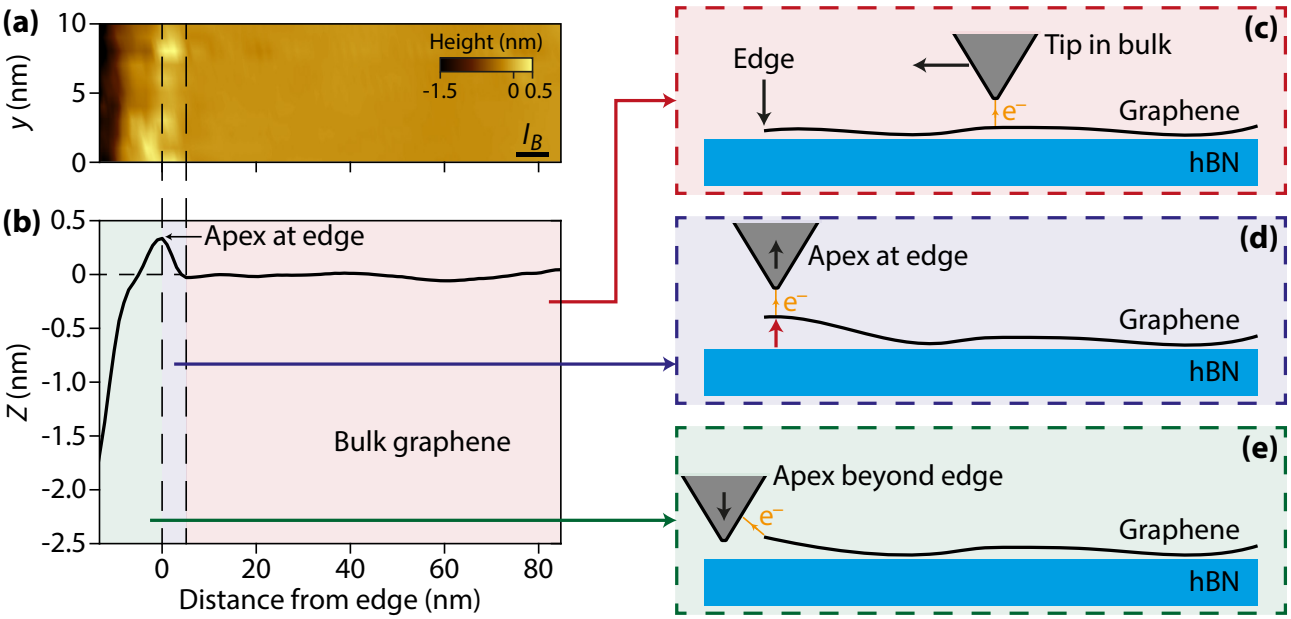

Figure 6.4: CITS toward graphene edge : edge localization. **(a)** $z(d_{\text{edge}}, y)$ topographic map and **(b)** $z(d_{\text{edge}})$ profile obtained with a CITS toward the armchair edge and beyond. We distinguish three regimes : the flat horizontal profile (red area) where the tip tunnels in bulk graphene, see **(c)**, the sharp increase of z (blue region) where the tip apex tunnels very close to the edge and where the sheet is strongly lifted, see **(d)**, and the decrease of z when the tip apex is moved outside the graphene sheet, where a residual tunneling happens between the edge of graphene and a side point of the tip, see **(e)**, preventing the tip from crashing into hBN. The edge position is taken at the position of the maximum of the topographic profile.

(either because the deformation follows the tip such that we eventually observe an overall flat background, or because the deformation of the graphene sheet on hBN is more difficult, since the adhesion interactions between both materials are more important due to their similar atomic structure [261]), we can assume the sheet is more easily deformed by the force of the tip at the edge and therefore the lifting is larger than in the bulk[3].

The lifting of the edge is well visible in the height profile of Figure 6.4(b), obtained by averaging the topographic map on the lateral dimension (parallel to the edge). The Z profile features a flat region corresponding to bulk graphene (with variations of less than 1 Å). When the tip reaches the edge, a hump appears in the Z profile due to the lifting of the edge, here on a height of 3 Å. After that, the tip quickly moves down of several nanometers until it meets the safety condition of the Z controller, which stops the CITS. We attribute this lowering of the Z position to the fact that the tip apex has gone beyond the edge of graphene, but tunneling remains possible with some other higher points close to it, see Figure 6.4(d). This makes the measurement of a tunneling current possible even when the apex itself is lying on hBN, yet this current is highly unstable and the tunneling spectra acquired in this situation are meaningless.

From this model we assume the position of the edge of graphene (i.e. the tip apex is atop the edge) is therefore given by the maximum of the hump in the Z profile, and from this origin we compute d_{edge} the distance from the edge that we use in the following figures.

[3]Consider the boundary conditions : the tip-induced deformation in the bulk of the sheet is radially constrained - the deformation must tend to zero asymptotically in the whole (x, y) plane - while at the edge the deformation is only constrained in the half-plane corresponding to the bulk.

6.2 Landau level edge dispersion spectroscopy

We show in this section the first tunneling spectroscopy of Landau levels at the edge of graphene on hBN. The results presented here were obtained at the armchair edge located in Figure 6.2 on which we focused our measurements.

6.2.1 LDOS evolution toward an armchair edge

We consider the tunneling conductance matrix $G(d_{\text{edge}}, y, eV_{\text{bias}})$ obtained by performing a CITS toward the graphene armchair edge, with the distance from the edge d_{edge} defined previously and y the coordinate parallel to the edge. We obtain the LDOS map $G(d_{\text{edge}}, eV_{\text{bias}})$ by averaging the tunneling spectra on the lateral dimension y. Such edge dispersion map is shown in Figure 6.5 for sample AC04 (hBN/SiO_2) at $B = 14\,\text{T}$, where we went down to 3 nm from the edge. We chose a back-gate voltage $V_g = -5\,\text{V}$ to bring graphene to charge neutrality, using a LDOS gate map at $B = 14\,\text{T}$. On the right side of the map, in bulk graphene, LLs are well resolved, as well as the two peaks of the LL_0 and the interaction-induced gap between.

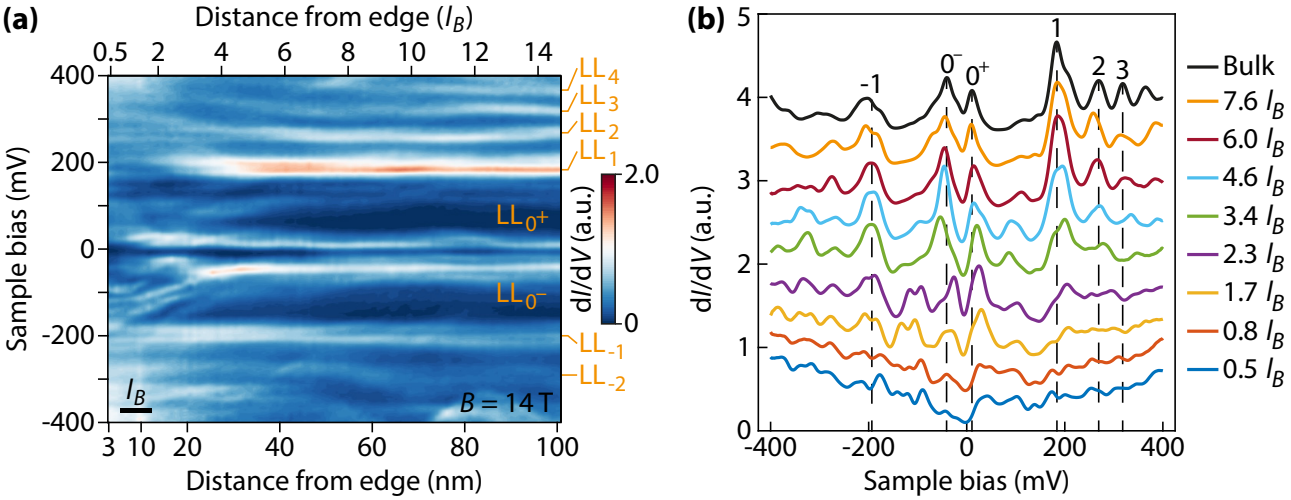

Figure 6.5: CITS toward graphene edge : LDOS spatial evolution. **(a)** $\mathrm{d}I_t/\mathrm{d}V_{\text{bias}}$ spectra as a function of the distance from graphene armchair edge, revealing the absence of visible LL bending when approaching the edge, but rather the continuous vanishing of LLs. **(b)** $\mathrm{d}I_t/\mathrm{d}V_{\text{bias}}$ spectra from (a) taken at different distances from the edge, in units of l_B. Bulk LLs are indexed and are seen to disappear when getting closer to the edge.

The first striking observation is the absence of visible LL bending upon approaching the edge. In fact we rather observe a continuous vanishing of LLs, such that the tunneling spectra measured in the last nanometers from the edge feature no LLs but a V-shape-like form. Notably, the lesser the Landau index N, the closer to the edge LL_N vanishes, which is characteristic of a crystallographic edge. For instance, LL_0 disappears at a distance around $2\,l_B$ from the edge.

As we mentioned in Chapter 3.7.2, similar observations were made by Li *et al.* [209] for graphene on conductive graphite, see Figure 3.19. On the contrary, this greatly differs from what Kim *et al.* [83] observed at a pn junction in bulk graphene, where a smooth dispersion of LLs occurs at the boundary on a scale of $150\,\text{nm} = 19\,l_B$ at $B = 10\,\text{T}$, see Figure 3.17.

Moreover note that the LL_0 gap does not close at the edge, indicating edge excitations in graphene/hBN/SiO_2 samples at charge neutrality are gapped, which is consistent with transport measurements and the observation of an insulating state at $\nu = 0$, see Figure 2.22.

Theoretical model In order to understand the apparent absence of LL band bending, we must consider the bandstructures studied in Chapter 2.2.2, where the LLs theoretically disperse at the edge on a distance of a few l_B only. However, one must remember that the LDOS measured with STS depends not only on the energy but also on the wave function :

$$\rho(\boldsymbol{r}, E) = \sum_{N,\xi=\pm 1} \left|\Psi_N^{\xi K}(\boldsymbol{r})\right|^2 \delta(E - E_N) \tag{6.1}$$

where $\Psi_N^{\xi K}$ are introduced in Chapter 2.1.2. The wave functions feature a spatial extent on the order of the cyclotron radius R_c given by Equation (2.24) and which scales as l_B and $N^{1/2}$. This scaling has an important consequence for the edge spectroscopy since the edge dispersion is theoretically expected to happen on this same length scale l_B [92] : when probing the edge states with the tip, we also probe states at a distance up to R_c, namely bulk states mainly - with large degeneracy, i.e. larger DOS - as well as other surrounding edge states, see Figure 6.6.

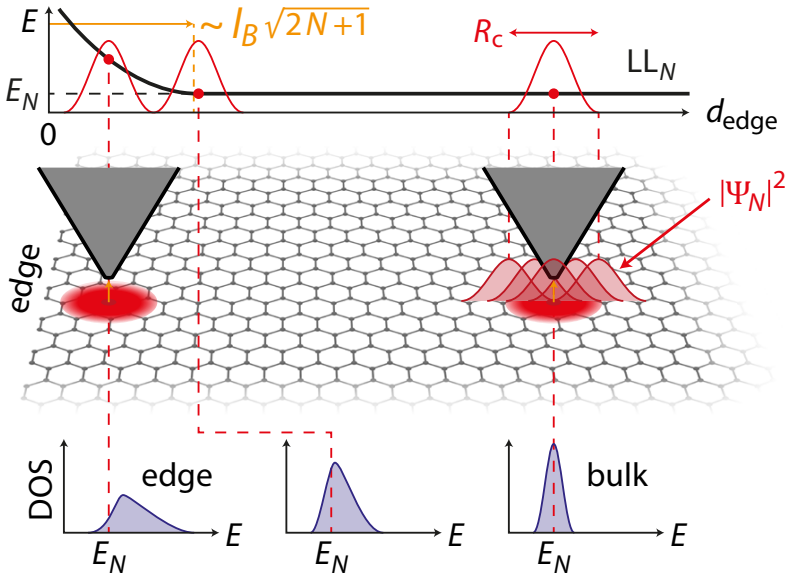

Figure 6.6: Probing edge states and bulk contribution. Due to the spatial extent $R_c = l_B(2|N|+1)^{1/2}$ of the LL_N wave functions Ψ_N, the tip probes at one point contributions from all states up to distances of about R_c (red gaussians in the top panel). In the bulk those states all have the same energy E_N, and the measured DOS (bottom panels) features a peak at this bulk energy. When approaching the edge, at a distance $d_{edge} \sim R_c$, the tip starts to probe more and more edge states at $E > E_N$ overlapping with the highly-degenerate bulk states and the LL_N peak in the DOS sees its spectral weight being redistributed toward higher energies.

Because of the resulting large contribution of the bulk states to the LDOS at the edge, LL peaks are not seen to disperse but rather stay at the bulk energies E_N. Nonetheless, getting closer to the edge, we probe less and less bulk states but more and more edge ones. The weight of the bulk states at energy E_N thus decreases whereas the weight of the edge states at energies greater than E_N increases : in other words, the edge dispersion is eventually observed in tunneling spectroscopy as a redistribution of the spectral weight of the LL peaks from lower to higher energies, and the LL peaks become broader and broader before they vanish close to the edge. Note that the greater the Landau index N, the further away from the edge this redistribution of the spectral weight happens, due to the scaling of the cyclotron radius as $N^{1/2}$.

Consequence on edge channels Our results shown in Figure 6.5 eventually imply that edge channels in graphene on hBN are squeezed in the last few l_B from the edge. In particular, this atomically sharp confinement potential induced at the edge leaves no room for edge reconstruction as described in GaAs by Chklovskii *et al.* [75] (see Chapter 2.2.1).

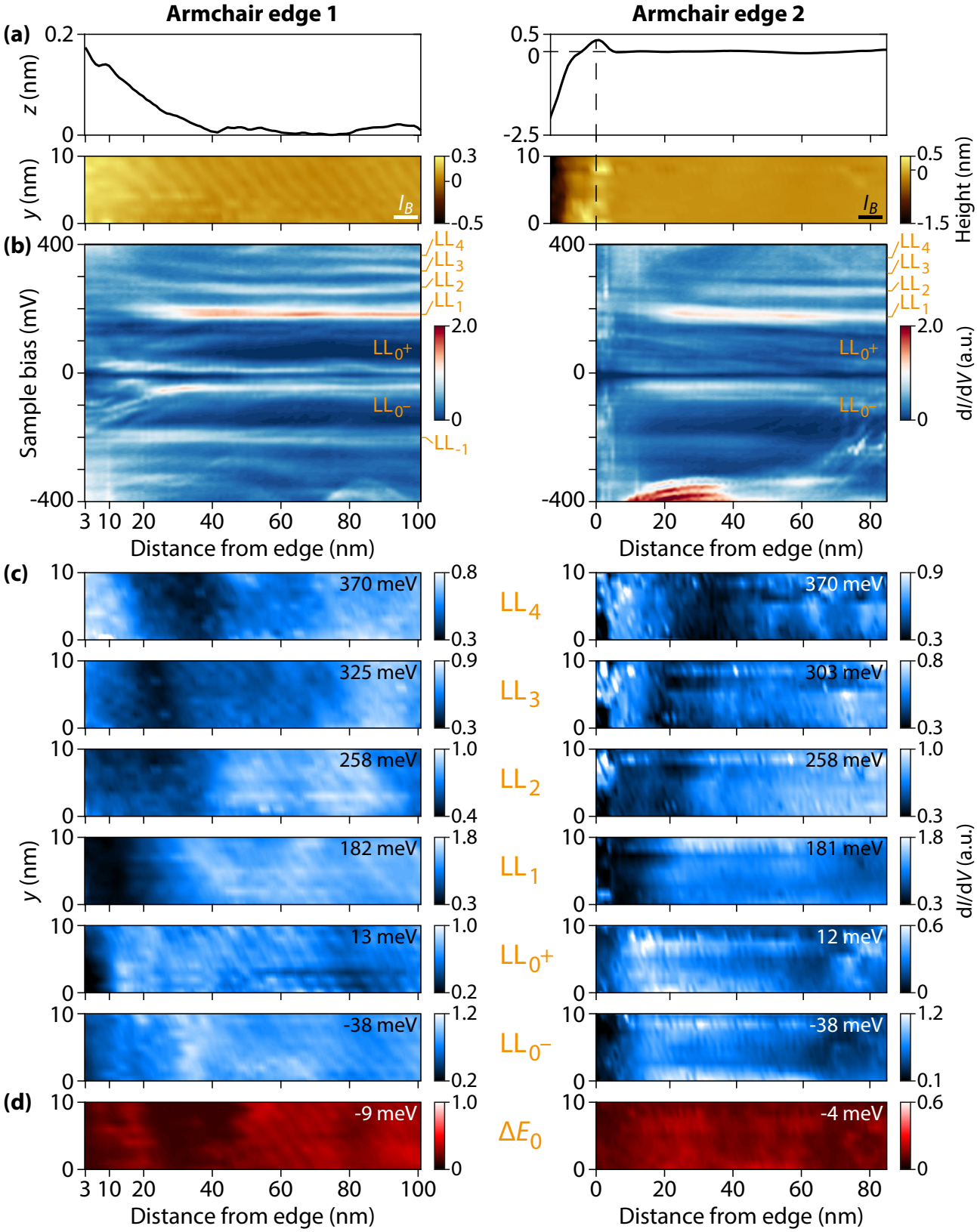

Figure 6.7: LL spectroscopy toward armchair edges 1 and 2. **(a)** Topographic profile $z(d_{\text{edge}})$ and map $z(d_{\text{edge}}, y)$ of graphene edge ($l_B = 6.85\,\text{nm}$ at $B = 14\,\text{T}$). **(b)** LDOS$(d_{\text{edge}}, eV_{\text{bias}})$ spatial evolution toward the edge. **(c)** LDOS$(d_{\text{edge}}, y, eV_{\text{bias}} = E_N)$ spatial maps for different LL energies. **(d)** $\nu = 0$ gap depth spatial map.

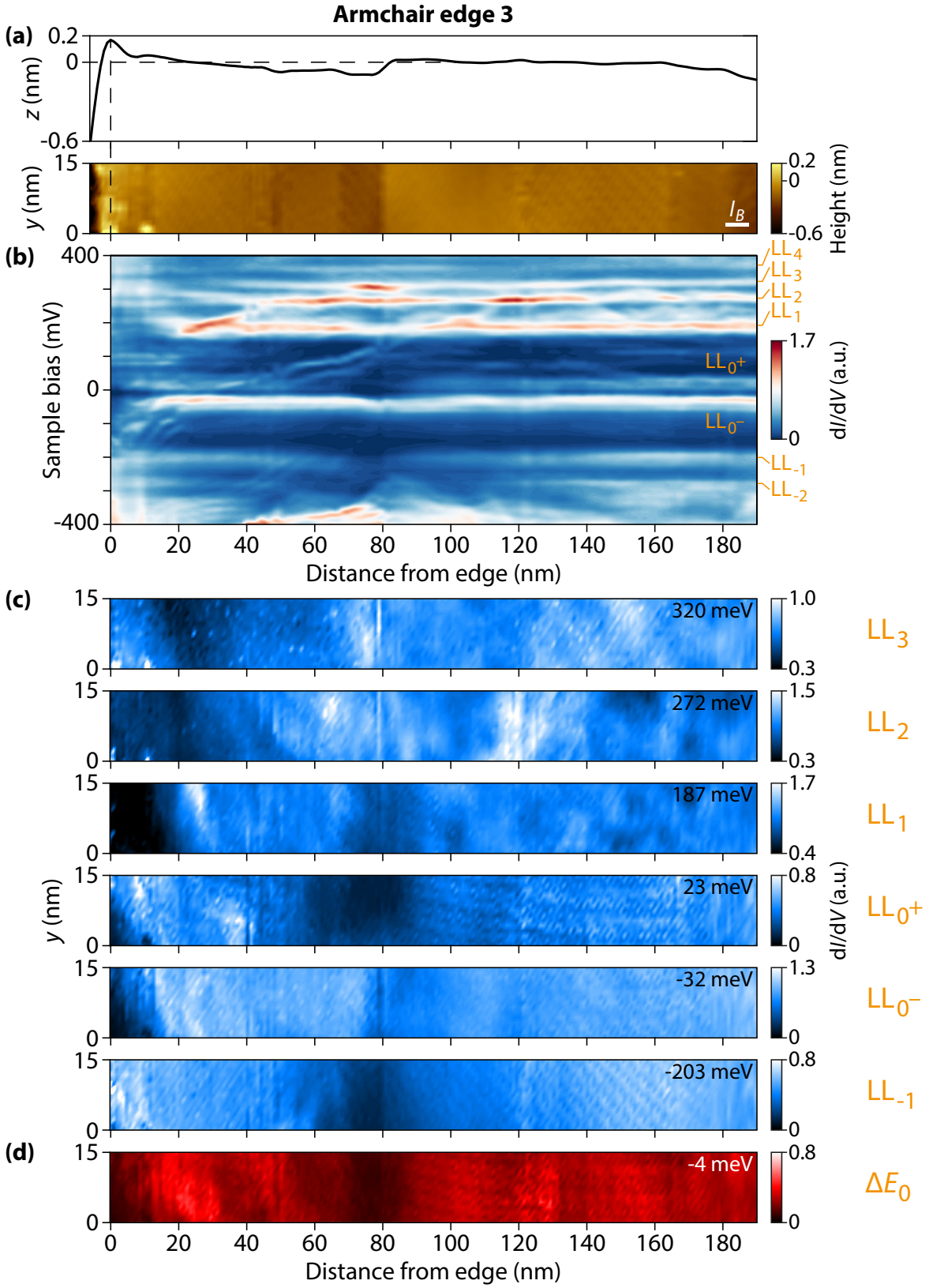

Figure 6.8: LL spectroscopy toward armchair edge 3. **(a)** Topographic profile $z(d_{\text{edge}})$ and map $z(d_{\text{edge}}, y)$ of graphene edge ($l_B = 6.85$ nm at $B = 14$ T). **(b)** LDOS$(d_{\text{edge}}, eV_{\text{bias}})$ spatial evolution toward the edge. **(c)** LDOS$(d_{\text{edge}}, y, eV_{\text{bias}} = E_N)$ spatial maps for different LL energies. **(d)** $\nu = 0$ gap depth spatial map.

6.2.1.a Spatial evolution of the LDOS

We show in Figures 6.7 and 6.8 CITS measurements at $B = 14\,\mathrm{T}$ and $\nu = 0$ at the armchair edge of Figure 6.2, with a distance of a few tens of nanometers along the edge between each CITS. The three studied edges are indexed 1, 2 and 3 in the figures, with the edge 1 the one featured in Figure 6.5. The grids of the CITS have a size of $100 \times 10\,\mathrm{nm}^2$ for Figure 6.7 and $200 \times 15\,\mathrm{nm}^2$ for Figure 6.8, with the lateral size greater than $l_B = 7\,\mathrm{nm}$, and are set to be parallel to the edge. The spatial resolution for the three CITS is 1 nm in both directions.

For each figure, the panels (a) show the topographic map $z(d_{\mathrm{edge}}, y)$ and the topographic profile $z(d_{\mathrm{edge}})$ obtained by averaging the map on the lateral dimension. Bulk graphene appears flat and clean, with a corrugation at most of 1 Å on a distance of 190 nm for edge 3. When approaching the edge on the left, $z(d_{\mathrm{edge}})$ increases by around $2-3$ Å due to the tip-induced lifting of the graphene sheet edge, before drastically decreasing. The maximum of $z(d_{\mathrm{edge}})$ gives the position of the edge where $d_{\mathrm{edge}} = 0$. For edge 1 the CITS grid did not go beyond the edge : the edge position is rather roughly estimated using the STM image in Figure 6.2.

The panels (b) show the LDOS$(d_{\mathrm{edge}}, eV_{\mathrm{bias}})$ evolution toward the armchair edges. The same qualitative observations can be made for the three edges : LLs do not disperse when approaching the edges but vanish. The splitting of the LL_0 is well visible and the gap stays open down to the edge where it even gets more pronounced.

In panels (c) we show LDOS$(d_{\mathrm{edge}}, y, eV_{\mathrm{bias}} = E_N)$ spatial maps at different bulk LL energies E_N. We first notice the spatial homogeneity of the area on a lateral scale of $1.5\,l_B$ for edges 1 and 2 and of $2.2\,l_B$ for edge 3. We also clearly observe the decrease of the height of the LL peaks when approaching the edge, with the map of the left part becoming darker, due to lower LDOS. The lower the Landau index N the closer to the edge the peak decreases in amplitude and the more abrupt the vanishing. Note nonetheless that an apparent increase of the LDOS happens at

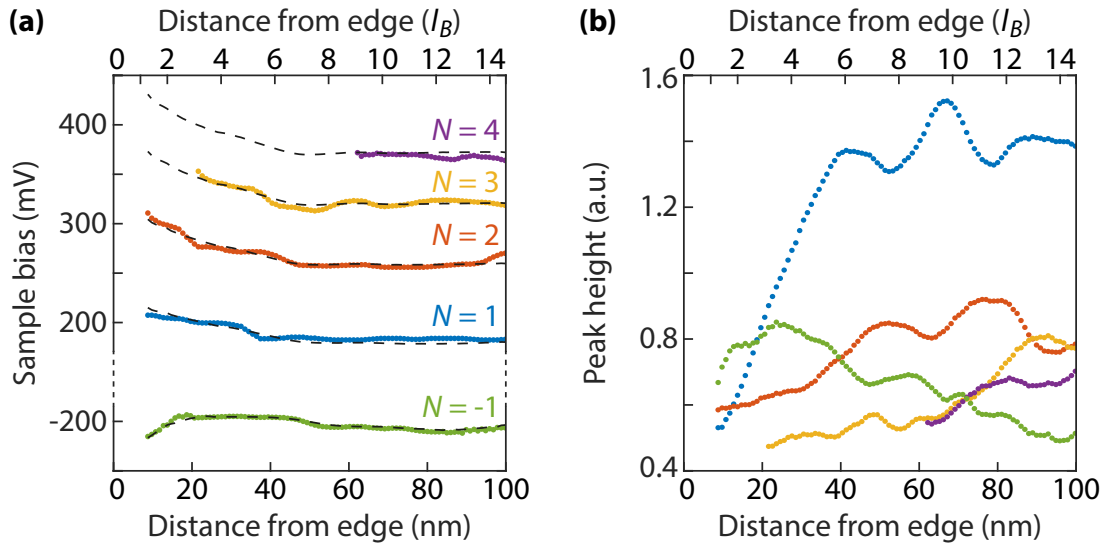

Figure 6.9: Evolution of LL peak positions and heights toward the armchair edge. **(a)** Peak position for LL_N as a function of the distance from the edge, extracted from the LDOS edge map in Figure 6.5. The dashed lines are the fitting curves given by Equation (5.6) using the parameters v_{F}^* and E_{D} obtained in Figure 6.10. **(b)** Peak height for the same LL_N (same color code). The redistribution of the spectral weight toward higher energies induces a weak dispersion of the LL peaks that coincides with the decreasing of the peak height.

the edge for LL_3 and LL_4. This is because of the V-shape background of the LDOS at the edge, which emerges due to the redistribution of the spectral weight of the LL peaks toward higher energies, background that becomes comparable in amplitude to those of the bulk LL_3 and LL_4 peaks.

Moreover, we remark the presence of steps in bulk graphene in Figure 6.8 evolving parallel to edge 3. The higher step occurring at $d_{\text{edge}} \simeq 80$ nm is 1 Å high, thus smaller than monolayer hBN step by a factor 3. We therefore attribute these small steps to the variations of the tip-induced lifting of the graphene sheet. Notably, these steps are also well visible in the LDOS spatial maps in panel (c), see for instance the steps at $d_{\text{edge}} \simeq 80$nm and at $d_{\text{edge}} \simeq 120$nm.

Finally, in panels (d) we show the LDOS spatial map at zero bias, that is, the DOS in the middle of the LL_0 gap. For the three CITS, the upper bound of the color bar is chosen as the lowest amplitude out of both bulk LL_0 peaks, while the lower bound is set to 0 : we thus map the depth of the LL_0 gap. We observe here as well a spatial homogeneity of the gap depth, with the gap becoming more pronounced (darker red areas in the maps) at the armchair edges as well sometimes in bulk graphene due to a local increase of the LL_0 splitting. In particular we do not see the LL_0 gap closing at any point toward the edge, which would have appeared as a white area in the maps. This is again consistent with the observation of gapped edge excitations in charge-neutral graphene.

We now consider once more the LDOS edge map shown in Figure 6.5 (armchair edge 1). We plot in Figure 6.9(a) the evolution of the positions E_N of the visible LL_N peaks and in Figure 6.9(b) the evolution of their height as a function of the distance from the edge. The amplitude of the LL peaks decreases as we approach the edge until it becomes comparable to the V-shape background which gradually grows at the edge, where LL peaks are no longer visible. In particular, LL_4 vanishes at $9\,l_B$ from the edge, LL_3 at $3\,l_B$ whereas LL_2 and $LL_{\pm1}$ disappear at l_B from the edge. The amplitude of LL_1 also vanishes way faster than the other LL_N of higher index N. If the peak vanishing at the edge is the main feature we observe in our measurements, we can also notice in Figure 6.9(a) a weak dispersion toward higher energy of the

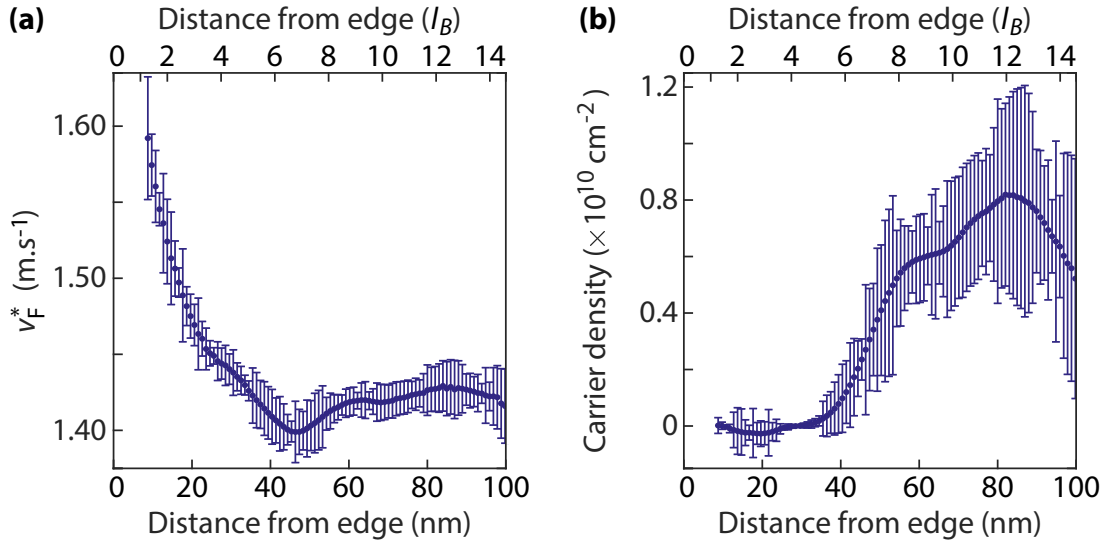

Figure 6.10: Evolution of the Fermi velocity and carrier density toward armchair edge, obtained with the fit of LL_{-1}, LL_1, LL_2, LL_3 and LL_4 positions (when visible). **(a)** The Fermi velocity v_F^*, renormalized in bulk at $\nu = 0$, increases toward the edge. **(b)** Carrier density n computed using Equation (5.5) and the Dirac point position E_D obtained from the fit. n presents a residual bulk value of $n_0 \approx 7 \times 10^9$ cm^{-2} and vanishes from 40 nm from the edge.

LL_N positions close to the edge (on a length of around $6\,l_B$ from the edge), resulting from the fact that we probe less bulk states and more edge states of higher energies. Those observations are similar to those of Li *et al.* [209] for graphene on graphite. We then fit the positions E_N of LL_N at each d_{edge} (for every visible LL at this point) with respect to Equation (5.6) to extract the Fermi velocity v_{F}^* and the Dirac point position E_{D} as a function of d_{edge}. These results are shown in Figure 6.10, where E_{D} was converted into the carrier density n using Equation (5.5). We retrieve a bulk value of the Fermi velocity $v_{\text{F,bulk}}^* = 1.42 \times 10^6$ m.s^{-1} consistent with the value at charge neutrality of the renormalized Fermi velocity in sample AC04, see Figure 5.17(a). Below $7\,l_B$ the Fermi velocity starts to diverge toward the armchair edge due to the weak dispersion of the LL peaks we observed, reaching $v_{\text{F,edge}}^* = 1.6 \times 10^6$ m.s^{-1} at l_B from the edge. As for the carrier density, we obtain a residual value of $n_0 \approx 7 \times 10^9$ cm^{-2} in bulk graphene. Below 60 nm the density is seen to decrease and eventually vanishes at 40 nm $= 5\,l_B$ from the edge. Li *et al.* [209] observed a similar decreasing of the density with respect to its bulk value from around l_B from graphene edge on graphite. We will go back to this result later when discussing charge accumulation at the edge. Finally, we use the $v_{\text{F}}^*(d_{\text{edge}})$ and $E_{\text{D}}(d_{\text{edge}})$ parameters to plot in Figure 6.9(a) the fitting curves in black dashed lines for each LL. We notice a good agreement with the experimental points, especially for the dispersing parts.

6.2.1.b LDOS gate maps toward the edge

We show in Figure 6.11 three LDOS gate maps at different distances from the armchair edge. The first one in Figure 6.11(a) was measured at $d_{\text{edge}} = 36$ nm where we retrieve the graphene bulk case with the typical staircase pattern of the LLs. Note also the opening of the LL_0 gap between $V_{\text{g}} = -6$ V and $V_{\text{g}} = -4.2$ V. The second LDOS gate map in Figure 6.11(b) was performed closer to the edge at $d_{\text{edge}} = 16$ nm. If the staircase pattern is still well observable, it also appears less defined. When considering the individual spectra in Figure 6.11(d) we remark the LL peaks are broader, consequence of their spectral weight redistribution. Eventually in the third LDOS gate map in Figure 6.11(c) realized at $d_{\text{edge}} = 5$ nm, the LL staircase pattern is barely visible due to the vanishing of the LL peaks at the edge, while the LLs in the individual spectra in Figure 6.11(f) can not be identified. Note that we can still resolve the LL_0 gap as indicated by the red dashed lines. Furthermore new bright peaks grow close to the edge, indicated by purple arrows in Figure 6.11(c,e,f). They disperse with a positive slope similarly to charging peaks, and eventually become predominant at the edge while washing out the LLs.

6.2.2 Charge accumulation at the edge

In this section we study the possible evolution of the carrier density n when approaching the graphene armchair edge. Silvestrov *et al.* [213] showed that a charge accumulation shall occur at graphene edges over a length l_{a} comparable to the thickness of the gate insulator, in our case $d_{SiO_2} + d_{BN} \simeq 300$ nm, due to electrostatic fringing effect of the back-gate electric field on the edge of graphene. This reveals to be an important topic since such accumulation at the edge may induce the appearance of additional edge channels.

6.2.2.a CITS toward the edge at $\nu = 0$

Such variations of carrier density at the edge should in principle be easy to observe in STS since it would translate into a dependence of the Dirac point position with the distance from the edge : $E_{\text{D}} \longmapsto E_{\text{D}}(d_{\text{edge}})$. However such a behavior is not noticeable in the three CITS at the graphene armchair edge shown in Figures 6.7 and 6.8, where LLs do not shift in energy while approaching the edge on a scale of 200 nm. In Figure 6.10(b) we computed the evolution of the carrier density as a function of the distance from the edge $n(d_{\text{edge}})$ for armchair edge 1 :

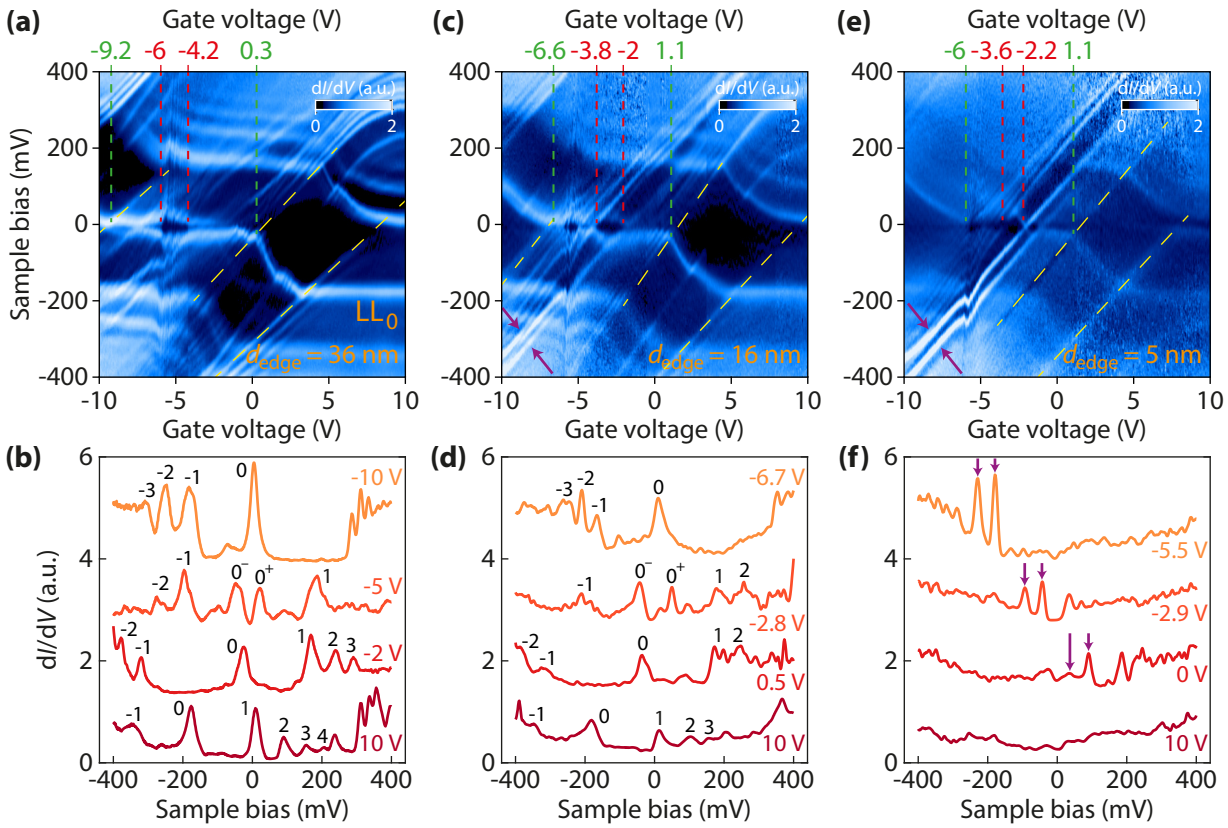

Figure 6.11: LDOS gate maps toward armchair edge 1. **(a)** $\mathrm{d}I_\mathrm{t}/\mathrm{d}V_\mathrm{bias}$ gate map as a function of sample bias and gate voltage for sample AC04 at $B = 14$ T in bulk graphene ($d_\mathrm{edge} = 36\,\mathrm{nm} = 5.3\,l_B$) where we retrieve the typical staircase patterns of LLs. **(b)** $\mathrm{d}I_\mathrm{t}/\mathrm{d}V_\mathrm{bias}$ spectra taken from (a) at different gate voltages. Landau levels are indexed. **(c)** Same than (a) but closer to the armchair edge ($d_\mathrm{edge} = 16\,\mathrm{nm} = 2.3\,l_B$). **(d)** $\mathrm{d}I_\mathrm{t}/\mathrm{d}V_\mathrm{bias}$ spectra taken from (c) at different gate voltages. **(e)** Same than (a) but close to the armchair edge ($d_\mathrm{edge} = 5\,\mathrm{nm} = 0.7\,l_B$). The LL pattern vanishes while bright peaks (indicated by purple arrows) grow and disperse similarly to charging peaks. **(f)** $\mathrm{d}I_\mathrm{t}/\mathrm{d}V_\mathrm{bias}$ spectra taken from (e) at different gate voltages. The peaks labeled by purple arrows correspond to the labeled ones in (e).

only a weak variation of $\delta n \approx 7 \times 10^9\ \mathrm{cm}^{-2}$ between bulk and edge is obtained, corresponding to a negligible variation of filling factor $\delta\nu = 0.02$ at $B = 14$ T.

We show in Figure 6.12 another CITS toward graphene armchair edge but on a larger scale of 300 nm, which is comparable to the length l_a where the charge accumulation should occur, yet no significant shift in energy of LLs as we approach the edge is visible.

Nonetheless, these CITS were done at $\nu = 0$ where the Fermi level is pinned inside LL_0. As we studied in Chapter 5.3.2, only a variation of the carrier density δn that would induce a variation of the filling factor $\delta\nu = \pm 2$, where E_F would transit from LL_0 to either $\mathrm{LL}_{\pm 1}$, could be observable in such measurements. This yields a lower limit to the density variation $\delta n_\mathrm{min} < \delta n$ between the bulk (set at $\nu = 0$) and the armchair edge that we can detect in STS. This minimal value is defined by half of the degeneracy of LL_0 - which depends on the magnetic field, see Equation (2.16) :

$$\delta\nu = 2 \quad \Longleftrightarrow \quad \delta n_\mathrm{min}(B) = 4.8 \times 10^{10}\ \mathrm{cm}^{-2} \times B[\mathrm{T}] \tag{6.2}$$

We give in Table 6.1 values of δn_min for different typical values of the magnetic field B. As a consequence, our LDOS edge maps obtained at $\nu = 0$ and $B = 14$ T give an upper limit for a possible charge accumulation which can not be greater than $\delta n_\mathrm{min} = 6.77 \times 10^{11}\ \mathrm{cm}^{-2}$.

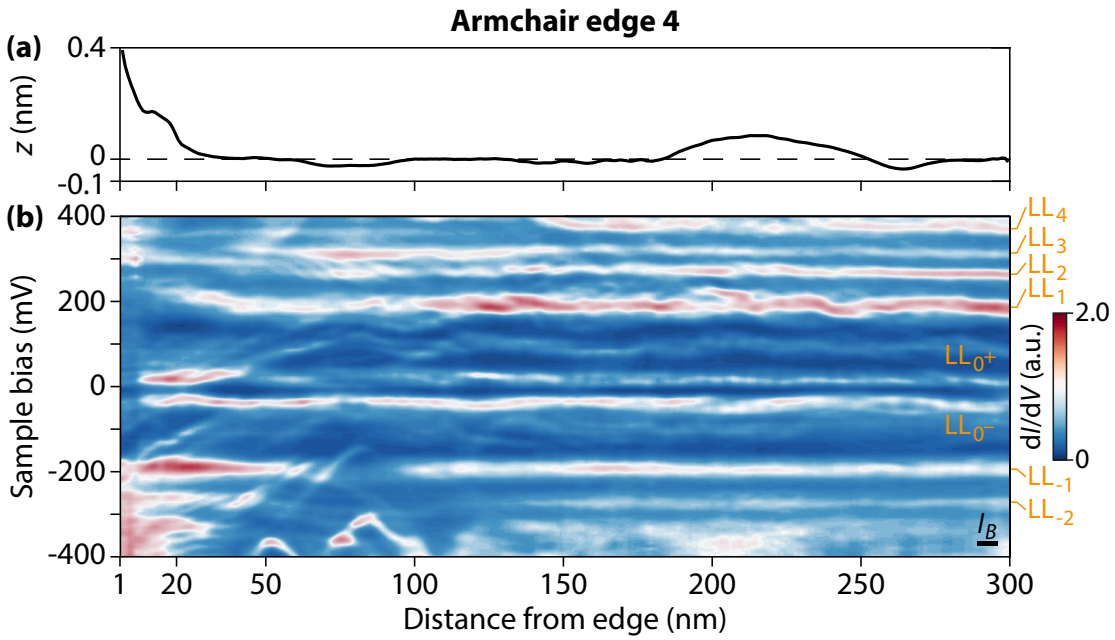

Figure 6.12: LL spectroscopy toward armchair edge 4. (a) Topographic profile $z(d_{\text{edge}})$ of graphene edge ($l_B = 6.85$ nm at $B = 14$ T). **(b)** LDOS spatial evolution toward the edge.

B (T)	1	3	5	7	14
δn_{min} ($\times 10^{11}$ cm^{-2})	0.48	1.45	2.42	3.39	6.77

Table 6.1: Minimal value δn_{min} of the variation of the density (corresponding to a change of $\delta\nu = 2$) that one can observe in STS with graphene at $\nu = 0$, for different magnetic fields B.

6.2.2.b LDOS gate maps toward the edge

In order to obtain a better quantitative result, let us consider again the LDOS gate maps shown in Figure 6.11 at different distances from the edge, which enables us to characterize the evolution of the charge-neutrality point V^{CNP} of graphene toward the armchair edge. We clearly observe in the three maps the opening of the interaction-induced gap of LL_0 at about $V_g \approx -5$ V, which is maximum at $\nu = 0$ due to the enhancement by exchange interactions (see Chapter 3.2). We estimate V^{CNP} at the middle of the range of gate voltage V_g where the gap is seen to increase and then decrease (red dashed lines), value at which the gap is also maximum. For Figure 6.11(a) at $d_{\text{edge}} = 36$ nm we obtain $V^{\text{CNP}}_{\text{bulk}} = (-5.1 \pm 0.9)$ V. This value is similar to the ones we already obtained in bulk graphene in the previous Chapter - at zero magnetic field, see Figure 5.3, and at $B = 5$ T, see Figure 5.10.

We further extract from additional LDOS gate maps realized at distances from the edge up to $d_{\text{edge}} = 500$ µm charge-neutrality points close to -5 V, such that no significant carrier density spatial variations (other than disorder fluctuations[4]) down to $d_{\text{edge}} = 25$ nm has been observed in LDOS gate maps, see Figure 6.13(a).

[4]Let us estimate the typical spatial variations of the charge-neutrality point induced by disorder. Considering Figure 5.6(f), we see that on an area of 100×100 nm^2 the density features spatial variations of $\delta n^{\text{dis}} \simeq 1.5 \times 10^{10}$ cm^{-2}. This therefore yields a variation of $\delta V^{\text{CNP}}_{\text{dis}} \simeq 0.2$ V. However it is still possible that one observes slightly greater variations on larger scales of several hundreds of nanometers.

Close to the armchair edge, in Figures 6.11(c,e), we observe a clear shift of the charge-neutrality point (and of the whole LL staircase pattern) toward higher gate voltages. We estimate $V_{\text{edge}}^{\text{CNP}} = (-2.9 \pm 0.9)$ V at $d_{\text{edge}} = 16$ nm and $V_{\text{edge}}^{\text{CNP}} = (-2.9 \pm 0.7)$ V at $d_{\text{edge}} = 5$ nm, hence a shift from bulk to edge of :

$$\delta V_{\text{b}\to\text{e}}^{\text{CNP}} = (2.2 \pm 1.6)\ \text{V} \tag{6.3}$$

The positive sign of $\delta V_{\text{b}\to\text{e}}^{\text{CNP}}$ means that there is a hole accumulation at the armchair edge which induces a negative density variation from bulk to edge of [5] :

$$\delta n_{\text{b}\to\text{e}} = (-1.5 \pm 1.1) \times 10^{11}\ \text{cm}^{-2} \tag{6.4}$$

This value is indeed smaller than $\delta n_{\text{min}}(B = 14\,\text{T})$, see Table 6.1, which is consistent with the absence of visible spatial dependence of the Dirac point E_{D} in our previous LDOS edge maps at $\nu = 0$: the resulting variation of the filling factor at the edge with respect to its bulk value is only of $\delta\nu_{\text{b}\to\text{e}} \simeq 0.2$ at $B = 14$ T.

Let us now extrapolate the effect of such charge accumulation at the edge as a function of the magnetic field B. Using $\nu = n\phi_0/B$ we can compute $\delta\nu_{\text{b}\to\text{e}}(B)$ for $\delta n_{\text{b}\to\text{e}}$ obtained previously, as shown in Figure 6.13(b) by the dark blue curve, while the surrounding blue area stands for the uncertainty on $\delta n_{\text{b}\to\text{e}}$. For $B > 3$ T the variation of the filling factor at the edge $\delta\nu_{\text{b}\to\text{e}} < -2$ is too small to induce a visible shift of the LLs in LDOS edge maps at $\nu = 0$. However at $B < 3$ T the charge accumulation induces $\delta\nu_{\text{b}\to\text{e}} > -2$: one should expect, starting from $\nu_{\text{bulk}} = 0$, to observe LLs shifting toward higher energies at a distance of a few l_B from the edge, such that eventually E_{F} is pinned at the edge inside LL_{-1}.

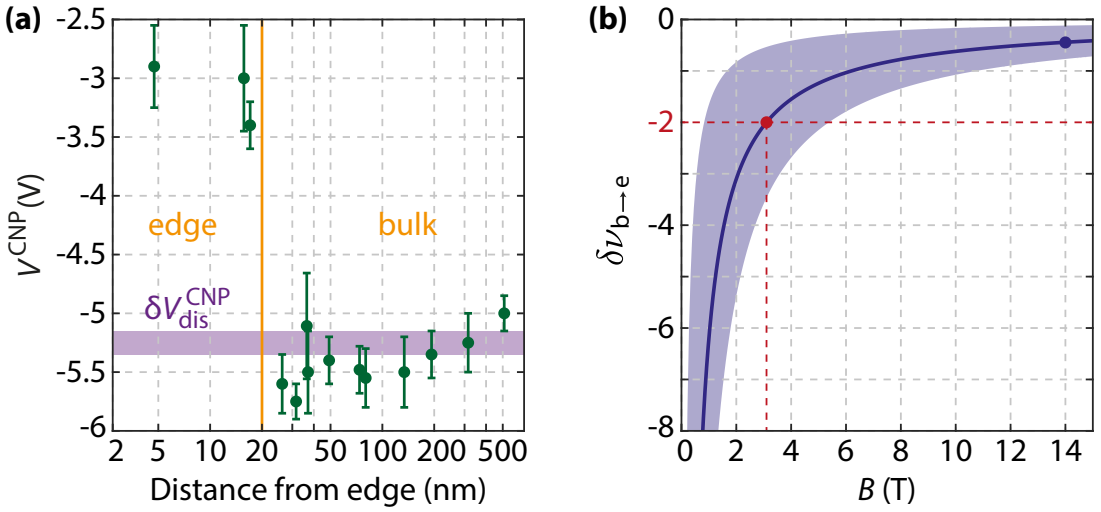

Figure 6.13: Charge accumulation at the graphene armchair edge. **(a)** Evolution of the charge-neutrality point V^{CNP} determined from LDOS gate maps at $B = 14$ T as a function of the distance from the edge d_{edge}. For $d_{\text{edge}} > 20$ nm, V^{CNP} stays around its bulk value $V_{\text{bulk}}^{\text{CNP}} = -5$ V. For $d_{\text{edge}} < 20$ nm, V^{CNP} shifts toward higher gate voltage at $V_{\text{edge}}^{\text{CNP}} = -2.9$ V. The boundary at $d_{\text{edge}} \simeq 20$ nm indicated by the yellow line is obtained from the CITS measurement at $\nu = 2$, see Figure 6.14. For comparison, we indicate in purple the range of disorder-induced variations of V^{CNP}. **(b)** Variation of the filling factor between the bulk and the edge $\delta\nu_{\text{b}\to\text{e}}$ as a function of the magnetic field B for a charge accumulation at the edge of $\delta n_{\text{b}\to\text{e}} = (-1.5 \pm 1.1) \times 10^{11}\ \text{cm}^{-2}$.

[5] We use here $\epsilon_{\text{r}} = 3.7$ for the gate insulator hBN/SiO_2 dielectric constant, as computed with Equation (5.3), such that the gating efficiency is $C_{\text{g}}/e = 6.82 \times 10^{10}\ \text{cm}^{-2}.\text{V}^{-1}$. This value indeed gives the accurate widths ΔV_{g} for the LL plateaus (variations of $\Delta\nu = \pm 4$) at $B = 5$ T in Figure 5.10.

6.2.2.c CITS toward the edge at $\nu = 2$

Finally, we performed a CITS on a scale of 100 nm from the armchair edge already studied at $\nu = 0$ in Figure 6.12, but this time at $\nu = 2$, see Figure 6.14. Contrary to the previous CITS at $\nu = 0$, E_F is here no longer pinned inside LL_0 but rather lies inside the cyclotron gap between LL_0 and LL_1. This drastically changes the behavior of the LL spectrum in presence of a possible variation of the carrier density. As we saw in the LDOS gate maps in Chapter 5.3.2, any spatial variation of the carrier density toward the edge would make E_F shift quickly until it either pins inside LL_0 or LL_1, giving a clear dispersion of the LL spectrum.

Still we do not observe any significant shift in energy of LL_0, down to $d_{edge} \simeq 20\,\text{nm} = 3\,l_B$ from the edge where it slightly moves toward higher energies before vanishing. This further strengthens the fact that no significant charge accumulation occurs at the graphene armchair edge on the scale of 100 nm away from it.

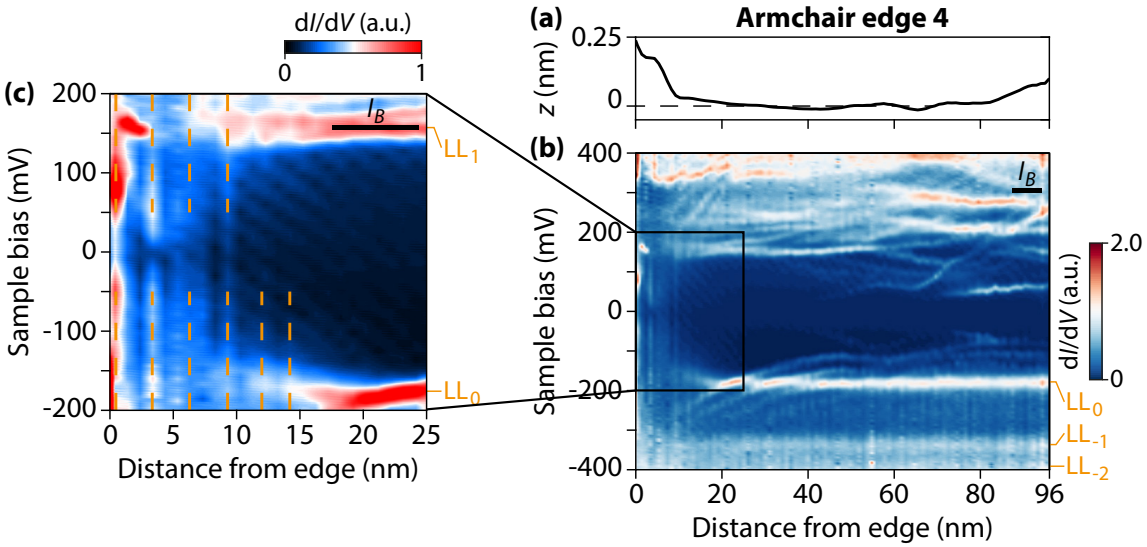

Figure 6.14: LL spectroscopy toward armchair edge 4 at $\nu = 2$. **(a)** Topographic profile $z(d_{edge})$ of graphene edge. **(b)** LDOS spatial evolution toward the edge at $\nu = 2$: if some states in the cyclotron gap disperse, the LLs themselves do not and vanish at the edge. In particular, LL_0 starts to move to higher energies at $d_{edge} \simeq 20$ nm. **(c)** In the cyclotron gap, some oscillations with a period of $3\,\text{nm} = 0.43\,l_B$ roughly appear close to the armchair edge, on a length of around $2\,l_B$.

We therefore conclude that our measurements at the graphene armchair edge enable us to observe a hole accumulation on a scale of $20\,\text{nm} = 3\,l_B$ from the edge, which is also the typical scale where the LLs start to feel the proximity of the boundary and so to vanish due to the redistribution of their spectral weight. Beyond a distance of 20 nm from the edge, the carrier density does not feature significant variations, and stays close to its bulk value. The weak charge accumulation we obtain $\delta n_{b\to e} = (-1.5 \pm 1.1) \times 10^{11}\,\text{cm}^{-2}$ has no impact on the LL spectrum at $\nu = 0$, and thus on the edge physics of charge-neutral graphene, for magnetic fields above $B = 3$T.

This is inconsistent with the theory of Silvestrov *et al.* [213], where they expected a density variation at the edges of graphene on SiO_2 on a scale of $l_a \sim 300$ nm comparable to the thickness of the gate insulator, hence on a scale 10 times larger than what we observe. In particular, the abrupt transition at $d_{edge} = 20$ nm of the charge-neutrality point, on a distance of about 10 nm only, rules out an electrostatic origin of the observed charge accumulation. Our results also contradict the hypothesis of a hole accumulation on a scale of 150 nm from the edge (one order of magnitude above the 20 nm we observe) put forward by Marguerite *et al.* [214] to explain the

dissipation and the simultaneous increase of the resistance they observed at the edge of their encapsulated-graphene device on SiO_2 at $B = 1\,\mathrm{T}$, which could rather be justified in terms of dopants at the edges introduced during the etching of their device.

The charge accumulation we observed here could have a different origin. It turns out that the $z(d_{\mathrm{edge}}, y)$ topographic maps, in Figures 6.12(a) and 6.14(a) for instance, show that the tip lifts up slightly by about 2-4 Å on a scale of $\sim 20\,\mathrm{nm}$ from the edge. This indicates that the graphene flake is lifted up by the tip interaction, as we already discussed in Section 6.1.b. The coincidence[6] between this lift up on 20 nm and the extension of the charge doping also on about 20 nm makes us conjecture that the charge accumulation occurs due to the decoupling between the graphene and hBN, which changes the orbital contacts. This hypothesis would furthermore imply an absence of charge accumulation at the edges in transport devices.

6.3 Edge dispersions of the $\nu = 0$ ground states

In this section we further study the LL edge dispersion with numerical simulations of the spatial evolution of the LDOS toward both armchair and zigzag edges. If many works derived the LL spectra toward graphene edges, see Chapter 2.2.2, either with a tight-binding model [85, 90] or with a continuum Dirac model [91, 92], few actually computed [92, 209] the resulting LDOS at the edges that one would measure in STS. Similarly, the edge dispersions of the different $\nu = 0$ ground states have been computed [119] but not the corresponding LDOS. We first describe the spatial evolution of the LDOS toward graphene edges at $\nu = 0$ in a generic case ignoring the opening of the interaction-induced gap in LL_0. We then consider the different polarizations of the $\nu = 0$ ground state as introduced in Chapter 2.3.3 : the Charge-Density Wave (CDW), the Ferromagnetic (F) and the Kekulé Distortion (KD) phases.

Figures in this section are numerical simulations of the tight-binding model provided to us by Adolfo G. Grushin from Néel Institute using the Kwant code [262, 263]. The system size is 42×42 unit cells. The magnetic flux per unit cell is $\phi = 0.003\phi_0$, corresponding to a magnetic field $B = 237\,\mathrm{T}$ for graphene cell. The LDOS is computed on the black dashed arrow toward the edge at the left, as shown in the insets of the following figures, and except for the sublattice-resolved LDOS maps, the LDOS is moreover averaged over the unit cell.

6.3.1 Unpolarized lattice

We start by considering the LDOS edge maps shown in Figure 6.15 where the LL_0 splitting is ignored. The energy axis is expressed in units of $t \simeq 2.7\,\mathrm{eV}$ the hopping energy. For the armchair edge, we find that the LL peaks display a similar behavior to that we observed experimentally : they do not disperse at the edge but rather vanish due to the broadening of their wave functions. Notably, the higher the Landau index N, the further from the edge LL_N starts to vanish, see the black dashed lines, consistent with the dependence of the cyclotron radius R_c with $N^{1/2}$. In particular the LL_0 peak disappears at the edge, as expected since it splits there into one electron-like and one hole-like bands both spin degenerate (see also Figure 2.14).

For the zigzag edge, similar behaviors are seen for the LLs except for LL_0 which here persists up to the edge. To better understand this, we show in Figure 6.16 the sublattice-resolved LDOS edge maps, where we suppose that the last row at the zigzag edge is made of atoms belonging

[6] Note also that the weaker charge accumulation observed at $\nu = 0$ in the LDOS edge map in Figure 6.10(b) matches as well with the lifting of the graphene sheet edge, see Figure 6.7(a).

to sublattice B. For sublattice A, we observe that LL_0 vanishes at the edge, consistently with the boundary conditions $\Psi_A|_{\text{edge}} = 0$, such that LL_0 splits at the edge into two dispersing bands. For sublattice B, the LL_0 connects to the dispersionless zigzag edge mode lying at zero energy and persists till the edge. When averaging both maps to obtain the one in Figure 6.15(b), the LL_0 peak eventually decreases in amplitude at the edge but does not vanish.

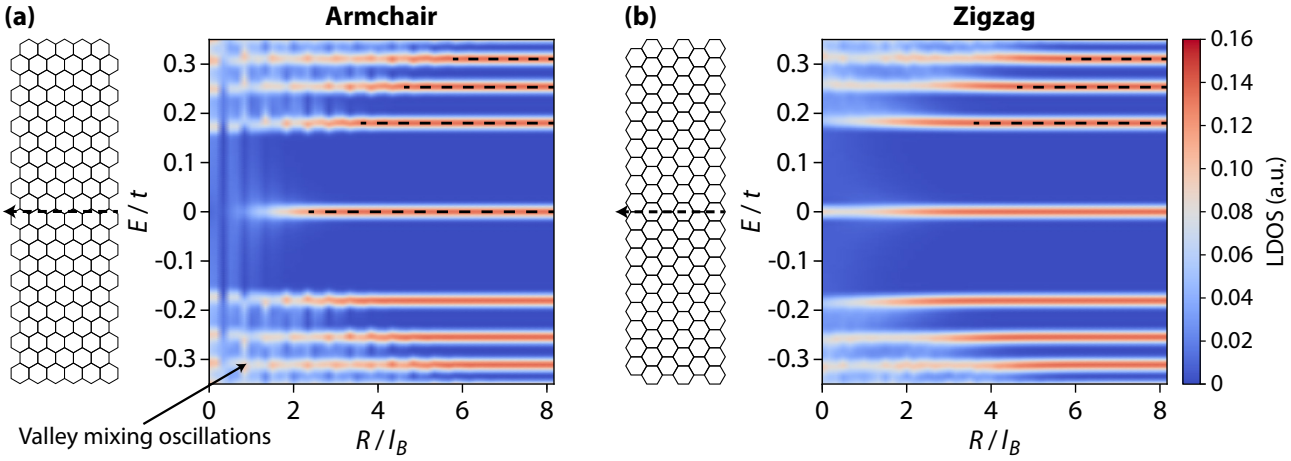

Figure 6.15: Landau levels edge dispersion at $\nu = 0$, (a) for an armchair edge and **(b)** for a zigzag edge. LLs are not seen to disperse but rather continuously vanish while approaching the edge. Simulations by [264].

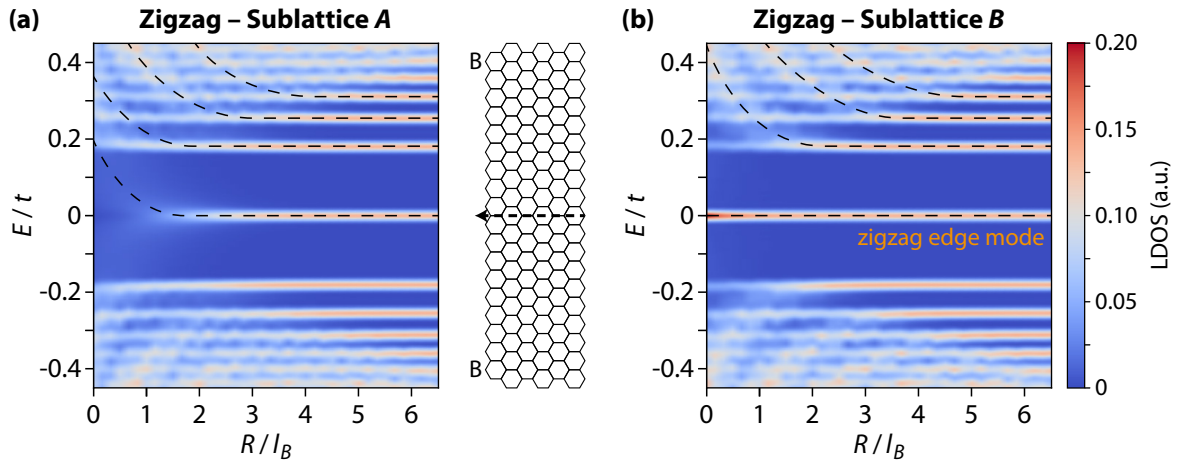

Figure 6.16: Sublattice-dependent Landau levels dispersion at $\nu = 0$ at a zigzag edge, with B atoms on the last row. **(a)** For sublattice A, the zeroth Landau level vanishes at the edge (yet both electron and hole-like bands can be roughly observed). **(b)** For sublattice B, the LL_0 morphs into the dispersionless zigzag edge mode and does not vanish at the edge (in particular its height increases close to the edge). Those figures can be compared to those obtained by Abanin *et al.* [92] in Figure 3.19 using a continuum model. Simulations by [264].

Non-zero LDOS in the cyclotron gaps The gradual redistribution of the LL peaks spectral weight at the edge toward higher energies is responsible for the vanishing of the peaks. Still we can roughly distinguish in Figure 6.16, as weak bright bands in the cyclotron gaps, both electron and hole-like bands resulting from the lifting of the valley degeneracy of LLs at the edge (see the dashed lines, reminiscent of the spectra in Figure 2.15, in particular notice that the dashed lines for LLs with $N > 0$ do not bend up at the same position in both figures). Eventually, this yields a non-zero LDOS in the cyclotron gaps below a distance from the edge of a few l_B, and gives a V-shape-like LDOS at the edge as we observed experimentally in Figure 6.5(b).

Valley mixing oscillations at armchair edge We note in Figure 6.15(a) that the non-zero LDOS inside the cyclotron gaps at the armchair edge is not homogeneous but rather displays alternating stripes. They arise from the oscillations of the wave function at the armchair edge due to the valley mixing, as expected by Brey and Fertig [90]. These oscillations feature here a period of $0.5\,l_B \simeq 8$ Å, twice the theoretical one of $3\sqrt{3}a/2 \simeq 3.7$ Å predicted by Ref. [90]. Their appearance coincides with where the gradual redistribution of the LLs spectral weight occurs (the higher the LL index N, the further from the edge the oscillations appear). For instance for LL_0 they are visible up to $2\,l_B$ from the armchair edge, which is consistent with the tight-binding calculations of Ref. [90]. Note also that the oscillations of one LL eventually interfere with those of higher LLs.

Experimentally, the oscillations we observed in Figure 6.14(c) at distances below $2\,l_B$ from the armchair edge and at $\nu = 2$ may be these valley-mixing oscillations, however the apparent large spatial period of 3 nm we measure is mostly due to the undersampling of our CITS (1 point per nm) which hinders an accurate estimation.

6.3.2 Charge-density wave

We now consider that the ground state of charge-neutral graphene features a charge-density-wave order. This is simulated by adding a staggered chemical potential $\pm M$ to sublattices A and B. Figure 6.18 shows the LDOS edge maps obtained for both armchair and zigzag edges. The LL_0 peak appears indeed split in two peaks of the broken-symmetry state, where the valley degeneracy is lifted (but not the spin one), with the opening of the interaction-induced gap that makes the bulk graphene insulating. For the armchair edge both LL_0 peaks disperse and thus disappear at the boundary.

However, for the zigzag edge, one LL_0 peak disappears while the other LL_0 peak connects to the zigzag edge mode and persists. Indeed, the addition of the staggered potential breaks the sublattice symmetry, and the atoms at the zigzag edge all display the same potential $+M > 0$, therefore shifting in energy the zigzag edge mode at $+M$ where lies one LL_0 broken-symmetry state. On the opposite, there is no zigzag edge mode at energy $-M$ such that the LL_0 peak at this energy vanishes at the edge. Furthermore, switching the sign of the staggered chemical potential to $+M < 0$, as shown in Figure 6.19, changes which LL_0 peak connects with the zigzag edge mode and persists at the edge.

Note also that the LDOS is zero at the edge inside the LL_0 gap for both edges (notably there is no oscillation of the LDOS at the armchair edge inside the gap), consistently with gapped edge excitations expected for the CDW phase.

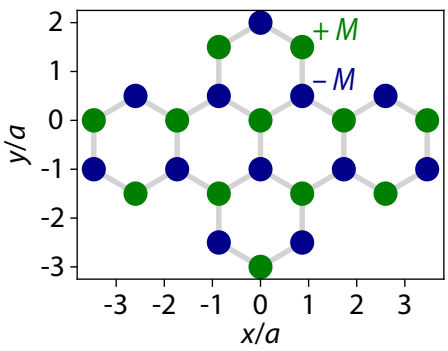

Figure 6.17: Graphene lattice with a charge-density wave. The CDW is simulated by adding a staggered chemical potential $\pm M$ to both sublattices.

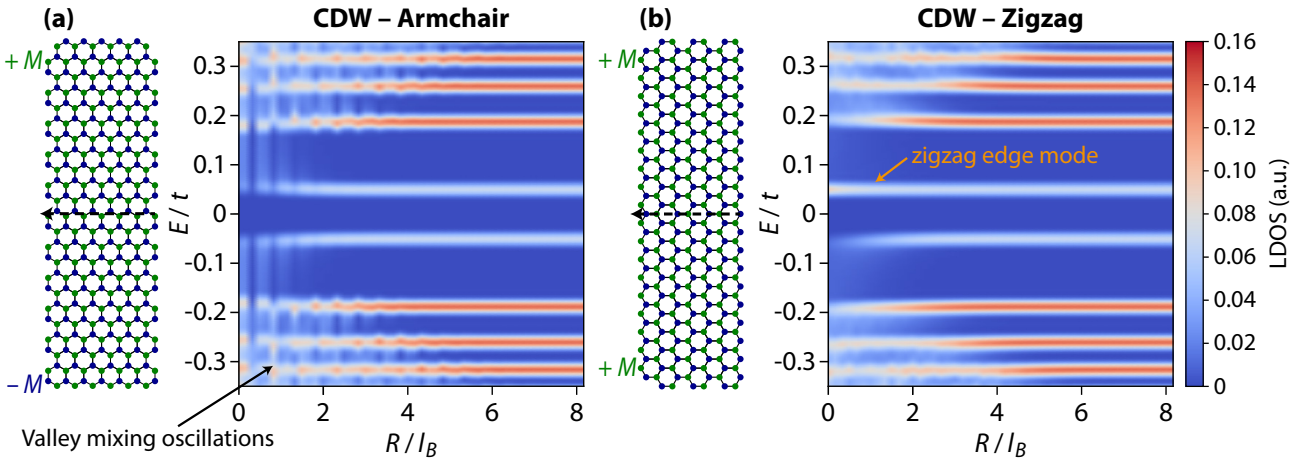

Figure 6.18: Landau levels edge dispersion at $\nu = 0$ with a CDW ground state, for a staggered potential $M = 0.05t$, **(a)** for an armchair edge, where both LL_0 peaks disappear at the edge, and **(b)** for a zigzag edge, where one LL_0 peak vanishes while the other LL_0 peak connects to the zigzag edge mode and persists at the edge. Simulations by [264].

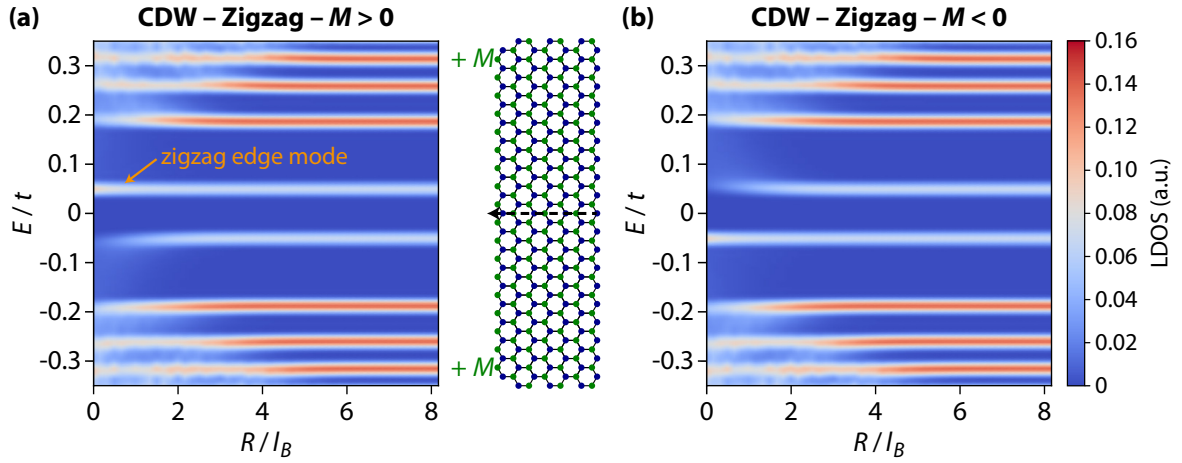

Figure 6.19: Landau levels edge dispersion at $\nu = 0$ at a zigzag edge with a CDW ground state, the sign of the staggered potential M at the edge defines which LL_0 peak connects with the zigzag edge mode. Simulations by [264].

6.3.3 Ferromagnetic phase

We now suppose a ferromagnetic polarization, simulated by adding a Zeeman splitting E_Z. Nonetheless note that here E_Z and the magnetic field B are two independent parameters. Figure 6.20 shows the LDOS edge maps for both armchair and zigzag edges obtained for $E_Z = 0.02t$. In the bulk we obtain a splitting of the LLs due to the spin degeneracy lifting (but not the valley). However unlike in the CDW phase, both doublets of LL_0 peaks split at the edges due to the consequent lifting of the valley degeneracy into, for each of them, one electron-like and one hole-like bands, although those dispersing bands would only appear in LDOS maps as peaks vanishing at the edges. Indeed, both LL_0 peaks disappear at the armchair edge in Figure 6.20, similarly to the CDW case, but they both persist at the zigzag edge, contrary to the CDW phase where one of them vanishes.

To understand the zigzag case we compute the sublattice-resolved LDOS edge maps in Figure 6.22, supposing the zigzag edge is comprised of B atoms. There the zigzag edge mode splits in two due to the Zeeman effect, similarly to LLs. We observe for sublattice A the vanishing of both LL_0 peaks and a non-zero density of states in the LL_0 gap (appearing as a brighter area

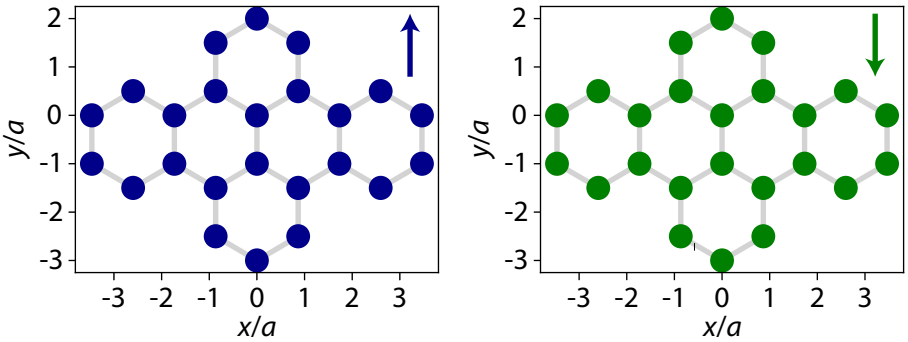

Figure 6.20: Graphene lattice with a ferromagnetic order, obtained by adding a Zeeman splitting E_Z (independent of the magnetic field B).

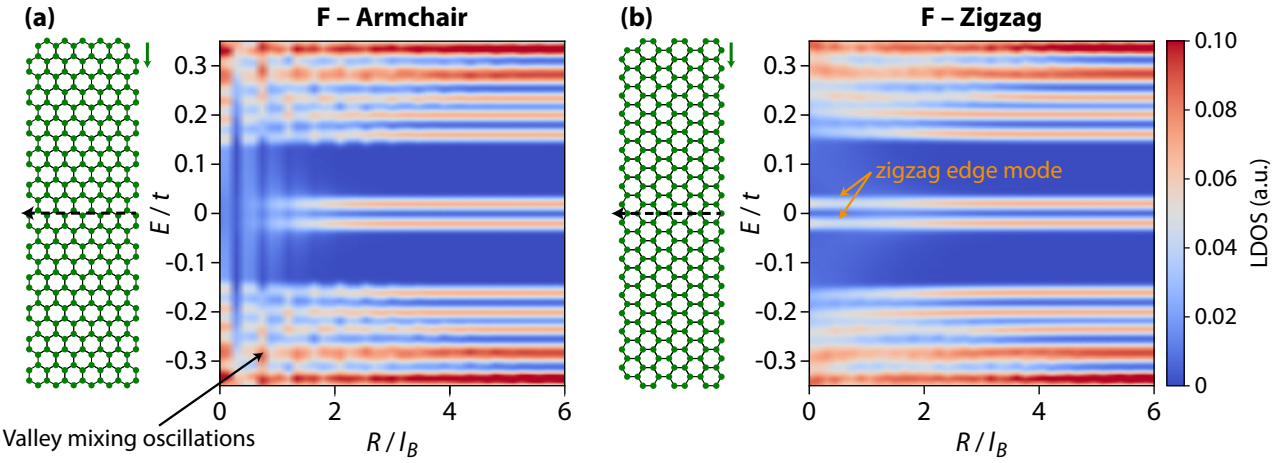

Figure 6.21: Landau levels edge dispersion at $\nu = 0$ with a F ground state, for a Zeeman splitting $E_Z = 0.02t$, **(a)** for an armchair edge, where both LL_0 peaks disappear at the edge, and **(b)** for a zigzag edge, where both LL_0 peaks persist at the edge. Simulations by [264].

compared to the bulk), consequence of the topological crossing of the dispersing electron and hole-like bands at the edge, see the red (spin up) and blue (spin down) dashed lines. On the contrary, for sublattice B, both LL_0 peaks connect to the Zeeman-split zigzag edge modes and persist at the edge while no state is visible in the LL_0 gap, since none LL_0 state disperses. The LDOS edge map of Figure 6.21(b), averaged on the unit cell, therefore features a weak non-zero LDOS inside the LL_0 gap as well as the two bright non-dispersing LL_0 peaks.

Increasing the ferromagnetic order and the resolution unveils in the global LDOS in Figure 6.23 the electron and hole-like dispersing bands at the zigzag edge. In particular we observe the band crossing expected theoretically, which gives a non zero LDOS at zero energy below $1.5\, l_B$ from the edge, and therefore makes the edge excitations in the F phase gapless. The same conclusions can be made for the armchair case where the valley-mixing oscillations of the LDOS at the edge are also visible inside the LL_0 gap, on the contrary to the CDW phase.

Comparison between the CDW and F phases

It is also possible to simulate spatial maps of the LDOS over the whole graphene sheet at a given energy. In Figure 6.24 are plotted the spatial LDOS maps at zero energy for both CDW and F phases, corresponding to graphene at $\nu = 0$. These maps are consistent with theory. Indeed, for the CDW ground state, there is no state at zero energy in the bulk and at the armchair edges, while the zigzag edge mode induces the appearance of a low LDOS localized on the very last row of atoms of both zigzag edges : there is no conduction through edge channels and charge-neutral

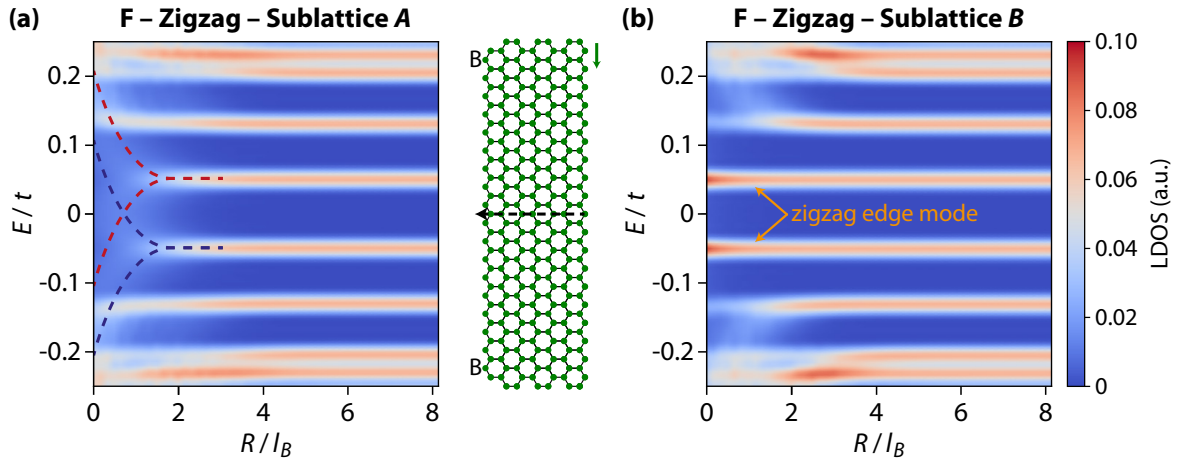

Figure 6.22: Sublattice-dependent Landau levels dispersion at $\nu = 0$ at a zigzag edge with a F ground state, for a Zeeman splitting $E_Z = 0.05t$ and B atoms on the last row. **(a)** For sublattice A, both peaks of LL_0 vanish at the edge. For each peak both electron and hole-like bands arising at the edge can be roughly observed, which gives a non-zero LDOS at zero energy. **(b)** For sublattice B, both peaks of LL_0 connect to the zigzag edge mode and do not disperse toward the edge. Simulations by [264].

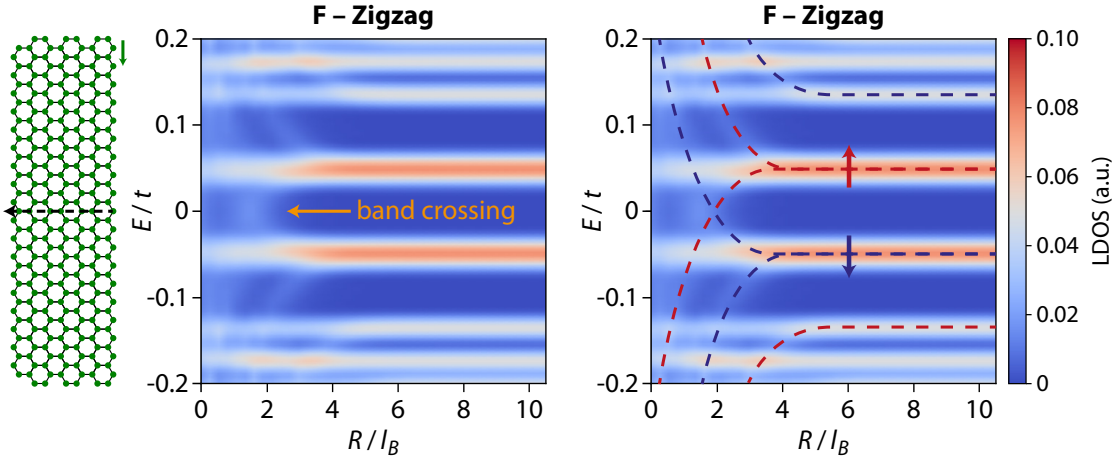

Figure 6.23: Landau levels edge dispersion at $\nu = 0$ at a zigzag edge with a F ground state, for a Zeeman splitting $E_Z = 0.05t$, where the band crossing at zero energy expected to occur at the edges in the F phase is visible as a weak feature compared to the height of the LL peaks. Right : overlay with the band diagram. Simulations by [264].

graphene is insulating. For the F ground state, the bulk is insulating but many states at zero energy exist at both armchair and zigzag edges, on a distance below $2\,l_B$ from the edge : conduction at zero energy is thus possible at the edges and charge-neutral graphene is conductive.

To study the transition between the CDW and F phases, we show in Figure 6.25 the tight-binding spectra computed at a zigzag edge for different staggered potentials M and Zeeman splitting E_Z, keeping the sum of both constant, for the two valleys K and K'. For $(M, E_Z) = (0, 0)$ we retrieve the tight-binding spectrum already computed by Brey and Fertig [90], see Figure 2.13(a), where for valley K the LL_0 splits into two dispersing branches at one edge and morphs into the dispersionless zigzag edge mode at the opposite edge, and conversely for valley K'. For $(M, E_Z) = (0.05t, 0)$ we obtain the tight-binding spectrum of the CDW phase, with the LL_0 gap between the two spin-degenerate dispersing branches, and gapped edge excitations, thus a zero LDOS at the edges inside the LL_0 gap.

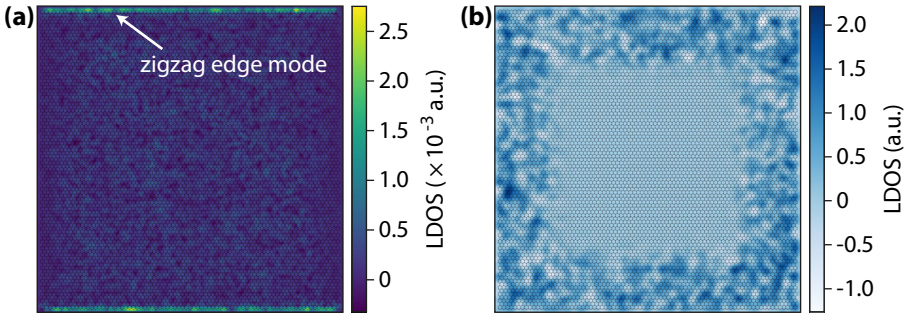

Figure 6.24: Spatial LDOS maps at zero energy for CDW and F ground states. **(a)** For the CDW phase, except the zigzag edge mode, there is no state at zero energy in bulk and at the edges. **(b)** For the F phase, there are edge states at zero energy while the bulk is insulating. Simulations by [264].

By adding a small Zeeman effect $(M, E_Z) = (0.04t, 0.01t)$ we lift the spin degeneracy of LLs and observe the four LL_0 broken-symmetry states, with the branches of identical spin dispersing in opposite directions. The edge excitations stay gapped until $E_Z > M$ where the topological inversion between the highest hole-type and the lowest electron-type bands occurs. This induces a band crossing at zero energy, which gives the non-zero LDOS at zero energy observed previously. Finally, the pure F phase is obtained for $(M, E_Z) = (0, 0.05t)$ with only two LL_0 spin-polarized states in the bulk, which disperse into four branches at the edge due to the lifting of the valley degeneracy.

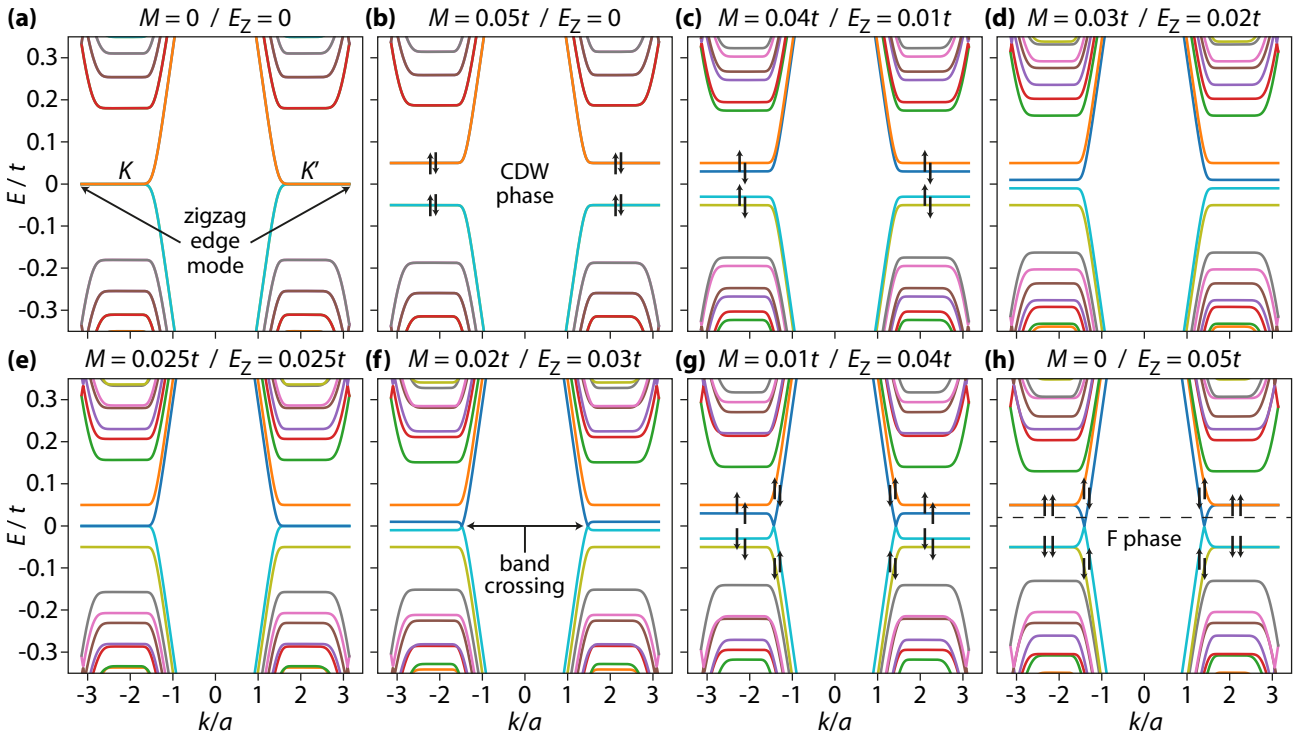

Figure 6.25: Tight-binding spectra of graphene for a zigzag edge with a CDW or F ground state, for different values of (M, E_Z). Simulations by [264].

Last, we plot in Figure 6.26(a) the spatial map of the LDOS at an energy $E = 0.01t$ slightly above zero, but still in the $\nu = 0$ gap, where we obtain as previously a concentration of the density of states at the edges while the bulk is insulating. Computing in the same conditions

the spin LDOS map shows spin puddles[7] at the edges. This spin texture is consistent with the crossing of the two bands of opposite spins at zero energy, from which arise the helical edge channels responsible for the quantum spin Hall effect observed in transport measurements [107, 122], as we described in Chapter 2.3.4.

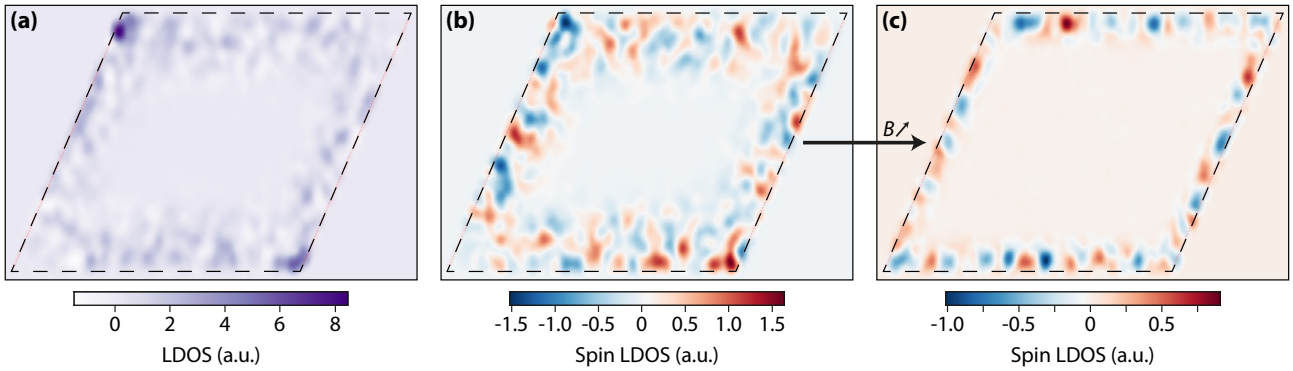

Figure 6.26: F ground state and conduction through the edges at $\nu = 0$. **(a)** Spatial LDOS map at $E = 0.01t$, corresponding to the dashed black line in the spectrum of Figure 6.25(h). The LDOS is zero in bulk graphene but non zero at the edges, for both zigzag and armchair ones. **(b)** Corresponding spatial spin LDOS map at $E = 0.01t$, showing that the edge states are spin-polarized as expected for the F phase. **(c)** Same than (b) but with higher B field. The spin-polarized edge states are squeezed closer to the edges. Simulations by [264].

6.3.4 Kekulé bond order

As for the last possible $\nu = 0$ ground state we study in this chapter, we suppose a Kekulé distortion of the honeycomb lattice. Each atom in graphene forms three bonds with its three nearest-neighbors, associated to three hopping energies t_1, t_2 and t_3. The Kekulé distortion is simulated by tuning the value of one t_i parameter while keeping the other two constant, for instance $t_1 > t_{2,3}$. This gives three possible and equivalent configurations for the KD ground state, labeled K1, K2 and K3, see Figure 6.27, where the unit cell is tripled in size with respect to the one of pristine graphene. Equivalent at least in the bulk, but inducing different edge configurations and thus LDOS edge maps : with the armchair and zigzag boundary types, there are six different LDOS edge maps, shown in Figure 6.28, with the two resulting LL_0 peaks.

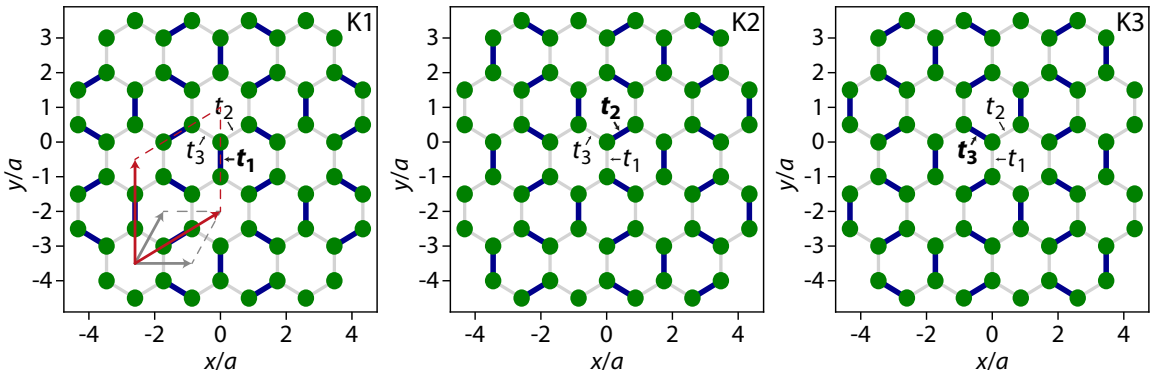

Figure 6.27: Graphene lattice with a Kekulé distortion. There are three possible configurations K_i for the KD ground state, obtained for $t_i > t_{j,k}$, which are equivalent in the bulk but give different patterns of strong and weak bonds at the edges. The unit cells of pristine and Kekulé-ordered graphene are represented in gray and red respectively.

[7] Note that this speckle-like pattern is most likely of numerical origin.

Let us start with the armchair edge (left panels). Depending on the configuration K_i but also on the size of the system, there are three possible patterns for the edge bonds. We index the three different bonds comprising the armchair edge with hopping parameters t_α (the bond at the edge), t_β (the nearest tilted bond to the edge) and t_γ (the next-nearest parallel bond to the edge), see the inset in panel (a). For both configurations $t_\gamma > t_{\alpha,\beta}$ in panel (c) and $t_\alpha > t_{\beta,\gamma}$ in panel (e) the LDOS edge maps are similar with the vanishing of the LL_0 peaks at the armchair edge and gapped edge excitations. Note also the absence here of valley-mixing oscillations, which might result from the change of unit cell. Nonetheless, for configuration $t_\beta > t_{\alpha,\gamma}$ in panel (a) the LL_0 gap unexpectedly seems to decrease at the edge, while the vanishing of the two peaks is less pronounced.

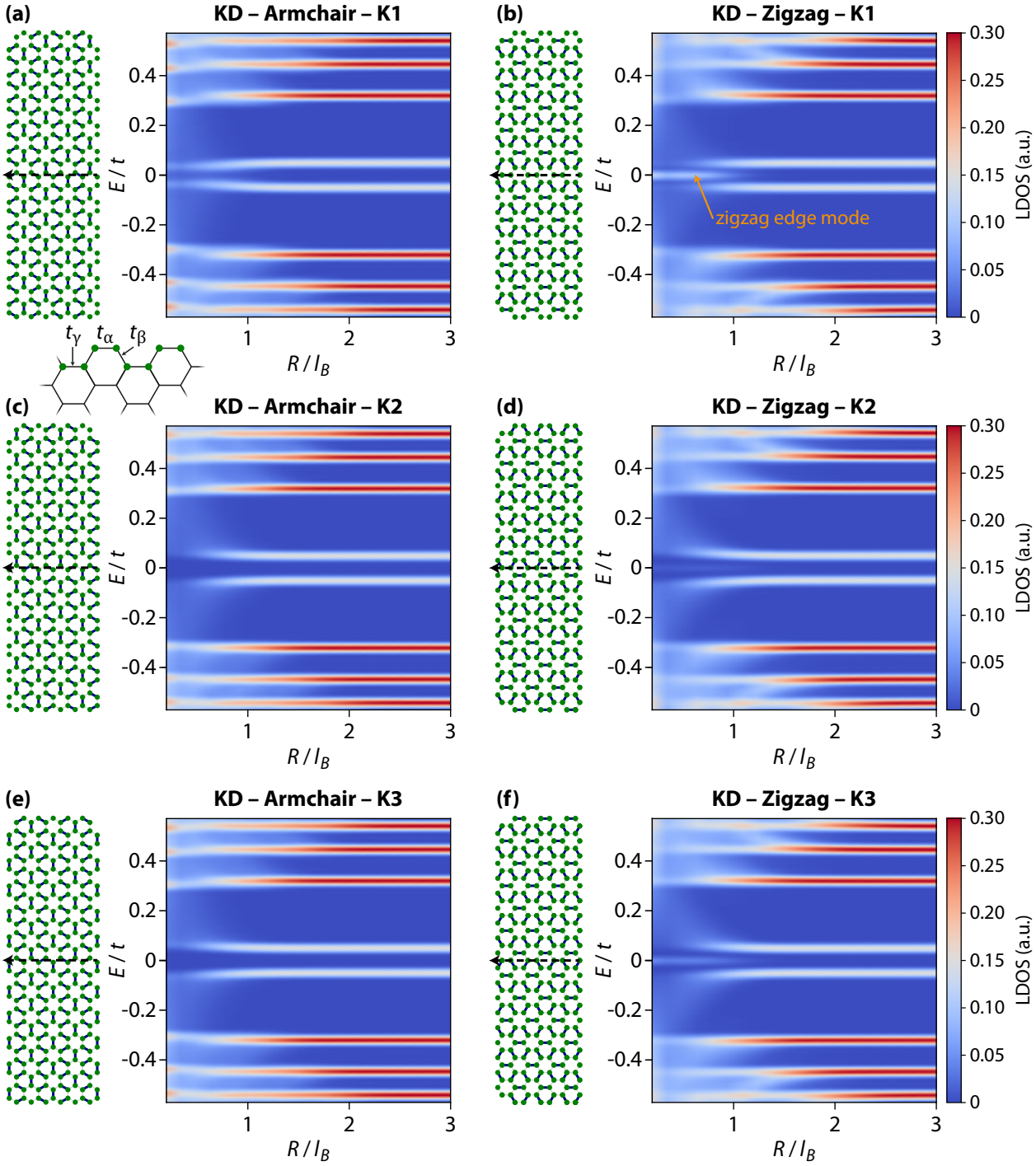

Figure 6.28: Landau levels edge dispersion at $\nu = 0$ with a KD ground state, for an armchair edge (left panels) and a zigzag edge (right panels) and for the three possible configurations of the KD phase. Simulations by [264].

We last discuss the zigzag case (right panels). As previously there are three different patterns for the edge bonds. In the three cases the two LL_0 peaks vanish at the edge, while the zigzag edge mode lies alone at zero energy. Its intensity depends on the panel, in particular the zigzag edge mode is brighter in panel (a) and the dispersion of the LL_0 peaks is less visible. This difference may be due to the symmetry of the edge bond pattern with respect to the axis on which the LDOS is calculated (black dashed line), while the other two patterns in panels (d,f) are asymmetric.

It therefore eventually seems that the LDOS edge maps for both edges depend on the symmetry of the bond patterns at the edge with respect to the computation axis. Nonetheless, experimentally the tip probes the LDOS at the edge on a scale of l_B and we would therefore measure the average of the three different configurations : for both armchair and zigzag edges, the LL_0 peaks vanish at the edge and edge excitations are gapped, while the zigzag edge mode stays at zero energy and does not connect to any of the LL_0 peaks.

Conclusion

We have shown in this chapter the first tunneling spectroscopy at an armchair edge of graphene on hBN/SiO_2, which is the same configuration in which the relativistic quantum Hall effect is observed by transport measurements. We obtained LDOS edge maps where the Landau level peaks do not disperse at the edge but rather vanish, due to the gradual redistribution of their spectral weight toward higher energies, as expected for an atomically sharp boundary. Those results are similar to those of Li *et al.* [209] for graphene on conductive graphite. The key feature here is the important bulk contribution to the LDOS at the edge probed by the tip, owing to the broadening of the Landau level wave functions on a scale of the magnetic length l_B. Our main result concerning the edge physics is that the edge channels of the quantum Hall effect are squeezed in the last few l_B from the edges, which leaves no room for the electrostatic edge reconstruction expected at smooth boundaries. This has important consequences for transport measurements, especially for devices which aim to control the propagation of edge channels in graphene, such as quantum Hall interferometry [265].

We also dealt with the topic of the charge accumulation that is expected to arise at the graphene edges due to the electrostatics of the back gate [213]. We have shown, however, that no significant carrier density variation occurs on the scale of several hundreds of nanometers and down to 20 nm from the edge. There, an abrupt decrease of the density happens, which can not originate from a smooth electrostatic potential, but that we rather supposed to come from the tip-induced lifting of the graphene sheet edge, which alters its dielectric environment. We might thus assume that no electrostatic charge accumulation occurs at the graphene edges. Nevertheless, the effect of the tip on the electrostatics at the edge of the graphene layer, and in particular the screening in the quantum Hall regime of this metallic tip which is a few angströms away from graphene, remains to be studied.

Finally, we investigated simulations of the LDOS evolution toward graphene armchair and zigzag edges as one would measure experimentally with STS. We also explored the behaviors of the LL_0 peaks when split for the CDW, F and KD phases. If both LL_0 peaks vanish at the armchair edge similarly for the three phases, their fate differs at the zigzag edge depending if the LL_0 peaks connect or not to the zigzag edge mode. We also retrieved that the F order features gapless edge excitations whereas the CDW and KD phases induce gapped edge excitations, this last case being consistent with our experimental data for sample AC04 on hBN/SiO_2.

Zeroth Landau level many-body ground states

CHAPTER 7

FINALLY, we focus in this chapter - see also its related publication [266] - on the physics of charge-neutral graphene, that is, at a filling factor $\nu = 0$. This broken-symmetry state appears at half-filling of the zeroth Landau level as a consequence of quantum Hall ferromagnetism, where exchange interactions play a fundamental role. The opening of the interaction-induced gap at $\nu = 0$ is notably responsible of the strong insulating behavior observed in transport measurements of charge-neutral graphene on hBN/SiO_2 samples. However, a direct spectroscopic measurement of this gap is still missing.

We start this chapter by presenting tunneling spectroscopy of the evolution of the $\nu = 0$ gap of graphene on hBN/SiO_2 as a function of the magnetic field, and we demonstrate it scales as the square root of the field, as expected for Coulomb interactions. We next similarly measure the $\nu = 0$ gap on hBN/$SrTiO_3$ and show it is significantly reduced as expected due to substrate-screening with respect to the hBN/SiO_2 unscreened case.

In the second part we focus on the different ground states of charge-neutral graphene for both hBN/SiO_2 and hBN/$SrTiO_3$ samples. We find that the $\nu = 0$ ground state of graphene on hBN/SiO_2 features a Kekulé distortion of the honeycomb lattice, rather than the canted-antiferromagnet phase expected from transport measurements [107].

Moreover, due to the screening of the Coulomb interaction, charge-neutral graphene on hBN/$SrTiO_3$ is driven in a different ground state at high magnetic field : a charge-density wave. Finally, contrary to the Kekulé distortion in hBN/SiO_2 samples, the charge-density-wave order in hBN/$SrTiO_3$ samples vanishes at low magnetic field, which is consistent with the observation in our group [122] of a conductive ferromagnetic phase in charge-neutral graphene in this low magnetic field regime. Our results constitute an evidence of a screening-induced quantum phase transition where the magnetic field tunes the efficiency of the $SrTiO_3$ substrate-screening of the Coulomb interaction.

Contents

7.1 Interaction-induced gap of the $\nu = 0$ state

We study in this section the gap that opens in the zeroth Landau level at partial filling. As we have already seen many times in previous LDOS gate maps, this gap opens when the LL_0 pins the Fermi level E_F, which lies at zero sample bias in the spectra. This is a consequence of the quantum Hall ferromagnetism, where interactions completely lift the spin and valley degeneracies in the partially filled flat LL bands, see Chapter 2.3.1.

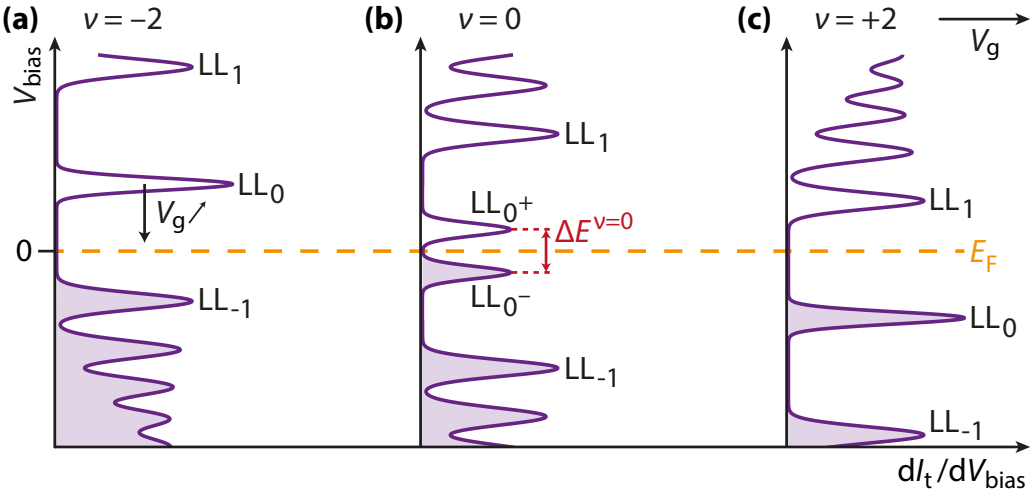

Figure 7.1: Quantum Hall ferromagnetism in half-filled LL_0. At $\nu = 0$, the zeroth Landau level is split in two due to exchange interactions and a gap opens at zero bias in tunneling spectroscopy.

In this chapter we consider four graphene samples : AC04 (hBN/SiO_2) and BNGrSTO-STM-07 / AC23 (hBN/$SrTiO_3$) that we have already characterized in Chapter 5, as well as AC24, a third hBN/$SrTiO_3$ sample. The thickness of the hBN spacer for each sample is indicated in Table 7.1.

Sample	AC04	BNGrSTO-STM-07	AC23	AC24
Substrate	Si^{++}/SiO_2	$SrTiO_3$	$SrTiO_3$	$SrTiO_3$
hBN thickness	14 nm	8 nm	12 nm	10 nm

Table 7.1: hBN spacer thickness d_{BN} of the four measured samples.

7.1.a Opening of the $\nu = 0$ gap

Let us start by examining how the $\nu = 0$ gap opens at zero bias. For this purpose we consider here for instance the sample BNGrSTO-STM-07 and the LDOS gate map measured at $B = 14$ T shown in Figure 5.10(c) with the successive pinning of the Fermi level E_F inside the LLs. We now focus on the pinning of E_F inside LL_0, of which a zoom is displayed in Figure 7.2(a). Below $V_g = 9$ V, LL_0 is empty and $\nu \approx -2$. As we increase the back-gate voltage, we clearly observe that LL_0 splits in two peaks of the $\nu = 0$ broken-symmetry state, labeled LL_{0^+} and LL_{0^-}, when it crosses the zero bias axis and starts to be filled ($-2 < \nu < 2$), with the opening of the LL_0 gap. Above $V_g = 16$ V, LL_{0^+} vanishes and we retrieve only one LL_0 peak, that eventually disperses toward negative biases when it has been completely filled ($\nu \approx 2$). We plot in Figure 7.2(b) individual dI_t/dV_{bias} taken at different gate voltages. The LL_0 peak is

readily seen to split in two peaks when it arrives at zero bias. As LL_0 is being filled, we also notice that the height of the LL_{0^+} peak (empty states) decreases while the height of the LL_{0^-} peak (filled states) increases, until every state of LL_0 has been filled and LL_{0^+} vanishes while LL_{0^-} becomes the new LL_0 peak and disperses toward negative biases.

Moreover note that the peaks of the broken-symmetry state are mostly asymmetric : it may be a signature of them being rather doublets of unresolved peaks, which would make us retrieve the four expected peaks of the broken-symmetry state with both spin and valley degeneracy lifting. This is consistent with the fact that, inside a doublet, the two peaks of the broken-symmetry state would be separated by a very small gap, much smaller than the interaction-induced gap which opens at E_F. This small gap would be given either by the Zeeman energy, which is only of $E_Z(B = 14\,\mathrm{T}) \simeq 1.6\,\mathrm{meV}$, or by the valley gap which is similar, see Chapter 2.3.1. In both cases, this negligible value is at most comparable with the energetic resolution of our LDOS gate maps, and this gap can thus not be resolved.

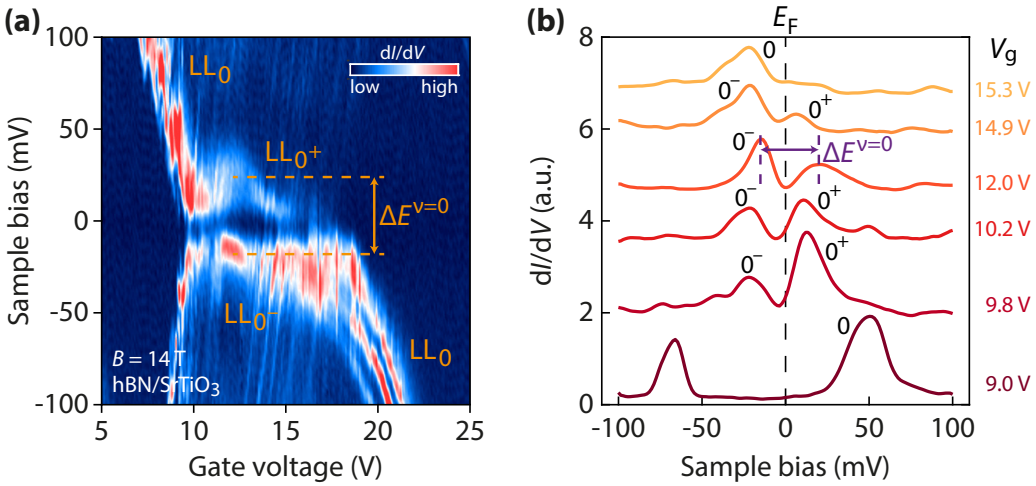

Figure 7.2: Opening of the interaction-induced gap of the $\nu = 0$ state. **(a)** $\mathrm{d}I_t/\mathrm{d}V_{bias}$ gate map as a function of sample bias and gate voltage for sample BNGrSTO-STM-07 at $B = 14\,\mathrm{T}$, zoom of Figure 5.10(c) and centered on the LL_0 gap. **(b)** $\mathrm{d}I_t/\mathrm{d}V_{bias}$ spectra taken from (a) at different gate voltages, showing the opening of the $\nu = 0$ gap when LL_0 crosses the Fermi level at zero bias.

7.1.b Measurement of the $\nu = 0$ gap

We observe in Figure 7.2 that the $\nu = 0$ gap, labeled $\Delta E^{\nu=0}$, is not constant with the back-gate voltage but rather increases and then decreases before it closes. This is a consequence of exchange energy which enhances the gap as a function of the filling factor. As we mentioned in Chapter 3.2, a similar feature happens in GaAs as observed by Dial *et al.* [146], where the gap which opens at odd filling factor (half-filling) is maximum when one spin-polarized state is completely filled while the other spin state is empty, thus maximizing the exchange interactions. An analogous effect is thus expected to happen in partially filled LLs in graphene, with an enhancement of the LL_0 gap at each quarter filling due to both spin and valley degeneracies. Nonetheless in most of our LDOS gate maps we observed this enhancement at $\nu = 0$ only and, for unknown reasons, we did not resolve the $\nu = \pm 1$ gaps.

In order to obtain the evolution of $\Delta E^{\nu=0}$ as a function of the filling factor, we now consider sample AC04 (hBN/SiO_2) and the LDOS gate map at $B = 7\,\mathrm{T}$ shown in Figure 7.3(a) (but note that the following observations hold for the other samples as well). Here the LL_0 gap

features a maximum around $V_g = -5$ V at the charge-neutral point of graphene. We plot in Figure 7.3(b) a series of dI_t/dV_{bias} tunneling spectra at different gate voltages and follow the evolution of the LL_0 peak(s) as the gate voltage is increased, see both blue dashed lines. The LL_{0^-} peak appears at $V_g = -7.0$ V indicating the zeroth Landau level starts to be filled, and becomes completely filled at $V_g = -1.5$ V where the LL_{0^+} peak disappears. The LL_0 gap is also clearly seen to increase around $V_g = -4.8$ V. We now compute the LL_0 gap as a function of gate voltage, see Figure 7.3(c), and we estimate the value of the interaction-induced gap at $\nu = 0$ as the maximum $\Delta E^{\nu=0}(B = 7\,\mathrm{T}) \simeq 39$ meV.

From now on, our methodology to estimate $\Delta E^{\nu=0}$ from the LDOS gate maps will consist in taking the maximum value of the LL_0 gap, as a function of gate voltage, that we extract from the individual spectra around charge neutrality.

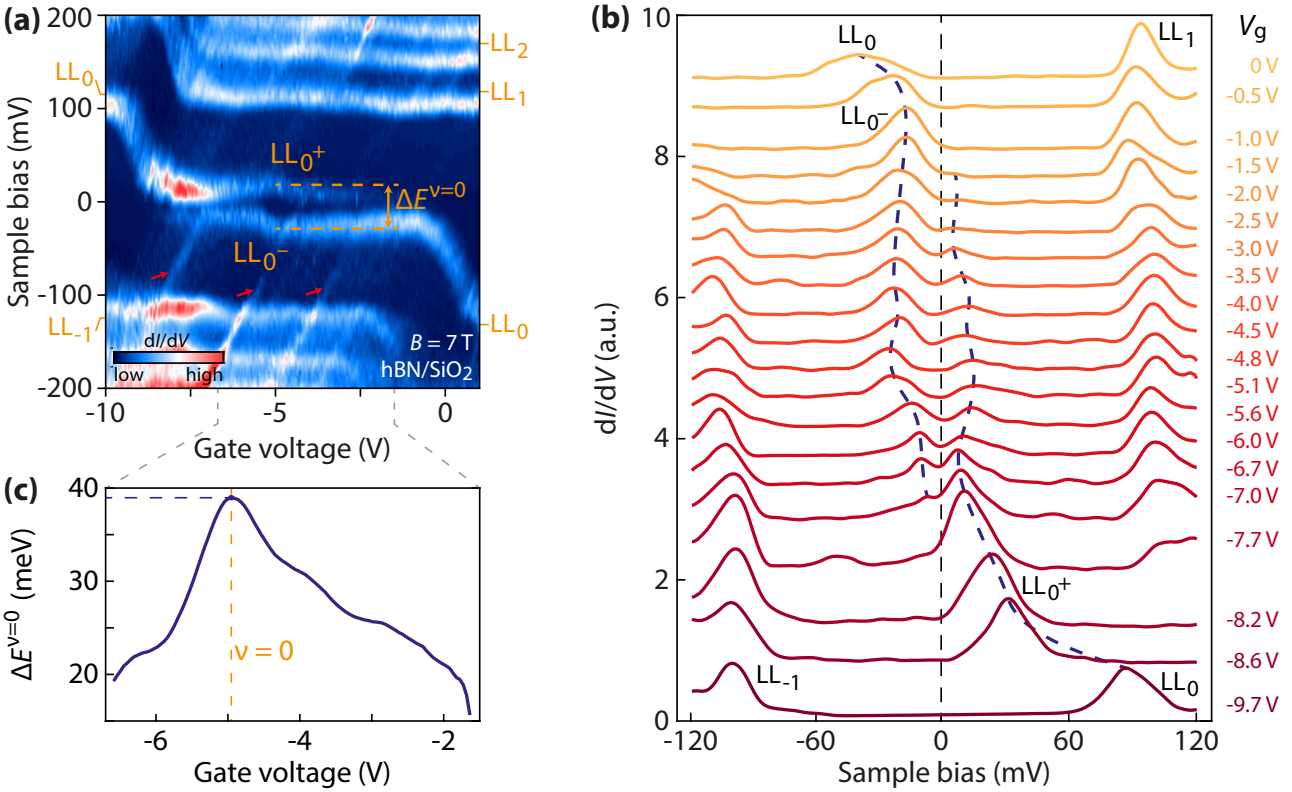

Figure 7.3: Evolution of the LL_0 gap with the gate voltage. **(a)** dI_t/dV_{bias} gate map as a function of sample bias and gate voltage for sample AC04 at $B = 7$ T centered on the LL_0 gap. **(b)** dI_t/dV_{bias} spectra taken from (a) at different gate voltages. **(c)** $\Delta E^{\nu=0}$ as a function of gate voltage. The maximum of the gap occurs at $\nu = 0$.

7.1.c Evolution of the LDOS gate maps with the magnetic field

We study in this section how the LDOS gate maps, and the opening of the LL_0 gap, evolve as a function of the magnetic field. We show in Figure 7.4 the typical evolution of the LDOS gate maps in sample BNGrSTO-STM-07 for decreasing magnetic fields from $B = 14$ T to $B = 1$ T. For each magnetic field, we perform the same gate sweep from $V_g = 80$ V to $V_g = -20$ V in order to keep the hysteresis cycle of the $SrTiO_3$ substrate constant. The full LDOS gate map at $B = 14$ T is shown in panel (a), and the zoom on the yellow rectangle centered on the LL_0 gap is displayed in panel (b). Next panels are as well zooms on the same area than (b). All those LDOS gate maps were done at the same position in graphene, up to the magnetic field drift.

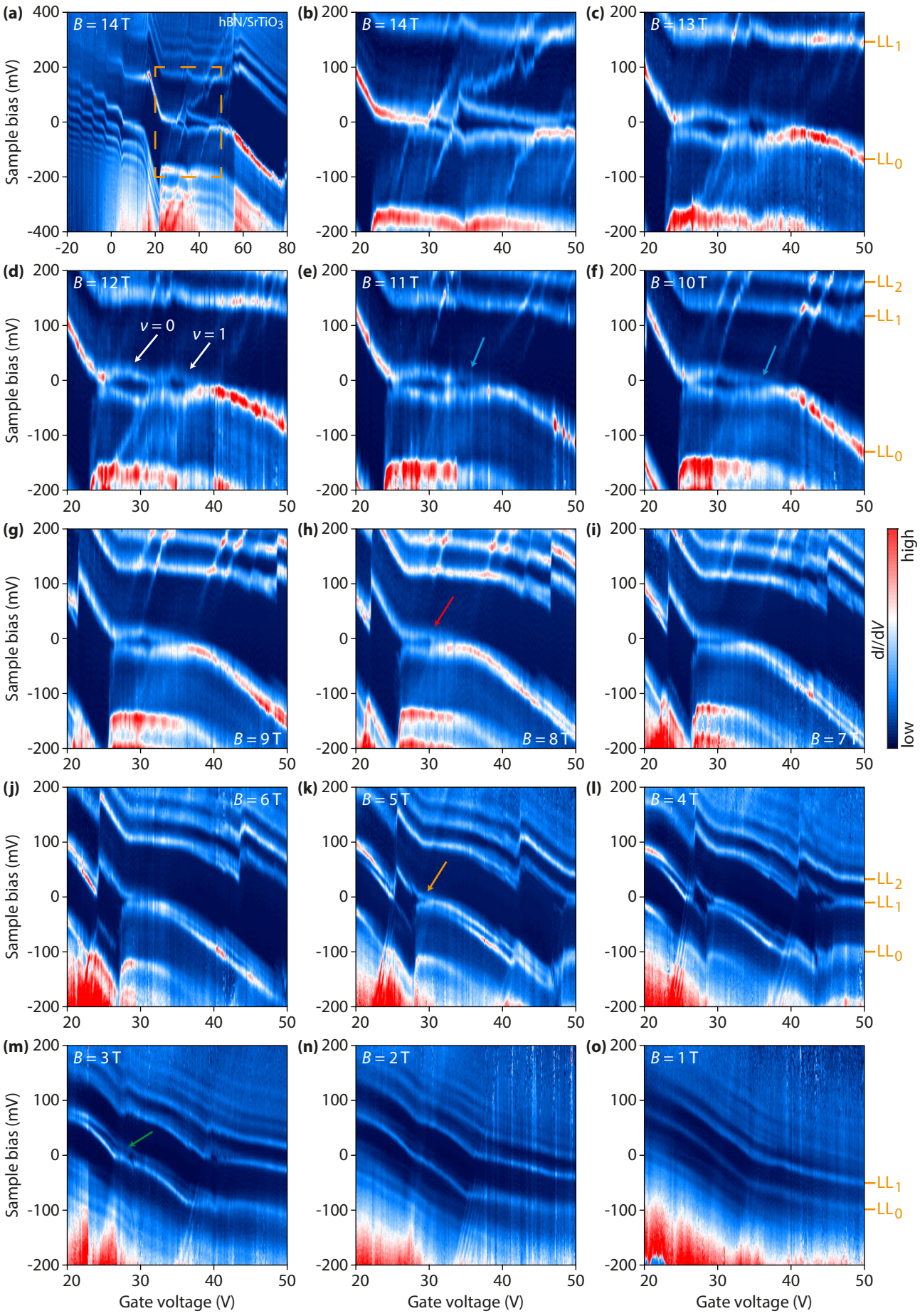

Figure 7.4: LDOS gate maps as a function of the magnetic field B on hBN/$SrTiO_3$, in sample BNGrSTO-STM-07 and at the same position.

Let us start at $B = 1$ T in the bottom right panel. Many peaks dispersing negatively with the gate voltage are visible, among them we can already distinguish LL_0 and LL_1. With increasing magnetic field the other resonant peaks eventually merge with each other to form LLs, as described by Gutiérrez *et al.* [82], see Figure 3.10. For instance LL_2 is formed at $B = 3$ T while LL_{-1} becomes distinguishable at $B = 5$ T. We also notice at $B = 1$ T that there is no pinning effect of E_F inside LLs, which thus disperse continuously with the gate voltage. We are still in the Shubnikov-de Haas regime where LLs are not fully separated. LLs start to pin the Fermi level at $B = 3$ T with the formation of a small plateau for LL_0 at $V_g = 27.5$ V, indicating the entrance into the quantum Hall regime. However note that the splitting of LL_0 in panel (m) is mostly due to the lifting of the orbital degeneracy, such that the apparent gap at zero bias (indicated by the green arrow) may be different from the interaction-induced gap we are aiming to. This orbital splitting is maximum at $B = 4$T and then decreases at higher magnetic fields.

The $\nu = 0$ gap finally opens at $B = 5$ T, see the yellow arrow in panel (k). Since the density of states of LL_0 grows as $B^{1/2}$, see Equation (2.31), the Fermi level stays pinned inside LL_0 for a wider and wider range of gate voltage with increasing B, and as a result the $\nu = 0$ gap develops on a larger LL_0 plateau. At $B = 8$ T the gap features a maximum due to its enhancement by exchange interactions, see the red arrow in panel (h). At $B = 10$ T, a second maximum appears on the right extremity of the LL_0 plateau, see the blue arrow in panel (f), while at $B = 12$ T we clearly distinguish two lobes marked by the white arrows in panel (d). The left lobe corresponds to the opening of the $\nu = 0$ gap whereas the right one is due to the opening of the $\nu = 1$ gap (however the $\nu = -1$ gap is not visible).

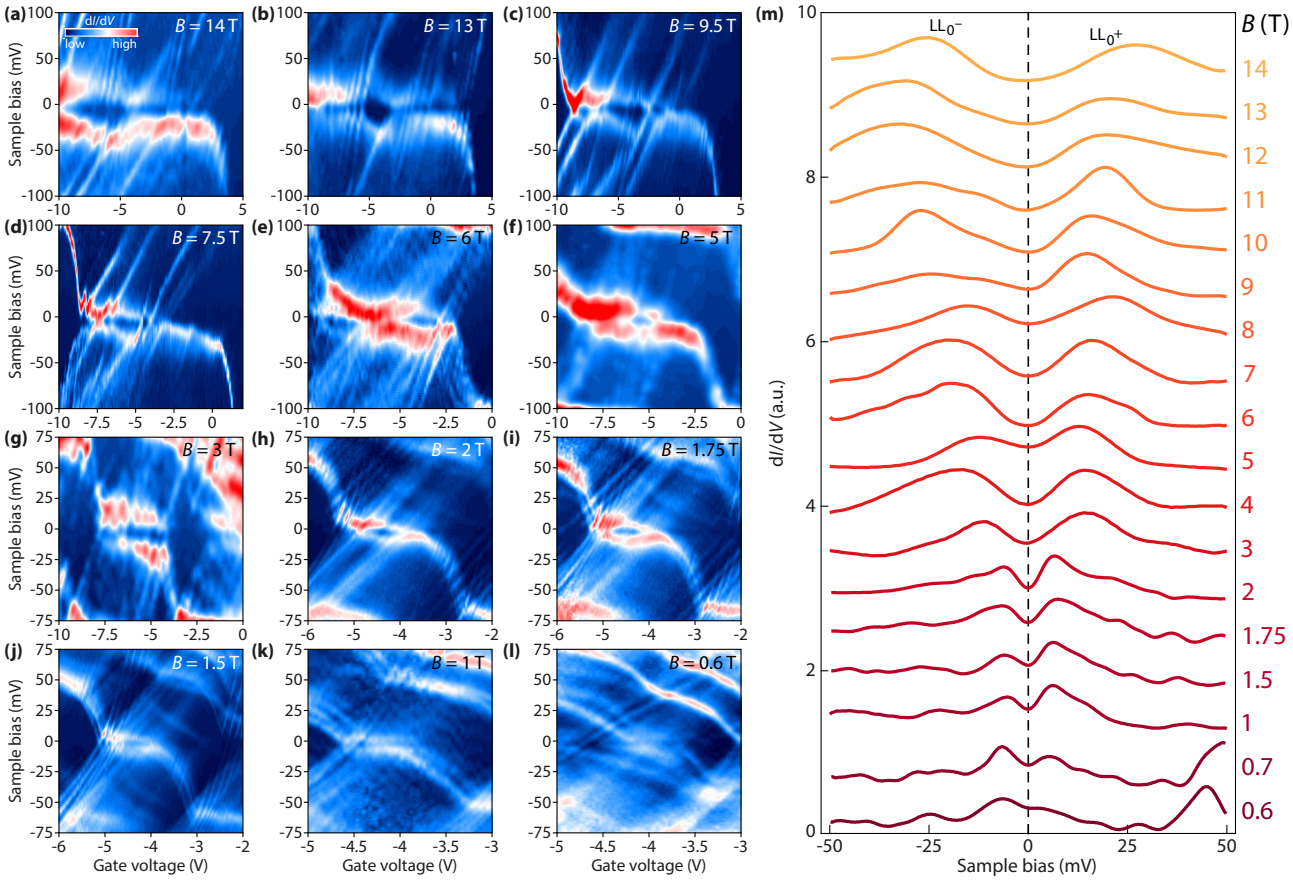

Figure 7.5: Evolution of $\Delta E^{\nu=0}$ with the magnetic field on hBN/SiO$_2$, in sample AC04. **(a-l)** LDOS gate maps at different magnetic fields. (b,c) were performed at the same position, same for (h-l). **(m)** Some dI_t/dV_{bias} spectra around (and centered at) zero bias we used to estimate $\Delta E^{\nu=0}$ from LDOS gate maps at different magnetic fields B.

7.1.d Evolution of the $\nu = 0$ gap with the magnetic field

With these LDOS gate maps[1] we can estimate the $\nu = 0$ gap at different magnetic fields B, using the methodology described previously. We compute the gap as the peak-to-peak energy, which gives an accurate estimation of the $\nu = 0$ gap since quasiparticles are here localized with no kinetic energy. We also ensured that the tip-induced band-bending is negligible (see Appendix C.2) and that tip-induced gating yields only a slight variation of filling factors of the order of 0.1 at most at the bias voltages of the split $LL_{0\pm}$ peaks (see Appendix C.7). Those gap measurements are carried out on the hBN/SiO_2 sample and the three hBN/$SrTiO_3$ ones. We show in Figure 7.5 some examples of $\Delta E^{\nu=0}$ estimations at different magnetic fields for the sample AC04 on hBN/SiO_2.

The evolution of the $\nu = 0$ gap $\Delta E^{\nu=0}$ as a function of the magnetic field B for the four samples is shown in Figure 7.6, which is one of the main results of this study.

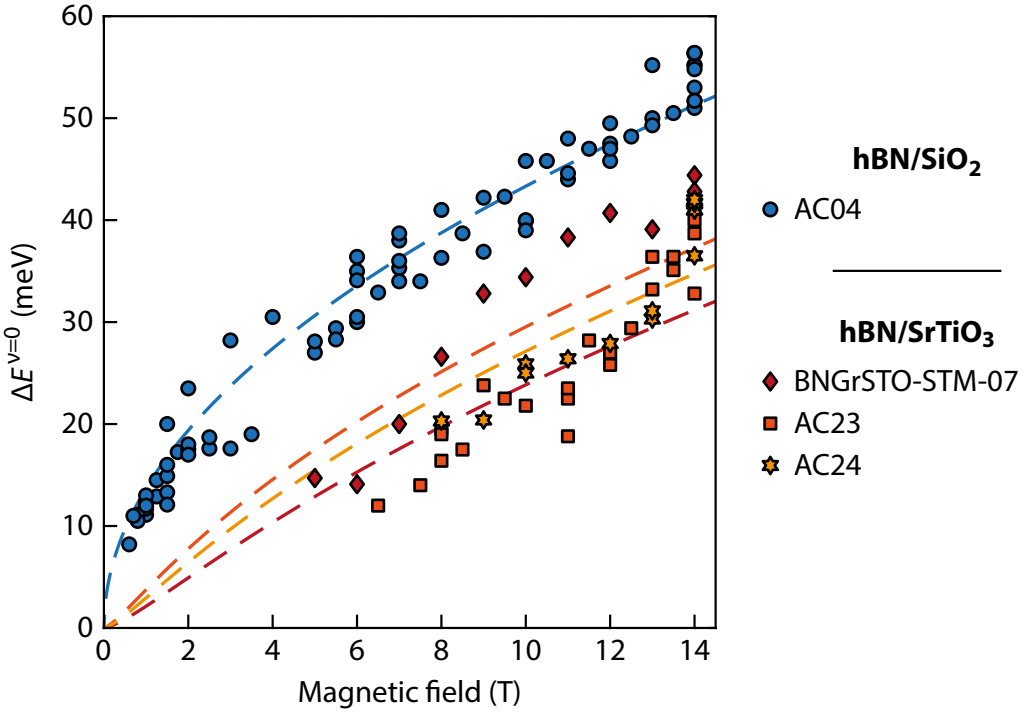

Figure 7.6: Evolution of the zeroth Landau level gap at $\nu = 0$ with the magnetic field. For sample AC04 on hBN/SiO_2 the interaction-induced gap $\Delta E^{\nu=0}$ scales as the Coulomb energy $E_C \propto \sqrt{B}$, drawn as the dashed blue line given by Equation (7.1). For the three samples on hBN/$SrTiO_3$ a clear decrease of $\Delta E^{\nu=0}$ due to substrate-screening is visible. The three dashed lines with matching colors for the three samples correspond to the substrate-screened Coulomb energy $\mathcal{E}_C$ given by Equation (7.5) with the hBN spacer thickness d_{BN}.

One can already remark that $\Delta E^{\nu=0}$ at a same magnetic field displays a dispersion of about $6 - 7$ meV : this is a consequence of the presence of weak charging features in our LDOS gate maps that intersect both $LL_{0\pm}$ peaks around $\nu = 0$ and may locally change the gap of a few meV. To minimize this effect and obtain pristine $\nu = 0$ gaps, the data points of Figure 7.6 come from LDOS gate maps where charging features are weak enough to prevent the formation of Coulomb diamonds, but nonetheless without completely disappearing, such as those of Figure 7.3(a) indicated by red arrows.

[1] One can remark in Figure 7.4 that the position of the maximum of the $\nu = 0$ gap, which is also the charge-neutrality point V^{CNP}, weakly fluctuates with the magnetic field. This prevents us from using LDOS magnetic field maps such as the one shown in Figure 5.9 to extract an accurate evolution of the $\nu = 0$ gap with the magnetic field B, since each dI_t/dV_{bias} at a given B would be done at a different filling factor around $\nu = 0$.

This dispersion also comes from the fact that, for our four samples, the different gap values at a given magnetic field in Figure 7.6 have been extracted from LDOS gate maps performed at different positions on graphene. This ensures the robustness of our measurements when it comes to spatial homogeneity, which is an important criterion to consider if we want to compare our local results with global transport measurements.

7.1.e Effect of screening

Unscreened $\nu = 0$ gap We first focus on the results for sample AC04 on hBN/SiO_2 (blue points). $\Delta E^{\nu=0}$ is clearly seen to increase as $B^{1/2}$, as expected for a gap induced by exchange interactions so that it scales like the Coulomb energy (see Chapter 2.3.1) :

$$E_C = \frac{e^2}{4\pi\epsilon_0\epsilon_m l_B} = \frac{e^{5/2}}{4\pi\epsilon_0\epsilon_m\hbar^{1/2}}\sqrt{B} \tag{7.1}$$

where $\epsilon_m = (1+\epsilon_{BN})/2$ is the effective dielectric constant felt by the graphene sheet lying between the hBN flake and vacuum. We were able to resolve both $LL_{0^\pm}$ peaks down to $B = 0.6$ T, with $\Delta E^{\nu=0}(B = 0.6\,\text{T}) \simeq 8.2$ meV. Below this magnetic field we could not resolve the opening of a gap inside LL_0, which is consistent with the width of the LL peaks, typically of $\Gamma \sim 15 - 20$ meV. Using Equation (7.1) we fit the blue points using ϵ_m as the fitting parameter. We obtain an excellent fit of the experimental data, represented by the blue dashed line for $\epsilon_m = 4.10 \pm 0.07$. However, for $\epsilon_{BN} = 3.6$ we rather expect $\epsilon_m = 2.3$ which is a value smaller than our experimental estimation.

Actually, the exchange gap is theoretically the energy of an infinitely separated skyrmion-antiskyrmion pair - namely, the cost to add an electron and a hole since skyrmions are quasiparticles for LL_0 - and so twice the energy of a skyrmion, computed as [112] :

$$E_{sk} = 4\pi\rho_s \tag{7.2}$$

with ρ_s the spin stiffness which is, for the zeroth Landau level [69] :

$$\rho_s = \frac{1}{16\sqrt{2\pi}}E_C \tag{7.3}$$

Therefore, $\Delta E^{\nu=0}$ is eventually expected to be [69] :

$$\Delta E^{\nu=0} = \frac{1}{2}\sqrt{\frac{\pi}{2}}E_C \tag{7.4}$$

With this exact scaling, the fit of the blue points now yields $\epsilon_m = 2.6 \pm 0.05$, which is consistent with the expected value for the relative permittivity $\epsilon_m = 2.3$. Such a quantitative agreement demonstrates the significance of our spectroscopy to assess the interaction-induced $\nu = 0$ gap.

Our result constitutes the first systematic study of the $\nu = 0$ gap directly probed by tunneling spectroscopy as a function of the magnetic field. Young *et al.* [62] also deduced that the broken-symmetry states in graphene arise from the Coulomb interaction, but they nonetheless observed an unexpected linear dependence with the magnetic field B of the activation energy of the $\nu = 0$ gap using transport measurements. We can conjecture that this transport characterization is related to edge transport which may have a smaller and different gap. On the contrary, Veyrat *et al.* [122] noticed a $B^{1/2}$ dependence of this same activation energy using also transport measurements. A similar $B^{1/2}$ dependence of the $\nu = 0$ gap was also observed by Kim *et al.* [83] using KPFM measurements for magnetic fields above $B = 8$ T, while below $B = 8$ T, $\Delta E^{\nu=0}$ rather increases linearly with decreasing B, see Figure 3.20. We here confirm the Coulomb origin of the $\nu = 0$ gap and directly observe its $B^{1/2}$ dependence from 0.6 T to 14 T.

Substrate-screened $\nu = 0$ gap We now discuss the results for the samples on hBN/$SrTiO_3$ (red, orange and yellow points). Here the $SrTiO_3$ substrate is expected to screen Coulomb interactions, which is at the origin of the formation of the ferromagnetic phase in graphene, see Chapter 2.3.4.b. The efficiency of this substrate-screening is furthermore supposed to depend on the hBN spacer thickness d_{BN} which must be smaller than the magnetic length l_B for electrons in graphene to feel the proximity of the $SrTiO_3$ substrate. This yields a substrate-screened Coulomb interaction $\mathcal{E}_{\mathrm{C}}$ calculated for hBN-encapsulated graphene samples :

$$\mathcal{E}_{\mathrm{C}} = \underbrace{\frac{e^2}{4\pi\epsilon_0\epsilon_{\mathrm{BN}} l_B}}_{E_{\mathrm{C}}} \times \underbrace{\left(1 - \frac{\epsilon_{\mathrm{STO}} - \epsilon_{\mathrm{BN}}}{\epsilon_{\mathrm{STO}} + \epsilon_{\mathrm{BN}}} \frac{l_B}{\sqrt{l_B^2 + 4d_{\mathrm{BN}}^2}}\right)}_{S(B)} \propto B^{3/2} \tag{7.5}$$

where E_{C} is the bare Coulomb energy and $S(B)$ the substrate-screening term.

In Figure 7.6, we indeed observe a strong reduction of $\Delta E^{\nu=0}$ for the three samples on hBN/$SrTiO_3$, of about 20 meV for $B > 6$ T which corresponds to a mitigation of about 40%. This therefore clearly confirms the substrate-screening of the Coulomb interaction in hBN/$SrTiO_3$ samples.

We were able to measure $\Delta E^{\nu=0}$ in sample AC23 down to $B = 6.5$ T, with a corresponding value $\Delta E^{\nu=0}(B = 6.5\,\mathrm{T}) = 12$ meV. Below this field, we were either limited by the width of LLs, which is about $\Gamma \sim 15 - 20$ meV, or by a sudden strong increase of the gap at zero bias. As we saw in Figure 7.4, our LDOS gate maps clearly show that this gap at low fields still exists away from charge neutrality - see Figure 7.4(l) for instance. We also noticed this gap did not clearly feature a dependence with the magnetic field, but at the opposite became strongly dependent on the position on graphene. It is therefore unlikely that this is the interaction-induced gap we study here and we did not consider those points.

We also notice that $\Delta E^{\nu=0}$ does not feature a $B^{1/2}$ dependence, which means the substrate-screening S in our samples indeed depends itself on the magnetic field, such as the screening term $S(B)$ described by Equation (7.5) for hBN-encapsulated graphene. Furthermore, Veyrat *et al.* [122] observed a similar linear behavior with the magnetic field of the activation energy at $\nu = 0$ in their hBN-encapsulated graphene devices on $SrTiO_3$ for $B > 7$ T.

We plot in Figure 7.6 the substrate-screened Coulomb energy $1/2\sqrt{\pi/2}\,\mathcal{E}_{\mathrm{C}}$ for the three hBN/$SrTiO_3$ samples as the red ($d_{\mathrm{BN}} = 8$ nm), yellow ($d_{\mathrm{BN}} = 10$ nm) and orange ($d_{\mathrm{BN}} = 12$ nm) dashed lines, using a modified Equation (7.5) where we have switched $\epsilon_{\mathrm{BN}} \longmapsto \epsilon_{\mathrm{m}} = (1 + \epsilon_{\mathrm{BN}})/2$ to adapt it to our graphene exposed to vacuum[2]. We consider the value $\epsilon_{\mathrm{m}} = 2.6$ we obtained with sample AC04 on hBN/SiO_2 since in Equation (7.5) the parameter ϵ_{m} describes the dielectric environment of graphene in absence of the $SrTiO_3$ substrate, which can thus be roughly estimated in our hBN/SiO_2 sample. We observe that the three dashed lines enable us to recover the good order of magnitude for $\Delta E^{\nu=0}$ for the three hBN/$SrTiO_3$ samples, even if we can not distinguish between the three of them as we should since they all possess a hBN spacer with a different thickness d_{BN}, and therefore more or less efficient substrate-screening. In particular, the data for sample BNGrSTO-STM-07 are above those of the other two samples although its hBN spacer is the thinner out of the three. With these fits we also retrieve a pretty good evolution with the magnetic field as $B^{3/2}$, see Equation (7.5).

[2]Note that this is a rough step : Equation (7.5) has been established for hBN-encapsulated graphene [122] where the presence of a thick top hBN flake enables to greatly simplify the electrostatic problem and to obtain an analytical expression for the substrate-screened Coulomb energy. In our case, the top hBN is missing and graphene is exposed to vacuum, which prevents us from obtaining a simple analytical formula.

7.2 Ground states of charge-neutral graphene

In this final section we deal with the question of the nature of the charge-neutral graphene ground state. As we have studied in Chapter 2.3.3, there are four possible $\nu = 0$ lattice-scale orders : the Ferromagnetic (F) phase, the Canted-AntiFerromagnet (CAF), the Charge-Density Wave (CDW) and the Kekulé Distortion (KD). The $\nu = 0$ phase diagram is shown in Figure 2.25. If the knowledge of the ground state in a graphene device holds important significance on the theoretical point of view, each phase possessing its own topological properties [267, 268, 269, 270, 271], it also induces different edge physics [116, 119] and therefore greatly influences the transport properties [107, 114, 122]. Notably the CAF, CDW and KD phases gives gapped edge excitations whereas the F phase induces gapless edge excitations.

Imaging the $\nu = 0$ ground state

The objective of this section is to image the $\nu = 0$ ground state in graphene on both hBN/SiO_2 and $hBN/SrTiO_3$ with STM. For this purpose we tune the back-gate voltage to bring graphene at charge neutrality, such that the $\nu = 0$ gap opens inside LL_0 at zero bias. We thus obtain in tunneling spectroscopy both $LL_{0^\pm}$ peaks, with LL_{0^-} the peak of the filled states of the $\nu = 0$ broken-symmetry state whereas LL_{0^+} is the peak of the empty states, see Figure 7.7(a).

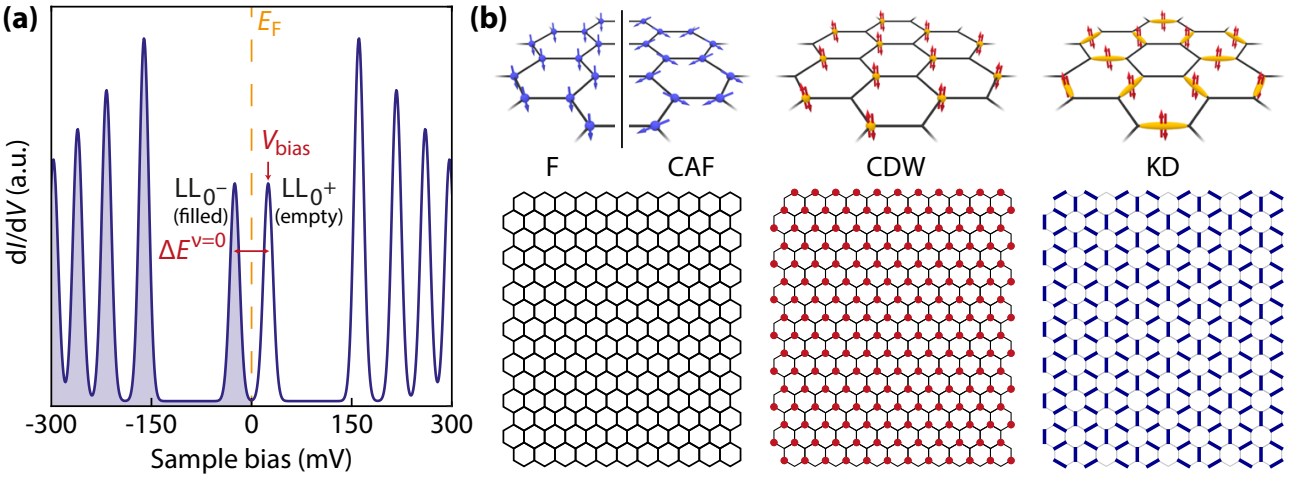

Figure 7.7: Imaging the $\nu = 0$ ground state in STM. (a) Simulated LL spectrum. Graphene is brought to charge neutrality with the gate voltage, so that the interaction-induced gap opens at zero bias. The sample bias V_{bias} is then set to either E_{0^+} or E_{0^-} to tunnel respectively into the empty or filled states of $\nu = 0$, before imaging graphene lattice in constant height mode. **(b)** Appearance in STM of the four possible ground states : since our tip is amagnetic, the F and CAF phases shall both appear as a pristine honeycomb lattice, while the CDW and KD phases would appear with a distinct sublattice polarization.

Starting from tunneling contact at ($V_{\text{bias}} = 300$ mV, $I_t = 1$ nA) with the Z-regulation on, we switch off the regulation and lower the bias voltage to either biases corresponding to the $LL_{0^\pm}$ peaks, which drastically decreases the tunneling current. We then manually approach the tip toward graphene until we get back a tunneling current of a few nA. STM scans with atomic resolution are subsequently realized to image the honeycomb lattice or its eventual polarization into one of the four possible $\nu = 0$ ground states. However, note that our tip is in amagnetic PtIr such that we can not resolve spin polarizations. As a consequence, the F and CAF phases which are not valley polarized would eventually appear in STM images as the usual honeycomb lattice and be indistinguishable. On the contrary, the CDW and KD phases which are valley polarized would appear with distinct sublattice polarizations, see Figure 7.7(b).

7.2.1 Kekulé distortion on hBN/SiO_2

Let us start with sample AC04 on hBN/SiO_2. Similar devices have been widely studied in transport and the nature of the charge-neutral graphene ground state has been a hot topic so far, in particular since the observation by Checkelsky in 2009 *et al.* [110, 111] of a strongly diverging resistance with magnetic field at $\nu = 0$ in graphene in SiO_2 devices, followed by a similar result obtained by Young *et al.* in 2012 [62] in graphene on hBN/SiO_2 devices. This insulating behavior already rules out the conductive F phase, notably Kim *et al.* [83] imaged the edge dispersion of LLs at a gate-induced pn-junction and clearly proved it features gapped edge excitations. The divergence of the resistance at charge neutrality has been predicted to be a signature of a magnetic-field induced Kosterlitz-Thouless transition toward a Kekulé instability of the graphene lattice [102, 114]. However, Young *et al.* [107] showed in 2014 that they could induce the formation of the F phase in graphene by tilting the magnetic field in order to boost the Zeeman effect (see Chapter 2.3.4.a). They justified their observations by considering that the strongly insulating phase at $\nu = 0$ at low magnetic field features a CAF order, such that by tilting the magnetic field all the spins would eventually tilt and align themselves toward its direction until the F phase arises, therefore inducing a phase transition which smoothly interpolates between the CAF and F phases. Since then, it has been believed that the ground state of insulating charge-neutral graphene on hBN/SiO_2 was a CAF phase.

7.2.1.a Observation of the Kekulé distortion of the honeycomb lattice

We demonstrate here that the $\nu = 0$ ground state of insulating graphene in fact features a Kekulé bond order, as shown in Figure 7.9 with a remarkably well-defined Kekulé distortion of the honeycomb lattice which appears as a bond-density wave. We have drawn in overlay the Kekulé lattice, with the enhanced bonds where spin-singlet pairs of electrons are localized as thick white lines. This phase appeared to be highly robust, as it was obtained in several different areas of graphene, after many reshaping of the tip on gold and also at different magnetic fields.

We describe in Figure 7.8 the Kekulé distortion lattice and we fix the conventions and notations we will use in this section. The KD is induced by a renormalization of the hopping parameters such that each C atom displays one strong bond out of the three it makes with its nearest-neighbors. The KD lattice is thus characterized by a unit cell three times larger than the one of pristine graphene. This lattice is shown in Figure 7.8(a). There are three possible and degenerate Kekulé distortions, represented in white, blue and red. Here, and in the following, we consider the white bonds to be the strong ones, while the red and blue are weak. The black arrows are the basis vector of the KD lattice. In Figure 7.8(b) we have drawn the unit cell only, which is comprised of three hexagons from the honeycomb lattice. We label each of them

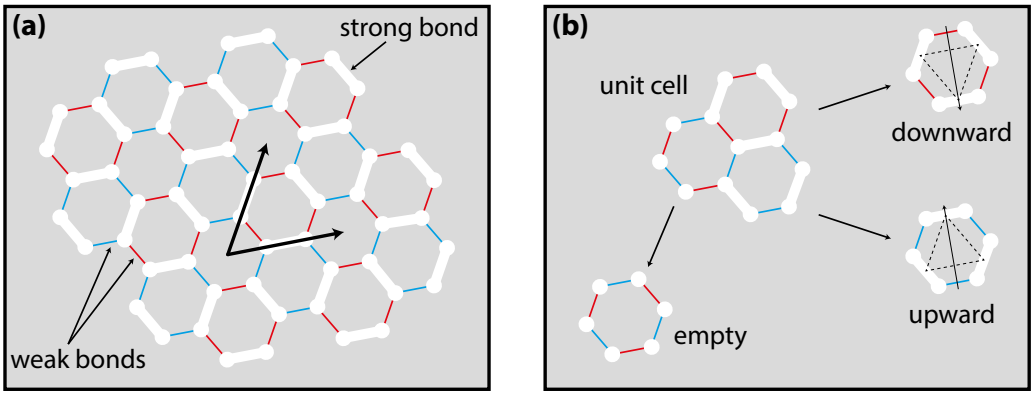

Figure 7.8: Kekulé distortion order - definitions and labels of the different cells.

as *upward* hexagons for those with three white strong bonds facing upward (see the dashed triangle, which is just a guide for the eye and not related to any physical bond) and three blue weak bonds, then *downward* hexagons for those with three white strong bonds facing downward and three red weak bonds, and last *empty* hexagons for those with no strong bond but only red and blue weak ones. For instance, in our STM image in Figure 7.9, empty hexagons appear moderately bright whereas upward and downward hexagons are dark regions encircled by three bright segments for their three strong bonds. Moreover, we will see later that we often observe an asymmetry between upward and downward hexagons.

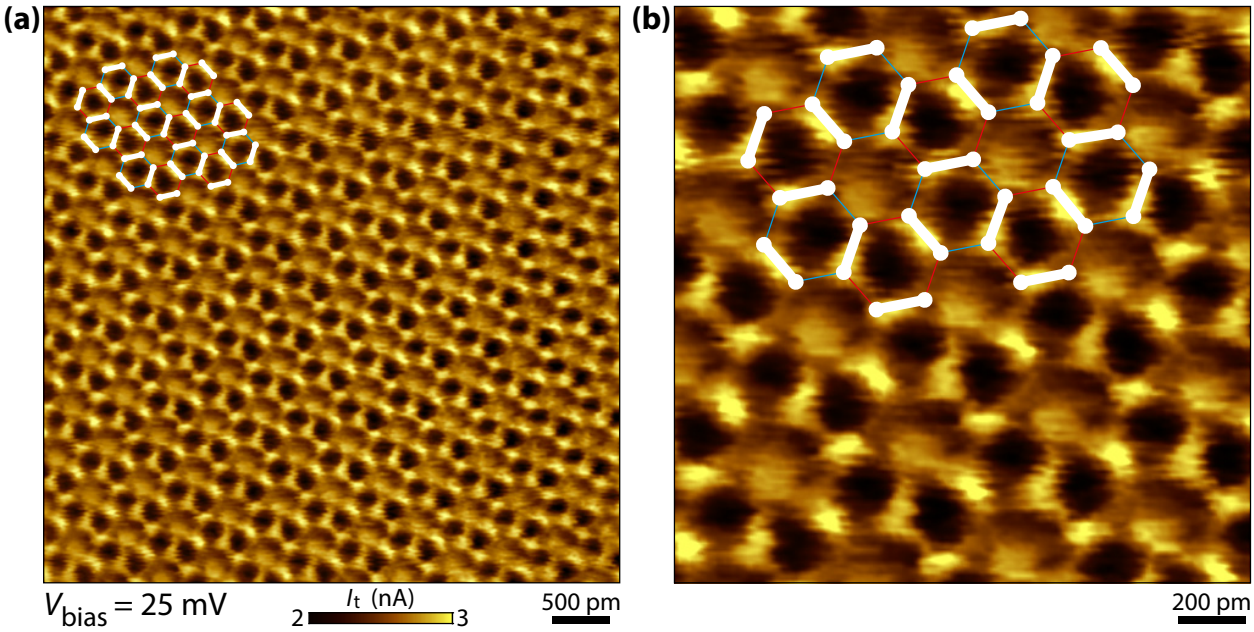

Figure 7.9: Kekulé distortion in charge-neutral graphene on hBN/SiO_2. $5 \times 5\,\mathrm{nm}^2$ image in constant height mode in sample AC04 at $T = 4\,\mathrm{K}$, $B = 14\,\mathrm{T}$ and at $V_{\mathrm{bias}} = 25\,\mathrm{mV}$ (LL_{0^+}). The KD lattice is shown in overlay. A zoom of (a) is displayed in (b).

As an aside, note that a similar Kekulé distortion was observed in STM by Li *et al.* [216] in graphene on graphite under magnetic field, see Figure 3.21. Furthermore, KD phases were also seen to emerge in other graphene systems with adatoms and at zero magnetic field [272, 273].

7.2.1.b Asymmetry of the Kekulé pattern

In fact, the imaging of this well-defined KD happened to be quite rare. We have rather most of the time obtained patterns such as the one shown in Figure 7.10(b). This is also a KD of the honeycomb lattice but there is an important asymmetry in the pattern. The stronger bonds in one specific direction (the nearly horizontal ones in the figure, drawn in gray instead of white) appear to blur toward the center of the upward hexagons, which enhances the adjacent blue bonds. The resulting asymmetry between the upward and downward hexagons gives this specific pattern with ball-like features, inducing an overall pattern similar to octopus suckers. Note also that the weak bonds of the KD are (barely) visible in this image.

In the following of this section, we will thus distinguish two types of KD patterns : the symmetric ones, where upward and downward hexagons look the same, and asymmetric ones where both hexagons appear quite differently with one of them having its three strong links sometimes merging into a circle.

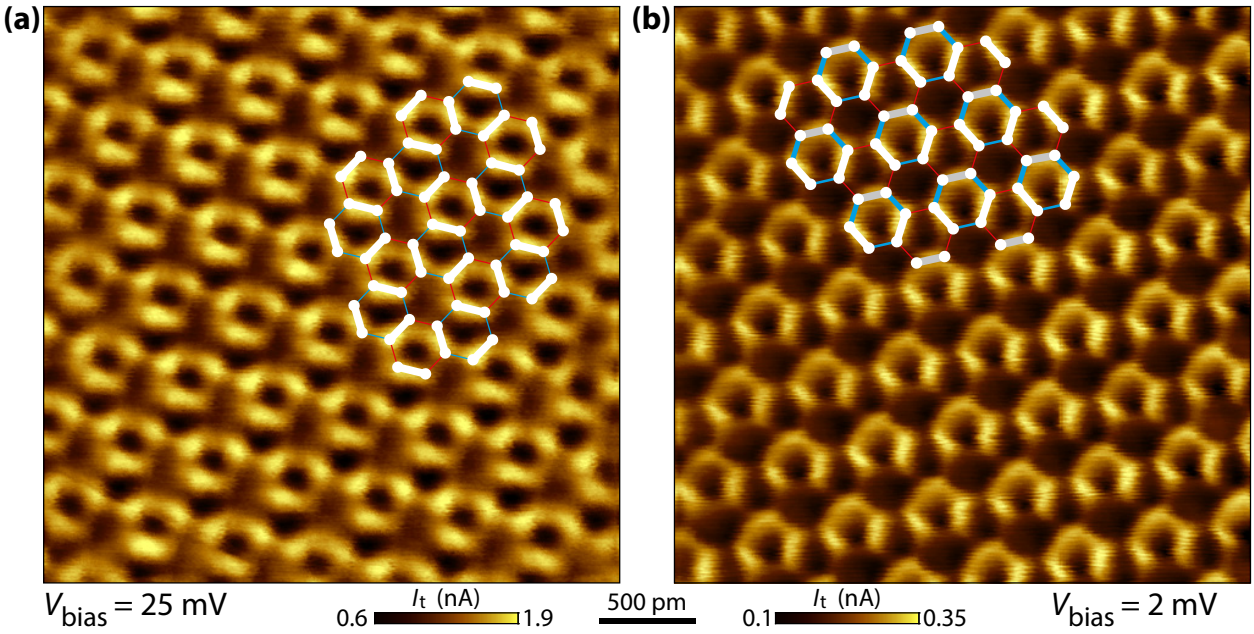

Figure 7.10: Asymmetry of the Kekulé distortion. $3 \times 3\,\mathrm{nm}^2$ images in constant height mode, **(a)** at $V_{\mathrm{bias}} = 25\,\mathrm{mV}$ with a mostly symmetric pattern, **(b)** at $V_{\mathrm{bias}} = 2\,\mathrm{mV}$ with an asymmetric pattern, arising from the blurring of the strong bond drawn in gray.

When we imaged the Kekulé ground state on a larger scale, see Figure 7.11, we most of the time observed asymmetric patterns. If on some images the strong bonds are still visible, see panel (b), they are usually not well resolved as they merge with each other, forming circles on upward or downward hexagons, which gives the octopus pattern visible in panels (a) and (c).

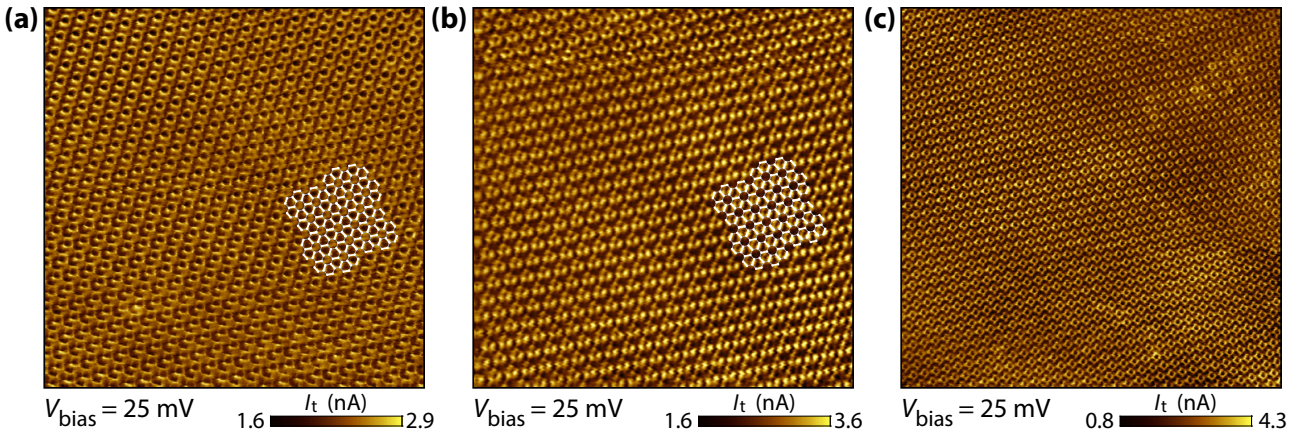

Figure 7.11: Long-range Kekulé distortion. (a,b) $10 \times 10\,\mathrm{nm}^2$ current STM images at $B = 14\,\mathrm{T}$ and $V_{\mathrm{bias}} = 25\,\mathrm{mV}$. **(c)** $15 \times 15\,\mathrm{nm}^2$ image under the same conditions.

7.2.1.c Characterization of the Kekulé distortion

We consider both KD patterns shown in Figure 7.10. We plot in Figure 7.12 the current profiles taken along the three directions perpendicular to the strong bonds of the KD (see the insets). For the mostly symmetric KD pattern, the three current profiles in Figure 7.12(a) are very similar. In particular, the three peaks which correspond to the strong bonds of the KD (indicated by black arrows) have almost the same height. On the contrary, for the asymmetric pattern, Figure 7.12(b) displays two very similar current profiles, the red and the green ones, whereas the blue profile (which goes across the blurred bonds) significantly differs from the other two. Notably, its peaks for the strong bonds are always smaller and broader.

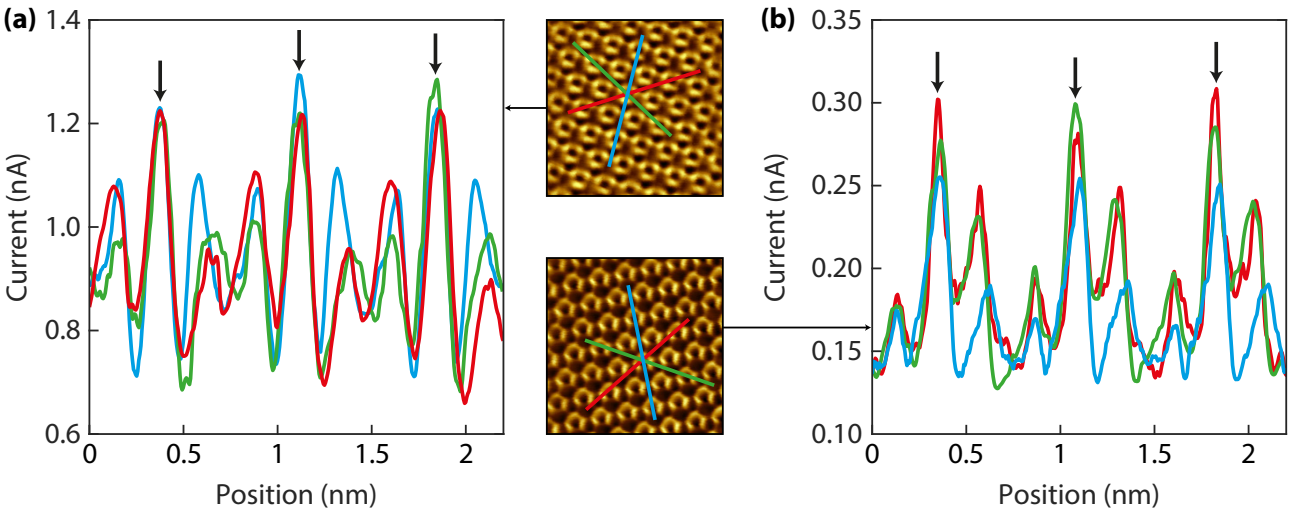

Figure 7.12: Current profiles of the Kekulé distortion. **(a)** Current profiles corresponding to the matching colored lines in the top inset (slightly asymmetric KD). **(b)** Current profiles corresponding to the matching colored lines in the bottom inset (asymmetric KD).

FFT analysis of the symmetric pattern In order to better understand this asymmetry of the Kekulé distortions, we study the 2D Fourier transforms of both patterns of Figure 7.10. We first consider the mostly symmetric KD pattern in Figure 7.10(a). We compute its 2D FFT and filter the STM image by considering only certain peaks of the FFT, see Figure 7.13. The 2D FFT is mainly comprised of three hexagons, defined by the yellow, red and blue encircled-peaks. We first filter the STM image by considering the yellow peaks only, which yields panel (c) : this is the usual honeycomb lattice. We now filter with the red peaks only, and obtain the image shown in panel (d) which features a triangular lattice. When we superimpose the honeycomb lattice in semi-transparency at the bottom right corner, we observe that each bright point of

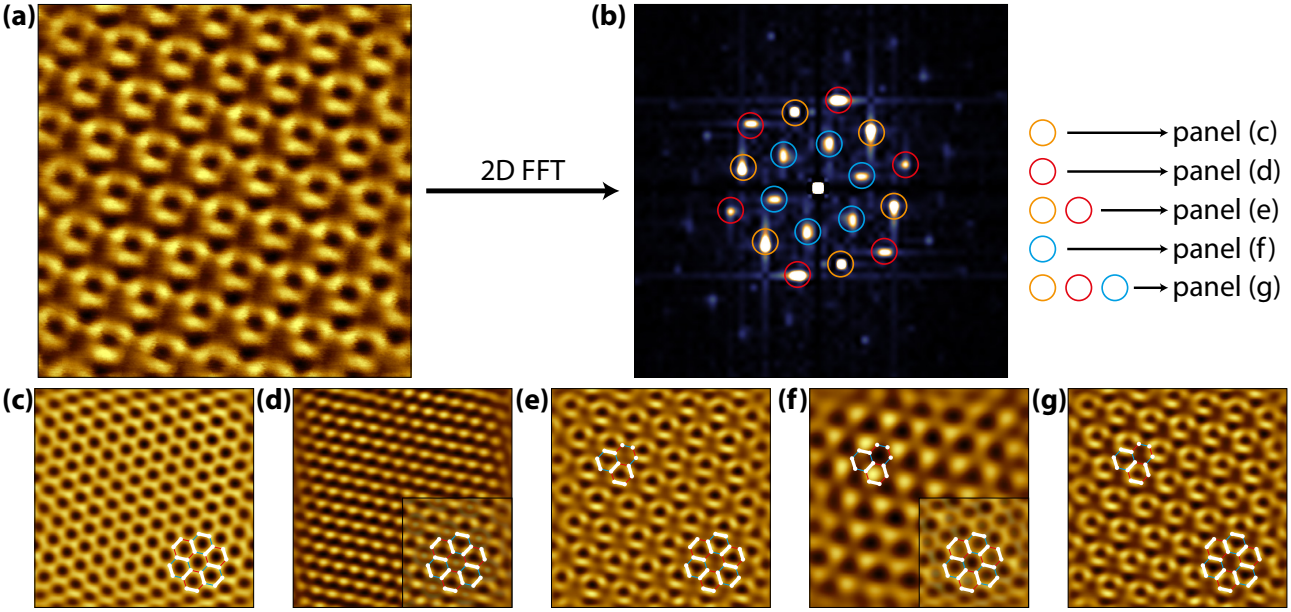

Figure 7.13: FFT decomposition of the symmetric Kekulé distortion. **(a)** Original image as obtained by STM in constant height mode and **(b)** its 2D FFT. The different peaks are marked by circles of different colors, notably the yellow peaks are those of honeycomb lattice. **(c-g)** Filtered images when considering only certain peaks, as indicated in (b). In the bottom right part of (d) and (f) we have superimposed the same area from (c) in semi-transparent.

this triangular lattice falls either on one C-C bond of the honeycomb lattice or at the center of one of its hexagons out of three (which happens to be the empty hexagon of the KD) : the addition of both images yields the Kekulé distortion, which is confirmed in panel (e) where we have filtered the STM image by considering this time both yellow and red peaks and obtained a symmetric KD pattern.

Last we show in panel (f) the image obtained after filtering using only the blue peaks. We observe a new triangular lattice with a period three times greater than the C-C distance in graphene, as visible in the bottom right part of the image where we have once again superimposed the honeycomb lattice. We have represented in the top left part of the image the unit cell of the KD : this second triangular lattice features the same periodicity than the KD pattern. We see that each of the three hexagons are weighted differently from this triangular lattice : the empty hexagon obtains no further weight, whereas both upward and downward hexagons get two different weights. Therefore, this triangular lattice, and the blue peaks in the FFT, are responsible of the asymmetry of the KD pattern we observe in our images. Here, this asymmetry happens to be rather weak. In panel (g) we show that we retrieve an accurate representation of our STM image, such that most of the information of our KD pattern is contained within the yellow, red and blue peaks of the FFT.

FFT analysis of the asymmetric pattern We now repeat this same FFT analysis for the asymmetric KD pattern of Figure 7.10(b), see Figure 7.14. The honeycomb lattice is retrieved in panel (a). However the image obtained in panel (e) by filtering using both yellow and red peaks only already displays a strong asymmetry, with upward hexagons forming ball-like features. This originates from the fact that two red peaks in the direction corresponding to the blurred gray bonds in Figure 7.10(b) are nearly halved in amplitude. Moreover, the triangular lattice obtained by filtering with the blue peaks only, see panel (f), is strongly asymmetric as well. This comes from a large asymmetry between the blue peaks in the FFT, where two peaks in

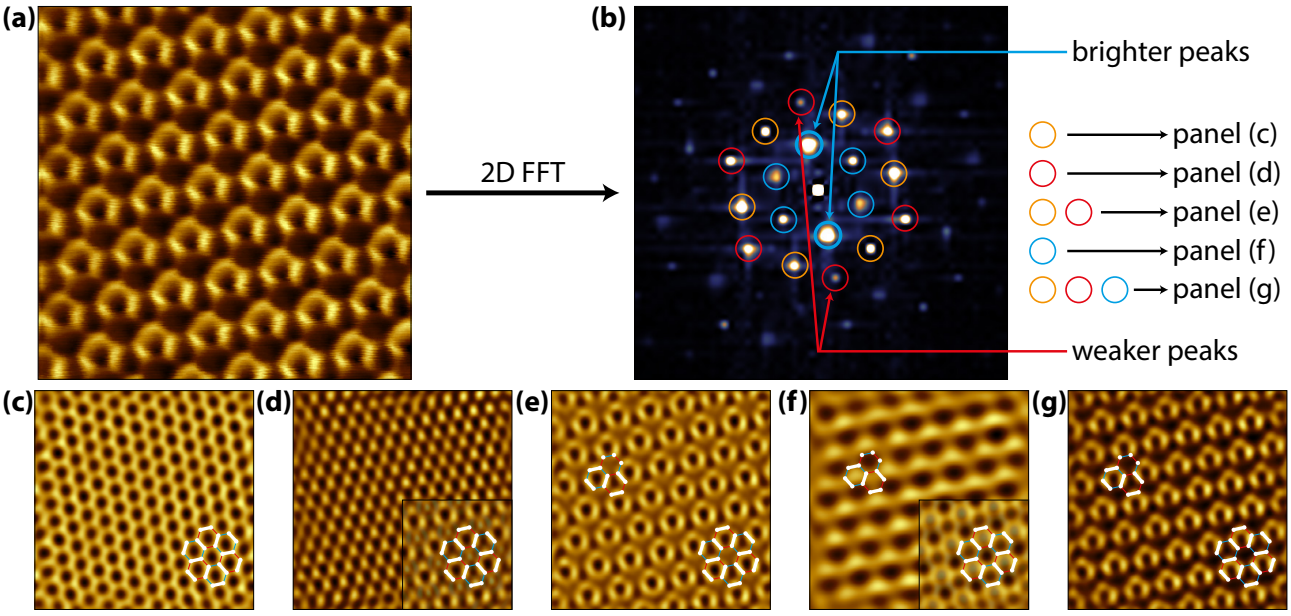

Figure 7.14: FFT decomposition of the asymmetric Kekulé distortion. (a) Original image as obtained by STM in constant height mode and **(b)** its 2D FFT. The different peaks are marked by circles of different colors, notably the yellow peaks are those of the honeycomb lattice. **(c-g)** Filtered images when considering only certain peaks, as indicated in (b). In the bottom right part of (d) and (f) we have superimposed the same area from (c) in semi-transparent.

one direction are twice as high as the others. The dissimilar weights this triangular lattice gives to upward and downward hexagons explains the strong asymmetry we observe in panel (a).

To conclude this FFT study, we have shown that the asymmetry in the KD patterns we observed in most of our STM images originates from the triangular lattice described by the blue peaks in the 2D FFT and which features a spatial modulation three times greater than that of graphene. It signifies that the KD phase coexists with a long-range charge-density wave (different from that predicted for the $\nu = 0$ ground state in Ref. [101]), that we label as K-CDW. Although it could be caused by the interactions between graphene and its hBN substrate, or by the tip which selects specific orbitals only, we will show latter that the K-CDW order varies with time, which shall rule out a stationary substrate or tip-induced effect.

7.2.1.d Kekulé distortion at negative bias

Previous images were measured at a positive bias, where we probed empty states. We show in Figure 7.15 images done at negative V_{bias} and at the same position than Figure 7.10(b). The top line displays the STM images, while the bottom line shows the same ones but with an inverted color map. The Kekulé pattern is plotted in overlay. At $V_{\text{bias}} = -43$ mV we tunnel outside the LL_0 gap and we observe the usual honeycomb lattice in the inverted image in panel (d). Still note that we can already see a slight distortion of the lattice that will give the KD at lower absolute bias. Indeed, at $V_{\text{bias}} = -25$ mV when we tunnel in the LL_{0^-} peak, the KD becomes well defined in both raw and inverted maps. We can also still observe the weak bonds between the ball-like features formed by the merging of the strong bonds in the downward hexagons. Eventually, at $V_{\text{bias}} = -12$ mV, only the balls are visible and the weak bonds are not.

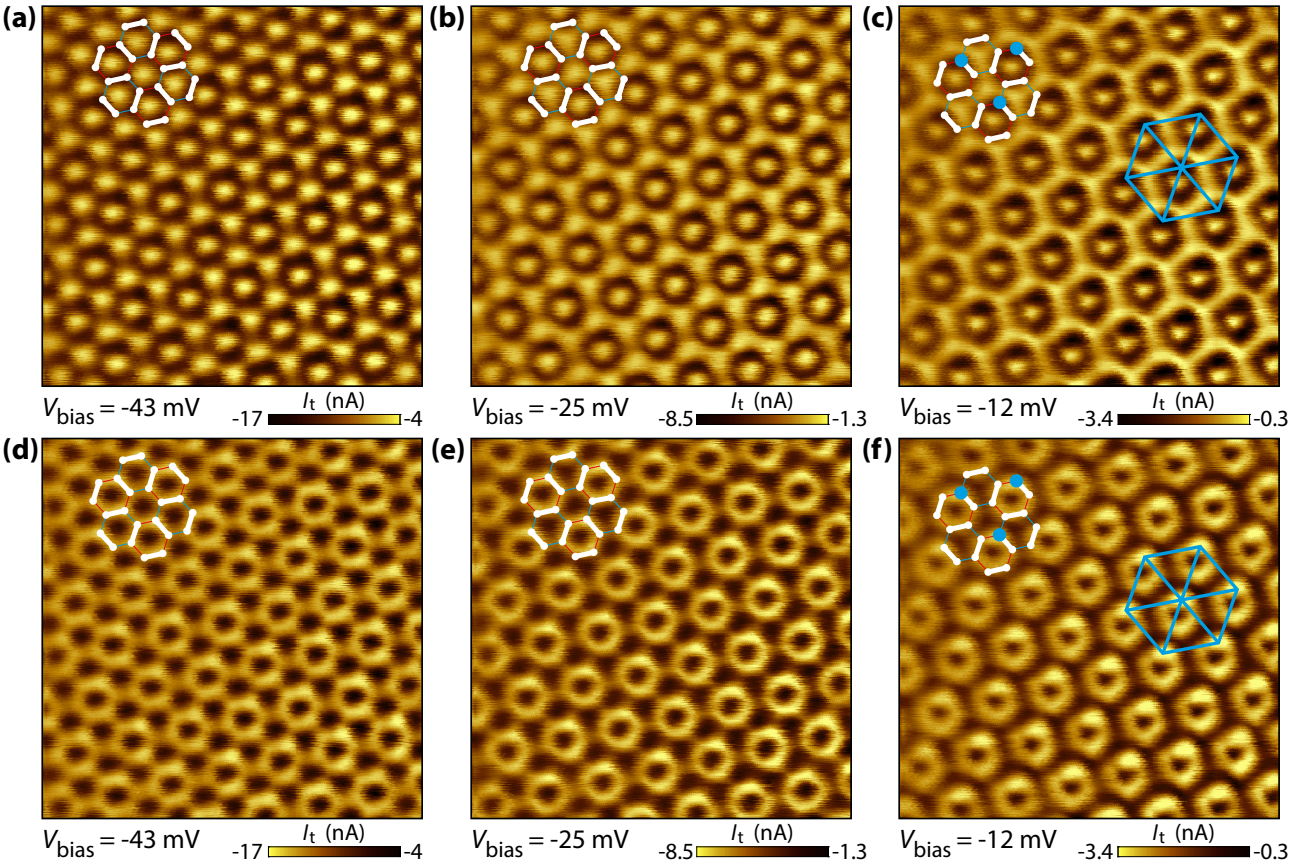

Figure 7.15: Kekulé distortion aspect at negative bias. (a-c) $3 \times 3\,\text{nm}^2$ current STM images at increasing negative bias voltages from top left to top right. **(d-f)** Same images than in the top panels but with inverted color map.

Moreover, we notice in Figure 7.15(c) the presence of dark spots which form a triangular lattice, represented in blue, with a parameter three times that of graphene. It is thus another signature of the K-CDW responsible for the asymmetry of the KD pattern we observed in the FFT analysis (blue peaks). Each of those dark spots corresponds to the same one atom in the KD unit cell (see the bigger blue atoms in the KD pattern at the top left). This triangular lattice is also visible in the other panels at lower bias, but less contrasted. It is in general not always visible (for instance in the first images of the KD we showed) and therefore the appearance of the K-CDW fluctuates with time.

7.2.1.e Contrast inversion

We now deal with the contrast inversion we should observe in our STM images by changing the sign of the bias, as we probe empty states at positive bias and filled states at negative bias, which should give, ideally, two complementary images. We show in Figure 7.16(a,b) constant height STM images where we have changed the sample bias V_{bias} as the scan was in progress. The arrows on the right of each panel show the direction of the slow axis of the scan, and their color corresponds to the actual sample bias, either on $\text{LL}_{0^\pm}$ peaks, which is indicated in the bottom insets. In both figures we clearly observe the contrast inversion with the continuity of the KD pattern at the interface. However, we sometimes obtained images with contrast inversion more complicated to explain. For instance, we show in Figure 7.16(c) such image which was measured at a constant bias (in opposition to the other two) of $V_{\text{bias}} = 25\,\text{mV}$. If we observe the expected asymmetric KD at the top of the figure, as the scan was ongoing a spontaneous contrast inversion occurred at the green arrow, such that we observe the inverted image at the bottom.

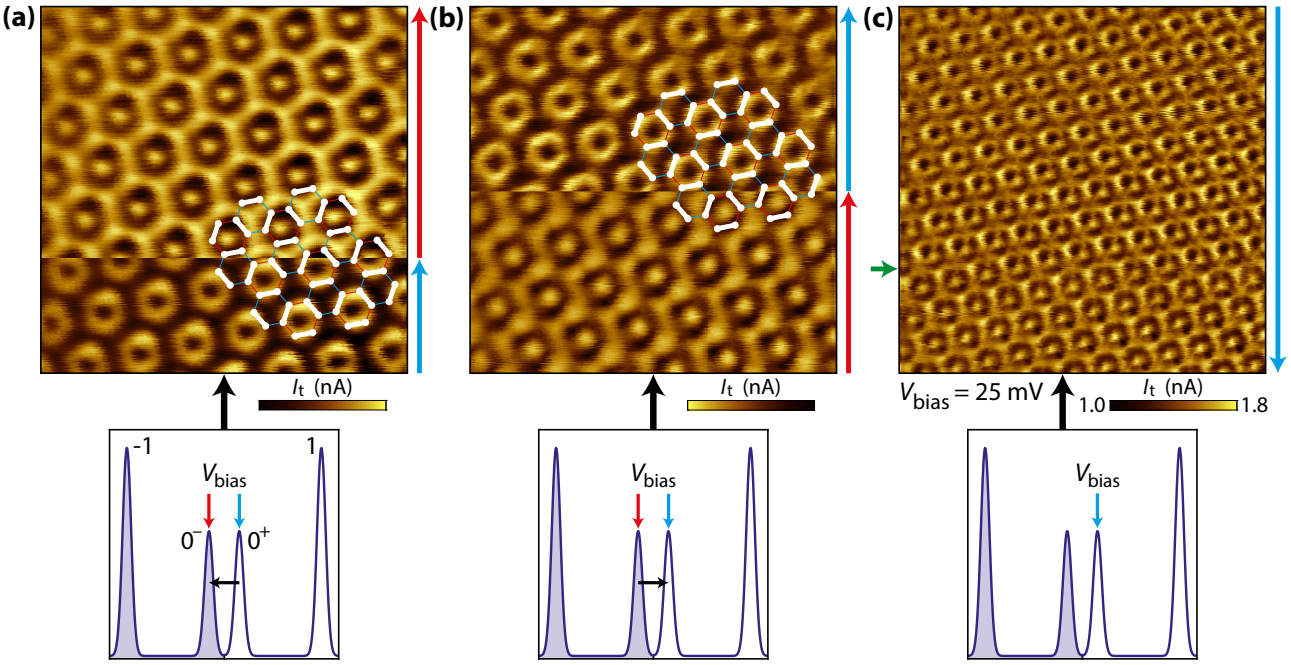

Figure 7.16: Kekulé distortion and contrast inversion. **(a)** $3 \times 3\,\text{nm}^2$ current STM image during which we changed the bias voltage (the current axis are tuned separately for each half of the map). We start (bottom) at $V_{\text{bias}} = 32\,\text{mV}$ (LL_{0^+}) and switch (top) to $V_{\text{bias}} = -12\,\text{mV}$ (LL_{0^-}) to observe the contrast inversion of the KD lattice. **(b)** Same than (a) but we start (bottom) at $V_{\text{bias}} = -11\,\text{mV}$ (LL_{0^-}) and switch (top) to $V_{\text{bias}} = 11\,\text{mV}$ (LL_{0^+}). We observe a similar contrast inversion. **(c)** $5 \times 5\,\text{nm}^2$ current STM image. While scanning at constant $V_{\text{bias}} = 25\,\text{mV}$, a spontaneous contrast inversion occurred at the line indicated by the green arrow.

7.2.1.f Emergence of the Kekulé phase

We now aim to visualize the emergence of the KD as a function of sample bias. We show in Figure 7.17(a,b) two images at different negative biases. Panel (a) was done at $V_{\text{bias}} = -43$ mV, outside the $\nu = 0$ gap but still in the tail of the LL_{0^-} peak. We observe the honeycomb lattice, but there is already one hexagon out of three which appears brighter than the others : this is the future empty hexagon of the KD lattice, which already starts to grow at this bias atop the honeycomb one. When changing the bias in panel (b) to $V_{\text{bias}} = -25$ mV, position of the LL_{0^-} peak, the KD phase appears. The KD lattice drawn in overlay clearly shows the bond-density wave, with a strong asymmetry as the upward hexagons are much darker than the downward ones.

We next performed in Figure 7.17(c) a new current image where we have changed the bias halfway and we clearly see the transition from the usual honeycomb lattice (top, $V_{\text{bias}} = -150$mV) to the KD pattern (bottom, $V_{\text{bias}} = -20$ mV). A similar image but for positive biases is shown in Figure 7.17(d). For both the KD pattern in overlay once again clearly shows the emergence of the bond-density wave and its continuity at the bias transition. Nonetheless the honeycomb lattices were there imaged at high biases (corresponding almost to $\text{LL}_{\pm 1}$). Last in Figure 7.17(e) we then show an image where we started from $V_{\text{bias}} = -43$ mV (top) just outside the $\nu = 0$ gap and changed to $V_{\text{bias}} = -25$ mV (bottom) which corresponds to the LL_{0^-} peak. We also observe the transition from the honeycomb lattice to the KD, which shows that the KD emerges only when we are tunneling inside the $\nu = 0$ gap.

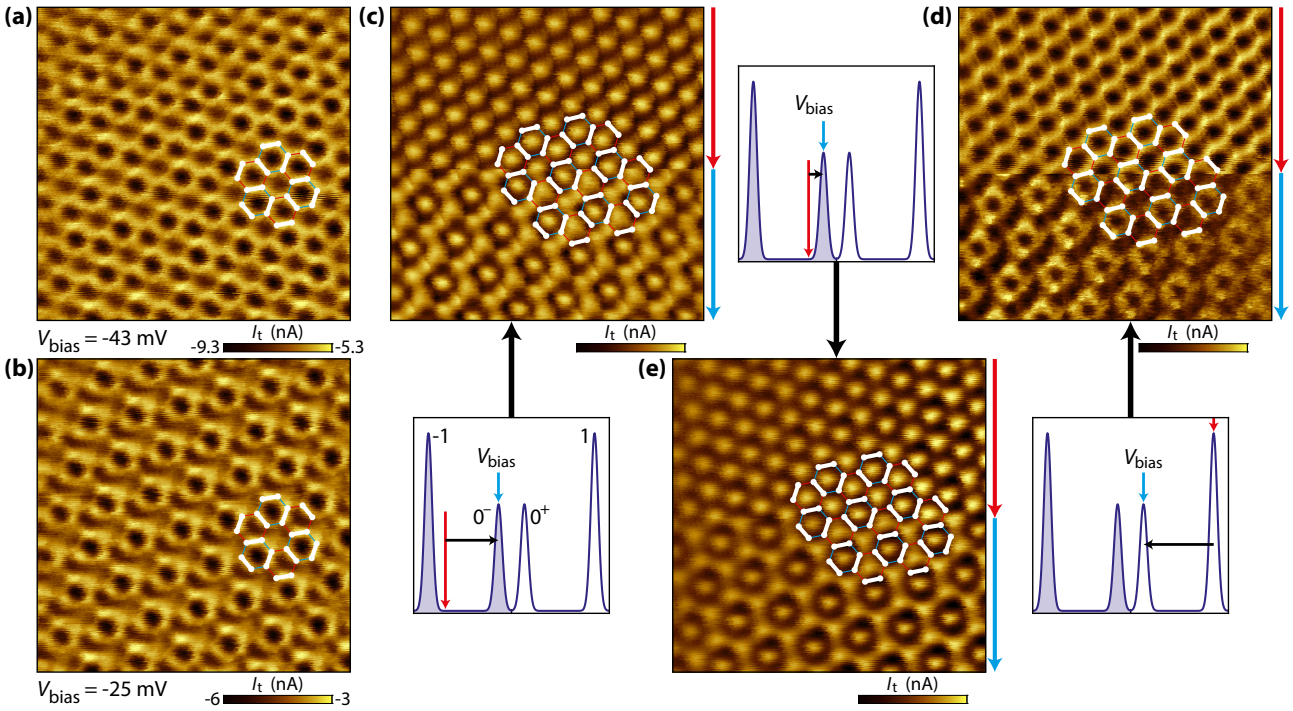

Figure 7.17: Emergence of the Kekulé distortion from the honeycomb lattice. (a,b) $3 \times 3\,\text{nm}^2$ constant height STM images at $B = 14$ T of the same area of graphene at $V_{\text{bias}} = -43$mV in (a) and at $V_{\text{bias}} = -25$ mV in (b) where the KD arises. **(c-e)** Images of the same region but where we changed the bias voltage at the middle of the scans (the current axis are tuned separately for each half of the maps). In (c) we start (top) at $V_{\text{bias}} = -150$ mV (cyclotron gap, close to LL_{-1}) where the honeycomb lattice is visible and switch (bottom) to $V_{\text{bias}} = -20$ mV (LL_{0^-}) where the KD appears. In (d) we start (top) at $V_{\text{bias}} = 200$ mV (LL_1) and switch (bottom) to $V_{\text{bias}} = 20$ mV (LL_{0^+}) to observe the emergence of the KD from the honeycomb lattice. In (e) we start (top) at $V_{\text{bias}} = -43$ mV (cyclotron gap, close to LL_{0^-}) and switch (bottom) to $V_{\text{bias}} = -20$ mV (LL_{0^-}) and observe a similar feature.

CITS experiment In order to observe the bias persistence of the KD pattern, we performed a CITS at $B = 14\,\mathrm{T}$ from $V_{\mathrm{bias}} = 300\,\mathrm{mV}$ to $V_{\mathrm{bias}} = -300\,\mathrm{mV}$. We show in Figure 7.18 spatial I_{t} and $\mathrm{d}I_{\mathrm{t}}/\mathrm{d}V_{\mathrm{bias}}$ maps at different V_{bias}, except in panel (a) where we show the topographic $z(x, y)$ map extracted from this CITS at $V_{\mathrm{bias}} = 300\,\mathrm{mV}$, with a well visible honeycomb lattice. At the same energy, the $\mathrm{d}I_{\mathrm{t}}/\mathrm{d}V_{\mathrm{bias}}$ map in panel (f) shows a homogeneous density of states. The same observation can be done for high negative bias, at $V_{\mathrm{bias}} = -290\,\mathrm{mV}$, see panels (o,t). Let us now see the evolution of the spatial maps as we increase the bias sample, starting from $V_{\mathrm{bias}} = -290\,\mathrm{mV}$. Below $V_{\mathrm{bias}} = -40\,\mathrm{mV}$, both I_{t} and $\mathrm{d}I_{\mathrm{t}}/\mathrm{d}V_{\mathrm{bias}}$ maps do not feature any significant spatial modulations. At $V_{\mathrm{bias}} = -40\,\mathrm{mV}$ in panel (s), the $\mathrm{d}I_{\mathrm{t}}/\mathrm{d}V_{\mathrm{bias}}$ map displays a weak spatial modulation : this corresponds to the case where we start tunneling in the tail of the LL_{0^-} peak inside the cyclotron gap. A residual honeycomb lattice is barely visible in the I_{t} map in panel (n).

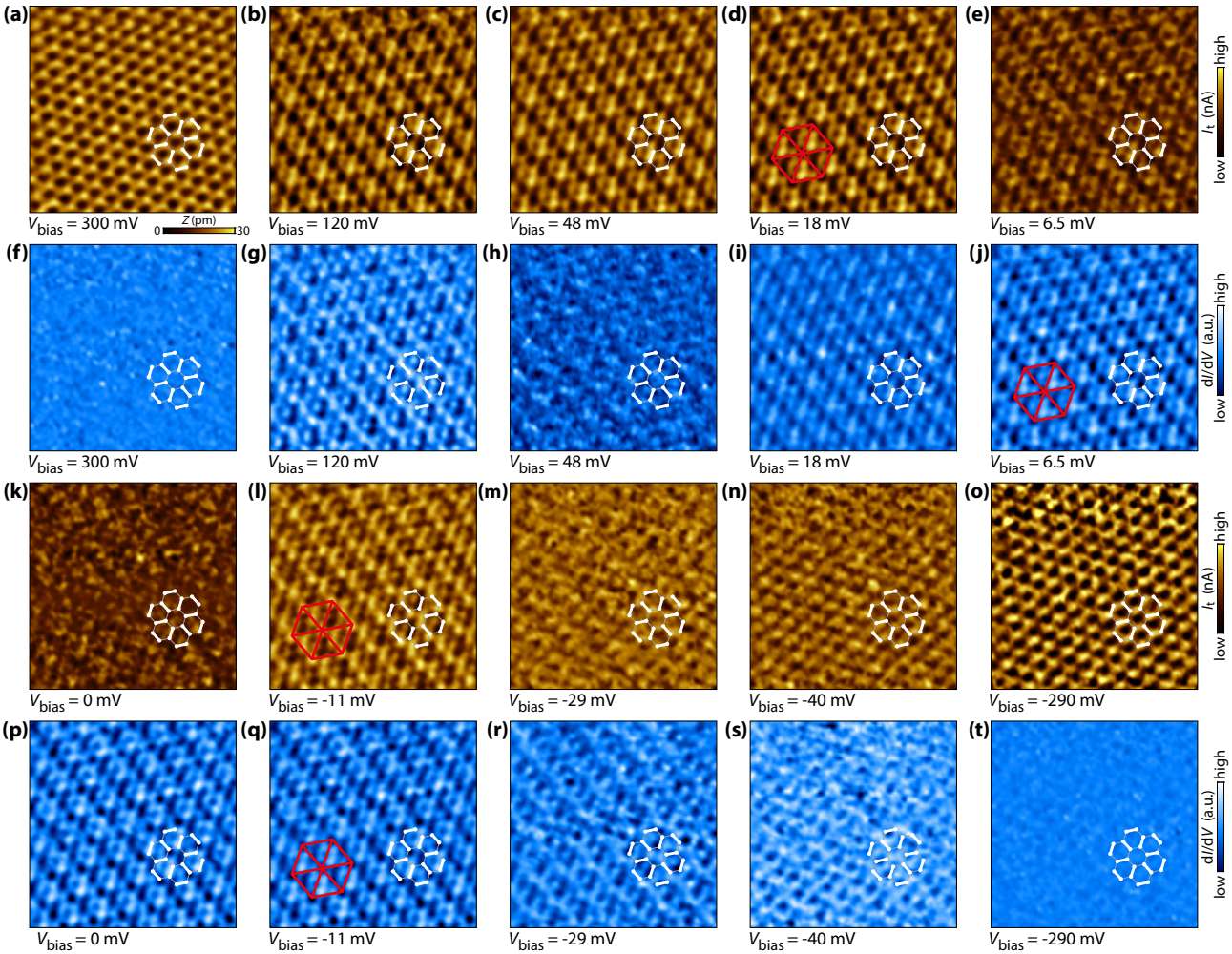

Figure 7.18: Emergence of the Kekulé ground state at low sample bias. Spatial I_{t} (first and third rows) and $\mathrm{d}I_{\mathrm{t}}/\mathrm{d}V_{\mathrm{bias}}$ (second and fourth rows) maps ($3 \times 3\,\mathrm{nm}^2$, 100×100 pixels) taken from a CITS at $B = 14\,\mathrm{T}$ and at different V_{bias}. (a) shows the topographic $z(x, y)$ map at ($I_{\mathrm{t}} = 1\,\mathrm{nA}$, $V_{\mathrm{bias}} = 300\,\mathrm{mV}$) of the area, where the honeycomb lattice is well defined.

At $V_{\mathrm{bias}} = -11\,\mathrm{mV}$, we probe states inside the $\nu = 0$ gap and the $\mathrm{d}I_{\mathrm{t}}/\mathrm{d}V_{\mathrm{bias}}$ map in panel (q) clearly shows a spatial modulation similar to the ball-like features visible in Figure 7.10(b). The KD order itself is nonetheless not well resolved. We also retrieve the K-CDW (red triangular lattice) which appears as dark spots. The I_{t} map as for her displays a weak modulation with bright spots at the same positions. The KD pattern in the $\mathrm{d}I_{\mathrm{t}}/\mathrm{d}V_{\mathrm{bias}}$ maps persists up to $V_{\mathrm{bias}} = 18\,\mathrm{mV}$ (LL_{0^+}) and vanishes above, see panel (h) at $V_{\mathrm{bias}} = 48\,\mathrm{mV}$, as we start tunneling inside the cyclotron gap between LL_{0^+} and LL_1. We therefore clearly show that the KD

order emerges only inside the LL_0 gap. On the contrary, the I_t maps show a more and more defined spatial modulation while increasing the sample bias inside the cyclotron gap and from $V_{bias} = 18\,mV$ (LL_{0^+}), modulation identical to that observed in the dI_t/dV_{bias} map for sample biases inside the LL_0 gap. This is simply understood by considering the I_t spatial maps as the integrals of the dI_t/dV_{bias} maps for energies from the Fermi level at $V_{bias} = 0$. Last, notice that at $V_{bias} = 120\,mV$, inside the cyclotron gap and nearly at the position of LL_1, an unexpected and non understood spatial modulation appears in the dI_t/dV_{bias} map, see panel (g), which looks like the inverted KD patterns shown in Figure 7.15(c).

7.2.1.g Vanishing at increasing filling factors

All the previous images were performed at charge neutrality, $V_g = V^{CNP} \simeq -5\,V$. Starting from this point, we increased the back-gate voltage by increments of 1 V and performed at each point current images to observe the evolution of the KD pattern as a function of the filling factor. If the KD stayed well visible up to $V_g = 0\,V$, it completely and abruptly disappeared at $V_g = 1\,V$, where only the usual honeycomb lattice was visible. Performing at this gate voltage a bias spectroscopy indeed showed us that we were at this point inside the cyclotron gap between LL_0 and LL_1, thus at a filling factor $\nu \approx 2$. This indicates that the appearance of the KD phase at low bias is a consequence of charge-neutral graphene physics.

7.2.1.h Persistence at low magnetic field

In this section we focus on the evolution of the KD phase as we decrease the magnetic field, starting from $B = 14\,T$ at which all the previous images were acquired. We show in Figure 7.19 images realized at $B = 14\,T$ in panel (a), at $B = 7\,T$ in panel (b) and at $B = 3\,T$ in panel (c). The three images were done at different locations and sample bias. At these three fields the $LL_{0^\pm}$ peaks are well defined and it is thus easy to tune the sample bias inside the $\nu = 0$ gap. At $B = 14\,T$ we recognize a highly asymmetric KD phase where the strong bonds form the same octopus-like pattern we have already observed in Figure 7.16. We retrieve the same pattern at $B = 7\,T$ and $B = 3\,T$, which proves that our KD phase persists at low magnetic field. This is consistent with the theory of the $\nu = 0$ state by Kharitonov [101] who predicted that no phase transition between the four possible ground states could be induced by increasing the perpendicular magnetic field B, since it would not change neither the signs nor the relative values of the anisotropy energies $u_{\perp,z}$ (defined in Chapter 2.3.3).

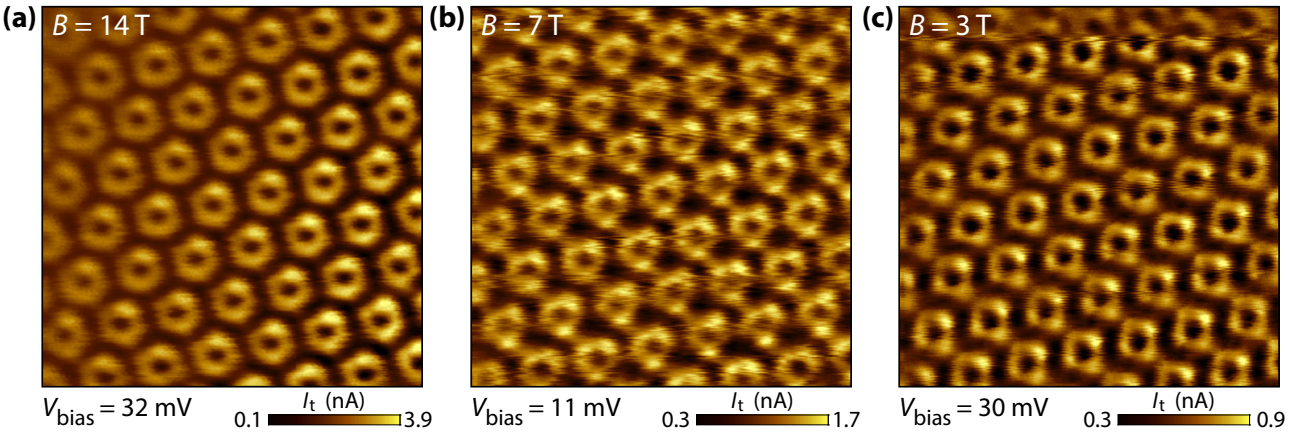

Figure 7.19: Persistence of the Kekulé distortion at low magnetic fields. **(a)** $3 \times 3\,nm^2$ current STM images at $B = 14\,T$ and $V_{bias} = 32\,mV$. **(b)** $3 \times 3\,nm^2$ current STM images at $B = 7\,T$ and $V_{bias} = 11\,mV$. **(c)** $3 \times 3\,nm^2$ current STM images at $B = 3\,T$ and $V_{bias} = 30\,mV$. The same asymmetric Kekulé pattern is well visible.

7.2.1.i Time evolution and moving defects

In this last section concerning the Kekulé distortion ground state on hBN/SiO_2, we describe some variations with time we observed during our measurements at $B = 14$ T. We first show in Figure 7.20(a) a strange image we acquired at the same location 15 minutes before we obtained the well-defined KD order shown in Figure 7.10(a), and recalled here in Figure 7.20(c). Both images were done at the same bias $V_{\text{bias}} = 25$ mV. By inverting the color map of panel (a), we eventually retrieve a KD pattern very similar to that in panel (c). This means that, for unknown reasons, a spontaneous contrast inversion occurred between the acquisitions of both images.

Moreover, the KD pattern differs when we compared panels (b) and (c). We have drawn the KD lattice in overlay at the same position in the three images. In panel (b), the red links correspond to the bright strong bonds in the image, whereas the blue and white links are not visible. On the contrary, in panel (c), the red and white bonds are not visible while the blue links correspond to the bright bonds in the image. We therefore observed a transition between two degenerate Kekulé configurations (out of the three possible, see Figure 7.8).

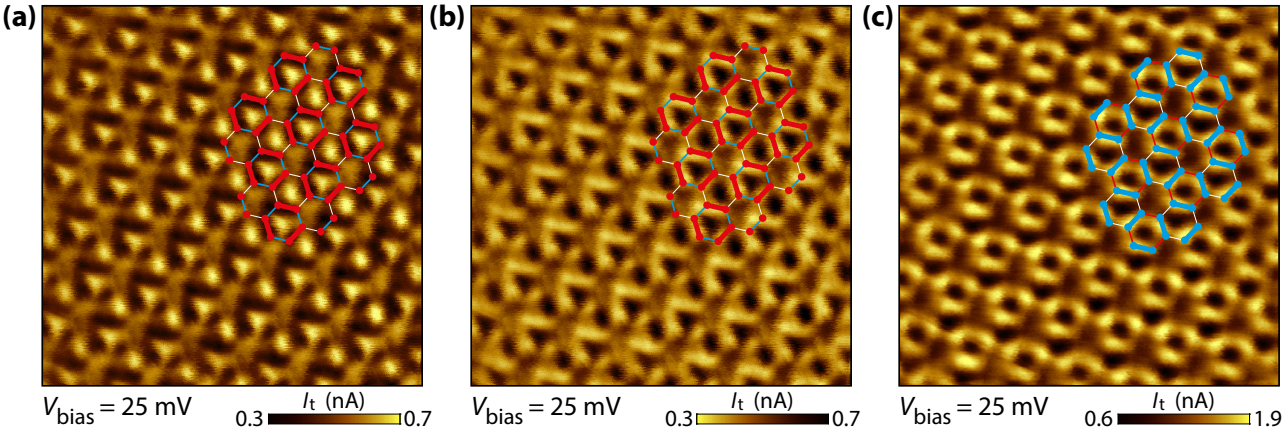

Figure 7.20: Transition between two Kekulé configurations. 3×3 nm^2 current STM images at $B = 14$ T, $V_{\text{bias}} = 25$ mV and at the same position. **(a,b)** Same image where the contrast is inverted in (b), which reveals the red Kekulé pattern. **(c)** Same image than in Figure 7.10(a) featuring a blue Kekulé pattern. The three lattices in overlay are at the same position. Note that we changed a few times the sample bias between the acquisitions of both images.

We now describe another kind of time variation of the KD phase. We show in Figure 7.21 three successive images acquired in a row at the same position and $V_{\text{bias}} = 2$ mV. The blue arrows on the left of each image indicate the direction of the slow axis of the scanning. The image in panel (a) is identical to that in Figure 7.10(b) (but taken a few minutes later). The lattice in overlay describes the asymmetric KD pattern, with the white links being the strong bonds of the KD, whereas the asymmetry that comes from the K-CDW makes the upward hexagons with blue weak bonds brighter than the downward hexagons with red bonds. The next image in panel (b) (duration of each image : 53 seconds) starts from the bottom, where we observe the same KD pattern. However a jump occurs at the line indicated by the red arrows and after that, in the top part of the image, the asymmetry of the KD pattern is reversed : using the lattice in overlay as a guide for the eye, we see that the downward red hexagons are brighter (due to the three strong white bonds almost merging together), such that the new pattern is the mirror of the previous one. Eventually, the next image in panel (c) displays this new pattern with brighter downward red hexagons on the whole area, and the next images we realized during several minutes happened to be identical. This means that the K-CDW changed at some point and reversed the asymmetry of the KD phase.

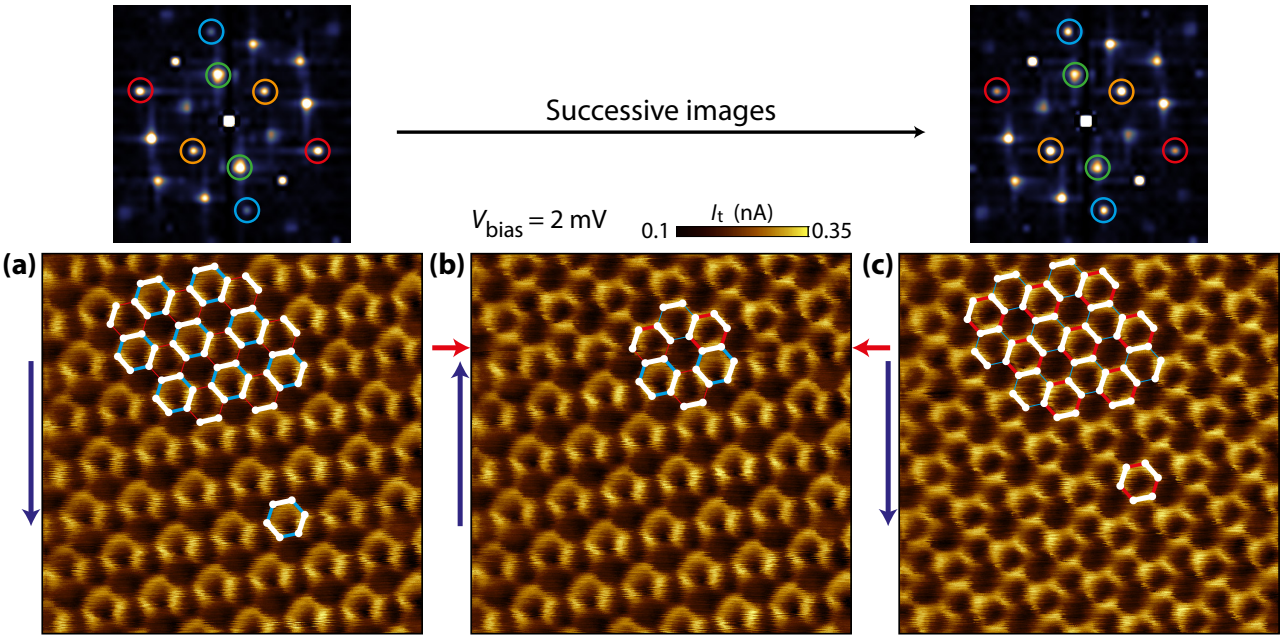

Figure 7.21: Asymmetry reversal of the Kekulé pattern. $3 \times 3\,\mathrm{nm}^2$ current STM images at $B = 14\,\mathrm{T}$ and at the same position and bias $V_{\mathrm{bias}} = 2\,\mathrm{mV}$. The three images were measured successively in a row (image time : 1 min). A jump occurs in (b) at the red arrows and reverses the asymmetry of the Kekulé pattern. The slow axis direction of the scanning is indicated by the blue arrows on the left of each image.

This is well seen in the 2D FFT of both images in panels (a) and (c), see the top insets. For panel (a), the K-CDW appears as the inner hexagon, where the two peaks encircled in green are twice as bright as the other four peaks. On the contrary, for panel (c), this is now the yellow peaks which are brighter, with the amplitude of the green peaks lowered. The change of the direction of the two brighter peaks induces the change of the asymmetry pattern of the KD. Interestingly, the outermost hexagon, which corresponds to the bond-density wave responsible of the KD, also features a change of the intensity of its peaks : in panel (a) the blue peaks are halved in amplitude while in panel (c) this is here the red peaks which are halved. This does not yield any significant change of the KD pattern but this may mean that the bond-density wave and the K-CDW are hybridized. We there recover the conclusion that the asymmetry of the KD we observed strongly depends on the time fluctuations of the K-CDW.

Moreover, the fact that we captured the line with the jump in panel (b) indicates that the K-CDW switches instantaneously on the time-scale of the scan speed. This can also point out either a change of the K-CDW on the entire sample in case of a homogeneous K-CDW, or the displacement of domains with different K-CDW configurations separated by domain walls[3]. Note this only concerns the K-CDW order, the KD order itself stays unchanged in the three images (the bright bond pattern remains the same).

The transitions of the K-CDW happened a few times during our measurements. In Figure 7.22(a) we show a $5 \times 5\,\mathrm{nm}^2$ image of a mostly symmetric KD pattern. In the top part of the image the ball-like features are again visible and emerge from brighter upward hexagons with blue weak bonds. When doing the same reasoning in the bottom part of the image, we find again the mirror pattern with downward hexagons with red weak links (see the overall KD lattice at the bottom right). The K-CDW background transited at the line indicated by the red arrows, where

[3]We point out that we cannot exclude a K-CDW configuration change induced by the action of the scanning tip. Still, such a tip-induced change also implies that the K-CDW is not pinned and can be subject to fluctuations.

we retrieve locally the KD pattern with no asymmetry between upward and downward hexagons. As previously, the KD lattice itself does not change, see the white dashed line which is a guide for the eye and shows that we have the same pattern of strong white bonds in both parts of the image.

A similar feature happened also in Figure 7.22(b) which displays a $10 \times 10\,\mathrm{nm}^2$ image. The jump between both CDW backgrounds is well visible at the line indicated by the red arrows, and the white dashed line which intercepts the balls in the top part of the image eventually passes between the balls in the bottom part.

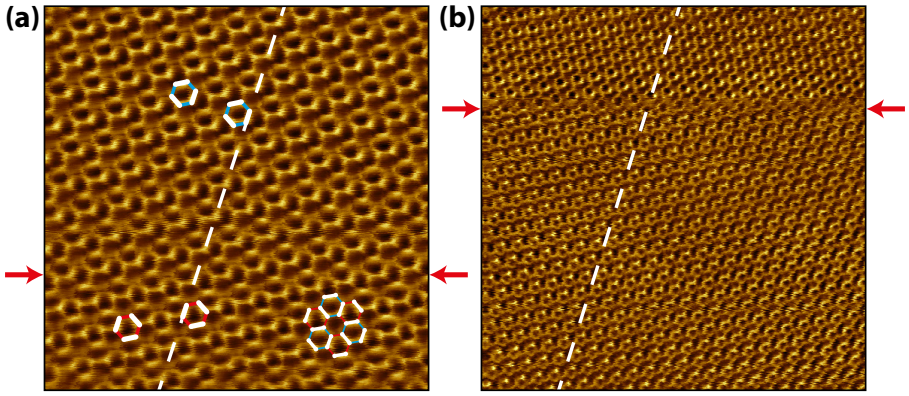

Figure 7.22: Variation of the Kekulé asymmetry pattern. **(a)** $5 \times 5\,\mathrm{nm}^2$ current STM image at $B = 14\,\mathrm{T}$ and $V_{\mathrm{bias}} = 25\,\mathrm{mV}$. The asymmetry pattern changes at the red arrows, see the white dashed line which is a guide to the eye. **(b)** $10 \times 10\,\mathrm{nm}^2$ current STM image at $B = 14\,\mathrm{T}$ and $V_{\mathrm{bias}} = 25\,\mathrm{mV}$. The asymmetry pattern changes as well at the red arrows.

Finally we show in Figure 7.23 a last $20 \times 20\,\mathrm{nm}^2$ image. The asymmetric KD pattern is well visible in the top part of the image, see the zoom in the red inset, whereas it is completely washed out in the bottom part, see the yellow inset where there is no longer a bond-density wave. However, the honeycomb lattice we observe in this area is highly deformed, see the zoom in the blue inset, and seems to display a Kekulé-Y distortion [273, 274]. It eventually revealed to be a transient defect as the next image we did right after in this same yellow area features the asymmetric KD lattice.

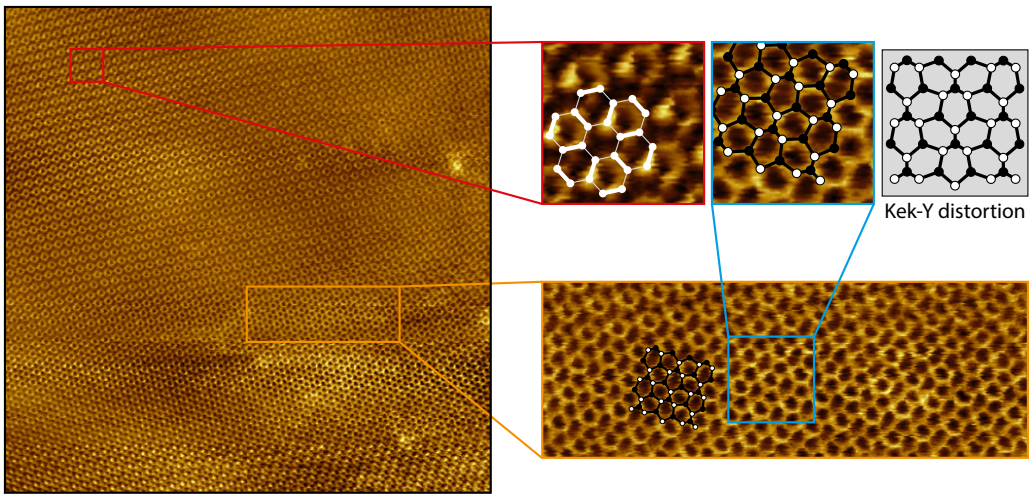

Figure 7.23: Domain with distorted honeycomb lattice in the asymmetric Kekulé pattern. (Left) $20 \times 20\,\mathrm{nm}^2$ current STM image at $B = 14\,\mathrm{T}$ and $V_{\mathrm{bias}} = 25\,\mathrm{mV}$. In the top part the asymmetric KD is well visible. In the bottom part the KD vanishes for the duration of this image only. In the yellow inset, the honeycomb lattice is highly distorted (see blue inset).

7.2.1.j Conclusion for graphene/hBN/SiO_2 samples

We imaged from $B = 14\,\mathrm{T}$ down to $B = 3\,\mathrm{T}$ a Kekulé distortion of the honeycomb lattice, which coexists with a long-range charge-density wave (K-CDW) with a parameter three times greater than the C-C distance. This induces a strong asymmetry of the KD pattern in most of our images. This sub-dominant K-CDW order adds a new flavor to the phase diagram, which was not anticipated thus far and deserves further theoretical attention. The observation of the KD order also contradicts the transition scenario from the conjectured CAF phase to the helical F phase tuned by the Zeeman field [62, 101, 107], as well as with recent magnon transmission experiments [275] that imply magnetism. Nonetheless, a recent prediction [276] suggests that both KD and CAF phases could co-exist, thus accounting for the experimental dissonance. One last point, the images shown in Figure 7.20 were acquired at about $d_{\mathrm{edge}} \simeq 20\,\mathrm{nm}$ from the armchair edge studied in Chapter 6.2, which indicates that the KD persists down to at least $3\,l_B$ from graphene edge.

7.2.2 Charge density wave on hBN/$SrTiO_3$

In this section we consider sample AC23 on hBN/$SrTiO_3$. In Ref. [122] we observed in hBN-encapsulated graphene samples on $SrTiO_3$ the emergence of the quantum spin Hall effect at $\nu = 0$ and low magnetic field, around $B = 1 - 3\,\mathrm{T}$, which is a signature of the formation of the conductive F phase in charge-neutral graphene. On the contrary, at higher magnetic fields, we remarked a divergence of the resistance at charge neutrality much weaker than the divergence observed in usual hBN/SiO_2 devices, suggesting in hBN/$SrTiO_3$ samples a magnetic-field induced phase transition from the conductive F phase to an insulating phase that might differ from the insulating Kekulé phase observed in our hBN/SiO_2 samples.

Indeed, we show in Figure 7.25 that the $\nu = 0$ ground state at high magnetic field ($B = 14\,\mathrm{T}$) features an outstanding charge-density-wave order with the spin-singlet pairs of electrons localized on a single sublattice of graphene. In both panels, the honeycomb lattice is drawn in overlay and placed using images acquired at the same location but at $V_{\mathrm{bias}} = 300\,\mathrm{mV}$ where the CDW vanishes and the honeycomb lattice appears instead.

Before we go further, we present the CDW lattice and the notations we will use in this section. We suppose both electrons of the $\nu = 0$ state are localized on sublattice A with blue atoms, while the second sublattice B with red atoms is empty, see Figure 7.24(a). We then introduce the different notations in Figure 7.24(b) for an interacting tight-binding model of graphene : t is the nearest-neighbor hopping parameter and V_1 is the nearest-neighbor interaction between atoms from different sublattices, whereas t_2 is the second-nearest-neighbor hopping parameter and V_2 is the second-nearest-neighbor interaction between atoms from the same sublattice A or B. For the usual honeycomb lattice, we have $t \gg t_{2,A} = t_{2,B}$ and $V_1 \gg V_2$.

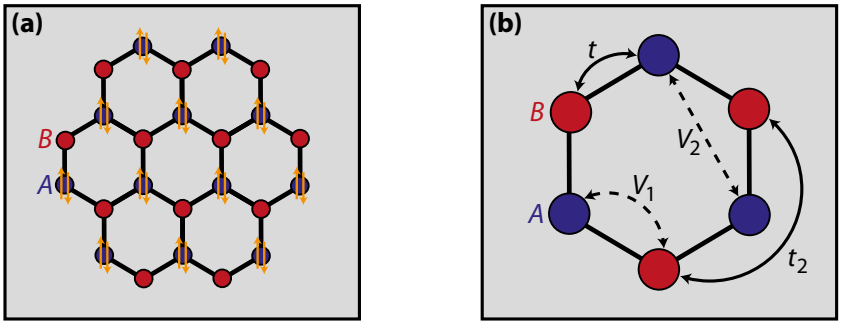

Figure 7.24: Charge-density wave - definitions and notations.

7.2.2.a Observation of the charge-density wave

In both images the CDW appears as bright or dark spots featuring a triangular symmetry corresponding to that of the atoms of a same sublattice, whereas the atoms of the other sublattice are not visible. Moreover, a contrast inversion occurs between the two images made at a negative (left) and positive (right) bias. However it is not a trivial inversion since in the image at negative bias the bright spots correspond to red atoms (see lattice in overlay), belonging to sublattice B, whereas dark spots in the image at positive bias correspond to blue atoms of sublattice A.

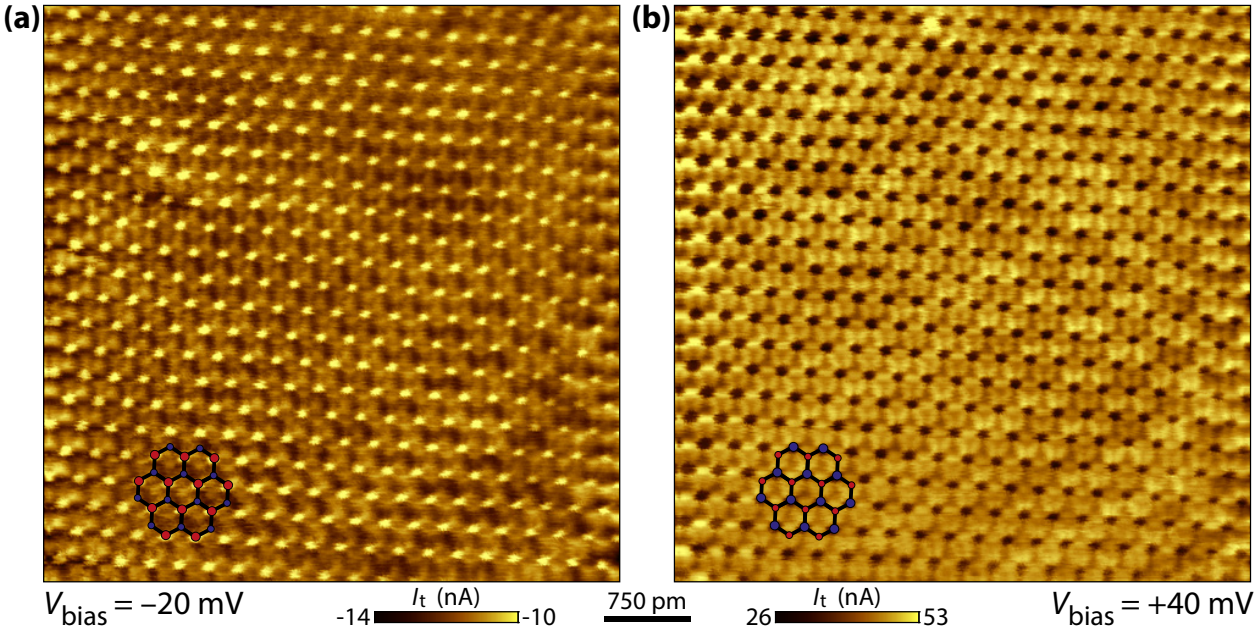

Figure 7.25: Charge-density wave in charge-neutral graphene on hBN/$SrTiO_3$, imaged at the same position in constant height mode in sample AC23 at $T = 4\,\mathrm{K}$ and $B = 14\,\mathrm{T}$, **(a)** at $V_{\mathrm{bias}} = -20\,\mathrm{mV}$, **(b)** at $V_{\mathrm{bias}} = 40\,\mathrm{mV}$.

In order to explain this feature, we first consider the case $V_{\mathrm{bias}} = E_{0^+} > 0$, which means that we are probing empty states in the LL_{0^+} peak of graphene. Since each orbital of LL_0 can at most be occupied by two electrons, there is no empty state at energy E_{0^+} on atoms of sublattice A accessible by electrons of the tip. Therefore the tunneling current I_t vanishes on sublattice A whose atoms appear as dark spots (of filled states) with low I_t. On the contrary LL_0 orbitals on atoms of sublattice B are empty and thus tunneling of electrons from the tip to those empty states in graphene is possible. Nonetheless, interestingly, we do not resolve bright spots of high tunneling current on sublattice B but rather weakly bright triangles between the dark spots of sublattice A - notice the red atoms in Figure 7.25(b) in overlay of such triangles. We will further discuss this a bit later.

We now suppose $V_{\mathrm{bias}} = E_{0^-} < 0$ and probe filled states in the LL_{0^-} peak. Here LL_0 orbitals on sublattice B are empty, thus there is no tunneling of electrons from atoms B of graphene to the tip at energy E_{0^-}. The tunneling current vanishes on sublattice B which appears as bright spots (of empty states) with low I_t in absolute value (note that the scale of current in Figure 7.25(a) is negative). Symmetrically to the previous case, tunneling from graphene is possible on atoms A where LL_0 orbitals are doubly occupied and sublattice A appears as triangles between the bright spots of sublattice B - see the blue atoms in Figure 7.25(a) in overlay of those triangles. We therefore clearly observe a contrast inversion between both images at $V_{\mathrm{bias}} = E_{0^\pm}$, as expected for a charge-density-wave phase.

7.2.2.b Characterization of the charge-density wave

Now that we have characterized the dark and brights spots in Figure 7.25, we describe the other features of this CDW. We plot in Figure 7.26 three enlarged images : the panel (a) is a zoom of 7.25(a) at $V_{\text{bias}} = -20$ mV, the panel (c) is a zoom of 7.25(a) at $V_{\text{bias}} = 40$ mV and, between both, panel (b) is a third scan measured at $V_{\text{bias}} = 20$ mV. For the three figures we show in overlay the CDW lattice with red atoms of sublattice B (empty) and blue atoms of sublattice A (doubly occupied).

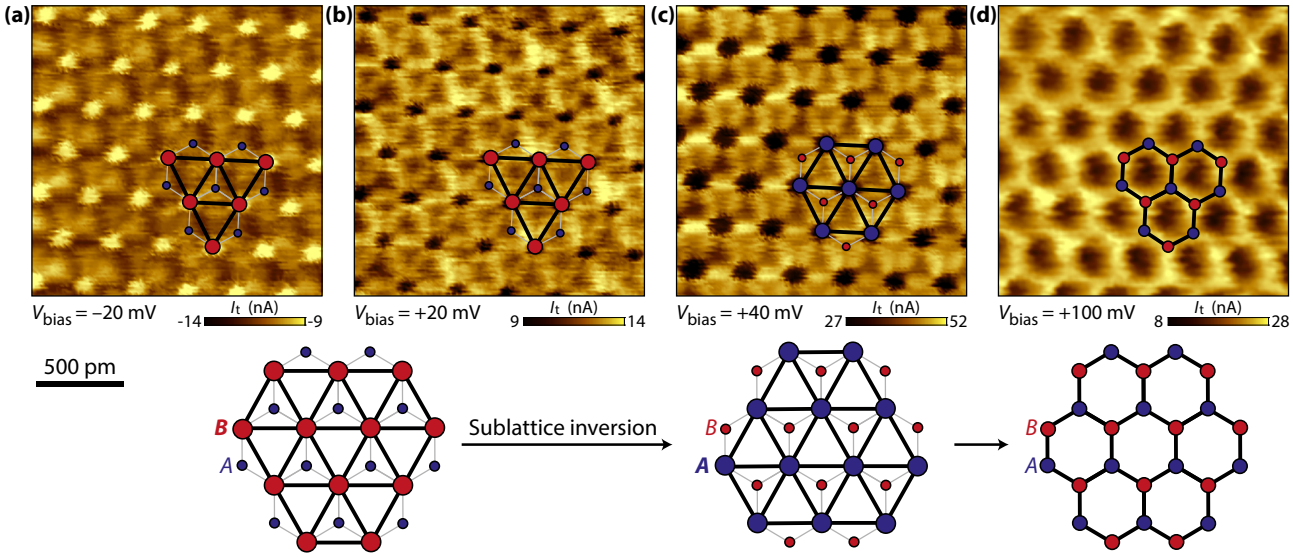

Figure 7.26: Charge-density-wave lattice. Constant-height STM images obtained at $B = 14$ T and at the same position while increasing V_{bias}. **(a)** Zoom of Figure 7.25(a) with the CDW lattice in overlay : sublattice B (empty) appears as bright spots at negative bias and intra-sublattice bonds are visible as dark lines. **(b)** The contrast inversion does not occur at zero bias as we observe at $V_{\text{bias}} = 20$ mV the same CDW pattern than at $V_{\text{bias}} = -20$ mV. The inversion eventually happens at $V_{\text{bias}} = 40$ mV. **(c)** Zoom of Figure 7.25(b) : sublattice A (doubly occupied) appears as dark spots at positive bias and intra-sublattice bonds are visible as bright lines. **(d)** At $V_{\text{bias}} = 100$ mV the CDW is no longer visible and the honeycomb lattice appears instead.

In Figure 7.26(c) at $V_{\text{bias}} = 40$ mV, we distinguish bright lines of large current (and thus of density of empty states) joining the dark spots of filled states on atoms A, which forms a triangular lattice. Those lines do not correspond to the C-C bonds of graphene honeycomb lattice but to bonds between next-nearest neighbor atoms A from the same sublattice. Conversely, in panel (a) at $V_{\text{bias}} = -20$ mV, dark lines of high absolute current (corresponding here to a large density of filled states) are visible and join the bright spots of empty states on atoms B. In both panels we have represented those intra-sublattice bonds as dark lines in the CDW lattices in overlay.

This puzzling observation could be justified as follows. It is expected in half-filled graphene at zero magnetic field that a charge-density wave renormalizes the interaction parameters V_1 and V_2 [277], which induces a related bond-density wave. However, the observation under strong magnetic field of this additional triangular order within our CDW images in panels (a) and (c) was not anticipated. Such a sublattice bond asymmetry, $t_{2,A} \neq t_{2,B}$, can appear when the pseudospin is partially polarized. We conjecture that this partial sublattice polarization could come from Landau level mixing, since sublattice and valley degrees of freedom are decoupled in higher LLs (see Ref. [266]).

For a same sublattice the charge and bond-density waves appear to be entangled. At $V_{\text{bias}} = 40\,\text{mV}$ the electronic density is completely localized on the atoms A whereas the bonds themselves are empty. On the opposite, at $V_{\text{bias}} = -20\,\text{mV}$, the electronic density is zero on the atoms B whereas it is strong on the bonds. This could be explained as the atoms A concentrate the density of filled states and polarize the intra-sublattice bonds with empty states, and vice versa for atoms B.

Moreover, in Figure 7.26(c), one triangle out of two of this lattice appears brighter : it coincides with where the red atoms of sublattice B are located and thus where the density of empty states is large, hence the high tunneling current. It is possible that the empty states of the atoms B hybridize with the empty states of the surrounding intra-sublattice A bonds, which could explain why we do not resolve bright spots for atoms B (as we do with dark spots for atoms A) but rather those brighter triangles delimited by the even brighter bond-density wave related to sublattice A. On the contrary, the other darker triangles coincide with the center of the hexagons of honeycomb lattice unit cells where the density of states is small - but unexpectedly non zero, in contrary to usual images of the honeycomb lattice such as Figure 5.1(c). The same observations hold for panel (a) with negative V_{bias}.

Last we consider Figure 7.26(b) at $V_{\text{bias}} = 20\,\text{mV}$. This image in fact greatly differs from panel (c) since the dark spots here correspond to red (empty) atoms B, and not to blue (doubly occupied) atoms A as in panel (c). This means that the contrast inversion does not occur at zero bias but between $V_{\text{bias}} = 20\,\text{mV}$ and $V_{\text{bias}} = 40\,\text{mV}$. This anomaly is a well-known feature of CDW imaging in STM for many 2D materials [278]. It could mean that the CDW gap does not open at E_{F}. Another possibility is that our graphene may not be strictly at charge neutrality but rather at $\nu = 0^{\pm}$. In some other images of the CDW state we do not observe any contrast inversion between positive and negative biases - see for instance Figures 7.29(a,b).

Analogy with the Kekulé distortion from hBN/SiO_2 samples It is intriguing to see that we retrieve here the opposite situation than what we observed in the previous section. For hBN/SiO_2 samples, the ground state is a Kekulé distortion (or bond-density wave) which coexists with the (more or less) weaker long-range K-CDW order with the same spatial modulation (three times the interatomic distance). Here for hBN/$SrTiO_3$ samples, the ground state is a charge-density wave which is entangled with a weaker short-range bond-density wave (compared to the KD) with the same periodicity (the honeycomb lattice parameter, or equivalently the distance between atoms from the same sublattice).

As a consequence, our results shall point toward the fact that, experimentally, charge-neutral graphene ground states are a combination of several of the ground states predicted theoretically [108, 118], but still with a predominant one.

Current profiles We now show in Figure 7.27 two current profiles of the CDW at negative and positive biases. Atoms of sublattice A appear at positive V_{bias} in panel (b) as pronounced dips, such as the one indicated by a blue arrow. On the contrary, sublattice B atoms appear at negative V_{bias} in panel (a) as pronounced peaks, see the red arrow. In panel (b) we observe three peaks (indicated by the green arrows) between two successive dips, and conversely in panel (a) three dips (see the green arrows as well) between two successive peaks : they correspond to the intra-sublattice bonds. The two other dips in panel (b) correspond to both sublattice B atoms (red arrow) and the center of the hexagons of the honeycomb lattice (yellow arrow), and symmetrically for panel (a).

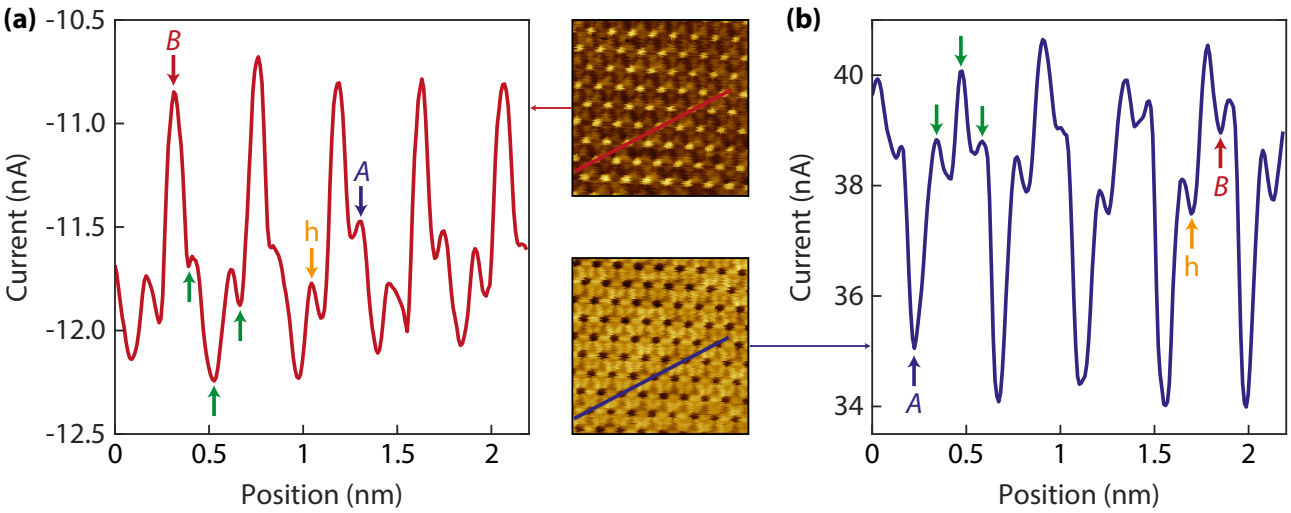

Figure 7.27: Current profiles of the CDW at negative and positive bias. (a) Current profile corresponding to the red line in the top inset, a zoom of Figure 7.25(a). **(b)** Current profile corresponding to the blue line in the bottom inset, a zoom of Figure 7.25(b).

FFT analysis Last we show in Figure 7.28(b) the 2D FFT of the CDW phase at positive V_{bias} [4], corresponding to Figure 7.25(b). The 2D FFT appears to be the superposition of both FFTs of the honeycomb lattice of graphene (yellow peaks) and of a triangular lattice (red, blue and other outer peaks). As previously, panels (c-f) are obtained after we filtered the image in panel (a) considering only certain peaks, as indicated in panel (b).

Panel (c) shows that the yellow peaks already encode the information on the asymmetry of the honeycomb lattice : sublattice A (blue atoms) appears dark, sublattice B (red atoms) appears bright and the center of the hexagon is between both. The image in panel (d) is obtained by filtering with red peaks only : we obtain a honeycomb lattice, but not that of graphene, see its unit cell in green in the middle left of the image. It is here smaller such that each C atom of graphene falls inside one hexagon of this smaller pattern, and it is also tilted by 30 degrees. By adding in semi-transparent, at the bottom right of the image, the asymmetric graphene honeycomb lattice from panel (c) we observe that this smaller honeycomb lattice eventually induces the bond-density waves we described previously, as the edges of the green hexagon coincide with the intra-sublattice bonds of graphene.

Nonetheless, the red peaks are only the main components of the triangular lattice. In panel (e) we added all the further blue peaks to the red peaks for the computation of the filtered image : the smaller honeycomb lattice now appears highly distorted, with some reminiscence of the Kekulé distortion pattern (but once again three times smaller here). We see in the bottom right part of the image where we have also superimposed graphene honeycomb lattice from panel (c) that if the dark spots corresponding to the blue atoms are not changed by this triangular lattice, red atoms are now surrounded by a wide bright area.

Eventually the CDW pattern from the original STM image is accurately recovered in panel (f) when considering yellow, red and blue peaks of the FFT, namely the asymmetric graphene honeycomb lattice and the short-range bond-density wave. Furthermore, adding the green peaks of the inner hexagon in the FFT does not change the outcome, see panel (g).

[4]Since the CDW patterns at negative and positive biases are eventually only translated with respect to each other (dark/bright spots on sublattice A or B), this merely yields a phase difference in the FFTs, which would not be visible here as we only plot the modulus.

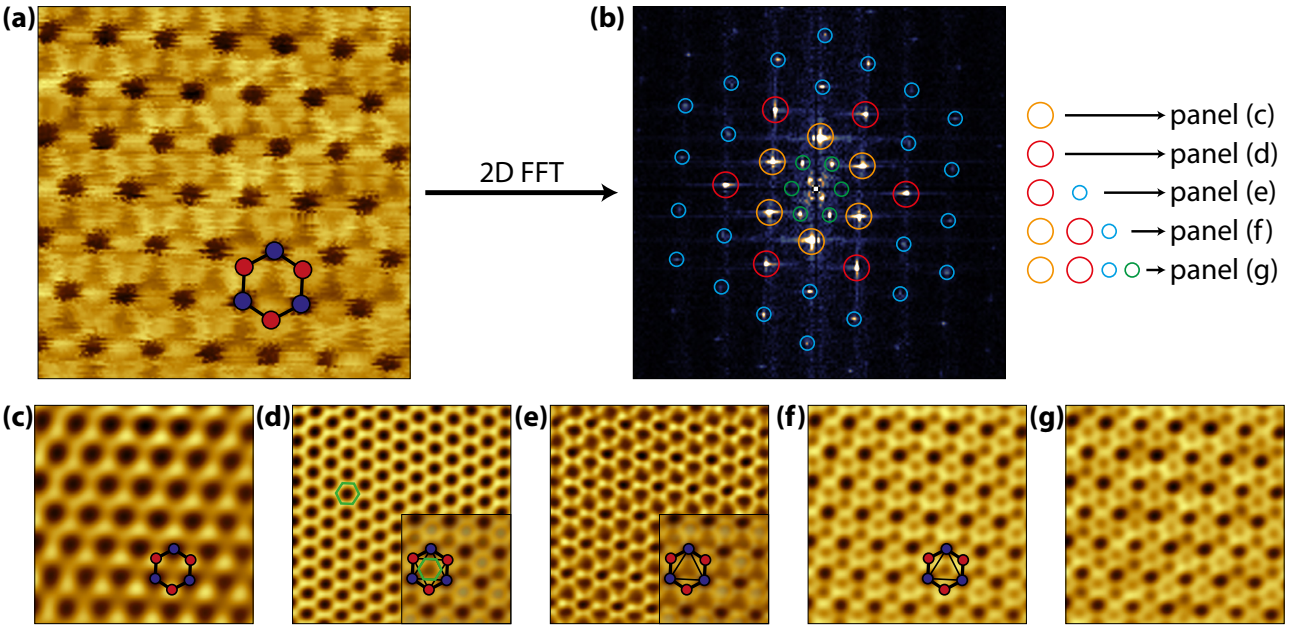

Figure 7.28: FFT decomposition of the charge-density wave. (a) Original image as obtained by STM in constant height mode and **(b)** its 2D FFT. The different peaks are marked by circles of different colors, notably the yellow peaks are those of graphene honeycomb lattice. **(c-g)** Filtered images when considering only certain peaks, as indicated in (b). In the bottom right part of (d,e) we have superimposed the same area from (c) in semi-transparent.

7.2.2.c Influence of the Moiré superlattice

We have shown in Figure 5.2(b,c) that this sample AC23 displays a weak Moiré superlattice (weak in the sense that is not always visible in our images). This therefore arises the question of whether the CDW phase we observed was induced by the Moiré pattern, which could also break the sublattice symmetry, or not. In such case, we should expect the CDW pattern to rely on that of the Moiré, with the sublattice polarization depending on the position inside the Moiré superlattice (due to the periodic potential it induces in graphene). Figure 7.29(b) displays a CDW phase observed at $B = 7\,\mathrm{T}$. The Moiré pattern is barely visible but appears as bright spots, such as the ones indicated by dashed white circles. However the CDW pattern itself is seen not to fluctuate in presence of this Moiré lattice, which as a result rules out the Moiré origin of our CDW phase.

Eventually, we also performed STM measurements in the similar sample AC24 (hBN/$SrTiO_3$). Contrary to sample AC23, we never notice any Moiré lattice in this second sample. In the same conditions, at $\nu = 0$, we eventually observed signatures of a CDW phase with a pattern identical to the one shown in Figure 7.29(a), which strengthens our conclusion that the CDW we observe in our hBN/$SrTiO_3$ samples is indeed an intrinsic consequence of many-body interactions at charge neutrality and not due to extrinsic substrate-induced sublattice symmetry breaking.

7.2.2.d Disappearance at low magnetic field

We last focus on the behavior of the CDW as we decrease the magnetic field. Figures 7.29(a,b) show that the CDW persists at $B = 9\,\mathrm{T}$ and $B = 7\,\mathrm{T}$. However, Figures 7.29(c-e) at $B = 4\,\mathrm{T}$ does not display the CDW anymore but just the usual honeycomb lattice. This is consistent with the observations in our group [122] where the quantum spin Hall effect - which is a signature of the formation of the F phase, that would appear as a honeycomb lattice in our STM measurements - is observed up to $B \approx 3\,\mathrm{T}$, beyond that charge-neutral graphene becomes

insulating, with a ground state featuring, as we now show here, a charge-density-wave phase. As a consequence, we suppose that a quantum phase transition occurred between $B = 4$ T and $B = 7$ T where charge-neutral graphene transits from a charge-density wave to a ferromagnetic ground state. The vanishing of the CDW comes from the renormalization of the anisotropy energies $u_\perp$ and u_z (see Chapter 2.3.3) due to the substrate-screening of the Coulomb interaction that we have demonstrated in Figure 7.6.

As an aside, we could not resolve the $\nu = 0$ gap below $B = 6$ T in sample AC23, which coincides with the disappearance of the CDW.

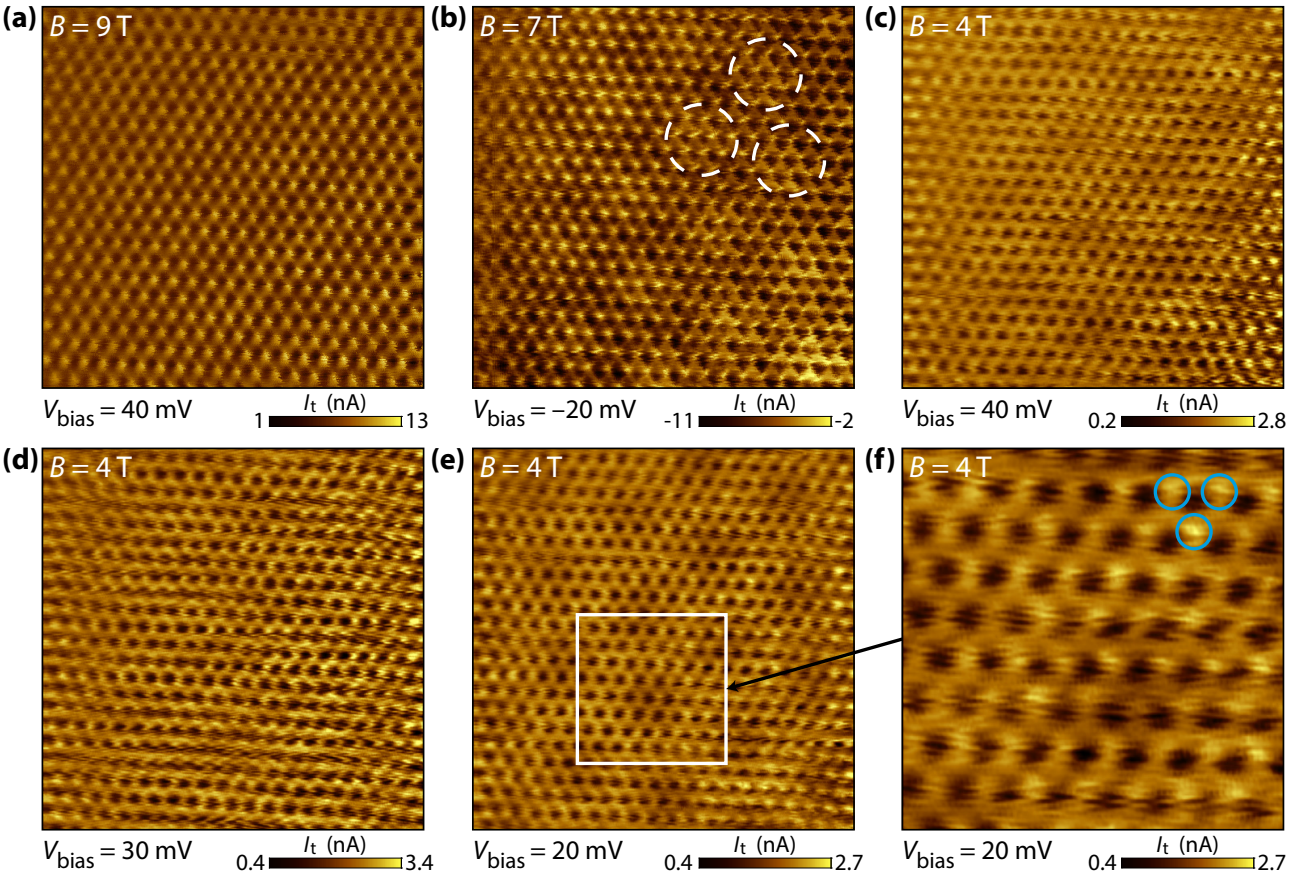

Figure 7.29: Disappearance of the charge-density wave at low magnetic field. (a) CDW at $B = 9$ T. **(b)** CDW at $B = 7$ T. The Moiré superlattice of sample AC23 is visible but does not perturb the CDW pattern. **(c,d)** Honeycomb lattice with no CDW at $B = 4$ T. **(e)** Honeycomb lattice at $B = 4$ T with residual traces of CDW, see the zoom in (f) of the white rectangle.

One last point, it is expected theoretically [101] that graphene undergoes a first-order phase transition from the CDW to the F phase. Such transition should induce the formation of domains in graphene with the coexistence of both phases around the magnetic field at which the transition occurs. When taking a closer look to Figure 7.29(e) taken at $B = 4$ T, see its zoom in Figure 7.29(f), one can notice that some bright dots appear in some parts of the image (see the blue circles) and this residual asymmetry of the honeycomb lattice is reminiscent of a charge-density wave. It is possible that it may constitute a signature of such domains between the CDW and F phases, which would therefore strengthen our hypothesis that the absence of a CDW pattern at low magnetic fields is indeed due to a first-order quantum phase transition toward the ferromagnetic phase.

7.2.3 Discussion of a screening-induced quantum phase transition

Our previous results now enable us to draw a scenario of a screening-induced quantum phase transition in our hBN/$SrTiO_3$ samples driven by the substrate-screening of electron-electron interactions in graphene, screening which is mitigated as the magnetic field is increased. Let us consider in Figure 7.30 the $\nu = 0$ phase diagram [108, 118] that we have studied in Chapter 2.3.3. We can infer three different regimes as a function of the magnetic field for our hBN/$SrTiO_3$ samples at charge neutrality :

- At low magnetic fields ($B \leq 4$ T) we only observe the usual honeycomb lattice, and consider it to be a signature of the F phase (blue point). In this regime charge-neutral graphene has been shown [122] to be conductive (featuring the quantum spin Hall effect).

- At high magnetic fields ($B = 7 - 14$ T) charge-neutral graphene features a CDW ground state (red point) and a weak insulating behavior [122].

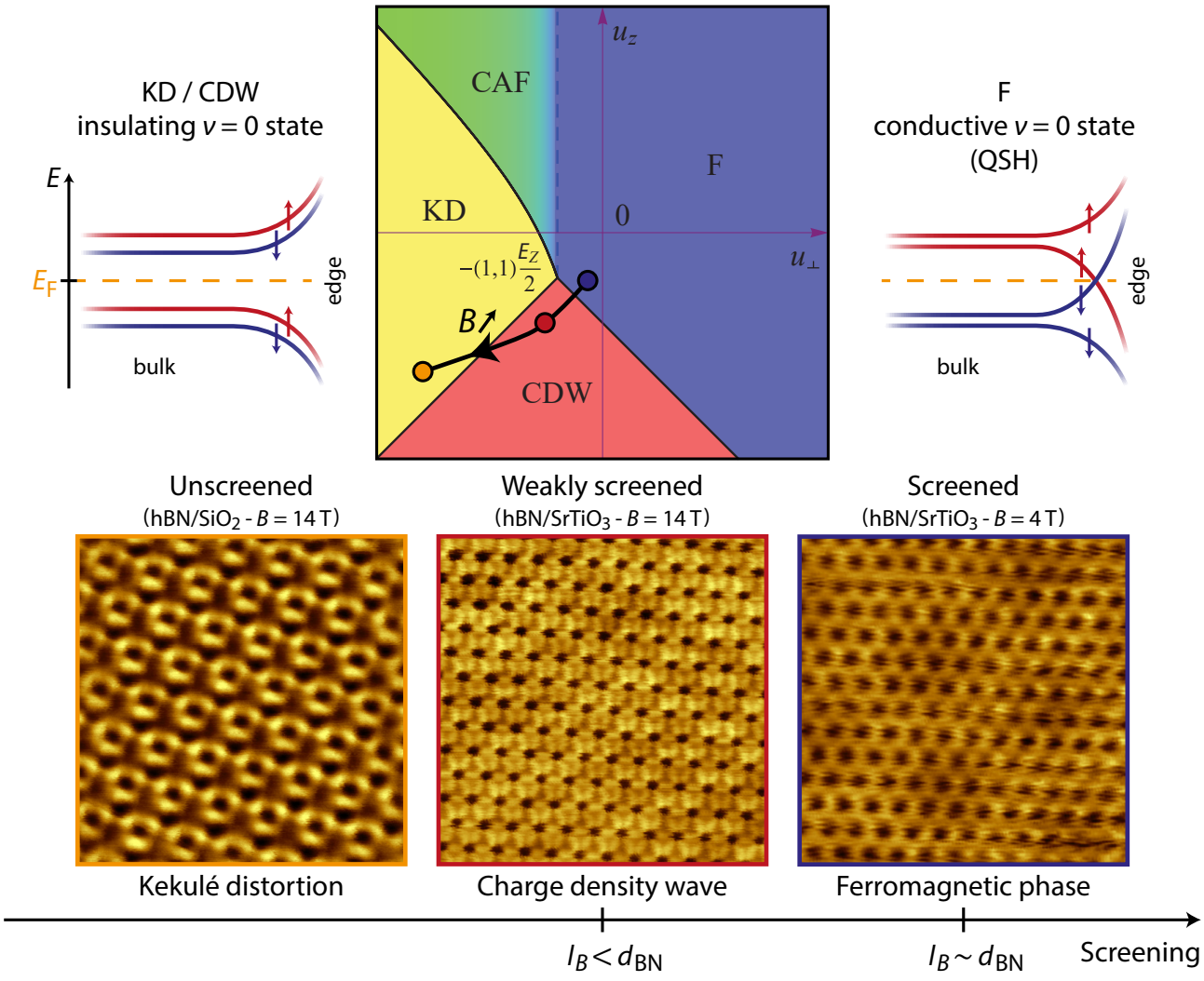

Figure 7.30: Model of a screening-induced quantum phase transition in charge-neutral graphene. For sample on hBN/$SrTiO_3$, increasing the magnetic field lowers the efficiency of the substrate-screening of the Coulomb interaction. At low magnetic fields (strong screening), the conductive F phase appears as the usual honeycomb lattice. At high magnetic fields (weak screening), a charge-density wave emerges and charge-neutral graphene becomes weakly insulating. At very high magnetic fields (no screening), the $\nu = 0$ ground state transits to a Kekulé distortion of the honeycomb lattice with a strong insulating behavior.

- At very high magnetic fields (such that $l_B \ll d_{\mathrm{BN}}$) the graphene plane is too far away from the $SrTiO_3$ substrate to feel any screening of the Coulomb interaction. We can suppose the unscreened physics that we have characterized in hBN/SiO_2 samples is restored and charge-neutral graphene would thus feature a Kekulé distortion (yellow point) as well as a strong insulating behavior [62, 122].

We therefore obtain a screening-induced quantum phase transition from the F phase to the KD ground state through a CDW order with increasing magnetic field, drawn as the black arrow[5] in Figure 7.30, where the magnetic field actually tunes the efficiency of the screening of the Coulomb interaction in graphene by the $SrTiO_3$ substrate.

7.2.4 A final curiosity

Before concluding this chapter and this thesis, we want to show a final striking observation. While we were scanning over sample AC23 (hBN/$SrTiO_3$) in order to image the CDW phase at $\nu = 0$ and $B = 10$ T, a strange defect of 1 nm spontaneously grew up in the CDW background and stayed pinned at the same location in graphene before it vanished 1h45 later. We show this unusual object in Figure 7.31.

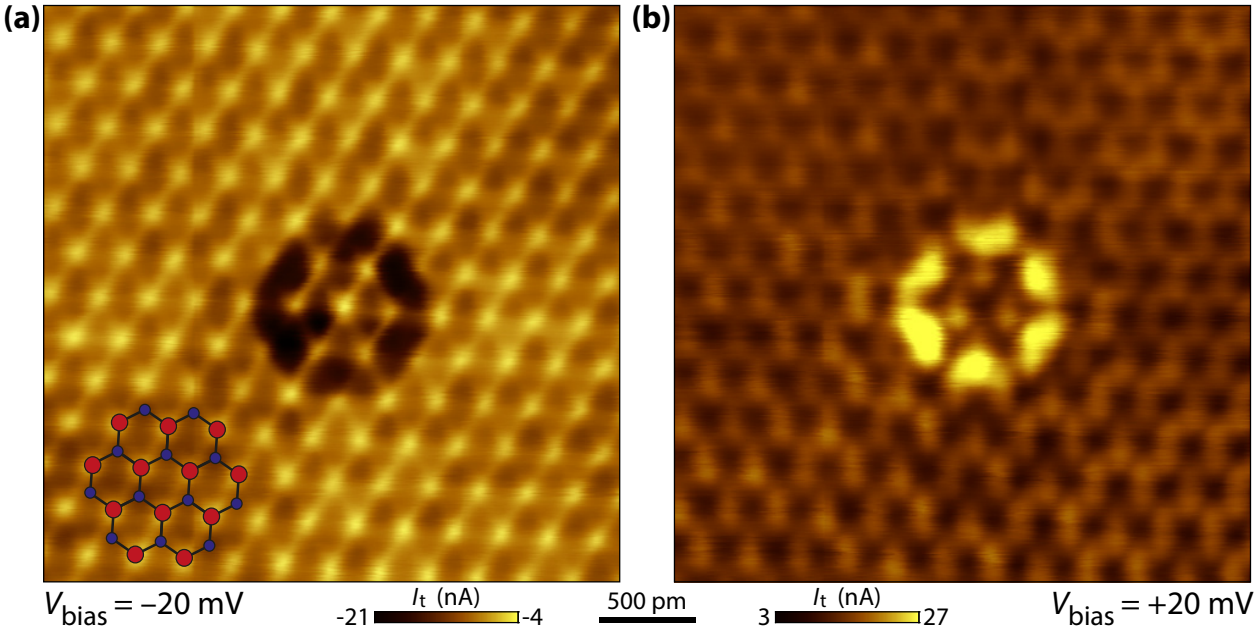

Figure 7.31: Observation of a charge-density wave-defect. Constant height STM images in sample AC23 at $T = 4$ K and $B = 10$ T, **(a)** acquired at $V_{\mathrm{bias}} = -20$ mV and **(b)** at $V_{\mathrm{bias}} = 20$ mV.

In Figure 7.31(a) at negative bias, we can clearly distinguish the CDW background that we have described in Section 7.2.2 and represented by the lattice in overlay. In the center of the image we see a dark area with at its center a slightly brighter lattice. The first remark we can do is that the CDW phase persists in the defect : there is no missing bright spot. Second the defect respects the symmetry of the CDW lattice, see Figure 7.32 where we have represented the pristine CDW triangular lattice (that we have characterized in Section 7.2.2.b) and next the same lattice in presence of the defect. If we consider the bright spot at the center of the

[5]Note that this arrow is only for illustration purposes only : we do not know the true functional in the phase space. If increasing the perpendicular magnetic field B is expected to not change the signs nor the relative values of the anisotropy energies $u_{\perp,z}$, we suppose that the mitigation of the Coulomb energy by our substrate-screening suppresses the renormalization of $u_{\perp,z}$ by the long-range Coulomb interaction.

defect in Figure 7.31(a), the nearest-neighbor bright spots define a bright circle which is in fact comprised of cells of the CDW triangular lattice. Similarly, the dark annulus between the first and second neighbor bright spots is also made of dark triangular cells of the CDW lattice. Since the CDW pattern is fully conserved in this defect, we label it a charge-density-wave defect.

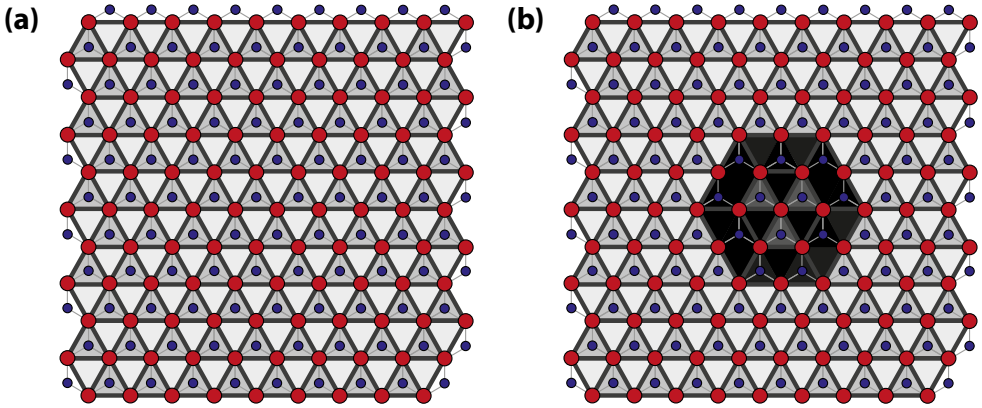

Figure 7.32: CDW lattice without (left) and with (right) the defect, for negative bias, with red atoms from sublattice B (appearing as bright spots in the STM image) and intra-sublattice bonds between them in dark gray.

We show in Figure 7.33 how the CDW defect appeared (top row) and later vanished (bottom row). Before its appearance, in panel (a), the CDW phase is well visible at positive bias except on the middle left, see the red circle, where the CDW pattern is highly distorted. This may already be the sign of a perturbation of the electronic density preceding the growth of the defect. In the next image in panel (b), done immediately after the first one (each scan lasts 52 seconds), the defect has appeared and the CDW pattern in its vicinity has become pristine. In panel (c) we moved the tip to bring the defect at the center of the scanned area : this shows by the way that the defect is not induced by the tip. In order to strengthen this hypothesis, we furthermore also moved the tip a few nanometers away from the defect and did not observed it anymore in the current image. After we brought back the tip on the area with the defect, we found it again at the same position. The defect was thus strongly pinned inside graphene. In the last panel (d), we show another image taken after the one in panel (c) but at negative bias.

The CDW defect did not move nor evolve during a stunning long time of about 1h45. Its inevitable disappearance eventually happened as we were scanning it by gradually lowering the bias at each new image, see the bottom row in Figure 7.33. In panel (e) we show the defect at $V_{\text{bias}} = -30$ mV. At $V_{\text{bias}} = -70$ mV in panel (f) the defect is less defined, though it could simply be because the CDW pattern itself is less visible as we tunnel at this bias in the cyclotron gap between LL_{0^-} and LL_1, and so outside the ν_0 gap. Eventually, as we were scanning from the bottom at $V_{\text{bias}} = -80$ mV in panel (g), we started to see the bottom of the defect but it suddenly vanished and left at its position only the CDW background. The next image we did in panel (h), and the other subsequent images, confirmed the defect was gone for good.

During its long lifetime we were able to image it at many different biases in order to study its bias dependence, see Figure 7.34 for current images with increasing bias. The CDW defect was already well defined at $V_{\text{bias}} = 10$ mV in panel (a) and did not vary with the bias until $V_{\text{bias}} = 100$ mV, far from the $\nu = 0$ gap. When we started to tunnel in the tail of the LL_1 peak in the cyclotron gap, at $V_{\text{bias}} = 120$ mV, the defect appeared to be less defined, see panel (g). It only got worse as we increased further the bias until the defect was completely washed out at $V_{\text{bias}} = 250$ mV, in the cyclotron gap between LL_1 and LL_2. However, scanning next the area back at $V_{\text{bias}} = 20$ mV in panel (l) immediately unveiled the CDW defect again.

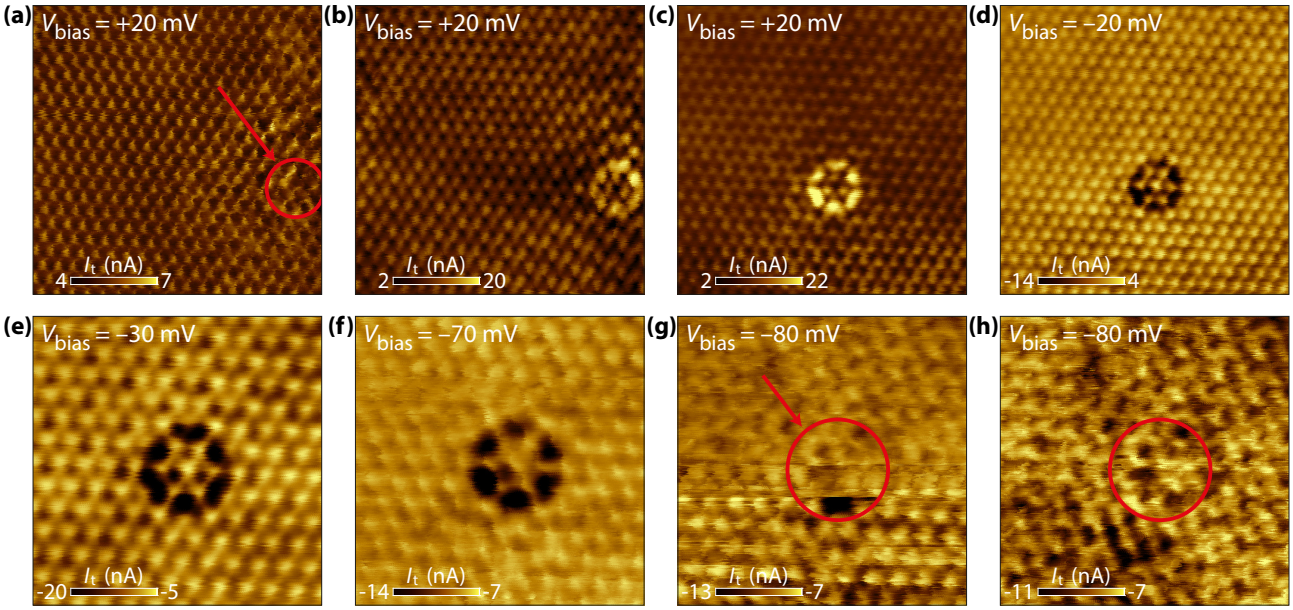

Figure 7.33: Spontaneous appearance and disappearance of the CDW defect. Images are in chronological order. Top row : the defect appeared spontaneously as we were imaging the CDW phase in (b). We have centered the defect in the next images from (c). Second row : similarly, as we were imaging the CDW defect at negative bias, it spontaneously vanished in (g).

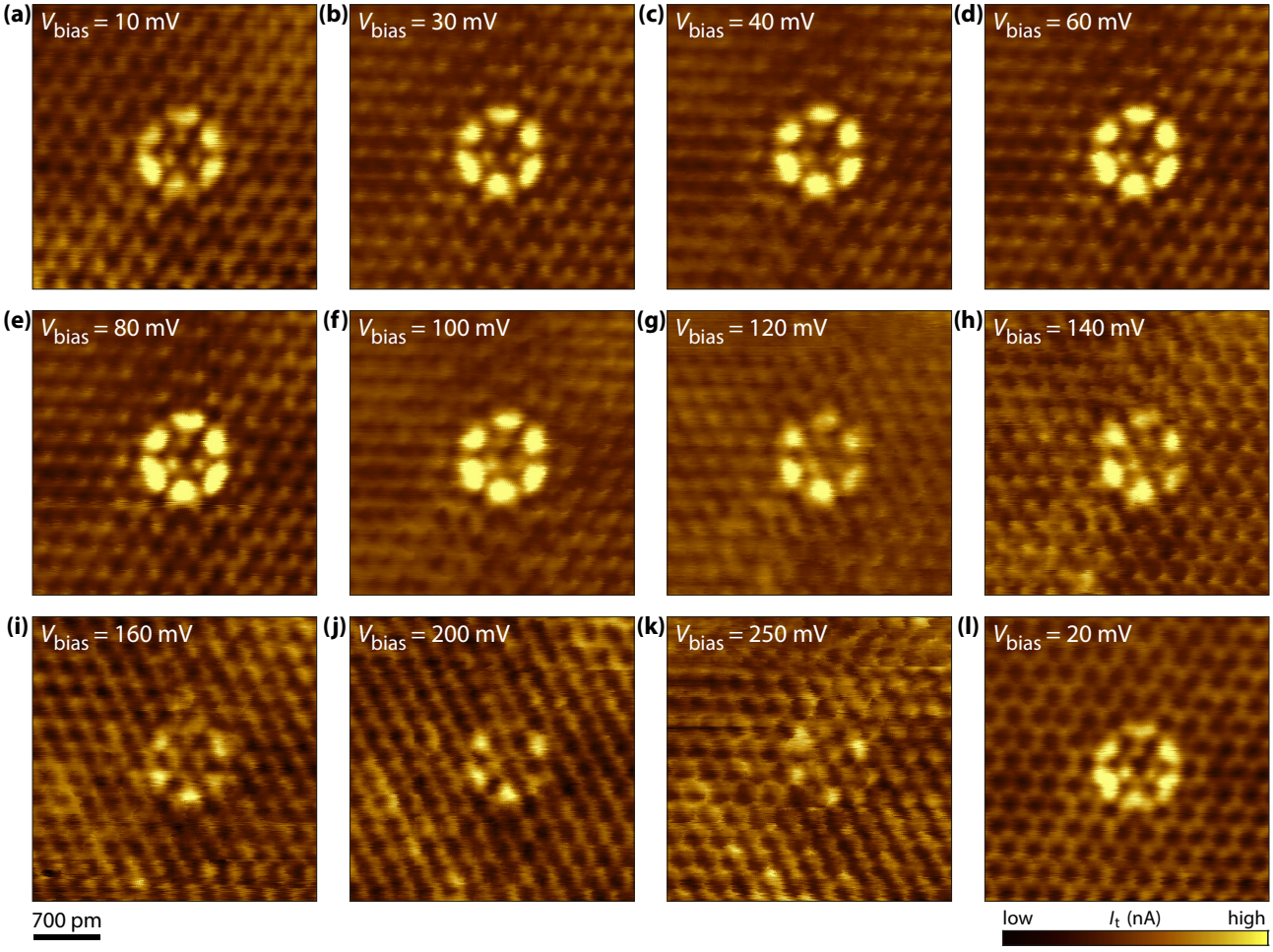

Figure 7.34: Evolution of the CDW defect with bias. Current images at the same position at different V_{bias}. The defect vanished when we started to tunnel inside the LL_1 peak at $V_{\text{bias}} \approx 150\,\text{mV}$, but instantly reappeared when we went back at $V_{\text{bias}} = 20\,\text{mV}$ in the LL_{0^+} peak.

The exact nature of this defect is still unknown. It remarkably features a length scale of four times the lattice parameter of graphene (1 nm), which corresponds to an extremely large energy scale. We discuss below different possible origins of the CDW defect and why we eventually exclude them :

- A charge which got trapped inside the hBN flake below the graphene sheet could induce the emergence of a dot inside graphene, however its length scale would be of the order of several times the magnetic length $l_B \simeq 8\,\text{nm}$ at $B = 10\,\text{T}$, much greater than the size of our defect.

- Since the CDW defect spontaneously appeared and vanished, we next suppose that it can be an excitation of the $\nu = 0$ state. Unfortunately, two points rule out this hypothesis. Atteia *et al.* [118] studied the skyrmionic excitations in charge-neutral graphene and showed that the phase inside a skyrmion should differ from that of the surrounding background. However both our defect and the neighboring background display the same CDW phase. The second point is once again the small size of our defect, as the size of a skyrmion is expected to be at least of l_B.

- Last we can conjecture that our CDW defect emerged due to the adsorption of a helium atom on graphene, since we used helium as exchange gas for the cooling of our STM, and later vanished when the He atom eventually desorbed. However we could expect that such atom, which would lie at the center of the defect, would be visible in our current images. Still note that there is no theory to our knowledge that models the interaction of an adsorbed atom on charge-neutral graphene in the quantum Hall regime.

Conclusion

In this last chapter, which concludes this thesis, we have established several important results concerning the physics of charge-neutral graphene in the quantum Hall regime. We realized the first systematic tunneling spectroscopy study of the $\nu = 0$ gap in graphene on hBN/SiO_2 samples. We showed that this gap scales as the square root of the magnetic field and thus opens due to the Coulomb interaction. We next proved that it is possible to efficiently screen this Coulomb interaction in charge-neutral graphene using the hBN/$SrTiO_3$ substrate.

We have then demonstrated that this screening strongly altered the lattice-scale order of charge-neutral graphene. In unscreened graphene on hBN/SiO_2, we observed a Kekulé distortion of the honeycomb lattice for the $\nu = 0$ ground state, although it was believed from transport measurements to be a canted antiferromagnet instead. We also found out that this KD phase persisted at low magnetic fields. Moreover we showed signatures that this KD order coexists with a long-range charge-density wave, labelled K-CDW, which has not been predicted theoretically. This result eventually gives further insights on the physics of charge-neutral graphene studied with transport measurements. In the substrate-screened graphene, we instead imaged a charge-density-wave order at $\nu = 0$. In this case, the CDW ground state happened to be not visible at low magnetic fields, which made us conjecture that a quantum phase transition toward the ferromagnetic phase occurred between 4 and 7 T. This is consistent with the increasing of the substrate-screening of the Coulomb energy at lower magnetic fields.

The observation of those many-body ground states of charge-neutral graphene is another major result of our study, and it enables us to draw a scenario of a screening-induced quantum phase transition where the efficiency of the substrate-screening is tuned by the magnetic field.

Conclusion

In this PhD thesis, we have successfully fabricated high-quality graphene samples that we characterized with scanning tunneling spectroscopy using our home-made AFM/STM. Two different substrates were employed : the standard SiO_2/Si substrate which is commonly used in transport measurements, and the high-k dielectric $SrTiO_3$ substrate which has been shown in our group to induce the formation of the ferromagnetic phase in charge-neutral graphene and the emergence of the quantum spin Hall effect. Three major and novel results were obtained during this PhD work : first about the quantum Hall edge states tunneling spectroscopy on hBN/SiO_2 samples, secondly concerning the scaling of the interaction-induced gap which opens at charge neutrality as the Coulomb energy, as well as the substrate-screening of the Coulomb interaction, and thirdly about the many-body ground states of charge-neutral graphene as a function of this screening of the Coulomb interaction.

Quantum Hall edge states spectroscopy

We performed the first tunneling spectroscopy of the quantum Hall edge states at the graphene native edge on its insulating hBN/SiO_2 substrate. We uncovered that Landau levels do not disperse at the edge as expected for a smooth confinement potential like in GaAs, but rather vanish a few magnetic lengths l_B away from the edge, due to the gradual redistribution of their spectral weight toward higher energies, as anticipated for an atomically sharp boundary. This implies that edge channels are squeezed in the last few l_B from the edge. This major result gives further insights on transport physics and is of great interest for transport devices that aim to manipulate the quantum Hall edge channels. We also found out that edge excitations at charge neutrality are gapped, in line with the observation in transport measurements of a strong insulating $\nu = 0$ state. Furthermore, we evidenced the absence of charge accumulation at the edges of graphene that was expected due to the electrostatic fringing effect of the back gate, which is another important result that shall greatly improve the comprehension of the edge physics in some transport observations.

We focused in this PhD thesis on the armchair edge of graphene, and a next step would be to perform similar measurements at the zigzag edge, where the edge dispersion of Landau levels should differ due to the existence of the zigzag edge mode. Another perspective would be to repeat those measurements on a hBN/$SrTiO_3$ substrate, where we have shown that graphene features a different ground state and thus probably a different Landau level edge dispersion. We have exhibited, as a preliminary study, numerical simulations of the evolution of the density of states at the edge for different lattice-scale orders of graphene.

Interaction-induced gap at $\nu = 0$ and screening of the Coulomb interaction

We realized the first systematic tunneling spectroscopy study of the interaction-induced gap which opens in charge-neutral graphene and we proved that this gap scales as the square root of the magnetic field in hBN/SiO_2 samples. This confirms that the $\nu = 0$ gap originates from the Coulomb interaction, which has been expected but never demonstrated quantitatively until now. This is a striking result that will significantly enhance the understanding of the strong insulating behavior of charge-neutral graphene observed in transport devices. We also showed that we can screen the Coulomb interaction in graphene with the use of the high-k $SrTiO_3$ substrate, screening whose efficiency can be tuned with the magnetic field (the lower the field, the stronger the screening). Moreover, the power law between the $\nu = 0$ gap and the magnetic field is also changed in substrate-screened graphene. We now aim in our group to obtain more measures of the $\nu = 0$ gap on hBN/$SrTiO_3$ samples, especially at low magnetic fields where data points are missing in our study.

Ground states of charge-neutral graphene and screening-induced quantum phase transition

We finally probed different lattice-scale orders of charge-neutral graphene in both hBN/SiO_2 and hBN/$SrTiO_3$ systems. We found out an unexpected Kekulé distortion ground state in unscreened graphene on hBN/SiO_2, although it has been believed for many years due to transport measurements that charge-neutral graphene in such samples would feature a canted antiferromagnetic phase. This groundbreaking result now implies that new theoretical models are required to understand some transport observations. Notably, the Kekulé bond order was observed to persist at low magnetic fields. We also investigated some signatures in our STM images that would infer the coexistence of this Kekulé phase with a weaker long-range charge-density wave (K-CDW) order, which is a hypothesis that has only been scarcely explored theoretically until now. The observation of the Kekulé distortion ground state eventually opens the path to the study by STM of many topological objects in graphene.

Next we demonstrated that substrate-screened charge-neutral graphene on hBN/$SrTiO_3$ features a charge-density wave lattice-scale order that vanishes at low magnetic field. We conjectured that this is due to a quantum phase transition toward the ferromagnetic phase, since the substrate-screening is increased as we lower the magnetic field. This is fully consistent with the observations in our group, first, of the quantum spin Hall effect in charge-neutral hBN-encapsulated graphene devices on $SrTiO_3$ at low magnetic field, which is the signature of the formation of the ferromagnetic phase, and secondly, of a transition to a weak insulating state at higher magnetic fields. A continuation of our work would consist in performing challenging spin-resolved STM to seek for a possible lattice-scale spin texture at low field in order to see if the ferromagnetic phase is not rather a canted antiferromagnetic phase.

Finally, our results presented in this PhD thesis point toward novel screening-induced quantum phase transitions in charge-neutral graphene in the quantum Hall regime.

Appendix

Scanning probe microscopy : STM and AFM

APPENDIX A

This chapter is intended to be an introduction to the two scanning probe techniques employed during this thesis : the Scanning Tunneling Microscopy (STM), the mainly used in this work, which probes the tunneling current between both conductive tip and sample like graphene to obtain atomic spatial resolution images of the sample and its density of states ; and the Atomic Force Microscopy (AFM), which probes the interactions between the tip and the sample and that we use to localize our device.

Contents

A.1 Scanning Tunneling Microscopy and Spectroscopy

We employ in this work Scanning Tunneling Microscopy (STM) and Scanning Tunneling Spectroscopy (STS) to measure the Density of States (DOS) and study the Landau levels of graphene. Developed in 1981 by Binnig, Rohrer, Gerber and Weibel [279, 280] in the laboratories of IBM Zurich, with the associated Nobel prize in physics in 1986 awarded to Binnig and Rohrer, STM enables the imaging of conductive surfaces with an atomic resolution and to directly probe the DOS of materials. A scanning tunneling microscope consists of a metallic tip that we approach toward the conductive sample at distances below the nanometer until a current starts flowing between both of them. This current originates from the tunneling effect and therefore depends exponentially on the tip-sample distance, granting the STM a spatial resolution down to the atomic scale - see the theory of STM developed by Tersoff and Hamann [281, 282] based on the Bardeen's formalism [283] of the tunneling current. However, this high sensibility of the tunneling current implies a very precise displacement and positioning system (with a sub angström precision) for the tip, made using piezoelectric actuators, but also requires to isolate the whole microscope from external mechanical vibrations.

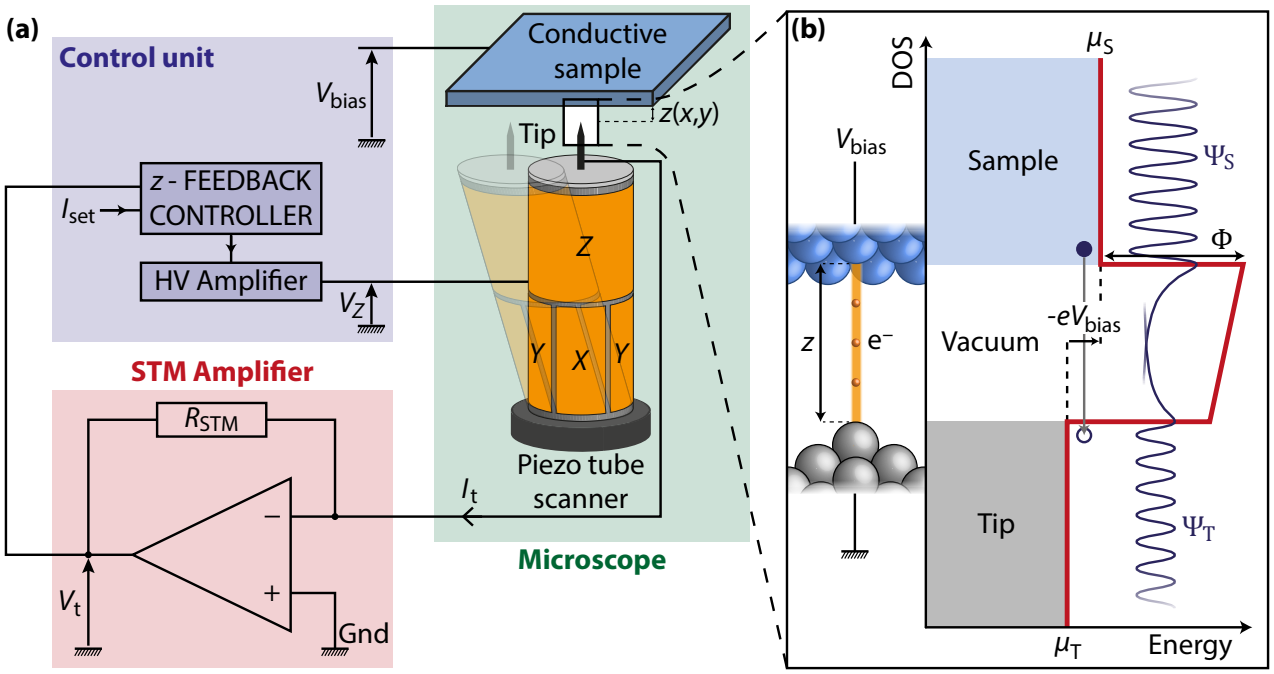

Figure A.1: Scanning Tunneling Microscopy (STM). (a) A metallic tip is mounted on a piezoelectric tube scanner which scans over a conductive sample biased at V_{bias}. For each point of the sample (x, y), the tip-sample distance z, controlled by the high voltage V_Z applied to the tube, is maintained constant by a feedback loop on the tunneling current I_t flowing between the tip and the sample. **(b)** Tunneling process between the tip and the sample across an insulating barrier (vacuum) : applying a bias voltage to the sample shifts its chemical potential μ_S with respect to that of the tip $\mu_T = E_F$ and a tunneling current flows through the barrier.

A.1.1 Quantum tunneling

We describe below the basics of the tunneling effect. We consider a free electron of mass m with energy E coming from $z < 0$ that arrives at $z = 0$ at a one-dimensional potential barrier $V(z)$ of height $\Phi > E$ and thickness z_{ts}. The barrier height $\Phi = (\Phi_T + \Phi_S)/2$ is related to the work functions of the tip Φ_T and the sample Φ_S, while z_{ts} is the tip-sample distance. The wave functions Ψ of the electron in the tip, the barrier and the sample, have to satisfy the stationary Schrödinger equation :

$$\left[-\frac{\hbar^2}{2m}\frac{\mathrm{d}^2}{\mathrm{d}z^2} + V(z)\right]\Psi(z) = E\Psi(z) \tag{A.1}$$

Using a plane wave ansatz, one can easily show that the probability for the electron to tunnel through the barrier is proportional to $\exp(-2\kappa z_{ts})$ where $\kappa = \sqrt{2m(\Phi - E)}/\hbar$. For most metals used in STM, the work function is typically $\Phi \sim 5$ eV (see [284]). We then suppose that we apply a bias voltage on the sample such that $eV_{\text{bias}} = E \ll \Phi$. The tunneling current flowing trough the barrier therefore depends exponentially on the tip-sample distance :

$$I_t \propto \exp(-2\kappa z_{ts}) \quad , \quad 2\kappa = 2\frac{\sqrt{2m\Phi}}{\hbar} \approx \sqrt{\Phi(\text{eV})}\ \text{Å}^{-1} \tag{A.2}$$

The probability of an electron to tunnel through the barrier becomes significant for tip-sample distances of the order of the angström, and the tunneling current I_t decreases by one order of magnitude for only a change of 1 Å of the tip-sample distance. This exponential dependence then makes likely that only the very last atom of the tip apex conducts the tunneling current, allowing the imaging of surfaces with atomic resolution without the need of very sharp tip.

A.1.2 STM mode

Although using the tunneling effect to study conductive surfaces arose quickly at the beginning of quantum physics, the first STM only appears in the 1980s thanks to the use of piezoelectric actuators, which allows very precise positioning of the tip with a picometric precision. Figure A.1(a) shows the working principle of a STM. The tip is mounted on a piezoelectric tube scanner. A bias voltage V_{bias} is applied to the sample, which shifts its chemical potential μ_{S} by $-eV_{\text{bias}}$ with respect to the chemical potential $\mu_{\text{T}} = E_{\text{F}}$ of the tip, hence $\mu_{\text{S}} = \mu_{\text{T}} - eV_{\text{bias}}$. Piezoelectric motors are used to move the tip toward the sample close enough so that a tunneling current flows between the tip and the sample.

The tunneling current I_{t} going through the tip is measured with the STM amplifier that converts this current, typically of the order of the nA, into a voltage, usually of the order of several hundreds of mV, which depends exponentially on the tip-sample distance. This signal serves as the input parameter of a feedback loop used to regulate the voltage V_Z applied to the Z electrode of the piezo tube in order to maintain I_{t} fixed at the setpoint value I_{set}. While scanning over a surface, the variations of V_Z are then converted in variations of the vertical position of the tip $z(x, y)$, and these spatial variations of z produce a topographic image of the sample surface. This imaging method is known as the *Constant-current imaging mode*. After ensuring that the surface of the scan area is flat, one can also use the *Constant-height imaging mode*, where the z-regulation on the tunneling current is turned off during the scanning and we image the spatial variations of the tunneling current due to surface corrugation, which gives a qualitative map of the topography of the sample.

Tunneling current We apply a bias voltage V_{bias} on the sample. At $T > 0\,\text{K}$, the measured net tunneling current is the sum of two contributions : the tunneling current from the tip to the sample and the one from the sample to the tip. Let us assume elastic tunneling of electrons through the vacuum barrier, which therefore conserve their energy. We now consider energies with respect to the Fermi level : $E_{\text{F}} = 0$. We note $\rho_{\text{T}}(E)$ the density of states of the tip while $\rho_{\text{S}}(E, \boldsymbol{r})$ is the local density of states of the sample at position $\boldsymbol{r}$. The number of electrons that can tunnel from occupied states of the tip with energy E to empty states of the sample with energy $E + eV_{\text{bias}}$ is given by :

$$\rho_{\text{T}}(E) f_{\text{FD}}(E, T) \times \rho_{\text{S}}(E + eV_{\text{bias}}, \boldsymbol{r}) \left[1 - f_{\text{FD}}(E + eV_{\text{bias}}, T)\right]$$

where $f_{\text{FD}}(E, T)$ is the Fermi-Dirac distribution function which gives the probability of an electronic state at energy E to be occupied at temperature T :

$$f_{\text{FD}}(E, T) = \left[\exp\left(\frac{E}{k_{\text{B}}T}\right) + 1\right]^{-1} \tag{A.3}$$

with k_{B} the Boltzmann constant. If at $T = 0\,\text{K}$ there is only one contribution to the net tunneling current, at $T > 0\,\text{K}$ appear electrons tunneling though thermally excited states that happen to be filled (resp. emptied) above (resp. below) the Fermi level.

Using the Fermi's golden rule, and taking into account the spin degeneracy, the total tunneling current flowing from the tip to the sample is then given by :

$$I_{\text{T}\to\text{S}} = \frac{4\pi e}{\hbar} \int_{-\infty}^{+\infty} |M|^2 \, \rho_{\text{T}}(E) \rho_{\text{S}}(E + eV_{\text{bias}}, \boldsymbol{r}) f_{\text{FD}}(E, T) \left[1 - f_{\text{FD}}(E + eV_{\text{bias}}, T)\right] \mathrm{d}E \tag{A.4}$$

$|M|^2$ is the tunneling matrix element which is proportional to the transmission probability of an electron through the barrier, and thus depends exponentially on the tip-sample distance z.

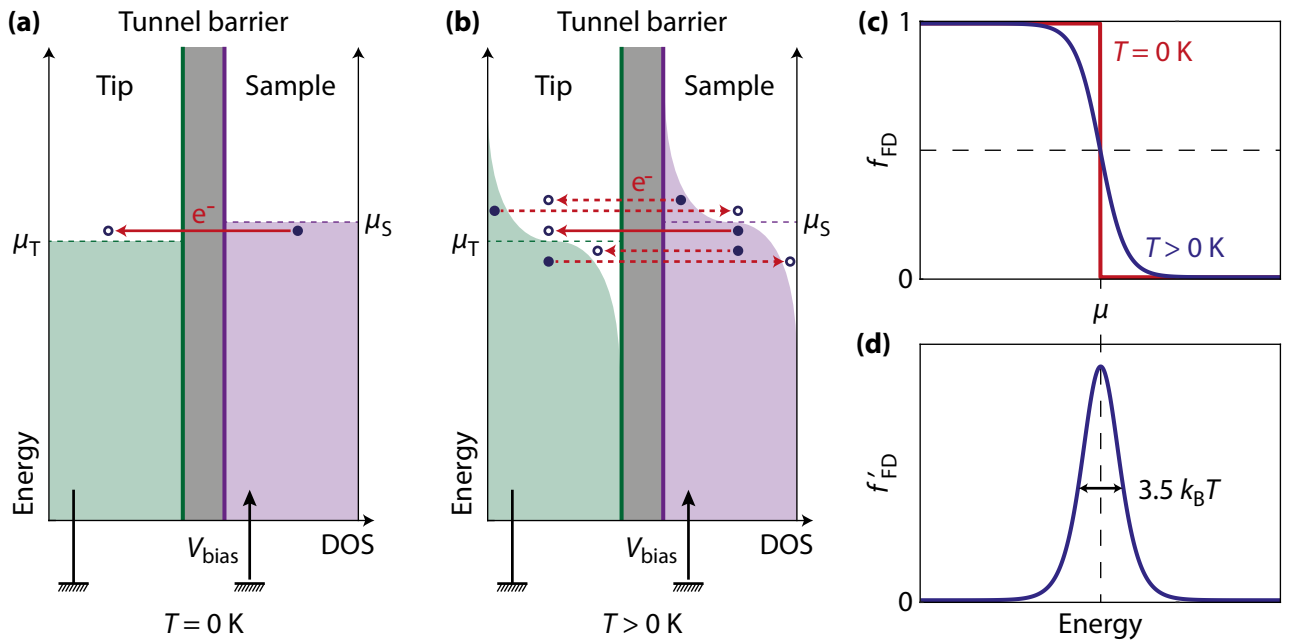

Figure A.2: Effect of temperature on the tunneling current. **(a)** At $T = 0\,\mathrm{K}$, only one tunneling process exists. **(b)** At $T > 0\,\mathrm{K}$, additional tunneling processes exist due to thermally exciting states. **(c)** Fermi-Dirac distribution and **(d)** its derivative.

Similarly, the number of electrons that can tunnel from occupied states of the sample with energy $E + eV_{\mathrm{bias}}$ to empty states of the tip with energy E is written as :

$$\rho_{\mathrm{T}}(E)\left[1 - f_{\mathrm{FD}}(E,T)\right] \times \rho_{\mathrm{S}}(E + eV_{\mathrm{bias}}, \boldsymbol{r}) f_{\mathrm{FD}}(E + eV_{\mathrm{bias}}, T)$$

and the total tunneling current flowing from the sample to the tip is :

$$I_{\mathrm{S}\to\mathrm{T}} = \frac{4\pi e}{\hbar}\int_{-\infty}^{+\infty} |M|^2\, \rho_{\mathrm{T}}(E)\rho_{\mathrm{S}}(E + eV_{\mathrm{bias}}, \boldsymbol{r})\left[1 - f_{\mathrm{FD}}(E,T)\right] f_{\mathrm{FD}}(E + eV_{\mathrm{bias}}, T)\mathrm{d}E \qquad \text{(A.5)}$$

The net total tunneling current I_{t} flowing from the sample to the tip is eventually the difference of Equations (A.5) and (A.4), which gives :

$$I_{\mathrm{t}}\left(z, V_{\mathrm{bias}}, \boldsymbol{r}\right) = \frac{4\pi e}{\hbar}\int_{-\infty}^{+\infty} |M|^2\, \rho_{\mathrm{T}}(E)\rho_{\mathrm{S}}(E + eV_{\mathrm{bias}}, \boldsymbol{r})\left[f_{\mathrm{FD}}(E + eV_{\mathrm{bias}}, T) - f_{\mathrm{FD}}(E,T)\right]\mathrm{d}E \qquad \text{(A.6)}$$

Since we assume $eV_{\mathrm{bias}} \ll \Phi$, $|M|^2 \propto \exp\left(-2\kappa z\right)$ is independent of the energy E and we finally obtain the expression of the tunneling current :

$$I_{\mathrm{t}}\left(z, V_{\mathrm{bias}}, \boldsymbol{r}\right) \propto \underbrace{\exp\left(-2\kappa z\right)}_{\textbf{STM}} \times \underbrace{\int_{-\infty}^{+\infty} \rho_{\mathrm{T}}(E)\rho_{\mathrm{S}}(E + eV_{\mathrm{bias}}, \boldsymbol{r})\left[f_{\mathrm{FD}}(E + eV_{\mathrm{bias}}, T) - f_{\mathrm{FD}}(E,T)\right]\mathrm{d}E}_{\textbf{STS}} \qquad \text{(A.7)}$$

The first term is the STM mode : at a given bias voltage V_{bias}, we regulate on the tunneling current I_{t} to image the surface topography $z(\boldsymbol{r})$, which in fact is rather the image of the sample density of states. On the other hand, the second term only depends on V_{bias} and is the convolution of both densities of states at $T = 0\,\mathrm{K}$: $I_{\mathrm{t}}(V_{\mathrm{bias}}) \propto \rho_{\mathrm{T}} \otimes \rho_{\mathrm{S}}$. Since this term depends on the local density of states of the sample $\rho_{\mathrm{S}}(E, \boldsymbol{r})$, if we fix the tip-sample distance z at a given point $\boldsymbol{r}$ and measure the evolution of I_{t} with V_{bias}, it is possible to probe ρ_{S}. This is the Scanning Tunneling Spectroscopy (STS) mode.

A.1.3 STS mode

Tunneling conductance In the following we fix z. We can therefore write the expression for the tunneling current, with a change a variable $E \longmapsto E + eV_{\text{bias}}$, as :

$$I_{\text{t}}\left(V_{\text{bias}}, \boldsymbol{r}\right) = \frac{4\pi e}{\hbar}\left|M\right|^2 \int_{-\infty}^{+\infty} \rho_{\text{S}}(E, \boldsymbol{r})\rho_{\text{T}}(E - eV_{\text{bias}})\left[f_{\text{FD}}(E, T) - f_{\text{FD}}(E - eV_{\text{bias}}, T)\right] \text{d}E \quad \text{(A.8)}$$

The tunneling conductance is then given by :

$$\frac{\partial I_{\text{t}}}{\partial V_{\text{bias}}} = \frac{4\pi e}{\hbar}\left|M\right|^2 \int_{-\infty}^{+\infty} \rho_{\text{S}}(E, \boldsymbol{r}) \frac{\partial}{\partial V_{\text{bias}}}\left[\rho_{\text{T}}(E - eV_{\text{bias}})\left[f_{\text{FD}}(E, T) - f_{\text{FD}}(E - eV_{\text{bias}}, T)\right]\right] \text{d}E \quad \text{(A.9)}$$

We now assume that the tip is metallic : its density of states around the Fermi energy can be considered constant and $\rho_{\text{T}}(E) = \rho_{\text{T}}$. The tunneling conductance thus becomes :

$$\frac{\partial I_{\text{t}}}{\partial V_{\text{bias}}}\left(V_{\text{bias}}, \boldsymbol{r}\right) = -\frac{4\pi e}{\hbar}\left|M\right|^2 \rho_{\text{T}} \int_{-\infty}^{+\infty} \rho_{\text{S}}(E, \boldsymbol{r}) \frac{\partial}{\partial V_{\text{bias}}} f_{\text{FD}}(E - eV_{\text{bias}}, T) \text{d}E \quad \text{(A.10)}$$

which can be written as the convolution of the local density of states of the sample with the derivative of the Fermi-Dirac distribution f'_{FD}, drawn in Figure A.2(d) :

$$\frac{\partial I_{\text{t}}}{\partial V_{\text{bias}}}\left(V_{\text{bias}}\right) \propto -\rho_{\text{S}} \otimes f'_{\text{FD}} \quad \text{(A.11)}$$

where :

$$f'_{\text{FD}}(E, T) = -\frac{1}{4T\cosh^2(E/2T)} \quad \text{(A.12)}$$

The tunneling conductance is therefore a direct way to probe the local density of states of the sample, but with a thermal broadening of about $3.5\, k_{\text{B}}T$. Eventually, at $T = 0\,\text{K}$, the tunneling conductance is proportional to the local density of states of the sample. Figure A.3 shows the principle of STS using a metallic tip to probe graphene Landau levels, where the tunneling current and conductance are computed numerically. At $T = 4\,\text{K}$, the resulting tunneling conductance is an accurate representation of the density of states of the sample. Indeed, the thermal broadening, which is about $3.5\, k_{\text{B}}T \simeq 1.2\,\text{meV}$, is negligible in the case of graphene compared to the cyclotron gaps ($\Delta E_{01} \simeq 36\,\text{meV}$ for the gap between the zeroth and first Landau levels at $B = 1\,\text{T}$). In our experiment of STS on graphene, the energy resolution is therefore not limited by the temperature.

Lock-in amplifier technique A simple way to obtain the tunneling conductance is by measuring the evolution of the tunneling current with the sample bias and then to compute numerically its derivative. However this method introduces an important numerical noise that is overcome by averaging the measured tunneling current over a large number of samples before computing the derivative of the mean current. Another way to measure directly the tunneling conductance is by using the *lock-in amplifier technique*.

We apply a bias V on the sample that is the sum of two voltages : the usual dc bias V_{bias} and a small sinusoidal ac modulation $V_{\text{mod}}\sin(2\pi f_{\text{mod}}t)$ generated by a lock-in amplifier. The amplitude of the modulation V_{mod} is such that $V_{\text{mod}} \ll V_{\text{bias}}$ (typically we choose $V_{\text{mod}} = V_{\text{bias}}/100$), while the frequency of the modulation f_{mod} is chosen to avoid the typical frequency domains of mechanical vibrations and electronic noise, coming mainly from the 50 Hz and its harmonics of the electric power supply (in our case we choose $f_{\text{mod}} = 263\,\text{Hz}$). Using a Taylor expansion, we can write the resulting tunneling current as :

$$I_{\text{t}}(V) = I_{\text{t}}(V_{\text{bias}}) + \left.\frac{\partial I_{\text{t}}}{\partial V}\right|_{V=V_{\text{bias}}} V_{\text{mod}}\sin(2\pi f_{\text{mod}}t) + \mathcal{O}(V_{\text{mod}}^2) \quad \text{(A.13)}$$

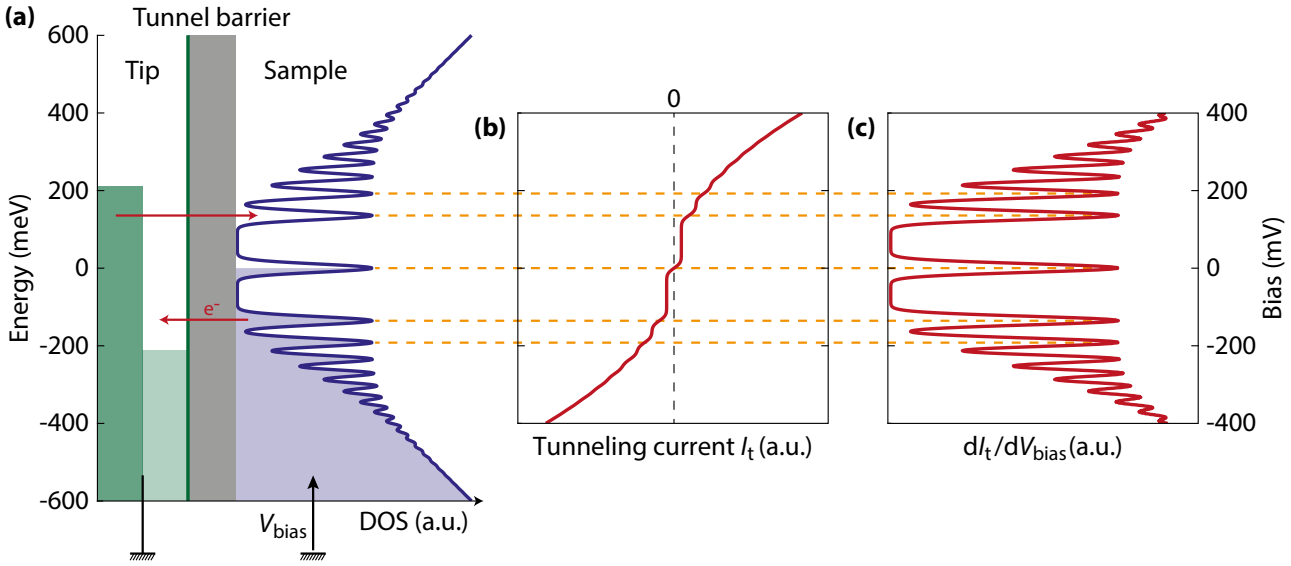

Figure A.3: Scanning Tunneling Spectroscopy (STS). (a) Elastic tunneling between a metallic tip (left), with a constant density of states (DOS) near the Fermi energy ($E_F = 0$), and a conductive sample (right), with a graphene-like DOS with Landau level peaks, through a tunnel barrier. By tuning the bias voltage V_{bias} applied to the sample, we change the relative position of the chemical potentials of the tip and sample, which gives access to different parts of the sample DOS. Two cases are shown for the tip DOS : translated to higher (resp. lower) energies for $V_{bias} > 0$ (resp. $V_{bias} < 0$). **(b)** Tunneling current I_t as a function of bias voltage V_{bias} calculated as the convolution of both density of states, see Equation (A.7), at $T = 4\,K$. **(c)** Tunneling conductance dI_t/dV_{bias} as a function of bias voltage V_{bias} at $T = 4\,K$: the tunneling conductance gives a direct access to the DOS of the sample.

At fixed V_{bias}, the ac component of the tunneling current is small compared to the dc one and thus does not affect the z-feedback loop that regulates the tip-sample distance for the usual STM mode. At fixed tip-sample distance corresponding to a setpoint $(V_{bias,0}, I_{t,0})$, we sweep the sample bias V_{bias} and measure the tunneling current as usual but, at the same time, the tunneling current is also measured with the lock-in amplifier, which gives as output the amplitude of the component corresponding to the reference frequency f_{mod} of the ac modulation of the bias :

$$A_{\text{lock-in}} = V_{mod} \left.\frac{\partial I_t}{\partial V}\right|_{V=V_{bias}} \tag{A.14}$$

Eventually, the lock-in amplifier directly gives the tunneling conductance, and therefore the local density of states of the sample. Nevertheless, we only obtain a qualitative measure of the tunneling conductance. The spectra measured with this method are clean and less noisy than those obtained by computing numerically the derivative of the tunneling current, but the broadening of the spectra can be important, with the removal of small features in the density of states. This broadening is reduced by keeping the amplitude of the modulation V_{mod} small compared to the typical energy width of the measured features in the sample density of states.

It is also possible to use STS to map the spatial variations of the local density of states of the sample. In the *Current Imaging Tunneling Spectroscopy* (CITS) mode, at each point (x, y) of the sample, the tip-sample distance is fixed and a spectrum dI_t/dV_{bias} is acquired. It enables to plot spatial maps at fixed sample bias of the sample LDOS. The inhomogeneities observed in CITS maps correspond to local variations of the density of states, for instance the presence of localized states or quantum dots. However such measures require a very stable tunneling junction since they easily last several hours in order to obtain a good spatial resolution.

A.2 Atomic Force Microscopy

Atomic Force Microscopy [285, 286], or AFM, is another scanning probe microscopy technique that we employed in this work, in a dynamic non-contact mode, for the localization of the device and of the edges of graphene. Indeed, a major drawback of STM is that it only works on conductive surfaces. If the tip happens to scan on an insulating part of the device, such as silicon oxide or hBN, it would inevitably crash. AFM is used to overcome this limitation.

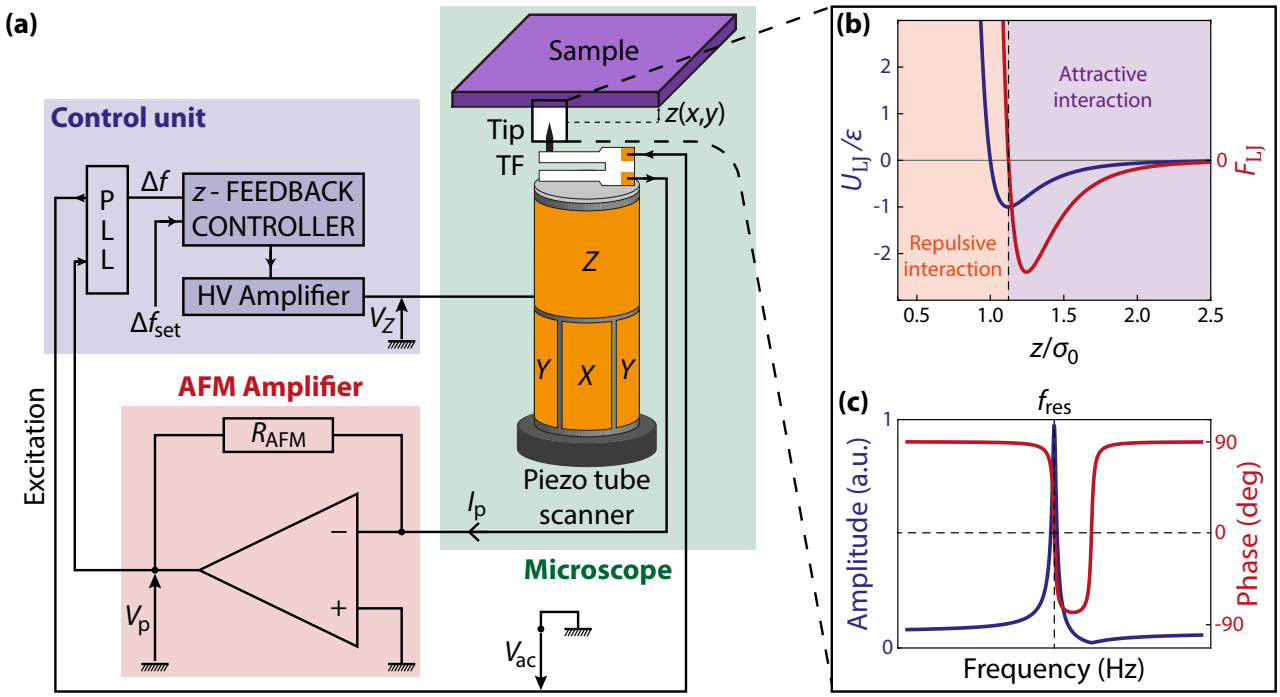

Figure A.4: Atomic Force Microscopy (AFM). (a) A tip glued on a tuning fork (TF) is used as a force sensor. The TF is excited on one of its electrode with a signal V_{ac} oscillating at the resonance frequency f_{res} of the TF, while we measure the resulting piezoelectric current I_{p} on the second electrode. A Phase-Locked Loop (PLL) determines the frequency shift Δf between the two signals, which results from the interaction between the tip and the sample. A feedback loop on Δf maintains constant the tip-sample distance z. **(b)** Lennard-Jones potential U_{LJ} describing the interaction between the tip and the sample and the corresponding force $F_{\mathrm{LJ}} = -\mathrm{d}U_{\mathrm{LJ}}/\mathrm{d}z$ as a function of tip-sample distance z. **(c)** Typical resonance of a tuning fork in both amplitude and phase in response to an oscillatory signal V_{ac}.

The working principle of an AFM is quite similar to that of a STM, see Figure A.4(a) : a tip is brought to close vicinity of a surface using piezoelectric actuators, and the tip-sample distance is regulated using a feedback loop that controls the voltage applied to the piezoelectric tube on which the tip is mounted. The main difference is that we probe the tip-sample interaction instead of a tunneling current. This interaction originates from van der Waals forces that appear at tip-sample distances of a few nanometers. To probe this interaction, we use quartz resonator tuning forks as force sensors on which we glue the tip at the extremity of one prong. When the tip is close enough to the surface so that the tip feels an attractive force, the resulting shift in the natural frequency of the resonator is used as the imaging signal, with the feedback loop adjusting the voltage on the piezoelectric tube to keep this frequency shift, and the tip-sample distance, constant. However, contrary to STM, it is more difficult to achieve atomic resolution in AFM due to the lower sensitivity of the frequency shift signal with the tip-sample distance. The shape of the tip apex also becomes here a crucial parameter for surface imaging.

A.2.1 Interactions between the tip and the sample

There are different kinds of interactions between the tip and the sample, depending on their range. At short range (a few angströms), chemical binding forces are repulsive due to the Pauli principle that prevents the electronic orbitals of the tip from penetrating those of the sample. At longer range (a few nanometers), the attractive van der Waals interactions take over. They originate from the interactions between electrostatic dipoles induced by the electronic cloud. The empirical way to represent those short-range tip-sample interactions is by using the Lennard-Jones potential, which describes the interaction between two electronically neutral atoms separated by a distance z :

$$U_{\mathrm{LJ}}(z) = 4\varepsilon\left[\left(\frac{\sigma_0}{z}\right)^{12} - \left(\frac{\sigma_0}{z}\right)^{6}\right] \tag{A.15}$$

where σ_0 is the distance at which the potential is zero (it is also regarded as the size of the particle), $z_{\mathrm{m}} = 2^{1/6}\sigma_0$ is the equilibrium distance where the Lennard-Jones potential is at its minimum value $U_{\mathrm{m}} = -\varepsilon$. Typically, $\sigma_0 \sim 3\,\text{Å}$ and $\varepsilon \sim 0.01\,\mathrm{eV}$. The positive and rapidly decaying term in $1/z^{12}$ describes the repulsive interactions, while the negative and slowly decaying term in $1/z^6$ describes the attractive van der Waals interactions. The resulting force between the two particles is given by :

$$F_{\mathrm{LJ}}(z) = -\frac{\mathrm{d}U_{\mathrm{LJ}}}{\mathrm{d}z} \tag{A.16}$$

$U_{\mathrm{LJ}}(z)$ and $F_{\mathrm{LJ}}(z)$ are represented in Figure A.4(b). The two particles repel each other at very close distance ($z < \sigma_0$) while the two particles attract each other at moderate distance $z > \sigma_0$. At long distances ($z \gg \sigma_0$), the particles do not interact.

At large distances (from tens to a few hundreds of nanometers), those short-range interactions disappear. Long-range interactions are dominated by attractive electrostatic forces between the tip and the sample if they are conducting. Applying a voltage V_{ts} between the tip and the sample, separated by a distance z, the electrostatic energy is given by :

$$U_{\mathrm{elec}}(z, V_{\mathrm{ts}}) = \frac{1}{2}C_{\mathrm{ts}}(z)V_{\mathrm{ts}}^2 \tag{A.17}$$

where the capacitance $C_{\mathrm{ts}}(z)$ between the tip and the sample depends on the distance z and the shape of the tip (assuming a planar sample). To the first order, the electrostatic energy varies as $1/z$ whereas the electrostatic force varies as $1/z^2$.

A.2.2 Dynamic AFM mode

AFM probes the short-range interactions between the tip and the sample. To detect those interactions, we use a quartz resonator with a characteristic eigen frequency of oscillation $\omega_0 = 2\pi f_0$ that varies when the tip and the sample interact with a force F_{ts}. The probe can be described as a damped harmonic oscillator subjected to a driving periodic force $F_0\cos(\omega_{\mathrm{d}}t)$ (to maintain its oscillation) and the tip-sample interaction force F_{ts}. The equation of motion is then given by :

$$m\ddot{z} + \alpha\dot{z} + k_0 z = F_0\cos(\omega_{\mathrm{d}}t) + F_{\mathrm{ts}} \tag{A.18}$$

where k_0 is the spring constant of the resonator, m its effective mass and α represents the dissipation. Introducing the quality factor Q and the resonance frequency of the free system $\omega_0 = \sqrt{k_0/m}$, we can write :

$$m\ddot{z} + \frac{m\omega_0}{Q}\dot{z} + k_0 z = F_0\cos(\omega_{\mathrm{d}}t) + F_{\mathrm{ts}} \tag{A.19}$$

A.2.2.a Dynamic of the oscillation

We consider the free resonator case with $F_{\text{ts}} = 0$ (tip far from the surface) and we write the solution of Equation (A.19) such as :

$$z(t) = A(\omega_{\text{d}}) \cos\left[\omega_{\text{d}} t - \varphi(\omega_{\text{d}})\right] \tag{A.20}$$

Using the complex notation $\underline{z}(t) = \underline{A}(\omega_{\text{d}}) \exp(j\omega_{\text{d}} t)$ with $\underline{A}(\omega_{\text{d}}) = A(\omega_{\text{d}}) \exp\left[-j\varphi(\omega_{\text{d}})\right]$ such as $z(t) = \Re[\underline{z}(t)]$, we can deduce the amplitude and phase of the solution to Equation (A.19) :

$$A(\omega_{\text{d}}) = \frac{A_{\text{d}}}{\sqrt{\left(1 - \frac{\omega_{\text{d}}^2}{\omega_0^2}\right)^2 + \left(\frac{\omega_{\text{d}}}{\omega_0 Q}\right)^2}} \qquad \text{and} \qquad \varphi(\omega_{\text{d}}) = \arctan\left[\frac{\omega_{\text{d}}}{\omega_0 Q\left(1 - \frac{\omega_{\text{d}}^2}{\omega_0^2}\right)}\right] \tag{A.21}$$

where $A_{\text{d}} = F_0/m\omega_0$. The amplitude $A(\omega_{\text{d}})$ is a lorentzian centered around ω_0. At the resonance, the amplitude of the oscillation is $A(\omega_{\text{d}} = \omega_0) = QA_{\text{d}}$. The quality factor quantifies the dissipation of energy in the resonator : if the driving excitation vanishes, the system relaxes with a characteristic time $\tau = 1/\alpha = 2Q/\omega_0$. It can also be defined as $Q = \omega_0/\Delta\omega$ where $\Delta\omega$ is the bandwidth of the resonator at half-power (corresponding to an attenuation of -3 dB). The working of AFM lies on this resonance and its shift in frequency when the tip and the sample are interacting. If the harmonic oscillator describes well the resonance of a tuning fork[1], one must keep in mind that a tuning fork also presents an anti-resonance, as shown in Figure A.4(c). A better modelization of the tuning fork is done in Chapter 4.3.1.

A.2.2.b Interaction with the surface

When the tip is close enough to the surface, the tip-sample force $F_{\text{ts}}(z)$ appears. In the regime of small tip displacement z around the position at equilibrium z_0, a Taylor expansion of the tip-sample interaction potential U_{ts} is used to write F_{ts} as :

$$F_{\text{ts}}(z) = -\frac{\mathrm{d}U_{\text{ts}}}{\mathrm{d}z} \approx -\frac{\mathrm{d}}{\mathrm{d}z}\left[U_{\text{ts}}(z_0) + \left.\frac{\mathrm{d}U_{\text{ts}}}{\mathrm{d}z}\right|_{z=z_0} z + \left.\frac{\mathrm{d}^2U_{\text{ts}}}{\mathrm{d}z^2}\right|_{z=z_0} \frac{z^2}{2} + \mathcal{O}(z^3)\right] \tag{A.22}$$

which gives, introducing $F_{\text{ts}}(z_0) = -\left.\frac{\mathrm{d}U_{\text{ts}}}{\mathrm{d}z}\right|_{z=z_0}$ and $k_{\text{ts}} = \left.\frac{\mathrm{d}^2U_{\text{ts}}}{\mathrm{d}z^2}\right|_{z=z_0}$:

$$F_{\text{ts}}(z) \approx F_{\text{ts}}(z_0) - k_{\text{ts}} z \tag{A.23}$$

We insert this back in Equation (A.19) to obtain :

$$m\ddot{z} + \frac{m\omega_0}{Q}\dot{z} + (k_0 + k_{\text{ts}})z = F_0 \cos(\omega_{\text{d}} t) + F_{\text{ts}}(z_0) \tag{A.24}$$

We get a new harmonic oscillator equation, with an effective stiffness $k_{\text{eff}} = k_0 + k_{\text{ts}}$ and a change of the eigen frequency into (assuming the resonator is stiff enough to have $k_0 \gg k_{\text{ts}}$) :

$$\omega_1 = \sqrt{\frac{k_0 + k_{\text{ts}}}{m}} = \left(\omega_0^2 + \frac{1}{m}\frac{\mathrm{d}^2U_{\text{ts}}}{\mathrm{d}z^2}(z_0)\right)^{1/2} \approx \omega_0\left(1 + \frac{1}{2k_0}\frac{\mathrm{d}^2U_{\text{ts}}}{\mathrm{d}z^2}(z_0)\right) \tag{A.25}$$

[1] Although a tuning fork is in fact two coupled vibrating prongs, which would require a better description of the oscillation dynamics, the tuning forks in our sensors are glued on one of their prong, that is eventually not able to oscillate anymore, such that the coupling is removed. We can therefore assume that the harmonic oscillator resonator models correctly our sensors.

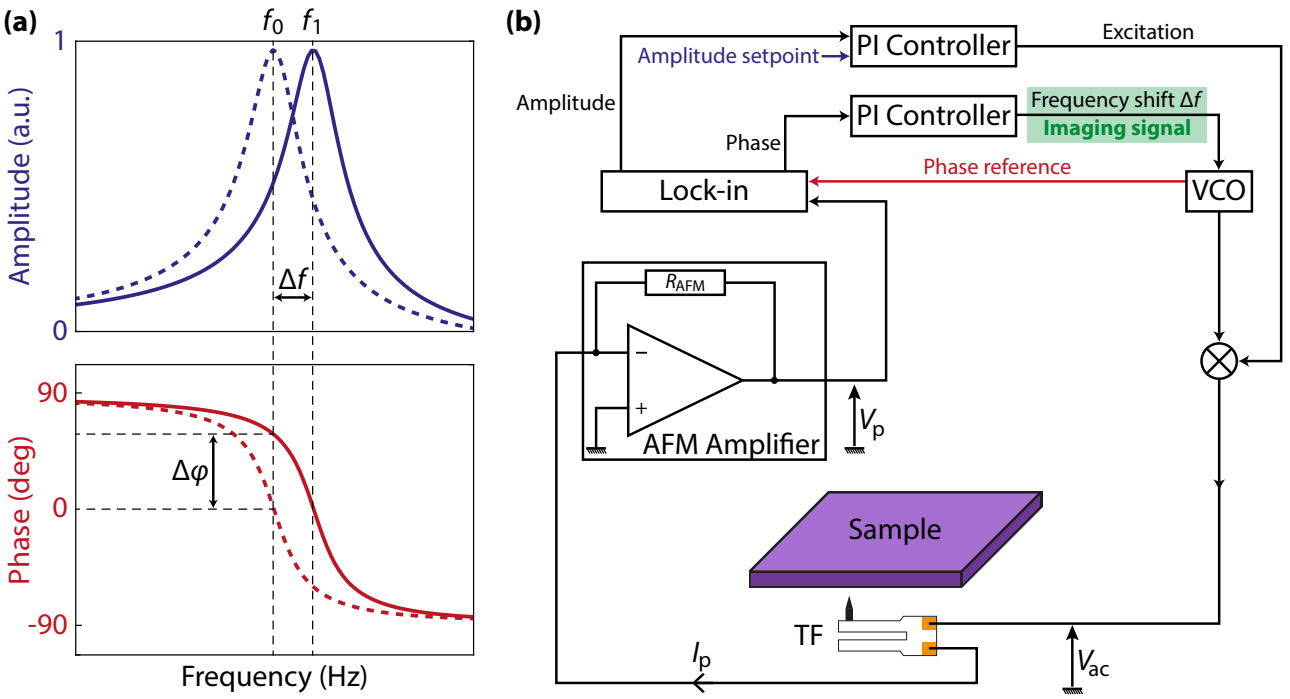

Figure A.5: Frequency Modulation AFM. (a) Response of the TF when the tip is interacting with the sample surface : resonance curves in the interacting case (solid line) and non-interacting case (dashed line). **(b)** Block diagram of the Frequency Modulation AFM feedback loop in order to maintain the TF at resonance while scanning.

The shift of the resonance frequency is therefore :

$$\Delta f = f_1 - f_0 \approx \frac{f_0}{2k_0} \left. \frac{\mathrm{d}^2 U_{\mathrm{ts}}}{\mathrm{d}z^2} \right|_{z=z_0} \tag{A.26}$$

Thus, when approaching the tip toward the sample, a shift of the resonance frequency appears and is related to the gradient of the interaction force between the tip and the sample. The response of the tuning fork to the tip-sample interaction is shown in Figure A.5(a). Probing the tip-sample interaction through the resulting frequency shift Δf of the resonator is the working principle of the Frequency Modulation AFM.

A.2.2.c Frequency Modulation AFM

We now describe how the frequency shift Δf of the resonator can be measured and used to regulate the tip-sample distance. Two techniques are mainly employed : the Amplitude Modulation (AM) and the Frequency Modulation (FM).

In AM-AFM, the resonator is excited at a frequency close to the resonance frequency, in a regime where the amplitude varies linearly with the frequency. The tip-sample distance is then kept constant using a regulation on the increase or decrease of the amplitude due to the tip-sample interaction force, which thus serves as a measure of Δf. However this technique presents a major drawback as the available bandwidth is limited by the quality factor Q of the resonator, since the response time of the system to a change of its environment is given by $\tau = 2Q/\omega_0$, which limits the scan velocity for high quality factor (typically for our tuning fork sensors, $Q \sim 10\,000$ and $f_0 \sim 20\,000$ kHz so $\tau \sim 0.2$ s).

The FM-AFM technique that we use in our setup, developed in 1991 by Albrecht [287], overcomes this limitation. The resonator is there constantly excited at its eigen frequency. Far

from the surface, the eigen frequency is f_0 and stays constant, but when the tip is brought close enough to the surface such that they interact, the eigen frequency of the resonator is modified to f_1. Measuring the frequency shift $\Delta f = f_1 - f_0$ and keeping it at a fixed value allows us to regulate the tip-sample distance and keep it constant. The problem now lies on how to measure efficiently the frequency shift Δf while scanning the surface. One can not simply measure the whole resonance, that would take several tens of seconds for high quality factors, at each point of the scan. The phase signal is rather used to stay at the resonance frequency, defined by $\varphi = 0$. Around this point, the phase is proportional to the frequency shift Δf, and a Phase-Locked Loop (PLL) is employed to maintain the tuning fork at resonance while scanning.

The working principle of FM-AFM is shown in Figure A.5(b). We use a quartz piezoelectric tuning fork, which is driven at its resonance with an oscillatory signal V_{ac}. The piezoelectric current I_{p}, that results from the mechanical deformation of the quartz, is measured with an AFM amplifier that converts I_{p} into a voltage V_{p} that serves as the input of a lock-in amplifier, which gives as outputs its amplitude and phase separately. The phase is calculated with respect to a reference phase, chosen to be zero when the probe is oscillating at resonance in the non-interacting regime, far from the sample.

The PLL is then comprised of two separated feedback loops with Proportional-Integral (PI) Controllers. The Amplitude Controller regulates the Excitation signal by comparing the measured amplitude with an amplitude setpoint, in order to maintain the amplitude of the resonator oscillation constant. The Phase Controller compares the input phase with the phase reference and acts on the VCO (Voltage Controlled Oscillator) to regulate the frequency of the resonator. A non-zero phase difference implies a frequency shift Δf due to the tip-sample interaction, and the feedback loop changes the frequency of the resonator by Δf to bring this phase difference back to zero. The signal Δf is then recorded as the main imaging signal. The excitation signal is finally combined with the signal oscillated at the new frequency generated by the VCO to form the signal V_{ac} that drives the tuning fork.

It is therefore possible to continuously track the resonance frequency of the tuning fork during the scan, to compare it with the resonance frequency far from the signal, and regulating using a z-feedback loop on the resulting frequency shift Δf enables to make topographic images of the sample surface. Other information can be obtained, for instance spatial maps of the excitation signal, that is related to the dissipation of the resonator depending on the material it is interacting with.

A.2.3 EFM mode

Electrostatic Force Microscopy (EFM) is another type of dynamic non-contact atomic force microscopy, where the electrostatic force between the tip and a charged sample is probed. The electrostatic interaction is a long-range force that can be sensed by the tip a few hundreds of nanometers away from the sample. It is therefore possible to image surfaces at such distances in EFM [288]. The shape of the tip and the capacitance it forms with the sample (and its modelization) become there fundamental parameters [289]. One can switch from AFM mode to EFM mode easily, starting from AFM contact, by turning off the z-regulation, then withdrawing the tip of some tens of nanometers and finally applying a voltage between the tip and the sample (see Figure A.4). The measure of the dependence of the frequency shift with this voltage gives information on the junction between the tip and the sample, especially the Contact Potential Difference (CPD) [2]. The CPD originates from the difference between the work functions of the

[2]The CPD can also be measured and mapped with Kelvin Probe Force Microscopy (KPFM) [207, 208].

two materials which leads to different positions of their Fermi level :

$$V_{\mathrm{CPD}} = \frac{\Phi_{\mathrm{S}} - \Phi_{\mathrm{T}}}{e} \tag{A.27}$$

When they are electrically connected, this electrochemical potential imbalance causes a transfer of charges between them until the Fermi levels are aligned, see Figure A.6(b). Moreover, this CPD causes an intrinsic electrostatic force between the tip and the sample that can be probed as a frequency shift. This force is nullifying by applying a compensating voltage between the tip and the sample.

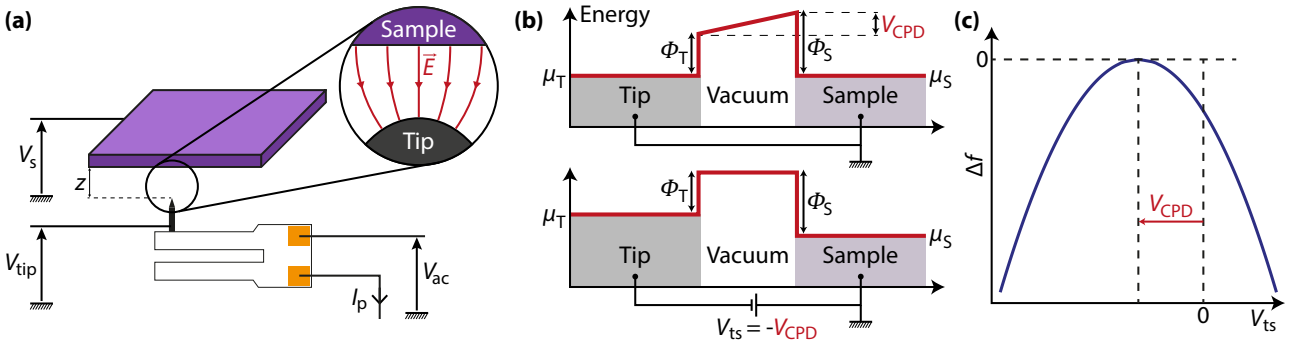

Figure A.6: Electrostatic Force Microscopy (EFM). (a) The tip probes the long-range electrostatic interaction with the sample, which shifts the resonance frequency of the tuning fork. **(b)** When both the tip and sample are grounded, the mismatch of their work function is called the Contact Potential Difference V_{CPD}. This is the voltage one has to apply between the tip and the sample to align their vacuum level. **(c)** Parabolic dependence of the frequency shift Δf with the voltage between the tip and the sample V_{ts}. The apex of the parabola lies at $V_{\mathrm{ts}} = -V_{\mathrm{CPD}}$.

A voltage $V_{\mathrm{ts}} = V_{\mathrm{tip}} - V_{\mathrm{s}}$ is applied between the tip and the sample, which are both conductive and separated by a distance z in vacuum. For $z > 10\,\mathrm{nm}$, the short-range interactions can be ignored. The tip and the sample form a capacitor where the capacitance $C_{\mathrm{ts}}(z)$ depends on the geometry of the tip (the sample is assumed to be flat) and the distance z. The electrostatic energy is given by Equation (A.17), and taking into account a non-zero CPD gives :

$$U_{\mathrm{elec}}(z, V_{\mathrm{ts}}) = \frac{1}{2} C_{\mathrm{ts}}(z) \left(V_{\mathrm{ts}} + V_{\mathrm{CPD}}\right)^2 \tag{A.28}$$

The corresponding electrostatic force between the tip and the sample $F_{\mathrm{ts}} = -\partial U_{\mathrm{elec}}/\partial z$ is :

$$F_{\mathrm{ts}} = -\frac{1}{2} \frac{\mathrm{d}C_{\mathrm{ts}}}{\mathrm{d}z} \left(V_{\mathrm{ts}} + V_{\mathrm{CPD}}\right)^2 \tag{A.29}$$

and using Equation (A.26), the frequency shift Δf which results from the electrostatic interaction is given by :

$$\Delta f = \frac{f_0}{4k_0} \frac{\mathrm{d}^2 C_{\mathrm{ts}}}{\mathrm{d}z^2} \left(V_{\mathrm{ts}} + V_{\mathrm{CPD}}\right)^2 \tag{A.30}$$

Since $\mathrm{d}C_{\mathrm{ts}}/\mathrm{d}z < 0$ (the capacitance between the tip and the sample decreases as they move away), the electrostatic force is always attractive. We there only consider the electrostatic force component perpendicular to the tip-sample surface, which has the dominant contribution in EFM. The frequency shift Δf as a function of V_{ts} presents a parabolic dependence, and the apex of the parabola lies at $V_{\mathrm{ts}} = -V_{\mathrm{CPD}}$. Since the electrostatic force is always attractive, $\Delta f < 0$. A typical evolution of Δf with V_{ts} is shown in Figure A.4(c). The curvature of the parabola decreases with the distance but can still be observed for distances of several hundreds of nanometers. Nevertheless, a good determination of the CPD requires measures at a few tens of nanometers of tip-sample distance at most.

Fabrication of graphene heterostructures for STM

APPENDIX B

NANOFABRICATION methods for the devices used in the STM measurements are described in this chapter. These samples consist of a graphene flake exfoliated from bulk graphite and placed on a hBN flake to improve its quality. The resulting graphene/hBN stack is consequently placed on a Si^{++}/SiO_2 or $SrTiO_3$ substrate. The graphene sheet is then contacted by metallic contacts patterned by electron-beam lithography and deposited by electron-beam metal evaporation. We finally describe the process used to clean the graphene surface from the resist and other organic residues. Some of the presented recipes were developed based on the work of K. Zimmermann [290].

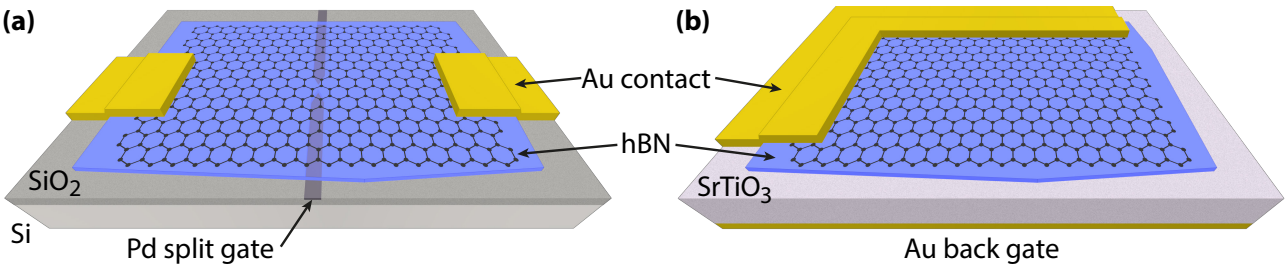

Figure B.1: Devices schematics. (a) Device on a SiO_2 substrate : graphene is contacted by a two (or four) probes configuration, and buried split gates in palladium have been pre-patterned in the substrate before the graphene/hBN stack was deposited above. **(b)** Device on a $SrTiO_3$ substrate : graphene is contacted on some of its edges while leaving the others accessible by the STM tip. In both cases, the carrier density in graphene is tunable by a back gate.

Contents

B.1 Exfoliation of graphene and hBN

We use the mechanical exfoliation technique to produce monolayers of graphene from bulk crystals of natural graphite, as developed in our team and based on the work of Geim and Novoselov [2]. Scotch tape is used to gradually cleave the graphite crystal into thinner and thinner layers. The same technique is used to exfoliated hBN flakes from high-quality hBN crystals produced by K. Watanabe and T. Taniguchi. Both flakes are exfoliated on $5 \times 5\,\mathrm{mm}^2$ highly p-doped silicon substrates with a 285 nm thick layer of SiO_2, which are beforehand cleaned in ultrasonic baths of acetone followed by isopropyl alcohol. Substrates are then treated 2 minutes in concentrate nitric acid to remove residues at the surface and charge traps.

B.1.a Exfoliation technique

Bulk crystals (graphite and boron nitride) are placed onto the adhesive side of a piece of Scotch tape to form a row. We use a binocular to select the crystal that appear to be mostly flat. The piece of tape is folded and peeled apart several times, see Figure B.2(a), to obtain a roughly homogeneous surface of $5 \times 5\,\mathrm{mm}^2$ covered by exfoliated crystals. The tape is then put onto a silicon substrate that has just been cleaned in nitric acid. Instead of applying any direct pressure onto the tape to stick it (which would deposit a lot of glue and mainly very thick flakes), we rather stroke it lightly with a flat edge of a pen for 2 minutes to make the tape contact the whole substrate. Afterwards, the tape is peeled off very slowly at a angle between the tape and the substrate of about 80°, as shown on Figure B.2(b), which leaves exfoliated flakes on the silicon chip.

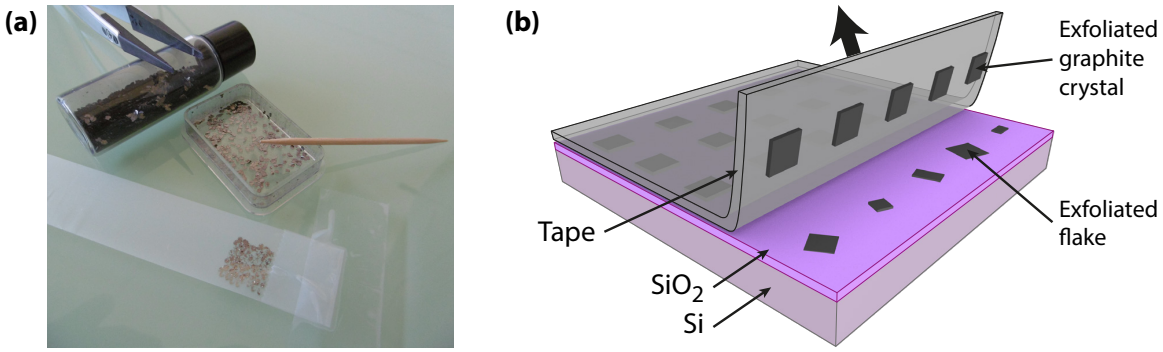

Figure B.2: Exfoliation of graphene. **(a)** The tape is repeatedly peeled off such that the graphite crystals are cleaved to gradually thinner and thinner layers, homogeneously spread on the tape. **(b)** The tape is slowly peeled off the substrate to exfoliate the flakes. The same technique applies for the exfoliation of hBN flakes.

B.1.b Optical research

The research of graphene and hBN flakes is done using an optical microscope. One of the main interest of using a silicon substrate with a SiO_2 layer is that the monoatomically-thick graphene flakes will get a boost of contrast thanks to optical interferences, the contrast depending on the thickness of the SiO_2 layer. In our case for a thickness of 285 nm, the optical contrast of a graphene flake is about 3 %. Graphene flake are then rather easy to observe. Figure B.3(a) shows a typical graphene flake observed using a $\times 100$ objective. For hBN, the color of the flake comes from its thickness : from azure blue for thick flakes (between 10 and 50 nm - see Figure B.3(b)) to dark blue for thin ones (below 10 nm - see Figure B.3(c)). The optical microscope can already be used to discriminate hBN flakes between those who are highly polluted by glue or not, and those who are flat or those who present several steps.

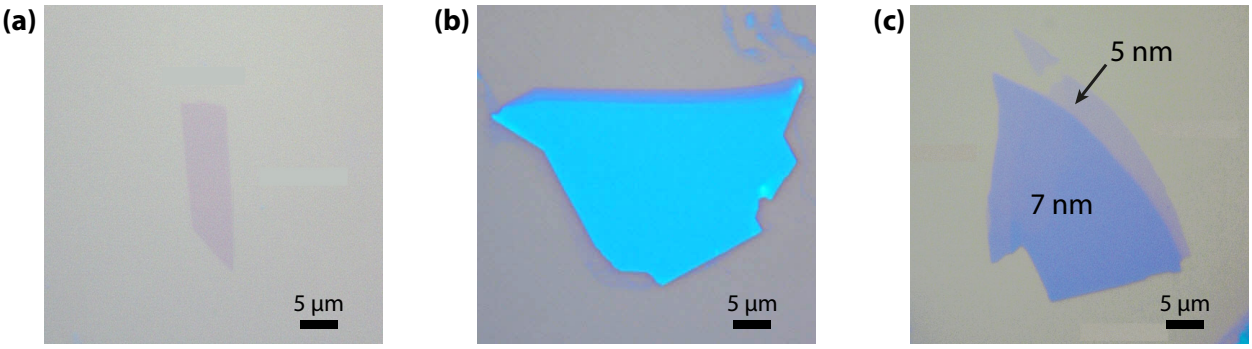

Figure B.3: Flakes exfoliated on SiO_2 and observed in optical microscope. **(a)** Graphene flake, whose contrast is boosted due to optical interferences. **(b)** Typical hBN flake used for devices on SiO_2 substrate. **(c)** Thin hBN flake used for devices on $SrTiO_3$ substrate. The thicknesses of the two steps, measured by AFM, are indicated. The scale bar is the same in the three figures : 5 µm.

B.1.c AFM characterization

The flakes chosen optically are finally characterized with an atomic force microscope, using the Néel Institute AFM platform. We are mainly interested by their cleanliness (flakes may have been polluted by the glue of the Scotch tape during exfoliation) and, for the hBN flakes, by their thickness[1] (thick flakes are used for devices on SiO_2 while thin ones are used for devices on $SrTiO_3$) and their flatness (atomically flat flake with no steps nor crystallographic imperfections).

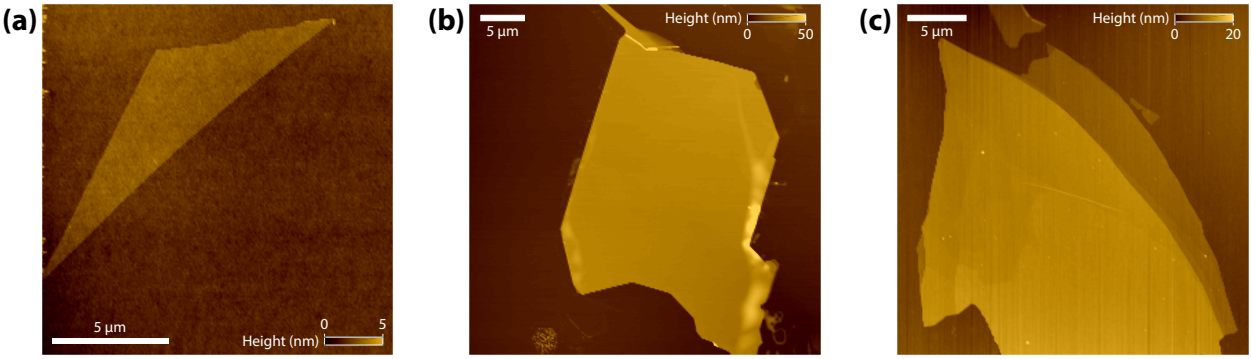

Figure B.4: Flakes exfoliated on SiO_2 and observed by AFM. **(a)** Clean graphene flake. **(b)** hBN flake used for devices on SiO_2 substrate. Some glue appears on some edges of the flake as bright spots. **(c)** Thin hBN flake used for devices on $SrTiO_3$ substrate with two steps (same flake as Figure B.3(c)). The scale bar is the same in the three figures : 5 µm.

For our heterostructures dedicated for STM measurements, we are interested by large graphene flakes, to have a maximum of surface to explore with the tip, and so we also need larger hBN flakes to place the graphene above. If atomically flat hBN flakes are our main interest, devices where graphene covered several steps in the hBN were also made to eventually study the influence of the hBN thickness on the physical properties on graphene (for instance concerning substrate screening). Indeed, since the measurements in STM are local, it is possible to combine using the same device different physical systems (for instance graphene on hBN flakes of decreasing thickness) that can be studied independently by tunneling spectroscopy.

[1] Due to the important roughness of the SiO_2 substrate, it is most of the time impossible to observe the atomic thickness of graphene.

B.2 Van der Waals stacking

Once both graphene and hBN flakes have been selected, the next step is to stack them on the chosen substrate. We use a transfer microscope that allows us to pick-up the flakes from the substrate they were exfoliated on, using the sticky polymer PolyPropylene Carbonate (PPC). This stacking process relies on the van der Waals interactions, namely, the first flake will be picked-up by the PPC since the van der Waals interactions with this sticky polymer exceed those with the SiO_2 substrate, and the same goes on with the next flakes that develop strong van der Waals interactions with the previous picked-up flake. The resulting stack is therefore known as a van der Waals heterostructure [291]. Although most graphene-based heterostructures consist of graphene encapsulated between two hBN flakes, e.g. for transport measurements, we here limit the stack to two flakes, hBN as the first one and then graphene, since the graphene flake must be accessible by the STM tip for tunneling measurements.

B.2.a Stamp preparation

We use a stamp of PPC to pick-up the different flakes one atop the other. The stamp is prepared on a glass slide where a droplet of transparent PDMS (PolyDiMethylSiloxane) was deposited and left to dry with the glass slide upside down, so that gravity shaped the droplet in a form of a dome. A film of PPC is spin-coated on a silicon chip[2] and is then transferred on a Scotch tape, where a hole has previously been cut, by sticking the tape on the chip and then peeling it off. This tape is finally stuck on the PDMS droplet, such that the hole in the tape is aligned with the apex of the droplet. The PPC film, which now lies between the PDMS and the tape, becomes accessible through the hole at the apex of the PDMS dome (see Figure B.5), and this is where the pick-up of the flakes will be done.

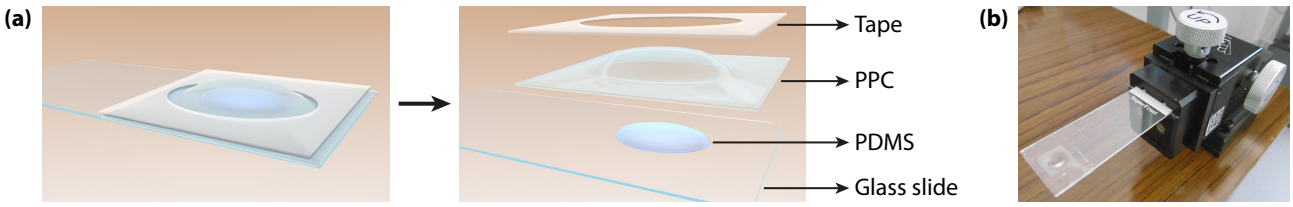

Figure B.5: Stamp used for the stacking. (a) On a glass slide, a transparent droplet of PDMS has been deposit and hardened in the shape of a dome. On top of it, a film of PPC is stuck by a transparent tape, with a hole above the apex of the PDMS droplet, to the glass slide. **(b)** Stamp in the micromanipulator.

B.2.b Transfer setup

The transfer setup is comprised of an optical microscope and a stage that can move in the three directions of space using piezoelectric motors (see Figure B.6). The substrate on which the flake we want to pick-up lies is put on the piezoelectric stage while the stamp of PPC is mounted on a micromanipulator that also allows displacement in the three directions as well. The substrate and the stamp can therefore both be moved in the three directions of space, independently. A second piezoelectric platform enables the rotation of the stage to precisely control the relative orientation of the flakes. Finally, the stage lies on a hotplate whose temperature is accurately adjusted in steps of 0.1 °C and can reach a maximum temperature of 180 °C. The sample is stuck to the stage with a vacuum pump during all the pick-up step.

[2]Solution of PPC prepared in anisole, in a ratio of 6 g of PPC for 40 mL of anisole. The solution is stored on a hotplate at 50 °C with stirring. Spin-coating parameters : 3750 rpm for 60 seconds at 2000 rpm/s. Backing : 90 °C for 2 minutes.

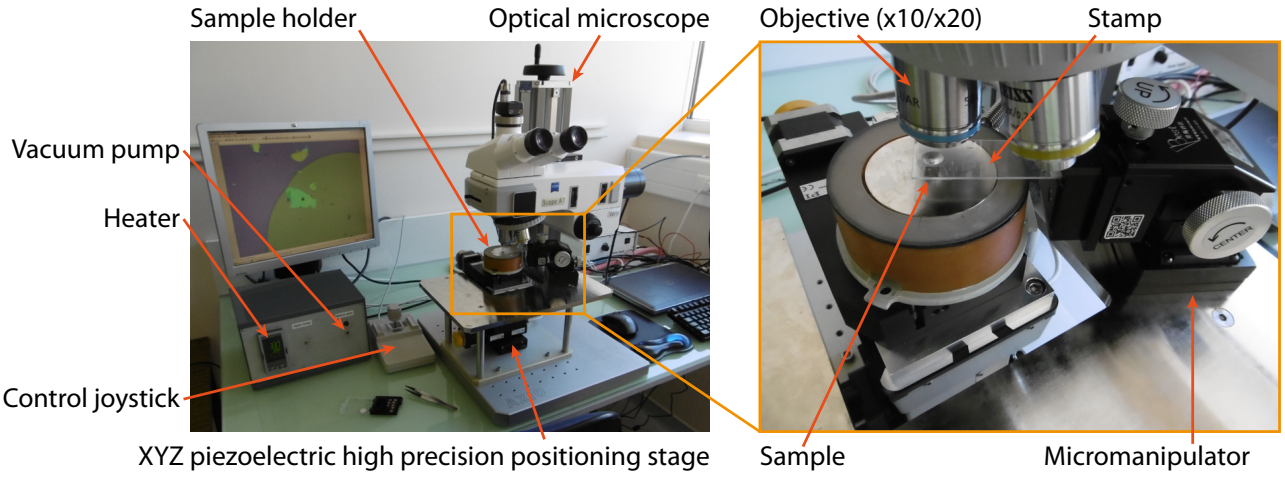

Figure B.6: Transfer setup for the fabrication of graphene heterostructures. The sample with the flake to pick up is placed on a positioning stage which moves in the three directions (controllable by a joystick). The sample is stuck using a vacuum pump and can be heated. The stamp is placed in a micromanipulator which also moves in the three directions.

B.2.c Stack fabrication

The sample with the hBN flake is put on the stage while the stamp of PPC is mounted upside down in the micromanipulator, such that the sample is observable with the optical microscope through the stamp. We heat the stage to 38 °C, temperature where the PPC becomes sticky. We start by putting the apex of the stamp to the focus, and then move up the sample just below the focus. We next place the targeted flake to about 50 µm of the apex : it is indeed much easier to control how the polymer expands and wets the sample surface after it has already contacted it, thanks to its thermal dilatation. After realizing the contact by moving the sample up, we precisely moves up again so that the PPC expands and starts to touch the flake. Increasing the temperature allows the PPC to wet more slowly the sample and we keep increasing, typically up to 50 °C, until the hBN flake is completely covered by PPC. We consequently turn down the heater back to 38 °C to cool down the PPC, which therefore starts to contract. Moving down the sample a little will make the PPC contract even more, which might favor the pick-up. Once cooled down, we slowly move down the chip until the PPC film starts to lift off, and at once quickly move the stamp and the sample apart. The hBN flake remains stuck to the PPC and is picked up with the stamp.

The next step is the pick-up of the graphene flake. Much of the process is identical to the pick-up of the hBN flake. However the key point is the alignment of the graphene flake with the hBN flake which lies on the stamp. The piezoelectric platforms, one for translation and the second for rotation, allow to precisely place the graphene flake below the hBN flake before stamp and substrate are brought in contact. We heat up the chip and hence the PPC to bring in contact both hBN and graphene flakes. Once the flow of the PPC covers the graphene, we quickly move down slightly the sample to contract the PPC film and prevent it from expanded further (we do not want the hBN flake on the stamp to fully contact the chip[3]). When the substrate is cooled down, we quickly separate the stamp from the sample and the graphene flake is picked up on the hBN flake, forming the hBN/graphene (BNGr) stack.

[3]One major problem is that due to van der Waals interactions, it is also possible, when we move apart the sample and the stamp, that the hBN flake remains stuck on the graphene flake and its SiO_2 substrate, rather than the graphene is picked up on the hBN on the stamp. To prevent this outcome, we avoid the hBN of the stamp to fully contact the chip with the graphene flake.

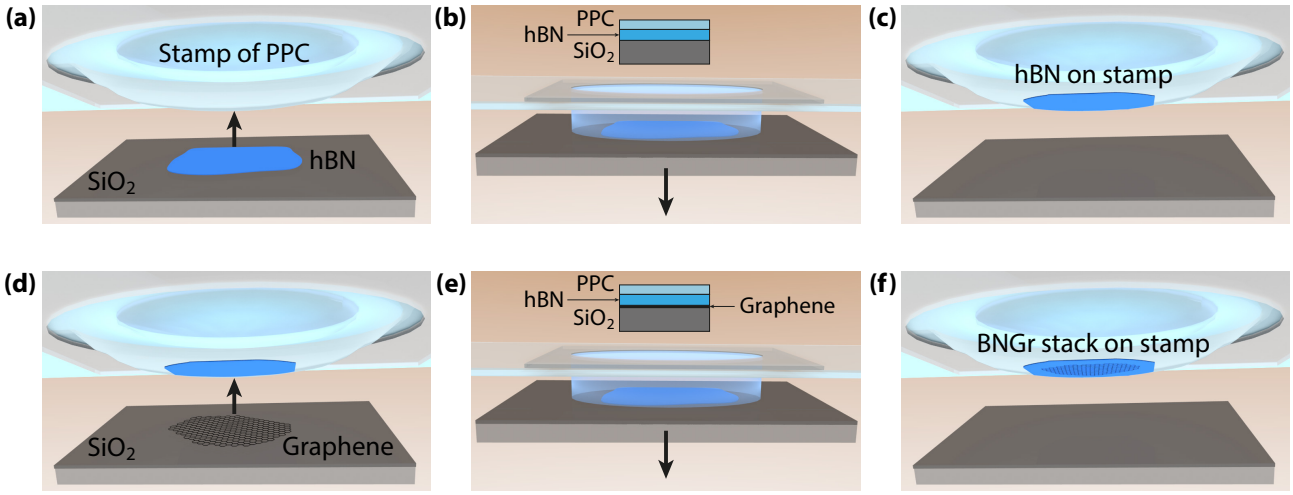

Figure B.7: Stacking process. The substrate with the hBN flake is brought to contact with the stamp of PPC (a). By increasing the temperature of the substrate, we control the dilatation of the PPC until it covers all the hBN flake (b), we then cool down the substrate and move it down to break the contact. The hBN flake is consequently picked up by the PPC stamp (c). We repeat the same process with the graphene flake. Before contacting the substrate with graphene and the stamp with the hBN flake, both flakes are precisely aligned, one above the other (d). Following the contact, the temperature is increased until all the graphene is recovered by the hBN flake (e), after what we cool down and break the contact. Graphene is picked up by the hBN flake, and the stack now lies on the stamp of PPC (f).

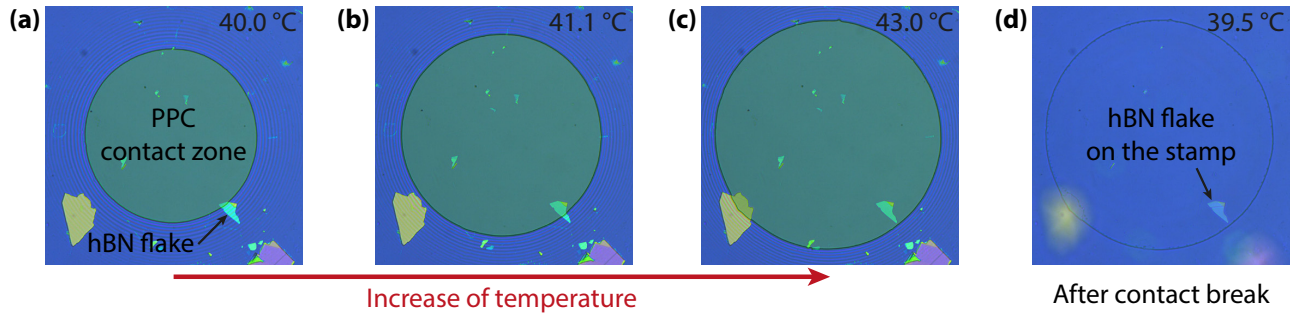

Figure B.8: Pick-up of the hBN flake. The chip with the flake is brought to contact with the stamp of PPC, creating a contact zone near the flake (a). Heating the substrate makes the PPC dilate and expand more toward the flake (b) until the PPC recovers the flake completely (c). After cooling down, the contact is broken by moving down the chip, and the hBN flake is picked up on the stamp (d).

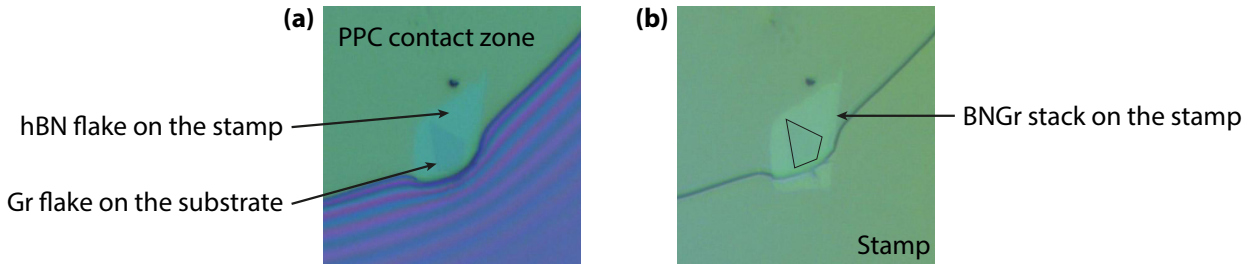

Figure B.9: Pick-up of the graphene flake. The stamp with the hBN flake is positioned above the chip with graphene by precisely aligning both flakes. The substrate is then brought to contact with the stamp and the temperature is increased until the graphene flake is completely covered, while avoiding complete contact for the hBN flake (a). After cooling down, the contact is broken by moving down the substrate, and the graphene flake is picked up by the hBN flake on the stamp, creating the BNGr stack (b).

B.3 Stack deposition on the substrate

With the BNGr stack on the stamp, we now have to deposit it on its substrate : either highly doped Si with a 285 nm layer of SiO_2 atop or $SrTiO_3$[4]. We developed two different methods.

Deposition of the PPC film directly on the substrate This procedure was developed based on Ref. [293] and is described in Figure B.10. The Scotch tape with the PPC film on the sticky side is slowly peeled off the stamp, flipped, and deposited on the substrate, centering the hole in the tape. The sample is then heated on a hotplate. The PPC film starts to wet the substrate at 80 °C. After the wetting is done, we heat at 120 °C, temperature at which the tape stops being sticky and can therefore be removed from the sample. The PPC film breaks between the part that was stuck on the tape, which is removed, and the part that was in the hole in the tape, with the stack above it, that stays on the substrate. The BNGr stack consequently lies on the PPC film that now has to be removed from the substrate.

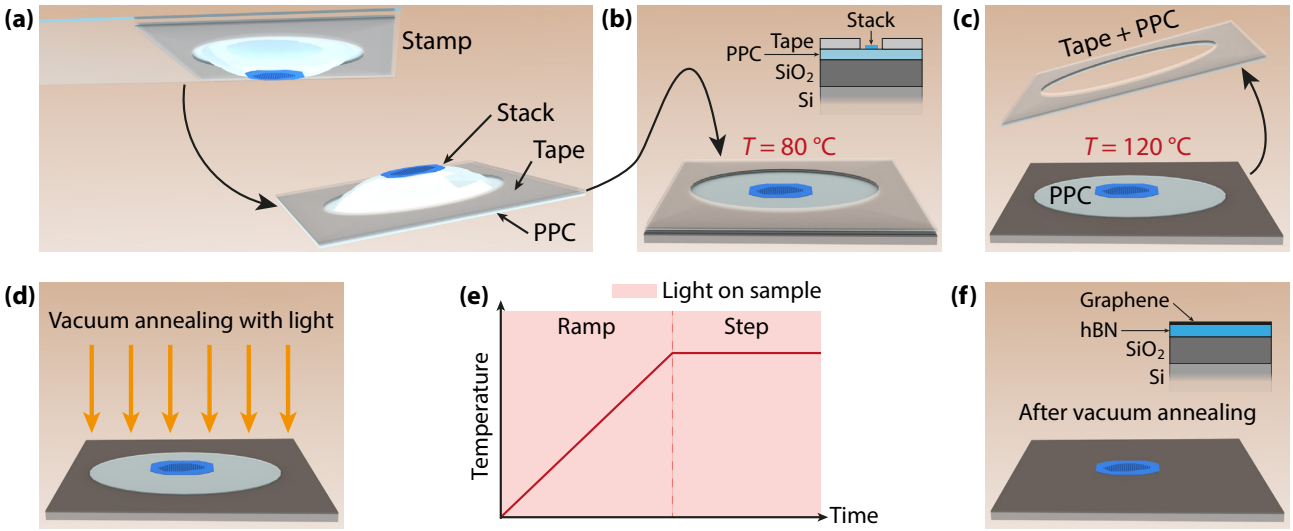

Figure B.10: Deposition of the stamp on the substrate. The tape is peeled off the stamp (a), with the PPC film on its sticky side, and then deposited on the substrate (b). Heating the substrate at 80 °C helps the PPC film to wet the surface. Once the wetting is done, we heat the substrate to 120 °C to remove the tape (with the piece of the PPC film that is stuck to it), leaving on the substrate only the piece of the PPC film that was in the hole of the tape, with the stack above it (c). To remove this PPC layer, a vacuum annealing with light is done (d), after which the stack henceforth lies on the substrate (f). The temperature profile of the annealing to remove the PPC film is shown in (e). Values for the different substrates are given in Table B.1. During all the annealing, the lamp is put on the sample.

The removal of the PPC film is done with a thermal annealing in a home-made oven (see Figure B.11). This oven is comprised of a vacuum chamber, reaching vacuum below 10^{-6} mbar, in which we put a block of copper as sample holder, and a halogen lamp used as a heater. A thermocouple whose sensor is put inside the piece of copper enables the regulation of temperature by a home-made software. A window in the vacuum chamber, above the copper holder, allows the halogen lamp to shine and heat the copper block. The lamp is located above the vacuum chamber, with its light beam focused on the window, and is free to move, such that we can move it wherever we want on the copper holder, for instance on the sample or away from it. For this step, the sample is placed on the copper holder directly under the lamp. While heating the

[4] $SrTiO_3$ substrates are beforehand etched 30 s in buffered HF acid [292] to obtain atomically flat surfaces.

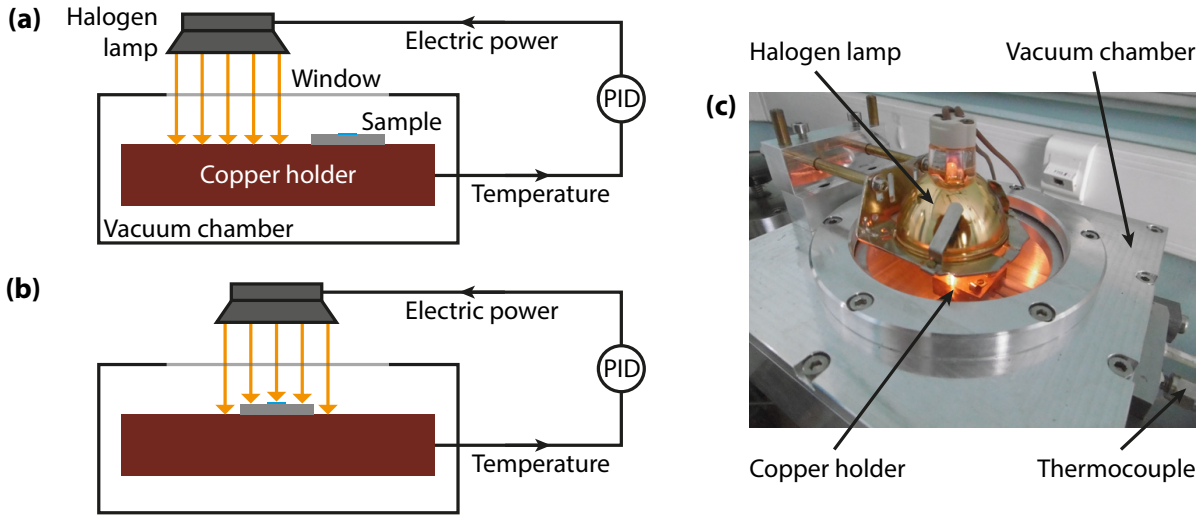

Figure B.11: Vacuum annealing oven. **(a)** *Annealing* mode : the sample is put on the copper holder away from the light beam. The temperature of the sample is measurable and regulated. **(b)** *Annealing with light* mode : the sample is put directly below the light beam so that light helps with the cracking of the polymer residues. The effective temperature of the sample is unknown and probably well above the regulated temperature of the copper holder. **(c)** Home-made oven for the vacuum annealing.

Substrate	Ramp of temperature	Lamp electric power	Step of temperature	Step time
SiO_2	4500 °C/h	110 W	350 °C	30 min
$SrTiO_3$	750 °C/h	52 W	350 °C	30 min

Table B.1: Annealing recipes to remove the PPC film and deposit the stack on the substrate. The lamp electric power is here the power received by the lamp to heat the sample during the ramp of temperature.

copper holder, the intense light beam also helps to crack the polymer chains of the PPC. The conjugated action of temperature[5] and light therefore completely removes the PPC film (see Table B.1 for recipes for SiO_2 and $SrTiO_3$ [6]). The stack consequently drops off on the substrate.

However odd things can quickly happen with this method. To be effective and complete, the evaporation of the PPC must be done at high temperature and under intense light, nevertheless it becomes uncontrollable since the effective temperature of the sample can not be known and probably reaches several hundreds of degrees above the temperature setpoint. Three major flaws can occur - see Figure B.12(c) :

- Some PPC residues - burnt polymer chains - can redeposit on the stack, and possibly on the graphene flake. After the annealing, those residues could not be removed by any tested solvents nor new annealing. As a result, graphene is severely polluted and unusable for STM measurements.

- Some PPC residues can also remain trapped below the stack when it lands on the substrate, and can not be removed afterward. These residues give very high topography (smoothed by the thickness of the stack) and represent potential threats for the STM tip.

[5] even if the effective temperature of the sample must be way higher due to the intensive light and thus remains unknown in this step.

[6] $SrTiO_3$ undergoes a phase transition during a vacuum annealing by doping with oxygen vacancies at high temperature, which limits the output power of the lamp and therefore the effectiveness of the annealing.

- Last, the evaporation of the PPC film can be so violent that the stack may be subjected to intense constraints that can tear apart the hBN flake and fold it, destroying the stack. The graphene flake can also be torn apart and folded, but as long as it becomes clean after the annealing, the stack remains interesting for STM. There is then a compromise between increasing the temperature of the annealing to efficiently remove PPC and limiting it to prevent damages to the stack.

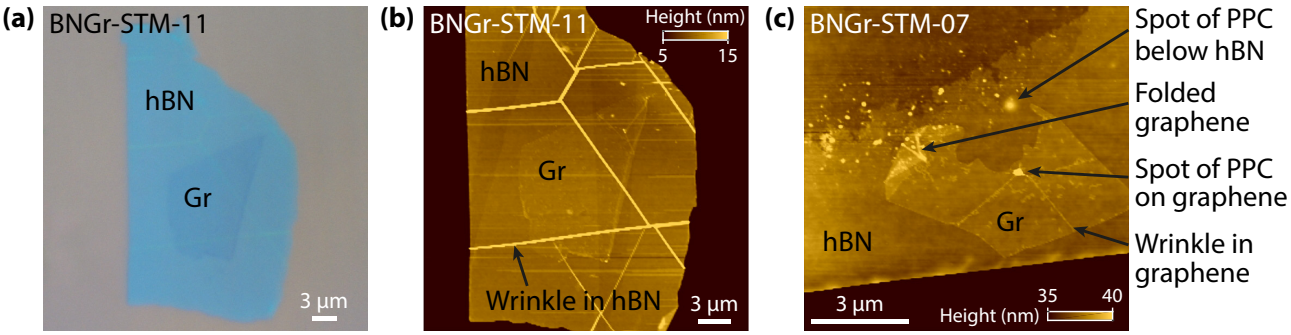

Figure B.12: BNGr stacks on SiO_2 after burning the PPC film. (a,b) Stack observed with an optical microscope (a) and with an AFM (b). The hBN flake is thin enough to see the graphene with the eye. The AFM reveals wrinkles in the hBN flake due to the annealing, but graphene is mostly clean. **(c)** Another stack observed with AFM, which unveils many defects, the main one being that the (originally rectangular) graphene flake has been torn apart and folded during the annealing. Many spots of PPC are also observable. The scale bar is the same in the three figures : 3 µm.

Nevertheless, in the best cases where none of those problems occurred, the stacks after annealing were clean as checked by AFM, see Figure B.12(b). A first series of samples on SiO_2 substrates was done using this process, followed by a series of samples on $SrTiO_3$ substrates. After this step, samples are ready for patterning.

Deposition of the flipped PPC film on a second stamp A second method has been developed, based on Ref. [294], to overcome these flaws by avoiding the annealing step. The Scotch tape with the PPC film and the stack upwards is also peeled off the stamp but this time the tape is flipped and deposited on the PDMS droplet of a second stamp, with the stack downwards. Heating the stamp up to 120 °C helps the PPC film to wet the PDMS droplet, whereas the tape does not stick anymore and can then be safely withdrawn. Therefore, the stack lies between the PDMS droplet and the PPC film. We remove the PPC film using acetone to expose the flipped stack that lies on the PDMS. Using the transfer setup, we put to contact the second stamp with the chosen substrate and increase the temperature so that the PDMS wets the substrate beyond the stack. Finally, we use the micromanipulator to move up the stamp very slowly until the stack is deposited on the substrate.

The main advantages of this method is that the stack can be deposited on an already pre-patterned chip, leaving only the graphene contacting step to do. However, it also presents some flaws :

- The step where we put the tape with the PPC film on the second stamp can be dangerous for the stack. Constraints may tear apart the PPC film before it completely wet the PDMS droplet and the stack might be torn and folded. In our stacks, if the hBN flake usually comes out unscathed, the graphene flake often comes out torn in several pieces.
- The graphene flake touches the PDMS, which may leave residues that need to be removed in a future annealing.

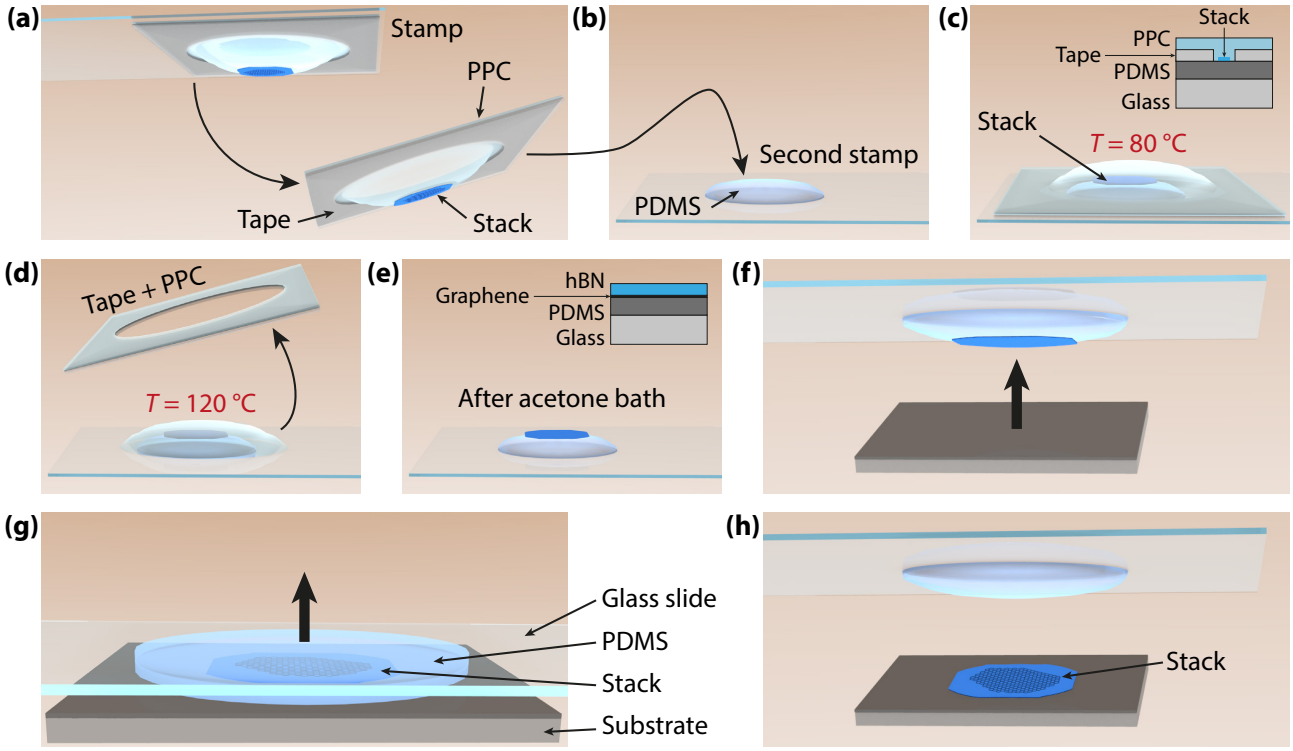

Figure B.13: Deposition of the flipped stack on the substrate. The tape is peeled off the stamp (a) and deposited on a second stamp (b), with the tape toward the glass slide, such that the PPC film is the topmost layer and the stack lies between the PPC film and the PDMS droplet. Heating the glass slide to 80 °C allows the PPC film to wet the PDMS droplet (c). Afterward, we heat the glass slide to 120 °C to remove the tape, leaving only the part of the PPC film that was located in the hole in the tape with the stack below (d). The stamp is then put in acetone to dissolve the PPC layer, which exposes the stack (e). Note that the stack is now reversed on the second stamp, with the graphene between the hBN flake and the PDMS. The second stamp is used to deposit the reversed stack on the substrate. The contact is done by moving up the substrate (f), and the dilatation of the PDMS is controlled by the temperature. When the stack completely touches the substrate, the stamp is moved up slowly (g) and after the contact breaks, the stack lies on the substrate (h).

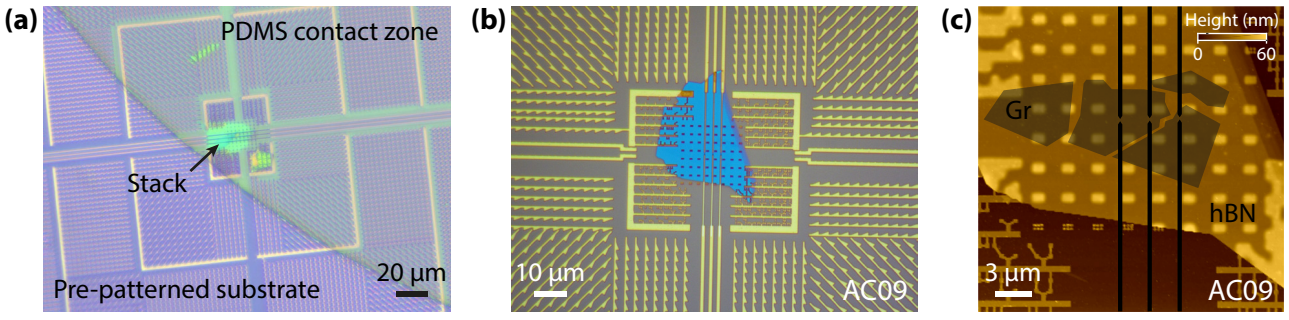

Figure B.14: BNGr stack deposition on a pre-patterned SiO_2 substrate. (a) Image corresponding to the step described in Figure B.13(g). The stack is precisely aligned with the targeted area on the pre-patterned substrate before contacting the PDMS stamp with the chip. Scale bar : 20 µm. **(b,c)** Stack observed with an optical microscope (b) and with an AFM (c). The stack has been precisely deposited on a pre-patterned substrate with a set of three buried split gates. Graphene is barely visible in AFM due to residues of PDMS (that will be removed in a latter step), but has been torn apart in several pieces during the transfer on the second stamp. The scale bar is 10 µm in (b) and 3 µm in (c).

A second series of samples on SiO_2 and $SrTiO_3$ was done using this process, with substrates where the guiding markerfield has already been patterned. Moreover, stacks on SiO_2 were precisely deposited on a set of pre-patterned buried split gates.

B.4 Device patterning

We describe in this section the different steps to pattern the device. These steps are done at the Nanofab clean room facility of Néel Institute. Every design was written by electron-beam lithography, etching steps were done using a Reactive Ion Etching (RIE) system and metallic depositions were done with a e-gun evaporator.

B.4.a E-beam lithography

Lithography is the main source of pollution for our devices since graphene is directly exposed to the resist that will systematically leave amounts of residues even after we dissolve it in acetone. We use PolyMethylMethAcrylate (PMMA) as resist[7], the PMMA presenting the advantage of being easily removed from the graphene surface with a thermal annealing. After the writing, exposed resist is developed using a mixture of MethylIsoButylKetone (MIBK) and IsoPropyl Alcohol (IPA) (ratio 1:3) for 1 minute.

E-beam lithography is more difficult with the insulating $SrTiO_3$ substrate since it does not drain the charges away during the exposure. The ensuing local accumulation of charges deflects the electron beam, and the written pattern is distorted and shifted. To avoid this, it is necessary to add a conductive layer above the PMMA one to drain the charges away. The first solution we used was to evaporate a layer of gold with a thickness of 5 nm atop the PMMA layer. After the writing, this gold layer was etched in a mixture solution of potassium iodide and iodine (KI,I_2), after what we could develop the PMMA layer. The second solution, more convenient, was to spin-coat a layer of conductive resist[8] above PMMA. This conductive layer was then dissolved in deionized water before the PMMA layer was developed.

B.4.b Alignment markers

Alignment markers are first patterned to allow very precise positioning of the next lithographies. Four sets of nine squares of 8 µm size, separated by 200 µm, are thus deposited in the four corners of the sample and will be used to locate precisely four given positions at each corner and realize focus.

B.4.c Split gates pre-patterning

In the second series of samples on SiO_2, the substrate was pre-patterned with a set of three buried split gates so that the quantum Hall edge channels in the graphene flake, placed above the split gates, under magnetic field, may be manipulated and reflected by Quantum Point Contacts (QPC). After the lithography and development of the split gates, an O_2 plasma is done during 15 seconds to remove resist residues. A CHF_3 plasma is then used for 90 seconds to etch 31 nm of the SiO_2 layer before we deposit a bilayer of Ti/Pd (5/27 nm). Titanium serves as an adhesion layer, and palladium is there used to obtain very flat metallic film, with a smaller grain size than gold (typically 10-20 nm for Pd and above 30 nm for Au).

[7] PMMA 950K (4% in ethyl lactate). Spin-coating parameters : 4000 rpm for 30 seconds at 4000 rpm/s. Backing : 180 °C for 5 minutes.

[8] Electra 92 (AR-PC 5090). Spin-coating parameters : 3500 rpm for 60 seconds at 3500 rpm/s. Backing : 90 °C for 2 minutes.

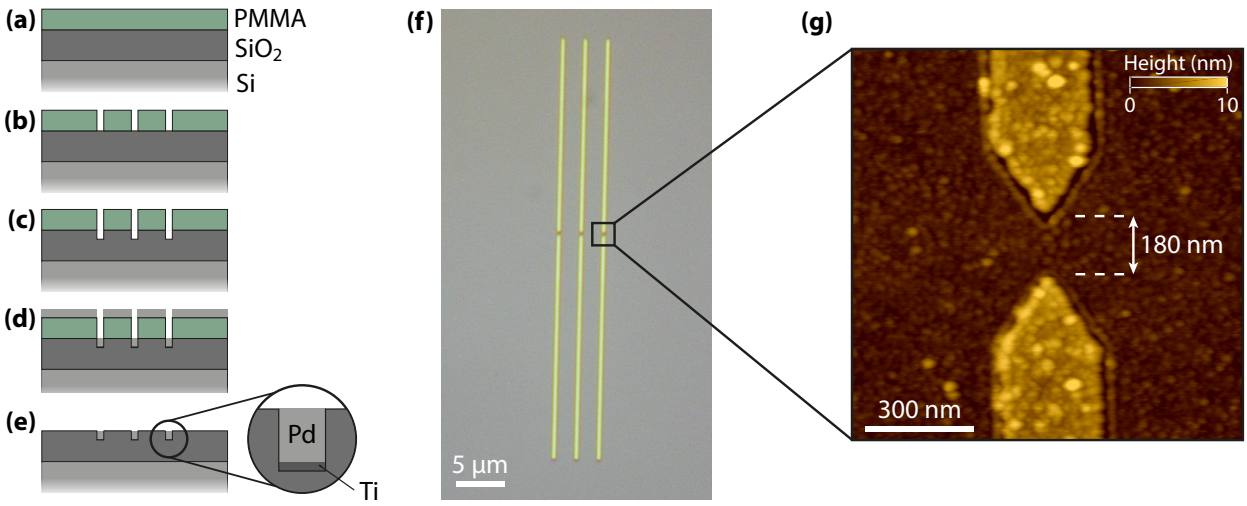

Figure B.15: Pre-patterning of buried split gates. (a-e) A layer of PMMA resist is spin-coated on the SiO_2 chip (a). After the e-beam exposure, the resist is developed (b). A first O_2 plasma removes resist residues, and a second CHF_3 plasma is used to etch the SiO_2 layer (c), immediately followed by the deposition of the bilayer Ti/Pd (d). The lift of the resist is done in acetone (e). **(f)** Optical image of a set of three buried split gates in SiO_2. Scale bar : 5 µm. **(g)** AFM image of a split gate, the observed gap of 180 nm is a little bit higher than the gap of 150 nm from the design. Scale bar : 300 nm.

B.4.d Guiding markerfield

The guiding markerfield is used to guide the STM tip toward the graphene device, from wherever the tip may land. It is patterned on the whole substrate and centred around the device. In order to minimize the number of steps and images needed to reach graphene, we want the code to be readable in one image. Since the full scanning view of our STM at 4 K is about $3 \times 3\,\mu m^2$, each code has to be separated from the next one by approximately 3 µm, which makes the guiding markerfield very dense.

Different codes are used depending on the distance from the device, from coarse to fine localization. The $5 \times 5\,mm^2$ sample surface is divided into 25 squares whose the sixteen closest[9] from the square containing the device are coded by a four-digit binary code, as shown in Figure B.16(g). The square containing the device is itself divided into eight concentric rings centered around the device, see Figure B.16(f). Each ring is coded by a second three-digit binary code alongside arrows pointing toward the device, as shown in Figure B.16(h,i). The final area surrounding the device is fully coded by a third four-digit binary code that allows precise localization of a $3 \times 3\,\mu m^2$ area, as shown in Figure B.16(h) in the center. Figure B.16(e) resumes the designs of the different binary codes. The guiding procedure using this markerfield and the different codes is explained in Chapter 4.4.1.

The whole markerfield is done in a single lithography. An O_2 plasma for 15 seconds is done to remove resist residues. The markerfield is consequently deposited with a bilayer Ti/Au (5/15 nm) for $SrTiO_3$ substrates and a trilayer Ti/Pt/Au (5/5/15 nm) for the SiO_2 substrates. The platinum layer is there used to prevent the diffusion of gold during later thermal annealing into the SiO_2 layer that might induce a short-circuit with the silicon back gate.

[9]The other squares are simply coded by vertical arrows pointing toward the middle of the sample.

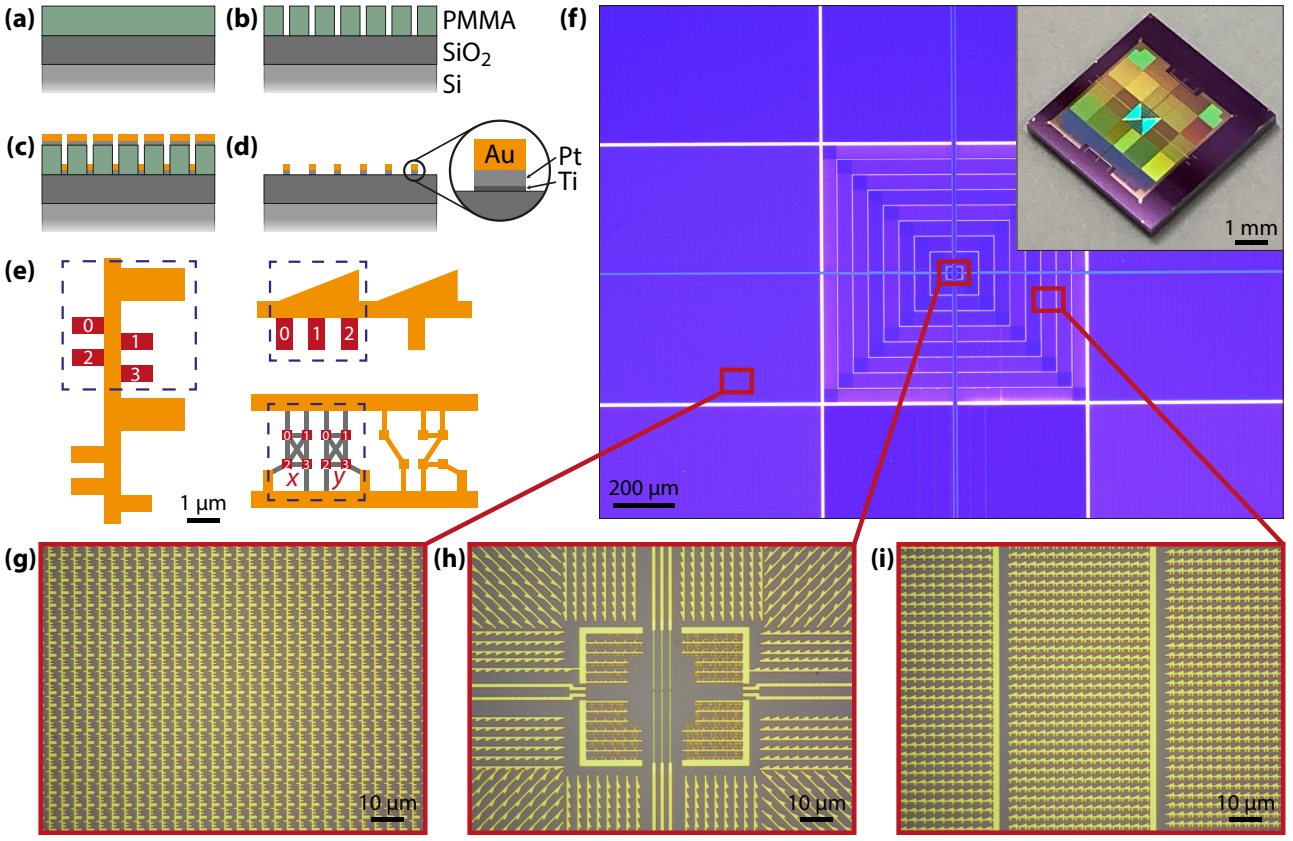

Figure B.16: Guiding markerfield. (a-d) A layer of PMMA resist is spin-coated on the SiO_2 substrate (a). After the e-beam exposure, the resist is developed (b). We then deposit a trilayer of Ti/Pt/Au (c) and use an acetone bath to remove the resist mask (d). The use of an ultrasonic bath is needed to completely lift the resist. **(e)** Schematics of the different codes used. Their architecture is shown in the blue dashed boxes, where the red parts constitute the binary code (the number of the digit is indicated) : 1 if the corresponding rectangle is present, 0 otherwise. Each code is chiral and allows unambiguous identification. (Left) Code for the different squares, for instance the marker below codes the square 13. (Upper right) Code for the different rings, for instance the marker on the right codes the ring 2. This marker is rotated, with the triangle pointing in the direction of graphene, as shown on (h) for the ring 0. (Lower right) Marker coding a $3 \times 3\ \mu m^2$ position in the final area around the device, which gives x and y coordinates, for instance the marker on the right codes the position (9;15). The digits of each group (for coordinate x and y) are connected by lines which gives a specific pattern for each value. **(f)** Optical image of the guiding markerfield centered around the device. Inset : chip as seen with the eye, each area with a different code diffracts the light differently, and so appears with a different color. **(g,i)** Optical images zooming on specific areas marked on (f). The graphene device will be located at the center of (h), where the buried split gates are.

B.4.e Graphene contacting

Last step is the contacting of the graphene flake. In the first series of samples, graphene is contacting by a huge gold contact which covers the whole sample[10], except graphene which is only contacted on one of its edges, making the graphene bulk and the other edges accessible by the STM tip. In the second series of samples (with the split gates), graphene is contacted with a two or four probes setup to enable transport measurements. The lithography pattern then

[10]The idea to have gold everywhere is to protect the STM tip during the guiding towards graphene. Indeed this layer of gold recovers any resist residues that might have polluted otherwise the tip, which therefore only touches (and sometimes picks up) gold, a conventional metal for STM tip.

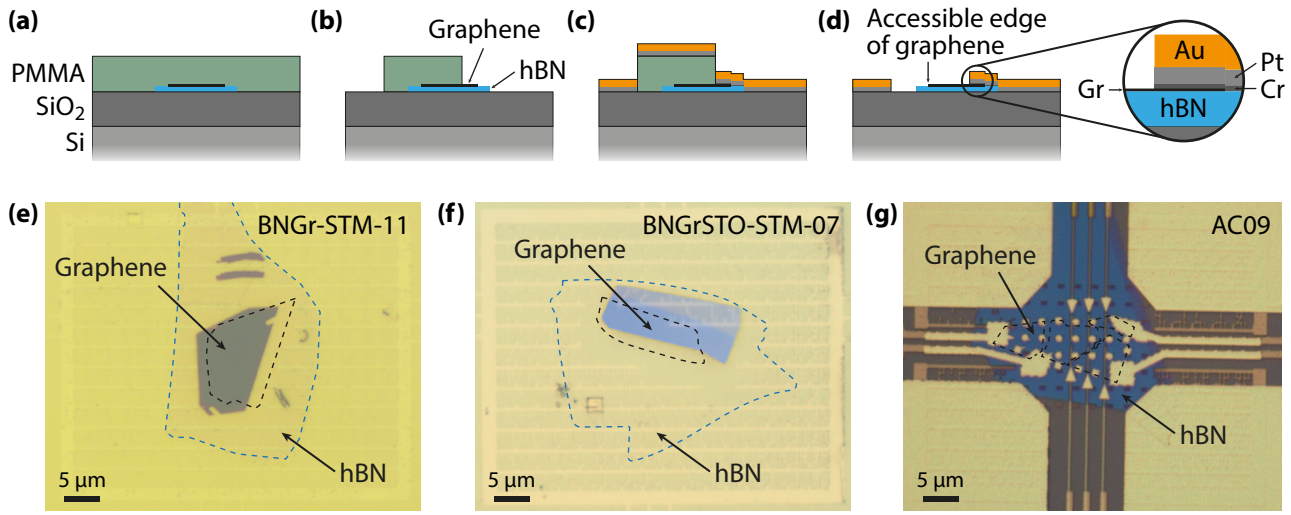

Figure B.17: Graphene contacting. (a-d) A layer of PMMA resist is spin-coated on the SiO_2 substrate (a). After the e-beam exposure, the resist is developed (b). We then deposit a trilayer of Cr/Pt/Au (c) and use an acetone bath to remove the resist mask (d). **(e)** Optical image of the stack BNGr-STM-11 on a SiO_2 substrate. Graphene is contacted by only one huge contact covering the whole substrate, except the bulk graphene and some of its edges that remain accessible by a STM tip. **(f)** Optical image of the stack BNGr-STO-STM-07 on a $SrTiO_3$ substrate. Graphene is contacted by the same kind of contact shown in (e). **(g)** Optical image of the stack AC09 on a SiO_2 substrate. Graphene is there contacted using a four-probe configuration (however the graphene flake itself was previously torn in four pieces). The four lines for the four probes, crossing the substrate horizontally, as well as the six lines of the split gates, crossing the substrate vertically, define four quadrants of the substrate that are covered by gold. The scale bar is the same for the three figures : 5 µm.

consists of the different contacts on graphene and the lines connecting them to pads locating on the opposite edges of the samples, as well as other lines connecting the split gates to other pads on the other two opposite edges of the samples, and four huge squares that cover the four quadrants of the sample defined by those lines. Metallic deposition for samples on SiO_2 substrate is done with a trilayer Cr/Pt/Au (5/15/30 nm). For samples on $SrTiO_3$ substrates, where the hBN flake is thin, a bilayer Cr/Au (5/25 nm) is deposited[11].

B.5 Graphene cleaning

After the patterning, the graphene flake comes out polluted by resist residues that need to be removed. We do a new vacuum thermal annealing to restore the graphene cleanliness. This step appears to be quite tricky since one can not simply increase the temperature to for instance 500 °C where polymer chains would crack and get away from graphene. Such temperature would melt gold thin films and lines. Moreover, gold would diffuse in the SiO_2 layer and short circuit the silicon back gate. That effect is mitigated by the presence of the platinum layer that prevents the diffusion of the gold layer above. On the other hand, the phase transition of $SrTiO_3$ by doping with oxygen vacancies happens at temperatures beyond those at which the gold thin films start to melt and therefore is not a problem here. The duration of the annealing is another important parameter, especially for the problem of gold diffusion. After the annealing, the cleanliness of the graphene flake is checked by AFM. We present in Table B.2 the final

[11] A final step for $SrTiO_3$ substrates consists of depositing a back gate on the back of the chip with a bilayer Ti/Au (20/80 nm).

recipes for both substrates that happen to give the best outcome with our home-made oven. For both substrates, the sample is firstly put on the piece of copper away from the light beam, that heats another part of the copper piece. For SiO_2 substrate, the sample is eventually put under the light beam after the heating, when the temperature is stabilized, during the whole step of temperature[12].

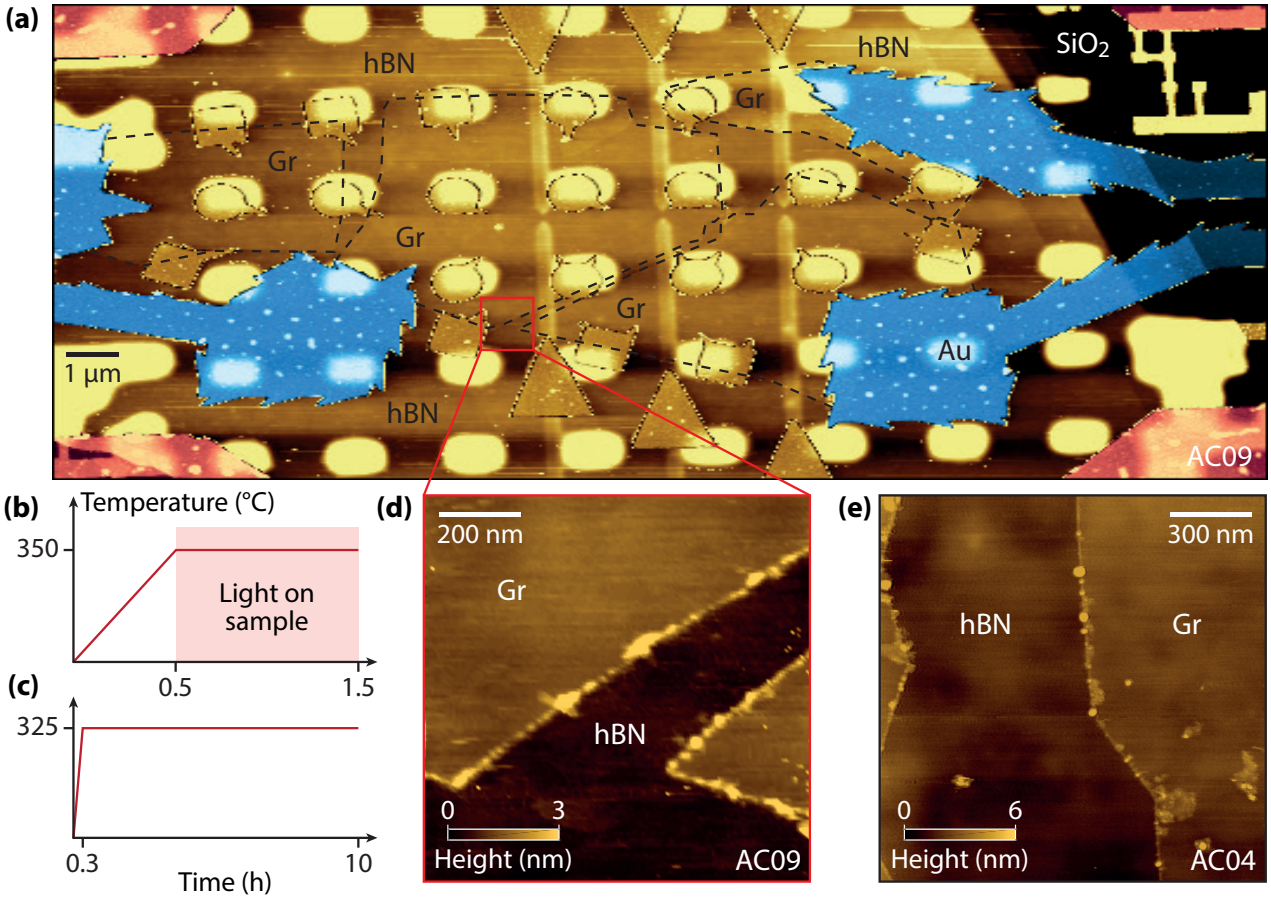

Figure B.18: Graphene cleaning. **(a)** AFM image of the sample AC09 after annealing. The four graphene flakes are mostly cleaned. The four contacts which are used to bias the flakes are colored in blue. Scale bar : 2 µm. **(b)** Annealing profile for samples on SiO_2 : once the temperature has reached its steady value, the sample is put under the light beam. **(c)** Annealing profile for samples on $SrTiO_3$. **(d,e)** AFM images of graphene/hBN interfaces on two different devices, AC09 in (d), AC04 in (e), : if the graphene bulk is cleaned, some residues are still visible on the edges. Scale bar for both images : 300 nm.

Substrate	Ramp of temperature	Step of temperature	Lamp electric power	Step time
SiO_2	600 °C/h	350 °C	25 W	1 hour
$SrTiO_3$	1000 °C/h	325 °C	-	10 hours

Table B.2: Annealing recipes to remove resist residues and clean graphene surface. For SiO_2, the lamp electric power is here the power received by the lamp to keep the temperature steady during the step of temperature.

[12]Note the difference with the annealing to remove the PPC film. For the PPC removing step, the sample is put under the light from the beginning, and therefore receives much power from the light during the temperature ramp when the light shines the most to heat the copper holder. For the graphene cleaning step, the sample is put under the light after the temperature ramp, and thus only receives from the light the power needed to keep the temperature of the copper holder steady.

After the annealing has been proven successful by AFM, a final vacuum annealing at 150 °C for 1 hour is done to remove water from the graphene surface. The sample is then immediately glued on the sample holder with silver paste (for the electrical contact with the back gate), bonded, and plugged in the STM.

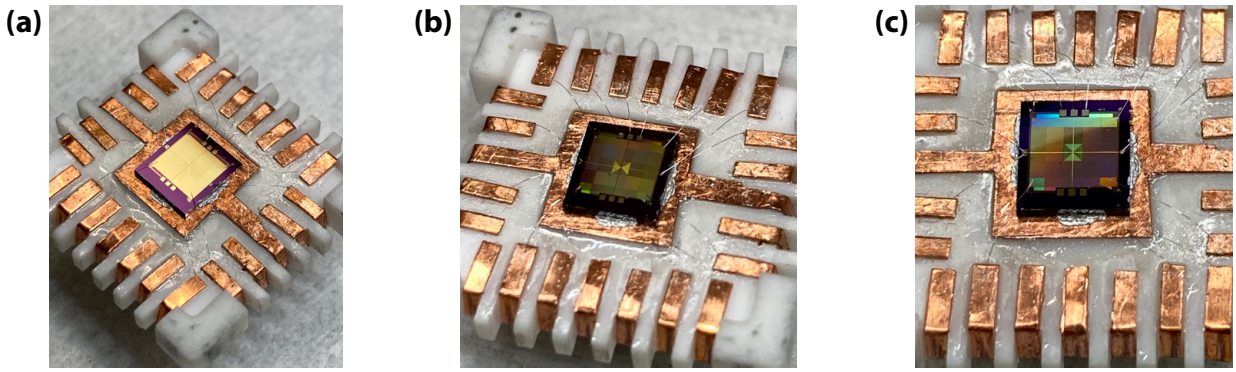

Figure B.19: Sample ready for STM. Three images from different points of view of the $5 \times 5\,\mathrm{mm}^2$ sample AC04 once glued and bonded on the sample holder. The graphene device lies in the center of the chip, which is well visible on the image on the right.

B.6 Device gallery

We present in this section the twelve samples that eventually arrived at the end of the fabrication process, and which are therefore ready for STM measurements (though only five of them were actually measured during this thesis). Each figure shows two optical images of the devices, the bright-field one on the left and the dark-field one on the right. The dashed blue lines outline the hBN flakes (when they are hidden by the gold layer above), while the black or white dashed lines outline the graphene flakes. For every image, the scale bar is 10 µm.

Devices BNGr-STM-07 and BNGr-STM-11 Graphene on hBN on SiO_2 substrate, where graphene flakes are contacted by only one contact for bias.

Devices BNGrSTO-STM-07 and BNGrSTO-STM-08 Graphene on thin hBN on $SrTiO_3$ substrate. The graphene flakes are contacted by only one contact for bias.

Devices AC01, AC03, AC04, AC09 and AC10 Graphene on hBN on SiO_2 substrate, where graphene flakes are contacted with a two- or four-probes configuration for bias and transport measurements. Buried split gates lie below the devices. For AC04 and AC09, it appeared that the graphene was torn apart in several pieces during the deposition of the stacks on the substrate.

Devices AC19, AC23 and AC24 Graphene on thin hBN on $SrTiO_3$ substrate. AC19 and AC23 are contacted respectively with a four- and six-probes configuration for bias and transport measurements, with one side gate. AC24 is contacted by only one contact for bias.

The results presented in this thesis come mostly from devices BNGrSTO-STM-07, AC04 and AC23 (mainly), as well as BNGrSTO-STM-08 and AC24.

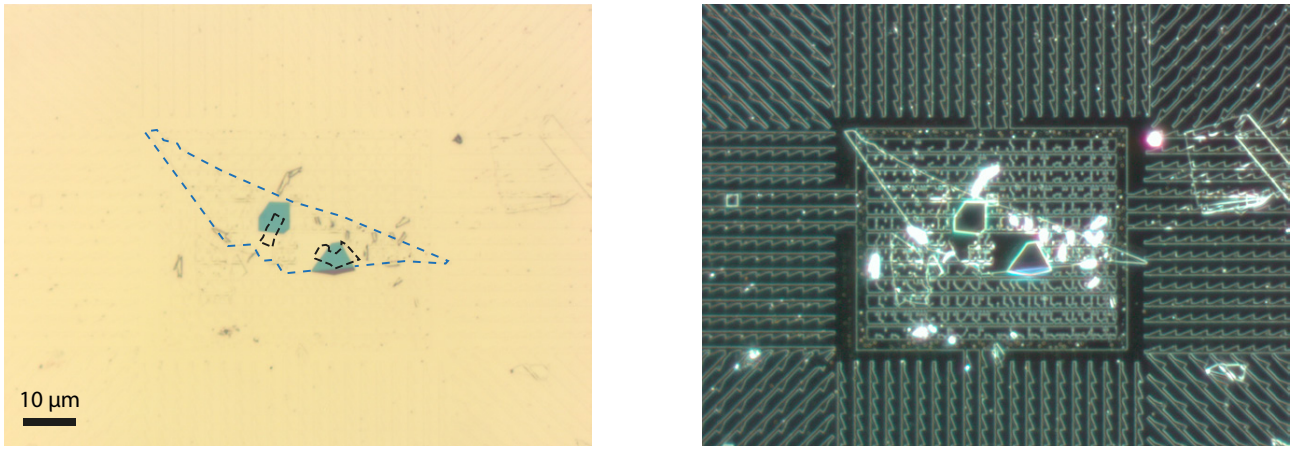

Figure B.20: Device BNGr-STM-07.

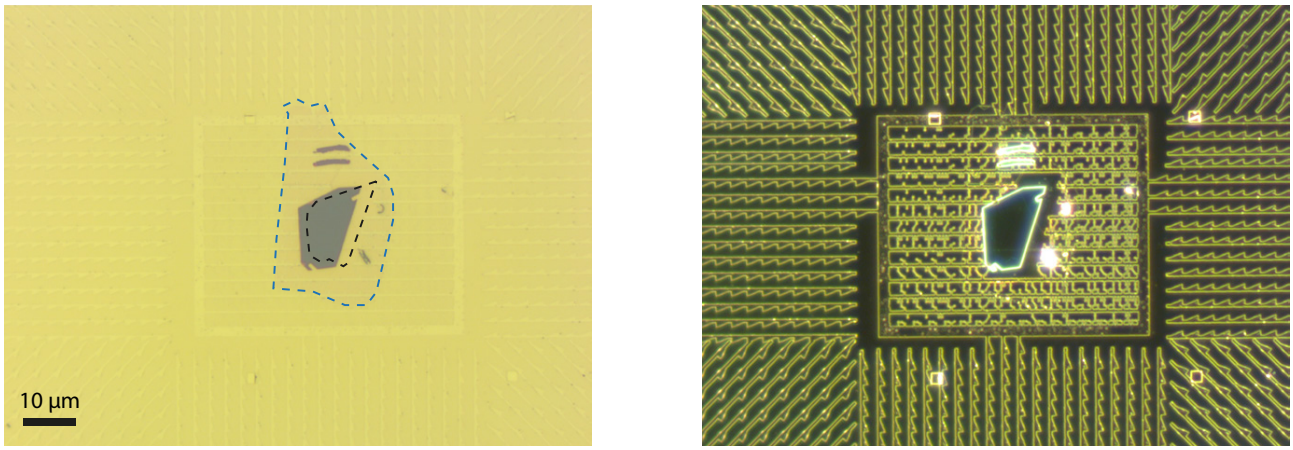

Figure B.21: Device BNGr-STM-11.

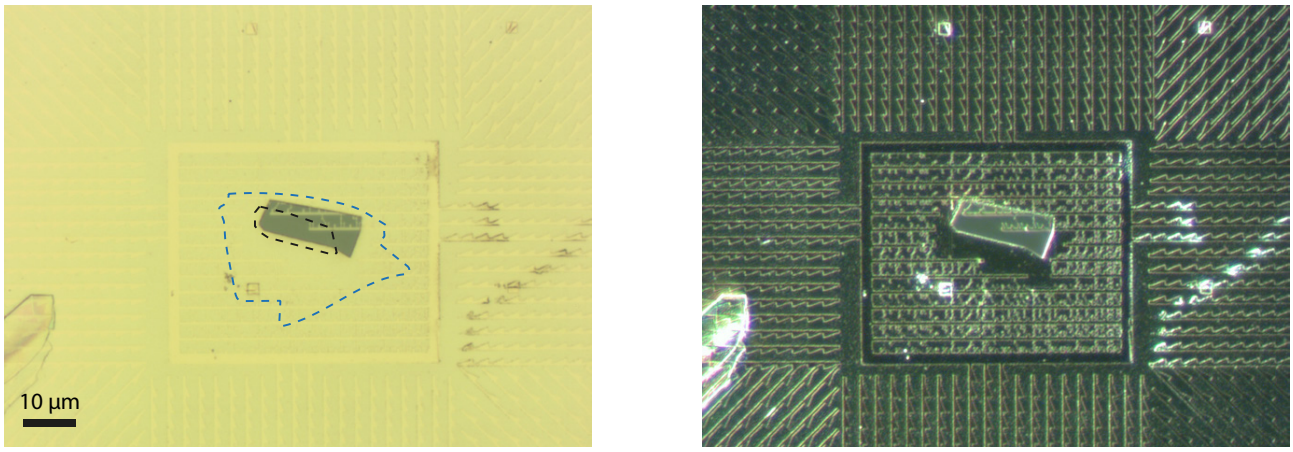

Figure B.22: Device BNGrSTO-STM-07.

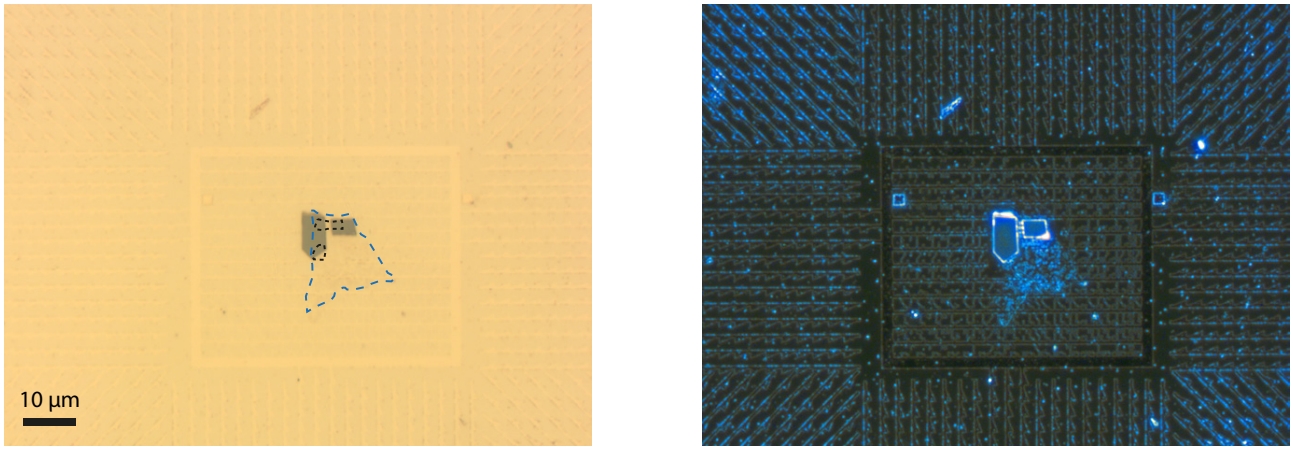

Figure B.23: Device BNGrSTO-STM-08.

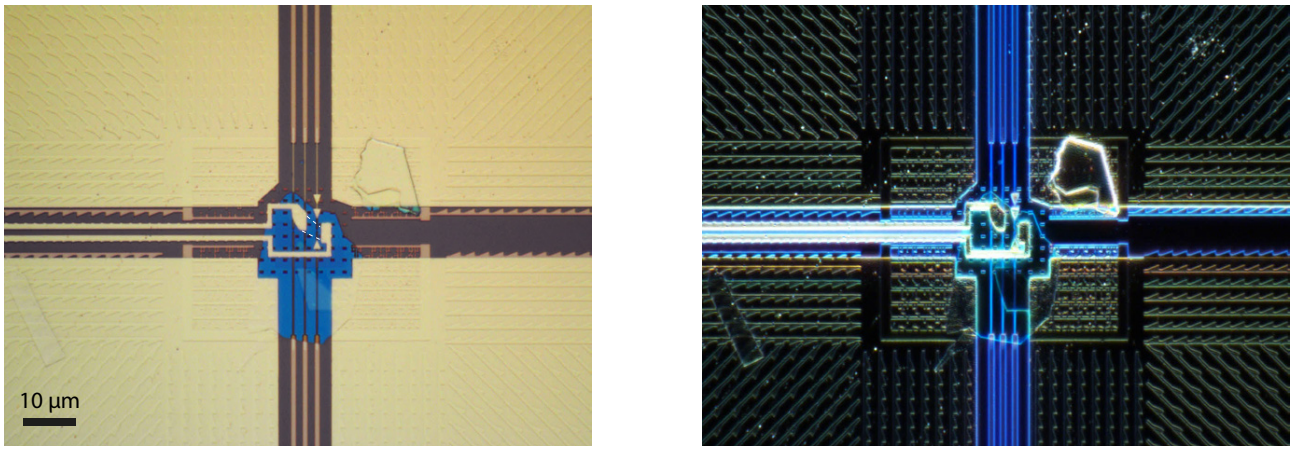

Figure B.24: Device AC01.

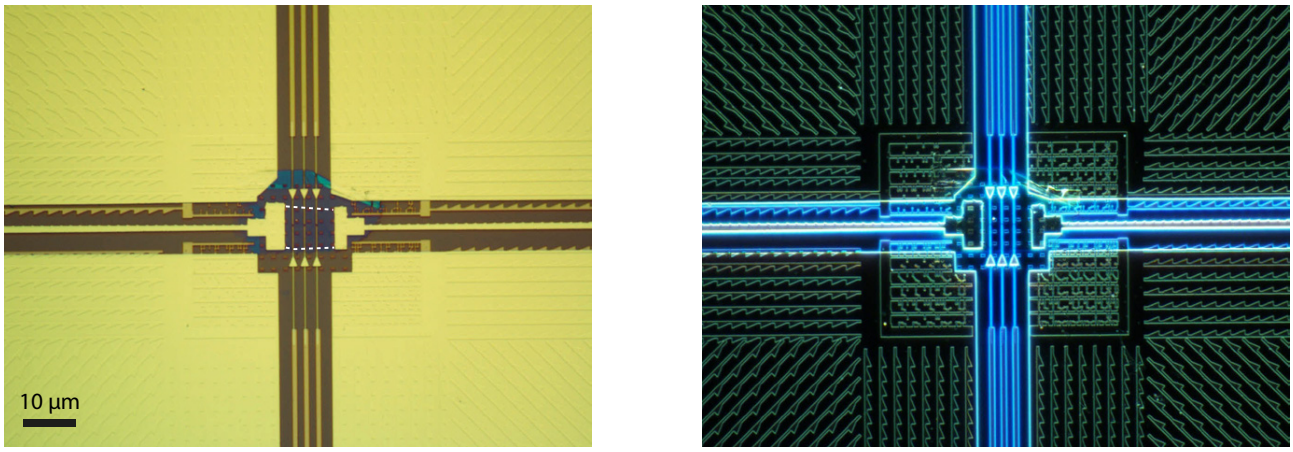

Figure B.25: Device AC03.

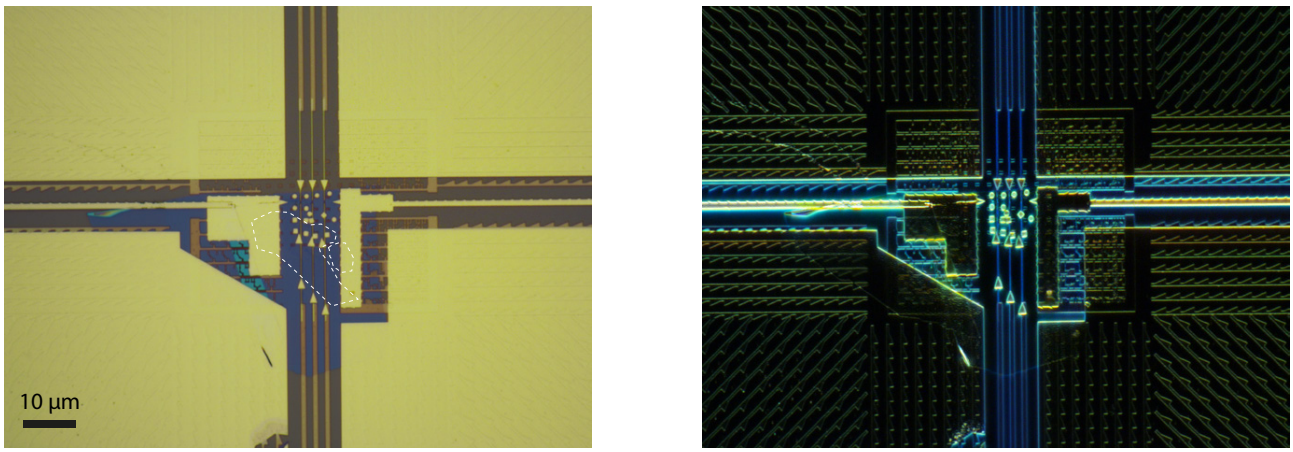

Figure B.26: Device AC04.

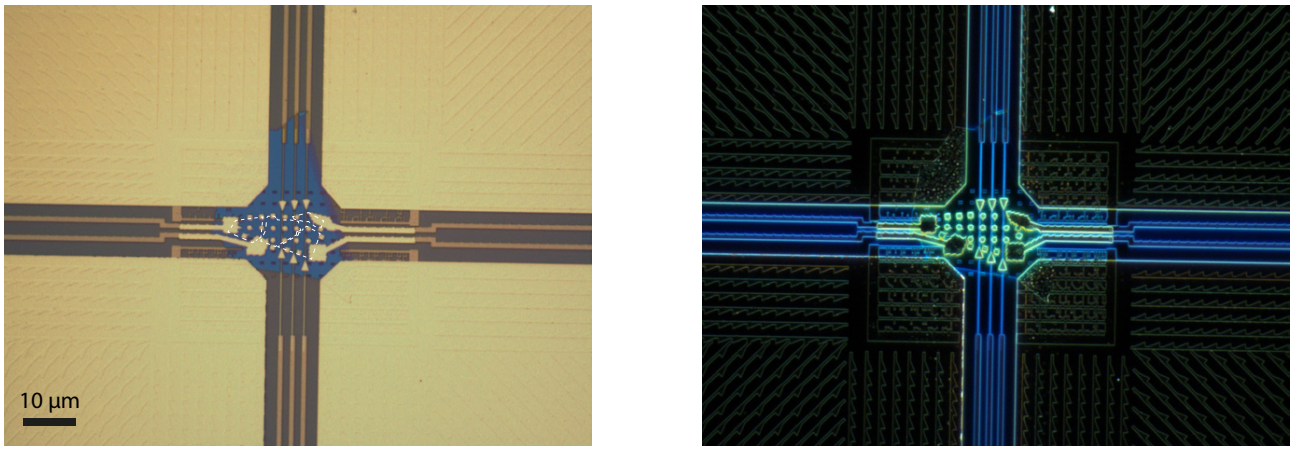

Figure B.27: Device AC09.

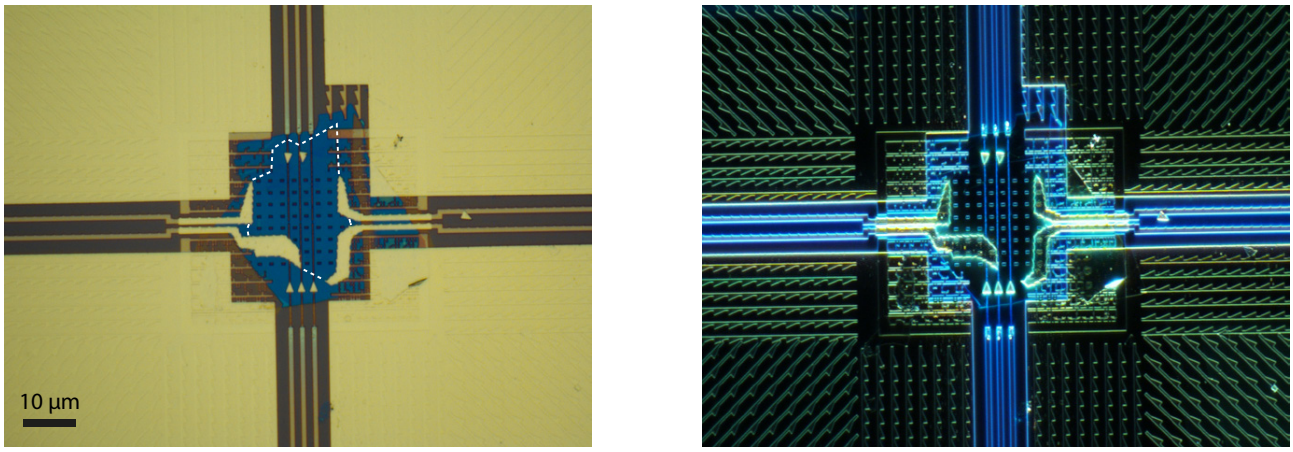

Figure B.28: Device AC10.

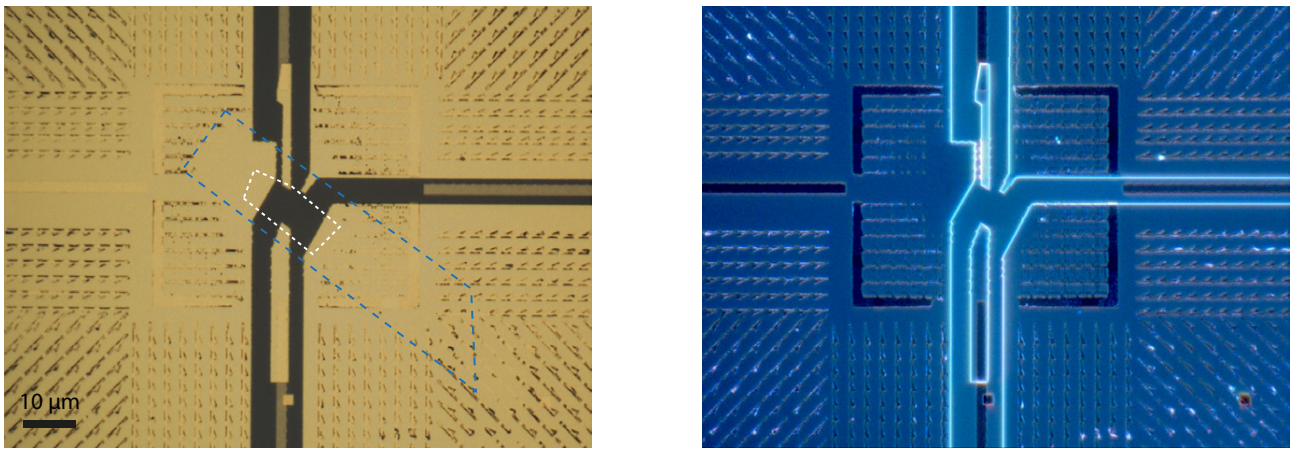

Figure B.29: Device AC19.

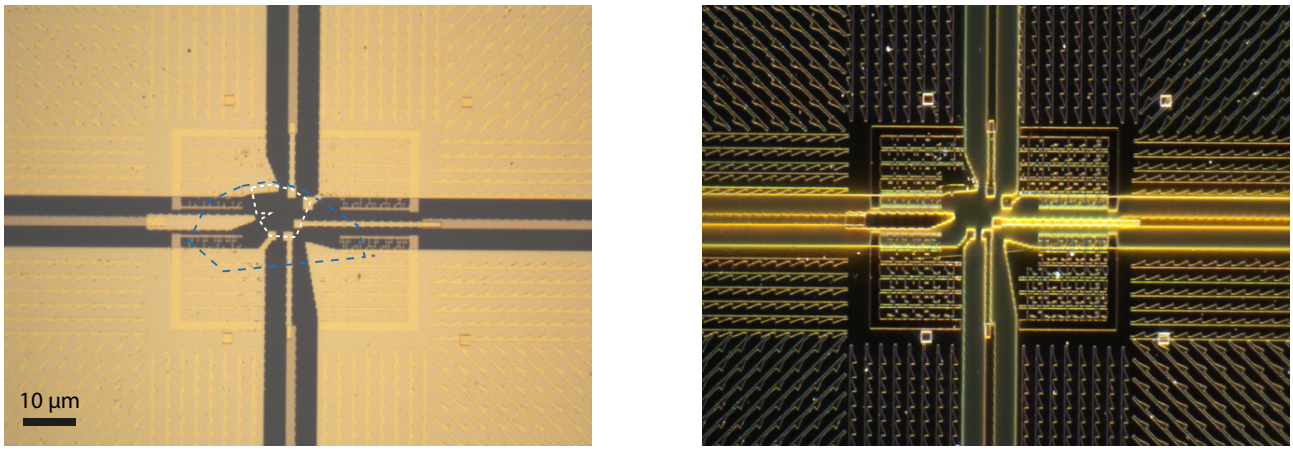

Figure B.30: Device AC23.

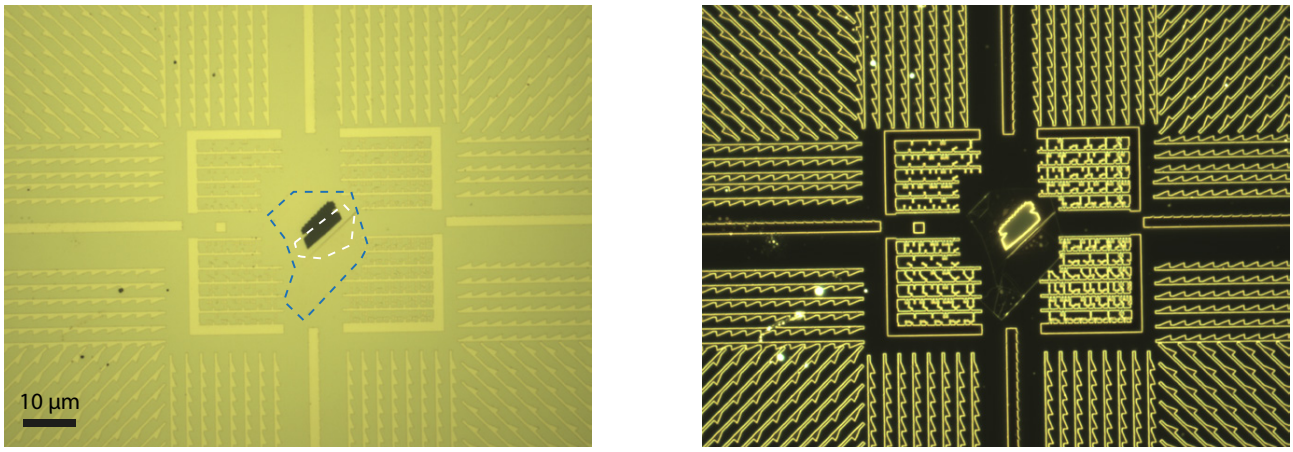

Figure B.31: Device AC24.

Supplementary results

Appendix C

We present in this chapter additional results obtained during this PhD thesis. We start with extra topographic data concerning the wrinkles and ripples that sometimes appear in our graphene samples, and which constitute typical areas we have avoided working on during our measurements. We then use EFM data to estimate the tip contact potential difference on graphene. We also show that the tunneling spectra measured with the lock-in amplifier method are, as expected, very similar to those obtained with the numerical computation of the tunneling conductance. We describe three further features observed during our STM measurements : the appearance of tip-induced resonant peaks (using numerical simulations), extra splitting of LLs (in addition to the interaction-induced gap at zero bias) and the formation of quantum dots, with the observation of Coulomb diamonds. Last, we estimate the tip-induced gating and the resulting variation of filling factor as we probe the $\nu = 0$ gap.

Contents

C.1 Graphene wrinkles and ripples

We observed in some samples the appearance of wrinkles in hBN, extending over several microns as shown in the AFM scan of Figure C.1(a), which deform the overlying graphene. Since these wrinkles were not visible in AFM scans at room temperature, they were formed during the cooling down to $T = 4$ K, probably owing to differences of thermal contraction coefficients. Notably, they disappeared when warming up the device, but new different ones emerged after a new cooling down. These wrinkles present typically an height of around 15 nm for a width of 150 nm, and are thus more prominent than those observed with STM in the graphene sheet itself by Xu *et al.* [295]. We also noticed the presence of ripples[1] in the graphene sheet, see Figure C.1(c), of less than 1 nm height and a few nanometers width [296, 297]. Since graphene electronic properties are altered by the strains that develop locally in the vicinity of these defects, we avoid those areas for our measurements and focus on flat graphene regions.

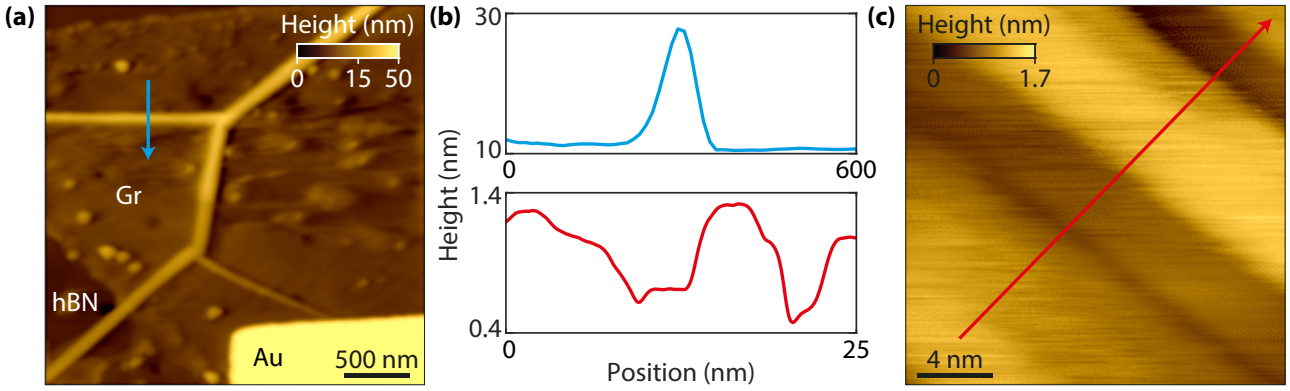

Figure C.1: Wrinkles and ripples in graphene. **(a)** $3 \times 3\,\mu m^2$ AFM image of graphene in AC23 showing the appearance of wrinkles in hBN at $T = 4$ K. **(b)** Topographic profiles corresponding to the blue and red arrows in (a) and (c). **(c)** $20 \times 20\,nm^2$ STM image of ripples in the graphene sheet in BNGrSTO-STM-07, the underlying honeycomb lattice is also visible.

Notably, we remarked a strain-induced distortion of graphene honeycomb lattice on the side of a ripple, see Figure C.2, which is consistent with the valley-polarized triangular lattice expected to arise in strained regions due to pseudo-magnetic field [187], see Chapter 3.6.2.

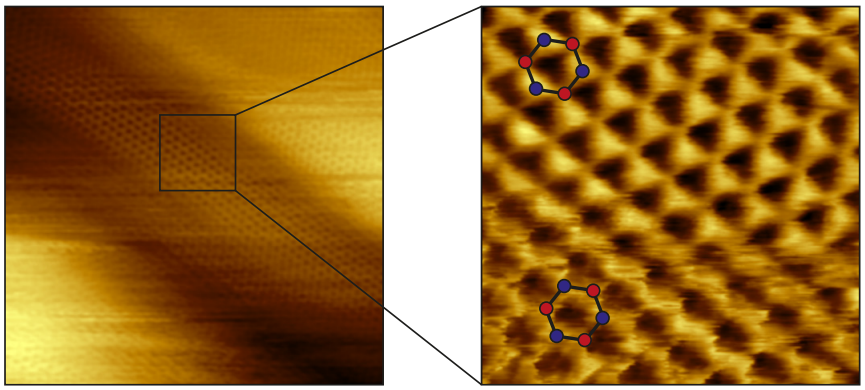

Figure C.2: Honeycomb lattice in graphene ripple. (Left) $10 \times 10\,nm^2$ STM image at $B = 14$ T of graphene ripples with visible honeycomb lattice. (Right) $2 \times 2\,nm^2$ STM image ($I_t = 1$ nA and $V_{bias} = 400$ mV) showing on the top part a strain-induced distortion of the honeycomb lattice.

[1] These ripples visible in sample BNGrSTO-STM-07 may be due to the structural phase transition of $SrTiO_3$ below 110 K and the appearance of domain walls, see Section 5.2.1.b.

C.2 Contact potential difference measurements

We show here contact potential difference V_{CPD} measurements in EFM mode (see Appendix A.2.3) on graphene as a function of the tip-sample distance, which enables us to extract the band-bending beneath the tip due to the work-function difference between the tip and graphene. We start from the contact in AFM mode, at $z = z_{\mathrm{AFM}}$, and then retract the tip at a position z_{scan}. The frequency shift Δf of the tuning fork is measured as the sample voltage V_{bias} is swept from $-5\,\mathrm{V}$ to $+5\,\mathrm{V}$ while the tip is kept grounded. We obtain a parabola such as the one shown in Figure C.3(a) described by Equation (A.30) that we write here as :

$$\Delta f = C\,(V_{\mathrm{bias}} - V_{\mathrm{CPD}}) + \Delta f_{\mathrm{min}} \tag{C.1}$$

V_{CPD} is estimated as the position of the maximum of the parabola, using a quadratic polynomial to locally fit the curve.

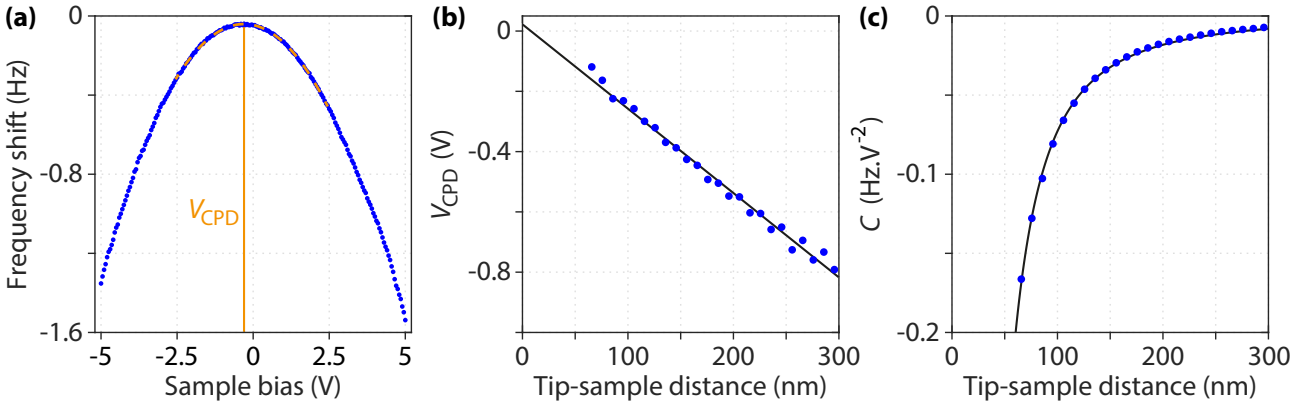

Figure C.3: Contact potential difference measurements on sample AC04 ($\mathbf{hBN/SiO_2}$). **(a)** Frequency shift Δf as a function of sample bias V_{bias} (blue points) at a tip-sample distance of $z = 115\,\mathrm{nm}$ from graphene. $V_{\mathrm{CPD}}(z)$ is determined as the maximum of the fitting parabola in dashed yellow. **(b)** V_{CPD} as a function of tip-sample distance z from graphene (blue points). The CPD between the tip and graphene is determined by the intercept of the linear fit (black line) with $z = 0$. **(c)** Evolution of the curvature C of the parabolas as a function of the tip-sample distance z from graphene (blue points). The fit using Equation (C.2) (black line) yields the tip-sample contact position z_0, from which we compute the tip-sample distance $z = z_{\mathrm{scan}} - z_0$.

This measure of the CPD is repeated at different distances from the sample, down to a few nanometers from the AFM contact. The variation of V_{CPD} with the tip-sample distance is shown in Figure C.3(b). A linear dependence is observed, and the intrinsic V^0_{CPD} between the tip and graphene can be determined by the intercept of the linear fit with $z = 0$. Here, z is the absolute distance between the tip and graphene, given by $z = z_{\mathrm{scan}} - z_0$, with z_0 the tip-sample contact position [298]. We also show in Figure C.3(c) the evolution of the curvature coefficient C of the parabolas with the tip-sample distance. As written in Equation (A.30), the curvature is proportional to $\mathrm{d}^2C_{\mathrm{ts}}/\mathrm{d}z^2$ where C_{ts} is the tip-sample capacitance. The negative sign of the curvatures is a consequence of the attractive nature of the electrostatic force between the tip and the sample, while the decrease as the tip is moved away from the sample is due to the ensuing decrease of the tip-sample capacitance with the distance.

In order to compute z_0, and the tip-sample distance z, we fit in Figure C.3(c) the evolution of the curvature coefficient C with the tip-sample distance using next equation, see Ref. [299] :

$$C = \frac{\beta}{(z_{\mathrm{scan}} - z_0)^2} \tag{C.2}$$

with z_0 and β, the force probe calibration parameter, as the two fitting parameters. The obtained value of z_0 enables us to plot Figures C.3(b,c) as a function of the absolute tip-sample distance z. From Figure C.3(b) we obtain a negligible contact potential difference of $V^0_{\mathrm{CPD}} = 0.02\,\mathrm{V}$ for a tip-sample distance in tunnel mode, that is, of the order of 1 nm. This very small potential can be accounted for by the fact that the tip apex is covered with gold due to the tip reshaping on the gold contact (see Chapter 4.4.2), and is not made of PtIr unlike the bulk of the wire. The work function of gold is about 4.8 eV [235] while graphene is given at 4.6 eV [300]. Our measurements show that these two work functions for our tip apex and graphene on hBN are actually very close and thus do not induce a significant band-bending. This must be compared to the work function of PtIr which is 5.7 eV [237], which would lead to a much more unfavorable situation with a significant band-bending.

This negligible contact potential difference, and hence negligible band-bending, is the ideal situation in which we aimed to realize our Landau levels spectroscopy. Nonetheless, note that this depends strongly on the tip apex shape and material, which change with each tip-cleaning procedure (see Chapter 4.4.2). Therefore, after each cleaning, we ensured that the band-bending was indeed negligible by achieving tunneling conductance gate maps on graphene where charging features, which would appear due to tip-induced confinement of charge carriers, are absent. Otherwise, the presence of charging peaks and/or Coulomb diamonds indicates a significant contact potential difference. In particular, we show in Appendix C.4 that the resulting electrostatic force between the tip and graphene in STM mode induces the appearance of some resonant peaks in the LDOS of graphene, see for instance Figure 5.4.

Besides, the fit parameter β can be used to obtain an estimation of the tip apex size, if we assume it to be spherical with a radius R, considering the following equation from Ref. [299] :

$$\beta = -\frac{f_{\mathrm{res}} R \pi \epsilon_0}{2k} \tag{C.3}$$

where f_{res} is the free resonance frequency and k the cantilever stiffness.

In a simplified mechanical model [224], each prong of the tuning fork behaves as a clamped beam, whose stiffness is given by :

$$k = \frac{Ew}{4}\left(\frac{t}{L}\right)^3 \tag{C.4}$$

with $E = 78.7\,\mathrm{GPa}$ the Young's modulus of quartz, $L = 2.3\,\mathrm{mm}$ the length of the prong, $t = 0.2\,\mathrm{mm}$ its thickness and $w = 0.1\,\mathrm{mm}$ its width (see Figure 4.12), such that we obtain an estimation of the cantilever stiffness as $k \simeq 1.3\,\mathrm{kN/m}$.

Besides, in this same simplified mechanical model, the resonance frequency of the free prong, without the tip glued at its extremity, can be determined as :

$$f_{\mathrm{res}} = \frac{3.516}{2\pi}\sqrt{\frac{E}{12\rho}}\frac{t}{L^2} \tag{C.5}$$

where $\rho = 2\,650\,\mathrm{kg/m^3}$ is quartz density, which gives $f_{\mathrm{res}} \simeq 33.2\,\mathrm{kHz}$, close enough to the expected value of 32.768 kHz up to the precision of the measurements of the geometrical parameters L, t and w.

Using now the value of the resonance frequency of the tuning fork with the tip, $f_{\mathrm{res}} = 24.5\,\mathrm{kHz}$, and the value of the stiffness $k \simeq 1.3\,\mathrm{kN/m}$ computed above, we estimate the tip apex radius from the fit parameter β with Equation (C.3) as $R \approx 2.8\,\mu\mathrm{m}$, consistent with a tip apex roughly cut by hand, see for instance the SEM images from Figure 4.14.

C.3 LDOS measurement : lock-in method versus numerical derivation

Every tunneling spectrum presented in this thesis was measured with the lock-in amplifier method, see Appendix A.1.3. The other and more direct method simply consists of computing numerically the derivative of the tunneling current. However this requires an important smoothing of both I_t and the resulting dI_t/dV_{bias} to filter the important high frequency noise and obtain the physical features.

If the lock-in amplifier method gives a better signal to noise ratio than what we obtain with the numerical derivation, it also requires a much longer measurement time. The integration time for each point of V_{bias} is 5 ms while the time constant of the lock-in is either $\tau = 10$ or 30 ms. The dI_t/dV_{bias} spectra obtained this way are smooth with low noise, yet one can wonder if the integration over τ of the modulated current, time during which the bias is swept, may lead to an important smearing of the spectrum.

We compare in Figure C.4(b) spectra obtained with both methods : the raw lock-in signal and the numerical derivative after an important smoothing. Very similar features are observed, in particular LLs peaks in both spectra have close widths. The energetic resolution is thus similar : no information is lost with the lock-in amplifier method.

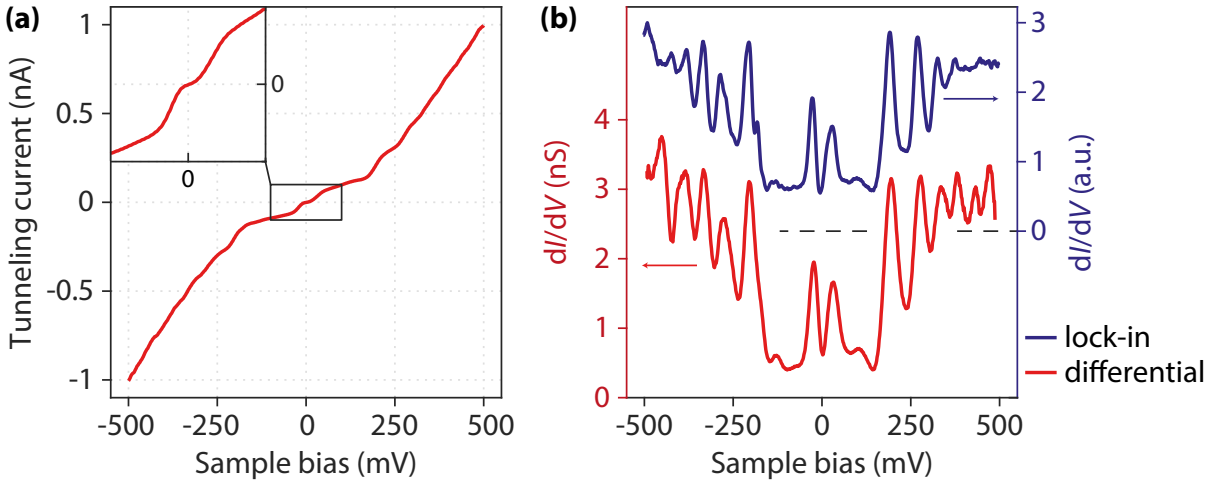

Figure C.4: Numerical derivation of the tunneling conductance. **(a)** Tunneling current I_t as a function of sample bias V_{bias} at $B = 14$ T and $V_g = 13$ V in sample BNGrSTO-STM-07, taken from Figure 5.8. Inset : zoom around zero sample bias showing the $\nu = 0$ gap appearing with a soft - but non zero - slope. **(b)** Tunneling conductance $G = dI_t/dV_{bias}$ determined with two methods : from a numerical derivation of the tunneling current I_t with respect to sample bias V_{bias} (red curve), and with a lock-in amplifier measurement (blue curve). Both spectra display very similar features.

On a side note, one remarks that both spectra do not fall to zero in the cyclotron gaps as we would expect (in particular between LL_0 and $LL_{\pm 1}$) : there is a flat non-zero background, which is clearly visible in Figure C.4(a) as the plateaus of the tunneling current I_t, obtained when tunneling inside the gaps, display positive slopes. We show in Section 5.3.3 that the observation of such plateaus, rather than the strictly horizontal ones expected for a zero DOS in the gaps, is eventually consistent with the experimental LDOS gate maps we measured assuming the existence of a background density of localized states [56].

C.4 Tip-induced resonant peaks

We investigate here the emergence of tip-induced resonant peaks at $B = 0\,\mathrm{T}$ in the LDOS spectra, for instance those that appear in Figure 5.4. Figures in this section are numerical simulations performed by Adolfo G. Grushin from Néel Institute using the Kwant code [262, 263].

C.4.a Quantum well generated by a carbon nanotube

We first consider a quantum well in graphene in the y direction created by a carbon nanotube placed a few nanometers away. Guided modes were shown to arise in the well by Cheng *et al.* in 2019 [257]. The well potential can be written as :

$$V(y) = \frac{V_0}{1 + y^2/d^2} \tag{C.6}$$

with V_0 the depth of the well, related to the voltage applied between the graphene sheet and the carbon nanotube, and d the width of the well, which increases with the distance between graphene and the nanotube.

Figure C.5(a) shows the density of states at zero energy of a graphene nanoribbon, without the quantum well ($V_0 = 0$). The corresponding band diagram in Figure C.5(d) gives the bandstructure we already studied in Chapter 2.2.2.b, in particular we observe the dispersionless

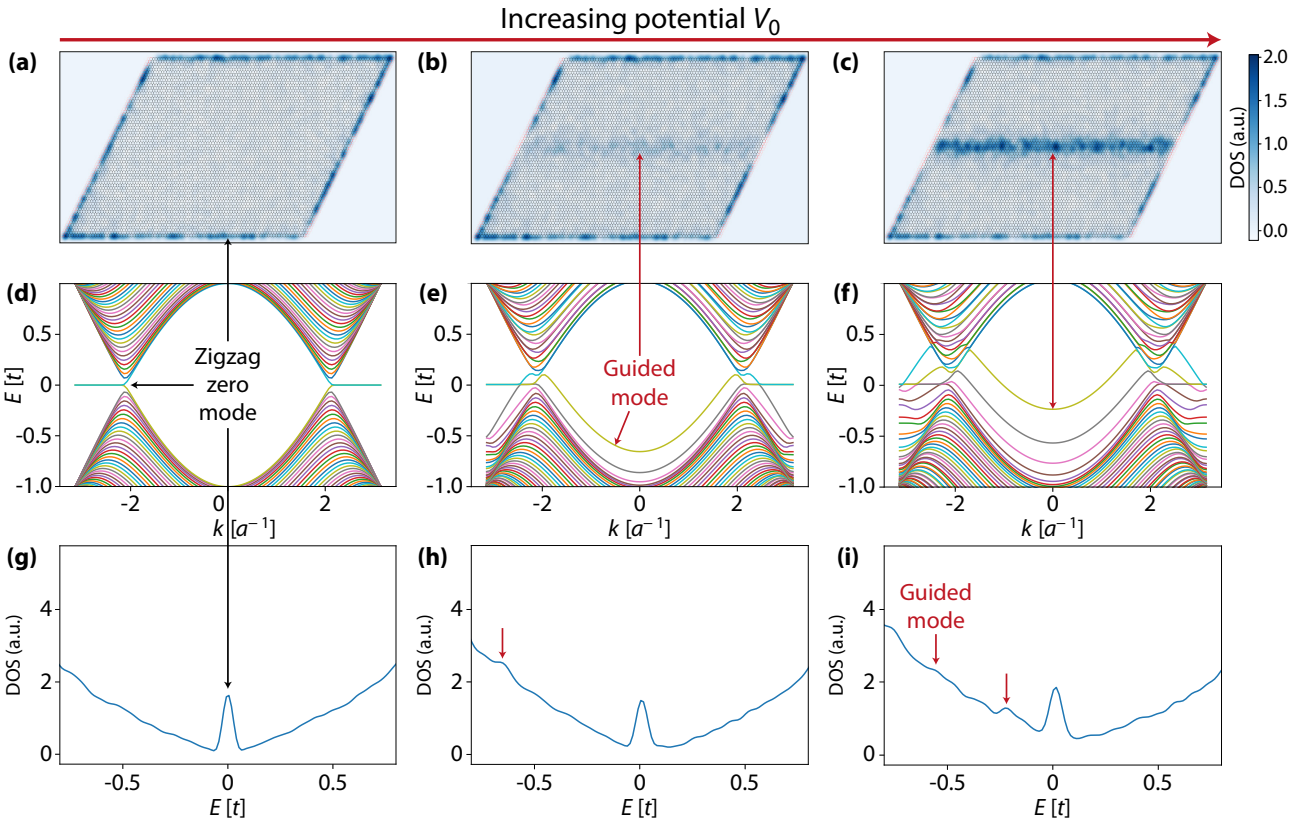

Figure C.5: Nanotube on top of graphene (tight-binding model). (a,b,c) Density of states at zero energy of a graphene ribbon (30×30 lattice sites) with increasing potential V_0 ($d = 3$ lattice sites). **(d,e,f)** Corresponding band diagrams (energy axis in units of $t = 2.7\,\mathrm{eV}$ the hopping energy). By increasing V_0, more and more modes are separated from the continuum. **(g,h,i)** Corresponding density of states, integrated on the whole surface, where the guided modes appear as resonant peaks. Simulations by [264].

zigzag zero mode. This zero mode appears in the density of states (integrated on the whole surface) of Figure C.5(g) as a peak at zero energy. By increasing V_0 we clearly see the quantum well appearing at the middle of the ribbon in Figure C.5(b,c). In the bandstructures of Figure C.5(e,f) emerge guided modes separated from the continuum, the greater V_0 the more guided modes. These modes appear in the density of states in Figure C.5(h,i) as resonant peaks.

We show in Figure C.6 the evolution of the integrated density of states of the graphene ribbon with increasing V_0. Besides the zigzag zero mode appearing as a peak at zero energy, many resonant peaks emerge with increasing V_0, dispersing with V_0 and featuring a strong electron-hole asymmetry. Finally, the number of guided modes in the bandstructure, and so that of resonant peaks in the density of states, increase with the well width d, see Figure C.7.

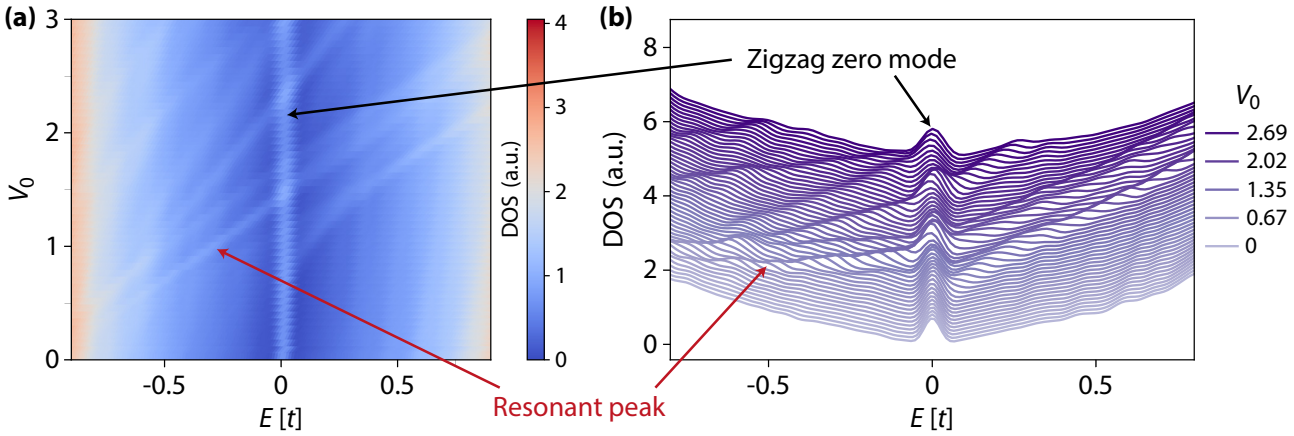

Figure C.6: Nanotube on top of graphene and resonant peaks (tight-binding model). **(a)** DOS map as a function of energy E and well potential V_0. The zigzag zero mode appears as a dispersionless peak at zero energy. Many resonant peaks emerge with increasing V_0. **(b)** DOS spectra taken from (a) at different V_0. Simulations by [264].

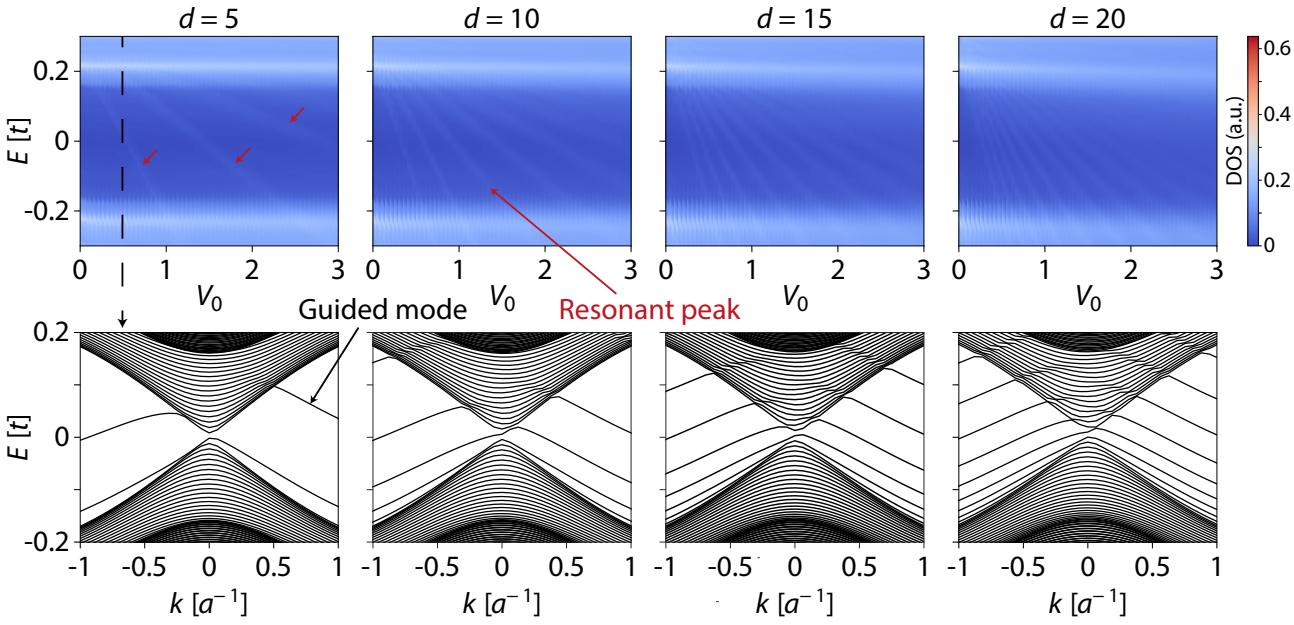

Figure C.7: Nanotube on top of graphene and resonant peaks (continuum model). (Top) DOS maps as a function of energy E and well potential V_0 for increasing well width d. The larger d, the more resonant peaks we observe. (Below) Band diagrams for increasing d taken at $V_0 = 0.5$: the number of guided modes is clearly seen to increase with d. Simulations by [264].

C.4.b Tip-induced quantum dot

By analogy with the 1D previous model, we suppose in our sample the existence of a tip-induced dot in graphene of radius R beneath the tip. Such dot is delimited by the circular pn junction created by the contact potential difference $V_0 = V_{\text{CPD}}$ between the tip and graphene. The dot potential in graphene can be written as :

$$V(r) = \frac{V_0}{1 + r^2/d^2} \tag{C.7}$$

with d the radius of the potential well in the dot, which increases with the tip apex radius and distance.

Figure C.8(a) shows such tip-induced dot on which the computed density of states at zero energy is overlaid. The zigzag zero mode appears as dark blue regions on the zigzag edges of the dot. Inside the dot appear some localized states - the larger the dot, the more structures there are. Figure C.8(b) displays the density of states integrated on the whole dot as a function of energy and the potential V_0. Many resonant peaks are visible and disperse with V_0, similarly to our experimental gate map in Figure 5.4.

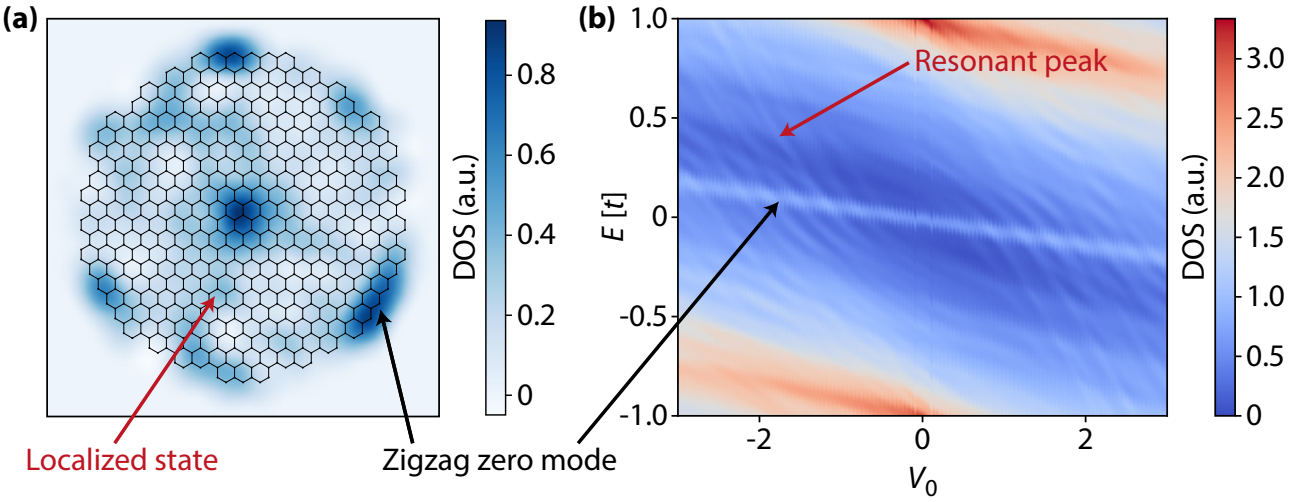

Figure C.8: Tip-induced dot in graphene and resonant peaks (tight-binding model). **(a)** Zero-energy density of states in graphene tip-induced dot in which emerge localized states. **(b)** Density of states integrated on the whole dot as a function of energy and contact potential difference $V_0 = V^{\text{CNP}}$, where we clearly see many resonant peaks. Simulations by [264].

C.5 Splitting of Landau level peaks

We noticed many different LL splitting in our LDOS gate maps, some among them occurring in ways we still do not understand. Yet we identified four robust kinds of splitting. The first one is the interaction-induced gap that opens in the LLs at zero bias, see Figure C.9(a,b). If the gap that opens in the zeroth Landau level is the focus of Chapter 7, we also noticed the opening of similar but smaller gaps in the $N = \pm 1$ and $N = -2$ LLs.

Secondly, we remarked LLs tend to split when E_{F} lies in a cyclotron gap between two plateaus, forming a series of peaks that disperse in parallel with the gate voltage, see Figure C.9(b-d). We suppose this is due to the lifting of the orbital degeneracy as observed by Luican-Mayer *et*

al. [152] and induced by the proximity of a charged impurity, which is not screened for integer filling factors, see Chapter 2.2.1. We show in Figure C.10(a,b) some $\mathrm{d}I_\mathrm{t}/\mathrm{d}V_\mathrm{bias}$ spectra taken from Figure 5.10(c) at $\nu = \pm 2$. The split peaks are indexed by the orbital index m as defined in Chapter 2.1.2. For both LL_0 and LL_{-1} we remark the rightmost peak is less defined and larger than the rest of the series : we suppose this results from the merging into a continuum of the unresolved higher orbital sublevels. We note $\Delta^\circ_{N,m} = E_{N,m+1} - E_{N,m}$ the orbital gap between orbital states m and $m+1$ in LL_N. The different values of these gaps are reported in Table C.1. Values for LL_0 are taken from Figure C.10(a) while those for LL_1 are computed from Figure C.10(b). We observe $\Delta^\circ_{N,m}$ decreases with increasing m and $|N|$ as expected from [167].

$\Delta^\circ_{N,m}$ (meV)	$m = 0$	$m = 1$	$m = 2$
$N = 0$	37.2	24.3	14.3
$N = -1$	25.8	18.5	13.0

Table C.1: Landau level orbital splitting in sample BNGrSTO-STM-07 at $B = 14\,\mathrm{T}$.

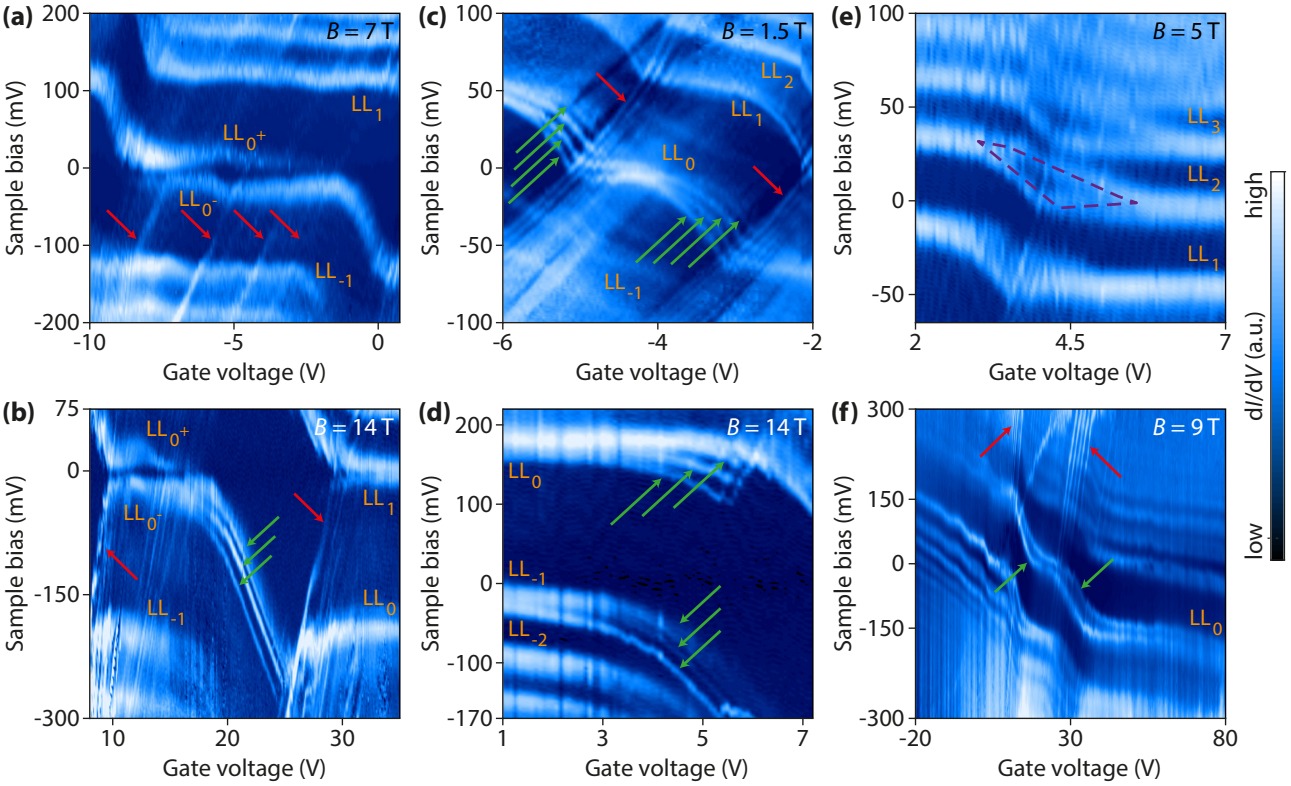

Figure C.9: Landau level splitting observed in LDOS gate maps. (a,c,e) maps were measured on sample AC04 ($\mathrm{hBN/SiO_2}$), (b,d) maps on sample BNGrSTO-STM-07 ($\mathrm{hBN/SrTiO_3}$) and (f) map on sample AC23 ($\mathrm{hBN/SrTiO_3}$). The opening of the interaction-induced gap in LL_0 at zero bias is well visible in (a,b). The lifting of the orbital degeneracy when E_F lies in a cyclotron gap is observable for LL_0 in (b,c,d), as well as for LL_{-1} in (d), with the orbital states indicating by green arrows. LLs are also seen to split in two between two plateaus in (e). Another splitting in two peaks of LL_0 is visible in (f) on a large range of gate voltage. Red arrows indicate charging features.

The third type of LL splitting we observed also occurs at integer filling factors, except this time LLs split in two peaks that do not disperse in parallel, but rather smoothly interpolates between the consecutive LL plateaus for one peak while the second displays a steep variation, see Figure C.9(e) and Figure C.10(c) where this splitting is clearly resolved for many positive LLs in sample AC04 ($\mathrm{hBN/SiO_2}$). Similar features were also noticed for negative LLs in

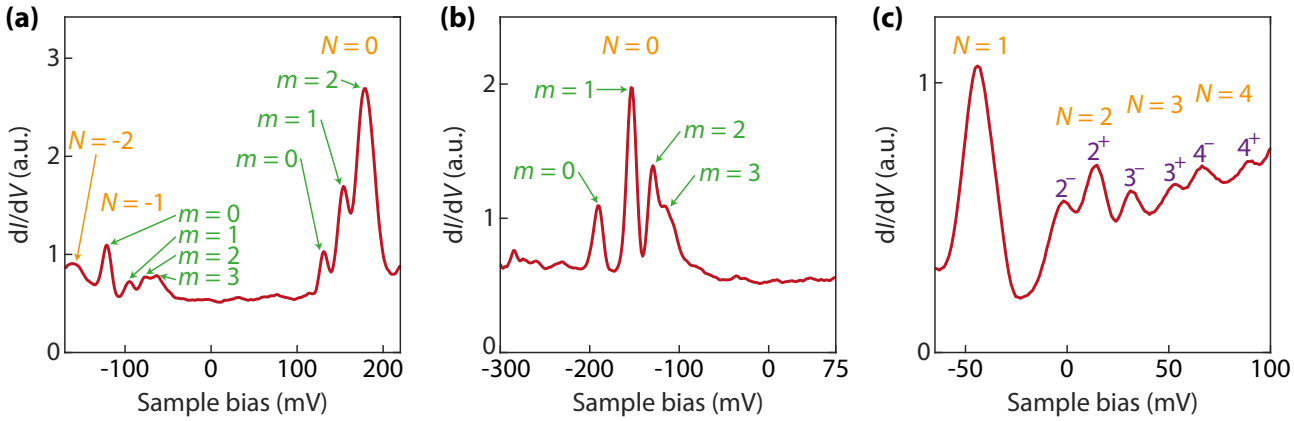

Figure C.10: Landau level splitting at integer filling factors. (a,b) Orbital splitting of the LL_0 and LL_{-1} in sample BNGrSTO-STM-07 at $B = 14$ T. Spectrum (a) taken from Figure C.9(d) at $V_g = 4.6$ V ($\nu = -2$). Spectrum (b) taken from Figure C.9(b) at $V_g = 22$ V ($\nu = 2$). **(c)** Splitting of the LL_2, LL_3 and LL_4 in sample AC04 at $\nu = 6$ and $B = 5$ T. Spectrum taken from Figure C.9(e) at $V_g = 4.5$ V.

other gate maps. The gap between those peaks varies with the gate voltage but its maximum value increases with N, contrary to what is expected for the orbital splitting that also happens at integer filling factors. However the gap is quickly blurred for $|N| > 5$ due to the merging of LLs.

Finally, we remarked in some LDOS gate maps the splitting in two peaks of LL_0 on a large range of gate voltage, including both regimes where E_F is pinned inside LL_0 and conversely, with no closure of the resulting gap at the transitions, see Figure C.9(f). Those two peaks move in parallel and an interaction-induced gap can open in the peak which pins E_F at zero bias (while the second peak forms a plateau at a higher energy and does not split). We also observed sometimes a clear difference between the intensity of the peaks, one being much brighter than the other. We suppose this splitting may be another signature of the lifting of the orbital degeneracy of LL_0.

C.6 Quantum dots and Coulomb diamonds

Some charging effects also emerge in our LDOS gate maps. Charging peaks disperse with a positive slope with gate voltage, contrary to LLs that move in the opposite direction. Notably they still disperse with gate voltage even when LLs form plateaus due to the pinning of E_F. The charging effects arise from the electrostatic confinement of LLs, forming graphene quantum dots, either due to the local disorder potential (charging peaks intensity and spacing change after moving the tip elsewhere on graphene) and/or from the electrostatic action of the tip (charging peaks intensity and spacing change after reshaping the tip), see Chapter 3.5.1 and 3.6.1.

In this last case charging peaks are highly dependent on the tip apex shape : the bigger the apex radius, the bigger the capacitive coupling between the tip and graphene, the smaller the charging energy $E_c = e^2/C_{tot}$ of the induced quantum dot in graphene and the more perturbed the tunneling spectrum by all these charging peaks. We therefore aim when reshaping the tip on gold to obtain the sharpest tip apex to reduce the emergence of those charging peaks that not only hinder the good mapping of the LLs, but also interact with the LL peaks, overshadowing them by forming Coulomb diamonds, which prevents for instance a good determination of the interaction-induced gap of LL_0.

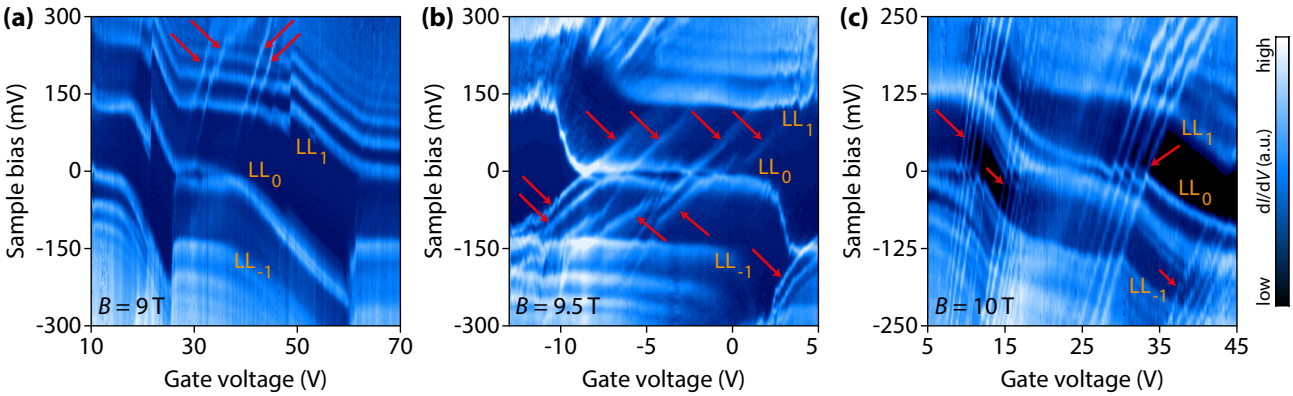

Figure C.11: Charging features in LDOS gate maps, indicated by red arrows. **(a)** LDOS gate map from sample BNGrSTO-STM-07 taken at $B = 9$ T. A quadruplet of charging peaks appears when E_F is pinned inside LL_0 and intersects LLs. **(b)** LDOS gate map from sample AC04 taken at $B = 9.5$ T. Charging peaks emerge in the cyclotron gap when E_F is pinned inside LL_0 and intersect the split LL_0 peak. **(c)** LDOS gate map from sample AC23 taken at $B = 10$ T. Different series of charging peaks arise when filling the different LLs, forming Coulomb diamonds.

Charging features occurred and behaved in many different ways during our measurements. Most of the time, charging peaks appear as quartets, due to spin and valley degeneracies. A charging series arises for each LL and intersects it as it forms its plateau at zero sample bias : each individual peak corresponds to the single-electron charging of the graphene quantum dot, following the Coulomb blockade physics [27] (see Chapter 3.5.1). In worst cases, the orbital degeneracy is also lifted and many charging peaks appear in the whole LDOS gate map, as shown in Figure C.11(c), owing to the progressive filling of each LL dot [82, 176] (see Chapter 3.5.2).

Charging peaks also appear more prominent around the LL_0 plateau, with decreasing brightness for higher N. In this case the LL spectrum is only slightly distorted and is still well visible. Figures C.11(a,b) show those typical charging quartets, indicated by red arrows. We notice two behaviors. Either the charging peaks are prominent at high sample bias and are seen to intersect $|N| > 1$ Landau levels, see Figure C.11(a) but also the peaks indicated by red triangles in Figure 5.10(c), and disappear in the cyclotron gap between LL_0 and $LL_{\pm1}$, or on the contrary they appear brighter in the cyclotron gap while being not visible at higher bias.

We show in Figure C.12 typical Coulomb diamond structures we observed during our experiments. In Figure C.12(a) a quartet of charging peaks intersects LL_0 at zero bias in sample AC23 ($hBN/SrTiO_3$) and forms a series of three diamonds. A similar series was observed in LL_{-1} in sample BNGrSTO-STM-07 ($hBN/SrTiO_3$), see Figure C.12(b), and (c) as well where an additional splitting of LL_{-1} yields two peaks and a series of Coulomb diamonds forms for both of them when they cross the zero bias.

In those three figures the central diamond appears bigger than its two neighbors, owing to the peaks inside the quadruplet not being equidistant. This is due to the opening of the interaction-induced gap in LLs at zero bias, gap which adds to the charging energy E_c in the peak spacing, see Figure 3.14. For each figure we estimate E^i_{add} the addition energy between the charging peaks i and $i+1$, see Table C.2. We indeed observe that $E^2_{add} > E^{1,3}_{add}$ for both LL_0 and LL_{-1}. Although we can extract a value of the LL_0 gap of $\Delta E_0 = E^2_{add} - E^1_{add} \simeq 19$ meV at $B = 10$ T, this method is rather imprecise and does not enable a systematic study of the LL_0 gap (charging peaks disappear at low magnetic field, and sometimes also at higher fields).

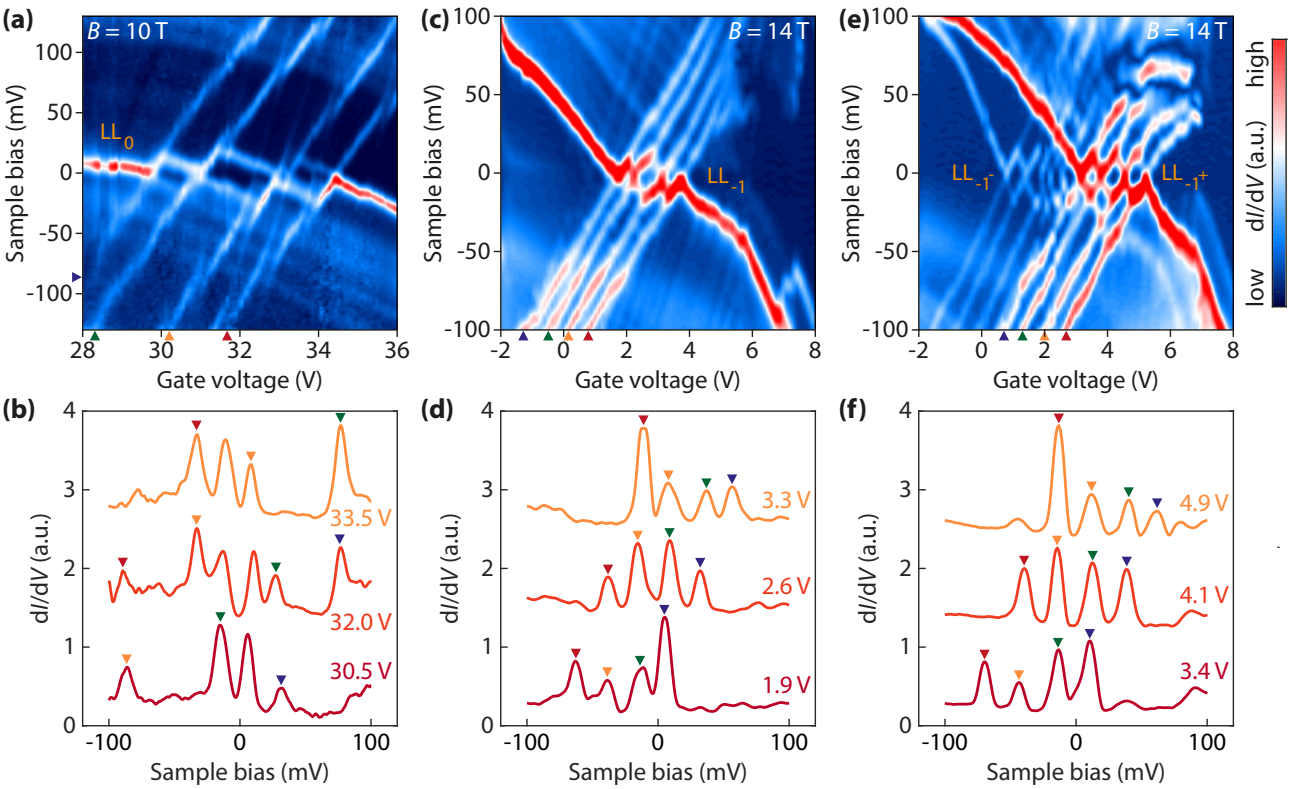

Figure C.12: Coulomb diamonds in LDOS gate maps. **(a)** LDOS gate map from sample AC23 (hBN/$SrTiO_3$) taken at $B = 10$ T, showing the formation of Coulomb diamonds in LL_0 due to its intersection by a quartet of charging peaks (marked by colored triangles). **(b)** Tunneling spectra from (a) at different gate voltages. The charging peaks are marked by triangles using the same color code than in (a). **(c)** LDOS gate map from sample BNGr-STO-STM-07 (hBN/$SrTiO_3$) taken at $B = 14$ T, showing the formation of Coulomb diamonds in LL_{-1}. **(d)** Tunneling spectra from (c) at different gate voltages. **(e)** Another LDOS gate map from sample BNGr-STO-STM-07 taken at $B = 14$ T, showing the formation of Coulomb diamonds in the split LL_{-1}. **(f)** Tunneling spectra from (e) at different gate voltages.

	LL_0 - Panel (a)	LL_{-1} - Panel (c)	LL_{-1} - Panel (e)
E^1_{add}	71 meV	22 meV	25 meV
E^2_{add}	90 meV	30 meV	30 meV
E^3_{add}	74 meV	19 meV	24 meV

Table C.2: Addition energies of the LL_0 dot in sample AC23 (hBN/$SrTiO_3$) at $B = 10$ T and of the LL_{-1} dot in sample BNGrSTO-STM-07 (hBN/$SrTiO_3$) at $B = 14$ T obtained from the corresponding panels of Figure C.12.

Moreover, one can estimate the size of the graphene quantum dot from which emerge those charging peaks. We consider Figure C.12(b), where the charging energy of the dot is given by the minimum of the addition energy, in absence of additional splitting term, hence either $E^{1,3}_{\text{add}}$. We thus obtain $E_c \simeq 20$ meV. As we saw in Chapter 3.5.1.a, the charging energy of the dot is determined by :

$$E_c = \frac{e^2}{C_{\text{tot}}} \quad \Rightarrow \quad C_{\text{tot}} \simeq 8.0 \times 10^{-18}\ \text{F} \tag{C.8}$$

where $C_{\text{tot}} = C_g + C_s + C_d$ is the total capacitance of the system. The ratio between the capacitances C_g, C_s and C_d are obtained from the slopes of the Coulomb diamonds, see Figure 3.8, as $C_d : C_s : C_g = 2.33 : 2.22 : 1$, such that $C_{\text{tot}} = 4.55\, C_g$ and $C_g \simeq 1.76 \times 10^{-18}$ F.

Finally, using Equation (3.4) with $d_{\mathrm{STO}} = 500\,\mu\mathrm{m}$ and $\epsilon_\mathrm{r} \approx 9300$ estimated from Figure 5.12(b) at $V_\mathrm{g} = 2\,\mathrm{V}$, we obtain the radius of the graphene dot :

$$C_\mathrm{g} = \epsilon_0 \epsilon_\mathrm{r} \frac{\pi R_\mathrm{dot}^2}{d_\mathrm{STO}} \quad \Rightarrow \quad R_\mathrm{dot} \approx 58\,\mathrm{nm} \tag{C.9}$$

which is consistent with the size of the dot observed in Figure 5.8(b).

C.7 Tip-induced gating

Probing graphene density of states in tunneling spectroscopy induces an unintentional local doping of graphene due to the field effect of the tip (see Chapter 3.6), which then modifies locally the filling factor of graphene beneath the tip. This could modify the $\nu = 0$ broken-symmetry state that we study in Chapter 7. We aim here to obtain an estimation of the variation of the filling factor due to tip-induced gating $\delta\nu_\mathrm{tip}$. The total doping of graphene from field effects of both the back gate and the tip is given by :

$$n = \frac{1}{e}\left(C_\mathrm{g} V_\mathrm{g} - C_\mathrm{tip} V_\mathrm{bias}\right) \tag{C.10}$$

with the capacitances C_g between graphene and the back gate and C_tip between the tip and graphene, as shown in Figure 3.12. Constant-carrier-density lines in tunneling conductance gate maps feature a slope given by :

$$\frac{\mathrm{d}n}{\mathrm{d}V_\mathrm{g}} = 0 \Rightarrow \frac{\mathrm{d}V_\mathrm{bias}}{\mathrm{d}V_\mathrm{g}} = \frac{C_\mathrm{g}}{C_\mathrm{tip}} \tag{C.11}$$

and thus do not appear as vertical lines at constant back-gate voltages, but rather as tilted lines, see for instance the red line in Figure 5.12(c) which shows that the Landau levels staircase transitions do not occur at the same back-gate voltage. Since the back-gate capacitance (per unit area) C_g can be estimated as $C_\mathrm{g} = \epsilon_0\epsilon_\mathrm{r}/d$, with d the thickness of the back-gate insulator and ϵ_r its relative dielectric constant, and the slope $C_\mathrm{g}/C_\mathrm{tip}$ of the isodensity lines can be obtained from the gate maps, following Ref. [47], it is possible to deduce the capacitance C_tip. The variation of the carrier density due to tip-induced gating at constant back-gate voltage is then :

$$\delta n_\mathrm{tip} = \frac{1}{e} C_\mathrm{tip} V_\mathrm{bias} \tag{C.12}$$

and the resulting tip-induced variation of the filling factor is :

$$\delta\nu_\mathrm{tip} = \frac{\delta n_\mathrm{tip} \phi_0}{B} \tag{C.13}$$

with ϕ_0 the flux quantum and B the magnetic field.

C.7.a SiO_2 sample

The back-gate insulator is here comprised of the SiO_2 layer and the hBN flake. Its thickness is $d = d_{\mathrm{SiO_2}} + d_{\mathrm{BN}} \simeq 300\,\mathrm{nm}$ (see Table 5.1). Its dielectric constant is given by Equation (5.3) as $\epsilon_\mathrm{r} \simeq 3.7$. The back-gate capacitance is thus :

$$C_\mathrm{g} = \frac{\epsilon_0 \epsilon_\mathrm{r}}{d} \simeq 10.9\,\mathrm{nF.cm^{-2}} \tag{C.14}$$

From several tunneling conductance gate maps we compute the slopes of the isodensity lines around charge neutrality to be of the order of 0.1 (the tip capacitance changes with the tip apex shape). We then obtain an estimation of the tip capacitance as :

$$\frac{C_g}{C_{tip}} \approx 0.1 \Rightarrow C_{tip} \approx 110\,\text{nF.cm}^{-2} \tag{C.15}$$

We now focus on the tip-induced gating at $\nu = 0$ at the bias positions of the two peaks of the split $LL_{0^\pm}$, positions that we used to estimate the $\nu = 0$ gap $\Delta E^{\nu=0}(B)$ in Chapter 7.1. The tip-induced gating at those biases, $V_{bias} = \pm\Delta E^{\nu=0}(B)/2$, is given by :

$$|\delta n_{tip}| = \frac{C_{tip}}{e}\frac{\Delta E^{\nu=0}(B)}{2} \tag{C.16}$$

which yields for the tip-induced variation of the filling factor ($\nu = 0$ at $V_{bias} = 0$, set by the gate voltage) :

$$|\delta\nu_{tip}| = \frac{\phi_0 C_{tip}\Delta E^{\nu=0}(B)}{2eB} \tag{C.17}$$

Numerically, at $B = 14$ T, we measured $\Delta E^{\nu=0} \simeq 55$ meV (see Figure 7.6), which gives $|\delta\nu_{tip}| \simeq 0.06$. At $B = 1.5$ T, we measured $\Delta E^{\nu=0} \simeq 15$ meV, which gives $|\delta\nu_{tip}| \simeq 0.14$. In both cases, the tip-induced variation of the filling factor is negligible and we can assume that it does not alter the physics of the $\nu = 0$ state we are probing. Note also that since $\Delta E^{\nu=0}$ scales as the Coulomb energy $E_C \propto \sqrt{B}$, this yields $|\delta\nu_{tip}| \propto B^{-1/2}$ and the effect of the tip on the filling factor decreases at higher magnetic fields.

C.7.b $SrTiO_3$ samples

The back-gate insulator is here comprised of the $SrTiO_3$ substrate and the hBN flake. Its thickness is $d \simeq d_{STO} = 500$ µm and its dielectric constant ϵ_r can be determined as explained in Chapter 5.3.2. From Figure 5.12 we can estimate $\epsilon_r \approx 7\,500$ at charge neutrality for sample BNGrSTO-STM-07. We then compute the back-gate capacitance as :

$$C_g = \frac{\epsilon_0\epsilon_r}{d} \simeq 13.3\,\text{nF.cm}^{-2} \tag{C.18}$$

We obtain from several tunneling conductance gate maps a similar ratio of the capacitances of the order of :

$$\frac{C_g}{C_{tip}} \approx 0.1 \Rightarrow C_{tip} \approx 133\,\text{nF.cm}^{-2} \tag{C.19}$$

Using Equation (C.17), we estimate at $B = 14$ T where we measured $\Delta E^{\nu=0} \simeq 40$ mV (see Figure 7.6) a tip-induced variation of the filling factor around $\nu = 0$ of $|\delta\nu_{tip}| \simeq 0.05$. At $B = 6$ T where $\Delta E^{\nu=0} \simeq 15$ meV, we have $|\delta\nu_{tip}| \simeq 0.04$. The effect of the tip on the filling factor is therefore also negligible.

Bibliography

[1] P. R. Wallace. The Band Theory of Graphite. *Phys. Rev.*, vol. 71:622, 1947. (Cited on page 6.)

[2] K. Novoselov, A. Geim, S. Morozov, D. Jiang, M. Katsnelson, I. Grigorieva, S. Dubonos, and A. Firsov. Two-dimensional gas of massless Dirac fermions in graphene. *Nature*, vol. 438:197–200, 2005. (Cited on pages 6, 13, 14, 31, 32, 69, and 220.)

[3] J. C. Slonczewski and P. R. Weiss. Band Structure of Graphite. *Phys. Rev.*, vol. 109:272–279, 1958. (Cited on page 8.)

[4] A. H. Castro Neto, F. Guinea, N. M. R. Peres, K. S. Novoselov, and A. K. Geim. The electronic properties of graphene. *Rev. Mod. Phys.*, vol. 81:109–162, 2009. (Cited on pages 8, 13, and 47.)

[5] T. Ando, T. Nakanishi, and R. Saito. Berry's phase and absence of back scattering in Carbon nanotubes. *J. Phys. Soc. Jpn*, vol. 67:2857–2862, 1998. (Cited on pages 8 and 13.)

[6] M. S. Dresselhaus and G. Dresselhaus. Intercalation Compounds of Graphite. *Advances in Physics*, vol. 51:1, 2002. (Cited on page 8.)

[7] Y. Barlas, K. Yang, and A. H. MacDonald. Quantum Hall effects in graphene-based two-dimensional electron systems. *Nanotechnology*, vol. 23:052001, 2012. (Cited on page 12.)

[8] X. Du, I. Skachko, A. Barker, and E. Y. Andrei. Approaching ballistic transport in suspended graphene. *Nature Nanotechnology*, vol. 3:491, 2008. (Cited on page 12.)

[9] K. I. Bolotin, K. J. Sikes, Z. Jiang, M. Klima, G. Fudenberg, J. Hone, P. Kim, and H. L. Stormer. Ultrahigh electron mobility in suspended graphene. *Solid State Commun.*, vol. 146:351, 2008. (Cited on page 12.)

[10] J. H. Chen, C. Jang, S. Adam, M. S. Fuhrer, E. D. Williams, and M. Ishigami. Charged impurity scattering in graphene. *Nature Physics*, vol. 4:377, 2008. (Cited on page 12.)

[11] F. V. Tikhonenko, A. A. Kozikov, A. K. Savchenko, and R. V. Gorbachev. Transition between electron localization and antilocalization in graphene. *Phys. Rev. Lett.*, vol. 109:226801, 2009. (Cited on page 12.)

[12] N. W. Ashcroft and N. D. Mermin. *Solid State Physics*. Saunders College, Philadelphia, PA, 1976. (Cited on page 13.)

[13] Y. Zhang, Y. Tan, H. Stormer, and P. Kim. Experimental observation of the quantum Hall effect and Berry's phase in graphene. *Nature*, vol. 438:201–204, 2005. (Cited on pages 13, 14, 15, 26, 31, and 69.)

[14] R. S. Deacon, K.-C. Chuang, R. J. Nicholas, K. S. Novoselov, and A. K. Geim. Cyclotron resonance study of the electron and hole velocity in graphene monolayers. *Phys. Rev. B*, vol. 76:081406(R), 2007. (Cited on page 13.)

[15] Z. Jiang, E. A. Henriksen, L. C. Tung, Y.-J. Wang, M. E. Schwartz, M. Y. Han, P. Kim, and H. L. Stormer. Infrared Spectroscopy of Landau Levels of Graphene. *Phys. Rev. Lett.*, vol. 98:197403, 2007. (Cited on page 13.)

[16] M. V. Berry. Quantal phase factors accompanying adiabatic changes. *Proc. R. Soc. Lond. A*, vol. 392:45, 1984. (Cited on page 13.)

[17] D. Xiao, M. C. Chang, and Q. Niu. Berry phase effects on electronic properties. *Rev. Mod. Phys.*, vol. 82:1959, 2010. (Cited on page 13.)

[18] T. Ando. Theory of Electronic States and Transport in Carbon Nanotubes. *J. Phys. Soc. Jpn.*, vol. 74:777–817, 2005. (Cited on page 13.)

[19] M. O. Goerbig. Electronic properties of graphene in a strong magnetic field. *Rev. Mod. Phys.*, vol. 83:1193, 2011. (Cited on pages 13, 27, and 31.)

[20] S. Das Sarma, S. Adam, E. H. Hwang, and E. Rossi. Electronic transport in two-dimensional graphene. *Rev. Mod. Phys.*, vol. 83:407–470, 2011. (Cited on pages 13, 20, and 26.)

[21] K. Bennaceur. *Electronic transport in graphene*. PhD thesis, Université Paris Sud - Paris XI, 2010. (Cited on page 13.)

[22] E. Y. Andrei, G. Li, and X. Du. Electronic properties of graphene: a perspective from scanning tunneling microscopy and magnetotransport. *Rep. Prog. Phys.*, vol. 75:056501, 2012. (Cited on pages 13, 17, and 67.)

[23] K. S. Novoselov, A. K. Geim, S. V. Morozov, D. Jiang, M. I. Katsnelson, I. V. Grigorieva, S. V. Dubonos, and A. A. Firsov. Two-dimensional gas of massless Dirac fermions in graphene. *Nature*, vol. 438:197, 2005. (Cited on page 15.)

[24] M. I. Katsnelson, K. S. Novoselov, and A. K. Geim. Chiral tunnelling and the Klein paradox in graphene. *Nat. Phys.*, vol. 2:620–625, 2006. (Cited on pages 15, 18, and 73.)

[25] P. E. Allain and J. N. Fuchs. Klein tunneling in graphene: optics with massless electrons. *Eur. Phys. J. B*, vol. 83:301, 2011. (Cited on pages 15, 18, and 73.)

[26] Y. Zhang, V. W. Brar, F. Wang, C. Girit, Y. Yayon, M. Panlasigui, A. Zettl, and M. F. Crommie. Giant phonon-induced conductance in scanning tunnelling spectroscopy of gate-tunable graphene. *Nature Physics*, vol. 4:627–630, 2008. (Cited on pages 16 and 119.)

[27] S. Jung, G. M. Rutter, N. N. Klimov, D. B. Newell, I. Calizo, A. R. Hight-Walker, N. B. Zhitenev, and J. A. Stroscio. Evolution of microscopic localization in graphene in a magnetic field from scattering resonances to quantum dots. *Nature Physics*, vol. 7:245–251, 2011. (Cited on pages 16, 67, 69, 73, 74, 75, 121, 122, 124, 125, 127, and 249.)

[28] Y. Zhang, V. W. Brar, C. Girit, A. Zettl, and M. F. Crommie. Origin of spatial charge inhomogeneity in graphene. *Nature Physics*, vol. 5:722–726, 2009. (Cited on pages 17, 18, 65, 116, 122, and 124.)

[29] J. Martin, N. Akerman, G. Ulbricht, T. Lohmann, J. H. Smet, K. Von Klitzing, and A. Yacoby. Observation of electron-hole puddles in graphene using a scanning single-electron transistor. *Nat. Phys.*, vol. 4:144–148, 2008. (Cited on pages 17 and 69.)

[30] T. Stauber, N. M. R. Peres, and F. Guinea. Electronic transport in graphene: A semi-classical approach including midgap states. *Phys. Rev. B*, vol. 76:205423, 2007. (Cited on page 17.)

[31] S. Samaddar, I. Yudhistira, S. Adam, H. Courtois, and C. B. Winkelmann. Charge Puddles in Graphene Near the Dirac Point. *Phys. Rev. Lett.*, vol. 116:126804, 2016. (Cited on pages 18, 65, and 122.)

[32] S. Samaddar. *Charge disorder and screening in graphene*. PhD thesis, Université Grenoble Alpes, 2015. (Cited on pages 18, 65, 113, and 122.)

[33] A. W. W. Ludwig, M. P. A. Fisher, R. Shankar, and G. Grinstein. Integer quantum Hall transition: An alternative approach and exact results. *Phys. Rev. B*, vol. 50:7526–7552, 1994. (Cited on page 18.)

[34] N. H. Shon and T. Ando. Quantum Transport in Two-Dimensional Graphite System. *J. Phys. Soc. Jpn.*, vol. 67:2421–2429, 1998. (Cited on page 18.)

[35] R. Decker, Y. Wang, V. W. Brar, W. Regan, H.-Z. Tsai, Q. Wu, W. Gannet, A. Zettl, and M. F. Crommie. Local Electronic Properties of Graphene on a BN Substrate via Scanning Tunneling Microscopy. *Nano Lett.*, vol. 11:2291–2295, 2011. (Cited on pages 18, 65, 116, 119, and 124.)

[36] C. R. Dean, A. F. Young, I. Meric, C. Lee, L. Wang, S. Sorgenfrei, K. Watanabe, T. Taniguchi, P. Kim, K. L. Shepard, and J. Hone. Boron nitride substrates for high-quality graphene electronics. *Nature Nanotechnology*, vol. 5:722–726, 2010. (Cited on pages 19, 31, and 65.)

[37] H. Aoki and M. S. Dresselhaus. *Physics of Graphene*. Springer International Publishing, 2014. (Cited on page 19.)

[38] M. Yankowitz, J. Xue, D. Cormode, J. D. Sanchez-Yamagishi, K. Watanabe, T. Taniguchi, P. Jarillo-Herrero, P. Jacquod, and B. J. LeRoy. Emergence of superlattice Dirac points in graphene on hexagonal boron nitride. *Nature Physics*, vol. 8:382–386, 2012. (Cited on pages 19, 20, and 117.)

[39] J. González, F. Guinea, and M. A. H. Vozmediano. Marginal-Fermi-liquid behavior from two-dimensional Coulomb interaction. *Phys. Rev. B*, vol. 59:R2474, 1999. (Cited on pages 20, 68, and 69.)

[40] S. Das Sarma, E. H. Hwang, and W.-K. Tse. Many-body interaction effects in doped and undoped graphene: Fermi liquid versus non-fermi liquid. *Phys. Rev. B*, vol. 75:121406(R), 2007. (Cited on pages 20 and 69.)

[41] M. Polini, R. Asgari, Y. Barlas, T. Pereg-Barnea, and A. H. MacDonald. Graphene: A pseudochiral Fermi liquid. *Solid State Communications*, vol. 143:58–62, 2007. (Cited on pages 20 and 69.)

[42] F. de Juan, A. G. Grushin, and M. A. H. Vozmediano. Renormalization of Coulomb interaction in graphene: Determining observable quantities. *Phys. Rev. B*, vol. 82:125409, 2010. (Cited on pages 20 and 69.)

[43] V. N. Kotov, B. Uchoa, V. M. Pereira, F. Guinea, and A. H. Castro Neto. Electron-Electron Interactions in Graphene: Currents Status and Perspectives. *Rev. Mod. Phys.*, vol. 84:1067, 2012. (Cited on pages 20 and 69.)

[44] S. Das Sarma and E. H. Hwang. Velocity renormalization and anomalous quasiparticle dispersion in extrinsic graphene. *Phys. Rev. B*, vol. 87:045425, 2013. (Cited on pages 20 and 69.)

[45] J. González, F. Guinea, and M. A. H. Vozmediano. Unconventional Quasiparticle Lifetime in Graphite. *Phys. Rev. Lett.*, vol. 77:3589, 1996. (Cited on page 20.)

[46] D. C. Elias, R. V. Gorbachev, A. S. Mayorov, S. V. Morozov, A. A. Zhukov, P. Blake, L. A. Ponomarenko, I. V. Grigorieva, K. S. Novoselov, F. Guinea, and A. K. Geim. Dirac cones reshaped by interaction effects in suspended graphene. *Nature Physics*, vol. 7:701–704, 2011. (Cited on pages 20, 70, and 71.)

[47] J. Chae, S. Jung, A. F. Young, C. R. Dean, L. Wang, Y. Gao, K. Watanabe, T. Taniguchi, J. Hone, K. L. Shepard, P. Kim, N. B. Zhitenev, and J. A. Stroscio. Renormalization of the Graphene Dispersion Velocity Determined from Scanning Tunneling Sprectroscopy. *Phys. Rev. Lett.*, vol. 109:116802, 2012. (Cited on pages 20, 67, 68, 69, 71, 72, 128, 135, 136, 137, and 251.)

[48] G. L. Yu, R. Jalil, B. Belle, A. S. Mayorov, P. Blake, F. Schedin, S. V. Morozov, L. A. Ponomarenko, F. Chiappini, S. Wiedmann, U. Zeitler, M. I. Katsnelson, A. K. Geim, K. S. Novoselov, and D. C. Elias. Interaction phenomena in graphene seen through quantum capacitance. *PNAS*, vol. 110:3282–3286, 2013. (Cited on pages 20 and 50.)

[49] J. W. McClure. Diamagnetism of Graphite. *Phys. Rev.*, vol. 104:666, 1956. (Cited on page 25.)

[50] Y. Zheng and T. Ando. Hall conductivity of a two-dimensional graphite system. *Phys. Rev. B*, vol. 65:245420, 2002. (Cited on page 27.)

[51] Cohen-Tannoudji, C. and Diu, B. and Laloë, F. *Mécanique quantique I*. Hermann, éditeurs des sciences et des arts, 1973. (Cited on page 27.)

[52] T. Champel and S. Florens. High magnetic field theory for the local density of states in graphene with smooth arbitrary potential landscapes. *Phys. Rev. B*, vol. 82:045421, 2010. (Cited on pages 27, 29, and 132.)

[53] G. Li, A. Luican, and E. Y. Andrei. Scanning Tunneling Spectroscopy of Graphene on Graphite. *Phys. Rev. Lett.*, vol. 102:176804, 2009. (Cited on pages 29, 66, 69, and 88.)

[54] D. L. Miller, K. D. Kubista, G. M. Rutter, M. Ruan, W. A. de Heer, P. N. First, and J. A. Stroscio. Observing the Quantization of Zero Mass Carriers in Graphene. *Science*, vol. 324:924, 2009. (Cited on pages 29 and 66.)

[55] M. Monteverde, C. Ojeda-Aristizabal, R. Weil, K. Bennaceur, M. Ferrier, S. Guéron, C. Glattli, H. Bouchiat, J. N. Fuchs, and D. L. Maslov. Transport and Elastic Scattering Times as probes of the Nature of Impurity Scattering in Single-Layer and Bilayer Graphene. *Phys. Rev. Lett.*, vol. 104:126801, 2010. (Cited on page 30.)

[56] G. Gobsch, D. Schulze, and G. Paasch. Interpretation of Shubnikov-de Haas oscillations and the quantum Hall effect in a heterojunction with two populated subbands. *Phys. Rev. B*, vol. 38:10943, 1988. (Cited on pages 30, 133, and 243.)

[57] K. von Klitzing, G. Dorda, and M. Pepper. New Method for High-Accuracy Determination of the Fine-Structure Constant Based on Quantized Hall Resistance. *Phys. Rev. Lett.*, vol. 45:494, 1980. (Cited on page 31.)

[58] D. C. Tsui, H. L. Stormer, and A. C. Gossard. Two-Dimensional Magnetotransport in the Extreme Quantum Limit. *Phys. Rev. Lett.*, vol. 48:1559, 1982. (Cited on page 31.)

[59] V. P. Gusynin and S. G. Sharapov. Unconventional Integer Quantum Hall Effect in Graphene. *Phys. Rev. Lett.*, vol. 95:146801, 2005. (Cited on page 31.)

[60] Y. Zhang, Z. Jiang, J. P. Small, M. S. Purewal, Y.-W. Tan, M. Fazlollahi, J. D. Chudow, J. A. Jaszczak, H. L. Stormer, and P. Kim. Landau-Level Splitting in Graphene in High Magnetic Fields. *Phys. Rev. Lett.*, vol. 96:136806, 2006. (Cited on pages 31 and 52.)

[61] X. Du, I. Skachko, F. Duerr, A. Luican, and E. Y. Andrei. Fractional quantum Hall effect and insulating phase of Dirac electrons in graphene. *Nature*, vol. 462:192–195, 2009. (Cited on pages 31 and 53.)

[62] A. F. Young, C. R. Dean, L. Wang, H. Ren, P. Cadden-Zimansky, K. Watanabe, T. Taniguchi, J. Hone, K. L. Shepard, and P. Kim. Spin and valley quantum Hall ferromagnetism in graphene. *Nature Physics*, vol. 8:550, 2012. (Cited on pages 31, 48, 49, 50, 53, 174, 177, 190, and 198.)

[63] K. I. Bolotin, F. Ghahari, M. D. Shulman, H. L. Stormer, and P. Kim. Observation of the fractional quantum Hall effect in graphene. *Nature*, vol. 462:196–199, 2009. (Cited on pages 31 and 53.)

[64] C. R. Dean, A. F. Young, P. Cadden-Zimansky, L. Wang, H. Ren, K. Watanabe, T. Taniguchi, P. Kim, J. Hone, and K. L. Shepard. Multicomponent fractional quantum Hall effect in graphene. *Nature Physics*, vol. 7:693–696, 2011. (Cited on page 31.)

[65] M. O. Goerbig. Quantum Hall Effects. *arXiv*:0909.1998, 2009. (Cited on page 31.)

[66] J. Weis and K. von Klitzing. Metrology and microscopic picture of the integer quantum Hall effect. *Phil. Trans. R. Soc. A*, vol. 369:3954–3974, 2011. (Cited on pages 31 and 84.)

[67] D. K. Ferry, S. M. Goodnick, and J. Bird. *Transport in Nanostructures*. Cambridge University Press, 2009. (Cited on page 31.)

[68] T. Ihn. *Semiconductor Nanostructures: Quantum states and electronic transport*. Oxford University Press, 2010. (Cited on page 31.)

[69] Z. F. Ezawa. *Quantum Hall Effects: Recent Theoretical and Experimental Developments*. World Scientific Publishing, 2013. (Cited on pages 31 and 174.)

[70] B. I. Halperin. Quantized Hall conductance, current-carrying edge states, and the existence of extended states in a two-dimensional disordered potential. *Phys. Rev. B*, vol. 25:2185, 1982. (Cited on pages 32, 40, and 42.)

[71] A. H. MacDonald and P. Středa. Quantized Hall effect and edge currents. *Phys. Rev. B*, vol. 29:1616, 1984. (Cited on page 32.)

[72] B. I. Halperin. Theory of the quantized Hall conductance. *Helv. Phys. Acta*, vol. 56:75–102, 1983. (Cited on page 34.)

[73] M. Büttiker. Absence of backscattering in the quantum Hall effect in multiprobe conductors. *Phys. Rev. B*, vol. 38:9375–9389, 1988. (Cited on page 34.)

[74] K. Hashimoto, C. Sohrmann, J. Wiebe, T. Inaoka, F. Meier, Y. Hirayama, R. A. Römer, R. Wiesendanger, and M. Morgenstern. Quantum Hall Transition in Real Space: From Localized to Extended States. *Phys. Rev. Lett.*, vol. 101:256802, 2008. (Cited on page 35.)

[75] D. B. Chklovskii, B. I. Shklovskii, and L. I. Glazman. Electrostatics of edge channels. *Phys. Rev. B*, vol. 46:4026, 1992. (Cited on pages 36, 37, 38, 39, 40, 47, 76, 84, and 147.)

[76] C. W. J. Beenakker. Edge Channels for the Fractional Quantum Hall Effect. *Phys. Rev. Lett.*, vol. 64:216, 1990. (Cited on page 36.)

[77] A. M. Chang. A unified transport theory for the integral and fractional quantum Hall effects: phase boundaries, edge currents, and transmission/reflection probabilities. *Solid State Commun.*, 74:871, 1990. (Cited on page 36.)

[78] D. B. Chklovskii, K. A. Matveev, and B. I. Shklovskii. Ballistic conductance of interacting electrons in the quantum Hall regime. *Phys. Rev. B*, vol. 47:12605–12617, 1993. (Cited on pages 36 and 76.)

[79] K. Lier and R. R. Gerhardts. Self-consistent calculations of edge channels in laterally confined two-dimensional electron systems. *Phys. Rev. B*, vol. 50:7757–7767, 1994. (Cited on page 36.)

[80] A. L. Efros. Density of states of 2D electron gas and width of the plateau of IQHE. *Solid State Commun.*, vol. 65:1281, 1988. (Cited on page 36.)

[81] A. L. Efros. Non-linear screening and the background density of 2DEG states in magnetic field. *Solid State Commun.*, vol. 67:1019, 1988. (Cited on page 36.)

[82] C. Gutiérrez, D. Walkup, F. Ghahari, C. Lewandowski, J. F. Rodriguez-Nieva, K. Watanabe, T. Taniguchi, L. S. Levitov, N. B. Zhitenev, and J. A. Stroscio. Interaction-driven quantum Hall wedding cake-like structures in graphene quantum dots. *Science*, vol. 361:789–794, 2018. (Cited on pages 40, 76, 77, 122, 172, and 249.)

[83] S. Kim, J. Schwenk, D. Walkup, Y. Zeng, F. Ghahari, S. T. Le, M. R. Slot, J. Berwanger, S. R. Blankenship, K. Watanabe, T. Taniguchi, F. J. Giessibl, N. B. Zhitenev, C. R. Dean, and J. A. Stroscio. Edge channels of broken-symmetry quantum Hall states in graphene visualized by atomic force microscopy. *Nature Communications*, vol. 12:2852, 2021. (Cited on pages 40, 84, 85, 88, 89, 141, 146, 174, and 177.)

[84] N. M. R. Peres, F. Guinea, and A. H. Castro Neto. Electronic properties of disordered two-dimensional carbon. *Phys. Rev. B*, vol. 73:125411, 2006. (Cited on pages 41 and 47.)

[85] P. Delplace and G. Montambaux. WKB analysis of edge states in graphene in a strong magnetic field. *Phys. Rev. B*, vol. 82:205412, 2010. (Cited on pages 41, 42, 43, 47, and 157.)

[86] M. Fujita, K. Wakabayashi, K. Nakada, and K. Kusakabe. Peculiar Localized State at Zigzag Graphite Edge. *J. Phys. Soc. Jpn.*, vol. 65:1920–1923, 1996. (Cited on pages 41 and 86.)

[87] K. Nakada, M. Fujita, G. Dresselhaus, and M. S. Dresselhaus. Edge state in graphene ribbons: Nanometer size effect and edge shape dependence. *Phys. Rev. B*, vol. 54:17954, 1996. (Cited on page 41.)

[88] S. Ryu and Y. Hatsugai. Topological Origin of Zero-Energy Edge States in Particle-Hole Symmetric Systems. *Phys. Rev. Lett.*, vol. 89:077002, 2002. (Cited on page 41.)

[89] L. Brey and H. A. Fertig. Electronic states of graphene nanoribbons studied with the Dirac eqation. *Phys. Rev. B*, vol. 73:235411, 2006. (Cited on page 41.)

[90] L. Brey and H. A. Fertig. Edge states and the quantized Hall effect in graphene. *Phys. Rev. B*, vol. 73:195408, 2006. (Cited on pages 42, 157, 159, and 162.)

[91] D. A. Abanin, P. A. Lee, and L. S. Levitov. Spin-Filtered Edge States and Quantum Hall Effect in Graphene. *Phys. Rev. Lett.*, vol. 96:176803, 2006. (Cited on pages 43, 44, 45, 52, 57, and 157.)

[92] D. A. Abanin, P. A. Lee, and L. S. Levitov. Charge and spin transport at the quantum Hall edge of graphene. *Solid State Communications*, vol. 143:77–85, 2007. (Cited on pages 43, 44, 45, 46, 47, 57, 86, 147, 157, and 158.)

[93] D. P. DiVincenzo and E. J. Mele. Self-consistent effective-mass theory for intralayer screening in graphite intercalation compounds. *Phys. Rev. B*, vol. 29:1685, 1984. (Cited on page 43.)

[94] A. H. Castro Neto, F. Guinea, and N. M. R. Peres. Edge and surface states in the quantum Hall effect in graphene. *Phys. Rev. B*, vol. 73:205408, 2006. (Cited on page 47.)

[95] N. M. R. Peres, A. H. Castro Neto, and F. Guinea. Dirac fermion confinement in graphene. *Phys. Rev. B*, vol. 73:241403(R), 2006. (Cited on page 47.)

[96] V. P. Gusynin, V. A. Miransky, S. G. Sharapov, and I. A. Shovkovy. Edge states, mass and spin gaps, and quantum Hall effect in graphene. *Phys. Rev. B*, vol. 77:205409, 2008. (Cited on page 47.)

[97] P. Delplace. *États de bord et cônes de Dirac dans des cristaux bidimensionnels*. PhD thesis, Université Paris Sud - Paris XI, 2010. (Cited on page 47.)

[98] Y. J. Song, A. F. Otte, Y. Kuk, Y. Hu, D. B. Torrance, P. N. First, W. A. de Heer, H. Min, S. Adam, M. D. Stiles, A. H. MacDonald, and J. A. Stroscio. High-resolution tunnelling spectroscopy of a graphene quartet. *Nature*, vol. 467:185–189, 2010. (Cited on pages 48, 66, 69, 88, and 89.)

[99] J. F. Janak. g factor of the Two-Dimensional Interacting Electron Gas. *Phys. Rev.*, vol. 178:1416–1418, 1969. (Cited on page 49.)

[100] J. Alicea and M. P. A. Fisher. Graphene integer quantum Hall effect in the ferromagnetic and paramagnetic regimes. *Phys. Rev. B*, vol. 74:075422, 2006. (Cited on page 49.)

[101] M. Kharitonov. Phase diagram for the $\nu = 0$ quantum Hall state in monolayer graphene. *Phys. Rev. B*, vol. 85:155439, 2012. (Cited on pages 49, 53, 54, 55, 57, 182, 186, 190, and 196.)

[102] C.-Y. Hou, C. Chamon, and C. Mudry. Deconfined fractional electric charges in graphene at high magnetic fields. *Phys. Rev. B*, vol. 81:075427, 2010. (Cited on pages 49 and 177.)

[103] K. Nomura and A. H. MacDonald. Quantum Hall Ferromagnetism in Graphene. *Phys. Rev. Lett.*, vol. 96:256602, 2006. (Cited on pages 50 and 51.)

[104] K. Yang, S. Das Sarma, and A. H. MacDonald. Collective modes and skyrmion excitations in graphene SU(4) quantum Hall ferromagnets. *Phys. Rev. B*, vol. 74:075423, 2006. (Cited on page 50.)

[105] E. Stoner. Collective electron ferromagnetism. *Proc. R. Soc. London, Ser. A*, vol. 165:372, 1938. (Cited on page 50.)

[106] H. A. Fertig and L. Brey. Luttinger Liquid at the Edge of Undoped Graphene in a Strong Magnetic Field. *Phys. Rev. Lett.*, vol. 97:116805, 2006. (Cited on page 52.)

[107] A. F. Young, J. D. Sanchez-Yamagishi, B. Hunt, S. H. Choi, K. Watanabe, T. Taniguchi, R. C. Ashoori, and P. Jarillo-Herrero. Tunable symmetry breaking and helical edge transport in a graphene quantum spin Hall state. *Nature*, vol. 505:528–532, 2014. (Cited on pages 52, 59, 60, 164, 167, 176, 177, and 190.)

[108] M. Kharitonov, S. Juergens, and B. Trauzettel. Interplay of topology and interactions in quantum Hall topological insulators: U(1) symmetry, tunable Luttinger liquid, and interaction-induced phase transitions. *Phys. Rev. B*, vol. 94:035146, 2016. (Cited on pages 52, 54, 59, 193, and 197.)

[109] D. A. Abanin, K. S. Novoselov, U. Zeitler, P. A. Lee, A. K. Geim, and L. S. Levitov. Dissipative Quantum Hall Effect in Graphene near the Dirac Point. *Phys. Rev. Lett.*, vol. 98:196806, 2007. (Cited on pages 52 and 53.)

[110] J. G. Checkelsky, L. Li, and N. P. Ong. Zero-Energy State in Graphene in a High Magnetic Field. *Phys. Rev. Lett.*, vol. 100:206801, 2008. (Cited on pages 53 and 177.)

[111] J. G. Checkelsky, L. Li, and N. P. Ong. Divergent resistance at the Dirac point in graphene: Evidence for a transition in a high magnetic field. *Phys. Rev. B*, vol. 79:115434, 2009. (Cited on pages 53 and 177.)

[112] M. O. Goerbig, R. Moessner, and B. Douçot. Electron interactions in graphene in a strong magnetic field. *Phys. Rev. B*, vol. 74:161407(R), 2006. (Cited on pages 54 and 174.)

[113] J. Jung and A. H. MacDonald. Theory of the magnetic-field-induced insulator in neutral graphene sheets. *Phys. Rev. B*, vol. 80:235417, 2009. (Cited on page 54.)

[114] K. Nomura, S. Ryu, and D.-H. Lee. Field-Induced Kosterlitz-Thouless Transition in the $N = 0$ Landau Level of Graphene. *Phys. Rev. Lett.*, vol. 103:216801, 2009. (Cited on pages 54, 176, and 177.)

[115] L. Zhang, J. Camacho, H. Cao, Y. P. Chen, M. Khodas, D. E. Kharzeev, A. M. Tsvelik, T. Valla, and I. A. Zaliznyak. Breakdown of the $n = 0$ quantum Hall state in graphene: Two insulating regimes. *Phys. Rev. B*, vol. 80:241412(R), 2009. (Cited on page 54.)

[116] M. Kharitonov. Edge excitations of the canted antiferromagnetic phase of the $\nu = 0$ quantum Hall state in graphene: A simplified analysis. *Phys. Rev. B*, vol. 86:075450, 2012. (Cited on pages 54, 57, 58, and 176.)

[117] D. M. Basko and I. L. Aleiner. Interplay of Coulomb and electron-phonon interactions in graphene. *Phys. Rev. B*, vol. 77:041409(R), 2008. (Cited on page 54.)

[118] J. Atteia, Y. Lian, and M. O. Goerbig. Skyrmion zoo in graphene at charge neutrality in a strong magnetic field. *Phys. Rev. B*, vol. 103:035403, 2021. (Cited on pages 56, 59, 193, 197, and 201.)

[119] A. Knothe and T. Jolicoeur. Edge structure of graphene monolayers in the $\nu = 0$ quantum Hall state. *Phys. Rev. B*, vol. 92:165110, 2015. (Cited on pages 59, 157, and 176.)

[120] A. H. Knothe. *Quantum Hall Ferromagnetism in Multicomponent Systems*. PhD thesis, Université Paris-Saclay; Albert-Ludwigs-Universität, 2017. (Cited on page 59.)

[121] T. Jolicoeur and B. Pandey. Quantum Hall skyrmions at $\nu = 0, \pm 1$ in monolayer graphene. *Phys. Rev. B*, vol. 100:115422, 2019. (Cited on page 59.)

[122] L. Veyrat, C. Déprez, A. Coissard, X. Li, F. Gay, K. Watanabe, T. Taniguchi, Z. Han, B. A. Piot, H. Sellier, and B. Sacépé. Helical quantum Hall phase in graphene on $SrTiO_3$. *Science*, vol. 367:781–786, 2020. (Cited on pages 59, 61, 62, 63, 119, 125, 164, 167, 174, 175, 176, 190, 195, 197, and 198.)

[123] A. Roth, C. Brüne, H. Buhmann, L. W. Molenkamp, J. Maciejko, X.-L. Qi, and S.-C. Zhang. Nonlocal Transport in the Quantum Spin Hall State. *Science*, vol. 325:294–297, 2009. (Cited on page 60.)

[124] T. Sakudo and H. Unoki. Dielectric Properties of $SrTiO_3$ at Low Temperatures. *Phys. Rev. Lett.*, vol. 26:851–853, 1971. (Cited on pages 61 and 121.)

[125] K. A. Müller and H. Burkard. $SrTiO_3$: An intrinsic quantum paraelectric below 4 K. *Phys. Rev. B*, vol. 19:3593, 1979. (Cited on pages 61 and 121.)

[126] J. Hemberger, M. Nicklas, R. Viana, P. Lunkenheimer, A. Loidl, and R. Böhmer. Quantum paraelectric and induced ferroelectric states in $SrTiO_3$. *J. Phys.: Condens. Matter*, vol. 8:4673–4690, 1996. (Cited on pages 61 and 121.)

[127] N. J. G. Couto, B. Sacépé, and A. F. Morpurgo. Transport through Graphene on $SrTiO_3$. *Phys. Rev. Lett.*, vol. 107:225501, 2011. (Cited on page 61.)

[128] L. Wang, I. Meric, P. Y. Huang, Q. Gao, Y. Gao, H. Tran, T. Taniguchi, K. Watanabe, L. M. Campos, D. A. Muller, J. Guo, P. Kim, J. Hone, K. L. Shepard, and C. R. Dean. One-Dimensional Electrical Contact to a Two-Dimensional Material. *Science*, vol. 342:614–617, 2013. (Cited on page 61.)

[129] J. D. Jackson. *Classical electrodynamics*. Wiley, New York, 1975. (Cited on page 61.)

[130] P. Barcellona, R. Bennett, and S. Y. Buhmann. Manipulating the Coulomb interaction: a Green's function perspective. *J. Phys. Commun.*, vol. 2:035027, 2018. (Cited on page 61.)

[131] M. Ishigami, J. H. Chen, W. G. Cullen, M. S. Fuhrer, and E. D. Williams. Atomic Structure of Graphene on SiO_2. *Nano Lett.*, vol. 7:1643–1648, 2007. (Cited on page 65.)

[132] V. W. Brar, Y. Zhang, Y. Yayon, T. Ohta, J. L. McChesney, A. Bostwick, E. Rotenberg, K. Horn, and M. F. Crommie. Scanning tunneling spectroscopy of inhomogeneous electronic structure in monolayer and bilayer graphene on SiC. *Appl. Phys. Lett.*, vol. 91:122102, 2007. (Cited on pages 65 and 119.)

[133] V. W. Brar. *Scanning Tunneling Spectroscopy of Graphene and Magnetic Nanostructures*. PhD thesis, University of California, Berkeley, 2010. (Cited on page 65.)

[134] E. Stolyarova, K. Taeg Rim, S. Ryu, J. Maultzsch, P. Kim, L. E. Brus, T. F. Heinz, M. S. Hybertsen, and G. W. Flynn. High-resolution scanning tunneling microscopy imaging of mesoscopic graphene sheets on an insulating surface. *PNAS*, vol. 104:9209–9212, 2007. (Cited on page 65.)

[135] G. M. Rutter, J. N. Crain, N. P. Guisinger, T. Li, P. N. First, and J. A. Stroscio. Scattering and Interference in Epitaxial Graphene. *Science*, vol. 317:219–222, 2007. (Cited on pages 65 and 121.)

[136] J. Sabio, C. Seoánez, S. Fratini, F. Guinea, A. H. Castro Neto, and F. Sols. Electrostatic interactions between graphene layers and their environment. *Phys. Rev. B*, vol. 77:195409, 2008. (Cited on pages 65, 72, 73, and 82.)

[137] V. Geringer, M. Liebmann, T. Echtermeyer, S. Runte, M. Schmidt, R. Rückamp, M. C. Lemme, and M. Morgenstern. Intrinsic and extrinsic corrugation of monolayer graphene deposited on SiO_2. *Phys. Rev. Lett.*, vol. 102:076102, 2009. (Cited on page 65.)

[138] A. Deshpande, W. Bao, F. Miao, C. N. Lau, and B. J. LeRoy. Spatially resolved spectroscopy of monolayer graphene on SiO_2. *Phys. Rev. B*, vol. 79:205411, 2009. (Cited on pages 65 and 124.)

[139] S. Adam, S. Jung, N. N. Klimov, N. B. Zhitenev, J. A. Stroscio, and M. D. Stiles. Mechanism for puddle formation in graphene. *Phys. Rev. B*, vol. 84:235421, 2011. (Cited on page 65.)

[140] J. Xue, J. Sanchez-Yamagishi, D. Bulmash, P. Jacquod, A. Deshpande, K. Watanabe, T. Taniguchi, P. Jarillo-Herrero, and B. J. LeRoy. Scanning tunnelling microscopy and spectroscopy of ultra-flat graphene on hexagonal boron nitride. *Nature Materials*, vol. 10:282–285, 2011. (Cited on pages 65, 123, and 124.)

[141] D. Wong, J. Velasco Jr, L. Ju, J. Lee, S. Kahn, H.-Z. Tsai, C. Germany, T. Taniguchi, K. Watanabe, A. Zettl, F. Wang, and M. F. Crommie. Characterization and manipulation of individual defects in insulating hexagonal boron nitride using scanning tunnelling microscopy. *Nature Nanotechnology*, vol. 10:949–953, 2015. (Cited on page 65.)

[142] G. Li and E. Y. Andrei. Observation of Landau levels of Dirac fermions in graphite. *Nature Physics*, vol. 3:623–627, 2007. (Cited on page 66.)

[143] A. Luican, G. Li, and E. Y. Andrei. Scanning tunneling microscopy and spectroscopy of graphene layers on graphite. *Solid State Communications*, vol. 149:1151–1156, 2009. (Cited on page 66.)

[144] L.-J. Yin, J.-B. Li, S.-Y. Qiao, J.-C. Nie, and L. He. Landau quantization in graphene monolayer, Bernal bilayer, and Bernal trilayer on graphite surface. *Phys. Rev. B*, vol. 91:115405, 2015. (Cited on pages 66 and 69.)

[145] A. Luican, G. Li, and E. Y. Andrei. Quantized Landau level spectrum and its density dependence in graphene. *Phys. Rev. B*, vol. 83:041405(R), 2011. (Cited on pages 67, 68, 69, 70, 126, and 128.)

[146] O. E. Dial, R. C. Ashoori, L. N. Pfeiffer, and K. W. West. High-resolution spectroscopy of two-dimensional electron systems. *Nature*, vol. 448:176–179, 2007. (Cited on pages 67, 68, and 169.)

[147] V. G. Popov. Self-consistent equilibrium of a two-dimensional electron system with a reservoir in a quantizing magnetic field: Analytical approach. *Phys. Rev. B*, vol. 73:125310, 2006. (Cited on page 67.)

[148] T. Ando and Y. Uemura. Theory of Oscillatory g factor in an MOS Inversion Layer under Strong Magnetic Fields. *J. Phys. Soc. Jpn.*, vol. 37:1044, 1974. (Cited on page 68.)

[149] A. H. MacDonald, H. C. A. Oji, and K. L. Liu. Thermodynamic properties of an interacting two-dimensional electron gas in a strong magnetic field. *Phys. Rev. B*, vol. 34:2681–2689, 1986. (Cited on page 68.)

[150] I. L. Aleiner and L. I. Glazman. Two-dimensional electron liquid in a weak magnetic field. *Phys. Rev. B*, vol. 52:11296, 1995. (Cited on page 68.)

[151] A. A. Sokolik, A. D. Zabolotskiy, and Y. E. Lozovik. Many-body effects if Coulomb interaction on Landau levels in graphene. *Phys. Rev. B*, vol. 95:125402, 2017. (Cited on pages 69 and 70.)

[152] A. Luican-Mayer, M. Kharitonov, G. Li, C.-P. Lu, I. Skachko, A.-M. Gonçalves, K. Watanabe, T. Taniguchi, and E. Y. Andrei. Screening Charged Impurities and Lifting the Orbital Degeneracy in Graphene by Populating Landau levels. *Phys. Rev. Lett.*, vol. 112:036804, 2014. (Cited on pages 69, 72, 73, and 247.)

[153] W.-X. Wang, L.-J. Yin, J.-B. Qiao, T. Cai, S.-Y. Li, R.-F. Dou, J.-C. Nie, X. Wu, and L. He. Atomic resolution imaging of the two-component Dirac-Landau levels in a gapped graphene monolayer. *Phys. Rev. B*, vol. 92:165420, 2015. (Cited on pages 69 and 90.)

[154] L. A. Ponomarenko, R. Yang, R. V. Gorbachev, P. Blake, A. S. Mayorov, K. S. Novoselov, M. I. Katsnelson, and A. K. Geim. Density of States and Zero Landau Level Probed through Capacitance of Graphene. *Phys. Rev. Lett.*, vol. 105:136801, 2010. (Cited on page 69.)

[155] M. L. Sadowski, G. Martinez, M. Potemski, C. Berger, and W. A. de Heer. Landau Level Spectroscopy of Ultrathin Graphite Layers. *Phys. Rev. Lett.*, vol. 97:266405, 2006. (Cited on page 69.)

[156] M. Orlita, C. Faugeras, P. Plochocka, P. Neugebauer, G. Martinez, D. K. Maude, A.-L. Barra, M. Sprinkle, C. Berger, W. A. de Heer, and M. Potemski. Approaching the Dirac Point in High-Mobility Multilayer Epitaxial Graphene. *Phys. Rev. Lett.*, vol. 101:267601, 2008. (Cited on page 69.)

[157] Z. Jiang, E. A. Henriksen, L. C. Tung, Y.-J. Wang, M. E. Schwartz, M. Y. Han, P. Kim, and H. L. Stormer. Infrared Spectroscopy of Landau Levels in Graphene. *Phys. Rev. Lett.*, vol. 98:197403, 2007. (Cited on page 70.)

[158] Z.-G. Chen, Z. Shi, W. Yang, X. Li, Y. Lai, H. Yan, F. Wang, G. Zhang, and Z. Li. Observation of an intrinsic bandgap and Landau level renormalization in graphene/boron-nitride heterostructures. *Nature Communications*, vol. 5:4461, 2014. (Cited on page 70.)

[159] C. Hwang, D. A. Siegel, S.-K. Mo, W. Regan, A. Ismach, Y. Zhang, A. Zettl, and A. Lanzara. Fermi velocity engineering in graphene by substrate modification. *Scientific Reports*, vol. 2:590, 2012. (Cited on page 70.)

[160] C. Faugeras, S. Berciaud, P. Leszczynski, Y. Henni, K. Nogajewski, M. Orlita, T. Taniguchi, K. Watanabe, C. Forsythe, P. Kim, R. Jalil, A. K. Geim, D. M. Basko, and M. Potemski. Landau Level Spectroscopy of Electron-Electron Interactions in Graphene. *Phys. Rev. Lett.*, vol. 114:126804, 2015. (Cited on page 70.)

[161] Y. E. Lozovik, A. A. Sokolik, and A. D. Zabolotskiy. Quantum capacitance and compressibility of graphene: The role of Coulomb interactions. *Phys. Rev. B*, vol. 91:075416, 2015. (Cited on page 71.)

[162] J. Sonntag, S. Reichardt, L. Wirtz, B. Beschoten, M. I. Katsnelson, F. Libisch, and C. Stampfer. Impact of Many-Body Effects on Landau Levels in Graphene. *Phys. Rev. Lett.*, vol. 120:187701, 2018. (Cited on page 71.)

[163] A. A. Sokolik and Y. E. Lozovik. Many-body filling factor dependent renormalization of Fermi velocity in graphene in strong magnetic field. *Phys. Rev. B*, vol. 99:085423, 2019. (Cited on pages 71, 72, and 138.)

[164] B. J. Russel, B. Zhou, T. Taniguchi, K. Watanabe, and E. A. Henriksen. Many-Particle Effects in the Cyclotron Resonance of Encapsulated Monolayer Graphene. *Phys. Rev. Lett.*, vol. 120:047401, 2018. (Cited on pages 71 and 72.)

[165] T. Ando, A. B. Fowler, and F. Stern. Electronic properties of two-dimensional systems. *Rev. Mod. Phys.*, vol. 54:437, 1982. (Cited on page 72.)

[166] O. V. Gamayun, E. V. Gorbar, and V. P. Gusynin. Magnetic field driven instability of a charged center in graphene. *Phys. Rev. B*, vol. 83:235104, 2011. (Cited on page 72.)

[167] Y. Zhang, Y. Barlas, and K. Yang. Coulomb impurity under magnetic field in graphene: A semiclassical approach. *Phys. Rev. B*, vol. 85:165423, 2012. (Cited on pages 72 and 247.)

[168] L. Veyrat, A. Jordan, K. Zimmermann, F. Gay, K. Watanabe, T. Taniguchi, H. Sellier, and B. Sacépé. Low-Magnetic-Field Regime of a Gate-Defined Constriction in High-Mobility Graphene. *Nano Lett.*, vol. 19:635–642, 2019. (Cited on page 73.)

[169] G. Giavaras, P. A. Maksym, and M. Roy. Magnetic field induced confinement-deconfinement transition in graphene quantum dots. *J. Phys.: Condens. Matter*, vol. 21:102201, 2009. (Cited on page 73.)

[170] G. Giavaras and F. Nori. Tunable quantum dots in monolayer graphene. *Phys. Rev. B*, vol. 85:165446, 2012. (Cited on page 73.)

[171] L. P. Kouwenhoven, Ch. M. Marcus, P. L. McEuen, S. Tarucha, R. M. Westervelt, and N. S. Wingreen. Electron transport in quantum dots. In *Mesoscopic Electron Transport*. Springer Netherlands, 1997. (Cited on pages 74 and 76.)

[172] M. M. Fogler, E. I. Levin, and B. I. Shklovskii. Chemical potential and magnetization of a Coulomb island. *Phys. Rev. B*, vol. 49:13767, 1994. (Cited on page 76.)

[173] J. Lee, D. Wong, J. Velasco, J. F. Rodriguez-Nieva, S. Kahn, H.-Z. Tsai, T. Taniguchi, K. Watanabe, A. Zettl, F. Wang, L. S. Levotov, and M. F. Crommie. Imaging electrostatically confined Dirac fermions in graphene quantum dots. *Nature Physics*, vol. 12:1032, 2016. (Cited on pages 76 and 122.)

[174] J. Velasco, L. Ju, D. Wong, S. Kahn, J. Lee, H.-Z. Tsai, C. Germany, S. Wickenburg, J. Lu, T. Taniguchi, K. Watanabe, A. Zettl, F. Wang, and M. F. Crommie. Nanoscale Control of Rewriteable Doping Patterns in Pristine Graphene/Boron Nitride Heterostructures. *Nano Lett.*, vol. 16:1620, 2016. (Cited on page 76.)

[175] F. Ghahari, D. Walkup, Ch. Gutiérrez, J. F. Rodriguez-Nieva, Y. Zhao, J. Wyrick, F. D. Natterer, W. G. Cullen, K. Watanabe, T. Taniguchi, L. S. Levitov, N. B. Zhitenev, and J. A. Stroscio. An on/off Berry phase switch in circular graphene resonators. *Science*, vol. 356:845, 2017. (Cited on pages 76 and 122.)

[176] D. Walkup, F. Ghahari, C. Gutiérrez, K. Watanabe, T. Taniguchi, N. B. Zhitenev, and J. A. Stroscio. Tuning single-electron charging and interactions between compressible Landau level islands in graphene. *Phys. Rev. B*, vol. 101:035428, 2020. (Cited on pages 76, 77, 78, and 249.)

[177] P. L. McEuen, E. B. Foxman, J. Kinaret, U. Meirav, M. A. Kastner, N. S. Wingreen, and S. J. Wind. Self-consistent addition spectrum of a Coulomb island in the quantum Hall regime. *Phys. Rev. B*, vol. 45:11419(R), 1992. (Cited on page 76.)

[178] R. C. Ashoori. Electrons in artificial atoms. *Nature*, vol. 379:413, 1996. (Cited on page 76.)

[179] Y. Zhao, J. Wyrick, F. D. Natterer, J. F. Rodriguez-Nieva, C. Lewandowski, K. Watanabe, T. Taniguchi, L. S. Levitov, N. B. Zhitenev, and J. A. Stroscio. Creating and probing electron whispering-gallery modes in graphene. *Science*, vol. 348:672–675, 2015. (Cited on pages 76, 80, and 122.)

[180] N. M. Freitag, L. A. Chizhova, P. Nemes-Incze, C. R. Woods, R. V. Gorbachev, Y. Cao, A. K. Geim, K. S. Novoselov, J. Burgdörfer, F. Libisch, and M. Morgenstern. Electrostatically Confined Monolayer Graphene Quantum Dots with Orbital and Valley Splittings. *Nano Lett.*, vol. 16:5798–5805, 2016. (Cited on page 80.)

[181] N. M. Freitag, T. Reisch, L. A. Chizhova, P. Nemes-Incze, C. Holl, C. R. Woods, R. V. Gorbachev, Y. Cao, A. K. Geim, K. S. Novoselov, J. Burgdörfer, F. Libisch, and M. Morgenstern. Large tunable valley splitting in edge-free graphene quantum dots on boron nitride. *Nature Nanotechnology*, vol. 13:392–397, 2018. (Cited on page 81.)

[182] I. P. Batra, N. García, H. Rohrer, H. Salemink, E. Stoll, and S. Ciraci. A study of graphite surface with STM and electronic structure calculations. *Surface Science*, vol. 181:126–138, 1987. (Cited on page 82.)

[183] D. Moldovan, M. Ramezani Masir, and F. M. Peeters. Electronic states in a graphene flake strained by a Gaussian bump. *Phys. Rev. B*, vol. 88:035446, 2013. (Cited on page 82.)

[184] M. Neek-Amal, L. Covaci, Kh. Shakouri, and F. M. Peeters. Electronic structure of a hexagonal graphene flake subjected to triaxial stress. *Phys. Rev. B*, vol. 88:115428, 2013. (Cited on page 82.)

[185] R. Carrilo-Bastos, D. Faria, A. Latgé, F. Mireless, and N. Sandler. Gaussian deformations in graphene ribbons: Flowers and confinement. *Phys. Rev. B*, vol. 90:041411(R), 2014. (Cited on page 82.)

[186] K.-I. Sasaki and R. Saito. Pseudospin and Deformation-Induced Gauge Field in Graphene. *Prog. Theor. Phys. Suppl.*, vol. 176:253–278, 2008. (Cited on page 82.)

[187] A. Georgi, P. Nemes-Incze, R. Carrillo-Bastos, D. Faria, S. V. Kusminskiy, D. Zhai, M. Schneider, D. Subramaniam, T. Mashoff, N. M. Freitag, M. Liebmann, M. Pratzer, L. Wirtz, C. R. Woods, R. V. Gorbachev, Y. Cao, K. S. Novoselov, N. Sandler, and M. Morgenstern. Tuning the Pseudospin Polarization of Graphene by a Pseudomagnetic Field. *Nano Lett.*, vol. 17, 4:2240–2245, 2017. (Cited on pages 82, 83, 144, and 240.)

[188] N. Levy, S. A. Burke, K. L. Meaker, M. Panlasigui, A. Zettl, F. Guinea, A. H. Castro Neto, and M. F. Crommie. Strain-Induced Pseudo-Magnetic Fields Greater Than 300 Tesla in Graphene Nanobubbles. *Science*, vol. 329:544–547, 2010. (Cited on page 82.)

[189] V. M. Pereira and A. H. Castro Neto. Strain Engineering of Graphene's Electronic Structure. *Phys. Rev. Lett.*, vol. 103:046801, 2009. (Cited on page 82.)

[190] S. Zhu, J. A. Stroscio, and T. Li. Programmable Extreme Pseudomagnetic Fields in Graphene by a Uniaxial Stretch. *Phys. Rev. Lett.*, vol. 115:245501, 2015. (Cited on page 82.)

[191] F. Guinea, M. I. Katsnelson, and A. K. Geim. Energy gaps and a zero-field quantum Hall effect in graphene by strain engineering. *Nature Physics*, vol. 6:30–33, 2010. (Cited on page 83.)

[192] N. N. Klimov, S. Jung, S. Zhu, T. Li, C. A. Wright, S. D. Solares, D. B. Newell, N. B. Zhitenev, and J. A. Stroscio. Electromechanical Properties of Graphene Drumheads. *Science*, vol. 336:1557–1561, 2012. (Cited on page 83.)

[193] S. Zhu, Y. Huang, N. N. Klimov, D. B. Newell, N. B. Zhitenev, J. A. Stroscio, S. D. Solares, and T. Li. Pseudomagnetic fields in a locally strained graphene drumhead. *Phys. Rev. B*, vol. 90:075426, 2014. (Cited on page 83.)

[194] K.-K. Bai, Y.-C. Wei, J.-B. Qiao, S.-Y. Li, L.-J. Yin, W. Yan, J.-C. Nie, and L. He. Detecting giant electron-hole asymmetry in a graphene monolayer generated by strain and charged-defect scattering via Landau level spectroscopy. *Phys. Rev. B*, vol. 92:121405(R), 2015. (Cited on page 83.)

[195] S.-Y. Li, K.-K. Bai, L.-J. Yin, J.-B. Qiao, W.-X. Wang, and L. He. Observation of unconventional splitting of Landau levels in strained graphene. *Phys. Rev. B*, vol. 92:245302, 2015. (Cited on page 83.)

[196] S.-Y. Li, Y. Su, Y.-N. Ren, and L. He. Valley Polarization and Inversion in Strained Graphene via Pseudo-Landau Levels, Valley Splitting of Real Landau Levels, and Confined States. *Phys. Rev. Lett.*, vol. 124:106802, 2020. (Cited on page 83.)

[197] A. Yacoby, H. F. Hess, T. A. Fulton, L. N. Pfeiffer, and K. W. West. Electrical imaging of the quantum Hall state. *Solid State Commun.*, vol. 111:1–13, 1999. (Cited on page 84.)

[198] G. Finkelstein, P. I. Glicofridis, S. H. Tessmer, and R. C. Ashoori. Imaging of low-compressibility strips in the quantum Hall liquid. *Phys. Rev. B*, vol. 61:R16323, 2000. (Cited on page 84.)

[199] P. Weitz, E. Ahlswede, J. Weis, K. von Klitzing, and K. Eberl. Hall-potential investigations under quantum Hall conditions using scanning force microscopy. *Physica E*, vol. 6:247–250, 2000. (Cited on page 84.)

[200] H. Ito, K. Furuya, Y. Shibata, S. Kashiwaya, M. Yamaguchi, T. Akazaki, H. Tamura, Y. Ootuka, and S. Nomura. Near-Field Optical Mapping of Quantum Hall Edge States. *Phys. Rev. Lett.*, vol. 107:256803, 2011. (Cited on page 84.)

[201] K. Lai, W. Kundhikanjana, M. A. Kelly, Z.-X. Shen, J. Shabani, and M. Shayegan. Imaging of Coulomb-Driven Quantum Hall Edge States. *Phys. Rev. Lett.*, vol. 107:176809, 2011. (Cited on page 84.)

[202] M. E. Suddards, A. Baumgartner, M. Henini, and C. J. Mellor. Scanning capacitance imaging of compressible and incompressible quantum Hall effect edge strips. *New Journal of Physics*, vol. 14:083015, 2012. (Cited on page 84.)

[203] J. R. Williams, L. DiCarlo, and C. M. Marcus. Quantum Hall Effect in a Gate-Controlled p-n Junction of Graphene. *Science*, vol. 317:638–641, 2007. (Cited on page 85.)

[204] B. Özyilmaz, P. Jarillo-Herrero, D. Efetov, D. A. Abanin, L. S. Levitov, and P. Kim. Electronic Transport and Quantum Hall Effect in Bipolar Graphene p-n-p Junctions. *Phys. Rev. Lett.*, vol. 99:166804, 2007. (Cited on page 85.)

[205] N. N. Klimov, S. T. Le, J. Yan, P. Agnihotri, E. Comfort, J. U. Lee, D. B. Newell, and C. A. Richter. Edge-state transport in graphene p-n junctions in the quantum Hall regime. *Phys. Rev. B*, vol. 92:241301(R), 2015. (Cited on page 85.)

[206] A. Uri, Y. Kim, K. Bagani, C. K. Lewandowski, S. Grover, N. Auerbach, E. O. Lachman, Y. Myasoedov, T. Taniguchi, K. Watanabe, J. Smet, and E. Zeldov. Nanoscale imaging of equilibrium quantum Hall edge currents and of the magnetic monopole response in graphene. *Nature Physics*, vol. 16:164–170, 2020. (Cited on page 85.)

[207] M. Nonnenmacher, M. P. O'Boyle, and Wickramasinghe. Kelvin probe force microscopy. *Appl. Phys. Lett.*, vol. 58:2921, 1991. (Cited on pages 85, 88, and 217.)

[208] W. Melitz, J. Shen, A. C. Kummel, and S. Lee. Kelvin probe force microscopy and its application. *Surface Science Reports*, vol. 66:1–27, 2011. (Cited on pages 85, 88, and 217.)

[209] G. Li, A. Luican-Mayer, D. Abanin, L. Levitov, and E. Y. Andrei. Evolution of Landau levels into edge states in graphene. *Nature Communications*, vol. 4:1744, 2013. (Cited on pages 85, 86, 87, 90, 141, 146, 152, 157, and 166.)

[210] Y. Kobayashi, K.-I. Fukui, T. Enoki, and K. Kusakabe. Edge state of hydrogen-terminated graphite edges investigated by scanning tunneling microscopy. *Phys. Rev. B*, vol. 73:125415, 2006. (Cited on page 85.)

[211] Y. Niimi, T. Matsui, H. Kambara, K. Tagami, M. Tsukada, and H. Fukuyama. Scanning tunneling microscopy and spectroscopy of the electronic local density of states of graphite surfaces near monoatomic step edges. *Phys. Rev. B*, vol. 73:085421, 2006. (Cited on pages 85 and 86.)

[212] L.-J. Yin, Y. Zhang, J.-B. Qiao, S.-Y. Li, and L. He. Experimental observation of surface states and Landau levels bending in bilayer graphene. *Phys. Rev. B*, vol. 93:125422, 2016. (Cited on page 87.)

[213] P. G. Silvestrov and K. B. Efetov. Charge accumulation at the boundaries of a graphene strip induced by a gate voltage: Electrostatic approach. *Phys. Rev. B*, vol. 77:155436, 2008. (Cited on pages 87, 152, 156, and 166.)

[214] A. Marguerite, J. Birkbeck, A. Aharon-Steinberg, D. Halbertal, K. Bagani, I. Marcus, Y. Myasoedov, A. K. Geim, D. J. Perello, and E. Zeldov. Imaging work and dissipation in the quantum Hall state in graphene. *Nature*, vol. 575:628–633, 2019. (Cited on pages 87 and 156.)

[215] E. A. Henriksen, P. Cadden-Zimansky, Z. Jiang, Z. Q. Li, L.-C. Tung, M. E. Schwartz, M. Takita, Y.-J. Wang, P. Kim, and H. L. Stormer. Interaction-Induced Shift of the Cyclotron Resonance of Graphene Using Infrared Spectroscopy. *Phys. Rev. Lett.*, vol. 104:067404, 2010. (Cited on page 88.)

[216] S.-Y. Li, Y. Zhang, L.-J. Yin, and L. He. Scanning tunneling microscope study of quantum Hall isospin ferromagnetic states in the zero Landau level in a graphene monolayer. *Phys. Rev. B*, vol. 100:085437, 2019. (Cited on pages 88, 90, and 178.)

[217] I. Keren, T. Dvir, A. Zalic, A. Iluz, D. LeBoeuf, K. Watanabe, T. Taniguchi, and H. Steinberg. Quantum-dot assisted spectroscopy of degeneracy-lifted Landau levels in graphene. *Nature Communications*, vol. 11:3408, 2020. (Cited on page 88.)

[218] Y. Zhang, Q.-Q. Guo, S.-Y. Li, and L. He. Nanoscale probing of broken-symmetry states in graphene induced by individual atomic impurities. *Phys. Rev. B*, vol. 101:155424, 2020. (Cited on page 88.)

[219] A. A. Zibrov, E. M. Spanton, H. Zhou, C. Kometter, T. Taniguchi, K. Watanabe, and A. F. Young. Even-denominator fractional quantum Hall states at an isospin transition in monolayer graphene. *Nature Physics*, vol. 14:930–935, 2018. (Cited on pages 88 and 89.)

[220] R. Ribeiro-Palau, C. Zhang, K. Watanabe, T. Taniguchi, J. Hone, and C. R. Dean. Twistable electronics with dynamically rotatable heterostructures. *Science*, vol. 361:690–693, 2018. (Cited on page 88.)

[221] D. L. Miller, K. D. Kubista, G. M. Rutter, M. Ruan, W. A. de Heer, M. Kindermann, P. N. First, and J. A. Stroscio. Real-space mapping of magnetically quantized graphene states. *Nature Physics*, vol. 6:811–817, 2010. (Cited on page 89.)

[222] S. Martin. *Systèmes nanoélectroniques hybrides : cartographies de la densité d'états locale*. PhD thesis, Université Grenoble Alpes, 2012. (Cited on pages 91 and 122.)

[223] S. H. Pan, E. W. Hudson, and J. C. Davis. ^{3}He refrigerator based very low temperature scanning tunneling microscope. *Review of Scientific Instruments*, vol. 70:1459, 1999. (Cited on page 91.)

[224] J.-M. Friedt and É. Carry. Introduction to the quartz tuning fork. *Am. J. Phys.*, vol. 75:415, 2007. (Cited on pages 102 and 242.)

[225] P. Günther, U. Ch. Fischer, and K. Dransfeld. Scanning near-field acoustic microscopy. *Appl. Phys. B*, vol. 48:89–92, 1989. (Cited on page 102.)

[226] K. Karrai and R. D. Grober. Piezoelectric tip-sample distance control for near field optical microscopes. *Appl. Phys. Lett.*, vol. 66:1842, 1995. (Cited on page 102.)

[227] J. Senzier, P. S. Luo, and H. Courtois. Combined scanning force microscopy and scanning tunneling spectroscopy of an electronic nanocircuit at very low temperature. *Appl. Phys. Lett.*, vol. 90:043114, 2007. (Cited on page 102.)

[228] F. J. Giessibl, S. Hembacher, M. Herz, Ch. Schiller, and J. Mannhart. Stability considerations and implementation of cantilevers allowing dynamic force microscopy with optimal resolution: the qPlus sensor. *Nanotechnology*, vol. 15:S79–S86, 2004. (Cited on page 104.)

[229] J. Rychen, T. Ihn, P. Studerus, A. Hermann, K. Ensslin, H. J. Hug, P. J. A. van Schendel, and H. J. Güntherodt. Operation characteristics of piezoelectric quartz tuning forks in high magnetic fields at liquid helium temperatures. *Rev. Sci. Instrum.*, vol. 71:1695, 2000. (Cited on page 105.)

[230] K. L. Ekinci and M. L. Roukes. Nanoelectromechanical systems. *Rev. Sci. Instrum.*, vol. 76:061101, 2005. (Cited on page 105.)

[231] H. Le Sueur. *Cryogenic AFM-STM for mesoscopic physics*. PhD thesis, Université Pierre et Marie Curie - Paris VI, 2007. (Cited on page 112.)

[232] C. Sabater, C. Untiedt, J. J. Palacios, and M. J. Caturla. Mechanical Annealing of Metallic Electrodes at the Atomic Scale. *Phys. Rev. Lett.*, vol. 108:205502, 2012. (Cited on page 112.)

[233] A. Castellanos-Gomez, G. Rubio-Bollinger, M. Garnica, S. Barja, A. L. Vázquez de Parga, R. Miranda, and N. Agraït. Highly reproducible low temperature scanning tunneling microscopy and spectroscopy with *in situ* prepared tips. *Ultramicroscopy*, vol. 122:1–5, 2012. (Cited on page 112.)

[234] S. Tewari, K. M. Bastiaans, M. P. Allan, and J. M. van Ruitenbeek. Robust procedure for creating and characterizing the atomic structure of scanning tunneling microscope tips. *Beilstein J. Nanotechnol.*, vol. 8:2389–2395, 2017. (Cited on page 112.)

[235] P. A. Anderson. Work Function of Gold. *Phys. Rev.*, vol. 115:553, 1959. (Cited on pages 113 and 242.)

[236] J. Chen. *Introduction to Scanning Tunneling Microscopy*. Oxford University Press, New York, 1993. (Cited on page 113.)

[237] J. A. Morán-Meza, J. Polesel-Maris, C. Lubin, F. Thoyer, A. Makky, A. Ouerghi, and J. Cousty. Reverse electrochemical etching method for fabricating ultra-sharp platinum/iridium tips for combined scanning tunneling microscope/atomic force microscope based on a quartz tuning fork. *Current Applied Physics*, vol. 15:1015–1021, 2015. (Cited on pages 113 and 242.)

[238] G. Giovannetti, P. A. Khomyakov, G. Brocks, V. M. Karpan, J. van den Brink, and P. J. Kelly. Doping Graphene with Metal Contacts. *Phys. Rev. Lett.*, vol. 101:026803, 2008. (Cited on page 113.)

[239] S. J. Altenburg and R. Berndt. Local work function and STM tip-induced distortion of graphene on Ir(111). *New J. Phys.*, vol. 16:053036, 2014. (Cited on page 113.)

[240] L. Wang, Y. Pu, A. K. Soh, Y. Shi, and S. Liu. Layers dependent dielectric properties of two dimensional hexagonal boron nitridenanosheets. *AIP Advances*, vol. 6:125126, 2016. (Cited on page 118.)

[241] A. Laturia, M. L. Van de Put, and W. G. Vandenberghe. Dielectric properties of hexagonal boron nitride and transition metal dichalcogenides: from monolayer to bulk. *npj 2D Materials and Applications*, vol. 2:6, 2018. (Cited on page 118.)

[242] T. O. Wehling, I. Grigorenko, A. I. Lichtenstein, and A. V. Balatsky. Phonon-Mediated Tunneling into Graphene. *Phys. Rev. Lett.*, vol. 101:216803, 2008. (Cited on page 119.)

[243] J. Hemberger, P. Lunkenheimer, R. Viana, R. Böhmer, and A. Loidl. Electric-field-dependent dielectric constant and nonlinear susceptibility in $SrTiO_3$. *Phys. Rev. B*, vol. 52:13159, 1995. (Cited on page 119.)

[244] R. Sachs, Z. Lin, and J. Shi. Ferroelectric-like $SrTiO_3$ surface dipoles probed by graphene. *Scientific Reports*, vol. 4:3657, 2014. (Cited on page 119.)

[245] S. Chen, X. Chen, E. A. Duijnstee, B. Sanyal, and T. Banerjee. Unveiling Temperature-Induced Structural Domains and Movement of Oxygen Vacancies in $SrTiO_3$ with Graphene. *ACS Appl. Mater. Interfaces*, vol. 12:52915–52921, 2020. (Cited on page 119.)

[246] J. F. Scott, E. K. H. Salje, and M. A. Carpenter. Domain Wall Damping and Elastic Softening in $SrTiO_3$: Evidence for Polar Twin Walls. *Phys. Rev. Lett.*, vol. 109:187601, 2012. (Cited on page 119.)

[247] E. K. H. Salje, O. Aktas, M. A. Carpenter, V. V. Laguta, and J. F. Scott. Domains within Domains and Walls within Walls: Evidence for Polar Domains in Cryogenic $SrTiO_3$. *Phys. Rev. Lett.*, vol. 111:247603, 2013. (Cited on page 119.)

[248] H. J. Harsan Ma, S. Scharinger, S. W. Zeng, D. Kohlberger, M. Lange, A. Stöhr, X. Renshaw Wang, T. Venkatesan, R. Kleiner, J. F. Scott, J. M. D. Coey, D. Koelle, and Ariando. Local Electrical Imaging of Tetragonal Domains and Field-Induced Ferroelectric Twin Walls in Conducting $SrTiO_3$. *Phys. Rev. Lett.*, vol. 116:257601, 2016. (Cited on page 119.)

[249] Y. Frenkel, N. Haham, Y. Shperber, C. Bell, Y. Xie, Z. Chen, Y. Hikita, H. Y. Hwang, E. K. H. Salje, and B. Kalisky. Imaging and tuning polarity at $SrTiO_3$ domain walls. *Nature Materials*, vol. 16:1203–1208, 2017. (Cited on page 119.)

[250] D. E. Grupp and A. M. Goldman. Giant Piezoelectric Effect in Strontium Titanate at Cryogenic Temperatures. *Science*, vol. 276:392–394, 1997. (Cited on page 120.)

[251] M. Honig, J. A. Sulpizio, J. Drori, A. Joshua, E. Zeldov, and S. Ilani. Local electrostatic imaging of striped domain order in $LaAlO_3/SrTiO_3$. *Nature Materials*, vol. 12:1112–1118, 2013. (Cited on page 120.)

[252] A. Matulis and F. M. Peeters. Quasibound states of quantum dots in single and bilayer graphene. *Phys. Rev. B*, vol. 77:115423, 2008. (Cited on page 121.)

[253] J. F. Rodriguez-Nieva and L. S. Levitov. Berry phase jumps and giant nonreciprocity in Dirac quantum dots. *Phys. Rev. B*, vol. 94:235406, 2016. (Cited on page 121.)

[254] C. Gutiérrez, L. Brown, C.-J. Kim, J. Park, and A. N. Pasupathy. Klein tunnelling and electron trapping in nanometre-scale graphene quantum dots. *Nature Physics*, vol. 12:1069–1075, 2016. (Cited on page 121.)

[255] F. D. Natterer, Y. Zhao, J. Wyrick, Y.-H. Chan, W.-Y. Ruan, M.-Y. Chou, K. Watanabe, T. Taniguchi, N. B. Zhitenev, and J. A. Stroscio. Strong Asymmetric Charge Carrier Dependence in Inelastic Electron Tunneling Spectroscopy of Graphene Phonons. *Phys. Rev. Lett.*, vol. 114:245502, 2015. (Cited on page 122.)

[256] Y. Zhang, Q. Yang, Y.-N. Ren, and L. He. Observation of phonon peaks and electron-phonon bound states in graphene. *Phys. Rev. B*, vol. 100:075435, 2019. (Cited on page 122.)

[257] A. Cheng, T. Taniguchi, K. Watanabe, P. Kim, and J.-D. Pillet. Guiding Dirac Fermions in Graphene with a Carbon Nanotube. *Phys. Rev. Lett.*, vol. 123:216804, 2019. (Cited on pages 122 and 244.)

[258] Y.-N. Ren, Q. Cheng, S.-Y. Li, C. Yan, Y.-W. Liu, K. Lv, M.-H. Zhang, Q.-F. Sun, and L. He. Spatial and magnetic confinement of massless Dirac fermions. *Phys. Rev. B*, vol. 104:L161408, 2021. (Cited on page 127.)

[259] C. E. Malec and D. Davidović. Transport in graphene tunnel junctions. *J. Appl. Phys.*, vol. 109:064507, 2011. (Cited on page 135.)

[260] M. Kim, S. G. Xu, A. I. Berdyugin, A. Principi, S. Slizovskiy, N. Xin, P. Kumaravadivel, W. Kuang, M. Hamer, R. Krishna Kumar, R. V. Gorbachev, K. Watanabe, T. Taniguchi, I. V. Grigorieva, V. I. Fal'ko, M. Polini, and A. K. Geim. Control of electron-electron interaction in graphene by proximity screening. *Nature Communications*, vol. 11:2339, 2020. (Cited on page 138.)

[261] B. Sachs, T. O. Wehling, M. I. Katsnelson, and A. I. Lichtenstein. Adhesion and electronic structure of graphene on hexagonal boron nitride substrates. *Phys. Rev. B*, vol. 84:195414, 2011. (Cited on page 145.)

[262] C. W. Groth, M. Wimmer, A. R. Akhmerov, and X. Waintal. Kwant: a software package for quantum transport. *New J. Phys.*, vol. 16:063065, 2014. (Cited on pages 157 and 244.)

[263] Kwant. `https://kwant-project.org/`. (Cited on pages 157 and 244.)

[264] Simulation performed by Adolfo. G. Grushin. Institut Néel, CNRS and Université Grenoble Alpes, Grenoble, France. (Cited on pages 158, 160, 161, 162, 163, 164, 165, 244, 245, and 246.)

[265] C. Déprez, L. Veyrat, H. Vignaud, G. Nayak, K. Watanabe, T. Taniguchi, F. Gay, H. Sellier, and B. Sacépé. A tunable Fabry-Pérot quantum Hall interferometer in graphene. *Nature Nanotechnology*, vol. 16:555–562, 2021. (Cited on page 166.)

[266] A. Coissard, D. Wander, H. Vignaud, A. G. Grushin, C. Repellin, K. Watanabe, T. Taniguchi, F. Gay, C. Winkelmann, H. Courtois, H. Sellier, and B. Sacépé. Imaging tunable quantum Hall broken-symmetry orders in graphene. *Nature*, in press, 2022. (Cited on pages 167 and 192.)

[267] C.-Y. Hou, C. Chamon, and C. Mudry. Electron Fractionalization in Two-Dimensional Graphenelike Structures. *Phys. Rev. Lett.*, vol. 98:186809, 2007. (Cited on page 176.)

[268] Y. Hatsugai, T. Fukui, and H. Aoki. Topological low-energy modes in $N = 0$ Landau levels of graphene: A possibility of a quantum-liquid ground state. *Physica E*, vol. 40:1530–1532, 2008. (Cited on page 176.)

[269] P. San-Jose, J. L. Lado, R. Aguado, F. Guinea, and J. Fernández-Rossier. Majorana Zero Modes in Graphene. *Phys. Rev. X*, vol. 5:041042, 2015. (Cited on page 176.)

[270] F. Liu, M. Yamamoto, and K. Wakabayashi. Topological Edge States of Honeycomb Lattices with Zero Berry Curvature. *J. Phys. Soc. Jpn*, vol. 86:123707, 2017. (Cited on page 176.)

[271] T. Kariyado and X. Hu. Topological States Characterized by Mirror Winding Numbers in Graphene with Bond Modulation. *Scientific Reports*, vol. 7:16515, 2017. (Cited on page 176.)

[272] C. Gutiérrez, C.-J. Kim, L. Brown, T. Schiros, D. Nordlund, E. B. Lochocki, K. M. Shen, J. Park, and A. N. Pasupathy. Imaging chiral symmetry breaking from Kekulé bond order in graphene. *Nature Physics*, vol. 12:950–958, 2016. (Cited on page 178.)

[273] C. Bao, H. Zhang, T. Zhang, X. Wu, L. Luo, S. Zhou, Q. Li, Y. Hou, W. Yao, L. Liu, P. Yu, J. Li, W. Duan, H. Yao, Y. Wang, and S. Zhou. Experimental Evidence of Chiral Symmetry Breaking in Kekulé-Ordered Graphene. *Phys. Rev. Lett.*, vol. 126:206804, 2021. (Cited on pages 178 and 189.)

[274] E. Andrade, G. G. Naumis, and R. Carrillo-Bastos. Electronic spectrum of Kekulé patterned graphene considering second neighbor-interactions. *J. Phys.: Condens. Matter*, vol. 33:225301, 2021. (Cited on page 189.)

[275] A. Assouline, M. Jo, P. Brasseur, K. Watanabe, T. Taniguchi, Th. Jolicoeur, D. C. Glattli, N. Kumada, P. Roche, F. D. Parmentier, and P. Roulleau. Excitonic nature of magnons in a quantum Hall ferromagnet. *Nature Physics*, vol. 17:1369–1374, 2021. (Cited on page 190.)

[276] A. Das, R. K. Kaul, and G. Murthy. Coexistence of Canted Antiferromagnetism and Bond-order in $\nu = 0$ Graphene. *arXiv*:2109.07515, 2021. (Cited on page 190.)

[277] J. Motruk, A. G. Grushin, F. de Juan, and F. Pollmann. Interaction-driven phases in the half-filled honeycomb lattice: An infinite density matrix renormalization group study. *Phys. Rev. B*, vol. 92:085147, 2015. (Cited on page 192.)

[278] M. Spera, A. Scarfato, Á. Pásztor, E. Giannini, D. R. Bowler, and Ch. Renner. Insight into the Charge Density Wave Gap from Contrast Inversion in Topographic STM Images. *Phys. Rev. Lett.*, vol. 125:267603, 2020. (Cited on page 193.)

[279] G. Binnig, H. Rohrer, Ch. Gerber, and E. Weibel. Surface studies by Scanning Tunneling Microscopy. *Phys. Rev. Lett.*, vol. 49:57, 1982. (Cited on page 207.)

[280] G. Binnig, H. Rohrer, Ch. Gerber, and E. Weibel. Tunneling through a controllable vacuum gap. *Appl. Phys. Lett.*, vol. 40:178, 1982. (Cited on page 207.)

[281] J. Tersoff and D. R. Hamann. Theory and Application for the Scanning Tunneling Microscope. *Phys. Rev. Lett.*, vol. 50:1998, 1983. (Cited on page 207.)

[282] J. Tersoff and D. R. Hamann. Theory of the scanning tunneling microscope. *Phys. Rev. B*, vol. 31:805, 1985. (Cited on page 207.)

[283] J. Bardeen. Tunnelling from a Many-Particle Point of View. *Phys. Rev. Lett.*, vol. 6:57, 1961. (Cited on page 207.)

[284] H. B. Michaelson. The work function of the elements and its periodicity. *J. Appl. Phys.*, vol. 48:4729, 1977. (Cited on page 208.)

[285] G. Binnig, C. F. Quate, and Ch. Gerber. Atomic Force Microscope. *Phys. Rev. Lett.*, vol. 56:930, 1986. (Cited on page 213.)

[286] F. J Giessibl. Advances in atomic force microscopy. *Rev. Mod. Phys.*, vol. 75:949, 2003. (Cited on page 213.)

[287] T. R. Albrecht, P. Grütter, D. Horne, and D. Rugar. Frequency modulation detection using high-Q cantilevers for enhanced force microscope sensitivity. *Journal of Applied Physics*, vol. 69:668, 1991. (Cited on page 216.)

[288] P. Girard. Electrostatic force microscopy: principles and some applications to semiconductors. *Nanotechnology*, vol. 12:485–490, 2001. (Cited on page 217.)

[289] S. Belaidi, P. Girard, and G. Leveque. Electrostatic forces acting on the tip in atomic force microscopy: Modelization and comparison with analytic expressions. *J. Appl. Phys.*, vol. 81:1023–1030, 1997. (Cited on page 217.)

[290] K. Zimmermann. *Quantum point contact in high mobility graphene*. PhD thesis, Université Grenoble Alpes, 2016. (Cited on page 219.)

[291] A. K. Geim and I. V. Grigorieva. Van der Waals heterostructures. *Nature*, vol. 499:419–425, 2013. (Cited on page 222.)

[292] M. Kawasaki, K. Takahashi, T. Maeda, R. Tsuchiya, M. Shinohara, O. Ishiyama, T. Yonezawa, M. Yoshimoto, and H. Koinuma. Atomic Control of the $SrTiO_3$ Crystal Surface. *Science*, vol. 266:1540–1542, 1994. (Cited on page 225.)

[293] X.-X. Li, Z.-Q. Fan, P.-Z. Liu, M.-L. Chen, X. Liu, C.-K. Jia, D.-M. Sun, X.-W. Jiang, Z. Han, V. Bouchiat, J.-J. Guo, J.-H. Chen, and Z.-D. Zhang. Gate-controlled reversible rectifying behaviour in tunnel contacted atomically-thin MoS_2 transistor. *Nature Communications*, vol. 8:970, 2017. (Cited on page 225.)

[294] Y. Choi, J. Kemmer, Y. Peng, A. Thomson, H. Arora, R. Polski, Y. Zhang, H. Ren, J. Alicea, G. Refael, F. von Oppen, K. Watanabe, T. Taniguchi, and S. Nadj-Perge. Electronic correlations in twisted bilayer graphene near the magic angle. *Nature Physics*, vol. 15:1174–1180, 2019. (Cited on page 227.)

[295] K. Xu, P. Cao, and J. R. Heath. Scanning Tunneling Microscopy Characterization of the Electrical Properties of Wrinkles in Exfoliated Graphene Monolayers. *Nano Lett.*, vol. 9:4446–4451, 2009. (Cited on page 240.)

[296] J. C. Meyer, A. K. Geim, M. I. Katsnelson, K. S. Novoselov, T. J. Booth, and S. Roth. The structure of suspended graphene. *Nature*, vol. 446:60–63, 2007. (Cited on page 240.)

[297] A. Fasolino, J. H. Los, and M. I. Katsnelson. Intrinsic ripples in graphene. *Nature Materials*, vol. 6:858–861, 2007. (Cited on page 240.)

[298] A. Hadjadj, B. Equer, A. Beorchia, and P. Roca Cabarrocas. Contact potential measurements with a local Kelvin probe. *Philosophical Magazine B*, vol. 82:1257–1266, 2002. (Cited on page 241.)

[299] J. Laurent, H. Sellier, A. Mosset, S. Huant, and J. Chevrier. Casimir force measurements in Au-Au and Au-Si cavities at low temperature. *Phys. Rev. B*, vol. 85:035426, 2012. (Cited on pages 241 and 242.)

[300] R. Yan, Q. Zhang, W. Li, I. Calizo, T. Shen, C. A. Richter, A. R. Hight-Walker, X. Liang, A. Seabaugh, D. Jena, H. Grace Xing, D. J. Gundlach, and N. V. Nguyen. Determination of graphene work function and graphene-insulator-semiconductor band alignment by internal photoemission spectroscopy. *Appl. Phys. Lett.*, vol. 101:022105, 2012. (Cited on page 242.)

– *Suus 'non ut simplex ...*
– *Suus 'non falsum* !

Graphene exhibits a two dimensional electron gas directly exposed to vacuum, thus accessible by scanning tunneling microscopy (STM) and spectroscopy. In this PhD thesis we present a systematic STM spectroscopy study performed on high-quality graphene samples, where the charge carrier density is tuned with a back-gate, and in which we have investigated the physics of the graphene quantum Hall regime under strong magnetic fields using a home-made AFM/STM operating at 4 K and up to 14 T. By carrying out high-resolution Landau level spectroscopy we unveil the pinning of the Fermi level in the Landau levels, a key phenomenon in the quantum Hall physics. We performed the first Landau level spectroscopy at the native edges of a graphene flake residing atop an insulating substrate and we show that the quantum Hall edge channels are squeezed on few magnetic lengths from the edge. When the Fermi level fills the zeroth Landau level, we observed the opening in the bulk of the interaction-induced gap at charge neutrality, resulting from the magnetic-like Stoner instability. This gap is found to be in excellent agreement with the Coulomb energy scale. We further show that the Coulomb interaction can be screened using a suitable high-k dielectric substrate. Last, scanning graphene at the atomic scale enabled us to image the different ground states of charge-neutral graphene, which emerge as a function of the strength of the Coulomb interaction. Our results eventually point towards a quantum phase transition driven by the substrate-screening of the Coulomb interaction.

Le graphène présente un gaz d'électrons bidimensionnel directement exposé au vide, donc accessible par microscopie et spectroscopie à effet tunnel (STM). Dans cette thèse de doctorat, nous présentons une étude systématique de spectroscopie STM réalisée sur des échantillons de graphène de haute qualité, où la densité de porteurs de charge est contrôlée avec une grille, et dans lesquels nous avons étudié la physique du régime de Hall quantique du graphène sous de forts champs magnétiques, en utilisant un AFM/STM de notre conception fonctionnant à 4 K et jusqu'à 14 T. En effectuant des spectroscopies haute résolution des niveaux de Landau, nous avons observé le piégeage du niveau de Fermi dans les niveaux de Landau, un phénomène clé dans la physique de l'effet Hall quantique. Nous avons réalisé la première spectroscopie des niveaux de Landau aux bords natifs d'un échantillon de graphène reposant sur un substrat isolant et nous montrons que les canaux de bord de l'effet Hall quantique sont comprimés au bord sur quelques longueurs magnétiques. Lorsque le niveau de Fermi remplit le niveau de Landau zéro, nous avons observé l'ouverture du gap d'interaction à la neutralité de charge, résultant de l'instabilité de Stoner de type magnétique. Ce gap est en excellent accord avec l'échelle d'énergie de Coulomb. Nous montrons en outre que l'interaction de Coulomb peut être écrantée à l'aide d'un substrat diélectrique approprié. Enfin, l'imagerie du graphène à l'échelle atomique nous a permis de visualiser les différents états fondamentaux du graphène à la neutralité de charge, qui apparaissent en fonction de l'intensité de l'interaction de Coulomb. Nos résultats mettent finalement en évidence une transition de phase quantique pilotée par l'écrantage de l'interaction de Coulomb par le substrat.